

**Direct Strength Design of
Cold-Formed Steel Members
with Perforations**

by

Cristopher Dennis Moen

A dissertation submitted to Johns Hopkins University in conformity with the
requirements for the degree of Doctor of Philosophy

Baltimore, Maryland

August 2008

UMI Number: 3340033

INFORMATION TO USERS

The quality of this reproduction is dependent upon the quality of the copy submitted. Broken or indistinct print, colored or poor quality illustrations and photographs, print bleed-through, substandard margins, and improper alignment can adversely affect reproduction.

In the unlikely event that the author did not send a complete manuscript and there are missing pages, these will be noted. Also, if unauthorized copyright material had to be removed, a note will indicate the deletion.

UMI[®]

UMI Microform 3340033

Copyright 2009 by ProQuest LLC.

All rights reserved. This microform edition is protected against unauthorized copying under Title 17, United States Code.

ProQuest LLC
789 E. Eisenhower Parkway
PO Box 1346
Ann Arbor, MI 48106-1346

Abstract

Cold-formed steel (CFS) structural members are commonly manufactured with holes to accommodate plumbing, electrical, and heating conduits in the walls and ceilings of buildings. Current design methods available to engineers for predicting the strength of CFS members with holes are prescriptive and limited to specific perforation locations, spacings, and sizes. The Direct Strength Method (DSM), a relatively new design method for CFS members validated for members *without* holes, predicts the ultimate strength of a general CFS column or beam with the elastic buckling properties of the member cross-section (e.g., plate buckling) and the Euler buckling load (e.g., flexural buckling). This research project, sponsored by the American Iron and Steel Institute, extends the appealing generality of DSM to cold-formed steel beams and columns *with* perforations.

The elastic buckling properties of rectangular plates and cold-formed steel beams and columns, including the presence of holes, are studied with thin shell finite element eigenbuckling analysis. Buckled mode shapes unique to members with holes are categorized. Parameter studies demonstrate that critical elastic buckling loads either decrease or increase with the presence of holes, depending on the member geometry and hole size, spacing, and location. Simplified alternatives to FE elastic buckling analysis for members with holes are developed with classical plate stability equations and freely available finite strip analysis software.

Experiments on cold-formed steel columns with holes are conducted to observe the interaction between elastic buckling, load–deformation response, and ultimate strength. The experimental results are used to validate an ABAQUS nonlinear finite element protocol, which is implemented to simulate loading to collapse of several hundred cold-formed steel beams and columns with holes. The results from these simulations, supplemented with existing beam and column data, guide the development of design equations relating elastic buckling and ultimate strength for cold-formed steel members with holes. These equations and the simplified elastic buckling prediction methods are presented as a proposed design procedure for an upcoming revision to the American Iron and Steel Institute’s North American Specification for the Design of Cold-Formed Steel Structural Members.

Advisor: Dr. Benjamin William Schafer
Readers: Dr. Takeru Igusa
Dr. Jamie Guest

*In memory of Sandy Austin,
for her quiet encouragement over many years*

Acknowledgements

Many wonderful people have supported me on this journey. My wife Stela made the adventure possible with her willingness to support us while I returned to the life of a student for four long years. She often had more confidence I would finish than I did, and showered me with love and optimism all the way to the end. My parents Dennis and Nancy, my sister Rachel, my parents-in-law Greg and Linda Patron, and brother and sister-in-law Jeff and Glenda LaRue are consistently my biggest fans. Life would not be life without their love and encouragement.

My advisor Dr. Ben Schafer deserves much of the credit for coaching me up those long research hills and making sure that I didn't get lost along the way (except once during a 10 mile run out to Lake Roland). I knew two years before I came to Hopkins that Ben would be the advisor for me (thanks to Dr. Lori Graham-Brady!), and I hitched my cart to a rising star. It was risky for him to take a chance on a regular old bridge engineer, but he accepted the challenge and unselfishly invested the required time and energy to get me where I needed to be. I am happy that it worked out so well and yes, he won, I love cold-formed steel.

The bulk of my teaching experience at Hopkins came as a TA for a very talented educator, Dr. Sanjay Arwade. Sanjay mentored me, trusted me to teach his students, and always fully considered my input on course content. Although I never had a class with Dr. Tak Igusa, I learned so much from him. He pushed me and gently built my confidence in our GBO practice sessions, and his "small" contributions to my research

resulted in some of the work that I am most proud of. I am also indebted to Dr. Jamie Guest, who unknowingly encouraged me when I was questioning my choice to enter academia. He showed me that it is possible to have a fun and keep a positive attitude even with the pressures of a young professor (one example, bringing soft pretzels from Philadelphia to optimization class). He was also very patient with my hunger for computing power, a.k.a. the Beast.

You cannot survive the pressures of a Ph.D. without a little fun. Thank goodness for my fellow graduate students at Hopkins – especially Mazdak, Arghavan, Katherine, Rachel, Muthu, Yared, Mina, Vahid, Luiz, Zhanjie, and Ornella. My allegiance to Hopkins will always be tied to the great people I met here and the memories we shared. It was truly a pleasure to study in an atmosphere where everyone was so caring, thoughtful, and willing to maintain a comfortable atmosphere for all. I am proud to graduate from such a forward-thinking civil engineering department and will seize any opportunity, as a dedicated alumnus should, to publicize Johns Hopkins University.

CFS4EVER

Table of Contents

Chapter 1	Introduction	1
Chapter 2	Thin-shell finite element modeling in ABAQUS.....	8
2.1	Comparison of ABAQUS thin-shell elements	9
2.2	Modeling holes in ABAQUS.....	16
2.3	Modeling Rounded Corners in ABAQUS	18
2.4	Summary of modeling guidelines.....	21
Chapter 3	Elastic buckling of cold-formed steel cross-sectional elements with holes	22
3.1	Plate and hole dimensions	23
3.2	Finite element modeling assumptions.....	25
3.3	Stiffened element in uniaxial compression	25
3.4	Stiffened element in bending	43
3.5	Unstiffened element in uniaxial compression	58
Chapter 4	Elastic buckling of cold-formed steel members with holes	66
4.1	Finite element modeling assumptions.....	67
4.2	Elastic buckling of columns with holes	67
4.3	Elastic buckling of beams with holes.....	126
Chapter 5	Experiments on cold-formed steel columns with holes	159
5.1	Acknowledgements	160
5.2	Testing Program	160
5.3	Elastic buckling calculations.....	196
5.4	Experiment results	205
Chapter 6	Predicting residual stresses and plastic strains in cold-formed steel members	223
6.1	Stress-strain coordinate system and notation.....	226
6.2	Prediction method assumptions.....	227
6.3	Derivation of the residual stress prediction method	230
6.4	Derivation of effective plastic strain prediction method.....	240
6.5	Employing the prediction method in practice: quantifying the coil radius influence.....	244
6.6	Comparison of prediction method to measured residual stresses.....	248
6.7	Discussion	254
6.8	Acknowledgements	257
Chapter 7	Nonlinear finite element modeling of cold-formed steel structural members.....	258
7.1	Preliminary nonlinear FE studies.....	259
7.2	Nonlinear finite element modeling of columns with holes	288
Chapter 8	The Direct Strength Method for cold-formed steel members with holes	313
8.1	DSM for columns with holes	314
8.2	DSM for laterally braced beams with holes	373
Chapter 9	Conclusions and proposed future work	408
9.1	Conclusions.....	408
9.2	Future work	410
References.....		414
Appendix A	ABAQUS input file generator in Matlab.....	418
Appendix B	ABAQUS element-based elastic buckling results	424
Appendix C	Derivation of elastic buckling coefficients for unstiffened elements	433
Appendix D	Elastic buckling prediction method of cross-sectional elements with holes	439
Appendix E	Derivation of global critical elastic buckling load for a column with holes.....	443
Appendix F	Column experiment results	447
Appendix G	Residual stresses– backstress for kinematic hardening implementation	472
Appendix H	Experiment true stress-strain curves	474
Appendix I	Column experiment nonlinear FE simulation results	495
Appendix J	Contact simulation in ABAQUS	519
Appendix K	Simulated column experiments database.....	522
Appendix L	Simulated beam experiment database	526
Curriculum Vitae.....		529

List of Figures

Figure 1.1	Perforations are provided in structural studs to accommodate utilities in the walls of buildings	2
Figure 1.2	Hole patterns in storage rack columns	2
Figure 1.3	Column elastic buckling curve generated with CUF5M	4
Figure 1.4	DSM global buckling failure design curve and equations	4
Figure 1.5	DSM local buckling failure design curve and equations.....	5
Figure 1.6	DSM distortional buckling failure design curve and equations.....	5
Figure 2.1	ABAQUS S4\S4R shell element with four nodes and a linear shape function, ABAQUS S9R5 shell element with nine nodes and a quadratic shape function.....	10
Figure 2.2	Buckled shape of a stiffened plate	10
Figure 2.3	Accuracy of ABAQUS S9R5, S4, and S4R elements for a stiffened element with varying aspect ratios, 8:1 finite element aspect ratio for the S9R5 element, 4:1 element aspect ratio for the S4 and S4R elements	13
Figure 2.4	Accuracy of S4, S4R, and S9R5 elements as a function of the number of elements provided per buckled half-wavelength, stiffened element, square waves ($k=4$)	14
Figure 2.5	Buckled shape of an unstiffened element, $m=1$ shown.....	15
Figure 2.6	Accuracy of S9R5 elements as the number of finite elements provided along an unstiffened element varies, $L/h=4$	15
Figure 2.7.	Finite element mesh and plate dimensions: slotted, rectangular, and circular holes..	17
Figure 2.8	Hole discretization using S9R5 elements.....	18
Figure 2.9	The critical elastic buckling stress converges to a constant magnitude when the S9R5 element aspect ratio a/b is between 0.5 and 2 and element corner angles are skewed	18
Figure 2.10	ABAQUS S9R5 initial curvature limit requires at least five elements to model corner	19
Figure 2.11	SSMA 600S162-68 C-section corner modeled with a) one S9R5 element, b) three S9R5 elements	20
Figure 2.12	The number of S9R5 corner elements has a minimal influence on the critical elastic buckling loads of an SSMA 600162-68 C-section column with $L=48$ in.....	21
Figure 3.1	Stiffened and unstiffened elements in a lipped C-section.....	23
Figure 3.2	Element and hole dimension definitions.....	24
Figure 3.3	Definition of unstiffened strip "A" and "B" for a plate with holes.....	24
Figure 3.4	Definition of neutral axis location for stiffened elements in bending.	24
Figure 3.5	ABAQUS boundary conditions and loading conditions for a stiffened element in uniaxial compression.....	26
Figure 3.6	Influence of a slotted hole on the elastic buckling stress of a simply supported rectangular plate with varying length	27
Figure 3.7	Comparison of buckled shape and displacement contours for a rectangular plate with $h_{hole}/h=0.66$ and $L/L_{hole}=3$, (a) with slotted hole and (b) without hole. Notice the change in length and quantity of buckled cells with the addition of a slotted hole.	28
Figure 3.8	Buckled shape of a simply supported plate (a) with a slotted hole and (b) without a hole. $L=15L_{hole}$, $h_{hole}/h=0.66$. The slotted hole dampens buckling but does not significantly change the natural half-wavelength of the plate.	28
Figure 3.9	(a) Slotted hole causes local buckling ($h_{hole}/h=0.26$), compared to (b) buckled cells at the natural half-wavelength of the plate	29
Figure 3.10	Definition of center-to-center dimension for the slotted holes	30
Figure 3.11	Influence of slotted hole spacing on the elastic buckling load of a long simply supported rectangular plate.....	30

Figure 3.12	Comparison of buckled shapes for a long stiffened element ($L=24 L_{hole}$) with a slotted hole spacing of $S/L_{hole}=4$ and $h_{hole}/h=0.66, 0.44,$ and 0.26 .	31
Figure 3.13	Variation in f_{cr} with increasing h_{hole}/h for a stiffened element correspond to buckling mode shapes (see Figure 3.12 for examples of plate buckling and unstiffened strip buckling mode shapes)	33
Figure 3.14	Unstiffened strip elastic buckling stress conversion from the net to the gross section	35
Figure 3.15	Accuracy of stiffened element prediction method as a function of hole spacing S to plate width h (a) without and (b) with the dimensional limits in Eq. (3.8) and Eq.(3.9)	38
Figure 3.16	Accuracy of stiffened element prediction method as a function of hole spacing S to length of hole L_{hole} (a) without and (b) with the dimensional limits in Eq. (3.8) and Eq.(3.9)	38
Figure 3.17	Accuracy of the stiffened element prediction method as a function of hole width h_{hole} to plate width h (a) without and (b) with the dimensional limits in Eq. (3.8) and Eq.(3.9)	38
Figure 3.18	For plates where the unstiffened strip is narrow compared to the plate width, plate buckling occurs between the holes.	39
Figure 3.19	Plate buckling and unstiffened strip buckling may both exist for a plate with holes. These modes are predicted conservatively as unstiffened strip buckling.	40
Figure 3.20	Accuracy of prediction method for stiffened elements with square or circular holes as a function of hole width h_{hole} to plate width h .	40
Figure 3.21	Accuracy of the stiffened element elastic buckling prediction method as a function of unstiffened strip width h_{strip} versus plate width h for offset holes (a) without and (b) with the dimensional limits in Eq. (3.8) and Eq.(3.9)	41
Figure 3.22	Holes at the edge of a wide stiffened plate reduce the axial stiffness (and critical elastic buckling stress) but do not change the buckled shape.	42
Figure 3.23	Accuracy of the stiffened element elastic buckling prediction method as a function of hole offset δ_{hole} versus plate width h for offset holes (a) without and (b) with the dimensional limits in Eq. (3.8), Eq.(3.9), and Eq. (3.11)	43
Figure 3.24	Boundary and loading conditions for a stiffened element in bending	43
Figure 3.25	Stiffened plates loaded with a linear bending stress gradient exhibit buckling of the unstiffened strip adjacent to the hole in the compression region of the plate.	45
Figure 3.26	Influence of slotted holes on critical elastic buckling stress f_{cr} of stiffened elements in bending as a function of (a) hole size relative to plate width and (b) hole spacing as a function of hole length.	46
Figure 3.27	Hole location influence on critical elastic buckling stress f_{cr} for a stiffened plate in bending ($Y=0.50h$) (Buckled mode shapes corresponding to A, B, C, and D are provided in Figure 3.28.)	47
Figure 3.28	The buckled mode shape changes as slotted holes move from the compression region to the tension region of a stiffened element in bending ($h_{hole}/h=0.20$).	48
Figure 3.29	Hole location influence on critical elastic buckling stress f_{cr} for a stiffened plate in bending ($Y=0.75h$)	49
Figure 3.30	Derivation of stress ratio ψ_A for unstiffened strip "A"	51
Figure 3.31	Derivation ψ_B and conversion of the compressive stress at the edge of unstiffened strip "B" to the stress f_{crB} at the edge of the plate	52
Figure 3.32	Derivation of f_{crh} for the case when $h_A+h_{hole} \geq Y$ (when the hole is located partially in the compressed region and partially in the tension region of the plate)	53
Figure 3.33	Derivation of f_{crh} for the case when $h_A+h_{hole} < Y$ (hole lies completely in the compressed region of the plate)	54

Figure 3.34	Influence of L_{hole}/y_A on the accuracy of the prediction method for stiffened elements in bending (a) without and (b) with the dimensional limits defined in Eq. (3.9), Eq. (3.24), Eq. (3.25), and Eq. (3.26).	56
Figure 3.35	Influence of h_A/Y on the accuracy of the prediction method for stiffened elements in bending (a) without and (b) with the dimensional limits defined in Eq. (3.9), Eq. (3.24), Eq. (3.25), and Eq. (3.26).	56
Figure 3.36	Influence of S/h on the accuracy of the prediction method for stiffened elements in bending (a) without and (b) with the dimensional limits defined in Eq. (3.9), Eq. (3.24), Eq. (3.25), and Eq. (3.26).	57
Figure 3.37	Influence of S/L_{hole} on the accuracy of the prediction method for stiffened elements in bending (a) without and (b) with the dimensional limits defined in Eq. (3.9), Eq. (3.24), Eq. (3.25), and Eq. (3.26).	57
Figure 3.38	Influence of h/h_{hole} on the accuracy of the prediction method for stiffened elements in bending (a) without and (b) with the dimensional limits defined in Eq. (3.9), Eq. (3.24), Eq. (3.25), and Eq. (3.26).	58
Figure 3.39	ABAQUS boundary and loading conditions for unstiffened plate loaded uniaxially.	58
Figure 3.40	The presence of holes causes a decrease in critical elastic buckling load for unstiffened plates in uniaxial compression.	60
Figure 3.41	Buckled shapes of unstiffened plates with holes.	60
Figure 3.42	The critical elastic buckling stress of a stiffened plate decreases as holes are shifted toward the simply supported edge ($+\delta_{hole}$).	62
Figure 3.43	The critical elastic buckling stress for stiffened elements with (a) transversely offset holes and (b) centered holes (from Section 3.5.2) decreases as a function of hole length L_{hole} to h_A .	62
Figure 3.44	(a) Comparison of ABAQUS and empirical plate buckling coefficients for an unstiffened element with holes and (b) ABAQUS to predicted elastic buckling stress for an unstiffened element.	64
Figure 4.1	C-section and hole dimension notation	68
Figure 4.2	Columns are modeled with pinned warping-free boundary conditions and compressed from both ends	69
Figure 4.3(a)	SSMA 250S162-33 web plate and structural stud, and (b) SSMA 400S162-33 web plate and structural stud	71
Figure 4.4	Effect of a slotted hole on the elastic buckling load of simply supported plates and structural studs	72
Figure 4.5	The presence of a hole creates unique local buckling modes where unstiffened strip buckling adjacent to the hole occurs symmetrically (LH) or asymmetrically (LH2) increase the distortional tendency of the flanges	74
Figure 4.6	SSMA slotted hole location and local buckling LH mode, $L=48$ in., $x/L=0.06,0.125,0.25,0.375,0.50$. Note the distortional tendencies of the flanges at the hole.	74
Figure 4.7	Influence of a slotted hole on the (a) distortional (D) and (b) global flexural-torsional (GFT) modes of a cold-formed steel column.	75
Figure 4.8	Influence of SSMA slotted hole location on P_{cr} for a 362S162-33 C-section (refer to Figure 4.5, Figure 4.6, and Figure 4.7 for buckled shape summaries)	76
Figure 4.9	Connection detail for structural stud to exterior wall requires a screw or bolt hole placed in the stud flange (Western States Clay Products Association 2004)	77
Figure 4.10	Influence of flange hole diameter on the local (L), distortional (D), and global (GFT) elastic buckling loads of an SSMA 362S162-33 structural stud	78
Figure 4.11	Local (L) buckling is dominated by flange and web deformation near the holes as b_{hole}/b exceeds 0.70	78
Figure 4.12	Experimental program boundary conditions as implemented in ABAQUS	80

Figure 4.13	Influence of fixed-fixed boundary conditions versus warping free boundary conditions on P_{crd} for column experiments ($L/H < 4$) as a function of (a) column length to fundamental distortional half-wavelength calculated with CUFSM and (b) column length to member length.....	87
Figure 4.14	Influence of fixed-fixed boundary conditions versus warping free boundary conditions on P_{crd} for column experiments ($L/H < 4$) as a function of (a) hole width relative to column width and (b) hole length relative to column length	87
Figure 4.15	Influence of weak-axis pinned boundary conditions versus warping free boundary conditions on (a) P_{crd} as a function of hole length to column length and (b) P_{crd} as a function of column length to member length.	88
Figure 4.16	Rules for modeling a column net cross-section in CUFSM.....	91
Figure 4.17	Local elastic buckling curve of net cross-section when (a) hole length is less than L_{crh} and (b) when hole length is greater than L_{crh}	92
Figure 4.18	Comparison of CUFSM and ABAQUS predictions of unstiffened strip buckling.....	93
Figure 4.19	ABAQUS results verify CUFSM local buckling predictions for an SSMA 362S162-33 column with evenly spaced web holes.	94
Figure 4.20	CUFSM and ABAQUS local buckling mode shapes are consistent when considering a slotted flange hole.....	95
Figure 4.21	ABAQUS results verify CUFSM predictions for an SSMA 362S162-33 cross section with evenly spaced flange holes.	95
Figure 4.22	ABAQUS predicts local plate buckling with distortional buckling interaction which is not detected in CUFSM.	96
Figure 4.23	ABAQUS results are slightly lower than CUFSM predictions, CUFSM predicts correctly that plate local buckling controls over unstiffened strip buckling.	97
Figure 4.24	Predicted P_{crh} (CUFSM, buckling of the net cross-section) and P_{cr} (CUFSM, buckling of the gross cross section, no hole) are compared relative to the ABAQUS P_{crd} with experiment boundary conditions as a function of (a) hole width to flat web width and (b) hole length to column length.....	98
Figure 4.25	Predicted P_{crd} (CUFSM approximate method) is compared relative to the ABAQUS P_{crd} with experiment boundary conditions as a function of (a) hole width to flat web width and (b) hole length to column length	99
Figure 4.26	CUFSM approximate method for calculating P_{crd} for a column with holes.	101
Figure 4.27	Modified cross section to be used in CUFSM to predict P_{crd} for a column with holes.	102
Figure 4.28	ABAQUS boundary conditions and imposed rotations for web plate	103
Figure 4.29	Plate deformation from imposed edge rotations, $h_{hole}/h=0.50$	104
Figure 4.30	Transverse rotational stiffness of the plate is significantly reduced in the vicinity of the slotted hole	104
Figure 4.31	Comparison of CUFSM and ABAQUS distortional buckling mode shapes.....	107
Figure 4.32	CUFSM distortional buckling prediction method is conservative when considering an SSMA 262S162-68 column with uniformly spaced holes.	107
Figure 4.33	Warping-fixed boundary condition amplification of P_{crd}	109
Figure 4.34	Accuracy of the CUFSM approximate method for predicting P_{crd} improves as column length increases relative to the fundamental distortional half-wavelength for warping-fixed columns.....	110
Figure 4.35	A "weighted thickness" cross section can be input directly into a program that solves the classical cubic stability equation for columns (e.g. CUTWP).	113
Figure 4.36	Weak-axis flexural and flexural-torsional global buckling modes for an SSMA 1200S162-68 column with evenly spaced circular holes.	114
Figure 4.37	Variation in net section properties as circular hole diameter increases.	115
Figure 4.38	Comparison of "weighted thickness" and "weighted properties" cross-sectional area.	116

Figure 4.39 Comparison of “weighted thickness” and “weighted properties” strong axis moment of inertia. 117

Figure 4.40 Comparison of “weighted thickness” and “weighted properties” weak axis moment of inertia. 117

Figure 4.41 ABAQUS boundary conditions for warping free and applied unit twist at $x=0$ in. and warping free but rotation restrained at $x=100$ in. 119

Figure 4.42 Angle of twist decreases linearly in the SSMA 1200S162-68 column with warping free end conditions. 119

Figure 4.43 The “weighted properties” approximation for J_{avg} matches closely with the ABAQUS prediction for the SSMA 12S00162-68 column with holes. 120

Figure 4.44 ABAQUS boundary conditions for warping free and applied unit twist at $x=0$ in. and warping fixed and rotation restrained at $x=100$ in. 121

Figure 4.45 Angle of twist is nonlinear along the SSMA 1200S162-68 column with warping fixed end conditions at $x=100$ in. 122

Figure 4.46 Comparison of “weighted thickness” and “weighted properties” approximations to the ABAQUS derived warping torsion constant $C_{w,avg}$ 123

Figure 4.47 Comparison of “weighted thickness” and “weighted properties” prediction methods for the SSMA 1200S162-68 weak-axis flexural buckling mode. Predictions using net section properties are also plotted as a conservative benchmark. 124

Figure 4.48 Comparison of “weighted thickness” and “weighted properties” prediction methods for the SSMA 1200S162-68 flexural-torsional column buckling mode. Predictions using net section properties are also plotted as a conservative benchmark. 125

Figure 4.49 Cross section of beam specimen showing aluminum strap angles connected to C-flanges 127

Figure 4.50 C-section and hole dimension notation 127

Figure 4.51 Experiment test setup with hole spacing, location of lateral bracing, spacing of aluminum angle straps, and load points 129

Figure 4.52 Finite element model boundary conditions for beam eigenbuckling analyses 130

Figure 4.53 Channel and hole meshing details and modeling of aluminum angle straps 131

Figure 4.54 ABAQUS meshing details for C-section rounded corners 132

Figure 4.55 Modeling of the beam concentrated loads in ABAQUS 133

Figure 4.56 Local buckling modes for specimen 2B,20,1&2(H) with and without holes 135

Figure 4.57 Local buckling modes for specimen 3B,14,1&2(H) with and without holes 135

Figure 4.58 Local buckling modes for specimen 6B,18,1&2(H) with and without holes 136

Figure 4.59 Local buckling modes for specimen BP-40(H) with and without holes 136

Figure 4.60 Local buckling modes for specimen 12B,16,1&2(H) with and without holes 137

Figure 4.61 Distortional buckling modes for specimen 2B,20,1&2(H) with and without holes .. 138

Figure 4.62 Distortional buckling modes for specimen 3B,14,1&2(H) with and without holes .. 139

Figure 4.63 Distortional buckling modes for specimen 6B,18,1&2(H) with and without holes .. 139

Figure 4.64 Distortional buckling modes for specimen BP5-40(H) with and without holes 140

Figure 4.65 Distortional buckling modes for specimen 12B,16,1&2(H) with and without holes 140

Figure 4.66 Elastic buckling curve for 12” deep specimen with modal participation summarized, note that selected L and D are mixed local-distortional modes 141

Figure 4.67 Possible global buckling mode occurs about the compression flange lateral brace point 142

Figure 4.68 Influence of holes on beam specimen $M_{cr,l}$ (Channel 1 and Channel 2 plotted) considering (a) all local buckling modes and (b) the lowest local buckling mode 147

Figure 4.69 Influence of holes on beam specimen $M_{cr,d}$ (Channel 1 and Channel 2 plotted) as a function of hole depth to flat web depth considering (a) all distortional buckling modes and (b) the lowest distortional buckling mode 148

Figure 4.70	Influence of holes on beam specimen M_{crd} (Channel 1 and Channel 2 plotted) as a function of web depth to flange width considering (a) all distortional buckling modes and (b) the lowest distortional buckling mode.....	148
Figure 4.71	Influence of test boundary conditions on M_{cr}	149
Figure 4.72	Influence of test boundary conditions on (a) M_{crd} and (b) on the distortional half-wavelength	151
Figure 4.73	Boost in M_{crd} from the angle restraints increases as the fundamental distortional half-wavelength increases relative to the restraint spacing S_{brace}	151
Figure 4.74	Guidelines for restraining beam net cross-sections in the CUFSM local buckling approximate method	154
Figure 4.75	Comparison of ABAQUS to predicted M_{cr} for C-sections with holes in the beam database as a function of (a) web depth and (b) hole width relative to flat web depth	155
Figure 4.76	Comparison of “mechanics-based” and “weighted-average” prediction methods to ABAQUS results for the distortional buckling load M_{crd} of C-sections with holes in the elastic buckling database	156
Figure 4.77	ABAQUS boundary conditions and applied loading for an SSMA 1200S162-68 beam with holes ($h_{hole}/h=0.50$ shown)	157
Figure 4.78	Comparison of “weighted thickness” and “weighted properties” prediction methods for the SSMA 1200S162-68 lateral-torsional beam buckling mode. Predictions using net section properties are also plotted as a conservative benchmark.....	158
Figure 5.1	Column testing parameters and naming convention	161
Figure 5.2	Tested lengths of cold-formed steel columns with holes as a function of (a) column length L and and (b) L versus out-to-out column width H	163
Figure 5.3	Typical column specimens with slotted holes	164
Figure 5.4	Column test setup and instrumentation.....	165
Figure 5.5	Novotechnik position transducer with ball-jointed magnetic tip	166
Figure 5.6	Central Machinery metal band saw used to rough cut column specimens.....	167
Figure 5.7	362S162-33 short column specimen with bismuth end diaphragms	168
Figure 5.8	600S162-33 short column specimen oriented in CNC machine	169
Figure 5.9	An end mill is used to prepare the column specimens.....	169
Figure 5.10	The intermediate length specimens were end-milled in a manual milling machine	170
Figure 5.11	The specimens are clamped at the webs only to avoid distortion of the cross-section	170
Figure 5.12	Setup procedure for measuring specimen cross section dimensions	172
Figure 5.13	Procedure for measuring specimen cross-section dimensions.....	173
Figure 5.14	Procedure for measuring flange-lip and flange-web angles.....	174
Figure 5.15	Specimen measurement nomenclature	175
Figure 5.16	Base metal and zinc thickness definitions	177
Figure 5.17	Removal of tensile coupon zinc coating as a function of time.....	179
Figure 5.18	A height gauge is used to measure specimen length.....	180
Figure 5.19	Lengths are measured at the four corners of the C-section column	181
Figure 5.20	A dial gauge and precision stand are used to measure initial web imperfections	184
Figure 5.21	Web imperfection measurement grid and coordinate system.....	184
Figure 5.22	Column specimen alignment schematic	186
Figure 5.23	Influence of platen bending stiffness on end moments for a fixed-fixed eccentric column.....	188
Figure 5.24	Column specimen weak axis out-of-straightness schematic.....	189
Figure 5.25	Digital calipers are used to measure the distance from the column web to platen edge	190
Figure 5.26	Tensile coupons are first rough cut with a metal ban saw.....	192
Figure 5.27	Tensile coupon dimensions as entered in the CNC milling machine computer.....	192

Figure 5.28 A custom jig allows three tensile coupons to be milled at once in the CNC machine	193
Figure 5.29 ATS machine used to test tensile coupons	194
Figure 5.30 Gradually yielding stress-strain curve with 0.2% strain offset method	195
Figure 5.31 Sharp-yielding stress strain curve using an autographic method for determining F_y	195
Figure 5.32 (a) Local and distortional elastic buckled mode shapes for (a) short ($L=48$ in.) 362S162-33 specimens and (b) intermediate length ($L=48$ in.) 362S162-33 specimens.	198
Figure 5.33 Local and distortional elastic buckled mode shapes for (a) short ($L=48$ in.) 600S162-33 specimens and (b) intermediate length ($L=48$ in.) 600S162-33 specimens.	198
Figure 5.34 Local (L) and distortional (D) DSM strength predictions are similar in magnitude for both 362S162-33 and 600S162-33 cross-sections, indicating that L-D modal interaction will occur during the tested response of the columns.	201
Figure 5.35 Comparison of global mode shapes for intermediate length 362S162-33 and 600S162-33 specimens.....	205
Figure 5.36 Load-displacement progression for short column specimen 362-2-24-NH.....	207
Figure 5.37 Load-displacement progression for short column specimen 362-2-24-H	208
Figure 5.38 Load-displacement curve for a 362S162-33 short column with, without a slotted hole	208
Figure 5.39 Comparison of load-deformation response and lateral flange displacements for specimen 362-2-24-NH.....	210
Figure 5.40 Influence of a slotted hole on 362S162-33 short column lateral flange displacement.....	210
Figure 5.41 Load-displacement progression for short column specimen 600-1-24-NH	212
Figure 5.42 Load-displacement progression for short column specimen 600-1-24-H	212
Figure 5.43 Comparison of load-displacement response for short 600S162-33 column specimens with and without holes	213
Figure 5.44 Load-displacement progression, intermediate length column specimen 362-3-48-NH	215
Figure 5.45 Load-displacement progression for intermediate length column specimen 362-3-48-H	215
Figure 5.46 Load-displacement curve, 362S162-33 intermediate column with and without a hole	216
Figure 5.47 362S162-33 long column mid-height flange displacements show the global torsional failure mode.....	216
Figure 5.48 Load-displacement progression, intermediate length column specimen 600-1-48-NH	218
Figure 5.49 Load-displacement progression, intermediate length column specimen 600-1-48-NH	218
Figure 5.50 Load-displacement comparison of intermediate length 600S162-33 specimens with and without holes	219
Figure 5.51 Short 600S162-33 column flange-lip corner lifts off platen during post-peak portion of test.....	222
Figure 6.1 Cold-formed steel roll-forming: (left) Sheet coil enters roll-forming line, (right) steel sheet is cold-formed into C-shape cross-section (photos courtesy of Bradbury Group).	224
Figure 6.2 Forming a bend: plastic bending and elastic springback of thin sheets results in a nonlinear through-thickness residual stress distribution.	225
Figure 6.3 Stress-strain coordinate system as related to the coiling and cold-forming processes.	226
Figure 6.4 Roll-forming setup with sheet coil fed from the (a) top of the coil and (b) bottom of coil. The orientation of the coil with reference to the roll-forming bed influences the direction of the coiling residual stresses.....	229

Figure 6.5	Coiling of the steel sheet may result in residual curvature which results in bending residual stresses as the sheet is flattened.....	231
Figure 6.6	Longitudinal residual stress distribution from coiling.....	232
Figure 6.7	Predicted longitudinal residual stress distribution from coiling, uncoiling, and flattening of a steel sheet.....	233
Figure 6.8	Cold-forming of a steel sheet.....	235
Figure 6.9	Fully plastic transverse stress state from cold-forming.....	235
Figure 6.10	Force couple ($F_p \cdot \frac{1}{2}t$) applied to simulate the elastic springback of the steel sheet after the imposed radial deformation is removed.....	236
Figure 6.11	Cold-forming of a steel sheet occurs as plastic bending and elastic springback, resulting in a self-equilibrating transverse residual stress.....	237
Figure 6.12	Plastic bending and elastic springback from cold-forming in the transverse direction result in longitudinal residual stresses because of the plane strain conditions.	238
Figure 6.13	Flowchart summarizing the prediction method for residual stresses in roll-formed members.....	239
Figure 6.14	Plastic strain distribution from sheet coiling with a radius less than elastic-plastic threshold r_{ep}	241
Figure 6.15	Effective plastic strain in a cold-formed steel member from sheet coiling when the radius r_x is less than the elastic-plastic threshold r_{ep}	242
Figure 6.16	Effective von Mises true plastic strain at the location of cold-forming of a steel sheet.	243
Figure 6.17	Flowchart summarizing the prediction method for effective plastic strains in roll-formed members.....	244
Figure 6.18	Coil coordinate system and notation.	245
Figure 6.19	Influence of sheet thickness and yield stress on through-thickness longitudinal residual stresses (z-direction, solid lines are predictions for mean coil radius, dashed lines for mean radius +/- one standard deviation).....	247
Figure 6.20	The mean-squared error of the predicted and measured bending residual stresses for de M. Batista and Rodrigues (De Batista and Rodrigues 1992), Specimen CP1 is minimized when $r_x = 1.60r_{inner}$	251
Figure 6.21	(a) Histogram and (b) scattergram of bending residual stress prediction error (flat cross-sectional elements) for 18 roll-formed specimens.....	254
Figure 6.22	(a) Histogram and (b) scattergram of bending residual stress prediction error (corner cross-sectional elements) for 18 roll-formed specimens.....	254
Figure 6.23	Definition of apparent yield stress, effective residual stress, and effective plastic strain as related to a uniaxial tensile coupon test.....	256
Figure 7.1	True stress-strain curve derived from a tensile coupon test (Yu 2005).....	260
Figure 7.2	Simply supported boundary conditions with equation constraint coupling at loaded edges.....	261
Figure 7.3	Application of (a) uniform load and (b) uniform displacement to a stiffened element.....	262
Figure 7.4	Type 1 imperfection (Schafer and Peköz 1998).....	263
Figure 7.5	Modified Riks method load-displacement solutions and failure modes.....	265
Figure 7.6	Correlation between initial imperfection shape and fold line locations at failure.....	265
Figure 7.7	Artificial damping load-displacement solutions and failure modes.....	268
Figure 7.8	Stiffened element boundary conditions with rigid body coupling at loaded edges ...	269
Figure 7.9	Initial geometric imperfection field used for the stiffened element with and without a hole.....	270
Figure 7.10	Deformation at ultimate load of a stiffened element with a hole loaded in compression. The common failure mechanism is material yielding adjacent to the hole followed by plate folding.....	271
Figure 7.11	Load-displacement curve for the RIKS1 and RIKS2 models showing direction reversal along load path.....	272

Figure 7.12	RIKS1 and RIKS2 models experience convergence problems and return along the loading path, the RIKS3 model successfully predicts a peak load and finds a post-peak load path.....	274
Figure 7.13	STATIC1 and STATIC2 load-displacement curves demonstrate convergence difficulties near the peak load.....	275
Figure 7.14	STAB1 and STAB2 load-displacement curves demonstrate a highly nonlinear post-peak equilibrium path.....	277
Figure 7.15	The STAB1 and STAB2 models (artificial damping, displacement control) exhibit a sharp drop in load as folding of the plate initiates near the hole. The STAB3 model (artificial damping, load control) finds the compressive load at which a complete loss of stiffness occurs.....	279
Figure 7.16	Comparison of ultimate limit state and elastic buckling plate behavior, initial imperfections are not considered in these results.....	280
Figure 7.17	Load-displacement sensitivity to imperfection magnitude for a plate without a hole.....	282
Figure 7.18	Load-displacement sensitivity to imperfection magnitude for a plate with a slotted hole.....	282
Figure 7.19	Calculation of “effective width” at a cross-section along a stiffened element.....	284
Figure 7.20	Definition of longitudinal (S11) membrane stress.....	284
Figure 7.21	(a) longitudinal membrane stresses and (b) effective width of a stiffened element at failure.....	285
Figure 7.22	(a) longitudinal membrane stresses and (b) effective width of a stiffened element with a slotted hole at failure.....	286
Figure 7.23	Effective width comparison for a plate with and without a slotted hole.....	286
Figure 7.24	Through the thickness variation of effective width of a plate without a hole.....	287
Figure 7.25	Through the thickness variation of effective width of a plate with a slotted hole.....	287
Figure 7.26	Through thickness variation in longitudinal (S11) stresses in a plate at failure.....	288
Figure 7.27	ABAQUS boundary conditions simulating column experiments.....	290
Figure 7.28	ABAQUS plastic strain curve for specimen 362-1-24-NH assuming (a) plasticity initiates at the proportional limit and (b) plasticity initiates at 0.2% offset yield stress.....	293
Figure 7.29	ABAQUS plastic strain curve for specimen 600-1-24-NH assuming (a) plasticity initiates at the proportional limit and (b) plasticity initiates at the beginning of the yield plateau (refer to Appendix H for the details on the development of this curve)......	293
Figure 7.30	Influence of ABAQUS material model on the load-deformation response of specimen 600-1-24-NH (work this figure with Figure 7.29).....	294
Figure 7.31	Slotted holes are filled with S9R5 elements to obtain no hole imperfection shapes.....	295
Figure 7.32	L and D imperfection magnitudes described with a CDF (Schafer and Peköz 1998).....	297
Figure 7.33	Method for measuring distortional imperfection magnitudes from experiments.....	297
Figure 7.34	Definition of out-of-straightness imperfections implemented in ABAQUS.....	298
Figure 7.35	ABAQUS element local coordinate system for use with residual stress definitions.....	300
Figure 7.36	Transverse residual stress distribution applied at the corners of the cross-section.....	300
Figure 7.37	Longitudinal residual stress distribution applied at the corners of the cross-section.....	300
Figure 7.38	Equivalent plastic strain distribution at the corners of the cross-section.....	301
Figure 7.39	Influence of section points on the unbalanced moment (accuracy) of the transverse residual stress distribution as implemented in ABAQUS.....	302
Figure 7.40	Load-displacement response of specimen 362-1-24-NH.....	306
Figure 7.41	Load-displacement response of specimen 362-1-24-H.....	306
Figure 7.42	Load-displacement response of specimen 362-1-48-NH.....	307
Figure 7.43	Load-displacement response of specimen 362-1-48-H.....	307
Figure 7.44	Load-displacement response of specimen 600-1-24-NH.....	308

Figure 7.45	Load-displacement response of specimen 600-2-24-H	308
Figure 7.46	Load-displacement response of specimen 600-1-48-NH	309
Figure 7.47	Load-displacement response of specimen 600-3-48-H	309
Figure 7.48	Influence of residual stresses (RS) and plastic strains (PS) on the FE load-displacement response of specimen 600-1-24-NH	311
Figure 7.49	Influence of residual stresses (RS) and plastic strains (PS) on the FE load-displacement response of specimen 362-1-24-NH.	312
Figure 8.1	ABAQUS simulated column experiments boundary conditions and application of loading.....	315
Figure 8.2	SSMA 800S250-97 structural stud with web holes considered in the DSM distortional buckling study.....	318
Figure 8.3	SSMA 800S250-97 structural stud failure mode transition from distortional buckling to yielding at the net section	320
Figure 8.4	Comparison of simulated column strengths ($A_{net}/A_g=1.0$) to (a) the existing DSM distortional buckling design curve and to (b) the proposed DSM distortional buckling curve for columns with holes	321
Figure 8.5	Comparison of simulated column strengths ($A_{net}/A_g=0.90$) to (a) the existing DSM distortional buckling design curve and to (b) the proposed DSM distortional buckling curve for columns with holes	321
Figure 8.6	Comparison of simulated column strengths ($A_{net}/A_g=0.80$) to (a) the existing DSM distortional buckling design curve and to (b) the proposed DSM distortional buckling curve for columns with holes	322
Figure 8.7	Comparison of simulated column strengths ($A_{net}/A_g=0.70$) to (a) the existing DSM distortional buckling design curve and to (b) the proposed DSM distortional buckling curve for columns with holes	322
Figure 8.8	Comparison of simulated column strengths ($A_{net}/A_g=0.60$) to (a) the existing DSM distortional buckling design curve and to (b) the proposed DSM distortional buckling curve for columns with holes	322
Figure 8.9	Comparison of simulated column strengths ($A_{net}/A_g=1.00$) to (a) the existing DSM global buckling design curve and to (b) the proposed DSM distortional buckling curve for columns with holes.....	325
Figure 8.10	Comparison of simulated column strengths ($A_{net}/A_g=0.90$) to (a) the existing DSM global buckling design curve and to (b) the proposed DSM distortional buckling curve for columns with holes.....	326
Figure 8.11	Comparison of simulated column strengths ($A_{net}/A_g=0.80$) to (a) the existing DSM global buckling design curve and to (b) the proposed DSM distortional buckling curve for columns with holes.....	326
Figure 8.12	Comparison of column test-to-prediction ratios for columns ($A_{net}/A_g=1.0$) failing by local-global buckling interaction as a function of (a) local slenderness (b) global slenderness	328
Figure 8.13	Comparison of column test-to-prediction ratios for columns failing by local-global buckling interaction with P_{ne} calculated (a) without the influence of holes (b) and with the influence of holes.....	330
Figure 8.14	Comparison of column test-to-prediction ratios for columns failing by local-global buckling interaction as a function of P_{ynet}/P_{ne} where P_{ne} is calculated (a) without the influence of holes (b) and with the influence of holes	330
Figure 8.15	SSMA 350S162-68 column failure mode changes from distortional-flexural torsional buckling failure to weak axis flexure as hole size increases ($L=34$ in.).....	331
Figure 8.16	SSMA 800S250-43 ($L=74$ in.) column web local buckling changes to unstiffened strip buckling at peak load as hole size increases	331
Figure 8.17	Comparison of DSM local buckling design curve options when $P_{ynet}=0.80 P_{yg}$ and (a) $P_{cre}=100P_{yg}$, (b) $P_{cre}=5P_{yg}$, and (c) $P_{cre}=P_{yg}$	334

Figure 8.18	Comparison of simulated test strengths to predictions for columns with local buckling-controlled failures as a function of local slenderness (tested strength is normalized by P_{ne}).....	344
Figure 8.19	Comparison of simulated test strengths to predictions for columns with local buckling-controlled failures as a function of local slenderness (tested strength is normalized by P_{ye}).....	345
Figure 8.20	Comparison of simulated test strengths to predictions for columns with distortional buckling-controlled failures as a function of distortional slenderness.....	346
Figure 8.21	Comparison of simulated test strengths to predictions for columns with global buckling-controlled failures (i.e., no local interaction) as a function of global slenderness	347
Figure 8.22	Test-to-predicted ratios for local buckling-controlled simulated column failures as a function of local slenderness	348
Figure 8.23	Test-to-predicted ratios for distortional buckling-controlled simulated column failures as a function of distortional slenderness	349
Figure 8.24	Test-to-predicted ratios for simulated global buckling-controlled column failures (i.e., no local buckling interaction) as a function of global slenderness.....	350
Figure 8.25	Test-to-predicted ratios for simulated local buckling-controlled column failures as a function of net cross-sectional area to gross cross-sectional area.....	351
Figure 8.26	Test-to-predicted ratios for simulated distortional buckling-controlled column failures as a function of net cross-sectional area to gross cross-sectional area.....	352
Figure 8.27	Test-to-predicted ratios for simulated global buckling-controlled column failures as a function of net cross-sectional area to gross cross-sectional area.....	353
Figure 8.28	Test-to-predicted ratios for simulated local buckling-controlled column failures as a function of column length, L , to flat web width, h	354
Figure 8.29	Test-to-predicted ratios for simulated distortional buckling-controlled column failures as a function of column length, L , to flat web width, h	355
Figure 8.30	Test-to-predicted ratios for simulated global buckling-controlled column failures as a function of column length, L , to web width, h	356
Figure 8.31	Comparison of experimental test strengths to predictions for columns with local buckling-controlled failures as a function of local slenderness (tested strength is normalized by P_{ne}).....	359
Figure 8.32	Comparison of experimental test strengths to predictions for columns with local buckling-controlled failures as a function of local slenderness (tested strength is normalized by P_y).....	360
Figure 8.33	Comparison of experimental test strengths to predictions for columns with distortional buckling-controlled failures as a function of distortional slenderness ..	361
Figure 8.34	Comparison of experimental test strengths to predictions for columns with global buckling-controlled failures as a function of global slenderness	362
Figure 8.35	Test-to-predicted ratios for experiment local buckling-controlled column failures as a function of local slenderness	363
Figure 8.36	Test-to-predicted ratios for experiment distortional buckling-controlled column failures as a function of distortional slenderness	364
Figure 8.37	Test-to-predicted ratios for experiment global buckling-controlled column failures as a function of global slenderness	365
Figure 8.38	Test-to-predicted ratios for experiment local buckling-controlled column failures as a function of net cross-sectional area to gross cross-sectional area.....	366
Figure 8.39	Test-to-predicted ratios for experiment distortional buckling-controlled column failures as a function of net cross-sectional area to gross cross-sectional area.....	367
Figure 8.40	Test-to-predicted ratios for experiment global buckling-controlled column failures as a function of net cross-sectional area to gross cross-sectional area.....	368
Figure 8.41	Test-to-predicted ratios for experiment local buckling-controlled column failures as a function of column length, L , to flat web width, h	369

Figure 8.42	Test-to-predicted ratios for experiment distortional buckling-controlled column failures as a function of column length, L , to flat web width, h	370
Figure 8.43	Test-to-predicted ratios for experiment global buckling-controlled column failures as a function of column length, L , to web width, h	371
Figure 8.44	ABAQUS simulated beam experiments boundary conditions and application of loading.....	374
Figure 8.45	SSMA 800S162-43 beam with web holes considered in the DSM local buckling study	377
Figure 8.46	Comparison of simulated beam strengths ($I_{net}/I_g=1.0$, no holes) to (a) the existing DSM local buckling design curve and to (b) the proposed DSM local buckling curve for beams with holes	379
Figure 8.47	Comparison of simulated beam strengths ($I_{net}/I_g=0.95$) to (a) the existing DSM local buckling design curve and to (b) the proposed DSM local buckling curve for beams with holes.....	379
Figure 8.48	Comparison of simulated beam strengths ($I_{net}/I_g=0.90$) to (a) the existing DSM local buckling design curve and to (b) the proposed DSM local buckling curve for beams with holes.....	380
Figure 8.49	Comparison of simulated beam strengths ($I_{net}/I_g=0.85$) to (a) the existing DSM local buckling design curve and to (b) the proposed DSM local buckling curve for beams with holes.....	380
Figure 8.50	SSMA 550S162-54 structural stud failure mode transition from distortional buckling to yielding at the net section	382
Figure 8.51	Comparison of simulated beam strengths ($I_{net}/I_g=1.0$) to (a) the existing DSM distortional buckling design curve and to (b) the proposed DSM distortional buckling curve for beams with holes	383
Figure 8.52	Comparison of simulated beam strengths ($I_{net}/I_g=0.95$) to (a) the existing DSM distortional buckling design curve and to (b) the proposed DSM distortional buckling curve for beams with holes	383
Figure 8.53	Comparison of simulated beam strengths ($I_{net}/I_g=0.90$) to (a) the existing DSM distortional buckling design curve and to (b) the proposed DSM distortional buckling curve for beams with holes	384
Figure 8.54	Comparison of simulated test strengths to predictions for laterally braced beams with local buckling-controlled failures as a function of local slenderness.....	393
Figure 8.55	Comparison of simulated test strengths to predictions for laterally braced beams with distortional buckling-controlled failures as a function of distortional slenderness ..	394
Figure 8.56	Test-to-predicted ratios for local buckling-controlled simulated laterally braced beam failures as a function of local slenderness	395
Figure 8.57	Test-to-predicted ratios for distortional buckling-controlled simulated laterally braced beam failures as a function of distortional slenderness.....	396
Figure 8.58	Test-to-predicted ratios for simulated local buckling-controlled laterally braced beam failures as a function of net cross-sectional moment of inertia to gross cross-sectional moment of inertia	397
Figure 8.59	Test-to-predicted ratios for simulated distortional buckling-controlled laterally braced beam failures as a function of net cross-sectional moment of inertia to gross cross-sectional moment of inertia.....	398
Figure 8.60	Test-to-predicted ratios for simulated local buckling-controlled laterally braced beam failures as a function of column length, L , to beam depth, H	399
Figure 8.61	Test-to-predicted ratios for simulated distortional buckling-controlled laterally braced beam failures as a function of column length, L , to H	400
Figure 8.62	Comparison of experimental test strengths to predictions for laterally braced beams with local buckling-controlled failures as a function of local slenderness	403

Figure 8.63 Comparison of experimental test strengths to predictions for laterally braced beams with distortional buckling-controlled failures as a function of distortional slenderness	404
Figure 8.64 Test-to-predicted ratios for experimental local buckling-controlled laterally braced beam failures as a function of net cross-sectional moment of inertia to gross cross-sectional moment of inertia	405
Figure 8.65 Test-to-predicted ratios for experimental distortional buckling-controlled laterally braced beam failures as a function of net cross-sectional moment of inertia to gross cross-sectional moment of inertia	406
Figure C.1 CUFSM finite strip modeling definition for an unstiffened element in compression	433
Figure C.2 The plate buckling coefficient k_A for an unstiffened element in compression (the multiple curves represent $0 \leq \psi_A \leq 1$ with a step of 0.1, 11 curves total).....	434
Figure C.3 The fitted curve for k_A is a conservative predictor when $L_{hole}/y_A \leq 2$	435
Figure C.4 CUFSM finite strip modeling definition for an unstiffened element with compression on the free edge, tension on the simply-supported edge	436
Figure C.5 Variation in plate buckling coefficient k_B for an unstiffened element with ψ_B ranging from 0 to 10	436
Figure C.6 Curve fit to minimum k_B for ψ_B ranging from 0 to 10	437
Figure C.7 Family of curves used to simulate boost in k_B when $L_{hole}/h_B \leq 2$, ψ_B ranges from 0 to 10	438
Figure E.1 Long column with two holes spaced symmetrically about the longitudinal midline.	443

List of Tables

Table 3.1 Plate widths corresponding to SSMA structural stud designations.....	26
Table 3.2 Parameter ranges in stiffened element verification study.	36
Table 3.3 Parameter range for stiffened element verification study with offset holes.....	41
Table 3.4 Parameter ranges considered for stiffened elements in bending with holes.....	44
Table 3.5 Study parameter limits for stiffened element in bending ($Y/h=0.50$) with offset holes .	46
Table 3.6 Parameter range for study of regularly-spaced holes on unstiffened elements.	59
Table 3.7 Parameter range considered for unstiffened element study with offset holes.....	61
Table 4.1 SSMA structural stud and plate dimensions	70
Table 4.2 Summary of column experimental data	79
Table 4.3 Fixed-fixed column experiment dimensions and material properties	82
Table 4.4 Fixed-fixed column experiment elastic buckling properties	83
Table 4.5 Weak-axis pinned column experiment dimensions and material properties	84
Table 4.6 Weak-axis pinned column experiment elastic buckling properties.....	84
Table 4.7 Parameter ranges for fixed-fixed and weak-axis pinned column specimens with holes	85
Table 4.8 DSM prequalification limits for C-sections.....	85
Table 4.9 DSM prequalification limits for beam C-sections	143
Table 4.10 Parameter ranges for beam specimens with holes.....	143
Table 4.11 Beam experiment cross-section dimensions, material properties, and tested strengths	144
Table 4.12 Beam experiment elastic buckling results.....	145
Table 5.1 FSM local and distortional buckling half-wavelengths for nominal 362S162-33 and 600S162-33 cross-sections	162
Table 5.2 Voltage conversion factors for column test instrumentation	166
Table 5.3 Summary of measured cross section dimensions	175
Table 5.4 Summary of measured lip-flange and flange-web cross section angles	176
Table 5.5 Specimen bare steel and zinc coating thicknesses.....	178
Table 5.6 Measured column specimen length	181
Table 5.7 Specimen end flatness.....	182
Table 5.8 Measured slotted hole dimensions and locations	183
Table 5.9 Initial web imperfections (deviations from the average elevation of the web).....	185
Table 5.10 Specimen gross centroid and offset from applied load during tests	187
Table 5.11 Summary of out-of-straightness calculations	190
Table 5.12 Voltage conversion factors for tensile coupon testing.....	194
Table 5.13 Summary of column specimen steel yield stress.....	195
Table 5.14 Column specimen steel yield stress statistics	196
Table 5.15 Critical elastic buckling loads, influence of holes on elastic buckling.....	200
Table 5.16 Specimen ultimate strength results	206
Table 6.1 Statistics of the residual stresses in roll-formed members.....	249
Table 6.2 Radial location in the coil that minimizes the sum of the mean square prediction error for roll-formed members	252
Table 7.1 Summary of nonlinear finite element models and associated solution controls	271
Table 7.2 Local and distortional imperfection magnitudes	297
Table 7.3 Out-of-straightness imperfection magnitudes.....	298
Table 7.4 Comparison of nonlinear FE simulation peak loads to experiments	303
Table 8.1 DSM test-to-predicted statistics for column simulations	343
Table 8.2 DSM test-to-predicted ratio statistics for column experiments.....	358
Table 8.3 DSM test-to-predicted ratio statistics for column experiments (stub columns only).....	358
Table 8.4 DSM test-to-predicted statistics for laterally braced beam simulations.....	392
Table 8.5 DSM test-to-predicted ratio statistics for column experiments.....	402

Chapter 1 Introduction

The goal of this research work is to develop a general design method for cold-formed steel structural members with holes. Cold-formed steel beams and columns are typically manufactured with perforations. For example, in low and midrise construction, holes are prepunched in structural studs to accommodate the passage of utilities in the walls and ceilings of buildings as shown in Figure 1.1. In cold-formed steel storage rack columns, perforation patterns are provided to allow for variable shelf configurations as shown in Figure 1.2. (Members with discrete holes, for example C-sections with punched holes as shown in Figure 1.1, are the research focus in this thesis, although many of the tools and methods developed here can be extended to perforation patterns in storage racks with additional research effort.) Existing design procedures for cold-formed steel members with holes are limited to certain hole sizes, shapes, and configurations. These limitations can hamper an engineer's design flexibility and decrease the reliability of cold-formed steel components where holes exceed these prescriptive limits.

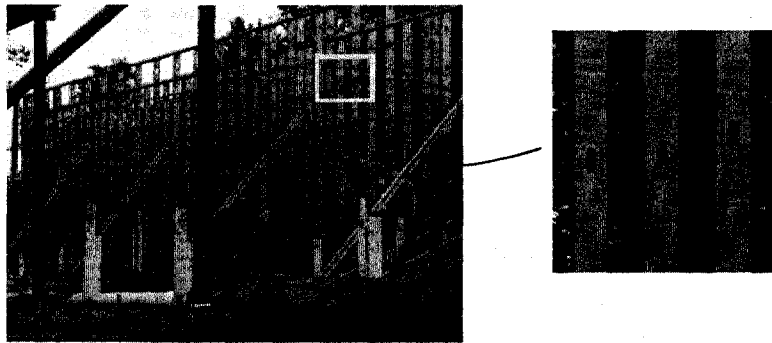


Figure 1.1 Perforations are provided in structural studs to accommodate utilities in the walls of buildings

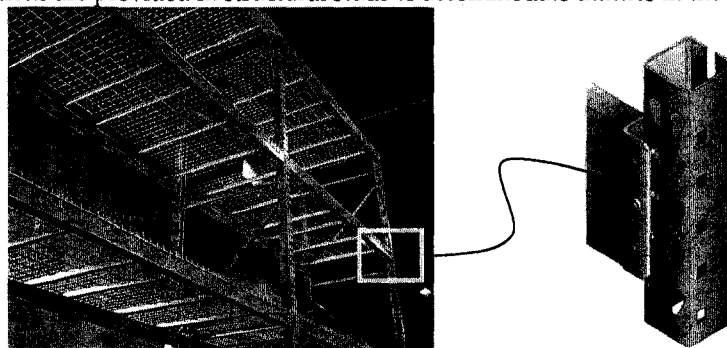


Figure 1.2 Hole patterns in storage rack columns

The basic framework of the design procedure developed in this thesis is the Direct Strength Method (DSM) (AISI-S100 2007, Appendix 1). DSM is relatively new and represents a major advancement in cold-formed steel design because it provides engineers and cold-formed steel manufacturers with the tools to predict the strength of a member with any general cross-section. Cold-formed steel members are manufactured from thin sheet steel, and therefore member resistance is influenced by cross-section instabilities (e.g., plate buckling and distortion of open cross-sections) in addition to the global buckling influence considered in thicker hot-rolled steel sections. DSM explicitly defines the relationship between elastic buckling and load-deformation response with empirical equations to predict ultimate strength.

To calculate the capacity of a cold-formed steel member with DSM, the elastic buckling properties of a general cold-formed steel cross-section are obtained from an elastic buckling curve. The curve can be generated with software employing the finite strip method to perform a series of eigenbuckling analyses over a range of buckled half-wavelengths. In this research work the freely available program CUFSM is utilized (Schafer and Adány 2006). An example of an elastic buckling curve is provided in Figure 1.3 for a cold-formed steel C-section column and highlights the three categories of elastic buckling considered in DSM – local buckling, distortional buckling, and global buckling. Local buckling occurs as plate buckling of individual slender elements in a cross-section. Distortional buckling exists only for open cross-sections such as a C-section, where the compressed flanges buckle inward or outward along the length of a member. Global buckling, also known as Euler buckling, defines buckling of the full member at long half-wavelengths including both flexural and flexural-torsional effects (and lateral-torsional effects in beams).

The critical elastic buckling loads associated with local, distortional, and global buckling – $P_{cr,l}$, $P_{cr,d}$, and $P_{cr,e}$ for columns ($M_{cr,l}$, $M_{cr,d}$, and $M_{cr,e}$ for beams), can be obtained directly from the elastic buckling curve. The critical elastic buckling loads are then used to predict the ultimate strength with three empirical design curves presented in Figure 1.4 to Figure 1.6 for cold-formed steel columns. (The current DSM column design equations for members *without holes* are also provided in these figures.) The local, distortional, and global slenderness of a member (λ_l , λ_d , λ_c) are calculated from the critical elastic buckling loads, defining a member's sensitivity to each type of buckling at

failure (high slenderness corresponds to high sensitivity, low slenderness to low sensitivity). The nominal resistances (P_{nl} , P_{nd} , and P_{ne}) are obtained by inserting the slenderness magnitudes into the DSM design equations. The minimum of the local, distortional, and global nominal strengths is taken as the strength of the member.

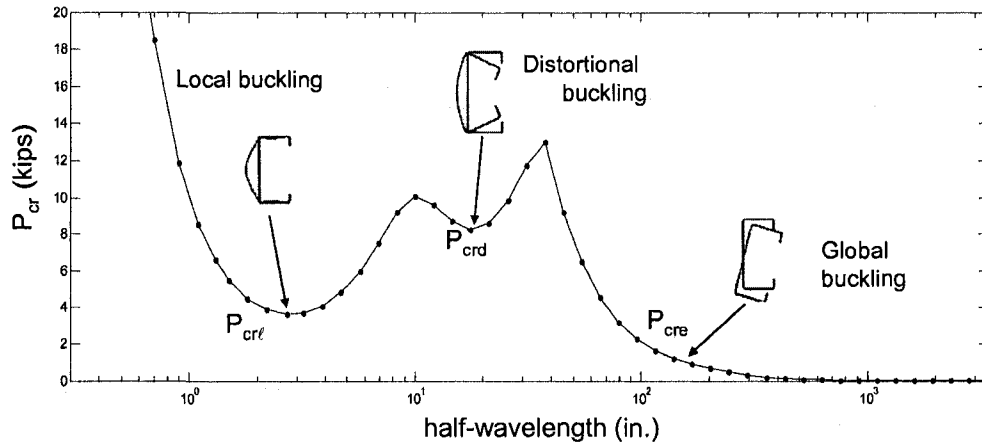


Figure 1.3 Column elastic buckling curve generated with CUFSM

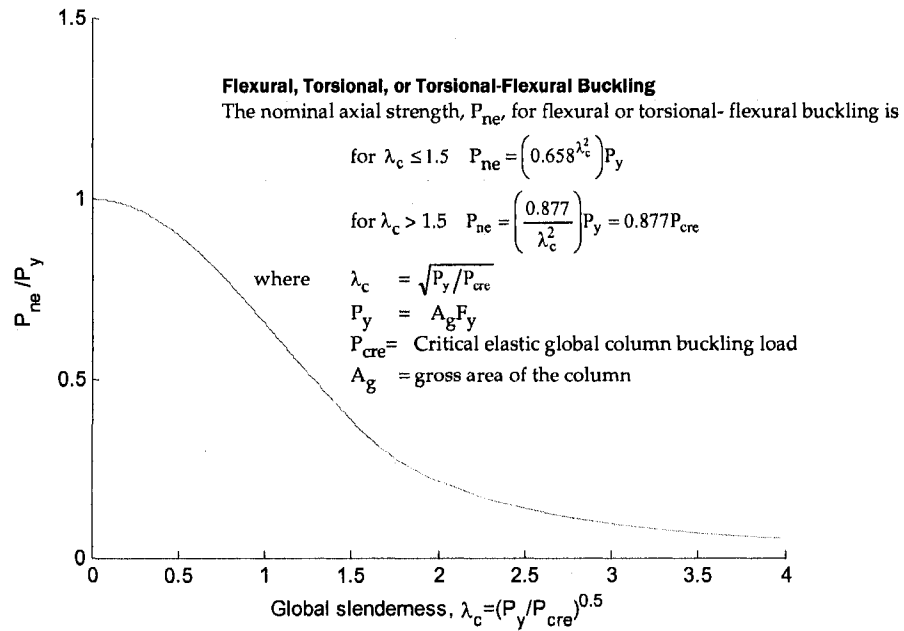


Figure 1.4 DSM global buckling failure design curve and equations

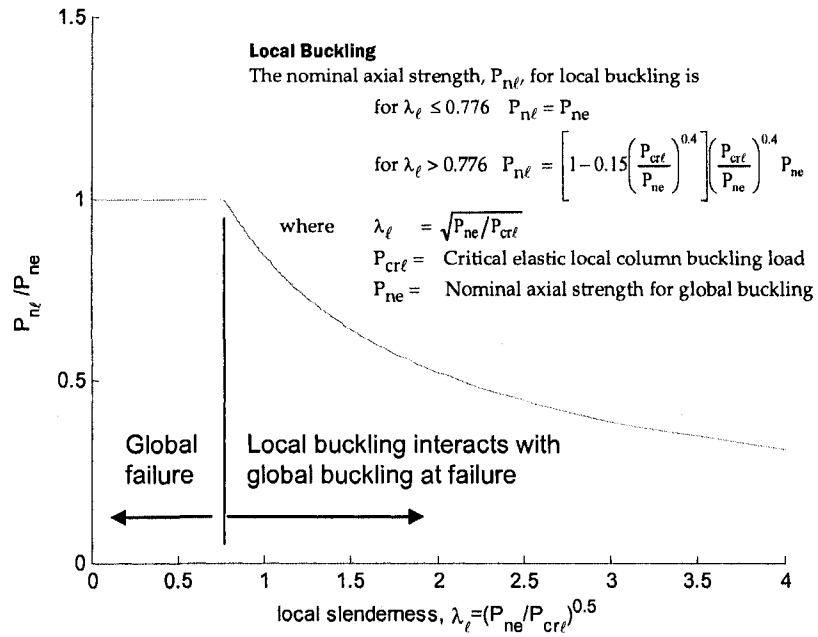


Figure 1.5 DSM local buckling failure design curve and equations

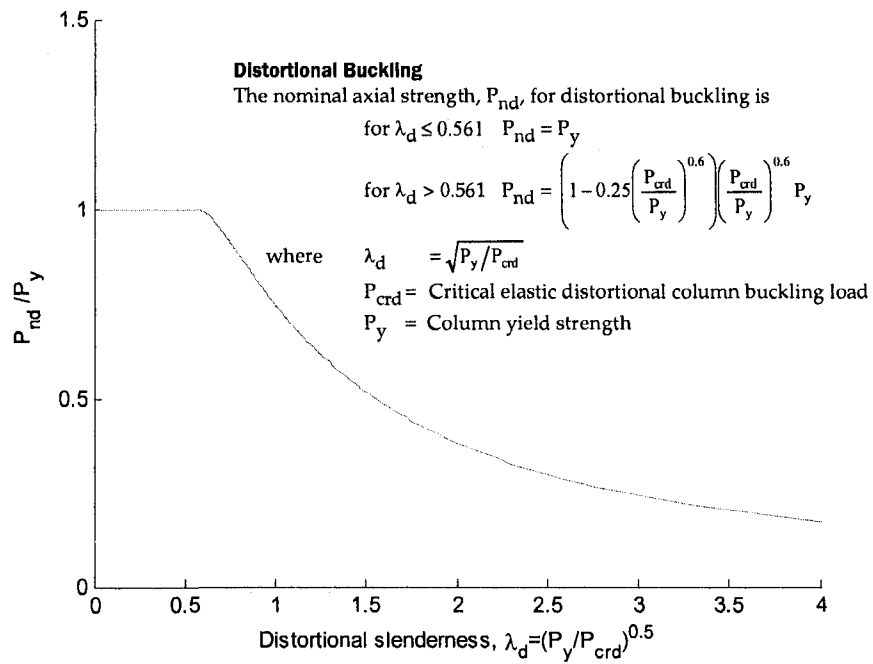


Figure 1.6 DSM distortional buckling failure design curve and equations

This research aims to extend the appealing generality of DSM to cold-formed steel members with perforations. The primary research goals are to study and quantify the influence of holes on the elastic buckling of cold-formed steel beams and columns and then to develop modifications to the existing DSM design equations which relate elastic buckling to ultimate strength. The research plan is implemented in three phases:

Phase I (Chapters 2-4)

1. Study the influence of holes on the elastic buckling of thin plates, and then on cold-formed steel beams and columns.
2. Evaluate the viability of DSM for members with holes by comparing existing experiments on members with holes to the current DSM specification.

Phase II (Chapters 5-7)

1. Conduct experiments on cold-formed steel columns to observe the influence of holes on ultimate strength and post-buckling response.
2. Define and validate a nonlinear finite element modeling protocol through parameter studies on thin plates and comparison to experimental results.

Phase III (Chapters 7-8)

1. Formalize the relationship between elastic buckling and ultimate strength for members with holes using nonlinear finite element simulations and existing data.
2. Modify the current DSM specification to account for members with holes

Phase I research is primarily focused on elastic buckling. Chapter 2 describes preliminary thin shell finite element eigenbuckling studies which are used to evaluate the accuracy of different shell element types in ABAQUS and to define finite element meshing guidelines. Chapter 3 extends this elastic buckling research with eigenbuckling analyses of typical cross-sectional elements considered in cold-formed steel design. For

example, a stiffened element is a simply-supported plate used to model the web of a cold-formed steel C-section and an unstiffened element is a plate simply-supported on three edges and free on the fourth edge to simulate the behavior of the free leg of a cold-formed steel hat section. Chapter 4 examines the elastic buckling of full cold-formed steel beams and columns with holes and develops useful simplified methods to predict elastic buckling, including the influence of holes, without finite element analysis. The elastic buckling properties of existing beam and column experiments are also calculated and merged with the tested strengths into a database. This database is employed near the end of the project to validate the proposed modifications to the DSM design equations for members with holes.

Phase II marks a shift from elastic buckling to the study of the influence of holes on load-deformation response and ultimate strength. Chapter 5 describes an experimental program on short and intermediate length cold-formed steel columns with holes. Chapter 6 initiates the development of a nonlinear finite element protocol with a significant effort to define the residual stresses and initial plastic strains from the manufacturing process. The capabilities of the commercial program ABAQUS (ABAQUS 2007a) are explored at the beginning of Chapter 7 with preliminary nonlinear finite element simulation studies on rectangular plates with holes. The experimental results from Chapter 5 are then employed in Phase III to fully develop and verify the modeling protocol. The research culminates in Chapter 8 with the development of a database of simulated tests which are used in combination with existing experimental data to validate the DSM design method for cold-formed steel members with holes.

Chapter 2

Thin-shell finite element modeling in ABAQUS

A set of ABAQUS modeling guidelines is formalized in this chapter to provide a consistent methodology for the finite element studies conducted in this thesis research. Finite element eigenbuckling analysis is a valuable tool for studying the elastic buckling properties of thin-walled structures. The accuracy of an analysis is influenced by decisions made while implementing the finite element model, including the choice of finite element type and the meshing geometry and density. Studies are presented here which compare finite element eigenbuckling predictions of plate buckling problems to known theoretical solutions. The eigenbuckling analyses are performed with the commercial finite element program ABAQUS (ABAQUS 2007a). The accuracy of ABAQUS thin shell elements are evaluated, and finite element convergence studies are presented to identify limits on element aspect ratio. Rules for modeling rounded corners and meshing around holes are also provided with supporting elastic buckling studies.

2.1 Comparison of ABAQUS thin-shell elements

Three ABAQUS finite elements commonly employed in the elastic buckling analysis of thin-walled structures are the S9R5, S4, and S4R elements as shown in Figure 2.1. The S4 and the S4R finite elements are four node general purpose shell elements valid for both thick and thin shell problems (ABAQUS 2007a). Both elements employ linear shape functions to interpolate deformation between nodes. The S9R5 element is a doubly-curved thin shell element with nine nodes derived with shear flexible Mindlin strain definitions and Kirchoff constraints (classical plate theory with no transverse shear deformation) enforced as penalty functions (Schafer 1997). This element employs quadratic shape functions (resulting from the increase in the number of nodes from 4 to 9) which provide two important benefits when modeling thin-walled structures: (1) the ability to define initially curved geometries and (2) the ability to approximate a half sine wave with just one element. The “5” in S9R5 denotes that each element node has 5 degrees of freedom (three translational, two rotational) instead of 6 (three translational, three rotational). The rotation of a node about the axis normal to the element mid-surface is removed from the element formulation to improve computational efficiency. The “R” in the S9R5 (and S4R) designation denotes that the calculation of the element stiffness is not exact; the number of Gaussian integration points is reduced to improve computational efficiency and to avoid shear locking. This “reduced integration” approach underestimates element stiffness and sometimes results in artificial element deformation modes with zero strain across the element, commonly referred to as “hourglass” modes (Schafer 1997). The accuracy of eigenbuckling finite element models

are compared here for each of these ABAQUS element types against the exact solutions for two common plate buckling problems.

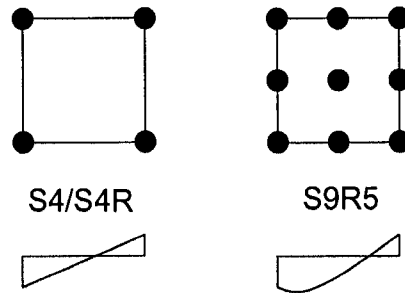


Figure 2.1 ABAQUS S4/S4R shell element with four nodes and a linear shape function, ABAQUS S9R5 shell element with nine nodes and a quadratic shape function

2.1.1 Modeling accuracy for a stiffened element

Elastic buckling analyses of a stiffened element were performed in ABAQUS to compare the accuracy of the ABAQUS S9R5, S4, and S4R elements against a known solution. A stiffened element is a common term used in thin-walled structures to describe a cross-sectional element restrained on both edges (see Figure 3.1) which is approximated as a thin simply-supported plate (with sides free to wave) and loaded uniaxially as shown in Figure 2.2.

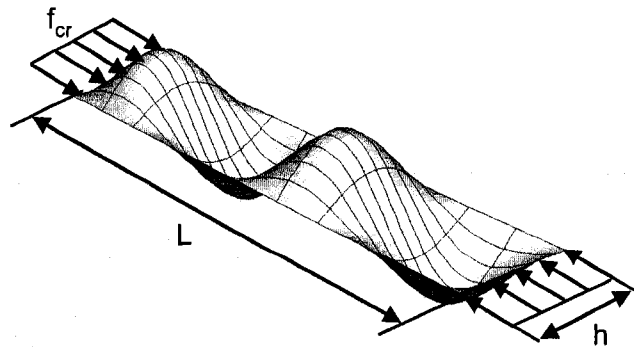


Figure 2.2 Buckled shape of a stiffened plate

The theoretical buckling stress for a stiffened element is:

$$f_{cr} = k \frac{\pi^2 E}{12(1-\nu^2)} \left(\frac{t}{h} \right)^2, \quad (2.1)$$

where h is the width of the plate, E is the modulus of elasticity of the plate material, ν is the Poisson's ratio, and t is the thickness of the plate.

The buckling coefficient k is:

$$k = \left(\frac{mh}{L} + \frac{n^2 L}{mh} \right)^2, \quad (2.2)$$

where L is the length of the plate and m and n are the number of half-wavelengths in the longitudinal and transverse directions, respectively (Chajes 1974). In Figure 2.2, $m=4$ and $n=1$.

Plate buckling coefficients (k) are approximated in ABAQUS by performing eigenbuckling analyses of stiffened elements with ABAQUS S4, S4R, and S9R5 elements. The element aspect ratio is set at 8:1 for the S9R5 element and 4:1 for the S4R and S4 elements to ensure a consistent comparison between finite element models (i.e., similar numbers of nodes and computational demand). These particular element aspect ratios were also chosen because they are expected to be towards the upper limit of what is required to discretize the geometry of cold-formed steel members (especially at rounded corners where the element aspect ratio can be quite high). The plate thickness is set to $t=0.0346$ in. $E=29500$ ksi and $\nu=0.30$ for all finite element models. The ABAQUS boundary and loading conditions are implemented as shown in Figure 3.1.

Figure 2.3 compares the theoretical k from Eq. (2.1) to the ABAQUS buckling coefficients for varying plate aspect ratios (L/h). The S9R5 element performs accurately over the range of element aspect ratios considered, with a maximum error of 1.3 percent. The S4 and S4R elements are not as accurate, with maximum errors of 11.4 percent and 9.7 percent, respectively. The accuracy of the plate models with S4 and S4R elements increase with increasing plate aspect ratio, which indirectly implies that solution accuracy increases as the number of elements per half-wave increase (in the loaded direction). This hypothesis is consistent with the element formulations, since the S9R5 element uses a quadratic shape function to estimate displacements (and can therefore capture the half-sine wave of a buckled plate with as little as one element) and the S4 and S4R elements use linear shape functions (requiring at least three elements to coarsely estimate the shape of a half sine wave). The S4R element is observed to be slightly less stiff than the S4 element in Figure 2.3, which is hypothesized to occur as a result of the reduced integration stiffness approximation.

Comparing the number of elements required to model a buckled half-wave is a more useful indicator of mesh density and model accuracy than just the element aspect ratio alone. Figure 2.4 verifies this supposition by demonstrating the improvement in modeling accuracy for a stiffened element as the number of finite elements per square half-wave increase. The S4 element experiences membrane locking when the number of elements per half wave is less than 2, resulting in exceedingly unconservative values for k . The S4R avoids this membrane locking with a reduced integration scheme that assumes the membrane stiffness is constant in the element (ABAQUS 2007a).

Regardless, the accuracy of the S4R element degrades when less than 5 elements per half-wavelength are used and neither four node element (i.e., the S4 or the S4R) is able to capture the sinusoidal shape of the buckled half-wave with less than three elements per buckled half-wave. The S9R5 accurately predicts the shape of the buckled half-wave and the buckling coefficient k with just one element. k is within 2.1 percent of the theoretical value for one element per half-wave and reduces to 0.1 percent for two elements per half-wave.

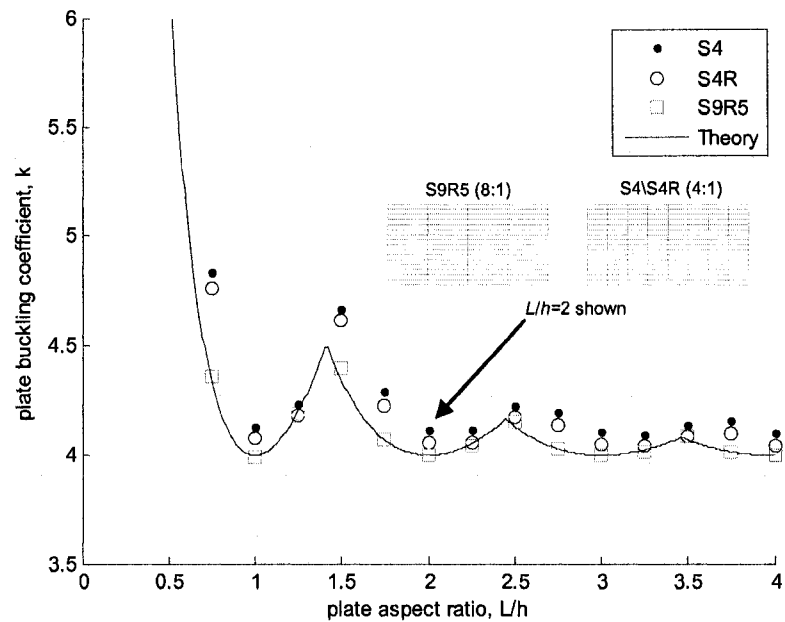


Figure 2.3 Accuracy of ABAQUS S9R5, S4, and S4R elements for a stiffened element with varying aspect ratios, 8:1 finite element aspect ratio for the S9R5 element, 4:1 element aspect ratio for the S4 and S4R elements

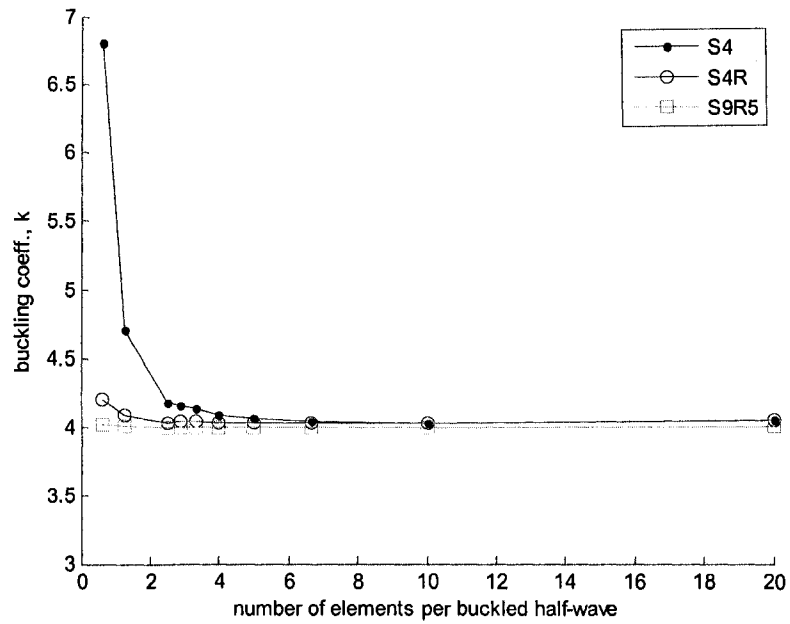


Figure 2.4 Accuracy of S4, S4R, and S9R5 elements as a function of the number of elements provided per buckled half-wavelength, stiffened element, square waves ($k=4$)

2.1.2 Modeling accuracy for an unstiffened element

An unstiffened element is another common cross-section component considered in the elastic buckling of thin-walled cross-sections (see Figure 3.1), the behavior of which is conservatively approximated as a plate simply-supported on three sides and free on the fourth side parallel to the direction of a uniaxially applied stress. The buckled shape of an unstiffened element is depicted in Figure 2.5.

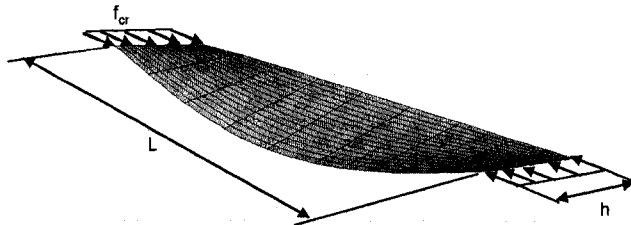


Figure 2.5 Buckled shape of an unstiffened element, $m=1$ shown

The theoretical buckling coefficient k of an unstiffened element can be calculated with the numerical solution of the following equations (Timoshenko 1961):

$$\beta \left(\alpha^2 - \nu \frac{m^2 \pi^2}{L^2} \right) \tanh(\alpha h) = \alpha \left(\beta^2 + \nu \frac{m^2 \pi^2}{L^2} \right) \tanh(\beta h), \quad (2.3)$$

$$\alpha = \left(\frac{m^2 \pi^2}{L^2} + \frac{m \pi^2}{Lh} k^{1/2} \right)^{1/2}, \text{ and } \beta = \left(-\frac{m^2 \pi^2}{L^2} + \frac{m \pi^2}{Lh} k^{1/2} \right)^{1/2}. \quad (2.4)$$

Figure 2.6 compares the theoretical to predicted k versus the number of S9R5 elements provided along the length L of an unstiffened element. The plate dimensions are held constant at $L/h=4$, while the element aspect ratio is varied from 1:1 to 64:1. The S9R5 element produces an error of 4.3 percent with an element aspect ratio of 16:1 and an error of 1.0 percent with an element aspect ratio of 8:1.

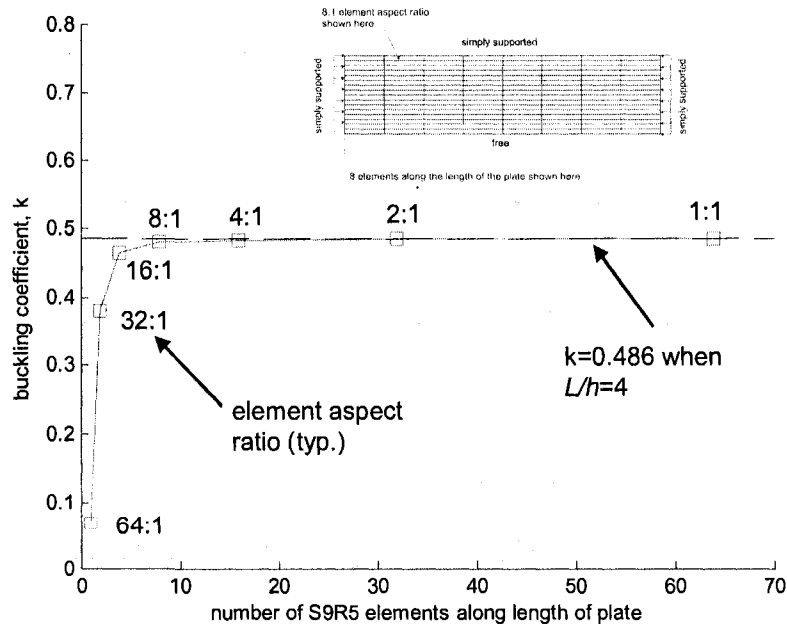


Figure 2.6 Accuracy of S9R5 elements as the number of finite elements provided along an unstiffened element varies, $L/h=4$

2.2 Modeling holes in ABAQUS

The ability to incorporate holes into the geometry of an ABAQUS finite element model is a key prerequisite to studying the influence of holes on the structural behavior of cold-formed steel structural members. To clear this hurdle, custom Matlab code was written by the author which generates a finite element mesh of a plate containing a hole (Mathworks 2007). The code discretizes the geometry around a hole by creating layers of S9R5 elements as shown in Figure 2.7 for a slotted hole, a circular hole, and a square hole. (See Appendix A for a description of the custom mesh generation program. Additional Matlab tools were developed to integrate the hole mesh geometry into an existing finite element model.) The discretization results in S9R5 elements with opposite edges which are not initially parallel. The initial geometry of 9 node quadrilateral elements without parallel edges can be defined without loss of accuracy as long as the midline nodes remain centered between the corner nodes (Cook 1989), which is an advantage over the S4 and S4R elements. ABAQUS recommends that the angle between isoparametric lines (i.e., corner angles of an element) should not be less than 45 degrees or greater than 135 degrees to ensure accurate numerical integration of the element stiffness matrix (ABAQUS 2007a). This limit coincides with the minimum and maximum S9R5 corner angles for the elements at the bisection of the 90 degree plate corners as shown in Figure 2.8.

This study establishes ABAQUS S9R5 finite element mesh guidelines for plates with holes by studying the convergence of the elastic stability solution as element aspect ratio

varies. Figure 2.7 provides the typical mesh layout and summarizes the plate dimensions considered in this study. The plate is modeled as a stiffened element in ABAQUS, simply supported on four sides and loaded uniaxially in compression (see Figure 3.5 for the ABAQUS implementation of the boundary and loading conditions). The plate thickness $t=0.0346$ in., $E=29500$ ksi, and $\nu=0.30$ for all finite element models.

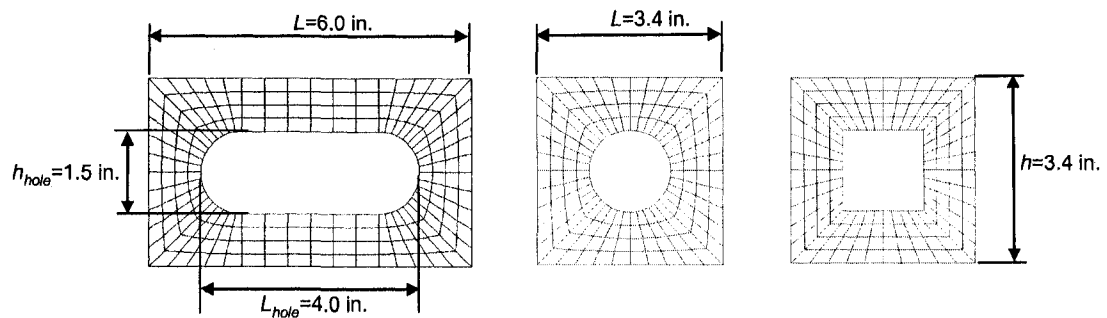


Figure 2.7. Finite element mesh and plate dimensions: slotted, rectangular, and circular holes

The convergence of the elastic buckling solution for the plates with holes is studied by varying the S9R5 element aspect ratio ($a:b$) at the bisection of the plate corners as shown in Figure 2.8, where a and b are defined as

$$a = \frac{h - h_{hole}}{N_{layers} \sqrt{2}}, \quad b = \frac{h_{hole}}{N_{elem}} \quad (2.5)$$

The aspect ratio is varied by increasing the number of finite element layers around the hole (N_{layers}) while maintaining the number of edge elements (N_{elem}) constant (i.e., the mesh density increases but the element corner angles remain constant).

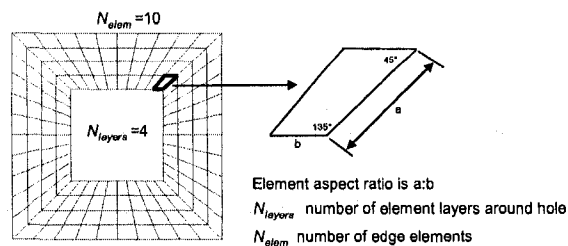


Figure 2.8 Hole discretization using S9R5 elements

Figure 2.9 demonstrates that the critical elastic buckling stress for the lowest buckling mode (a half sine wave in this case) for all hole types converges to a constant magnitude when $a:b$ is between 0.5 and 2. This result is employed as a modeling guideline for the research work in this thesis with the expressions for a and b in Eq. (2.5):

$$0.5 \leq \frac{N_{elem}}{N_{layers} \sqrt{2}} \left(\frac{h}{h_{hole}} - 1 \right) \leq 2. \quad (2.6)$$

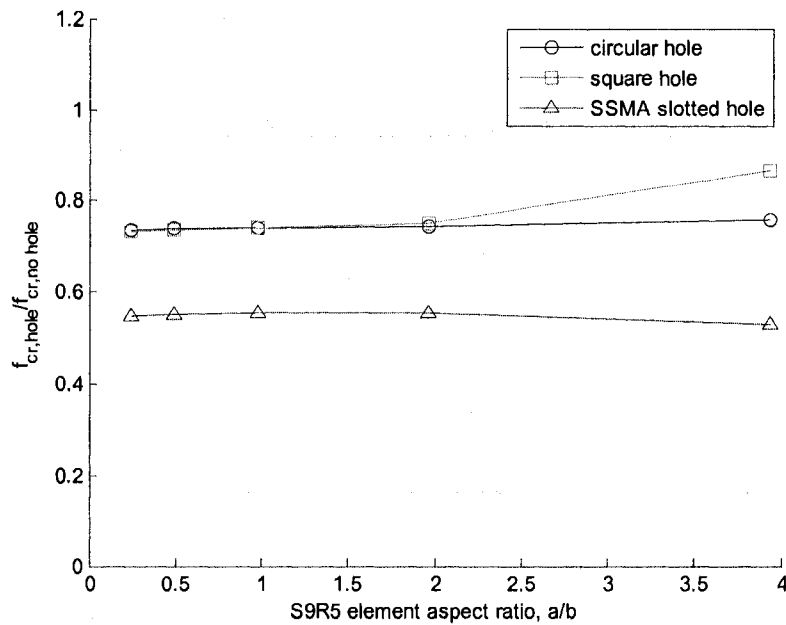


Figure 2.9 The critical elastic buckling stress converges to a constant magnitude when the S9R5 element aspect ratio a/b is between 0.5 and 2 and element corner angles are skewed

2.3 Modeling Rounded Corners in ABAQUS

The S9R5 element can be defined with an initial curved geometry in ABAQUS which makes it convenient for modeling rounded corners of a cold-formed steel cross-section.

ABAQUS recommends that the initial element curvature should be less than 10 degrees,

where curvature of an S9R5 element is defined as the angle subtended by the nodal normal and the average element normal as shown in Figure 2.10. The derivation in Figure 2.10 demonstrates that this curvature recommendation is met when five or more S9R5 elements form the 90 degree corner. This limit is unfavorable from a modeling perspective because the element aspect ratio increases as the number of elements around the corner increase, another potential source of accuracy degradation. Also, for a finite element model with four 90 degree corners (e.g., a cold-formed steel lipped C-section), increasing the number of elements at a corner can result in a considerable increase in computational demand if the corner elements comprise a large proportion of the total number of elements in a cross-section.

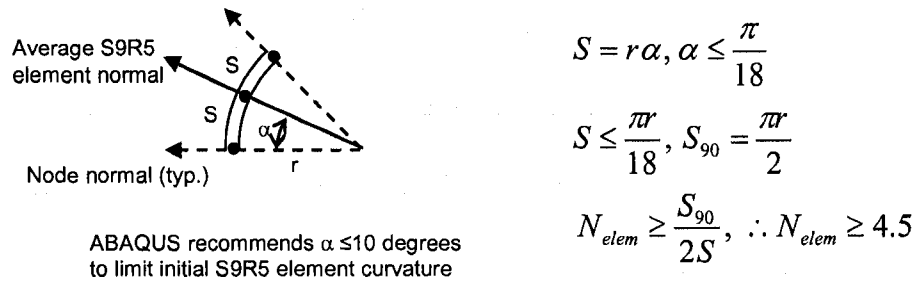


Figure 2.10 ABAQUS S9R5 initial curvature limit requires at least five elements to model corner

A parameter study was conducted to evaluate the influence of the number of S9R5 elements making up a 90 degree corner on the critical elastic buckling loads for local buckling ($P_{cr,l}$), distortional buckling ($P_{cr,d}$), and global buckling ($P_{cr,g}$) of an SSMA 600S162-68 C-section column. The number of corner elements were varied from 1 to 5, with the associated S9R5 aspect ratio $a:b$ varying from 5 to 22. The column length was held constant at $L=48$ inches for all models to accommodate multiple local and distortional half-waves. The columns were loaded uniaxially and modeled with warping-free ends

(CUFSM-style boundary conditions) as shown in Figure 4.2. $E=29500$ ksi and $\nu=0.30$ for all finite element models. P_y is the squash load of the column calculated with the steel yield stress $F_y=50$ ksi.

Figure 2.11 provides the typical mesh geometry of the column and compares a C-section corner modeled as a smooth surface with one S9R5 element and with three S9R5 elements. Figure 2.12 demonstrates that the number of S9R5 corner elements has a minimal influence on the elastic buckling behavior of the column, with a slight decreasing trend (less than 1%) in critical elastic buckling load with increasing element quantity. Mesh refinement at the corners does not influence solution accuracy because elastic buckling deformation occurs primarily within the more flexible cross-sectional elements. If the simulation of sharp folding of the corners is required, such as in the case of nonlinear finite element modeling to collapse, additional corner elements may be warranted to accurately capture localized deformation gradients.

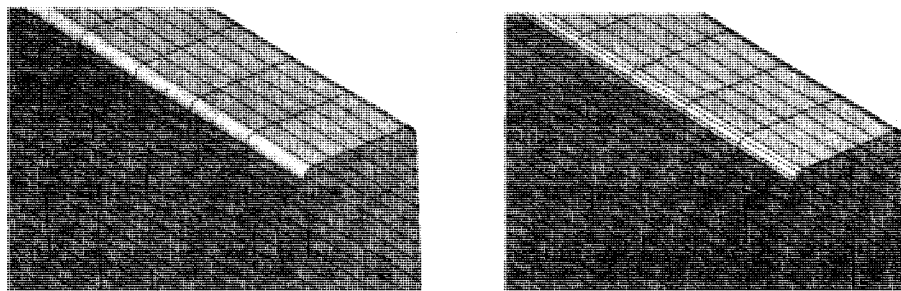


Figure 2.11 SSMA 600S162-68 C-section corner modeled with a) one S9R5 element, b) three S9R5 elements

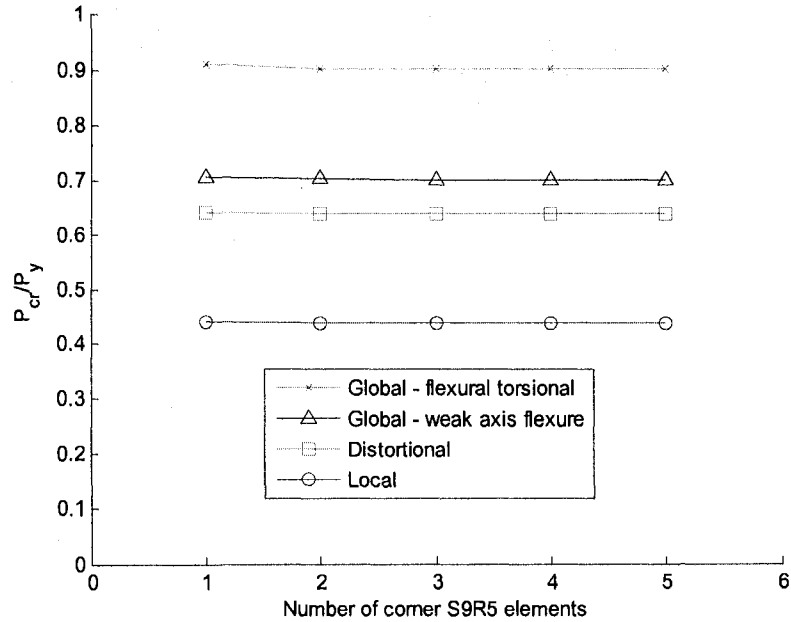


Figure 2.12 The number of S9R5 corner elements has a minimal influence on the critical elastic buckling loads of an SSMA 600162-68 C-section column with $L=48$ in.

2.4 Summary of modeling guidelines

The S9R5 element will be implemented in this research work based on its versatility and demonstrated accuracy. The results of the ABAQUS studies in this chapter form the basis of the ABAQUS modeling guidelines below which will be implemented for both eigenbuckling and nonlinear finite element studies in this thesis:

- A minimum of two S9R5 elements per half-wavelength shall be provided in stiffened elements in the direction normal to the applied load (e.g., flanges and web of a lipped C-section)
- The S9R5 element aspect ratio shall be less than or equal to 8:1 in unstiffened elements (e.g., flange lip in a C-section)
- The S9R5 element aspect ratio shall be between 0.5 and 2.0 when modeling holes with the discretization scheme described in Section 2.2 (where the element sides are not perpendicular)
- For both stiffened and unstiffened elements, at least two S9R5 elements shall be provided in the direction perpendicular to the application of load
- Rounded corners shall be modeled with at least two S9R5 elements, and the element aspect ratio of these elements shall be less than or equal to 16:1.

Chapter 3

Elastic buckling of cold-formed steel cross-sectional elements with holes

A simplified method for determining the elastic buckling properties of a thin-walled cross-section is to evaluate the contribution of each element in the cross-section separately. This element-by-element evaluation is the basis of the effective width design method for cold-formed steel beams and columns and can also be employed as a conservative predictor of the local critical elastic buckling load (P_{cr}) when designing cold-formed steel members with the Direct Strength Method (AISI-S100 2007, Appendix 1). The two common cross-section element types in an open thin-walled cross section are stiffened and unstiffened elements, examples of which are provided in Figure 3.1. The boundary conditions of a stiffened element are conservatively approximated as a simply-supported plate. The unstiffened element is treated as a plate simply-supported on three sides and free on the fourth edge parallel to the application of load.

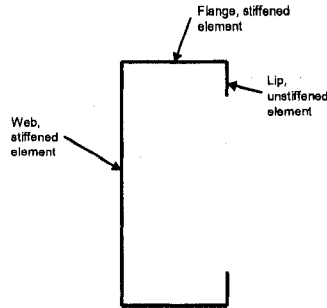


Figure 3.1 Stiffened and unstiffened elements in a lipped C-section

The influence of holes on the elastic buckling behavior of stiffened and unstiffened elements is evaluated in this chapter using thin shell finite element eigenbuckling analysis. The presence of holes can modify the buckled mode shape of an element and either increase or decrease its critical elastic buckling stress. Hole spacing and hole size relative to element size are studied for both stiffened and unstiffened elements, and approximate methods for predicting element critical elastic buckling stress are developed and presented for use in design. The research results presented here will be used as a framework for the elastic buckling studies of full cold-formed steel structural members with holes in Chapter 4.

3.1 Plate and hole dimensions

Plate and hole dimension nomenclature used throughout this chapter is summarized in Figure 3.2. The strips of plate between a hole and the plate edges will be referred to as unstiffened strip "A" and unstiffened strip "B", where the widths of these unstiffened strips are h_A and h_B respectively as shown in Figure 3.3. For stiffened elements in bending, the neutral axis location is defined as Y in Figure 3.4 and is measured from the compressed edge of the plate.

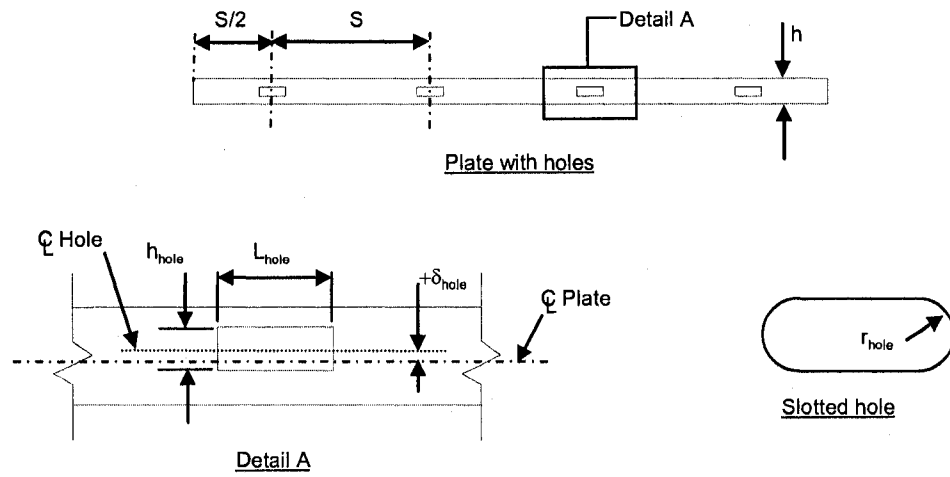


Figure 3.2 Element and hole dimension definitions

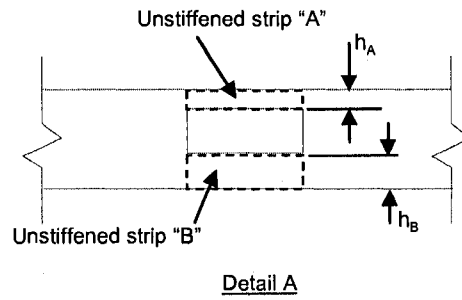


Figure 3.3 Definition of unstiffened strip "A" and "B" for a plate with holes.

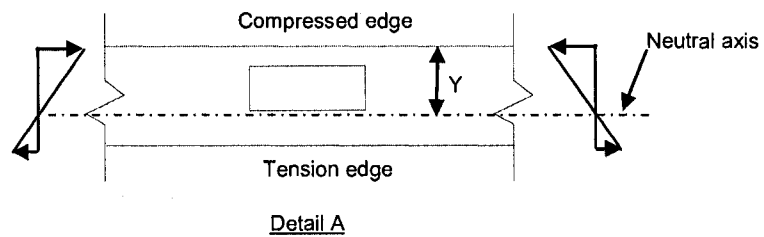


Figure 3.4 Definition of neutral axis location for stiffened elements in bending.

3.2 Finite element modeling assumptions

The elastic buckling behavior of stiffened and unstiffened elements with holes are obtained with eigenbuckling analyses of plates in ABAQUS (ABAQUS 2007a). All members are modeled with ABAQUS S9R5 reduced integration nine-node thin shell elements. The typical finite element aspect ratio is 1:1 and the maximum aspect ratio is limited to 8:1 (refer to Chapter 2 for a discussion on ABAQUS thin shell finite element types and finite element aspect ratio limits). Element meshing was performed with a Matlab (Mathworks 2007) program written by the author (refer to Appendix A for a description of the program). The plate models are loaded from each end with stress distributions applied as consistent nodal loads in ABAQUS. Converting a stress distribution to consistent nodal loads for the S9R5 element requires a different procedure than that followed for a 4-node finite element (Schafer 1997). Cold-formed steel material properties are assumed as $E=29500$ ksi and $\nu=0.3$ in all finite element models.

3.3 Stiffened element in uniaxial compression

3.3.1 Boundary and loading conditions

The stiffened element is modeled with simply-supported boundary conditions and loaded uniaxially with a uniform compressive stress as shown in Figure 3.5.

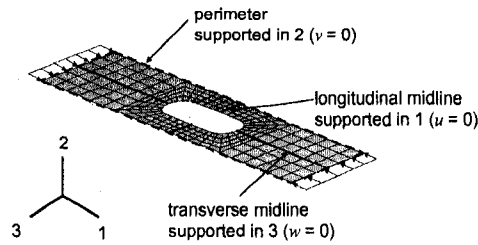


Figure 3.5 ABAQUS boundary conditions and loading conditions for a stiffened element in uniaxial compression

3.3.2 Influence of a single slotted hole

This study explores the influence of a single slotted hole on the elastic buckling stress of a stiffened element. The plate length L is varied from three to twenty-four times the slotted hole length, L_{hole} and the width of the plates are chosen to equal the flat web widths of four common Steel Stud Manufacturers Association (SSMA) structural studs listed in Table 3.1 (SSMA 2001). The slotted hole has dimensions of $h_{hole}=1.5$ in., $L_{hole}=4$ in., and $r_{hole}=0.75$ in. Holes are always centered transversely between the unloaded edges of the plate in this study. The plate thickness, t , is 0.0346 in.

Table 3.1 Plate widths corresponding to SSMA structural stud designs

SSMA Designation	h (in)	h_{hole}/h
250S162-33	2.28	0.66
362S162-33	3.40	0.44
600S162-33	5.78	0.26
800S162-33	7.78	0.19

The results of this study are presented in Figure 3.6 and demonstrate that as the length of a stiffened element increases relative to the length of the hole, the critical elastic buckling stress, f_{cr} , converges to a constant magnitude which is either equal to or lower than the buckling stress of a plate without a hole. The convergence occurs as L/L_{hole}

exceeds 5, suggesting that the influence of the hole is independent of the plate end conditions beyond this length.

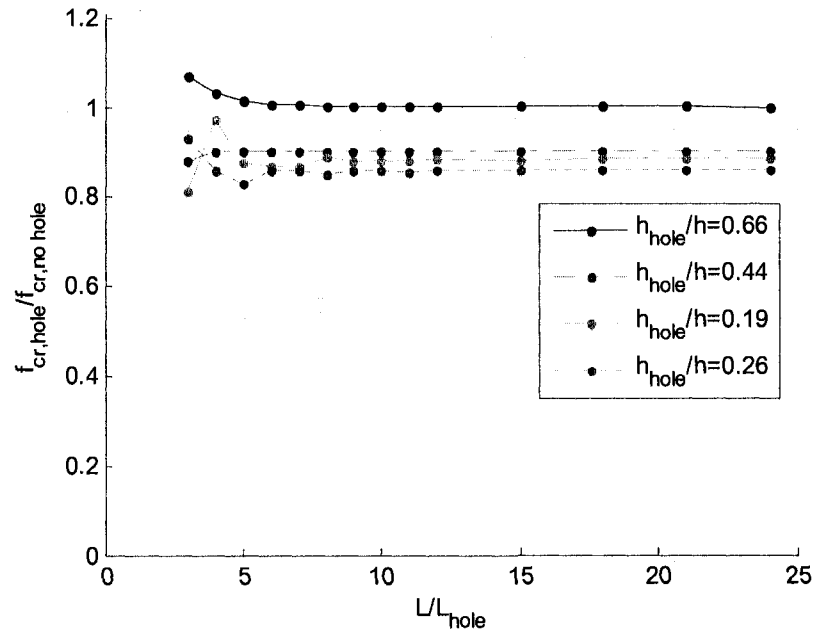


Figure 3.6 Influence of a slotted hole on the elastic buckling stress of a simply supported rectangular plate with varying length

When the hole is wide relative to the width of the plate ($h_{hole}/h=0.66$) and L/L_{hole} is small (see Figure 3.6), the elastic buckling stress of the plate with the hole is as much as 7 percent higher than for a plate without a hole. This increase in stress is explained by the buckled mode shapes in Figure 3.7. The plate with the hole in Figure 3.7a has a higher elastic buckling stress than the plate without the hole in Figure 3.7b because the natural pattern of buckled waves is modified by the hole. The buckled cells adjacent to the hole are shorter and therefore stiffer. The thin strips at the hole dampen buckling in this case because they have an axial stiffness higher than the buckled cells away from the hole.

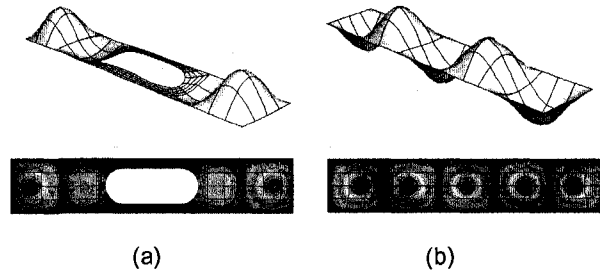


Figure 3.7 Comparison of buckled shape and displacement contours for a rectangular plate with $h_{hole}/h=0.66$ and $L/L_{hole}=3$, (a) with slotted hole and (b) without hole. Notice the change in length and quantity of buckled cells with the addition of a slotted hole.

As the plate length increases past $L/L_{hole}=5$ for the smallest plate width ($h_{hole}/h=0.66$), the buckling stress converges to that of a plate without a hole. Figure 3.8 demonstrates that for these long, slender stiffened elements the slotted hole dampens buckling near the hole but does not appreciably change the natural half-wavelength of the buckled cells as was observed for the shorter plates in Figure 3.7.

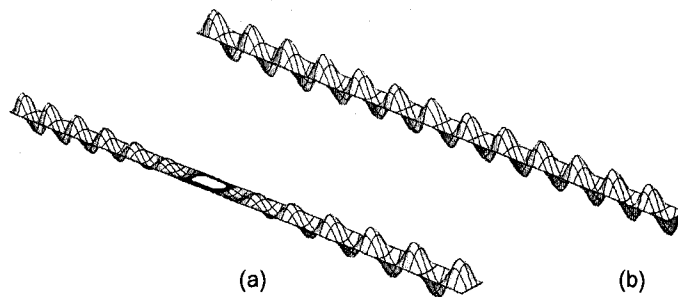


Figure 3.8 Buckled shape of a simply supported plate (a) with a slotted hole and (b) without a hole. $L=15L_{hole}$, $h_{hole}/h=0.66$. The slotted hole dampens buckling but does not significantly change the natural half-wavelength of the plate.

For plates with h_{hole}/h less than 0.66, the slotted hole causes a decrease in the elastic buckling stress which converges to a constant magnitude as the plate length exceeds $L/L_{hole}=5$. Figure 3.9a demonstrates that local buckling near the hole controls the

elastic buckling stress of these wider plates. The deformation at the hole results from the localized reduction in transverse plate bending stiffness.

As plate length decreases below $L/L_{hole} < 5$ and $h_{hole}/h = 0.19$, the influence of the hole on the critical elastic buckling stress fluctuates as shown in Figure 3.6. When the lowest elastic buckling mode shape results in an odd number of half-waves, the hole falls within the central half-wave and the critical elastic buckling stress decreases. For an even number of half-waves, the hole is located at the transition between two half sine-waves (because the hole is centered at the midlength of the plate), forcing the buckled cells to shorten and increasing the critical elastic buckling stress.

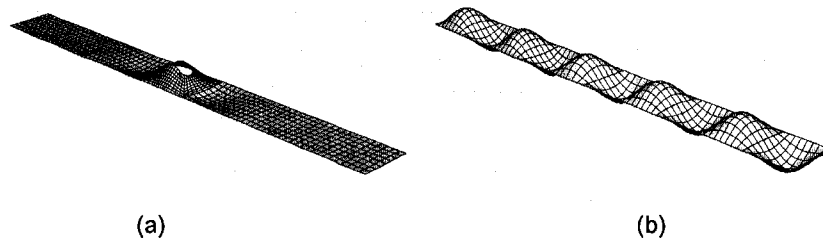


Figure 3.9 (a) Slotted hole causes local buckling ($h_{hole}/h=0.26$), compared to (b) buckled cells at the natural half-wavelength of the plate

3.3.3 Influence of slotted hole spacing

The previous study demonstrated that the elastic buckling behavior of a stiffened element with a single hole is sensitive to the size of the hole relative to the size of the plate. The focus now shifts to the influence of multiple slotted holes on the elastic buckling stress of a long fixed length stiffened element. In this study, slotted holes are added one by one to a stiffened element (where $L=24 L_{hole}$) such that the center-to-center spacing S varies as shown in Figure 3.10.

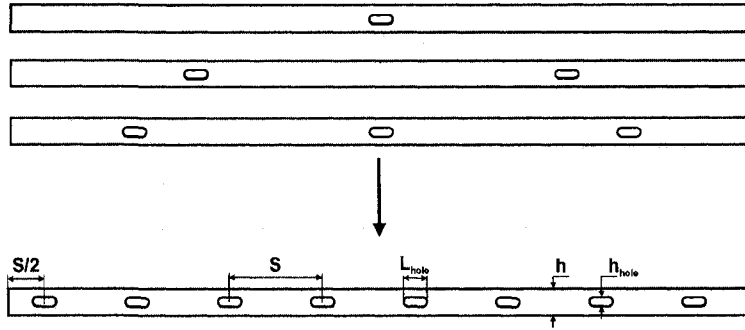


Figure 3.10 Definition of center-to-center dimension for the slotted holes

As hole spacing decreases, the elastic buckling stress in Figure 3.11 either increases or decreases depending on the ratio of hole width to plate width. When there are many large holes ($h_{hole}/h=0.66$, $S/L_{hole} < 4$), buckling is dampened at the holes and the buckled cells shorten their lengths to form between adjacent holes (see Figure 3.12 for buckled shape). The decrease in buckled half-wavelength causes an increase in elastic buckling stress of the plate.

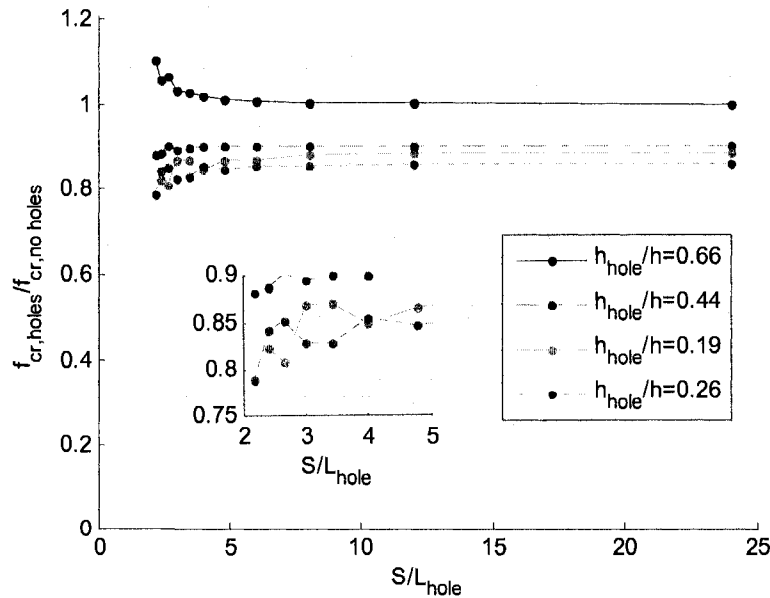


Figure 3.11 Influence of slotted hole spacing on the elastic buckling load of a long simply supported rectangular plate

When the holes are smaller relative to the plate width ($h_{hole}/h < 0.44$) and are spaced closely together ($S/L_{hole} < 4$), the local buckling influence of adjacent holes combine to sharply decrease the elastic buckling stress. The inset of Figure 3.11 highlights this reduction in elastic buckling stress for $h_{hole}/h=0.19$ and $h_{hole}/h=0.26$, and Figure 3.12 provides a summary of the associated buckled shapes. When hole spacing increases beyond $S/L_{hole}=5$, the elastic buckling stresses approach constant magnitudes for all plate widths considered, which is consistent with the trends presented in Figure 3.6. This observation is important from a design perspective because it serves as a rational basis for setting hole spacing limits in cold-formed steel members.

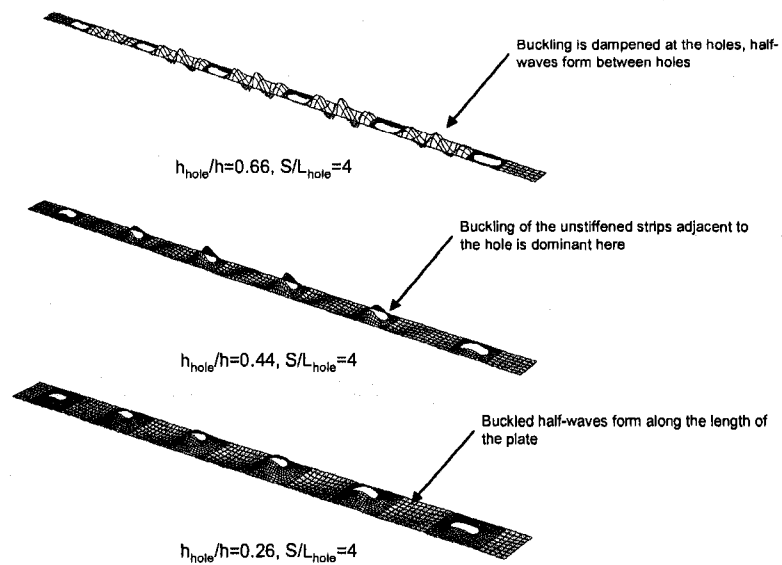


Figure 3.12 Comparison of buckled shapes for a long stiffened element ($L=24 L_{hole}$) with a slotted hole spacing of $S/L_{hole}=4$ and $h_{hole}/h=0.66, 0.44,$ and 0.26 .

Figure 3.12 highlights the two types of buckling modes that can occur in stiffened elements, plate buckling and unstiffened strip buckling. The influence of these buckling

modes on f_{cr} is reflected in Figure 3.13. The maximum decrease in f_{cr} occurs for a relatively small hole when compared to the plate width ($h_{hole}/h=0.30$) and lies at the transition between plate buckling, where axial stiffness of the buckled cells is reduced with the presence of holes, and unstiffened strip buckling. Unstiffened strip buckling occurs between $h_{hole}/h=0.30$ and $h_{hole}/h=0.55$ resulting in a relative increase in f_{cr} as the strips adjacent to the holes increase the axial stiffness of the plate. As h_{hole}/h increases past $h_{hole}/h=0.55$ the unstiffened strip adjacent to the hole becomes narrow and stiff, resulting in plate buckling away from the holes and an f_{cr} similar to a plate without a hole. (An increase in critical elastic buckling stress for large holes does not necessarily correspond to an increase in ultimate strength because the strength of the plate will be limited by the strength of the net cross-section.) This is another important observation that will be used when developing an elastic buckling prediction method for stiffened elements with holes in Section 3.3.4.

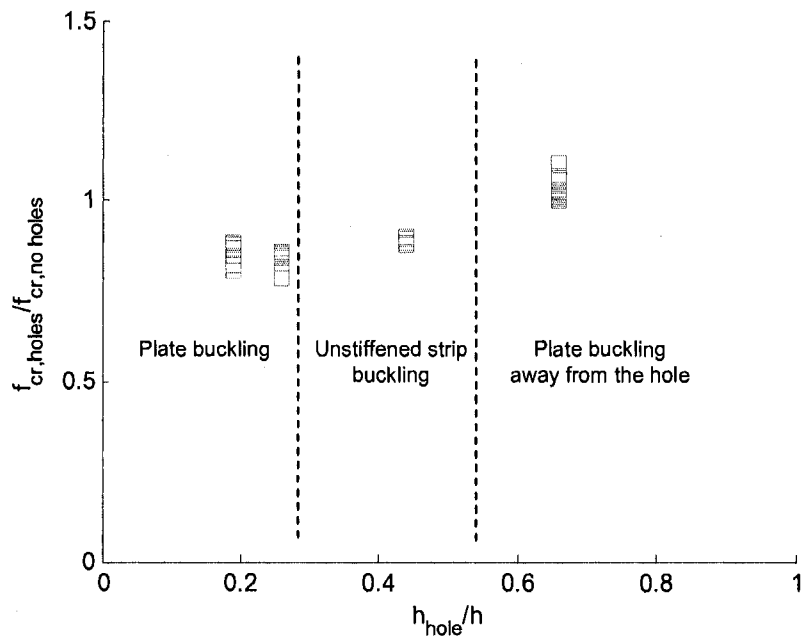


Figure 3.13 Variation in f_{cr} with increasing h_{hole}/h for a stiffened element correspond to buckling mode shapes (see Figure 3.12 for examples of plate buckling and unstiffened strip buckling mode shapes)

3.3.4 Approximate prediction method for use in design

Approximations for the critical elastic buckling stress of stiffened elements (e.g. column web or flange of a lipped C-section) with holes under uniaxial compression are developed in this section considering two elastic buckling states, buckling of the plate without hole influence and buckling of the unstiffened strips adjacent to the hole. The proposed prediction method is validated with thin shell finite element eigenbuckling analyses for a variety of hole shapes, sizes, and spacings. Mandatory dimensional tolerances on the prediction method are explicitly defined, and optional dimensional limits, marked with an asterisk (*), are provided to avoid excessive conservatism.

3.3.4.1 Definitions and assumptions

Figure 3.2 defines the plate and hole dimension notation used in the element prediction method, including the hole spacing S , plate width h , and hole length and hole width, L_{hole} and h_{hole} . δ_{hole} is the offset distance of a hole measured from the centerline of the plate. The elastic buckling prediction method for a stiffened element is developed assuming a long plate loaded uniaxially and simply-supported on all four sides with evenly spaced holes. A summary of all prediction method equations is provided in Appendix D.

3.3.4.2 Prediction Equations

The elastic buckling stress of a stiffened element with holes is approximated as

$$f_{crl} = \min[f_{cr}, f_{crh}]. \quad (3.1)$$

The critical elastic buckling stress for plate buckling (without hole influence) is

$$f_{cr} = k \frac{\pi^2 E}{12(1-\nu^2)} \left(\frac{t}{h}\right)^2, \quad (3.2)$$

where k is commonly taken equal to 4 when considering long rectangular plates ($L/h > 4$).

When elastic buckling of the stiffened element is governed by the buckling of an unstiffened strip adjacent to the hole, the critical elastic buckling stress of the governing unstiffened strip is:

$$f_{crh,net} = \min[f_{crA}, f_{crB}] \quad (3.3)$$

$$f_{cri} = k_i \frac{\pi^2 E}{12(1-\nu^2)} \left(\frac{t}{h_i} \right)^2 \text{ and } i = A \text{ or } B \quad (3.4)$$

The plate buckling coefficient k_i for unstiffened strips A and B are approximated by (Yu and Schafer 2007):

$$\text{for } L_{hole}/h_i \geq 1, \quad k_i = 0.425 + \frac{0.2}{(L_{hole}/h_i)^{0.95} - 0.6}, \quad (3.5)$$

$$\text{for } L_{hole}/h_i < 1, \quad k_i = 0.925, \text{ and } i = A \text{ or } B. \quad (3.6)$$

Eq. (3.5) accounts for the length of the unstiffened strip. As hole length shortens relative to the unstiffened strip width, k_i increases. This is an improvement over AISI-S100 which conservatively assumes the lowerbound $k=0.425$ regardless of hole length. When L_{hole}/h_i is less than 1, k may be conservatively assumed equal to 0.925 via Eq. (3.6) or calculated directly by solving the classical stability equations for an unstiffened element (Timoshenko 1961).

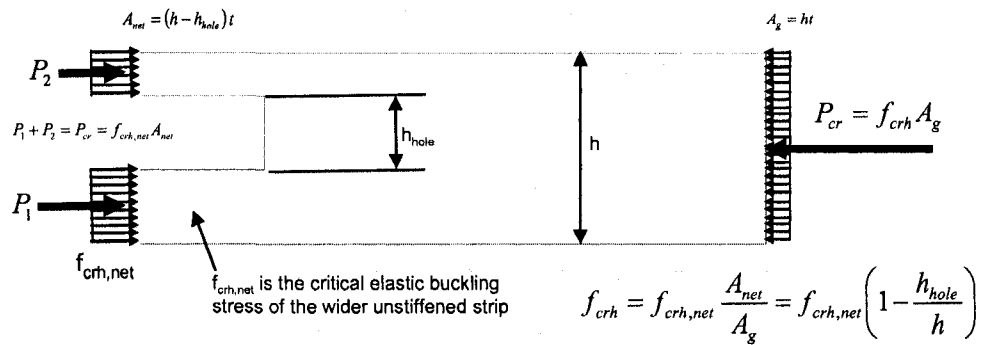


Figure 3.14 Unstiffened strip elastic buckling stress conversion from the net to the gross section

To compare the buckling stress from the unstiffened strip ($f_{crh,net}$) to that of the entire plate (f_{cr}) equilibrium between the net and gross section must be considered, as shown in Figure 3.14 and provided in the following:

$$f_{crh} = f_{crh,net} (1 - h_{hole}/h). \quad (3.7)$$

3.3.4.3 Verification and equation limits

3.3.4.3.1 Holes centered transversely in plate

Thin shell finite element eigenbuckling analysis in ABAQUS, as described in Section 3.2, is employed here to verify the accuracy of the approximate prediction method in Section 3.3.4.2. The boundary and loading conditions assumed for the stiffened element are described in Figure 3.5. The length of the slotted hole, L_{hole} , width of the plate h , the shape of hole (slotted, circular, square), the hole spacing S , length of the plate L , and plate thickness t are varied in the analyses. The plate and hole dimensions as well as the ABAQUS critical elastic buckling stress, f_{crh} , for the 145 models considered, are provided in Appendix B (the eigenbuckling results from the studies in Section 3.3.2 and Section 3.3.3 are included in the 145 models). The parametric ranges in this study are summarized for each hole type in Table 3.2.

Hole type		h_{hole}/h	S/L_{hole}	S/h	h/t	# of models
Slotted	Min	0.10	1.7	1.2	21	131
	Max	0.70	24.0	42.2	434	
Circular	Min	0.10	13.3	1.3	62	7
	Max	0.70	13.3	9.3	434	
Square	Min	0.10	13.3	1.3	62	7
	Max	0.70	13.3	9.3	434	

The results of the ABAQUS eigenbuckling analyses are compared to the stiffened element prediction method in Figure 3.15 and Figure 3.16. Figure 3.15 demonstrates that as hole spacing S becomes small relative to the plate width h , the prediction method is not always accurate. As hole spacing decreases, holes begin to coincide with the local buckling half-wavelengths (which have a length of h) and the influence of the individual holes act cumulatively to decrease the axial stiffness of the plate. A similar loss in stiffness is observed in Figure 3.16 as hole spacing decreases relative to hole length. From these observations, the following limits are imposed on the prediction method:

$$\frac{S}{h} \geq 1.5, \quad (3.8)$$

$$\frac{S}{L_{hole}} \geq 2. \quad (3.9)$$

If the parameter limit in Eq. (3.9) is substituted into Eq. (3.8), a third dimensional limit is automatically imposed:

$$\frac{L_{hole}}{h} \leq 0.75 \quad (3.10)$$

Eq. (3.10) prevents the hole length from being too long relative to the half-wavelength of the plate. The mean and standard deviation of the ABAQUS to predicted ratio for the stiffened elements within the limits of Eq. (3.8) and Eq. (3.9) are 1.02 and 0.04 respectively, demonstrating that the prediction method is viable.

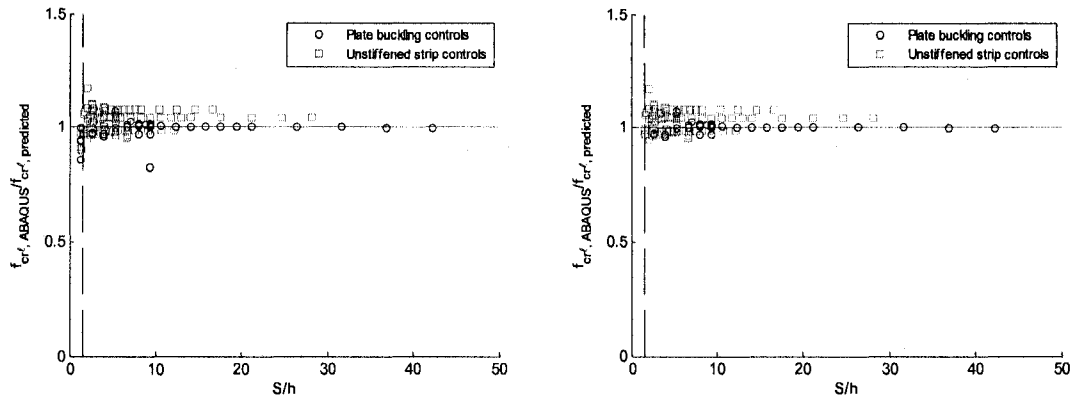


Figure 3.15 Accuracy of stiffened element prediction method as a function of hole spacing S to plate width h (a) without and (b) with the dimensional limits in Eq. (3.8) and Eq.(3.9)

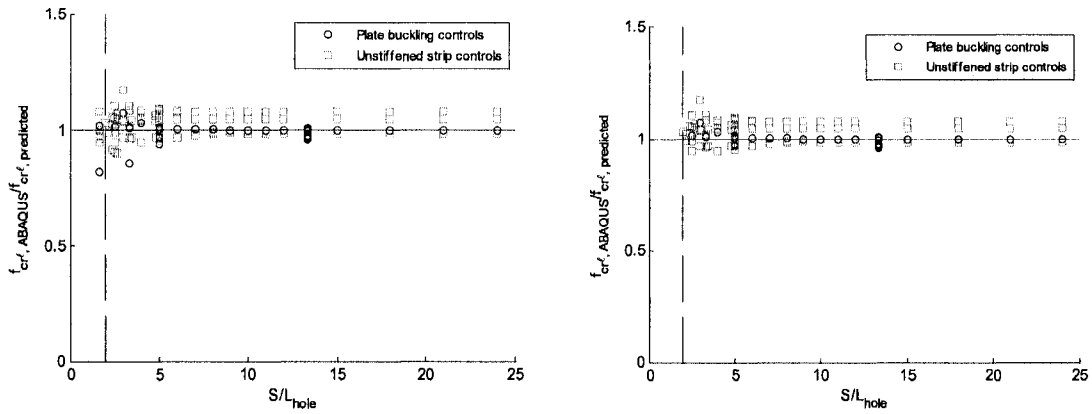


Figure 3.16 Accuracy of stiffened element prediction method as a function of hole spacing S to length of hole L_{hole} (a) without and (b) with the dimensional limits in Eq. (3.8) and Eq.(3.9)

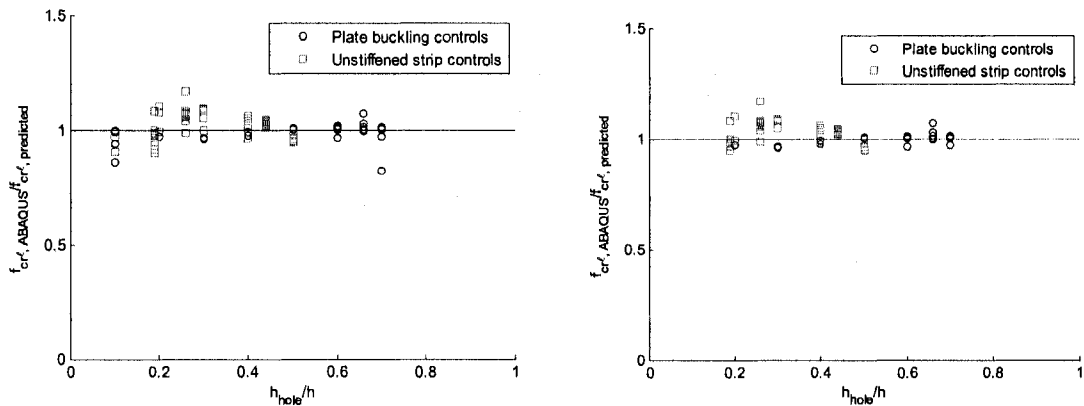


Figure 3.17 Accuracy of the stiffened element prediction method as a function of hole width h_{hole} to plate width h (a) without and (b) with the dimensional limits in Eq. (3.8) and Eq.(3.9)

As hole width increases relative to plate width in Figure 3.17, the controlling buckled state transitions from buckling of the unstiffened strip adjacent to plate buckling. The strips of web material adjacent to the holes have a higher axial stiffness than the sections of the plate without holes, causing plate buckling to occur between the holes as shown in Figure 3.18.

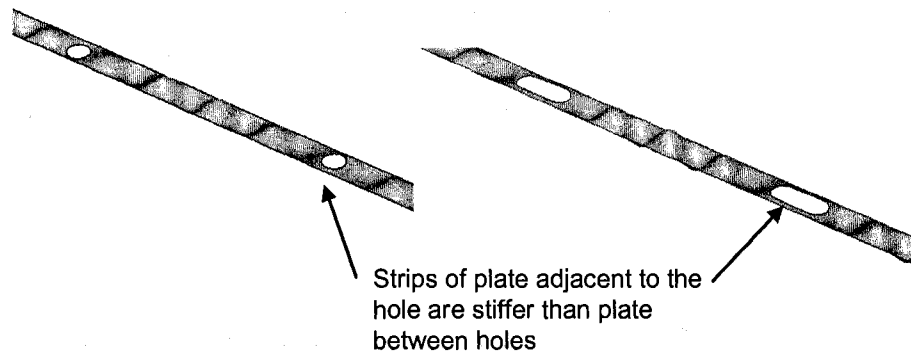


Figure 3.18 For plates where the unstiffened strip is narrow compared to the plate width, plate buckling occurs between the holes.

As the hole width becomes small relative to plate width, the unstiffened strip buckled state is predicted by the simplified method for slotted holes, although the actual behavior is a combination of plate buckling and local buckling at the holes, as shown in Figure 3.19. The assumption of unstiffened strip buckling when the slotted hole width is small relative to plate width is conservative, with a maximum ABAQUS to predicted ratio of 1.16 when h_{hole}/h is in the range of 0.30. Figure 3.19 also demonstrates that plate buckling dominates over unstiffened strip buckling for stiffened elements with square and circular holes. The prediction method identifies this elastic buckling behavior and accurately predicts f_{crit} as shown in Figure 3.20, where stiffened element results containing just square or just circular holes are plotted.

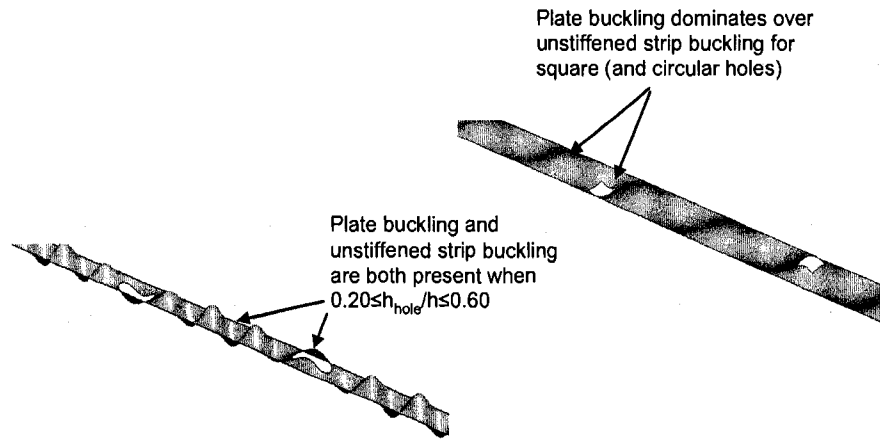


Figure 3.19 Plate buckling and unstiffened strip buckling may both exist for a plate with holes. These modes are predicted conservatively as unstiffened strip buckling.

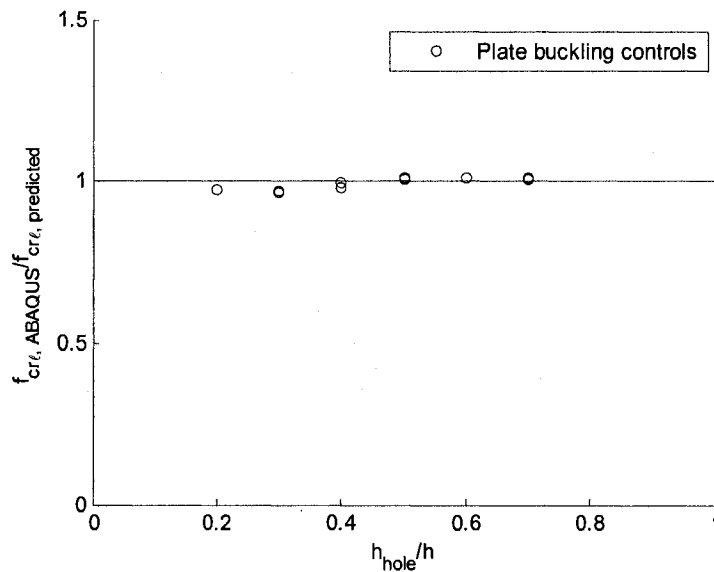


Figure 3.20 Accuracy of prediction method for stiffened elements with square or circular holes as a function of hole width h_{hole} to plate width h .

3.3.4.3.2 Offset holes

43 additional ABAQUS eigenbuckling analyses were performed to evaluate the accuracy of the simplified prediction method in Section 3.3.4.2, but now with transversely offset holes. For these models, the hole offset from the centerline of the

plate, δ_{hole} , and the plate width, h , were varied. All plate models in this study have regularly spaced slotted holes ($S=20$ in.) and constant plate length, L , of 100 in. The boundary and loading conditions assumed for the stiffened element are described in Figure 3.5. The model dimensions and critical elastic buckling stress, f_{cr} , for the 43 models considered, are summarized in Appendix B. h_{strip} is the widest unstiffened strip, either h_A and h_B . The parametric ranges for this study are summarized in Table 3.3.

Table 3.3 Parameter range for stiffened element verification study with offset holes.

Hole type		h_{hole}/h	S/L_{hole}	S/h	h/t	δ_{hole}/h	# of models
Slotted	Min	0.10	5.0	1.3	62	0.000	43
	Max	0.70	5.0	9.3	434	0.375	

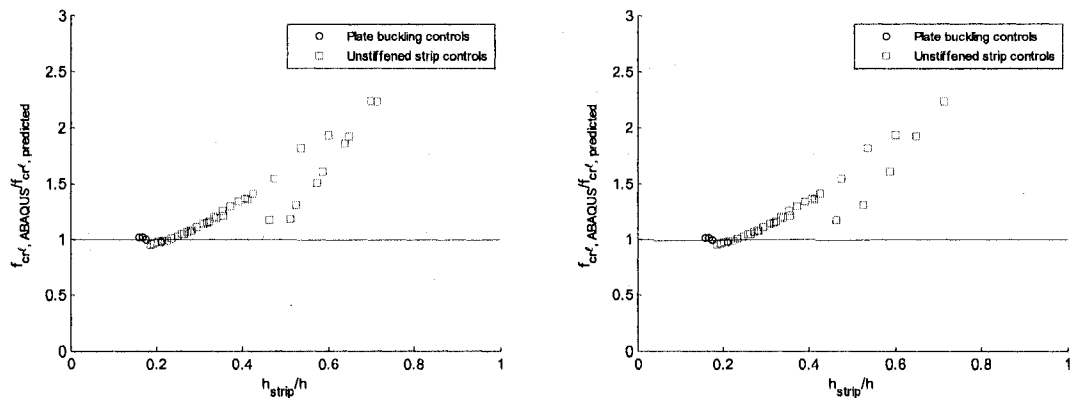


Figure 3.21 Accuracy of the stiffened element elastic buckling prediction method as a function of unstiffened strip width h_{strip} versus plate width h for offset holes (a) without and (b) with the dimensional limits in Eq. (3.8) and Eq.(3.9)

The ABAQUS critical elastic buckling stress results are compared to the prediction method in Figure 3.21, and demonstrate that the prediction method is conservative and that the accuracy of the method improves as h_{strip} decreases relative to the plate width h and hole length L_{hole} . The unstiffened strip buckled state is predicted to control for most of the plate models, primarily because the shift in hole location results in a wider

unstiffened strip with less axial stiffness than that provided by the plate material between holes. When the plate is relatively wide compared to the width of the hole and the hole is shifted near the edge of the plate as shown in Figure 3.22, the predictions can be very conservative. The wide unstiffened strip is not a good approximation of the actual behavior of the plate in this case. Prediction accuracy varies with hole offset, δ_{hole} , as shown in Figure 3.23a, and is most conservative as the hole offset becomes large relative to the plate width h . To avoid overly conservative results, the following limit on hole offset δ_{hole} is proposed for stiffened elements:

$$\frac{\delta_{hole}}{h} \leq 0.15^* \quad (3.11)$$

The mean and standard deviation of the ABAQUS to predicted ratio for the data within the dimensional limits of Eq. (3.8), Eq. (3.9), and Eq. (3.11) are 1.14 and 0.15 respectively (also see Figure 3.23b).

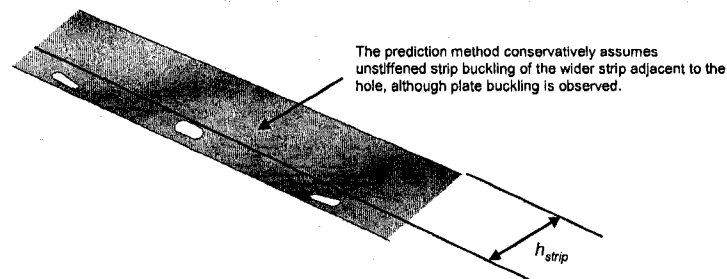


Figure 3.22 Holes at the edge of a wide stiffened plate reduce the axial stiffness (and critical elastic buckling stress) but do not change the buckled shape.

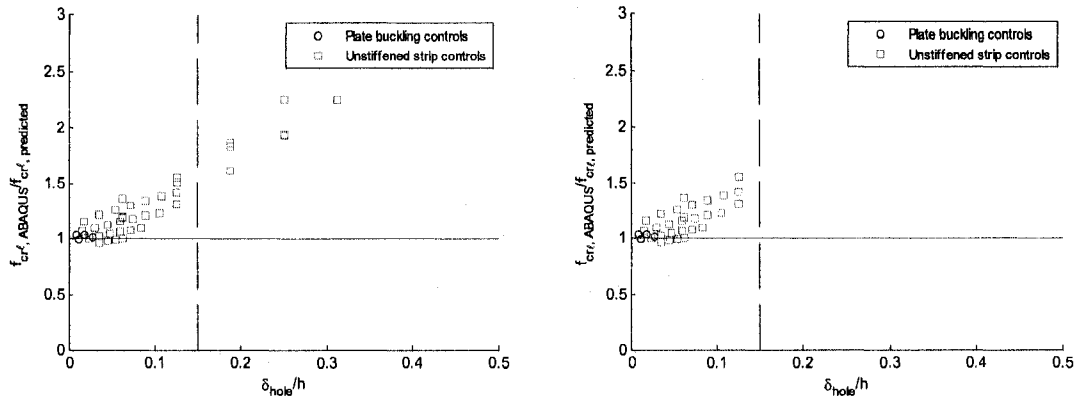


Figure 3.23 Accuracy of the stiffened element elastic buckling prediction method as a function of hole offset δ_{hole} versus plate width h for offset holes (a) without and (b) with the dimensional limits in Eq. (3.8), Eq.(3.9), and Eq. (3.11)

3.4 Stiffened element in bending

3.4.1 Boundary and loading conditions

The stiffened element is modeled with simply-supported boundary conditions and loaded with a bending compressive stress distribution as shown in Figure 3.24. The location of the neutral axis about which bending occurs, Y , is measured from the compressed edge of the plate.

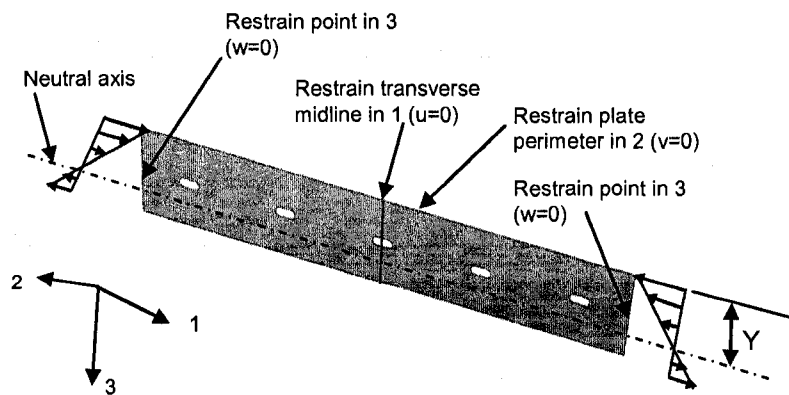


Figure 3.24 Boundary and loading conditions for a stiffened element in bending

3.4.2 Influence of transversely-centered slotted holes

Shell finite element eigenbuckling models of stiffened elements with regularly spaced slotted holes are evaluated in this study. The bending stress distribution is symmetric about the transverse centerline of the plate ($Y=0.50h$) for all models. The slotted holes are centered transversely in the plate ($\delta_{hole}=0$). The plate and hole dimensions and the critical elastic buckling stress, f_{cr} , for the 28 models considered, are summarized in Appendix B. The parametric ranges for this study are summarized in Table 3.4.

Table 3.4 Parameter ranges considered for stiffened elements in bending with holes.

Hole type		h_{hole}/h	S/L_{hole}	S/h	h/t	Y/h	# of models
Slotted	Min	0.10	1.67	1.33	61.93	0.50	28
	Max	0.70	5.00	9.33	433.53	0.50	

Figure 3.25 highlights the influence of hole width to plate width on stiffened elements in bending. As h_{hole}/h increases, the buckling mode transitions from plate buckling (similar to a plate without a hole) to buckling of the compressed unstiffened strip adjacent to the hole. The buckled half-wavelength of a plate in bending is between $0.25h$ to $0.50h$, which results in a shortened half-wavelength of the unstiffened strip (often less than the length of the hole) when compared to the equivalent unstiffened strip buckling mode for stiffened elements in uniaxial compression (See Section 3.3).

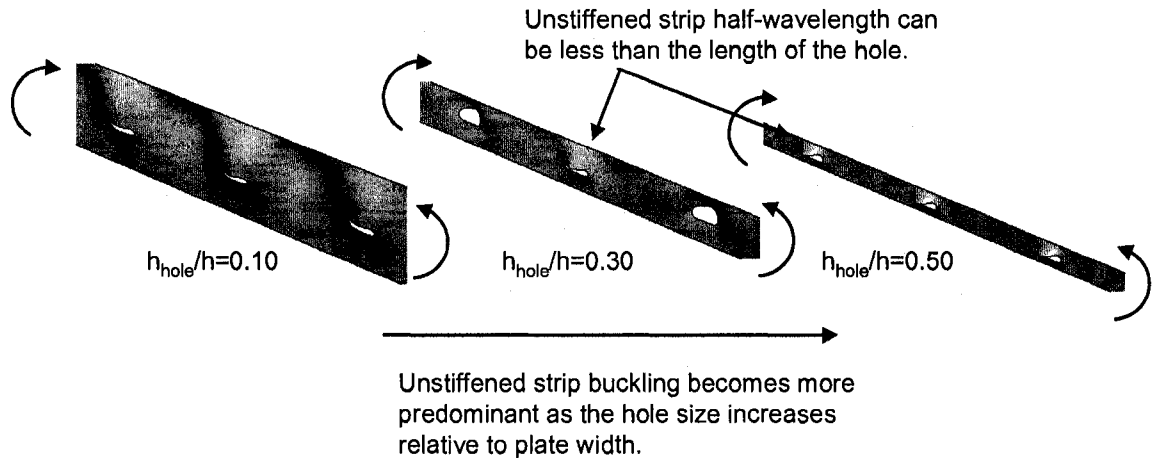


Figure 3.25 Stiffened plates loaded with a linear bending stress gradient exhibit buckling of the unstiffened strip adjacent to the hole in the compression region of the plate.

The maximum reduction in critical elastic buckling stress occurs in the range of $h_{hole}/h=0.30$ as shown in Figure 3.26a. This result is consistent with the elastic buckling results for stiffened plates under axial compression (See Figure 3.13). The elastic buckling behavior of stiffened elements in bending are different than in pure compression though as h_{hole}/h exceeds 0.50. Unstiffened strip buckling continues to dominate for plate bending (with an associated reduction in f_{cr}) while plate buckling away from the hole controls for uniaxially compressed plates (with minimal influence on f_{cr} even for very large holes). This distinction between compression (columns) and bending (beams) elastic buckling behavior of stiffened elements is important when considering how to approximate elastic buckling behavior. f_{cr} decreases as hole spacing becomes small relative to hole length as shown in Figure 3.26b, identifying S/L_{hole} as another important parameter when predicting elastic buckling of stiffened elements in bending (as it is for stiffened elements in compression, See Section 3.3).

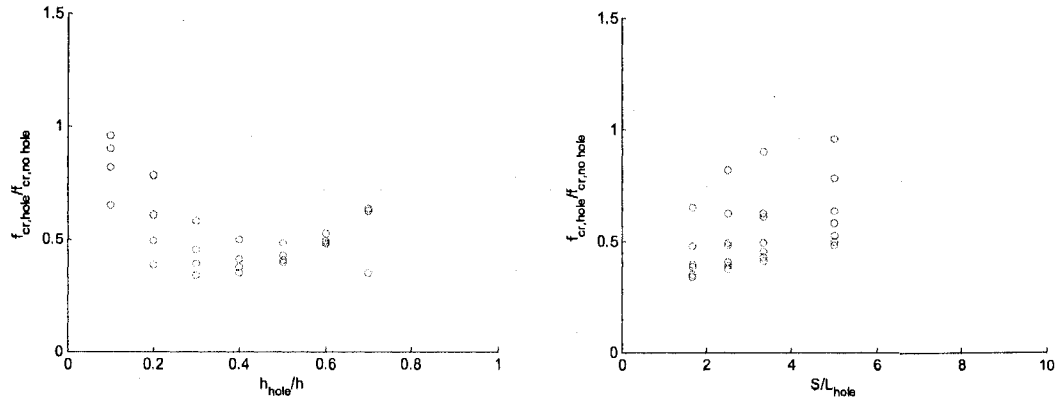


Figure 3.26 Influence of slotted holes on critical elastic buckling stress f_{cr} of stiffened elements in bending as a function of (a) hole size relative to plate width and (b) hole spacing as a function of hole length.

3.4.3 Influence of offset slotted holes

3.4.3.1 Neutral axis location at $Y=0.50h$

Shell finite element eigenbuckling models of stiffened elements with regularly spaced offset slotted holes are evaluated in this study. The bending stress distribution is symmetric about the transverse centerline of the plate ($Y=0.50h$) for all models. The hole offset, δ_{hole} , ranges from $-0.375h$ to $+0.375h$, where a positive shift moves the holes into the compression region of the plate. The plate and hole dimensions and the critical elastic buckling stress, f_{cr} , for the 92 models considered, are summarized in Appendix B. The parameter range considered in this study is provided in Table 3.5.

Table 3.5 Study parameter limits for stiffened element in bending ($Y/h=0.50$) with offset holes

Hole type		h_{hole}/h	S/L_{hole}	S/h	h/t	Y/h	δ_{hole}/h	# of models
Slotted	Min	0.10	5.00	1.33	61.93	0.50	-0.375	92
	Max	0.70	5.00	9.33	433.53	0.50	0.375	

The presence of holes in the compression region of a stiffened element in bending ($Y=h/2$) decreases the critical elastic buckling stress when compared to a plate without holes as shown in Figure 3.27. Depending upon the width of the unstiffened strip "A"

in the compressed region of the plate and the unstiffened strip “B” in the tensile region of the plate (see Figure 3.3 for definitions) relative to hole depth h , unstiffened strip buckling may occur above the hole, below the hole, or above and below the hole. f_{cr} varies with the transverse position of the holes in the plate (characterized as the width of unstiffened strip “A”, h_A) in Figure 3.27. The trends in f_{cr} can be related to the elastic buckling modes in Figure 3.28. If the holes are located in the tensile region of the stiffened element, the buckled mode shape (and f_{cr}) are unchanged when compared to a stiffened element without holes. The relationship between these buckled mode shapes and trends in f_{cr} will be used in Section 3.4.4 when developing an approximate elastic buckling prediction method for stiffened elements in bending.

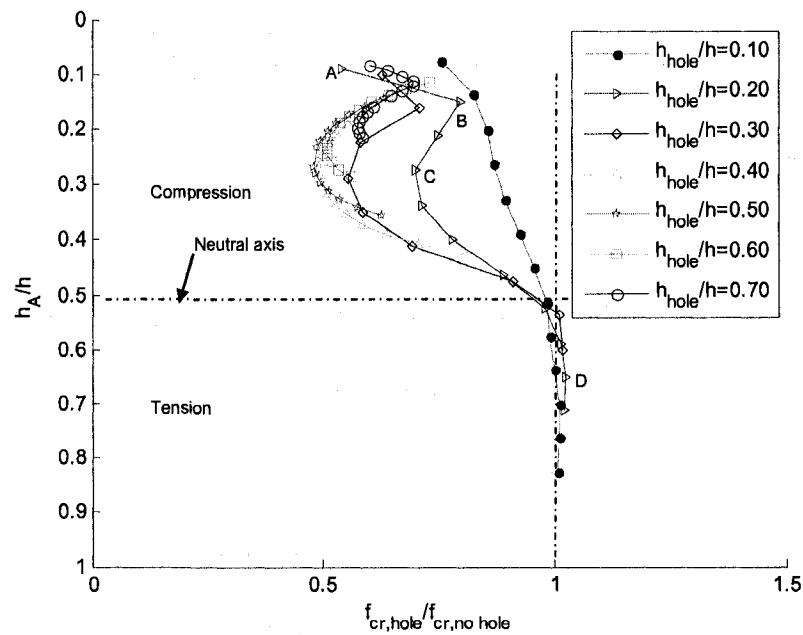


Figure 3.27 Hole location influence on critical elastic buckling stress f_{cr} for a stiffened plate in bending ($Y=0.50h$) (Buckled mode shapes corresponding to A, B, C, and D are provided in Figure 3.28.)

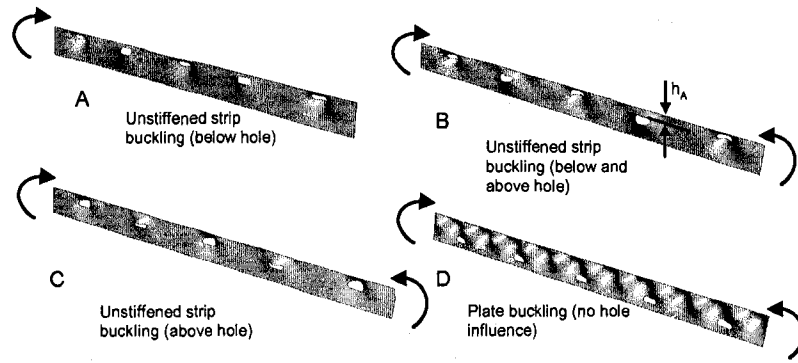


Figure 3.28 The buckled mode shape changes as slotted holes move from the compression region to the tension region of a stiffened element in bending ($t_{hole}/t=0.20$).

3.4.3.2 Neutral axis location at $Y=0.75h$

The neutral axis in the shell finite element eigenbuckling models from Section 3.4.3.2 is now modified to $Y=0.75h$. The trends in f_{cr} in Figure 3.29 are similar to those observed in Figure 3.27 ($Y=0.50h$). Elastic buckling of the unstiffened strip below the holes occurs when the hole is close to the compressed edge. The mode shape transitions to unstiffened strip buckling above the holes as the hole offset increases toward the tensile region of the plate. The plate and hole dimensions and the critical elastic buckling stress, f_{cr} , for the 92 models considered here, are summarized in Appendix B.

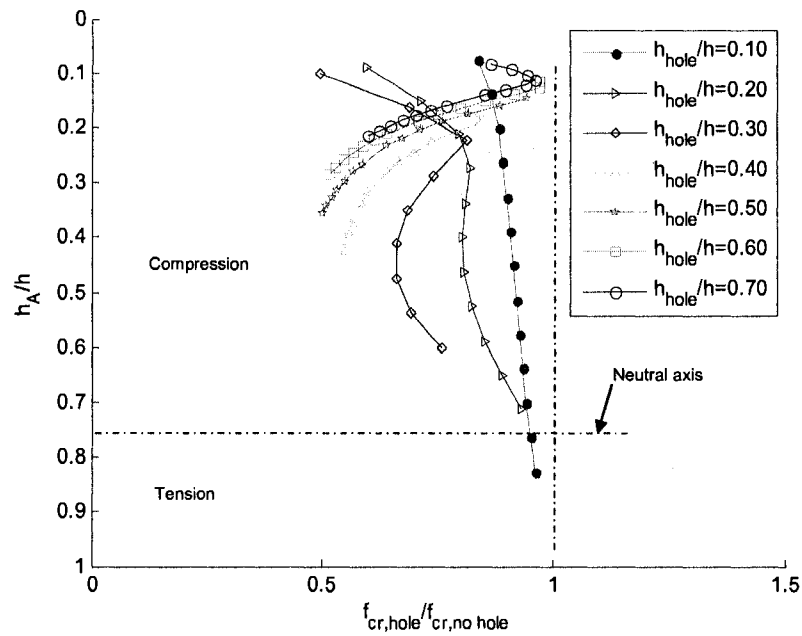


Figure 3.29 Hole location influence on critical elastic buckling stress f_{cr} for a stiffened plate in bending ($Y=0.75h$)

3.4.4 Approximate prediction method for use in design

In the previous section unique elastic buckling modes were identified for a stiffened element in bending with holes. Buckling of the unstiffened strip between the hole and the compressed edge of the plate (unstiffened strip "A") or between the hole and the tension edge of the plate (unstiffened strip "B") may occur depending upon the transverse location of the hole in the plate, the width of the hole (h_{hole}) relative to the depth of the plate (h), and the location of the plate neutral axis (Y). If the hole is completely contained within the tension region of the plate then the hole has a minimal influence on elastic buckling and the critical elastic buckling stress, f_{cr} , remains unchanged. These observations can be used to define an approximation for the critical elastic buckling stress of a stiffened element with holes in bending:

$$f_{crl} = \min[f_{cr}, f_{crh}] \quad (3.12)$$

The critical elastic buckling stress for a stiffened element in bending (without the influence of holes), f_{cr} , may be determined with Eq. (3.2) where the buckling coefficient k is calculated with AISI-S100-07 Eq. B2.3-2 (AISI-S100 2007):

$$k = 4 + 2(1 + \psi)^3 + 2(1 + \psi) \quad (3.13)$$

and ψ is the absolute value of the ratio of tensile stress to compressive stress applied to the stiffened element, i.e.:

$$\psi = |f_2 / f_1| = (h - Y) / Y \quad (3.14)$$

When elastic buckling of the stiffened element is governed by the buckling of an unstiffened strip adjacent to a hole, the critical elastic buckling stress is:

$$f_{crh,net} = \min[f_{crA}, f_{crB}] \quad (3.15)$$

Consideration of unstiffened strip "A" is required only if $h_A < Y$, i.e., at least a portion of the hole must lie in the compression region of the stiffened element. If that condition is met the elastic buckling stress for strip "A" is:

$$f_{crA} = k_A \frac{\pi^2 E}{12(1 - \nu^2)} \left(\frac{t}{h_A} \right)^2 \quad (3.16)$$

The plate buckling coefficient for the unstiffened strip "A" is approximated as

$$k_A = \frac{0.578}{\psi_A + 0.34} + \frac{2.70 - 1.76\psi_A}{0.024\psi_A + 0.035 + (L_{hole}/h_A)^2}, \text{ and } \psi_A = \frac{Y - h_A}{Y} \quad (3.17)$$

Eq. (3.17) is a modification of AISI-S100-07 Eq. B3.3-2 (AISI-S100 2007) This expression accounts for the gradient of the compressive stress distribution and the aspect ratio of

the unstiffened strip (see Appendix C for derivation). The equation for ψ_A is derived in Figure 3.30.

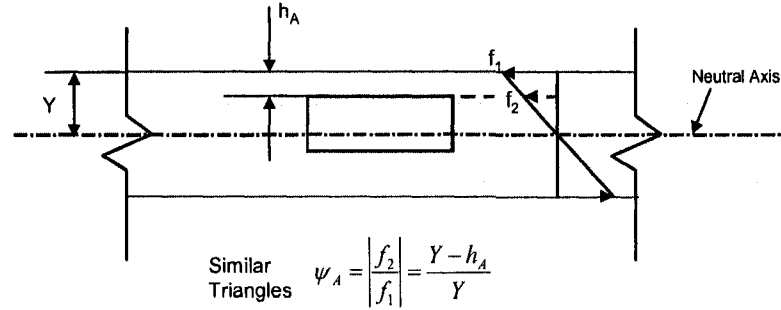


Figure 3.30 Derivation of stress ratio ψ_A for unstiffened strip "A".

Consideration of unstiffened strip "B" is required only if $h_A+h_{hole}<Y$, i.e., only when the entire hole lies within the compressed region of the plate. For this case the buckling stress of the unstiffened strip, converted to a stress at the compressed edge, is found as:

$$f_{crB} = k_B \frac{\pi^2 E}{12(1-\nu^2)} \left(\frac{t}{h_B} \right)^2 \left(\frac{Y}{Y-h_A-h_{hole}} \right), \quad (3.18)$$

where the final term in Eq. (3.18) converts the buckling stress from the edge of unstiffened strip "B" to the edge of unstiffened strip "A" as shown in Figure 3.31 so that the two stresses (f_{crA} and f_{crB}) may be compared in Eq. (3.15) to determine the minimum.

The plate buckling coefficient for the unstiffened strip "B" is approximated as:

for $L_{hole}/h_B > 2$

$$k_B = 0.340\psi_B^2 + 0.100\psi_B + 0.573, \quad (3.19)$$

for $L_{hole}/h_B \leq 2$

$$k_B = \frac{0.38\psi_B^{1.8} + 1.6\left(\frac{h_B}{L_{hole}}\right)^2 + 0.49}{-0.20\psi_B^{0.3} + \left(\frac{h_B}{L_{hole}}\right)^{0.1} + 0.14}, \quad (3.20)$$

and the ratio of tension to compressive stresses (derived in Figure 3.31) is:

$$\psi_B = \frac{h - Y}{Y - h_A - h_{hole}}, \quad 0 \leq \psi_B \leq 10. \quad (3.21)$$

The plate buckling coefficient k_B is applicable over a larger range of ψ_B than AISI-S100-07 Eq. B3.2-5 (AISI-S100 2007) and accounts for the increase in k_B as the unstiffened strip aspect ratio tends to zero (i.e., a wide, short strip resulting from a small hole). Refer to Appendix C for the derivation of k_B .

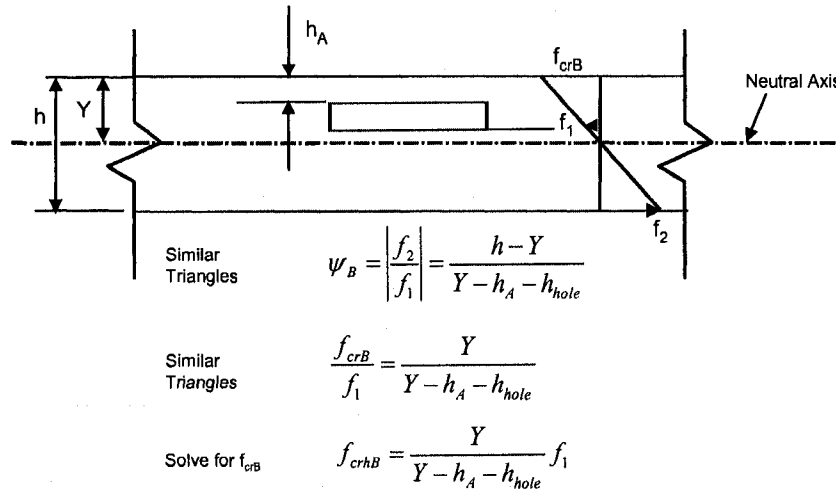


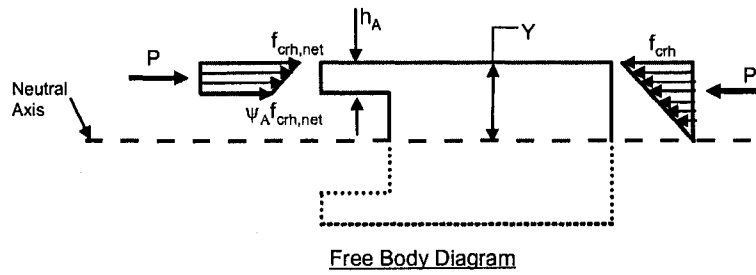
Figure 3.31 Derivation ψ_B and conversion of the compressive stress at the edge of unstiffened strip "B" to the stress f_{crB} at the edge of the plate

Conversion to the gross section for the comparison of stresses in Eq. (3.12) requires that:

$$\text{for } h_A + h_{hole} \geq Y, \quad f_{crh} = f_{crh,net} \left(1 + \psi_A\right) \frac{h_A}{Y}, \quad (3.22)$$

$$\text{for } h_A + h_{hole} < Y, \quad f_{crh} = f_{crh,net} \left[1 - \frac{h_{hole}}{Y} \left(2\psi_A - \frac{h_{hole}}{Y} \right) \right]. \quad (3.23)$$

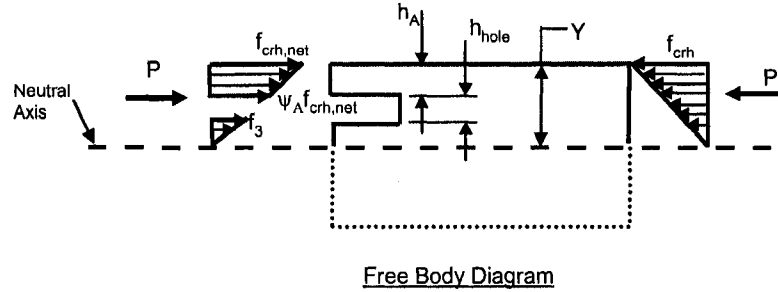
The conversion from $f_{crh,net}$ at the net section of the plate to f_{crh} on the gross cross-section is obtained with a similar method to that described in Figure 3.14 for stiffened elements in uniaxial compression; the total compressive force at the net and gross cross-sections are assumed in equilibrium as shown in Figure 3.32 and Figure 3.33. A summary of all prediction method equations is provided in Appendix D.



$$\text{Force Equilibrium} \quad P = \left(\frac{f_{crh,net} + \psi_A f_{crh,net}}{2} \right) h_A t = \frac{1}{2} f_{crh} Y t$$

$$\text{Solve for } f_{crh} \quad f_{crh} = f_{crh,net} (1 + \psi_A) \frac{h_A}{Y}$$

Figure 3.32 Derivation of f_{crh} for the case when $h_A + h_{hole} \geq Y$ (when the hole is located partially in the compressed region and partially in the tension region of the plate)



Force Equilibrium
$$P = \frac{1}{2} Y f_{cr,net} t - \left(\frac{\psi_A f_{crh,net} + f_3}{2} \right) h_{hole} t = \frac{1}{2} f_{crh} Y t$$

Define f_3 using similar triangles
$$\frac{f_3}{f_{crh,net}} = \frac{Y - h_A - h_{hole}}{Y} = \psi_A - \frac{h_{hole}}{Y}$$

Substitute f_3 and solve for f_{crh}
$$f_{crh} = f_{crh,net} - \frac{h_{hole}}{Y} \left(\psi_A f_{crh,net} + \left(\psi_A - \frac{h_{hole}}{Y} \right) f_{crh,net} \right)$$

Simplify
$$f_{crh} = f_{crh,net} \left[1 - \frac{h_{hole}}{Y} \left(2\psi_A - \frac{h_{hole}}{Y} \right) \right]$$

Figure 3.33 Derivation of f_{crh} for the case when $h_A + h_{hole} < Y$ (hole lies completely in the compressed region of the plate).

3.4.5 Verification and parameter limits

The elastic buckling prediction method for stiffened elements in bending is now evaluated with the ABAQUS eigenbuckling results presented in Section 3.4.2 and Section 3.4.3. The viability of the method is examined for evenly spaced slotted holes centered transversely or offset in a plate. Parameter limits on the prediction method, required when formalizing the method for use in design, are also identified.

ABAQUS results are compared to predictions in Figure 3.34a and Figure 3.38a. Figure 3.34a demonstrates that the simplified method underpredicts the elastic buckling stress as aspect ratio of the unstiffened strip "A" increases. A dimensional tolerance is imposed to avoid unconservative predictions:

$$\frac{L_{hole}}{h_A} \leq 10. \quad (3.24)$$

Eq. (3.24) also serves as a practical limit on the slenderness of an unstiffened strip, and therefore is also imposed on the unstiffened strip "B":

$$\frac{L_{hole}}{h_B} \leq 10. \quad (3.25)$$

The prediction method becomes increasingly conservative as h_A/Y approaches unity as shown in Figure 3.35a. When only a small portion of the hole exists in the compressed region of the plate, the observed buckling mode is more consistent with plate buckling than unstiffened strip buckling as predicted by the simplified method (See Figure 3.28, picture D). A dimensional limit is suggested to prevent excessive conservatism in this case:

$$\frac{h_A}{Y} \leq 0.6 * \quad (3.26)$$

The hole spacing limits defined in Section 3.3.4.3 for stiffened elements in uniaxial compression are also considered here for a stiffened element in bending. The prediction accuracy degrades when hole spacing S approaches the plate width h as shown in Figure 3.36a. Predictions can also be unconservative when S is 2 to 3 times the length L_{hole} as shown in Figure 3.37a. With the limits from Eq. (3.8), Eq. (3.9), Eq. (3.24), Eq. (3.25), and Eq. (3.26) imposed, the method is observed to be viable predictor over a wide range of h_{hole}/h as shown in Figure 3.38b. The mean and standard deviation of the ABAQUS to predicted ratio within the imposed dimensional limits are 1.22 and 0.11 respectively.

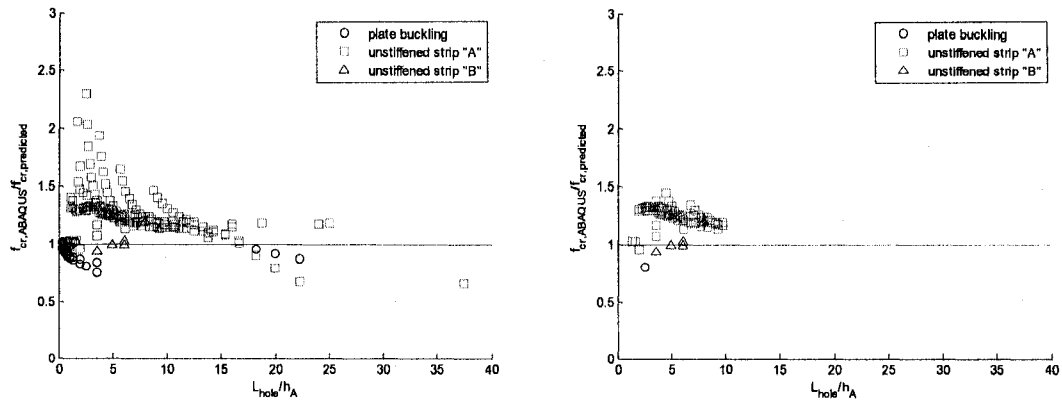


Figure 3.34 Influence of L_{hole}/y_A on the accuracy of the prediction method for stiffened elements in bending (a) without and (b) with the dimensional limits defined in Eq. (3.9), Eq. (3.24), Eq. (3.25), and Eq. (3.26).

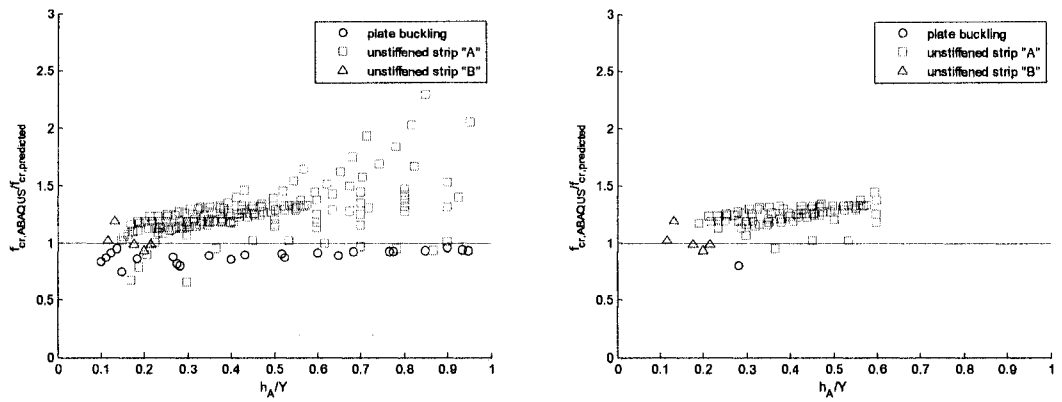


Figure 3.35 Influence of h_A/Y on the accuracy of the prediction method for stiffened elements in bending (a) without and (b) with the dimensional limits defined in Eq. (3.9), Eq. (3.24), Eq. (3.25), and Eq. (3.26).

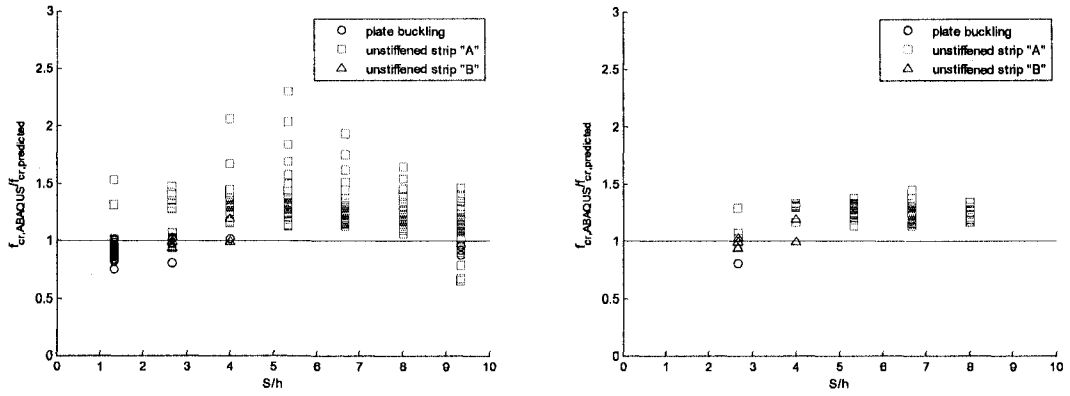


Figure 3.36 Influence of S/h on the accuracy of the prediction method for stiffened elements in bending (a) without and (b) with the dimensional limits defined in Eq. (3.9), Eq. (3.24), Eq. (3.25), and Eq. (3.26).

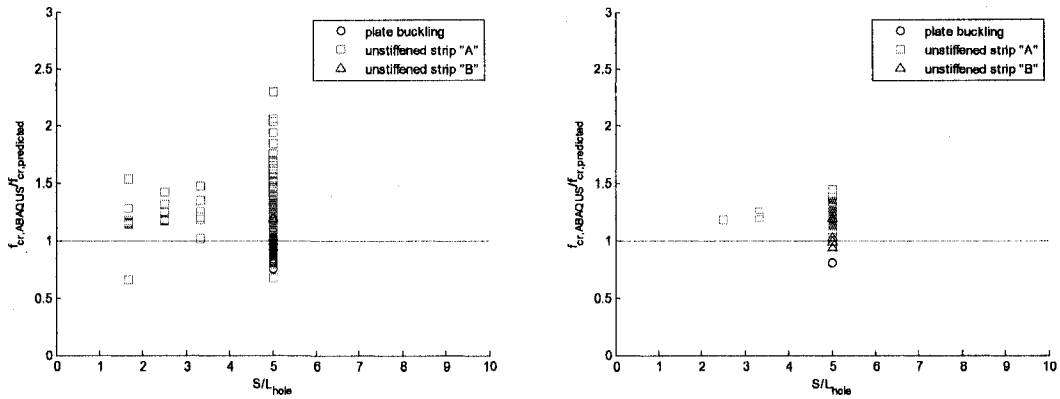


Figure 3.37 Influence of S/L_{hole} on the accuracy of the prediction method for stiffened elements in bending (a) without and (b) with the dimensional limits defined in Eq. (3.9), Eq. (3.24), Eq. (3.25), and Eq. (3.26).

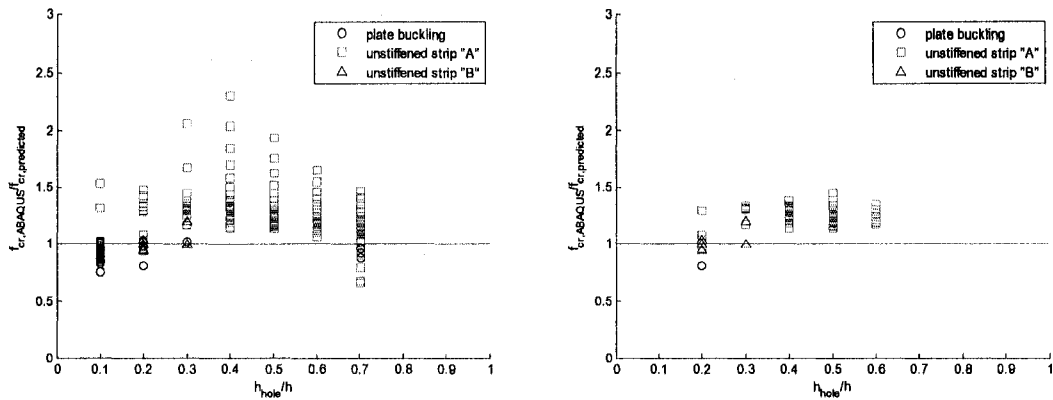


Figure 3.38 Influence of h/h_{hole} on the accuracy of the prediction method for stiffened elements in bending (a) without and (b) with the dimensional limits defined in Eq. (3.9), Eq. (3.24), Eq. (3.25), and Eq. (3.26).

3.5 Unstiffened element in uniaxial compression

3.5.1 Boundary and loading conditions

The unstiffened element is modeled with simply-supported boundary conditions on three sides and unsupported on the fourth side parallel to the application of a uniform compressive stress as shown in Figure 3.39.

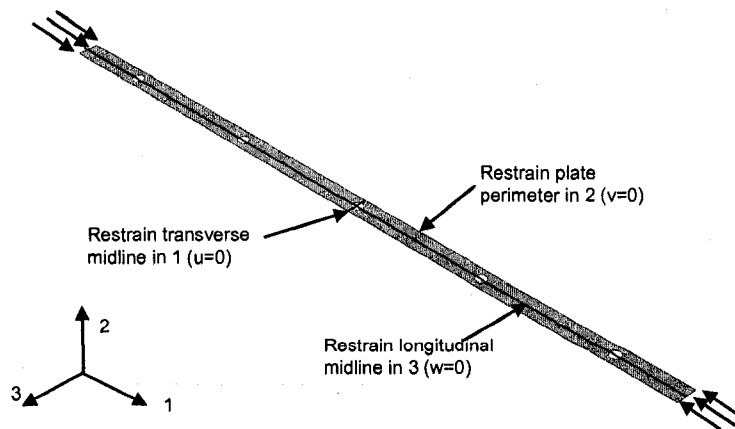


Figure 3.39 ABAQUS boundary and loading conditions for unstiffened plate loaded uniaxially.

3.5.2 Influence of regularly-spaced holes

Eigenbuckling analyses in ABAQUS are performed to evaluate the influence of evenly-spaced holes on the elastic buckling behavior of an unstiffened element. The model loading and boundary conditions are summarized in Figure 3.39 and the material properties and meshing procedures are the same as those described in Section 3.2. The plate width h , hole length L_{hole} , and hole type (slotted, circular, rectangular) are varied in this study. The hole width remains constant at $h_{hole}=1.5$ in. The plate and hole dimensions as well as the critical elastic buckling stress, f_{cr} , for the 91 models considered, are provided in Appendix B. The parametric ranges considered in this study for each hole type are summarized in Table 3.6.

Table 3.6 Parameter range for study of regularly-spaced holes on unstiffened elements.

Hole Type		h_{hole}/h	S/L_{hole}	S/h	h/t	# of models
Slotted	Min	0.10	1.7	1.0	21	77
	Max	0.70	24.0	42.2	434	
Circular	Min	0.10	13.3	1.3	62	7
	Max	0.70	13.3	9.3	434	
Square	Min	0.10	13.3	1.3	62	7
	Max	0.70	13.3	9.3	434	

A comparison of the ABAQUS results from the 91 models to the theoretical elastic buckling stress for a long unstiffened element ($k=0.425$) in Figure 3.40 demonstrates that the critical elastic buckling stress f_{cr} decreases as hole width h_{hole} increases relative to plate width h . Holes always reduce the critical elastic buckling stress of unstiffened elements in the cases studied. Buckling of the unstiffened strip "A" between the hole and the simply supported edge is not observed in the simulations because L/h is always greater than L_{hole}/h_A , although buckling of the unsupported strip "B" at the free edge occurs as the strip becomes slender (similar to Euler buckling) as shown in Figure 3.41. These

important observations are employed in Section 3.5.4 to develop an approximate prediction method for the critical elastic buckling stress of an unstiffened element with holes.

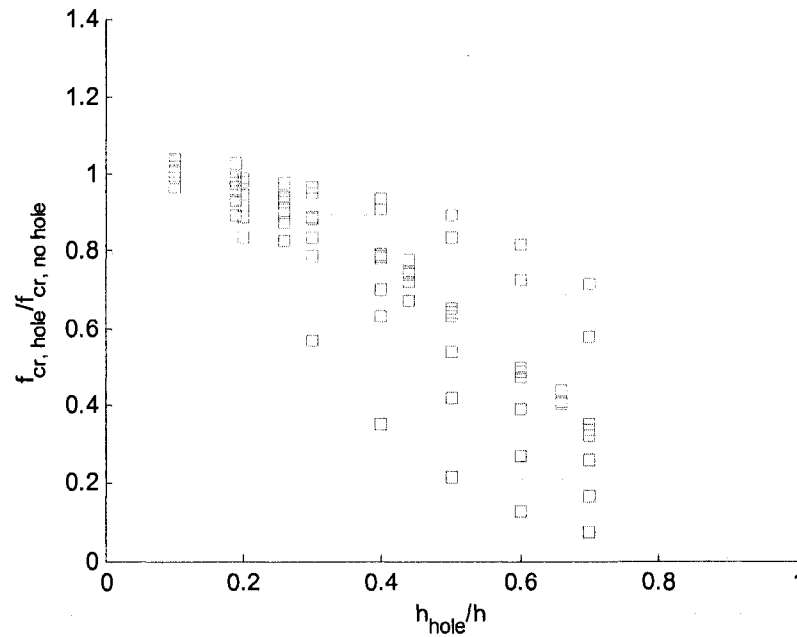


Figure 3.40 The presence of holes causes a decrease in critical elastic buckling load for unstiffened plates in uniaxial compression.

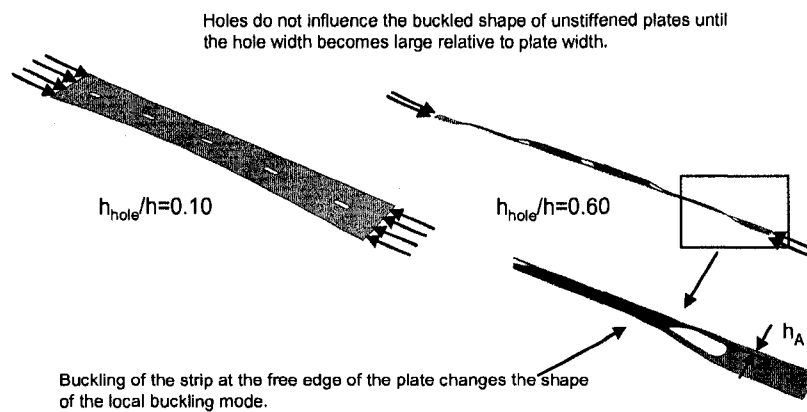


Figure 3.41 Buckled shapes of unstiffened plates with holes.

3.5.3 Influence of offset slotted holes

ABAQUS eigenbuckling analyses were performed to evaluate the influence of transversely offset slotted holes on the elastic buckling of an unstiffened element. The ratio of transverse offset, δ_{hole} , to plate width h was varied from -0.375 to 0.375, where a negative offset shifts the holes toward the simply supported edge and a positive offset shifts towards the free plate edge (refer to Figure 3.2 for a definition of δ_{hole}). The model loading and boundary conditions are summarized in Figure 3.39 and the material properties and meshing procedures are the same as those described in Section 3.2. The plate and hole dimensions as well as the critical elastic buckling stress, f_{cr} , for the 92 models considered, are summarized in Appendix B. The parametric ranges considered here are provided in Table 3.7.

Table 3.7 Parameter range considered for unstiffened element study with offset holes

		h_{hole}/h	S/L _{hole}	S/h	h/t	δ_{hole}/h	# of models
Slotted	Min	0.10	5.00	1.33	62	-0.375	92
	Max	0.70	5.00	9.33	434	0.375	

The axial stiffness of an unstiffened element is higher near the simply supported edge and lower near the free edge. It is hypothesized that holes shifted towards the simply-supported edge will reduce the critical elastic buckling stress more than hole material removed from near the free edge. This hypothesis is confirmed in Figure 3.43 where f_{cr} decreases more when holes are shifted towards the simply-supported edge. The dimension of the plate strip between the hole and the simply-supported edge, h_A (see Figure 3.3), is identified as a useful parameter when predicting f_{cr} . f_{cr} forms a trend line when plotted against L_{hole} relative to y_A as demonstrated in Figure 3.43a for offset

holes. The same plot is produced using the data from Section 3.5.2 for centered holes in Figure 3.43b with similar results. This important conclusion, that y_A and L_{hole} are key parameters influencing f_{cr} is used in the next section to develop an approximate elastic buckling prediction method for unstiffened elements with holes.

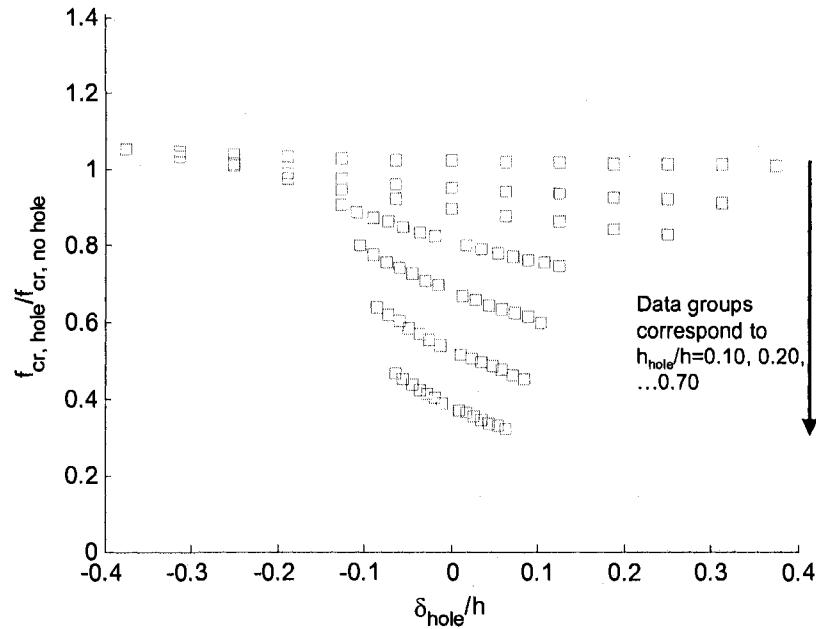


Figure 3.42 The critical elastic buckling stress of a stiffened plate decreases as holes are shifted toward the simply supported edge ($+\delta_{hole}$)

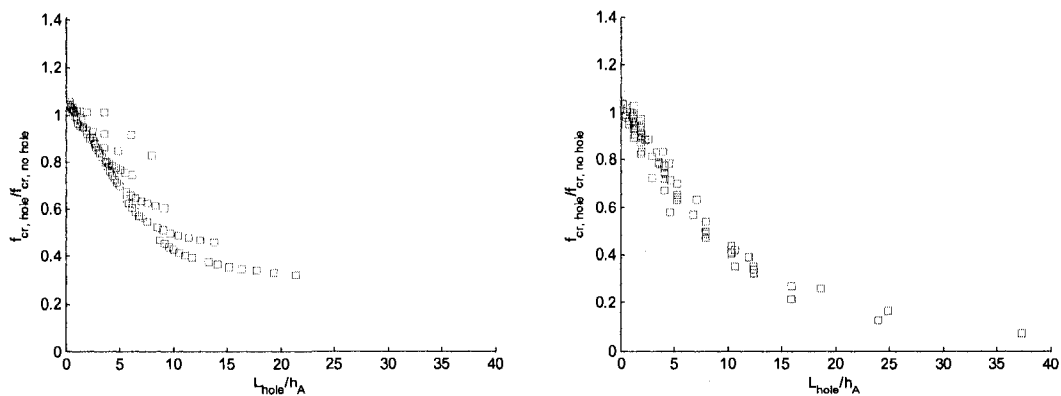


Figure 3.43 The critical elastic buckling stress for stiffened elements with (a) transversely offset holes and (b) centered holes (from Section 3.5.2) decreases as a function of hole length L_{hole} to h_A

3.5.4 Approximate prediction method for use in design

An approximate elastic buckling prediction method for an unstiffened element with holes is presented here. The method is based on the observations in Section 3.3.2 and Section 3.3.3 for long unstiffened elements with evenly spaced holes. The width of the strip between the hole and the simply supported edge, h_A , and the length of the hole L_{hole} are utilized as predictors of the critical elastic buckling stress. A summary of the prediction method equations are provided in Appendix D.

3.5.4.1 Derivation of empirical buckling coefficient

An empirical plate buckling coefficient is determined using a linear regression analysis of the data in Figure 3.43a and Figure 3.43b for both centered and offset slotted holes, which was then adjusted to have a slightly conservative bias. The regression minimizes the error between the ABAQUS results and the classical stability solution of an unstiffened element ($k=0.425$) for the plate models within the following parametric limits:

$$\frac{L_{hole}}{h_A} \leq 10 \quad (3.27)$$

$$\frac{L_{hole}}{h_B} \leq 10 \quad (3.28)$$

$$\frac{h_{hole}}{h} \leq 0.50 \quad (3.29)$$

Eq. (3.27) is imposed as a practical limit on the slenderness of the strip adjacent to the hole at the simply-supported plate edge. Eq. (3.28) prevents Euler buckling of

unstiffened strip “B” as shown in Figure 3.41. Eq. (3.29) is imposed because of the increased rate of degradation in f_{cr} observed in Figure 3.40 as holes become large relative to plate width. The empirical plate buckling coefficient is set as:

$$k = 0.425 \left(1 - 0.062 \frac{L_{hole}}{h_A} \right) \quad (3.30)$$

where the strip of plate between the hole and the simply supported edge, h_A , is calculated as

$$h_A = \frac{h - h_{hole}}{2} - \delta_{hole}. \quad (3.31)$$

A positive δ_{hole} (hole offset from the centerline of the plate, See Figure 3.2) shifts the hole towards the simply supported edge. The empirical buckling coefficient in Eq. (3.30) is shown in Figure 3.44a to be a slightly conservative but accurate representation of ABAQUS predicted buckling coefficients. The mean and standard deviation of the ABAQUS to empirical prediction ratio are 1.06 and 0.09 respectively.

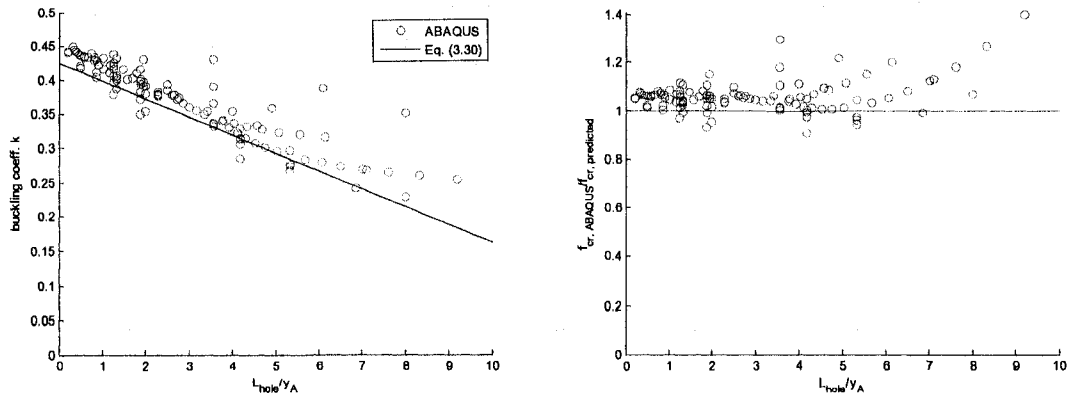


Figure 3.44 (a) Comparison of ABAQUS and empirical plate buckling coefficients for an unstiffened element with holes and (b) ABAQUS to predicted elastic buckling stress for an unstiffened element

3.5.4.2 Prediction equations

The elastic buckling stress of an unstiffened element in compression with holes is thus approximated as:

$$f_{crl} = \min[f_{cr}, f_{crh}]. \quad (3.32)$$

The critical elastic buckling stress prediction for plate buckling of the unstiffened element without holes (f_{cr}) is calculated with Eq. (3.2), where $k=0.425$ when considering long rectangular plates ($L/h>4$). The minimum critical elastic buckling stress of the unstiffened element with holes, f_{crh} , coincides with either buckling of the entire unstiffened element with holes or buckling of the unstiffened strip "A" adjacent to the hole and the simply supported edge, or:

$$f_{crh} = \min \left[k \frac{\pi^2 E}{12(1-\nu^2)} \left(\frac{t}{h} \right)^2, f_{crA} \left(1 - \frac{h_{hole}}{h} \right) \right] \quad (3.33)$$

where k is an empirical plate buckling coefficient derived from finite element eigenbuckling studies in Eq. (3.30). f_{crA} is calculated with Eq. (3.4) and modified by the factor $(1 - h_{hole}/h)$ to convert the stress on the unstiffened strip "A" to the stress at the end of the plate so that it can be compared to the buckling stress of the unstiffened element. f_{crh} will always be predicted as less than or equal to f_{cr} with this method.

Chapter 4

Elastic buckling of cold-formed steel members with holes

The elastic buckling properties of cold-formed steel lipped C-section beams and columns with holes are evaluated in this chapter using thin-shell finite element eigenbuckling analyses in ABAQUS. The elastic buckling studies are used to assess the influence of holes on the local, distortional, and global critical elastic buckling loads $P_{cr,t}$, $P_{cr,d}$, $P_{cr,e}$. The studies also identify elastic buckling modes unique to cold-formed steel members with holes. Elastic buckling properties of existing experiments on cold-formed steel columns and beams with holes are summarized and formal buckling modes are defined in preparation for the presentation of the Direct Strength Method for structural members with holes in Chapter 8.

4.1 Finite element modeling assumptions

The elastic buckling behavior of the cold-formed steel structural members with holes are obtained with eigenbuckling analyses in ABAQUS (ABAQUS 2007a). All members are modeled with ABAQUS S9R5 reduced integration nine-node thin shell elements. The typical finite element aspect ratio is 1:1 and the maximum aspect ratio is limited to 8:1 (refer to Chapter 2 for a discussion on ABAQUS thin shell finite element types and finite element aspect ratio limits). Element meshing is performed with a Matlab (Mathworks 2007) program written by the author (refer to Appendix A for a description of the program). Cold-formed steel material properties are assumed as $E=29500$ ksi and $\nu=0.3$ in the finite element models unless noted otherwise. P_y , the squash load of the column, is calculated by multiplying an assumed yield stress of 50 ksi by the gross cross-sectional area of the column.

4.2 Elastic buckling of columns with holes

4.2.1 Member and hole dimensions

Member and hole dimension notation used throughout this chapter is summarized in Figure 4.1. Uppercase dimensions (H, D, B) are out-to-out and lowercase dimensions (b, h) are flat lengths between points of curvature.

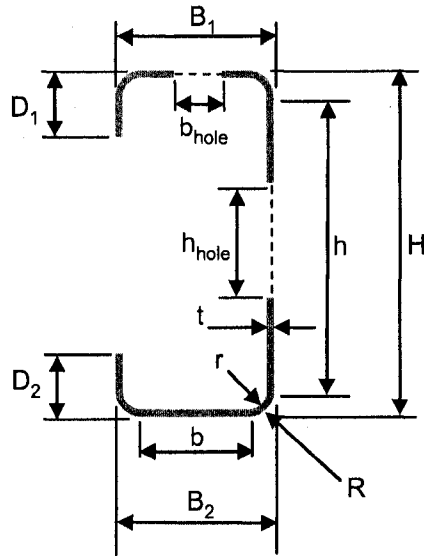


Figure 4.1 C-section and hole dimension notation

4.2.2 Loading and boundary conditions

The cold-formed steel column boundary conditions are modeled as warping free at the member ends and warping fixed at the midlength of the member as shown in Figure 4.2, which mimics the semi-analytical finite strip method (Schafer and Adány 2006). The columns are loaded at each end with stress distributions applied as consistent nodal loads in ABAQUS (see Section 3.2 for details on the loading implementation).

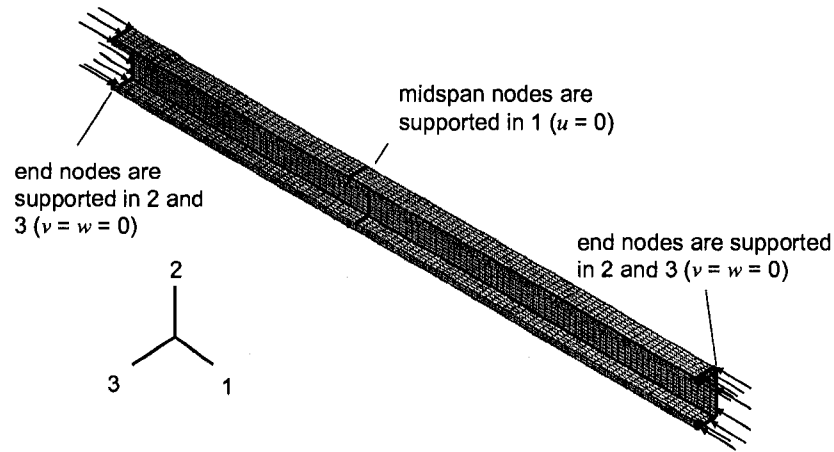


Figure 4.2 Columns are modeled with pinned warping-free boundary conditions and compressed from both ends

4.2.3 Elastic buckling comparison of short C-section columns versus isolated stiffened elements

This study builds on the results and observations in Chapter 3 for cross-sectional elements with holes and marks a transition in research focus from elements to full cold-formed steel members. The influence of one slotted hole on the elastic buckling behavior of a range of rectangular plates and SSMA cold-formed steel structural stud sections is compared, the goal being to quantify the relative influence of a web hole on one element in a cross-section (in this case a stiffened element, see Figure 3.1 for definition and Figure 3.5 for ABAQUS boundary conditions) versus a full C-section. The slotted hole has dimensions of $h_{hole}=1.5$ in., $L_{hole}=4$ in., and $r_{hole}=0.75$ in. The plate widths are chosen to correspond with the flat web widths of standard SSMA structural studs (SSMA 2001). Plate aspect ratios are held constant at 4:1. From each plate, a full structural stud finite element model is developed for comparison. The SSMA member

designations and cross section dimensions considered in this study are listed in Table 4.1.

Table 4.1 SSMA structural stud and plate dimensions

SSMA Designation	H in.	B in.	D in.	r in.	t in.	h in.	b in.	h_{hole}/h	$L=4h$ in.
250S162-33	2.50	1.63	0.50	0.0764	0.0346	2.28	1.40	0.66	9.1
350S162-33	3.50	↓	↓	↓	↓	3.28	↓	0.46	13.1
362S162-33	3.62	↓	↓	↓	↓	3.40	↓	0.44	13.6
400S162-33	4.00	↓	↓	↓	↓	3.78	↓	0.40	15.1
550S162-33	5.50	↓	↓	↓	↓	5.28	↓	0.28	21.1
600S162-33	6.00	↓	↓	↓	↓	5.78	↓	0.26	23.1
800S162-33	8.00	↓	↓	↓	↓	7.78	↓	0.19	31.1

Before examining the elastic buckling load, consider the observed changes in the first mode shape caused by the addition of a hole as given in Figure 4.3. For the buckled shape of the SSMA 250S162-33 in Figure 4.3a, the number of buckled half-waves changes from four to three for the isolated plate and from five to two for the full member, when the hole is added. The strips of plate adjacent to the hole are stiffened by the connected flange in the full member, causing buckled half-waves to form in the web away from the hole. Also, the length of the hole, L_{hole} , is approximately half of the length of the member L in the SSMA 250S162-33 member which also prevents local buckling in the web. In Figure 4.3b, the hole decreases the number of buckled half-waves from four to three in the SSMA 440S162-33 isolated plate but does not change the number of half-waves in the full member. The cross-section connectivity of the full member limits deformation at the hole and encourages buckling half-waves to form along the entire member. Also, there is more web material to accommodate local buckling along the length ($L_{hole}/L=0.26$) when compared to the SSMA 250S162-33 member.

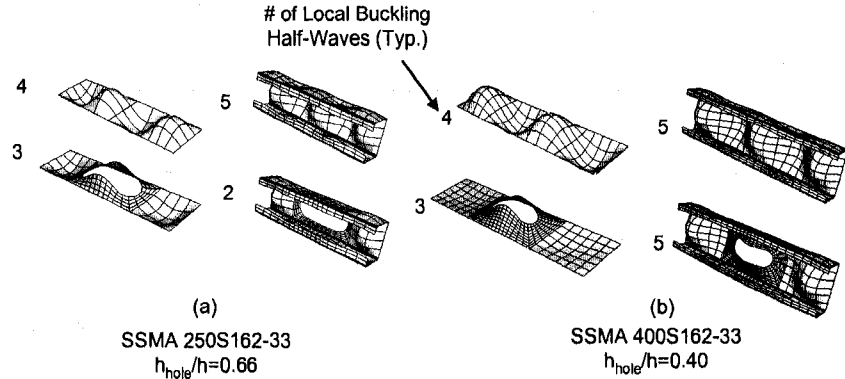


Figure 4.3(a) SSMA 250S162-33 web plate and structural stud, and (b) SSMA 400S162-33 web plate and structural stud

Figure 4.4 presents the influence of a slotted hole on the critical elastic buckling stress f_{cr} of the isolated web plates and full members with holes from Table 4.1. These results are compared to the elastic buckling prediction for a stiffened element with holes developed and presented in Section 3.3.4. The influence of the hole is minimal for small hole width to plate width ratios, but increases to a maximum at $h_{hole}/h=0.30$ for the ABAQUS plate results (consistent with the stiffened element prediction). f_{cr} increases with increasing h_{hole}/h for full members, demonstrating that the cross-section connectivity decreases a member's sensitivity to a hole (especially in the range of $h_{hole}/h=0.30$). The web is stiffened through beneficial web-flange interaction created by the relatively stable edge-stiffened flange.

As normalized hole width increases, the elastic buckling load exceeds that of a plate without a hole. This increase in buckling load is attributed to the increased axial stiffness from the strips adjacent to the hole, which causes local buckling to occur away from the holes (this "unstiffened strip" effect is discussed in Section 3.3). The length of hole relative to the length of the member also contributes to the increase in f_{cr} . L_{hole}/L increases

with increasing h_{hole}/h in this study since $L=4h$. As demonstrated in Figure 4.3a, the removal of web material restricts the formation of local buckling in the web of the member, resulting in shortened half-waves away from the hole with increased axial stiffness. The stiffened element prediction in Figure 4.4 is conservative here when compared to the plate results because it was developed for evenly spaced holes in long plates and does not account for the L_{hole}/L boost in f_{cr} .

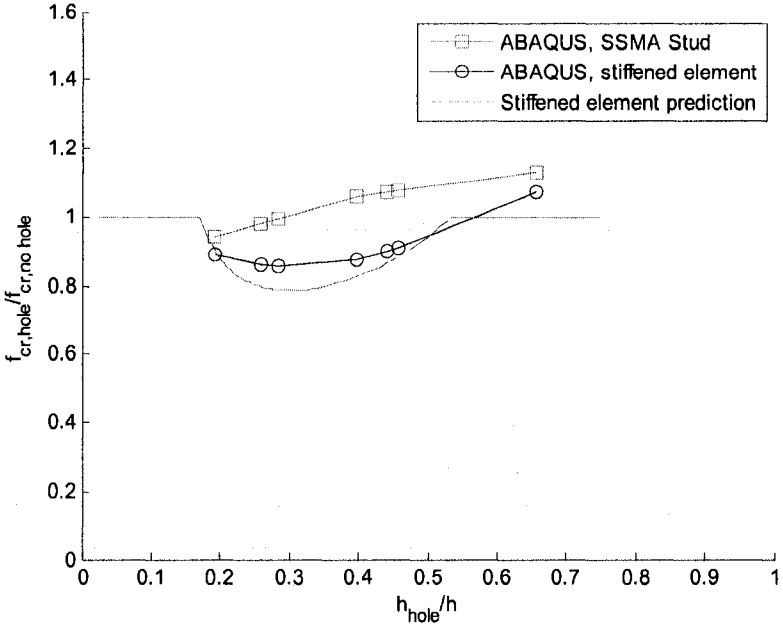


Figure 4.4. Effect of a slotted hole on the elastic buckling load of simply supported plates and structural studs

4.2.4 Influence of slotted hole location on elastic buckling of an intermediate length structural stud

This study investigates the elastic buckling behavior of an intermediate length cold-formed steel column with one slotted hole. The primary goal here is to identify and formally define the elastic buckling modes that will be used as predictors of ultimate strength within the Direct Strength Method. The elastic buckling behavior is compared

as the location of a slotted hole is varied along the length of the column. The typical compression member in this study has a length L of 48 inches and is modeled with an SSMA 362162-33 structural channel cross section. A single slotted hole is centered transversely in the web. The slotted hole has dimensions of $h_{\text{hole}}=1.5$ in., $L_{\text{hole}}=4$ in., and $r_{\text{hole}}=0.75$ in. Table 4.1 summarizes the dimensions of the SSMA 362162-33 cross section. The ABAQUS column boundary conditions are consistent with Figure 4.2.

Figure 4.5 compares the local buckling (L) mode shapes of the column with and without a slotted hole. The lowest buckling mode is local buckling (L) and exists for both the column with and without the hole. The location of the hole does not influence P_{cr} for this mode as observed in Figure 4.8. Plate buckling of the web away from the hole dominates for this mode, regardless of hole location.

Two unique local buckling modes to the column with a hole, LH and LH2, are also identified in the eigenbuckling analyses. These modes, shown in Figure 4.5, exhibit buckling of the unstiffened strip adjacent to the hole similar to that observed in the cross-sectional element studies with holes in Chapter 3. The LH mode occurs when both unstiffened strips buckle in the same direction normal to the web plane, which increases the distortional tendencies of the flange in the vicinity of the hole. This localized distortional buckling is observed in Figure 4.6, which compares the LH modes as the location of the hole varies along the column length. The LH mode is consistent with the elastic buckling mode shapes of stiffened elements, where the presence of a hole is observed to reduce the transverse bending stiffness causing localized deformation at the hole (see Figure 3.9a).

The LH2 mode occurs when the unstiffened strips buckle in opposite directions relative to the web plate, resulting in antisymmetric distortional deformation at the hole. Figure 4.8 demonstrates that P_{cr} for these two modes is similar and that both modes are minimally affected by the longitudinal location of the hole in the column.

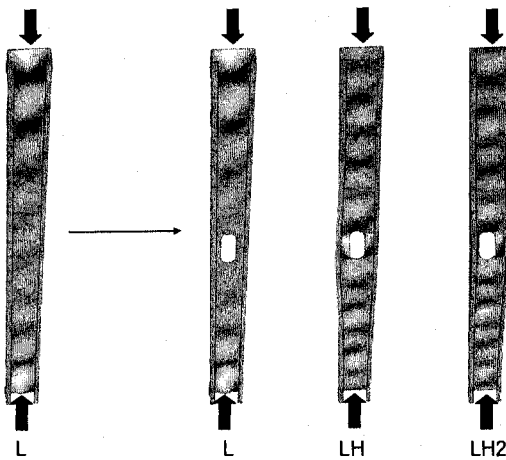


Figure 4.5 The presence of a hole creates unique local buckling modes where unstiffened strip buckling adjacent to the hole occurs symmetrically (LH) or asymmetrically (LH2) increase the distortional tendency of the flanges

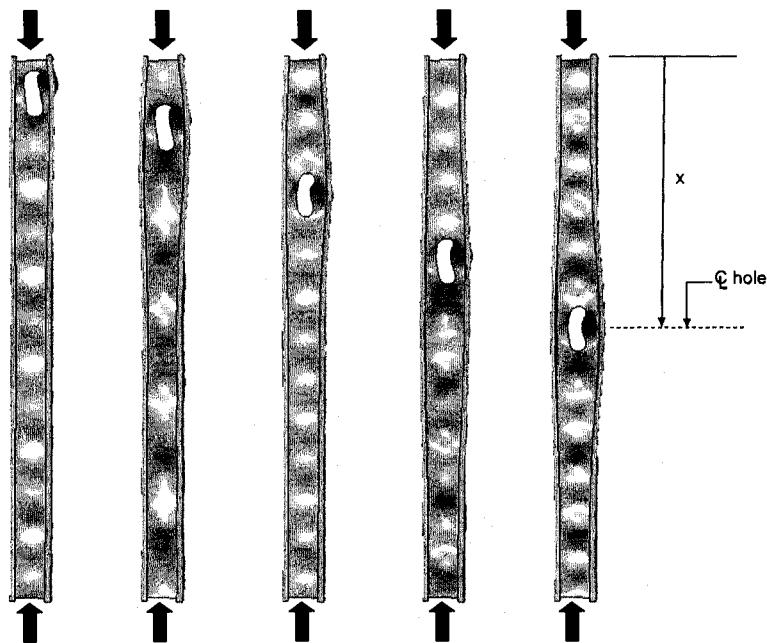


Figure 4.6 SSMA slotted hole location and local buckling LH mode, $L=48$ in., $x/L=0.06, 0.125, 0.25, 0.375, 0.50$. Note the distortional tendencies of the flanges at the hole.

The pure distortional buckling mode for the column, D, is compared for a column with and without a hole in Figure 4.7a. Note that distortional half-wavelength is unchanged with the presence of the hole, although local buckling with half-wavelengths shorter than the fundamental L half-wavelength (see Figure 4.5) mix with the D mode for the member with the hole. Figure 4.8 demonstrates that the presence of the hole has a minimal influence on P_{crd} regardless of longitudinal location.

The lowest global buckling mode is flexural-torsional buckling (GFT) as shown in Figure 4.7b. The presence of a hole results in a slight decrease in P_{cre} as the hole moves towards the end of the column as shown in Figure 4.8. As the hole shifts close to the loaded end of the column ($x/L=0.06$), local buckling at the hole combines with the GFT mode to reduce P_{cre} .

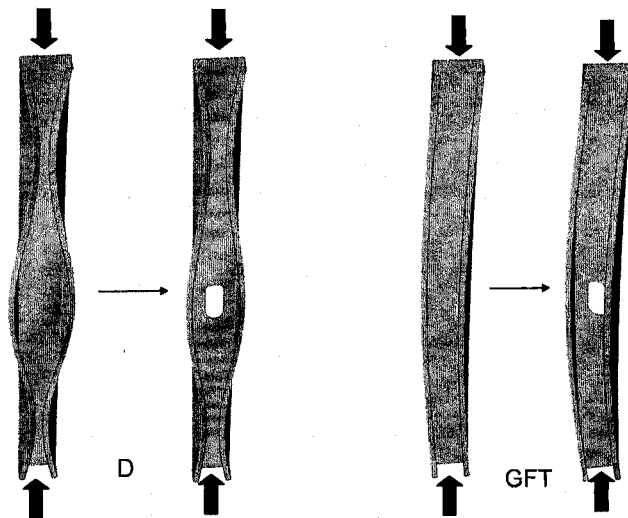


Figure 4.7 Influence of a slotted hole on the (a) distortional (D) and (b) global flexural-torsional (GFT) modes of a cold-formed steel column

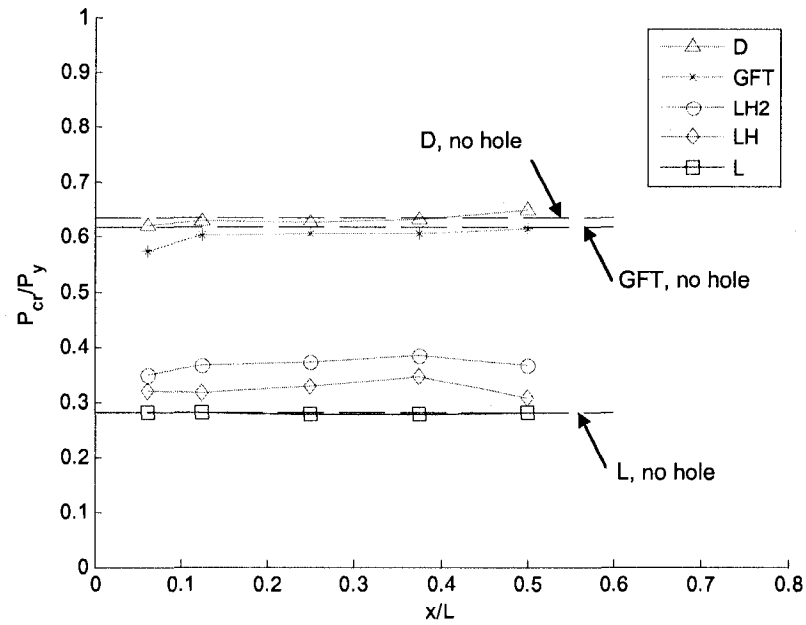


Figure 4.8 Influence of SSMA slotted hole location on P_{cr} for a 362S162-33 C-section (refer to Figure 4.5, Figure 4.6, and Figure 4.7 for buckled shape summaries)

4.2.5 Flange hole study

The research focus up until now has been on the elastic buckling modes of isolated web plates and cold-formed steel compression members with web holes. Holes are also commonly present in the flanges of C-section columns. A standard connection detail requiring a flange hole is shown in Figure 4.9, where gypsum sheathing is connected to steel studs with a bolted or screw attachment (Western States Clay Products Association 2004).

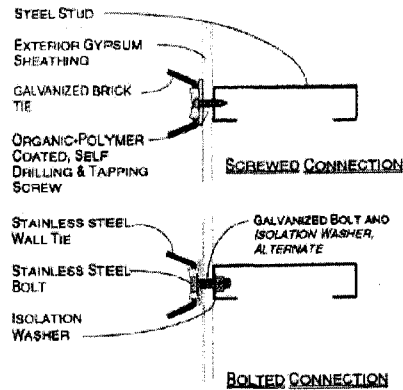


Figure 4.9 Connection detail for structural stud to exterior wall requires a screw or bolt hole placed in the stud flange (Western States Clay Products Association 2004)

This study evaluates the influence of circular flange holes on the elastic buckling behavior of an intermediate length SSMA 362S162-33 structural stud. A single hole is placed at the midlength of both the top and bottom flanges and centered between the web and lip stiffeners. Five hole diameters consistent with standard bolt holes are considered: $b_{hole}/b = 0.178, 0.356, 0.534, 0.713, \text{ and } 0.892$ ($1/4''$, $1/2''$, $3/4''$, $1''$, $1 1/4''$ holes in a $1 5/8''$ flange) where the flat flange width $b=1.40$ in. The length L is 48 in. for all members, corresponding to a common unbraced length of a SSMA structural stud.

Figure 4.10 presents the variation in elastic buckling loads for local, distortional, and global modes as the diameter of the flange holes increase. The local (L) buckling load, P_{crit} , is not influenced by small holes, but decreases as b_{hole}/b exceeds 0.70. Figure 4.11 demonstrates that for large flange holes local buckling is dominated by web and flange deformation near the holes. The large flange holes adversely affect the beneficial web-flange interaction inherent in structural studs (Figure 4.4 highlights this beneficial interaction for C-sections with web holes). The interruption of the web-flange interaction by the holes is also reflected in the pure distortional mode (D), as P_{crit}

decreases slightly as flange hole size increases relative to flange width. The flanges holes have a minimal effect on the global flexural-torsional mode (GFT) because their diameter is small relative to the column length.

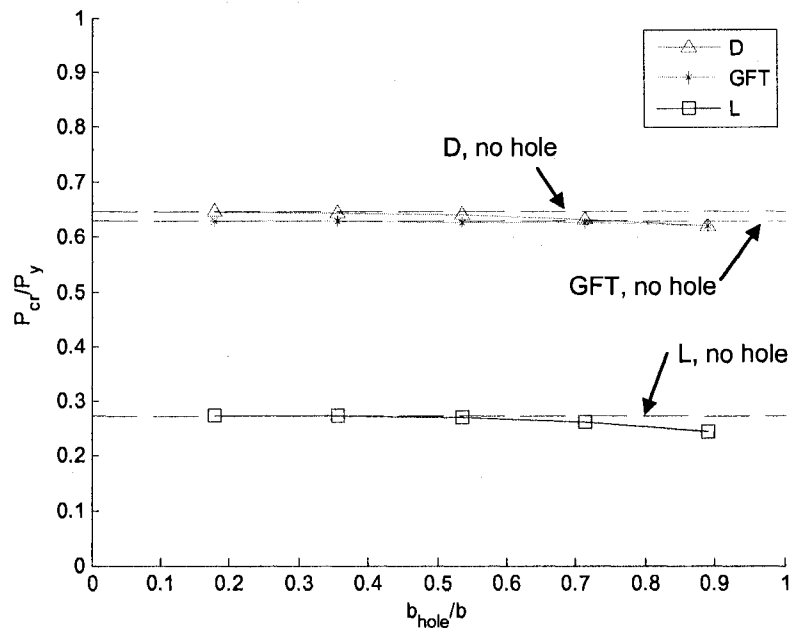


Figure 4.10 Influence of flange hole diameter on the local (L), distortional (D), and global (GFT) elastic buckling loads of an SSMA 362S162-33 structural stud

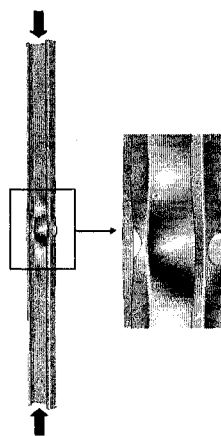


Figure 4.11 Local (L) buckling is dominated by flange and web deformation near the holes as b_{hole}/b exceeds 0.70

4.2.6 Analysis of existing experiments on columns

The Direct Strength Method employs the elastic buckling properties of a cold-formed steel member to predict its ultimate strength. To assist in the extension of DSM to columns with holes, a database is developed in this section which summarizes the elastic buckling properties and tested strengths of cold-formed steel columns experiments with holes from the past 30 years. This database is used Chapter 8 when developing and verifying DSM for columns with holes. Table 4.2 summarizes the experimental programs comprising the database.

Table 4.2 Summary of column experimental data

Author	Publication Date	Types of Specimens	Cross Section	End Conditions	# of Specimens
Ortiz-Colberg	1981	Stub Column	Lipped Cee Channel	Fixed-Fixed	8
Ortiz-Colberg	1981	Long Column	↓	Weak axis pinned	15
Miller and Peköz	1994	Stub Column		Fixed-Fixed	12
Sivakumaran	1987	Stub Column		Fixed-Fixed	14
Abdel-Rahman	1997	Stub Column		Fixed-Fixed	8
Pu et al.	1999	Stub Column		Fixed-Fixed	9
Moen and Schafer	2008	Short Column		Fixed-Fixed	6
Moen and Schafer	2008	Intermediate Column		Fixed-Fixed	6

4.2.6.1 Elastic buckling database for column experiments

ABAQUS eigenbuckling analyses were conducted for each specimen in the database. Member boundary conditions and loading conditions were modeled to be consistent with the actual experimental conditions. The ABAQUS implementations of the boundary conditions for each experimental program are described in Figure 4.12. Local (L, LH, LH2 – see Figure 4.5), distortional (D), and global (G) buckling modes were manually identified from the buckled modes in ABAQUS using the modal definitions described in 4.2.4.

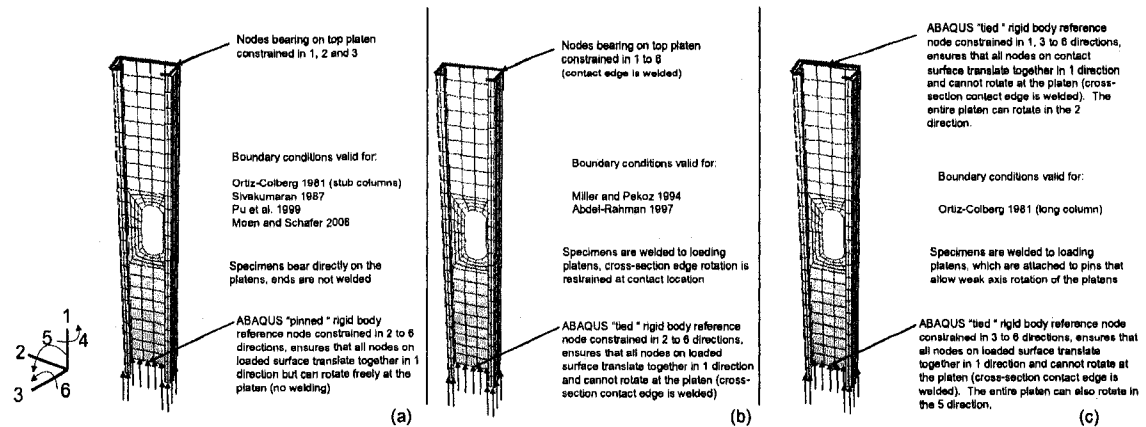


Figure 4.12 Experimental program boundary conditions as implemented in ABAQUS

Table 4.3 summarizes the fixed-fixed column specimen dimensions and material properties, including cross section and hole dimensions, tested ultimate load P_{test} , tested specimen yield stress F_y , specimen yield force $P_{y,g}$ (calculated with the gross cross-sectional area), and $P_{y,net}$ (calculated with the net cross-sectional area). Table 4.4 summarizes the fixed-fixed column specimen elastic buckling loads. ABAQUS eigenbuckling results are presented for two different types of boundary conditions, the experiment boundary conditions and CUFSM boundary conditions (warping-free at the ends, warping-fixed at the midlength of the column) except for the Moen and Schafer specimens which were only modeled with experiment boundary conditions. CUFSM elastic buckling results are also provided, including the distortional half-wavelength L_{crd} . The same experiment and elastic buckling information is summarized for the weak-axis pinned columns in Table 4.5 and Table 4.6 and together with Table 4.3 and Table 4.4 comprise the data set used to evaluate the DSM equations for cold-formed steel columns with holes Chapter 8.

Table 4.7 summarizes cross section and material property parameter ranges for the fixed-fixed specimens and weak-axis pinned specimens. Most of the weak-axis pinned specimens are long columns, while the majority of the fixed-fixed specimens are stub columns (the exception being the short and intermediate length fixed-fixed columns tested by Moen and Schafer). All column specimens in the database are common industry shapes and meet the DSM prequalification standards (for members without holes) summarized in Table 4.8 (AISI-S100 2007).

Table 4.7 Parameter ranges for fixed-fixed and weak-axis pinned column specimens with holes

Specimen type		D/t	H/t	B/t	H/B	D/B	L/H	h_{hole}/h	L_{hole}/L	F_y (ksi)
fixed-fixed columns	min	6.3	46.3	19.3	1.9	0.23	1.7	0.16	0.04	24.8
	max	20.0	172.7	65.0	4.9	0.32	13.3	0.60	0.46	62.0
weak-axis pinned columns	min	6.6	46.2	20.4	2.3	0.33	7.7	0.16	0.01	42.3
	max	10.3	71.6	31.7	2.3	0.30	17.9	0.47	0.06	51.5

Table 4.8 DSM prequalification limits for C-sections

Column parameter	DSM prequalification limit
Web slenderness	$H/t < 472$
Flange slenderness	$B/t < 159$
Lip slenderness	$4 < D/t < 33$
Web / flange	$0.7 < H/B < 5.0$
Lip / flange	$0.05 < D/B < 0.41$
Yield stress	$F_y < 86$ ksi.

4.2.6.2 Boundary condition influence on elastic buckling

The ABAQUS results in the column elastic buckling database, in addition to serving as a resource for extending DSM to columns with holes, can also be used to study the influence of column boundary conditions on elastic buckling. Consider the fixed-fixed columns in the database with $L/H < 4$ (most are considered stub columns). Figure 4.13 and Figure 4.14 and compare the influence of the experiment fixed-fixed boundary conditions for these columns relative to warping free boundary conditions (i.e. CUFSM style boundary conditions in Figure 4.2) on P_{crd} (distortional buckling) and $P_{cr\ell}$ (local buckling). The experiment boundary conditions are shown to increase P_{crd} for all of the column specimens considered while $P_{cr\ell}$ remains relatively unchanged, primarily because warping deformations are intimately tied to distortional buckling and not plate buckling (Schafer and Ádány 2006). For stub columns, the length of the fundamental distortional half-wave is often shorter than the length of the column, which results in an

increase in P_{crd} . The restrained warping at the column ends also contributes to the shortening of the half-wave and an increase in P_{crd} . The magnitude of this boost in P_{crd} decreases as L/L_{crd} increases as shown in Figure 4.13a because the wavelength shortening required to accommodate distortional buckling in the column can be distributed over multiple half-waves as column length increases. Figure 4.13b confirms this observation by demonstrating that P_{crd} increases with increasing L/H . H is inversely proportional to L_{crd} for a constant flange width B (i.e., a wider column will have a shorter distortional half-wavelength) and therefore as L/H increases, the distortional half-wavelength increases relative to the column length causing an increase in P_{crd} .

$P_{cr\ell}$ increases slightly with increasing hole size relative to column size (both for h_{hole}/h and L_{hole}/L) as shown in Figure 4.14 due to the fixed-fixed boundary conditions. For large holes relative to member size the local buckling half-waves form away from the hole near the column ends (see Section 3.3). These half-wavelengths are shortened relative to their fundamental half-wavelengths by the loaded column edges which are also restrained from rotating (from welding), resulting in a higher $P_{cr\ell}$ when compared to warping-free end conditions with loaded edges free to rotate.

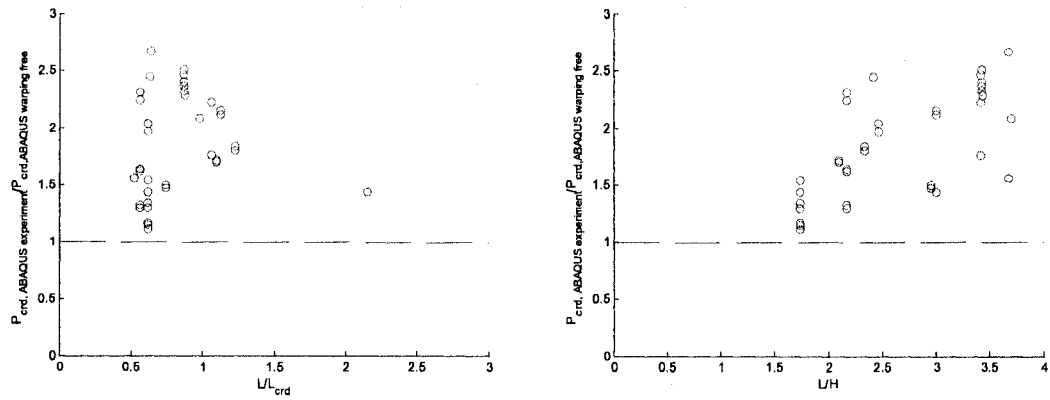


Figure 4.13 Influence of fixed-fixed boundary conditions versus warping free boundary conditions on P_{crd} for column experiments ($L/H < 4$) as a function of (a) column length to fundamental distortional half-wavelength calculated with CUFSM and (b) column length to member length.

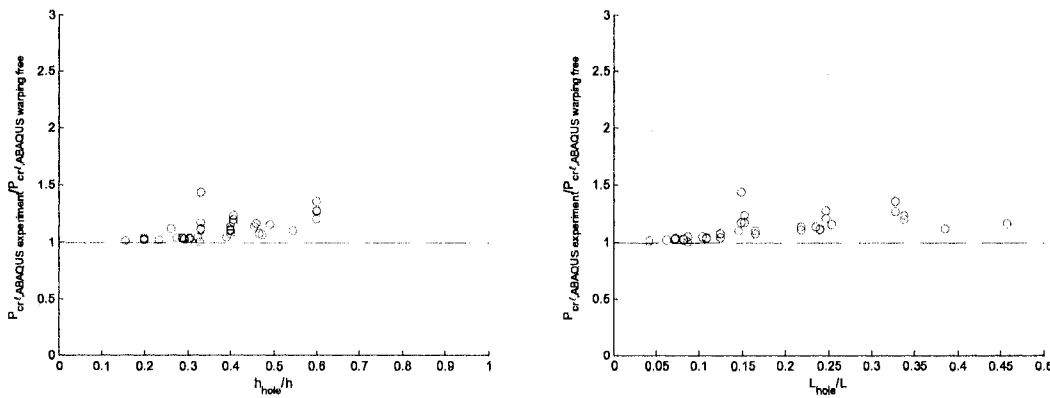


Figure 4.14 Influence of fixed-fixed boundary conditions versus warping free boundary conditions on $P_{cr\ell}$ for column experiments ($L/H < 4$) as a function of (a) hole width relative to column width and (b) hole length relative to column length

The weak-axis pinned boundary conditions have a minimal influence on $P_{cr\ell}$ and P_{crd} in Figure 4.15 when compared to the warping-free boundary conditions. These columns are still warping-fixed even though they are pinned (a plate is welded to the end of the member preventing warping deformation), but because the columns are all relatively long compared to the stub columns and hole size is small relative to column size, the wavelength shortening boost in $P_{cr\ell}$ and P_{crd} is not pronounced.

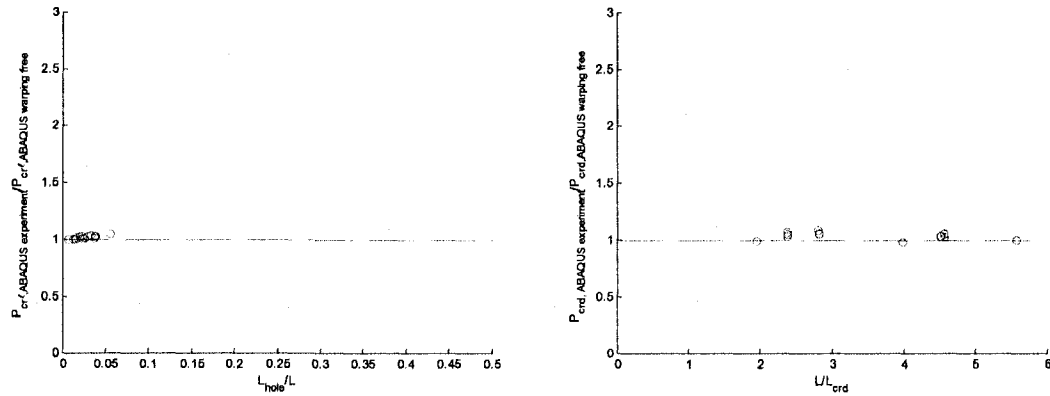


Figure 4.15 Influence of weak-axis pinned boundary conditions versus warping free boundary conditions on (a) P_{cr} as a function of hole length to column length and (b) P_{crd} as a function of column length to member length.

4.2.7 Approximate prediction methods for use in design

The ability to approximate local, distortional, and global critical elastic buckling loads is central to the extension of the Direct Strength Method (DSM) for cold-formed steel structural members with holes. To facilitate the use of DSM for members with holes, approximate (and conservative) methods for calculating elastic buckling are developed here which can be used in lieu of a full finite element eigenbuckling analysis. Elastic buckling approximations using the finite strip method (e.g. CUFSM) are derived for local and distortional buckling, and modifications to the classical column stability equations are proposed for global buckling. The simplified methods are intended to be general enough to accommodate the range of hole shapes, sizes, and spacings common in industry.

4.2.7.1 Local buckling

An approximate method for predicting the local elastic buckling behavior of cold-formed steel members with holes is presented in this section. This method extends the assumption in the “element-based” methods in Chapter 3 that local buckling occurs as either plate buckling of the entire cross-section or unstiffened strip buckling at the location of the hole. In this finite strip approximate method, local buckling is assumed to occur as the minimum of P_{cr} occurring from local buckling on the gross cross-section (as calculated in the Direct Strength Method) and local buckling of the unstiffened strip adjacent to the hole. The use of the finite strip method allows for a more realistic prediction of P_{cr} for unstiffened strip buckling by including the interaction of the cross-section on the unstiffened strip (i.e., the LH mode for the C-section in Figure 4.5). The method is presented through three examples considering industry standard cross-sections with holes which are then verified with ABAQUS thin shell finite element eigenbuckling results. The prediction method is also validated using the column elastic buckling database developed in Section 4.2.6.1.

4.2.7.1.1 Prediction method

The local critical elastic buckling load P_{cr} is calculated for a cold-formed steel member with holes as

$$P_{cr} = \min(P_{cr}, P_{crh}). \quad (4.1)$$

The calculation of the local critical elastic buckling load on the gross cross-section, P_{cr} , is performed using standard procedures defined in Appendix 1 of the AISI-S100 (AIS-

S100 2007). P_{ch} is calculated in CUFSM using the net cross-section, which is restrained to isolate local buckling from distortional buckling by fixing the column cross-section corners as shown in Figure 4.16. It is important to avoid fully restraining a cross-section element (i.e., flange or web), since this prevents Poisson-type deformations and artificially stiffens the cross-section. For example, Figure 4.16a restrains the corners in the z -direction only to prevent distortional buckling while still accommodating transverse deformation of the flanges. The only time a corner should be fixed in both the x and z directions is when two isolated elements intersect (i.e., C-section with a flange hole, see Figure 4.16a). Finally, when a hole isolates a strip of the net cross-section as shown in Figure 4.16b (e.g., a hat section with flange holes), the isolated portion of the cross-section should be deleted since it is assumed to no longer contributes to the stiffness of the cross-section over the length of the hole. If the isolated elements are not removed then the critical elastic buckling load calculated in CUFSM will correspond to Euler buckling of this isolated portion of the cross-section.

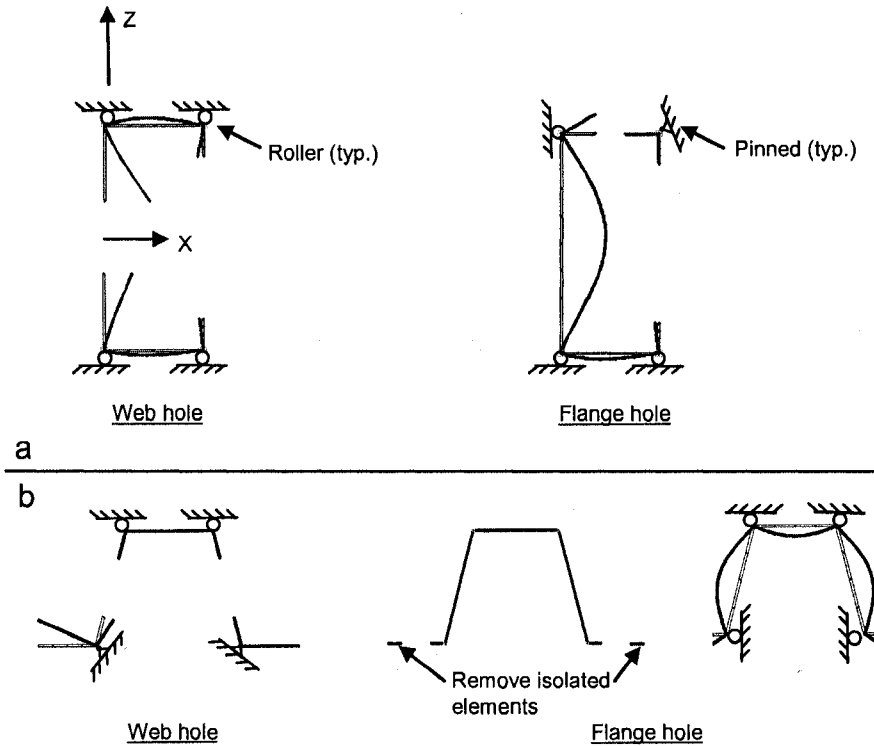


Figure 4.16 Rules for modeling a column net cross-section in CUFSM

Once the net-cross section is restrained, an eigenbuckling analysis is performed, and an elastic buckling curve similar to Figure 4.17 is generated. L_{crh} is identified on the curve as the half-wavelength corresponding to the minimum buckling load. When $L_{hole} < L_{crh}$ as shown in Figure 4.17a, P_{crh} is equal to the buckling load at the length of the hole. If $L_{hole} \geq L_{crh}$ as shown in Figure 4.17b, P_{crh} is the minimum on the buckling curve. When no local minimum exists, then P_{crh} is equal to the elastic buckling load corresponding to L_{hole} . Determining elastic buckling loads at specific half-wavelengths is a new and fundamentally different use of the finite strip method when compared to its primary application within DSM, which is calculating the lowest fundamental elastic buckling modes of cold-formed steel members.

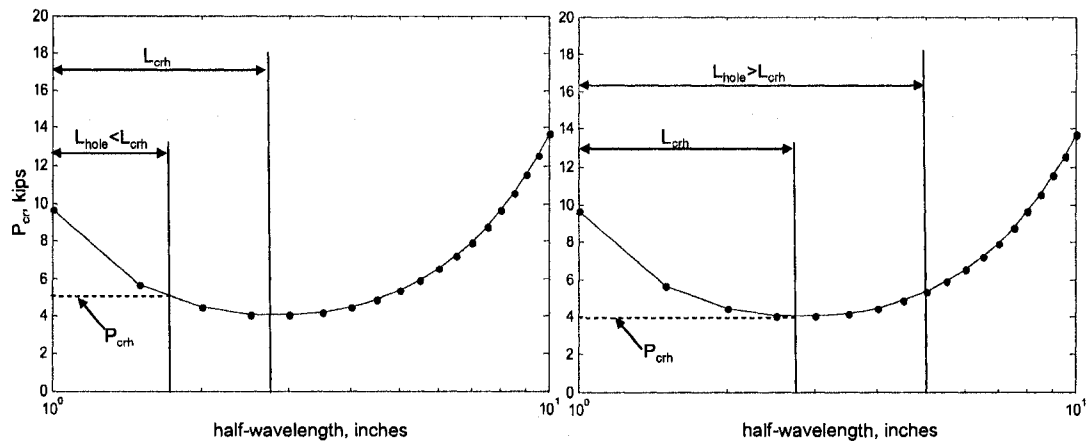


Figure 4.17 Local elastic buckling curve of net cross-section when (a) hole length is less than L_{crh} and (b) when hole length is greater than L_{crh}

4.2.7.1.2 Method examples

Three examples are presented here that approximate the local critical elastic buckling load $P_{cr\ell}$ for cold-formed steel columns with holes using CUFSM. For all examples, the length of the column $L=100$ inches and five slotted holes are spaced at $S=20$ inches. The typical length of the hole $L_{hole}=4$ inches. All ABAQUS eigenbuckling analyses are modeled with CUFSM-style boundary and loading conditions identical to those shown in Figure 4.2. The modulus of elasticity, E , is assumed as 29500 ksi and Poisson's ratio, ν , as 0.3 in all finite strip and finite element models. $P_{cr\ell}$ is normalized when plotted by $P_{y,g}$, the squash load of the column calculated with the gross cross-sectional area and a yield stress, F_y , of 50ksi.

The first example is an SSMA 362S162-33 cross section with a slotted web hole. Figure 4.18 compares the finite strip and ABAQUS mode shapes for $h_{hole}/h_c=0.14$ where h_c is the C-section web depth measured from the centerline flange to centerline flange. The CUFSM approximate method predictions are plotted for a range of h_{hole}/h_c in Figure 4.19,

and compared with ABAQUS eigenbuckling predictions to demonstrate the viability of the prediction method. For this example, smaller hole widths lead to reductions in P_{cr} when compared to a member without a hole or members with larger holes. This counterintuitive result occurs because for small holes the unstiffened strip controls the local buckling behavior (i.e., the LH mode) and for large holes, local plate buckling occurs between the holes (i.e., the L mode), which is consistent with the elastic buckling observations for plates (see Chapter 3). (One must keep in mind that for strength the net section in yielding, as well as the elastic buckling load, ultimately determine the capacity, not just P_{cr} .)

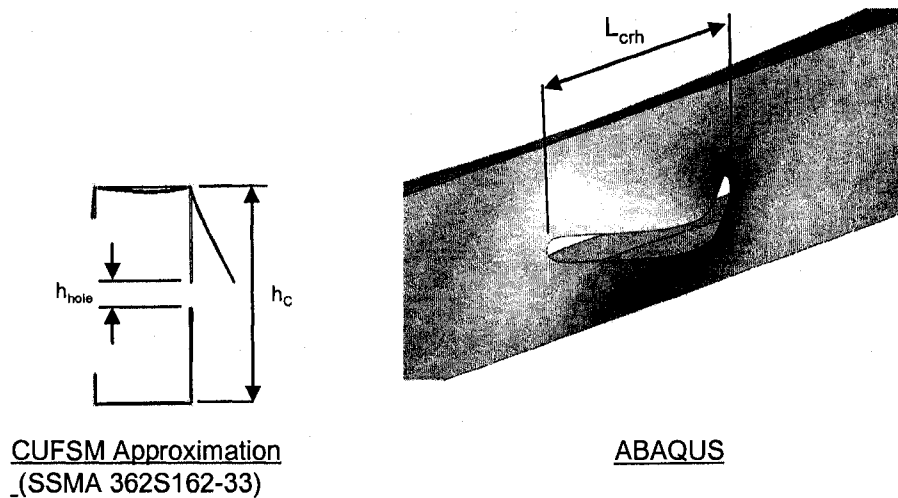


Figure 4.18 Comparison of CUFSM and ABAQUS predictions of unstiffened strip buckling.

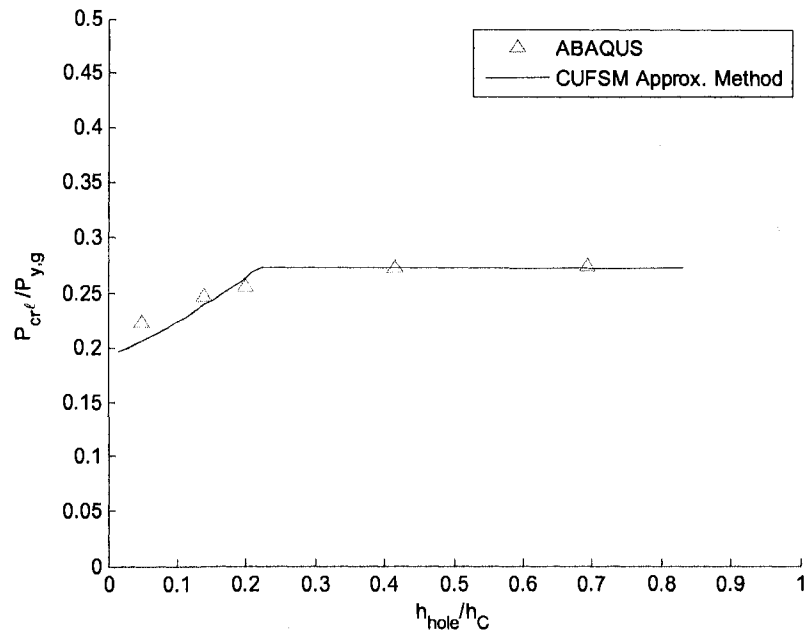


Figure 4.19 ABAQUS results verify CUFSM local buckling predictions for an SSMA 362S162-33 column with evenly spaced web holes.

The next example evaluates the influence of a slotted flange hole on P_{cr} for an SSMA 362S162-33 cross section. The unstiffened strip buckled mode shape for this cross-section from both finite strip and finite element predictions are compared in Figure 4.20. It is observed that for both CUFSM and ABAQUS mode shapes, buckling occurs primarily in the web and flange strip, and that the flange strip – lip portion of the cross-section remains stable at P_{crh} . The CUFSM prediction method results are plotted for varying flange hole width b_{hole} relative to centerline flange width b_C and compared to ABAQUS eigenbuckling predictions in Figure 4.21. P_{crh} decreases with increasing flange hole width for both CUFSM and ABAQUS results. The decreasing trend in the critical elastic buckling load demonstrates the importance of the flange in web local buckling dominated cross-sections.

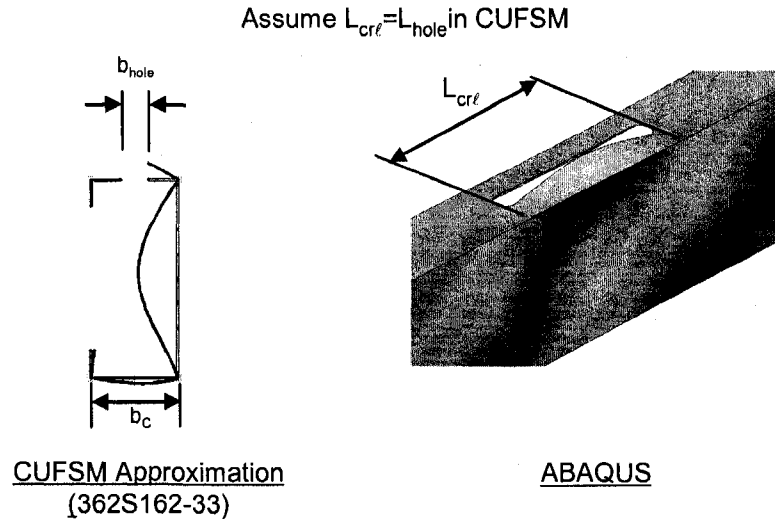


Figure 4.20 CUFSM and ABAQUS local buckling mode shapes are consistent when considering a slotted flange hole.

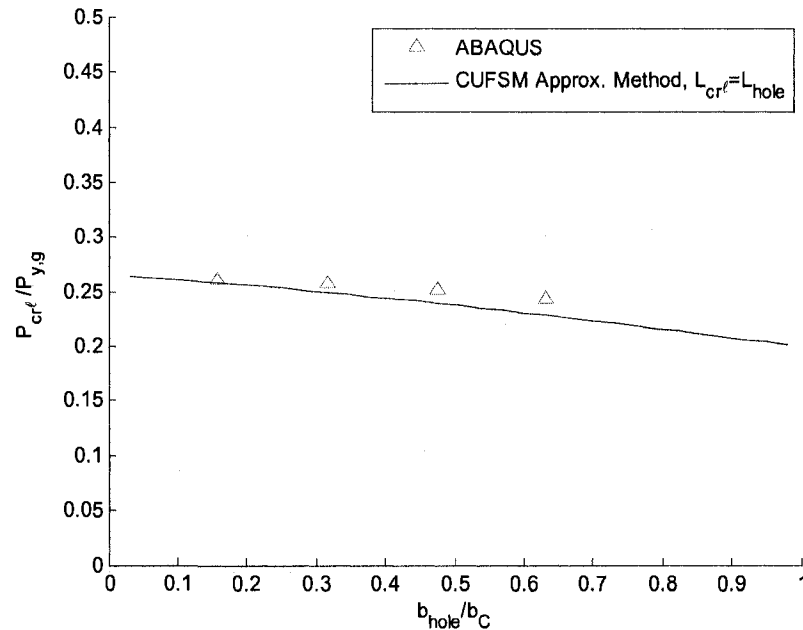


Figure 4.21 ABAQUS results verify CUFSM predictions for an SSMA 362S162-33 cross section with evenly spaced flange holes.

The third example is an SSMA 1200S162-68 cross section with a slotted hole centered in the web. Figure 4.22 provides the CUFSM and ABAQUS buckled shapes when $h_{hole}/h_c=0.16$. The assumption in the CUFSM prediction method that L_{crf} is equal to $L_{hole}=4$ in. produces a P_{crh} higher than P_{cr} without the hole (because L_{crf} is shorter than the local

buckling half-wavelength of the column) and therefore P_{cr} controls in the prediction method as shown in Figure 4.23. The approximate method correctly predicts that unstiffened strip buckling does not occur as observed in the ABAQUS buckled shape, and that the actual local buckling half-wavelength L_{cr} is similar to that of a column without holes. The prediction for P_{cr} is unconservative here though (ABAQUS results are 10% lower than P_{cr}), because the hole causes a mixed local-distortional mode that is not captured by the CUFSM net-section model (with pinned corners) or the CUFSM gross cross-section model (without the influence of the web hole). For sections such as this where local and distortional buckling have similar half-wavelengths and critical elastic buckling loads, a full finite element eigenbuckling analysis may be warranted to evaluate the presence of holes.

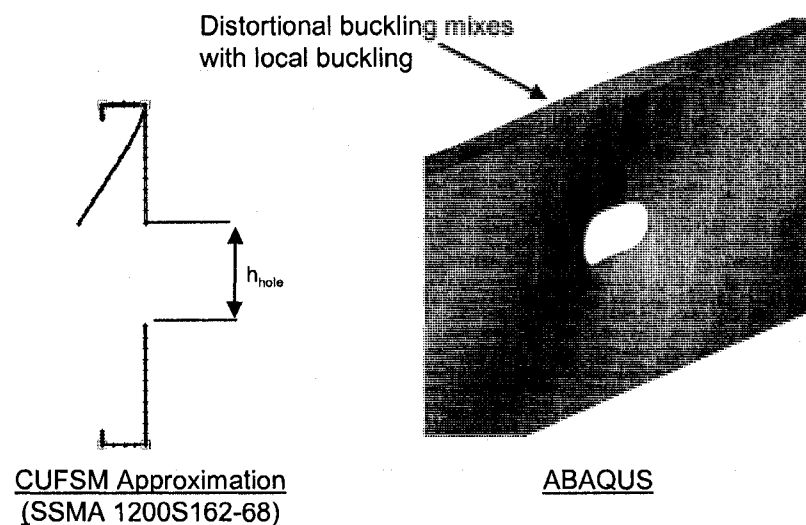


Figure 4.22 ABAQUS predicts local plate buckling with distortional buckling interaction which is not detected in CUFSM.

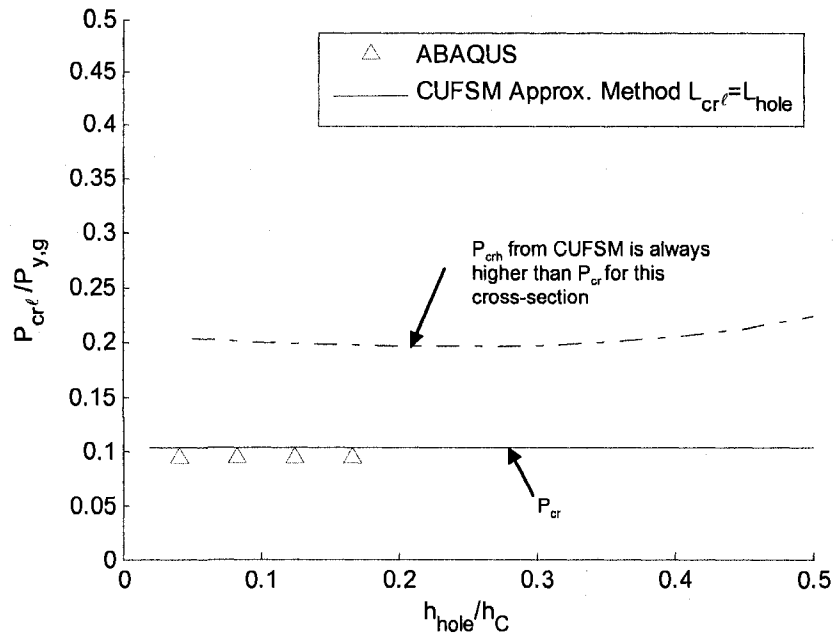


Figure 4.23 ABAQUS results are slightly lower than CUFSM predictions, CUFSM predicts correctly that plate local buckling controls over unstiffened strip buckling.

4.2.7.1.3 Method validation using elastic buckling database

The elastic buckling database developed in Section 4.2.6.1 is utilized here to evaluate the CUFSM approximate method for predicting $P_{cr\ell}$. Custom Matlab code was written to calculate P_{crh} for all 78 specimens in the database (Mathworks 2007). The code performed a CUFSM analysis of the net cross-section (cross-section containing a hole) with pinned corners (x - and z -directions). The predicted $P_{cr\ell}$ of each column specimen is the minimum of P_{crh} (unstiffened strip buckling at the net section) and P_{cr} (Table 4.4 and Table 4.6, CUFSM elastic buckling results, no hole).

Figure 4.24 compares $P_{cr\ell}$ reflecting the experimental boundary conditions in ABAQUS (from Table 4.4 and Table 4.6) relative to P_{cr} and P_{crh} . For all specimens, P_{cr} (no hole, gross cross-section) is lower than P_{crh} (hole, net cross-section) because the strips of web adjacent to the hole are stiffer than the cross-section away from the holes (similar to

the SSMA362S162-33 cross-section with $h_{hole}/h > 0.20$, see Figure 4.19). Even for those column specimens with small holes relative web width, the holes are often circular or square and therefore P_{crh} is predicted higher than P_{cr} since the buckling half-wavelength of the unstiffened strip is assumed equal to the diameter of the hole. This prediction result is consistent with the actual buckled behavior of stiffened elements with circular and square circular holes shown in Figure 3.19.

Figure 4.25 compares the ABAQUS experiment $P_{cr\ell}$ to the predicted $P_{cr\ell}$ and demonstrates the approximate method is accurate for smaller holes relative to column size and becomes increasing conservative as hole size increases relative to column size (h_{hole}/h and L_{hole}/L). The prediction becomes conservative because it does not take into account the wavelength stiffening effects (discussed in Section 3.3.2) which boost $P_{cr\ell}$ as the hole becomes large relative to the column. The mean and standard deviation of the ABAQUS to predicted ratio are 1.11 and 0.18 respectively, demonstrating the viability of the method for the specimens considered.

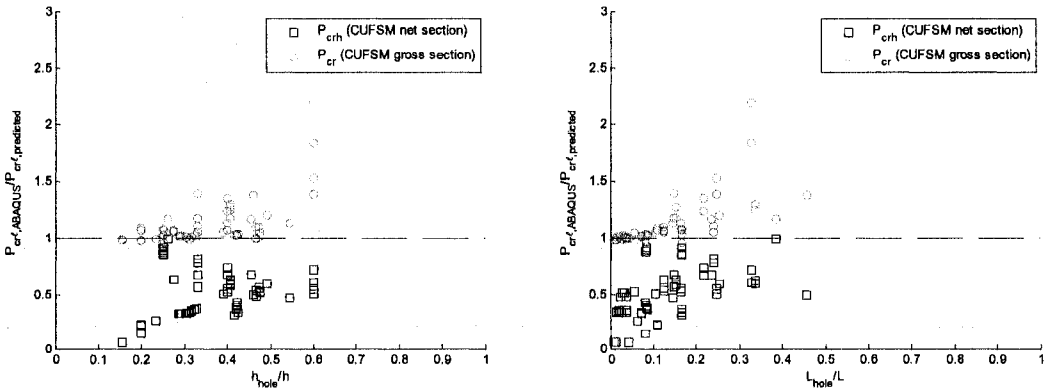


Figure 4.24 Predicted P_{crh} (CUFSM, buckling of the net cross-section) and P_{cr} (CUFSM, buckling of the gross cross section, no hole) are compared relative to the ABAQUS $P_{cr\ell}$ with experiment boundary conditions as a function of (a) hole width to flat web width and (b) hole length to column length

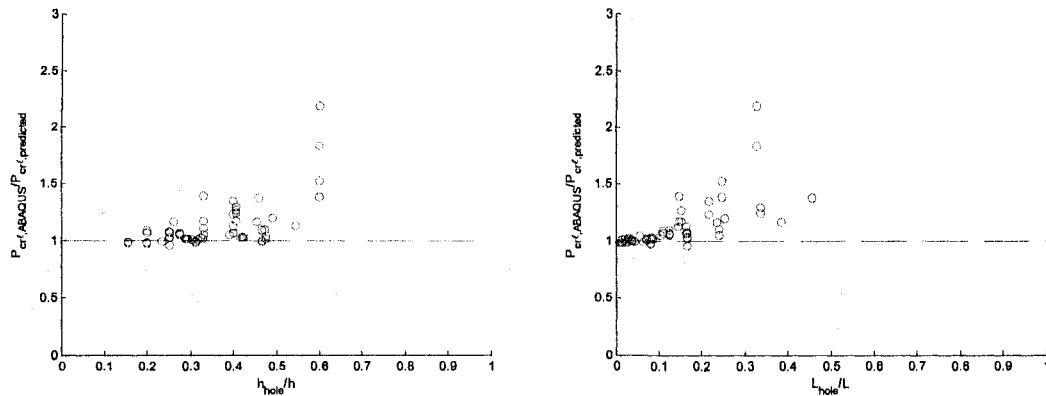


Figure 4.25 Predicted P_{cr} (CUFSM approximate method) is compared relative to the ABAQUS P_{cr} with experiment boundary conditions as a function of (a) hole width to flat web width and (b) hole length to column length

4.2.7.2 Distortional buckling

An approximate method utilizing the finite strip method is developed here for predicting the distortional critical elastic buckling load P_{crd} of cold-formed steel columns with holes. The method simulates the loss in bending stiffness of a cross-section within a distortional buckling half-wave by modifying the cross-section thickness in CUFSM. Two different approaches to simulating this loss in stiffness are evaluated. The first approach reduces the member thickness in the regions of the cross-section with holes based on the ratio of hole length to distortional half-wavelength. The second approach is developed for C-sections with web holes and is mechanics-based, where the thickness of the entire web is reduced based on an assumed relationship between web bending stiffness (derived with observations from ABAQUS thin shell elastic FE analyses) and the bending stiffness matrix terms of a finite strip element. The steps for implementing these methods in CUFSM are described, and an example is provided where the prediction method for P_{crd} is compared to ABAQUS eigenbuckling results for an industry

standard SSMA 250S162-68 cross-section with evenly spaced web holes along the length of a column. An empirical equation is derived to account for the increase in P_{crd} from warping fixed end conditions and then the viability of the approximate method is evaluated against P_{crd} from the column experiment database in Section 4.2.6.1.

4.2.7.2.1 Prediction method

The prediction method presented here for P_{crd} assumes that the change in cross-sectional stiffness within a distortional half-wave caused by the presence of a hole (or holes) can be simulated by assuming a reduced thickness of the cross-section. The distortional half-wavelength of the cross-section, L_{crd} , without holes is determined first. The elastic buckling curve is calculated using the gross section of the column in CUFSM and L_{crd} is read off of the curve at the location of the distortional local minimum as shown in Figure 4.26 (this elastic buckling curve corresponds to an SSMA 250S162-68 cross section, where $L_{crd}=12$ in.). The prediction method assumes that L_{crd} does not change with the presence of holes. The cross-section is then modified to approximate the presence of holes within a distortional half-wavelength. Two approaches for this modification step are presented next in Section 4.2.7.2.1.1 and Section 4.2.7.2.1.2. Once the cross section is modified to account for the presence of a hole in CUFSM, another elastic buckling curve is generated and P_{crd} (including the presence of the hole) is determined as the elastic buckling load occurring at L_{crd} as shown in Figure 4.26.

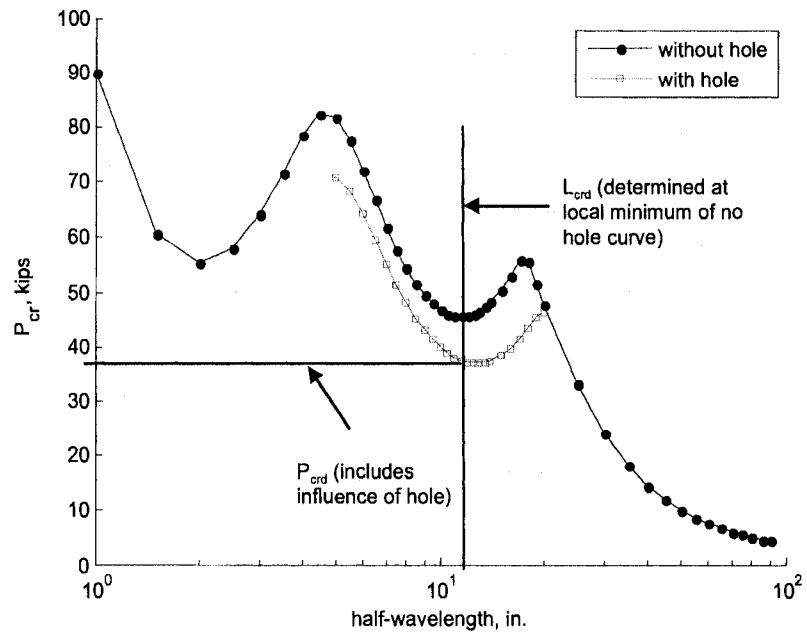


Figure 4.26 CUFSM approximate method for calculating P_{crd} for a column with holes.

4.2.7.2.1.1 “Weighted average” approach for predicting hole influence

The hole influence on distortional buckling of an open thin-walled cross section can be approximated by modifying the cross-section thickness in CUFSM at the location of a hole with the following equation:

$$t_{hole} = \left(1 - \frac{L_{hole}}{L_{crd}} \right) t. \quad (4.2)$$

The implementation of the reduced thickness in a C-section with a single web hole is provided in Figure 4.27. This approach is an intuitive first cut at approximating the reduction in bending stiffness of the cross section. A more refined mechanics-based approach is presented next.

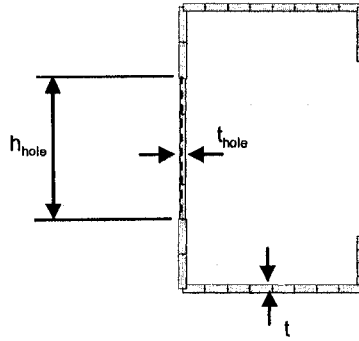


Figure 4.27 Modified cross section to be used in CUFSM to predict P_{crd} for a column with holes.

4.2.7.2.1.2 “Mechanics-based” approach for predicting hole influence

A plate model is developed in ABAQUS to study the influence of a hole on the bending stiffness of a SSMA 250S162-68 column experiencing distortional buckling. The stiffness reduction observed in ABAQUS is quantified and then equated to finite strip bending stiffness matrix terms to derive a reduced web thickness expression based on finite strip mechanics. The plate dimensions in ABAQUS are chosen to correspond to the web of the 250S162-68 section over one distortional half-wave. The plate width h is 2.4 in., the plate length $L=12$ inches (consistent with $L_{crd}=12$ in.), and $t=0.0713$ in. One slotted hole with $L_{hole}=4$ in. is centered in the plate. The width of the hole is varied, $h_{hole}=0.5$ in., 0.96 in., 1.20 in., 1.5 in., and 1.75 in. (and subsequently r_{hole} varies). The modulus of elasticity, E , is assumed as 29500 ksi and Poisson’s ratio, ν , as 0.3 for all finite element models considered here. The ABAQUS boundary conditions and applied loading are described in Figure 4.28. The plate is simply-supported and loaded with imposed rotations at the long edges of the plate with magnitudes varying as a half-sine wave to simulate distortional deformation over one half-wavelength.

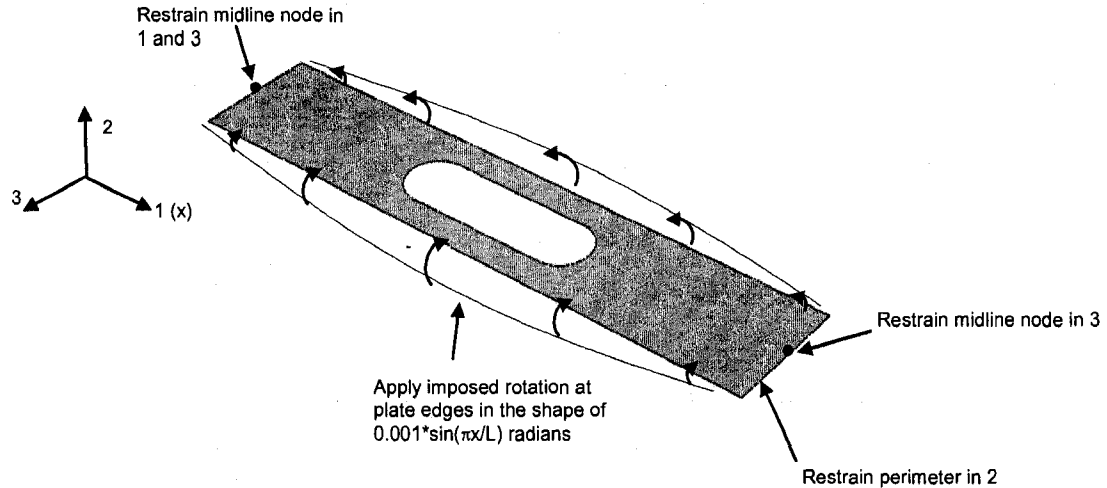


Figure 4.28 ABAQUS boundary conditions and imposed rotations for web plate

The deformed shape of the plate when $h_{hole}/h=0.50$ is provided in Figure 4.29. At each node where an imposed rotation is applied, the associated moment is obtained from ABAQUS and plotted in Figure 4.30 as a transverse bending stiffness per unit length. (Note that near $x=0$ in. and $x=12$ in., the deformed shape in ABAQUS results in a small negative bending stiffness which is not plotted in Figure 4.30 and does not affect the overall results here. The negative stiffness is not predicted in the finite strip formulation because the longitudinal shape function is enforced as a half-sine wave). The hole causes a sharp reduction in bending stiffness at the location of the hole, but has a minimal influence on bending stiffness away from the hole. The stiffness reduction is shown to be relatively insensitive to the ratio of hole width to plate width except for peaks in stiffness that increase with h_{hole}/h at the rounded edges of the slotted hole. The results in Figure 4.30 confirm the intuitive assumption employed to develop Eq. (4.2); the ratio of the length of the hole to the length of the distortional half-wave is an important parameter when predicting the loss in bending stiffness.

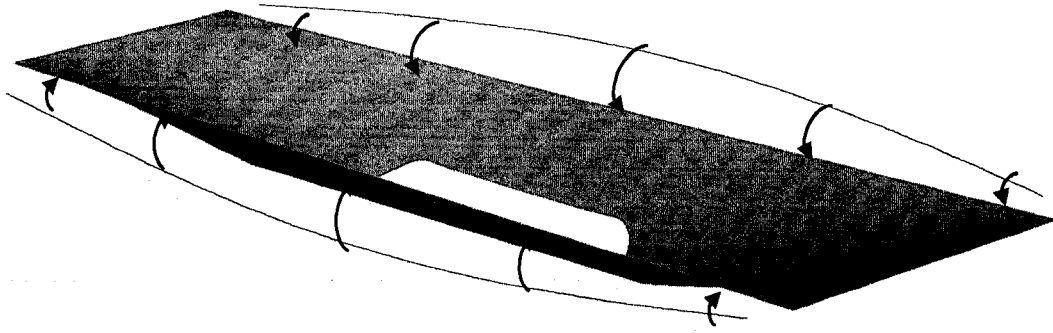


Figure 4.29 Plate deformation from imposed edge rotations, $h_{hole}/h=0.50$

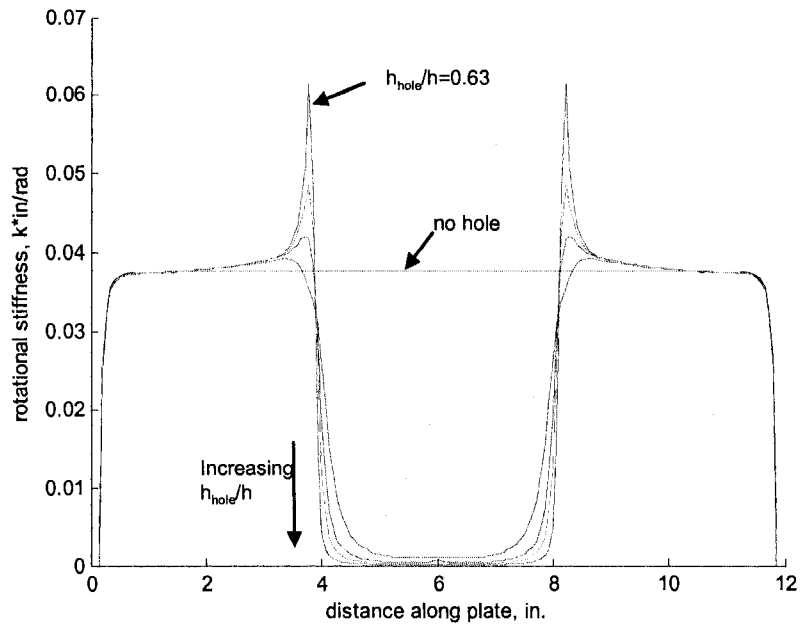


Figure 4.30 Transverse rotational stiffness of the plate is significantly reduced in the vicinity of the slotted hole

If K represents the cumulative transverse bending stiffness for the plate without a hole (area under the curve in Figure 4.30), then the reduced K including the presence of the hole can be approximated as:

$$K_{hole} = \left(1 - \frac{L_{hole}}{L_{crd}}\right) K. \quad (4.3)$$

The global bending stiffness K for a simply-supported finite strip element is derived by applying a unit rotation at the strip edges:

$$k_{eb} [d_{w\theta}]^T = \begin{bmatrix} k_{11} & k_{12} & k_{13} & k_{14} \\ k_{12} & k_{22} & k_{23} & k_{24} \\ k_{31} & k_{32} & k_{33} & k_{34} \\ k_{41} & k_{42} & k_{43} & k_{44} \end{bmatrix} \begin{Bmatrix} 0 \\ 1 \\ 0 \\ -1 \end{Bmatrix} = \begin{Bmatrix} V \\ K \\ V \\ K \end{Bmatrix}, \quad (4.4)$$

where the k_{eb} is the bending stiffness matrix and $d_{w\theta} = [w_1 \ \theta_1 \ w_2 \ \theta_2]$ (Schafer and Adányi 2006). Solving Eq. (4.4) for K :

$$K = k_{22} - k_{24}. \quad (4.5)$$

Since k_{22} and k_{24} are both functions of the web thickness $(t_{web})^3$, K and K_{hole} can be equated directly as:

$$\frac{K_{hole}}{K} = \frac{(t_{web,hole})^3}{(t_{web})^3}. \quad (4.6)$$

Substituting Eq. (4.6) and rearranging in terms of $t_{web,hole}$, the reduced web thickness corresponding to the reduced transverse bending stiffness from the hole is:

$$t_{web,hole} = \left(1 - \frac{L_{hole}}{L_{crd}}\right)^{1/3} t_{web}. \quad (4.7)$$

Eq. (4.7) is an improvement over Eq. (4.2) because it reflects the underlying plate bending mechanics involved in distortional buckling and is actually simpler to implement in CUFSM since the entire web thickness of a C-section is reduced to $t_{web,hole}$ instead of changing the sheet thickness just at the location of the hole as shown in Figure 4.27. A similar modification to t has been proposed for web-slotted thermal structural studs (Kesti 2000).

4.2.7.2.2 Method example

The distortional critical elastic buckling load P_{crd} is calculated here with the CUFSM prediction method for a long column ($L=100$ in.) with an SSMA 250S162-68 cross-section and five evenly spaced slotted web holes ($S=20$ in., $L_{hole}=4$ in.). The width of the hole is varied relative to the web width, and ABAQUS eigenbuckling results are used to evaluate the viability of the method. All ABAQUS finite element models have CUFSM style boundary and loading conditions as shown in Figure 4.2. The modulus of elasticity, E , is assumed as 29500 ksi and Poisson's ratio, ν , as 0.3 in all finite strip and finite element models. P_{crd} is normalized by $P_{y.g}$ when plotted. $P_{y.g}$ is the squash load of the column calculated with the gross cross-sectional area and assuming $F_y=50$ ksi.

A comparison of the CUFSM prediction method (employing the "weighted average" thickness approximation) and ABAQUS distortional buckling mode shapes are provided in Figure 4.31 when $h_{hole}/h=0.63$. Nine distortional half-waves form along the member in ABAQUS, with every other half-wave containing one slotted hole. The CUFSM prediction method employing both the "weighted average" and "mechanics-based" thickness modifications to the cross-section are compared over a range of h_{hole}/h to ABAQUS eigenbuckling results in Figure 4.32. P_{crd} for the pure ABAQUS distortional (D) buckling mode is plotted to demonstrate that prediction method is viable for this cross-section and hole spacing. The CUFSM prediction for P_{crd} with the "weighted average" thickness reduction at the hole decreases with increasing hole width since the web provides less bending stiffness to the flanges as more hole material is removed. The CUFSM prediction employing the "mechanics-based" reduction in web thickness is not

a function of h_{hole}/h and is shown to be a more realistic predictor of P_{crd} than the “weighted average” approach. These approximate methods are evaluated against ABAQUS distortional buckling predictions from the column database in Section 4.2.7.2.4.

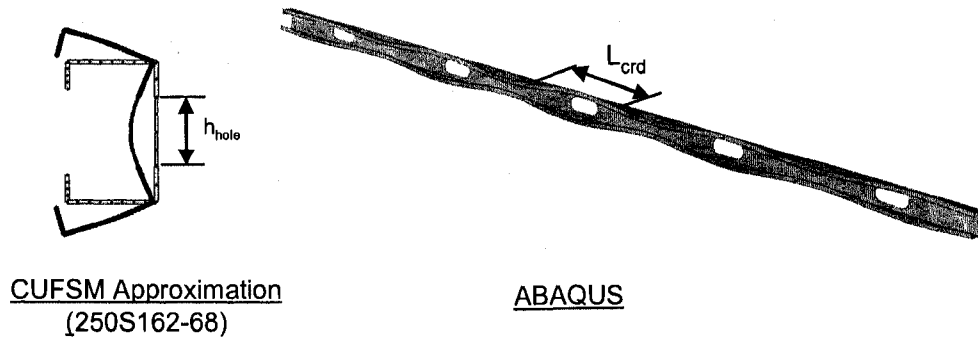


Figure 4.31 Comparison of CUFSM and ABAQUS distortional buckling mode shapes.

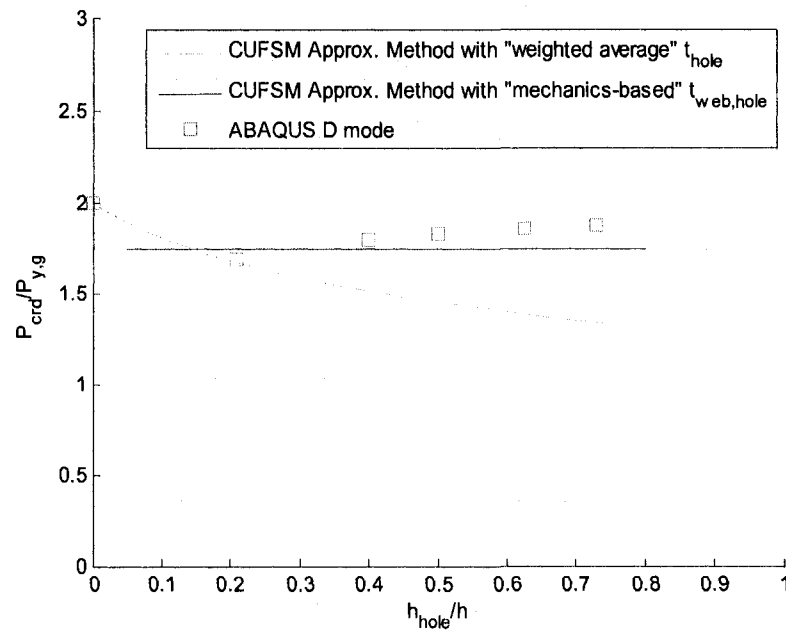


Figure 4.32 CUFSM distortional buckling prediction method is conservative when considering an SSMA 262S162-68 column with uniformly spaced holes.

4.2.7.2.3 Warping-fixed distortional amplification factor

Longitudinal warping deformations occur as a result of distortional buckling in cold-formed steel columns. When this warping deformation is restrained, the distortional buckling half-wavelength is shortened relative to the fundamental distortional half-wavelength of the column cross-section, L_{crd} . This change in half-wavelength results in an amplification of the distortional critical elastic buckling load of the column, P_{crd} (see Figure 4.13a for boost in P_{crd} for stub columns). The elastic buckling database developed in Section 4.2.6.1 (Table 4.4 and Table 4.6) provides an opportunity to derive an empirical amplification factor since for all columns in the database, P_{crd} for both warping-fixed (ABAQUS) and warping free (CUFSM) boundary conditions are known and the fundamental distortional half-wavelength, L_{crd} , has been calculated in CUFSM.

The warping-fixed boundary condition effect on P_{crd} is plotted for the 78 specimens in the column database in Figure 4.33. The boost in P_{crd} is highest when the column is short relative to L_{crd} because the wavelength shortening must be accommodated over just one half-wave. An empirical equation (also plotted in Figure 4.33) is fit to the data trend:

$$D_{\text{boost}} = 1 + \frac{1}{2} \left(\frac{L_{crd}}{L} \right)^2 \quad (4.8)$$

This amplification factor can be used with the CUFSM prediction method developed in Section 4.2.7.2.1 when the column being considered has warping-fixed boundary conditions. Eq. (4.8) is consistent with the distortional buckling boost factor provided in the DSM Design Guide (AISI 2006) as shown in Figure 4.33.

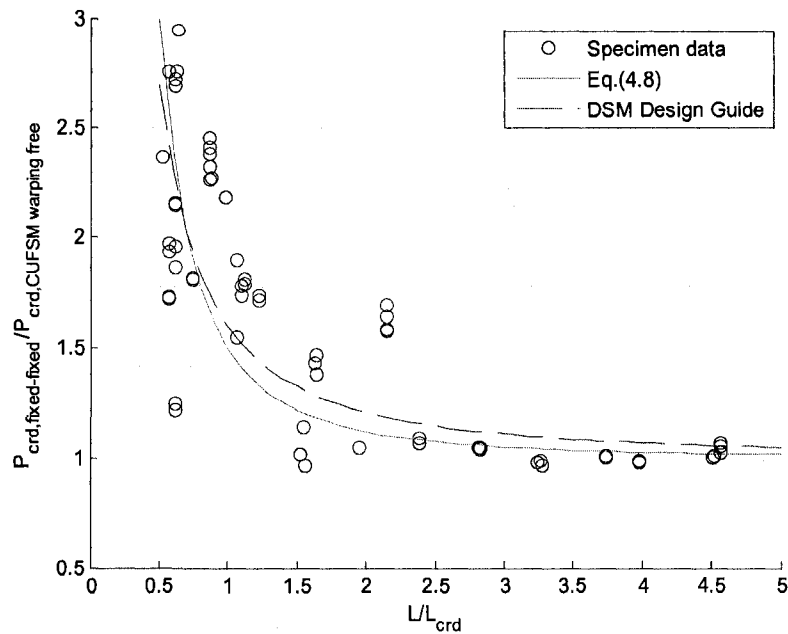


Figure 4.33 Warping-fixed boundary condition amplification of $P_{cr,d}$

4.2.7.2.4 Verification of CUFSM approximate method with column database

The CUFSM approximate method for distortional buckling is now evaluated using the elastic buckling properties of the 78 column specimens from the experiment database developed in 4.2.6.1. The ABAQUS distortional critical elastic buckling load $P_{cr,d}$ determined with the experiment boundary conditions, is plotted against the approximate method predictions in Figure 4.34. The predictions including the distortional amplification factor from Eq. (4.8). The approximate method employing the “weighted average” reduced web thickness at the hole from Eq. (4.2) and the “mechanics-based” reduced web thickness approach from Eq. (4.7) are both presented. The accuracy of the prediction method improves as the column length increases relative to the fundamental distortional half-wavelength $L_{cr,d}$. The prediction accuracy is highly

variable when $L/L_{crd} < 1$, primarily because of the variation in the boundary condition influence described in Section 4.2.7.2.3 for stocky columns. As expected, the “mechanics-based” thickness approach (with ABAQUS to predicted ratio mean and standard deviation of 1.19 and 0.29) is more accurate over the 78 columns than the “weighted average” approach (mean of 1.24 and standard deviation of 0.29).

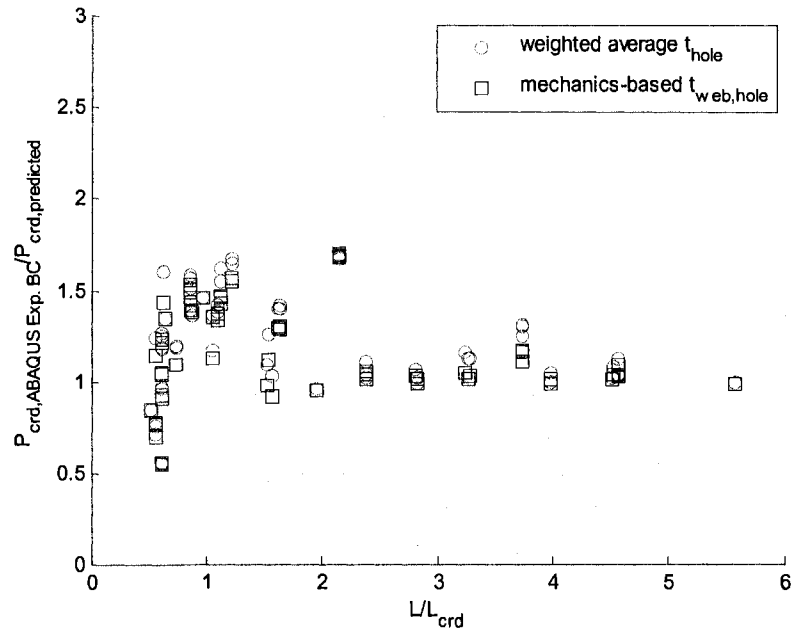


Figure 4.34 Accuracy of the CUFMS approximate method for predicting $P_{cr,d}$ improves as column length increases relative to the fundamental distortional half-wavelength for warping-fixed columns

4.2.7.3 Global buckling

Two different approximate methods for calculating the critical elastic buckling load of a column, $P_{cr,e}$, are evaluated in this section. Both methods employ weighted averages of the member section properties in the classical column stability equation to account for the influence of holes, one using a weighted cross-sectional thickness at the locations of the hole and the other using the weighted average of the gross and net cross sections. The

approximate methods are compared to ABAQUS eigenbuckling results for a long cold-formed steel column (SSMA 1200S162-68 cross section) with uniformly spaced circular holes. The average torsional constants, J and C_w , are calculated directly using ABAQUS for this column and then compared to their associated weighted average estimates. Based on these studies, recommendations are made regarding the approximate method most suitable for predicting P_{cre} for columns with holes.

4.2.7.3.1 Description of methods

4.2.7.3.1.1 Weighted Properties Method

The equation for predicting the global (flexural only) critical elastic buckling load P_{cre} of a column with holes along its length can be solved using energy methods, and is derived for a column with two holes located symmetrically about the longitudinal midline of the column in Appendix E. The equation that evolves from the Raleigh-Ritz derivation for this case is:

$$P_{cre} = \frac{\pi^2 E}{L^2} \left(\frac{I_g L_{NH} + I_{net} L_H}{L} \right) \quad (4.9)$$

where I_g is the moment of inertia of the gross cross-section, I_{net} is the moment of inertia of the net cross-section, L_{NH} is the length of column without holes and L_H is the length of column with holes (note that $L_{NH} + L_H = L$). The average moment of inertia of the column with holes is shown in Eq. (4.9) to be equivalent to the weighted average of the gross and net cross sections along the column length. An approximate method for calculating P_{cre} is proposed here which extends this “weighted properties” methodology in Eq. (4.9)

to all of the cross-section properties of the column required to solve the classical cubic buckling equation for columns (Chajes 1974):

$$(P_{cre,y} - P)(P_{cre,x} - P)(P_{cre,\phi} - P) - (P_{cre,y} - P)\frac{P^2 x_o^2}{r_o^2} - (P_{cre,x} - P)\frac{P^2 y_o^2}{r_o^2} = 0 \quad (4.10)$$

including the cross-sectional area A , moment of inertia I_x and I_y , St. Venant torsional constant J , and shear center location. The computer program CUTWP solves Eq. (4.10) for any general cross-section and is freely available (Sarawit 2006). The net section properties can be calculated in CUFSM (or CUTWP) by reducing the sheet strip thickness to zero at the location of the hole. This approximation is referred to as the “weighted properties” method. A general form of Eq. (4.9) is also derived in Appendix E which can be used with the “weighted properties” method for the case of a column with a single hole or multiple arbitrarily-spaced holes.

4.2.7.3.1.2 Weighted Thickness Method

This approximate method approaches the calculation of the average column section properties in a different way, by using a weighted member thickness at the location of the holes in the cross-section to calculate the average cross sectional properties:

$$t_{hole} = \frac{L - L_H}{L} t. \quad (4.11)$$

An example of a C-section with a reduced thickness at the location of a web hole is provided in Figure 4.35. This “weighted thickness” method is more convenient to implement than the “weighted properties” method presented in the previous section

because the modified cross-section (with reduced thickness) can be input directly into a computer program such as CUTWP.

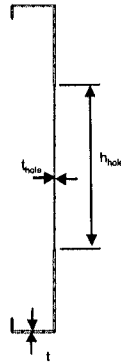


Figure 4.35 A “weighted thickness” cross section can be input directly into a program that solves the classical cubic stability equation for columns (e.g. CUTWP).

4.2.7.3.2 Example and verification

ABAQUS global eigenbuckling results are compared in this section to the “weighted properties” and “weighted thickness” prediction methods for an industry standard SSMA 1200S162-68 long column (SSMA 2001) with evenly spaced circular holes. The length of the column $L=100$ in., the hole spacing $S=20$ in., and the diameter of the circular hole is varied from $h_{hole}/H=0.10$ to $h_{hole}/H=0.90$ where H is the out-to-out depth of the cross-section (see Figure 4.1 for cross-section dimension notation). All ABAQUS finite element models are loaded in compression at the member ends and have warping free boundary conditions as shown in Figure 4.2. The modulus of elasticity, E , is assumed as 29500 ksi and Poisson’s ratio, ν , as 0.3 in all CUTWP and finite element models.

The three global buckling modes of this SSMA 1200S162-68 long column without holes are calculated in CUTWP: (1) weak axis flexural buckling occurs at $P_{\sigma}=7.91$ kips, (2) flexural-torsional buckling occurs at $P_{\sigma}=13.39$ kips, and (3) strong-axis flexural

buckling occurs at $P_{cr}=604.17$ kips. The first two buckling modes are the focus of this study since the strong-axis buckling mode is much higher than the squash load of the column ($P_{y,s}=56.30$ kips assuming $F_y=50$ ksi) and will not influence the design of the column. Figure 4.36 provides an example of the weak-axis flexural and flexural-torsional buckling modes when $h_{hole}/H=0.50$. Note that shell FE predicts local buckling mixing with the weak-axis flexural mode when $h_{hole}/H>0.50$ because P_{cr} is reduced by the presence of holes to a magnitude similar to the local critical elastic buckling load ($P_{cr}=6.69$ kips). Local buckling is not observed to mix with global buckling in the flexural-torsional (column) or lateral-torsional (beam) buckling in this study.

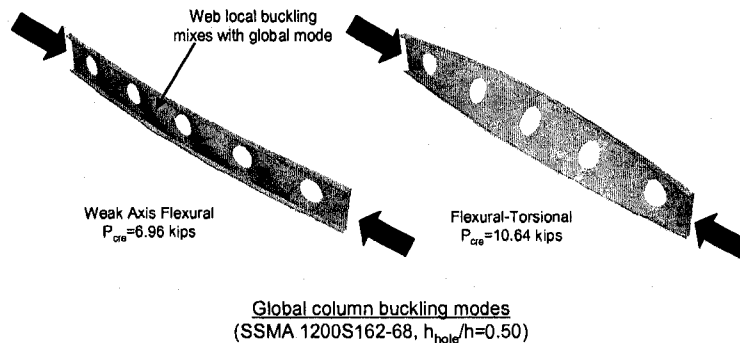


Figure 4.36 Weak-axis flexural and flexural-torsional global buckling modes for an SSMA 1200S162-68 column with evenly spaced circular holes.

4.2.7.3.2.1 Section property calculations at the net section

To draw meaningful conclusions regarding the “weighted properties” and “weighted thickness” prediction methods it is first helpful to understand how circular hole diameter influences the column’s section properties. Figure 4.37 compares the net section to the gross cross-sectional area A , the strong and weak axis moment of inertia I_x and I_y , the St. Venant torsional constant J , and the warping torsional constant C_w of the

column as they vary with h_{hole}/H . All net section properties in this figure are determined with the CUFSM section property calculator by reducing the sheet thickness to zero at the location of the hole. A and J decrease linearly with hole diameter while I_x and I_y decrease nonlinearly. I_y is most sensitive to the presence of the hole because the hole is located in the channel web for this case, which provides much of the contribution to the weak axis moment of inertia. C_w , calculated here assuming zero thickness but continuity through the hole, varies nonlinearly with h_{hole}/H . It is unclear if the net section C_w calculated in this way produces the best approximation of the column's actual physical behavior in torsional buckling. The magnitude of C_w is influenced heavily by cross-section continuity since a line integral around the cross-section is used to solve for the warping function. Further investigation of J and C_w for columns with holes is presented in Section 4.2.7.3.2.3.

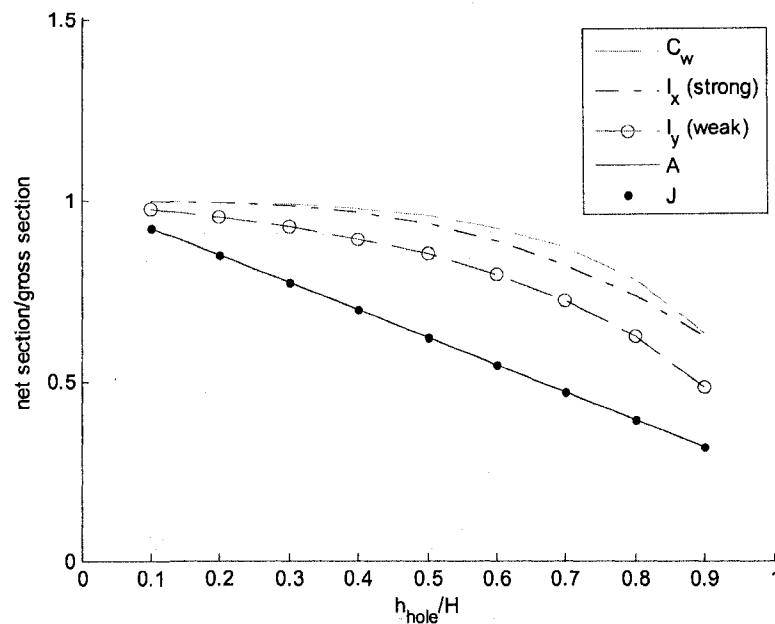


Figure 4.37 Variation in net section properties as circular hole diameter increases.

4.2.7.3.2 Average section property calculations for the column - A, I_x , and I_y

The average section properties of the 1200S162-68 column with circular holes calculated using the “weighted thickness” and “weighted properties” methods are compared in Figure 4.38 through Figure 4.40. For this example problem there are minimal differences between the methods for A and I_x , although I_y calculated with the “weighted properties” method decreases in stiffness relative to the “weighted thickness” method as hole diameter increases relative to column width.

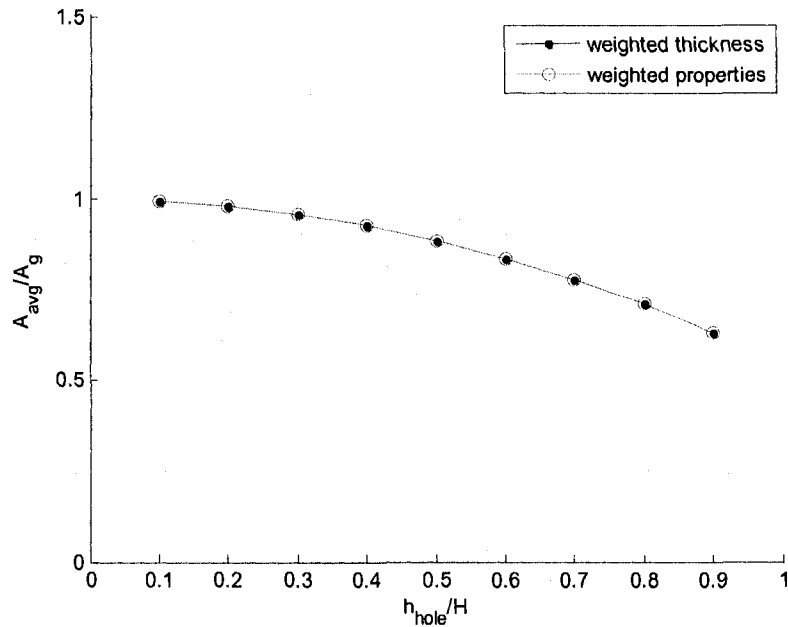


Figure 4.38 Comparison of “weighted thickness” and “weighted properties” cross-sectional area.

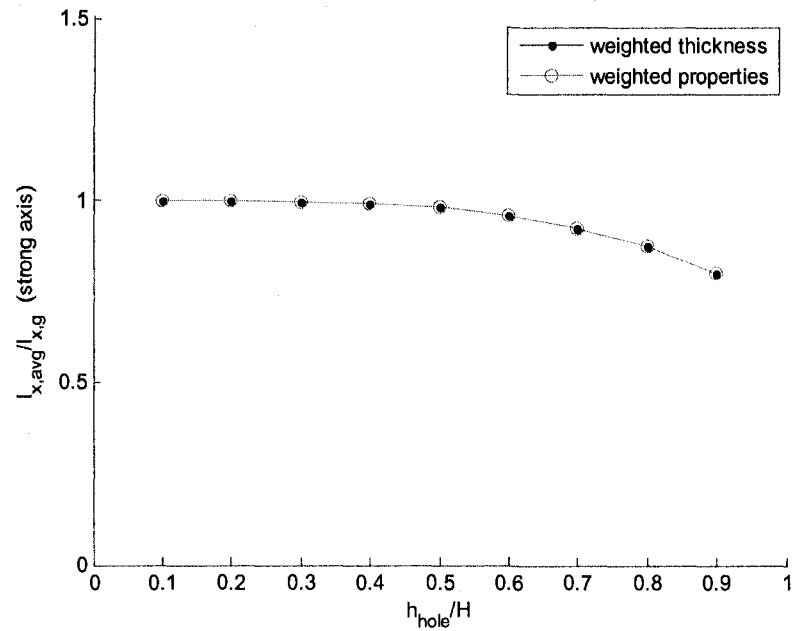


Figure 4.39 Comparison of “weighted thickness” and “weighted properties” strong axis moment of inertia.

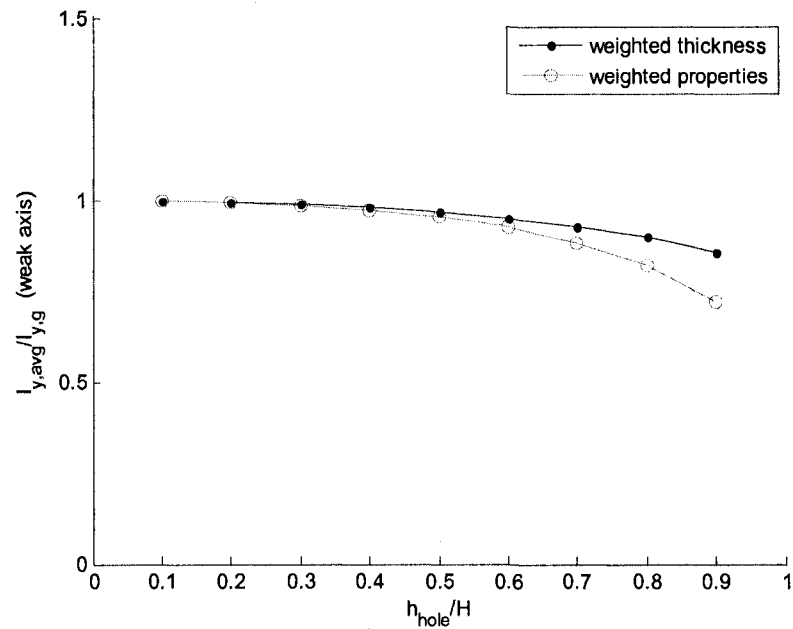


Figure 4.40 Comparison of “weighted thickness” and “weighted properties” weak axis moment of inertia.

4.2.7.3.2.3 Average section property calculations for the column - J and C_w

The average J and C_w of the 1200S162-68 column with circular holes is determined directly using ABAQUS and then compared to the “weighted properties” and

“weighted thickness” predictions in this section. The differential equation for torsion is defined as (Timoshenko 1961):

$$T = GJ \frac{d\beta}{dx} - EC_w \frac{d^3\beta}{dx^3}, \quad (4.12)$$

where β is the angle of twist of the cross section and G is the shear modulus of steel ($G=11346$ ksi in this case). Eq. (4.12) is used in conjunction with static ABAQUS analyses (not eigenbuckling!) to solve for J_{avg} and $C_{w,avg}$ of the column as h_{hole}/H varies from 0.10 to 0.90. J_{avg} is calculated by applying a unit twist at the end of the column about the gross cross-section shear center while keeping the opposite column end fixed against twist as shown in Figure 4.41. If both ends of the column are free to warp, the variation in twist along the column is constant as shown in Figure 4.42 and warping resistance does not contribute to the resulting torsion ($d^3\beta/dx^3=0$). The variation in twist was not sensitive to increasing hole diameter in this case, and therefore the line shown in Figure 4.42 is the same regardless of hole diameter. The twist β along the column is measured in ABAQUS as the relative rotation of the flange-web corners. The twist magnitude along the column length remains unchanged with increasing h_{hole}/H . J_{avg} for the warping free column is calculated by rearranging Eq. (4.12):

$$J_{avg} = \frac{T_o}{G} \frac{L}{\beta_o} \quad (4.13)$$

β_o , G , and L are known and T_o is the torque resulting from the unit rotation β_o , which is read directly from ABAQUS.

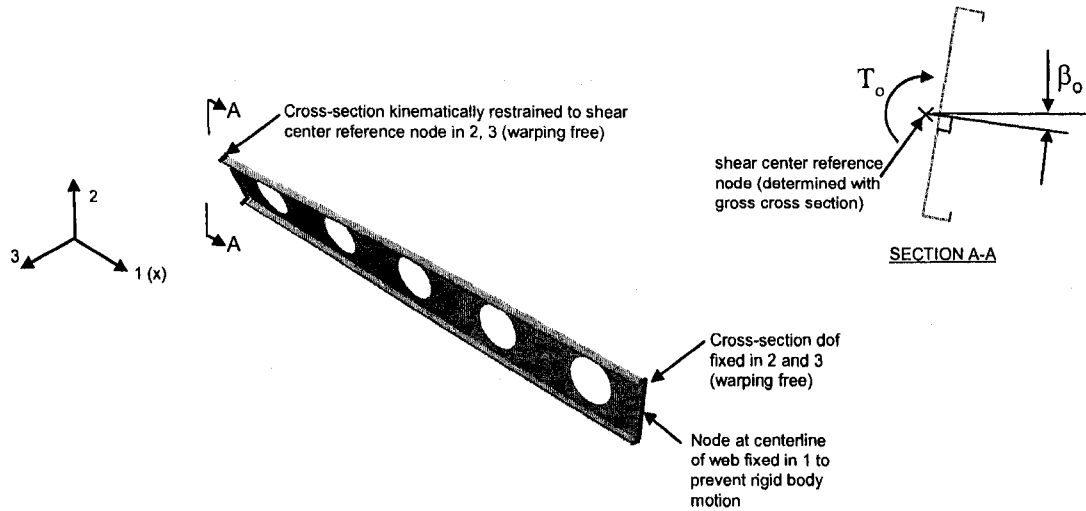


Figure 4.41 ABAQUS boundary conditions for warping free and applied unit twist at $x=0$ in. and warping free but rotation restrained at $x=100$ in.

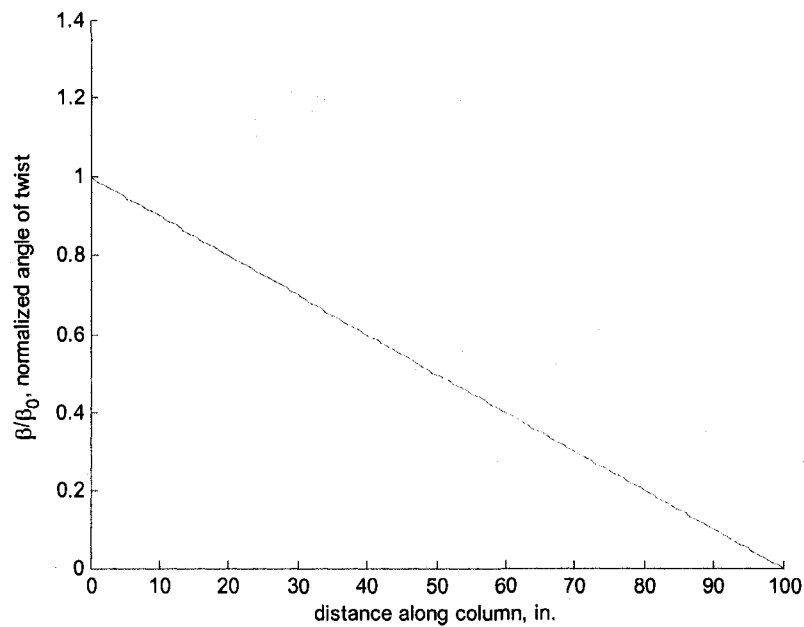


Figure 4.42 Angle of twist decreases linearly in the SSMA 1200S162-68 column with warping free end conditions.

The resulting J_{avg} from ABAQUS is compared against the “weighted properties” and “weighted thickness” calculations of J_{avg} . (Note that the “weighted properties” J_{avg} is calculated with J_{net} from Figure 4.37 using the CUFMS section property calculator and

assuming the thickness is zero at the hole). It is clear from Figure 4.43 that the “weighted properties” calculation of J_{avg} is most consistent with J_{avg} derived from ABAQUS.

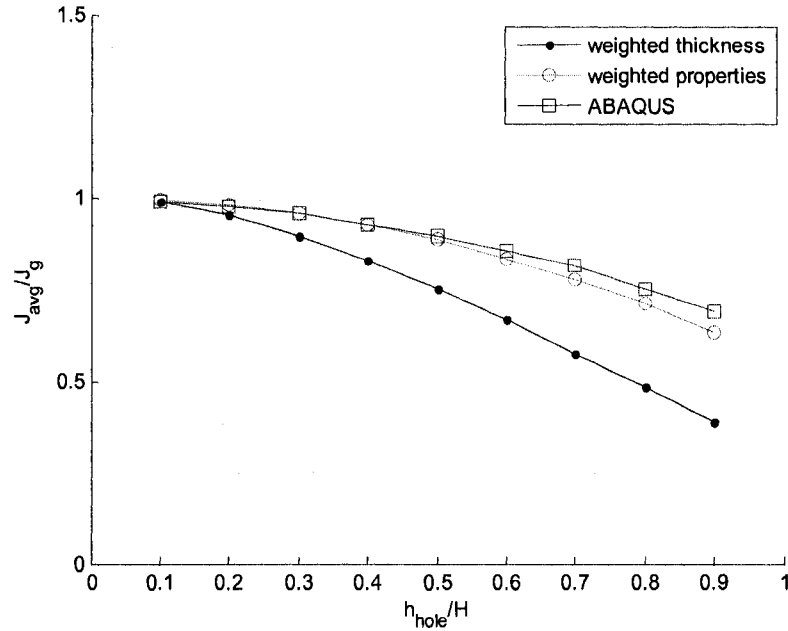


Figure 4.43 The “weighted properties” approximation for J_{avg} matches closely with the ABAQUS prediction for the SSMA 12S00162-68 column with holes

The ABAQUS boundary conditions are now modified such that warping is restrained at the fixed column end as shown in Figure 4.44. A unit twist, β_o , is again applied at the free end, and the resulting angle of twist β along the length of the column is measured in ABAQUS. Because of the warping-fixed end condition, β is nonlinear along the length of the column and warping resistance contributes to the torsional stiffness of the column. Since the distribution of β along the column is not influenced by h_{hole}/H as observed in ABAQUS, an indirect solution of $C_{w,avg}$ as a function of $C_{w,g}$ can be derived:

$$\frac{C_{w,avg}}{C_{w,g}} = \frac{T_o - GJ_{avg} \frac{d\beta}{dx}(x=0)}{T_{o,g} - GJ_g \frac{d\beta}{dx}(x=0)}, \quad (4.14)$$

where for each ABAQUS model ($h_{hole}/H=0.10$ to 0.90), the torque T_o associated with the unit twist β_o is read directly from ABAQUS and $d\beta/dx(x=0)$ is calculated from Figure 4.45. As was the case for the warping free case in Figure 4.42, the variation in twist was not sensitive to increasing hole diameter and therefore the line shown in Figure 4.45 is the same regardless of hole diameter. The influence of holes on the variation in twist is expected to be more pronounced as column length decreases relative to hole length. Future research is planned to evaluate the influence of member length on the torsional properties of columns with holes.

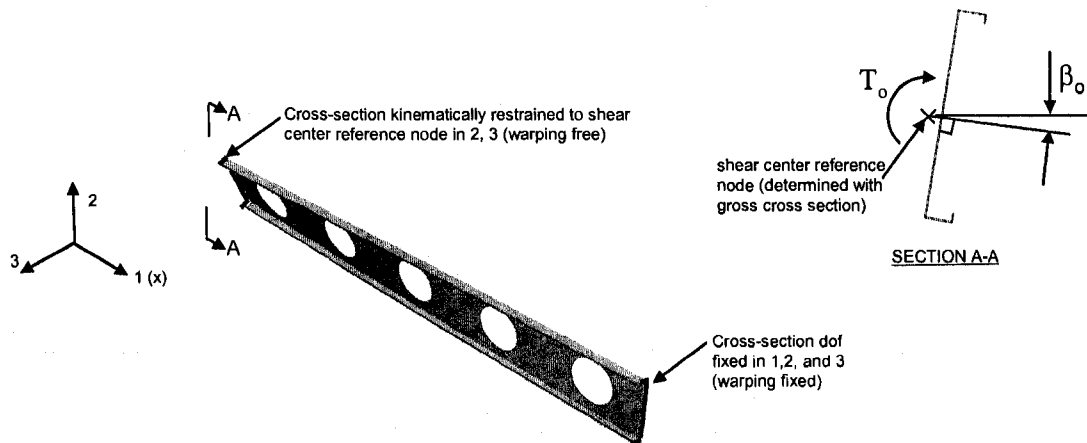


Figure 4.44 ABAQUS boundary conditions for warping free and applied unit twist at $x=0$ in. and warping fixed and rotation restrained at $x=100$ in.

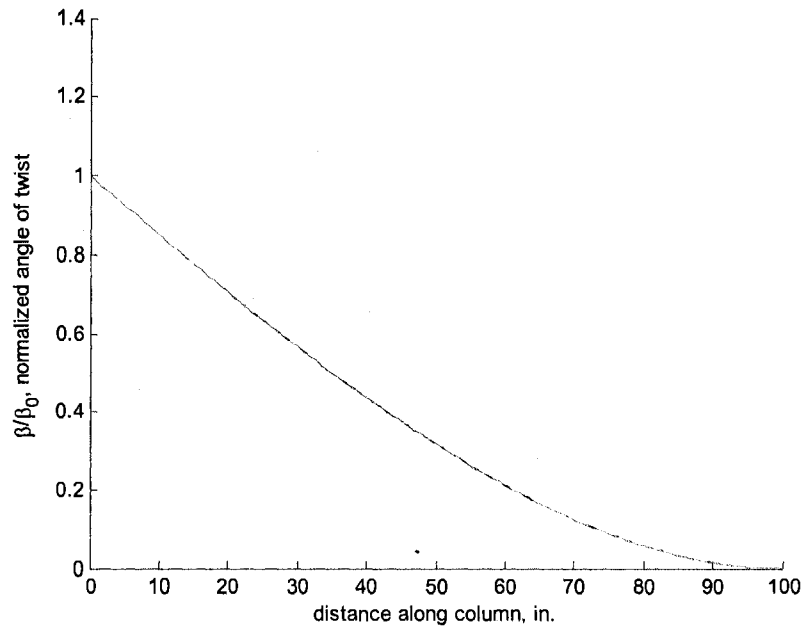


Figure 4.45 Angle of twist is nonlinear along the SSMA 1200S162-68 column with warping fixed end conditions at $x=100$ in.

Figure 4.46 demonstrates that the “weighted properties” and “weighted thickness” approximations both overestimate $C_{w,avg}$ when compared to the ABAQUS derived $C_{w,avg}$ demonstrating that neither is an accurate predictor of $C_{w,avg}$. A modified version of the “weighted properties” approximation is also plotted, where $C_{w,net}$ is taken equal to zero instead of $C_{w,net}$ taken from the results in Figure 4.37. This assumption for $C_{w,net}$ is motivated by the idea that the hole separates the cross section into two pieces, where each piece on its own contributes minimally to warping resistance. This modified “weighted properties” approximation results in a conservative lower bound on $C_{w,avg}$ which is useful from a design perspective until more accurate approximations are developed.

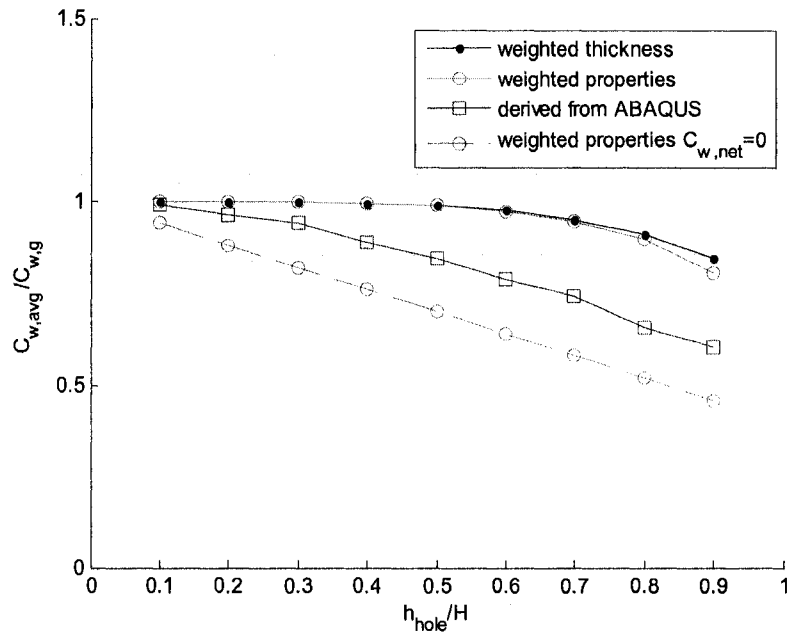


Figure 4.46 Comparison of “weighted thickness” and “weighted properties” approximations to the ABAQUS derived warping torsion constant $C_{w,avg}$.

4.2.7.3.2.4 Comparison of prediction accuracy between methods

Figure 4.47 compares the weak-axis flexural critical elastic buckling load of the 1200S162-68 column calculated with the “weighted thickness” and “weighted properties” prediction methods to ABAQUS eigenbuckling results. The ABAQUS calculation of P_{cre} is systematically 10% lower than the prediction method (even for a column without holes), which results from the assumption of a rigid cross-section in the classical stability equations. The column cross-section as modeled in ABAQUS is allowed to change shape along the length, resulting in a lower axial stiffness of the column. (The reduction in P_{cre} was also confirmed in CUFSM, which like ABAQUS, accounts for plate-type deformations in elastic buckling calculations.) Beyond this systematic difference, both approximate methods are accurate predictors of P_{cre} for

$h_{hole}/h \leq 0.60$ and the “weighted properties” method remains accurate for even larger holes.

The prediction of weak-axis flexure P_{cre} using the net section properties from Figure 4.37 is also plotted in Figure 4.47, demonstrating a conservative alternative to the “weighted properties” and “weighted thickness” methods.

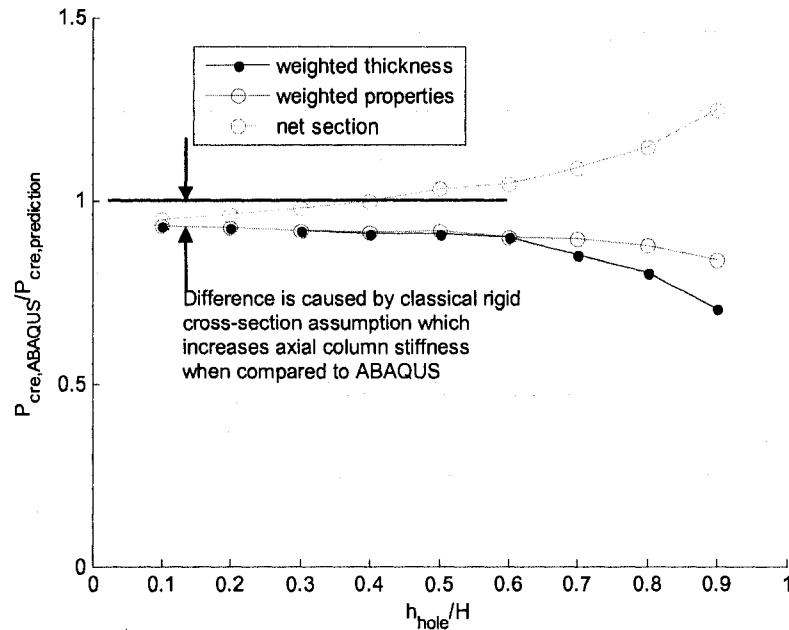


Figure 4.47 Comparison of “weighted thickness” and “weighted properties” prediction methods for the SSMA 1200S162-68 weak-axis flexural buckling mode. Predictions using net section properties are also plotted as a conservative benchmark.

Figure 4.48 compares the “weighted thickness” and “weighted properties” methods to ABAQUS results for the second global mode, flexural-torsional column buckling. The accuracy of the prediction methods decrease with increase h_{hole}/H for both methods, confirming what was observed in Figure 4.46, that the weighted approximations for C_w are not accurate representations of the average warping torsion stiffness, especially as h_{hole}/H becomes large. Warping torsion dominates over St. Venant torsion in this mode since both weighted average methods predict similar variations in P_{cre} , even though J varies between the two methods (see Figure 4.43). The “weighted properties” method

with $C_{w,avg}$ replaced with $C_{w,avg}$ predicted in ABAQUS (see Figure 4.46) accurately predicts P_{cre} until h_{hole}/H exceeds 0.80, although this method may not be practical from a design perspective since it requires thin shell FE analysis. The modified “weight properties” approach, calculated assuming $C_{w,net}=0$, is shown to be more accurate than using just the net section properties and is a conservative method for predicting P_{cre} of flexural-torsional buckling modes. Future research is planned to develop a mechanics-based approximation for the average C_w of a column including the influence of holes.

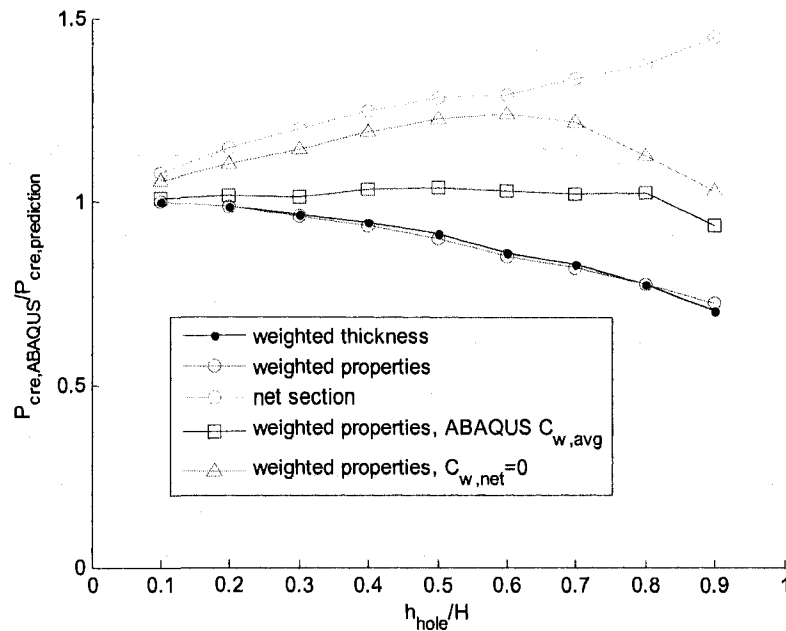


Figure 4.48 Comparison of “weighted thickness” and “weighted properties” prediction methods for the SSMA 1200S162-68 flexural-torsional column buckling mode. Predictions using net section properties are also plotted as a conservative benchmark.

4.3 Elastic buckling of beams with holes

4.3.1 Analysis of existing tests on beams

A column experiments database was assembled in Section 4.2.6.1 to serve as a resource in the development and validation of the Direct Strength Method for columns with holes. In this section, a similar database is developed that summarizes the elastic buckling properties and tested strengths of cold-formed steel beam experiments with holes. This database is used in Chapter 8 when developing and verifying DSM for beams with holes.

The beam experiments considered in this study were conducted by Shan, LaBoube, Schuster, and Batson in the early 1990's and consist of three separate test sequences (Batson 1992; Schuster 1992; Shan and LaBoube 1994). Test Sequences 1 and 2 were performed at the University of Missouri-Rolla (UMR) and Test Sequence 3 was executed at the University of Waterloo. Each specimen is made up of two C-sections oriented toe-to-toe as depicted in Figure 4.49. 3/4"x3/4"x1/8" aluminum angles connect the top and bottom flanges of the two channels with one self-drilling screw per flange. The angles provide a closed beam section that prevents lateral-torsional buckling of the individual channels.

4.3.1.1 Member and hole dimension notation

Beam cross-section and hole dimension notation is presented in Figure 4.50. The C-section inside corner radii are assumed to equal twice the measured thickness of the specimen. Two hole shapes were considered in the experiments, an industry standard

slotted hole and a tri-slotted hole with the curved hole ends replaced by triangular tips. The holes are centered in the web and are mechanically punched at 24 inches on center longitudinally with a hole at the center of the span.

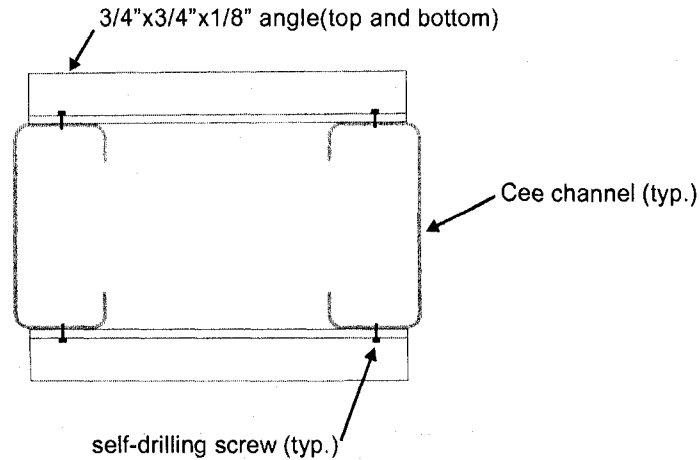


Figure 4.49 Cross section of beam specimen showing aluminum strap angles connected to C- flanges

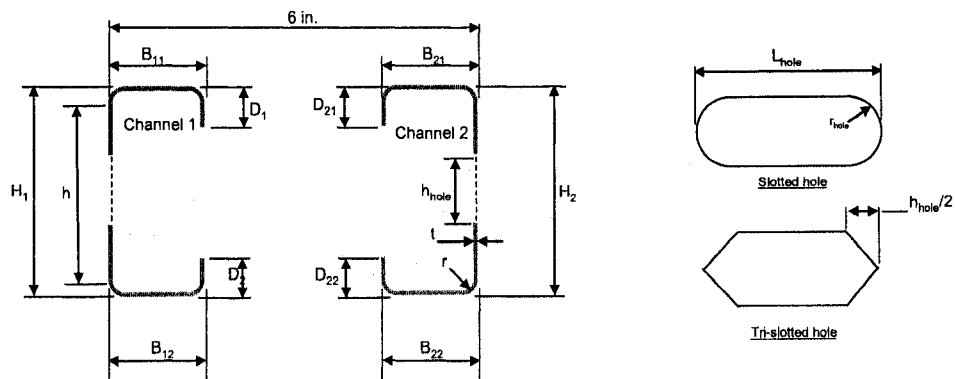


Figure 4.50 C-section and hole dimension notation

4.3.1.2 Tested boundary conditions and loading

All beam specimens are tested as simply supported in four-point bending to create a region of constant moment between the load points at the center of the beam.

The point loads are applied through stub channels attached to the beam webs with self-drilling screws. The stub channels prevent web crippling by distributing the concentrated load and by restraining the web. Lateral bracing is provided in the vicinity of the constant moment region by struts connecting the top flange aluminum angles to a reaction frame. The ends of the beam specimens are laterally braced by vertical rollers. A summary of the beam test setup is provided in Figure 4.51.

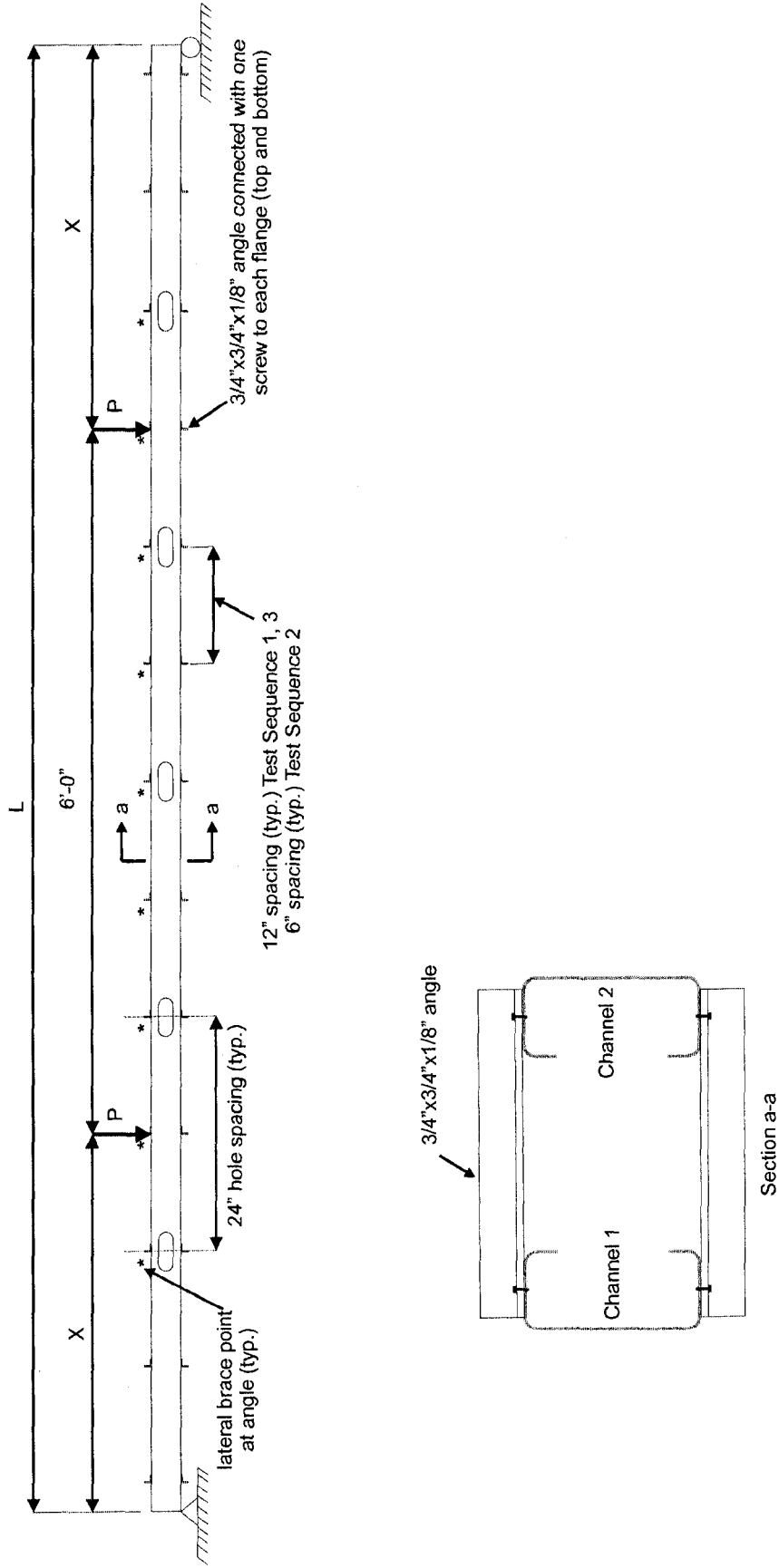


Figure 4.51 Experiment test setup with hole spacing, location of lateral bracing, spacing of aluminum angle straps, and load points

4.3.1.3 Finite Element Modeling

The elastic buckling properties of the 72 beam specimens are obtained with eigenbuckling analyses in ABAQUS (ABAQUS 2004). All beams are modeled with S9R5 reduced integration nine-node thin shell elements. Refer to Section 2.1 for a detailed discussion of the S9R5 element. Cold-formed steel material properties are assumed as $E=29500$ ksi and $\nu=0.3$.

Special care is taken to simulate the experimental boundary conditions when modeling in ABAQUS. The simple supports with vertical roller restraints, the aluminum angle straps connecting the top and bottom channel flanges, the lateral bracing of the top flange in the constant moment region, and the application of load through the webs and are all considered. Figure 4.52 summarizes the ABAQUS boundary condition assumptions.

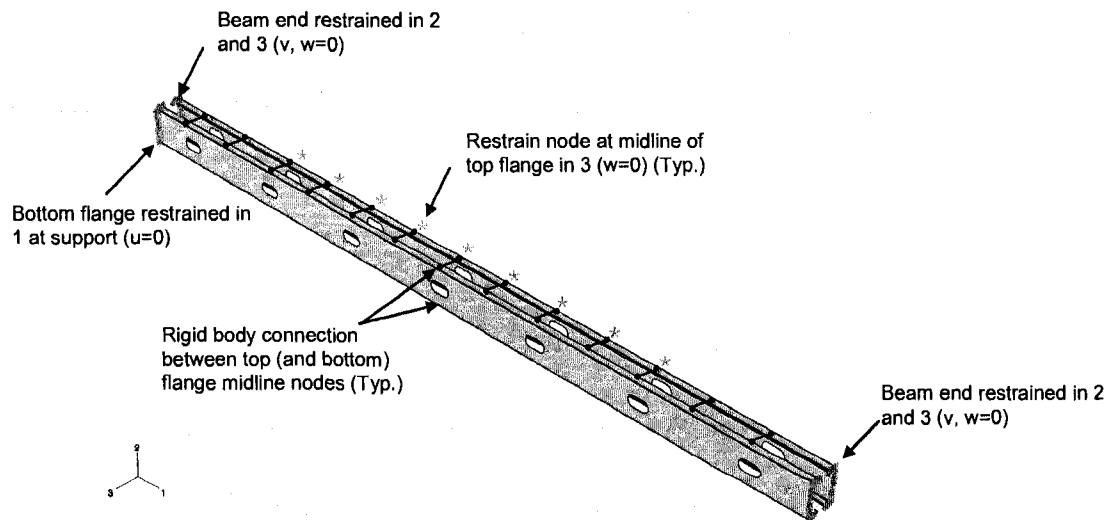


Figure 4.52 Finite element model boundary conditions for beam eigenbuckling analyses

To simulate the simply supported conditions with vertical rollers, the ends of the beams are modeled as warping free except for the bottom flange at one end which is

restrained to prevent longitudinal rigid body movement. The channel cross-sections are restrained from vertical and lateral translation at both beam ends.

A rigid body restraint is used to model the connectivity between the top and bottom C-section flanges provided by the aluminum angle straps connected with self-drilling screws. Figure 4.53 demonstrates how each angle is modeled as a rigid body made up of one midline flange node from each channel. The rigid body definition requires that the motion (both translational and rotational) of the two nodes is governed by a single reference node, in this case the midline flange node of Channel 1. The formulation allows for rigid body motion but requires that the relative position of the two nodes remains constant. A disadvantage of this rigid body restraint is that flange movements are only restrained at the midline node and do not simulate contact between the channel flange and aluminum angle, which sometimes results in distortional buckling modes that would not be physically possible.

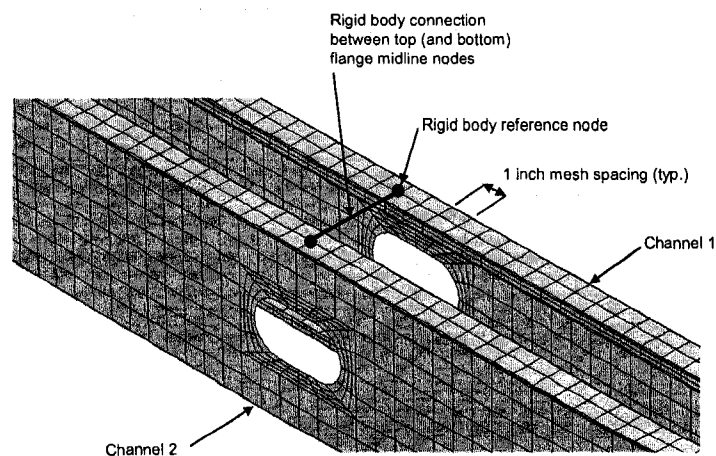


Figure 4.53 Channel and hole meshing details and modeling of aluminum angle straps

Element meshing is performed with a custom-built Matlab program written by the author (See Appendix A). Figure 4.53 provides an example of a typical FE mesh, where

the holes are defined with a series of element lines radiating from the opening. Figure 4.54 provides a close-up view of the rounded corner meshing of the channels. Two elements model the rounded corners here because S9R5 elements have quadratic shape functions which allow the initial curved geometry. Refer to Section 2.2 for more information on modeling rounded corners with S9R5 elements.

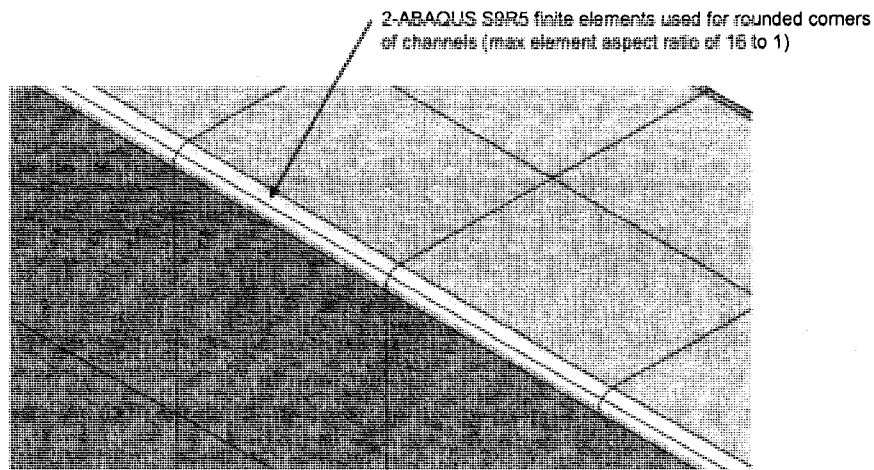


Figure 4.54 ABAQUS meshing details for C-section rounded corners

Concentrated loads are applied to the beam specimens through vertical stub channels connected to the beam webs with self-drilling screws. To simulate the distribution of the load into a channel web, the concentrated load is applied as a group of web point loads in ABAQUS. Figure 4.55 demonstrates how the concentrated loads are applied to the beam webs in the finite element models. The web local buckling restraint (essentially doubling up of the web at the loading point) provided by the stub channels is not modeled in ABAQUS because it was observed to have a negligible influence on the elastic buckling behavior in the relatively long constant moment regions of the beams.

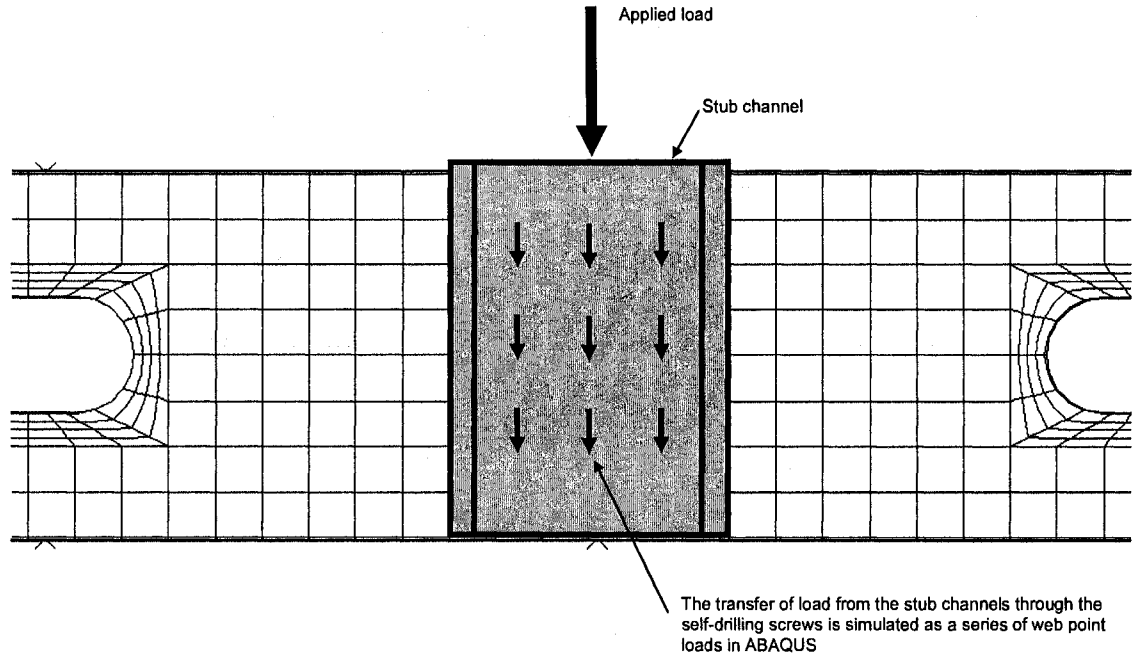


Figure 4.55 Modeling of the beam concentrated loads in ABAQUS

4.3.1.4 Elastic buckling results and mode definitions

The beam specimen elastic buckling modes were reviewed in ABAQUS by the author to identify the pure local (L) and distortional (D) buckling modes as well as any mixed elastic modes created by the addition of web holes. Lateral-torsional buckling is restrained by the top flange lateral bracing and aluminum angle straps (see Figure 4.51), although other possible global (G) buckling modes are possible as discussed in Section 4.3.1.4.3.

The mode identification process for beams with holes is guided by the experiences obtained in Section 4.2.4 for cold-formed steel compression members with holes. C-section columns with web holes exhibited unique mixed buckling modes where distortion of the flanges near the hole mixes with local buckling (LH mode). In

this beam study mixed local-distortional modes are again observed, as well as local web hole modes initiated by the compression component of the stress gradient from bending.

4.3.1.4.1 Local Buckling

Slotted holes in the beam specimen webs initiate unique local buckling modes and reduce the critical elastic local buckling moment $M_{cr\ell}$ in most cases. The shallow beam specimen without holes (nominal depth of 2.5 inches) in Figure 4.56 exhibits local buckling in both the top flange and web. The addition of slotted web holes creates a new local buckling mode, the LH2 mode. The LH2 mode occurs when the strip of web above the hole buckles in two half-waves. This mode occurs because the fundamental local buckling half-wavelength of the cross-section, $L_{cr\ell}$ is less than the length of the hole. The critical elastic buckling moment for the LH2 mode is 8 percent less than that of the pure L mode, suggesting that this local hole mode may influence the load-deformation response of the beam.

Figure 4.57 compares the elastic buckling behavior of a slightly deeper beam (nominal depth of 3.625 inches) with and without holes. The addition of slotted web holes again creates the LH2 mode with a critical elastic buckling moment that is 17 percent less than the pure L mode. Figure 4.58, Figure 4.59, and Figure 4.60 summarize the influence of slotted holes on the local buckling behavior of deeper beams with nominal heights of 6 inches, 8 inches, and 12 inches respectively. The LH mode is identified in these deeper beam depths as the buckling of the strip of web above the hole into a single half-wave. The LH2 mode is observed in the 6 in. and 8 in. deep beams but

with a higher critical elastic buckling moment than the LH mode. The LH2 mode is not observed for the 12 in. deep specimen since L_{cr} for this specimen exceeds the length of the hole.

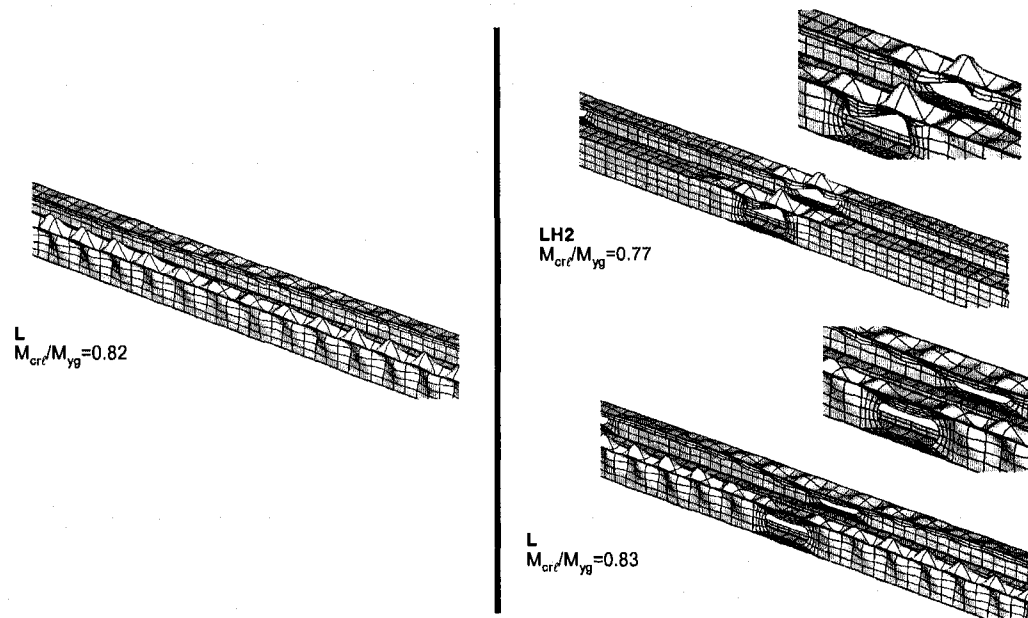


Figure 4.56 Local buckling modes for specimen 2B,20,1&2(H) with and without holes

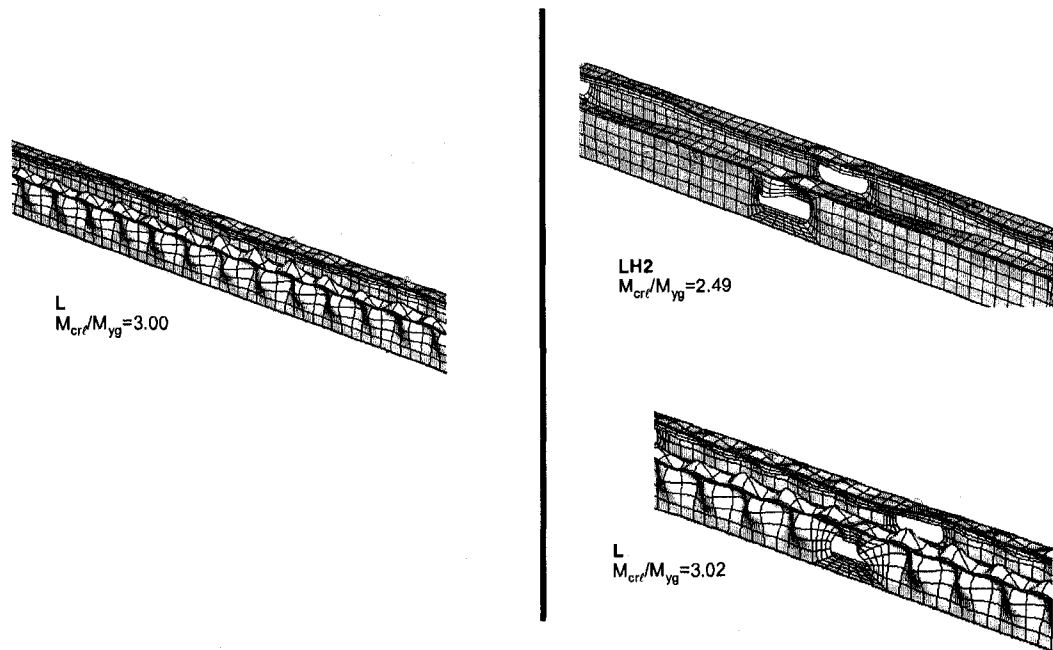


Figure 4.57 Local buckling modes for specimen 3B,14,1&2(H) with and without holes

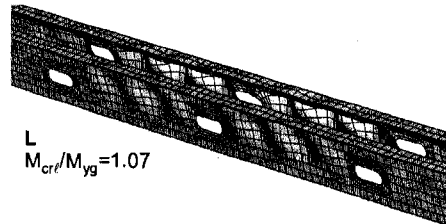
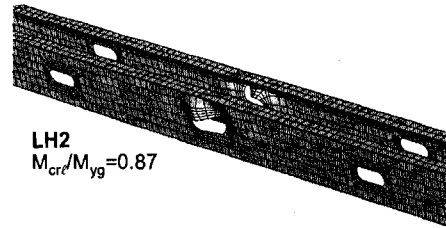
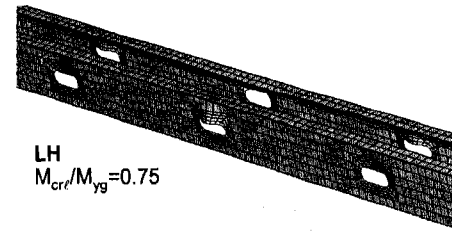
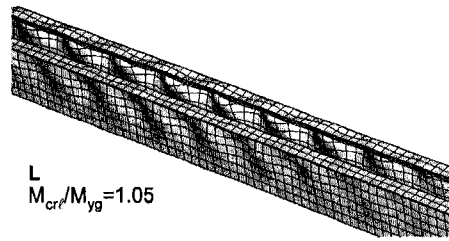


Figure 4.58 Local buckling modes for specimen 6B,18,1&2(H) with and without holes

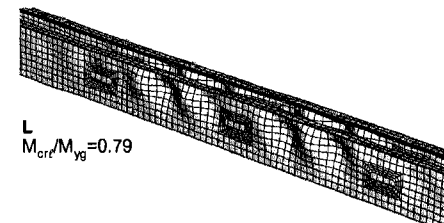
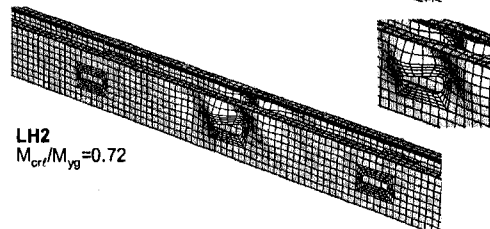
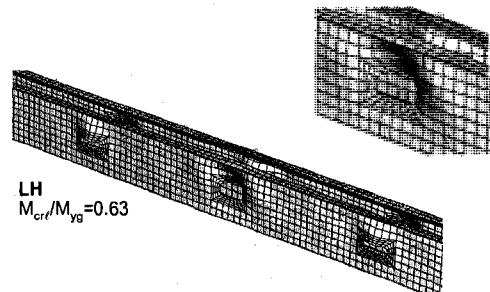
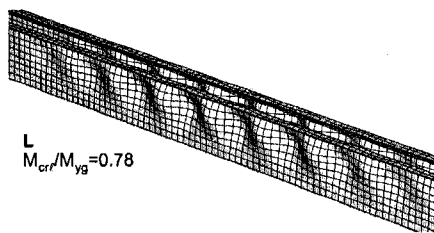


Figure 4.59 Local buckling modes for specimen BP-40(H) with and without holes

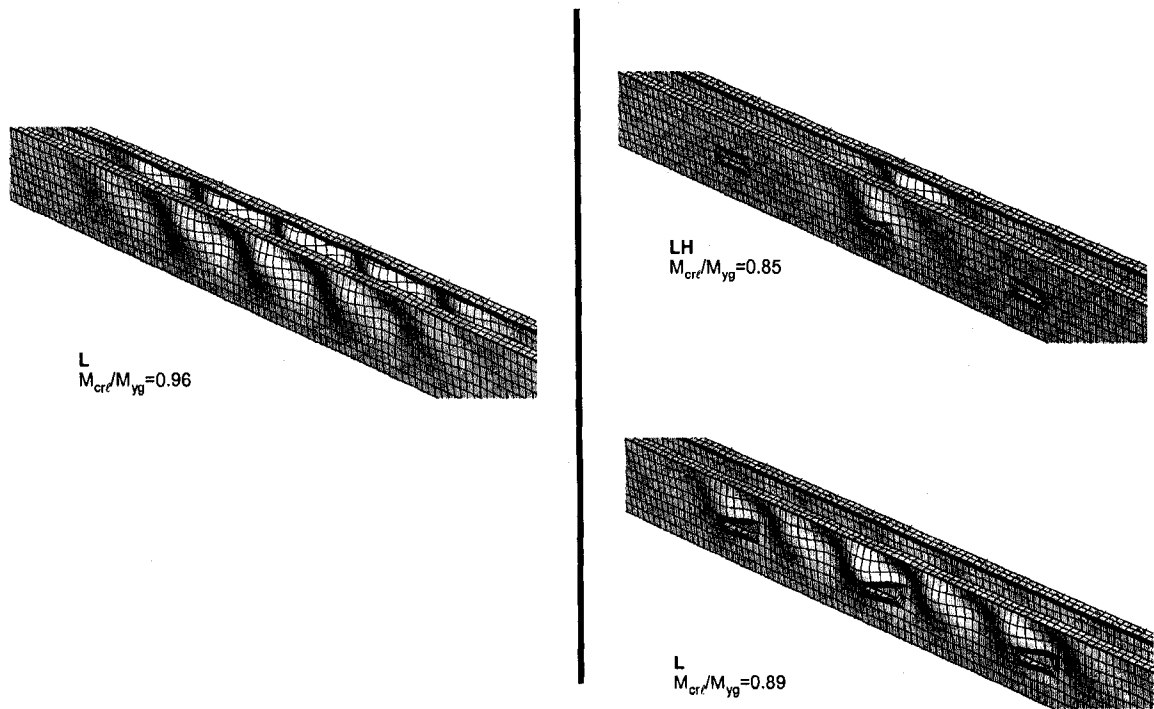


Figure 4.60 Local buckling modes for specimen 12B,16,1&2(H) with and without holes

4.3.1.4.2 Distortional Buckling

Figure 4.61 compares the influence of slotted web holes on the distortional buckling of a shallow beam specimen (nominal height of 2.5 inches). For the specimen with holes, a unique DH+L mode is observed with a critical elastic buckling moment 20 percent less than the pure D mode. This mode has similar characteristics to the LH mode in beams (see Section 4.3.1.4.1), especially the buckling of the strip above the hole into one half-wave. The DH+L mode is expressed more as a distortional mode though because the compression flange is wide relative to the unstiffened strip. The D mode without holes becomes a mixed distortional-local mode (D+L) when holes are added, although the critical elastic buckling moment is not significantly affected in this case. This specimen is sensitive to mixing of local and distortional modes because of the

relatively thin steel sheet thickness t of 0.0346 inches. It is also noted that the hole has only a small influence on the pure D mode half-wavelength for this specimen.

The DH distortional buckling mode at the hole is also observed for a slightly deeper beam specimen (nominal height of 3.625 inches) in Figure 4.62. The sheet thickness for these channels is roughly double that of the previously discussed specimen ($t=0.71$ inches) and the hole depth is unchanged. M_{crd} is higher than M_{crd} because of the increased thickness, resulting in DH and D modes without local buckling interaction when the slotted holes are present. The critical elastic buckling moment of the DH mode is 13 percent less than that of the pure D mode.

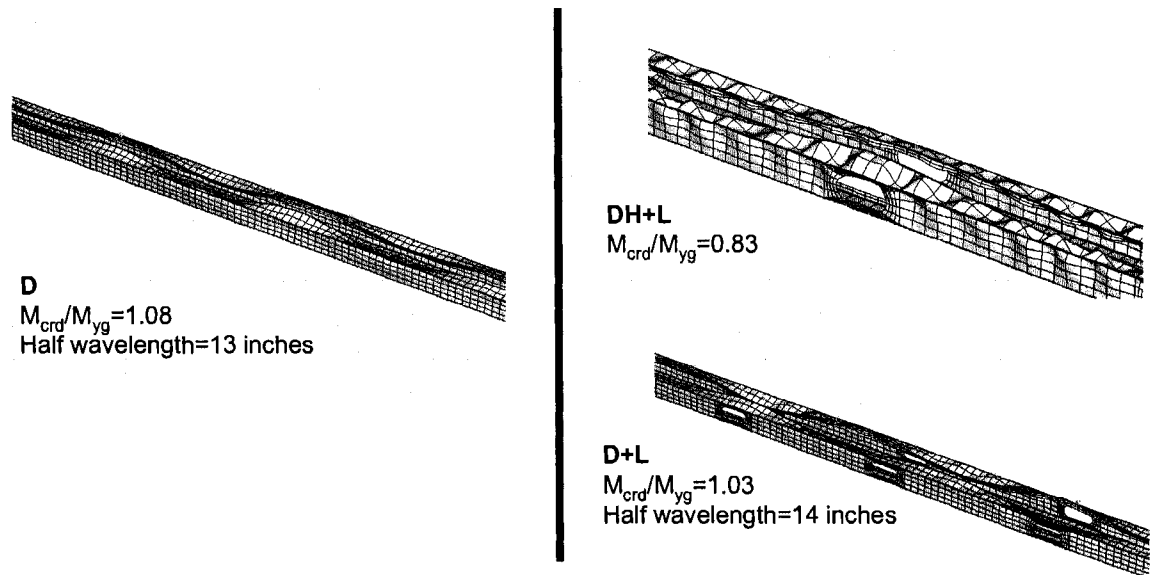


Figure 4.61 Distortional buckling modes for specimen 2B,20,1&2(H) with and without holes

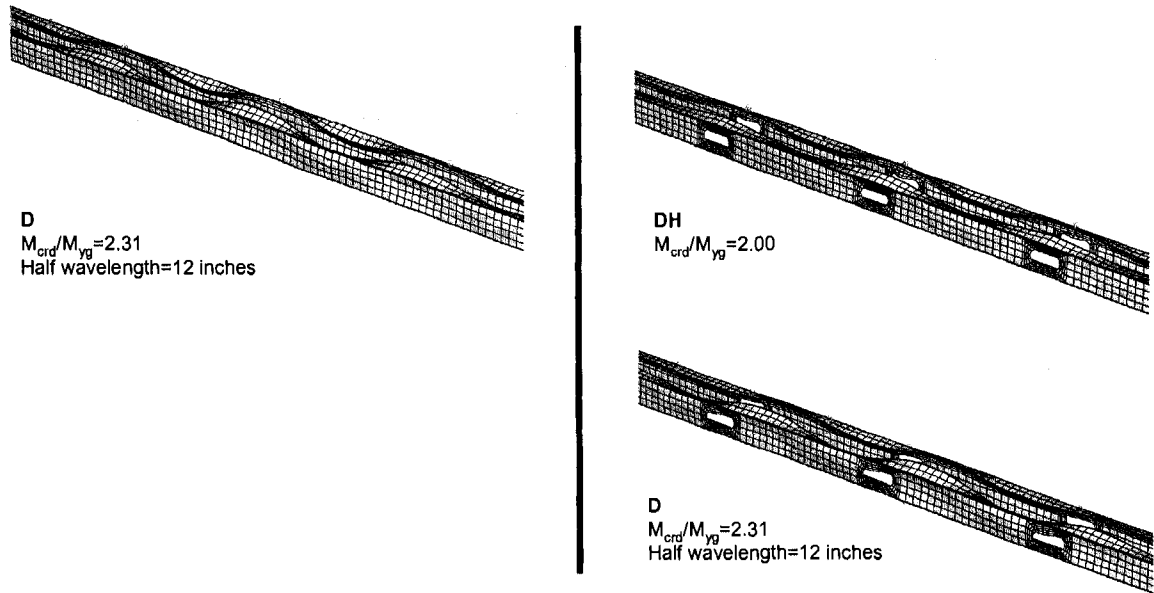


Figure 4.62 Distortional buckling modes for specimen 3B,14,1&2(H) with and without holes

Figure 4.63 and Figure 4.64 compare the influence of slotted web holes on beams with nominal heights of six inches and eight inches respectively, both having a steel sheet thickness of $t=0.047$ inches. For these specimens the unstiffened strip buckling mode above the hole is identified as LH buckling (see Figure 4.58, Figure 4.59) instead of DH buckling because the majority of the buckling deformation occurs in the web. The similarities between the LH and DH modes can make them difficult to classify in some cases. Research on a mechanics-based modal identification method is underway.

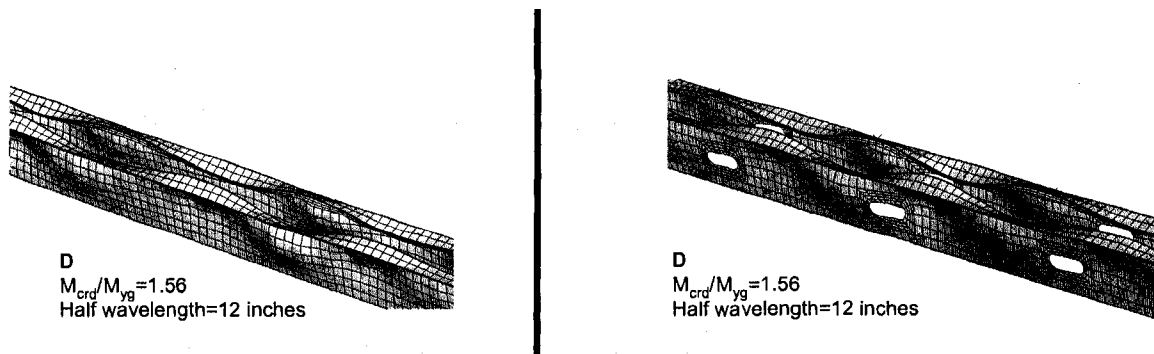


Figure 4.63 Distortional buckling modes for specimen 6B,18,1&2(H) with and without holes

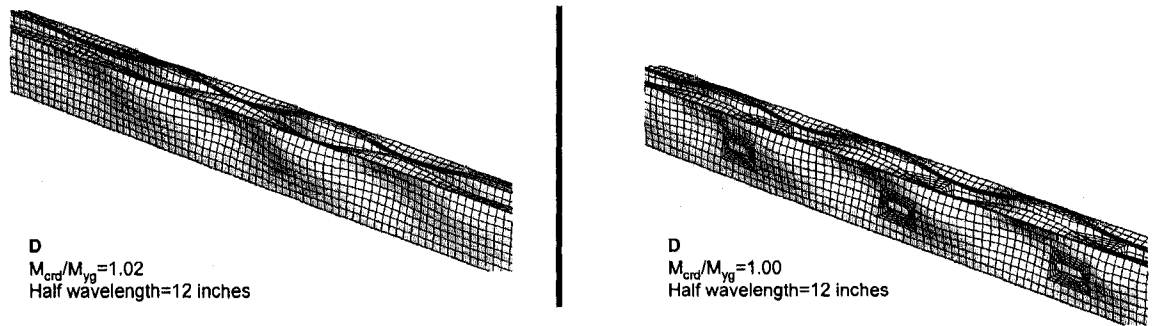


Figure 4.64 Distortional buckling modes for specimen BP5-40(H) with and without holes

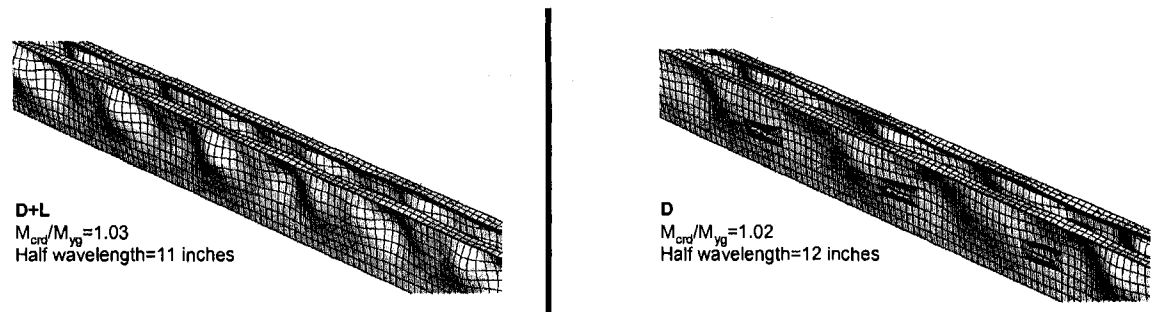


Figure 4.65 Distortional buckling modes for specimen 12B,16,1&2(H) with and without holes

The distortional buckling modes of the deepest beam specimen considered in this study (nominal depth of 12 inches) are provided in Figure 4.65. Identifying the distortional buckling modes for the channels making up this beam are inherently challenging because even for a member without holes, there is not a clear distinction between the L and D modes. The critical elastic buckling moments for a single C-section from the beam cross section are provided at various half-wavelengths from a finite strip analysis (CUFSM) in Figure 4.66 (including the modal participation factors calculated with the constrained finite strip method). Only one minimum exists, suggesting that the modes at or near the minimum buckling load are a mixture of L and D modes. The most suitable mode identified by the author (for the specimen without a hole) in Figure 4.65 alternates between larger distortional half-waves and shorter local buckling half-waves in the constant moment region of the channels. For the specimen with the web holes in

Figure 4.65, the local half-waves are not present and the mode resembles more of a “pure” D mode. The DH mode is not observed for this specimen, which is consistent with the buckling behavior of stiffened elements in bending (see Figure 3.25). Unstiffened strip buckling (the plate mode that is hypothesized to initiate the DH mode in beams) does not occur when h_{hole}/h is small.

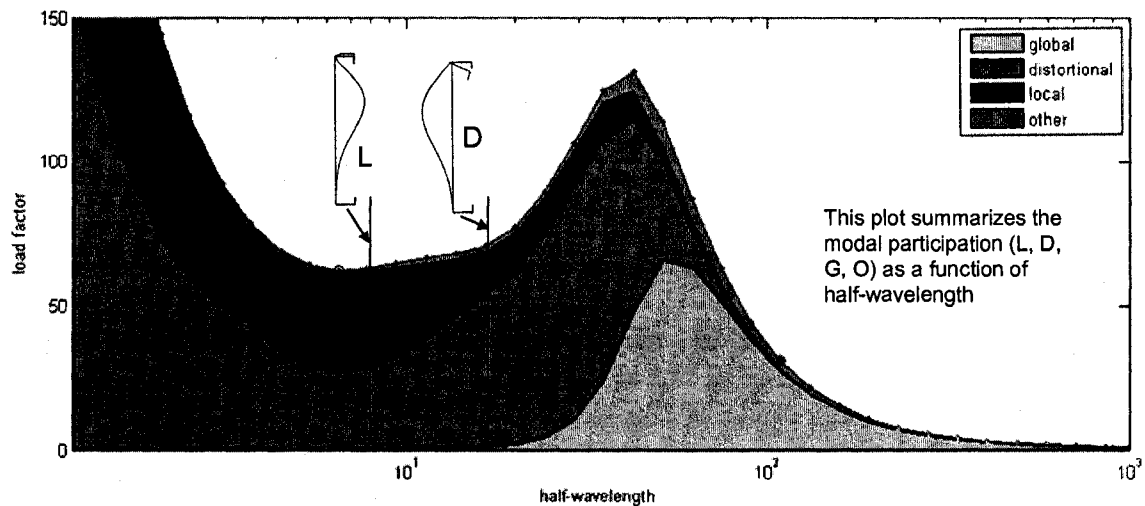


Figure 4.66 Elastic buckling curve for 12" deep specimen with modal participation summarized, note that selected L and D are mixed local-distortional modes

4.3.1.4.3 Global buckling

Lateral-torsional buckling is a common global (G) elastic buckling mode in beams, although this mode is eliminated for the specimens considered here by connecting the two C-sections toe-to-toe with aluminum angles and by providing lateral bracing at the compression flange in the constant moment region of the beams (see Figure 4.51). Twisting of an individual channel about its longitudinal axis is still possible though, even with the top flange restrained. Figure 4.67 depicts the potential twisting mode. CUFSM is used to conservatively quantify the elastic buckling moment for this mode, and it is determined that M_{cre} is more than ten times the yield moment M_y

for the specimens in this study. Since the M_{cre} does not influence the DSM prediction as long as $M_{cre} > 2.78 M_y$, the global twisting mode is not summarized in the database.

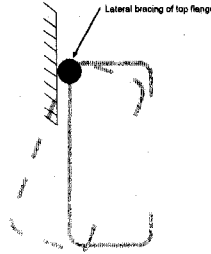


Figure 4.67 Possible global buckling mode occurs about the compression flange lateral brace point

4.3.1.5 Elastic buckling database for beams with holes

Table 4.11 summarizes the dimensions and material properties of each channel making up the beam (Channel 1 and Channel 2), including cross section and hole dimensions, tested ultimate point load P_{test} (for each channel) and ultimate moment M_{test} (for each channel), tested specimen yield stress F_y , specimen yield moment $M_{y,g}$ (calculated with the gross cross-section), and $M_{y,net}$ (calculated with the net cross-section). F_y varies from 22.0 ksi to 93.3 ksi with a mean of 48.6 ksi and standard deviation of 14 ksi. This large variation in yield stress was somewhat unexpected.

ABAQUS eigenbuckling results are summarized in Table 4.12 for each channel considering the experiment boundary conditions both with and without holes. These results are used in Section 4.3.1.6 to evaluate the influence of holes on M_{cre} and M_{crd} . The CUFSM elastic buckling results are also provided, including the fundamental distortional half-wavelength L_{crd} , which are used in Section 4.3.1.7 to evaluate the influence of experiment boundary conditions on M_{cre} and M_{crd} and the distortional half-wavelength.

Table 4.10 presents the cross-section parameter ranges of the beam C-sections contained in the experiment database. All of the beam specimens have cross-section dimensions that meet the DSM prequalification standards for ultimate strength prediction summarized in Table 4.9 (AISI-S100 2007). Four of the beam specimens exceed the yield stress prequalification limit of $F_y < 70$ ksi.

Table 4.9 DSM prequalification limits for beam C-sections

Beam parameter	DSM prequalification limit
Web slenderness	$H/t < 321$
Flange slenderness	$B/t < 75$
Lip slenderness	$0 < D/t < 34$
Web / flange	$1.5 < H/B < 17$
Lip / flange	$0 < D/B < 0.70$
Yield stress	$F_y < 70$ ksi

Table 4.10 Parameter ranges for beam specimens with holes

	D/t	H/t	B/t	H/B	D/B	h_{hole}/h	F_y (ksi)
min	5.5	40.5	16.3	1.5	0.18	0.13	22.0
max	22.1	257.1	58.3	7.7	0.42	0.67	93.3

4.3.1.6 Influence of holes on beam local and distortional critical elastic buckling loads

4.3.1.6.1 Local buckling

The ABAQUS local buckling eigenbuckling results for each beam specimen C-section (Channel 1 and Channel 2) with holes is compared to the same beam specimen but without holes in Figure 4.68. The variation in M_{cr} for the LH, LH2, and L modes (see Section 4.3.1.4.1 for definition) with hole size to flat web depth is highlighted in Figure 4.68a. The LH mode (buckling of the compressed unstiffened strip above a hole) is observed only when $0.20 < h_{hole}/h < 0.40$, and is always the lowest buckling mode when it exists. As h_{hole}/h exceeds 0.40 the lowest mode switches to the LH2 mode. This trend occurs because as h decreases, the local buckling half-wavelength decreases causing multiple half-waves to form in the unstiffened strip at the hole. When $h_{hole}/h < 0.20$ the unstiffened strip above the hole is relatively stiff (i.e., deep relative to hole length) and plate buckling controls as the lowest local buckling mode. The minimum M_{cr} for the LH, LH2, and L is plotted in Figure 4.68b exhibits a similar trend to that observed for stiffened elements in bending (see Figure 3.26a), where the maximum hole influence occurs when h_{hole}/h is between 0.30 and 0.40. Unstiffened strip buckling (LH and LH2) of full members controls for h_{hole}/h exceeding 0.50 which is also consistent with the behavior of a stiffened element in bending (and different from a column with holes, where web local buckling occurs away from the hole for large h_{hole}/h). The presence of the C-section flanges reduces the magnitude of the hole influence in a full member when compared to

a stiffened element, which is consistent with similar observations for compression members (see Figure 4.4).

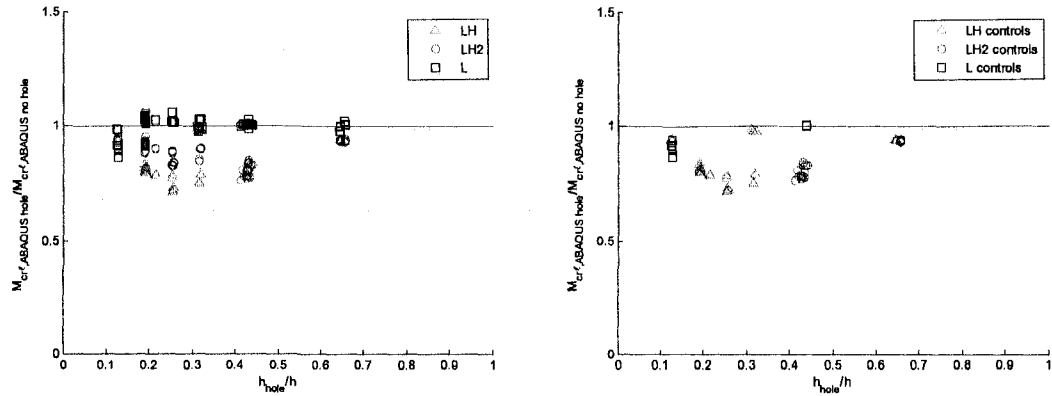


Figure 4.68 Influence of holes on beam specimen M_{cr} (Channel 1 and Channel 2 plotted) considering (a) all local buckling modes and (b) the lowest local buckling mode

4.3.1.6.2 Distortional buckling

The ABAQUS distortional buckling eigenbuckling results for each beam specimen C-section (Channel 1 and Channel 2) with holes is compared to the same beam specimen but without holes in Figure 4.69. The variation in M_{cr} for the DH and D modes (see Section 4.3.1.4.2 for definition) with hole size to flat web depth is highlighted in Figure 4.69a. The DH mode is often the lowest distortional mode in Figure 4.69b, especially when h_{hole}/h is between 0.20 and 0.40. This mode is initiated by unstiffened strip buckling and is related to the LH mode, and therefore its maximum influence in this region is expected.

The ratio of web depth to flange width is an important parameter to consider when differentiating between the LH and DH modes for beams with holes. The DH mode is most prevalent in the range $2 < H/B < 6$ as shown in Figure 4.70. As the beam depth increases relative to flange width ($H/B > 6$) the distortional tendency associated with

unstiffened strip buckling decreases and the DH mode transitions to the LH (or LH2) mode.

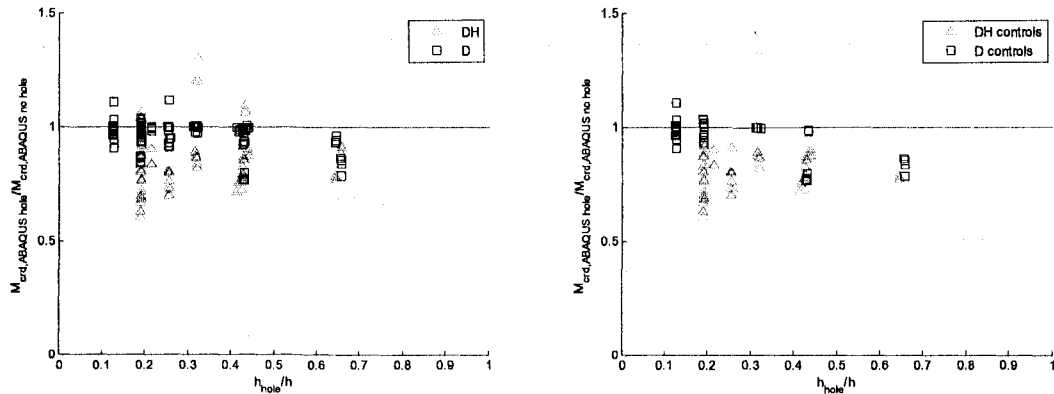


Figure 4.69 Influence of holes on beam specimen M_{crd} (Channel 1 and Channel 2 plotted) as a function of hole depth to flat web depth considering (a) all distortional buckling modes and (b) the lowest distortional buckling mode

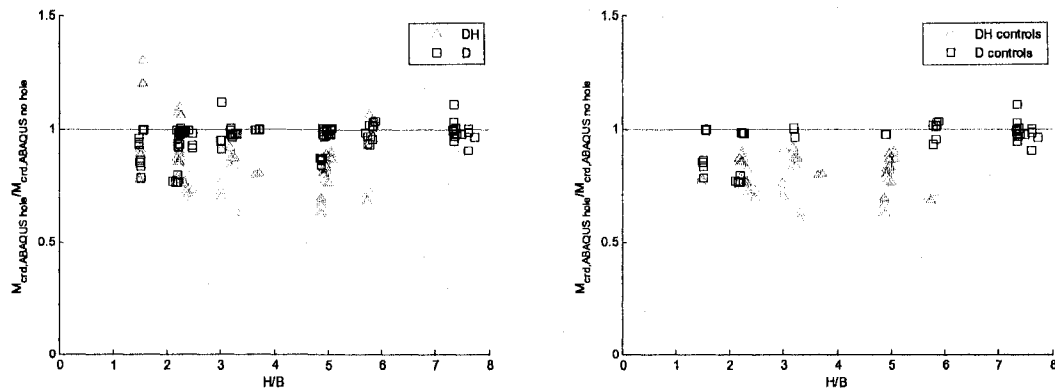


Figure 4.70 Influence of holes on beam specimen M_{crd} (Channel 1 and Channel 2 plotted) as a function of web depth to flange width considering (a) all distortional buckling modes and (b) the lowest distortional buckling mode

4.3.1.7 Influence of experiment boundary conditions on beam local and distortional critical elastic buckling loads

4.3.1.7.1 Local buckling

The influence of experiment boundary conditions on the elastic buckling behavior is evaluated by comparing the ABAQUS critical elastic buckling moment

M_{cr} (without holes) of each C-section making up the beam specimens to the local buckling moment determined with the finite strip software CUFSM. Since the finite strip method considers elastic buckling of each channel individually under a constant moment, the comparison of ABAQUS and CUFSM results isolate the influence of the aluminum angle straps at the top and bottom flanges, as well as the lateral bracing and the application of the constant moment as a series of point loads in the experiments. The experiment loading and boundary conditions have a minimal influence on M_{cr} for the specimens considered in this study as shown in Figure 4.71. This result is consistent with the local buckling mode shapes in Section 4.3.1.4.1, where it was observed that the formation of local buckling half-waves in the constant moment region were unimpeded by the angle straps.

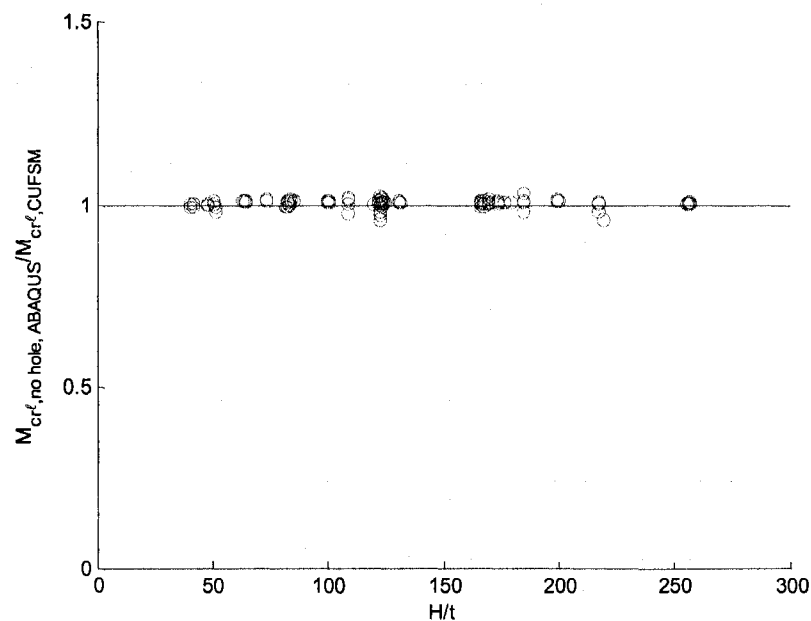


Figure 4.71 Influence of test boundary conditions on M_{cr}

4.3.1.7.2 Distortional buckling

The influence of the experiment boundary conditions on the distortional buckling behavior is evaluated by comparing the critical elastic buckling moment M_{crd} (without holes) from the ABAQUS eigenbuckling analyses to the buckling moment of each channel individually determined with the finite strip software CUFSM. The comparison of ABAQUS and CUFSM results isolates the influence of the aluminum angle straps, lateral bracing and the load application method on the critical elastic moment results. The experiment test conditions provide a significant boost to M_{crd} as shown in Figure 4.72b, which is hypothesized to be related to the restrained distortional buckling caused by the aluminum angle straps. This hypothesis is supported by existing research on unrestrained elastic distortional beam buckling (no compression flange connections), which observed similar CUFSM and ABAQUS eigenbuckling results (Yu and Schafer 2006). The pure D distortional half-wavelengths approximated from ABAQUS (for specimens without holes) in Figure 4.72b are often shorter relative to the predicted half-wavelengths from a finite strip analysis. This trend is a direct result of the angle spacing (12" on center for Test Sequences 1 and 3, 6" for Test Sequence 2), which is less than the fundamental L_{crd} for many of the C-sections. The change in half-wavelength away from the natural half-wavelength of the distortional mode increases the critical elastic buckling moment. This boost in M_{crd} decreases with increasing H/B as shown in Figure 4.72a, since the fundamental L_{crd} also decreases as beam web depth increases relative to flange width.

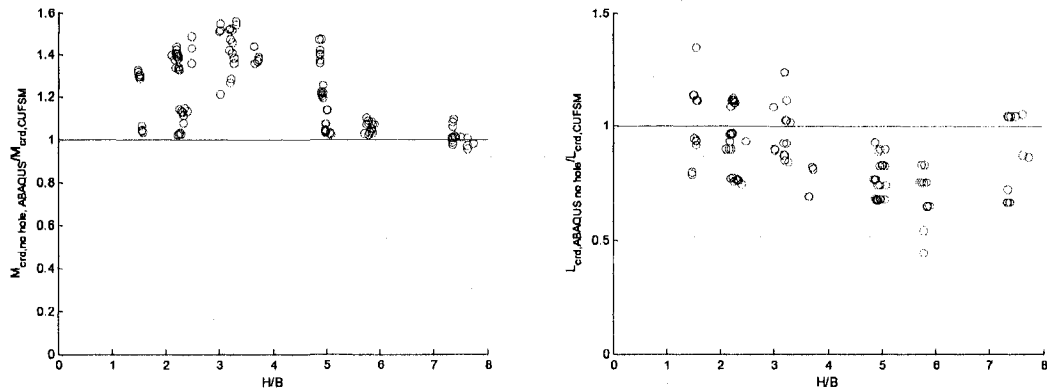


Figure 4.72 Influence of test boundary conditions on (a) $M_{cr,d}$ and (b) on the distortional half-wavelength

The boost in $M_{cr,d}$ from the restraint of the beam compression flanges exhibits a linear trend when plotted against the ratio of $L_{cr,d}$ (from CUFSM) versus the restraint spacing S_{brace} in Figure 4.73. A linear equation is fit to this trend, resulting in a useful approximation of the restraint boost:

$$D_{boost} = 0.15 \left(\frac{L_{cr,d}}{S_{brace}} \right) + 0.85, \quad \frac{L_{cr,d}}{S_{brace}} \geq 1 \quad (4.15)$$

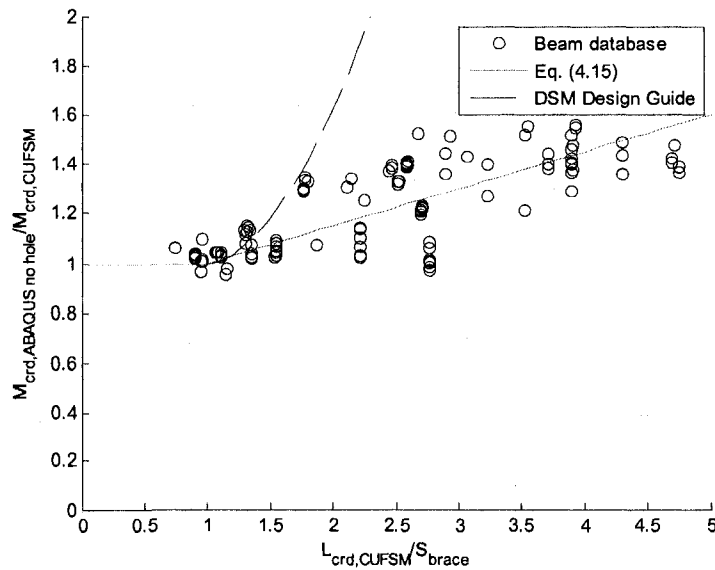


Figure 4.73 Boost in $M_{cr,d}$ from the angle restraints increases as the fundamental distortional half-wavelength increases relative to the restraint spacing S_{brace}

The DSM Design Guide's suggested modification to M_{crd} when $L \leq L_{crd}$ is also plotted in Figure 4.73 (AISI 2006, Section 4.2):

$$M_{crd}(L < L_{crd,CUF\text{SM}}) = M_{crd}^* (L/L_{crd,CUF\text{SM}})^{\ln(L/L_{crd,CUF\text{SM}})}, \quad (4.16)$$

where M_{crd}^* is the minimum distortional critical elastic buckling moment read from CUFSM. L is assumed equal to S_{brace} when plotted in Figure 4.73, i.e. the distortional half-wave is assumed to form between the flange braces. The DSM Design Guide prediction for M_{crd} is higher than that proposed by Eq. (4.16) because for many of the beams in the ABAQUS-generated elastic buckling database, L_{crd} was shortened but not completely restrained between braces. On the other hand, the ABAQUS eigenbuckling analyses did not simulate contact between the angles and the flanges (only the bending and shear stiffness of the angles), and therefore the actual M_{crd} most likely lies between the two predictions.

4.3.2 Approximate prediction methods for use in design

4.3.2.1 Local buckling

4.3.2.1.1 Prediction method

The approximate method for predicting the local elastic buckling behavior of cold-formed steel beams is similar to the method for columns presented in Section 4.2.7.1.1. Local buckling is assumed to occur as the minimum of M_{cr} of the gross cross-section (as calculated in the Direct Strength Method) and local buckling of the compressed unstiffened strip adjacent to the hole, M_{crh} . The method captures the lowest unstiffened

strip buckling mode, either the LH or LH2 mode, with the procedure described in Figure 4.17. When the hole length is longer than the fundamental half-wavelength of the net cross-section L_{crh} , then the LH2 mode governs. When the hole length is less than L_{crh} , the LH mode governs.

To predict M_{crh} from the net cross-section in CUFSM, the cross-section is restrained to isolate local buckling from distortional buckling as shown in Figure 4.74. Compressed corners should be restrained in the direction normal to the neutral axis about which bending occurs (corners experiencing tension need not be restrained). It is important to avoid fully restraining a cross-section element, since this prevents Poisson-type deformations and artificially stiffens the cross-section. The only time both the x and z directions of a corner should be restrained is if a hole isolates two compressed intersecting elements (as in the case of a flange hole in a C-section, see Figure 4.74a). Finally, when holes isolate two compressed elements of a cross-section (similar to the flange hole in the column hat section, see Figure 4.16b), the isolated element should be removed from the cross-section. This prediction method is validated in the next section using the beam elastic buckling database developed in Section 4.3.1.5.

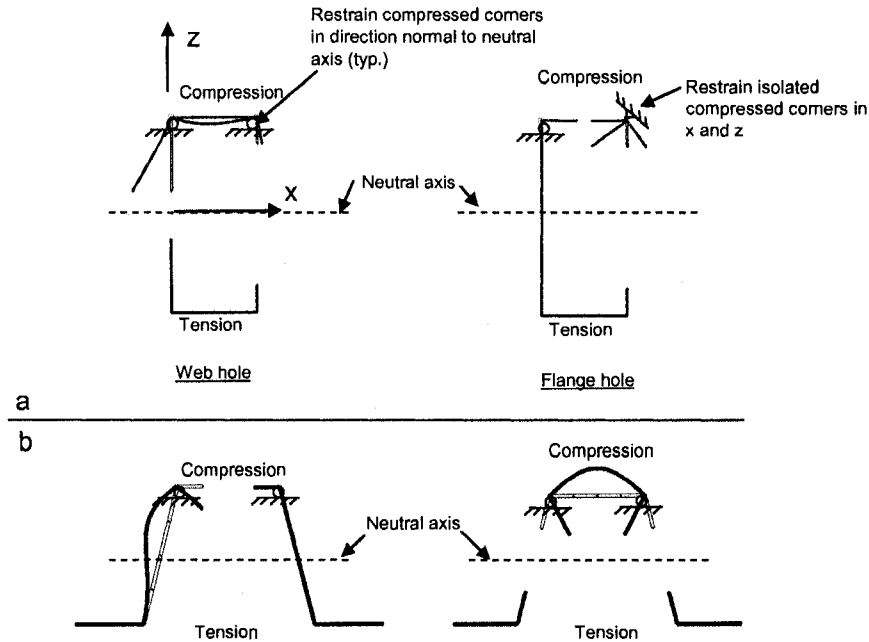


Figure 4.74 Guidelines for restraining beam net cross-sections in the CUFSM local buckling approximate method

4.3.2.1.2 Method verification using elastic buckling database

The finite strip prediction method is used to predict M_{cr} for the 144 C-sections described in Table 4.11. These predictions are compared to the ABAQUS eigenbuckling results from Table 4.12 (the minimum of L, LH, and LH2 modes), and demonstrates that the finite strip approximate method is viable and conservative over a wide range of hole widths and beam depths. A clear transition from L and LH2 buckling to LH buckling occurs as the C-sections increases in depth as shown in Figure 4.75a. This observation is consistent with finite element eigenbuckling observations (see Figure 4.56 to Figure 4.60), where as beam depth increases the half-wavelength of the net-section increases beyond the length of the hole, resulting in a switch from unstiffened strip buckling in two half-waves (LH2) to one half-wave (LH). The mean and standard deviation of the ABAQUS to predicted ratio for M_{cr} are 1.14 and 0.16 respectively.

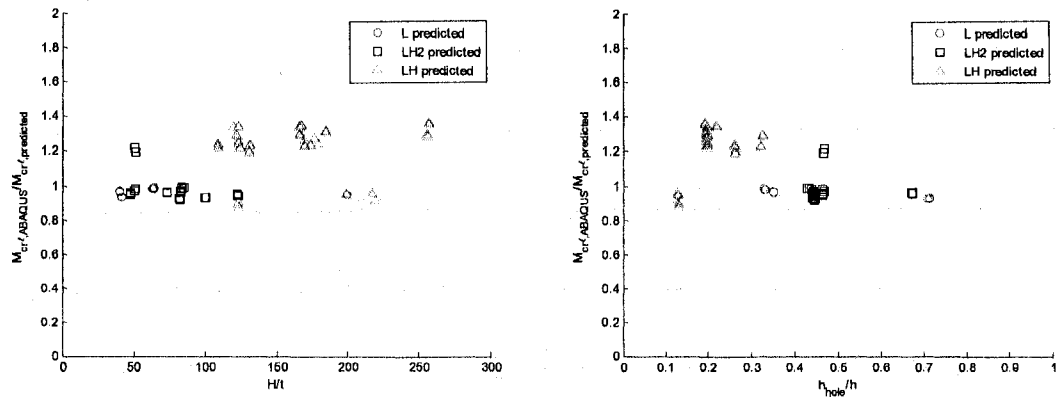


Figure 4.75 Comparison of ABAQUS to predicted M_{cr} for C-sections with holes in the beam database as a function of (a) web depth and (b) hole width relative to flat web depth

4.3.2.2 Distortional buckling

4.3.2.2.1 Prediction method

The “weighted average” and “mechanics-based” finite strip methods for predicting M_{crd} of columns with holes introduced in Section 4.2.7.2.1 are employed here to predict the distortional critical elastic buckling load of cold-formed steel beams with holes. These approximate methods are evaluated against the ABAQUS M_{crd} (the minimum of the DH and D modes) from the beam experiment database in Table 4.12.

4.3.2.2.2 Method verification using elastic buckling database

Figure 4.76 plots M_{crd} determined with ABAQUS versus the predictions using the “weighted-average” and “mechanics-based” approximate methods. The ABAQUS M_{crd} (with holes) is multiplied by the ratio of M_{crd} from CUFSM to M_{crd} from ABAQUS without holes to eliminate the influence of the boundary conditions and to allow for a consistent comparison between the ABAQUS results (with only the hole influence) and the prediction method. The ABAQUS to “mechanics-based” prediction ratio is more

accurate (ABAQUS to predicted mean of 1.04 and standard deviation of 0.02) than the “weighted-average” prediction (ABAQUS to predicted mean of 1.10 and standard deviation of 0.06), which is consistent with the verification study for columns with holes in Section 4.2.7.2.1.

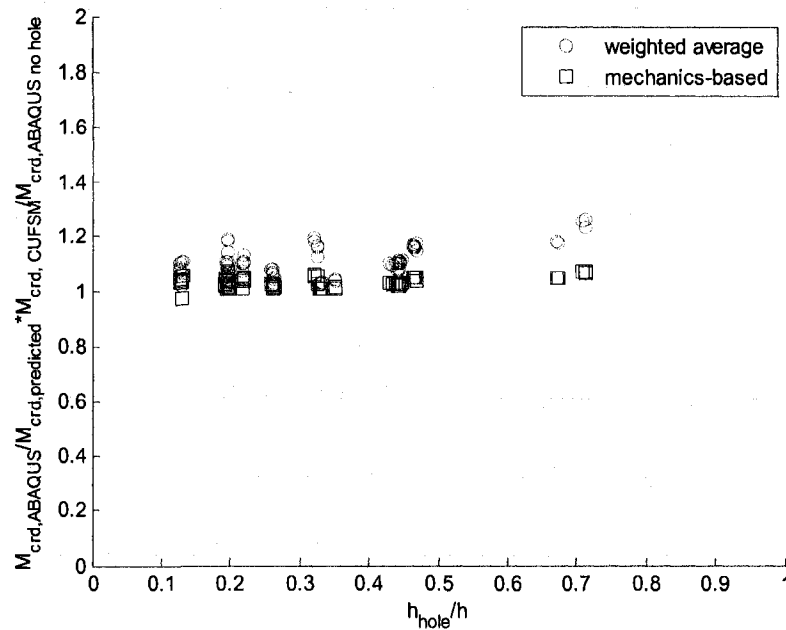


Figure 4.76 Comparison of “mechanics-based” and “weighted-average” prediction methods to ABAQUS results for the distortional buckling load M_{crd} of C-sections with holes in the elastic buckling database

4.3.2.3 Global buckling

The “weighted thickness” and “weighted properties” approximate methods presented in Section 4.2.7.3.1 are now implemented to predict M_{cre} for a beam with uniformly spaced holes loaded with a constant moment.

4.3.2.3.1 Description of Prediction Method

The “weighted thickness” and “weighted properties” approximates for I_y , J , and C_w are employed with the classical lateral-torsional stability equation to predict M_{cre} of a beam with holes (Chajes 1974):

$$M_{cre} = \sqrt{EI_y \left(GJ + EC_w \frac{\pi^2}{L^2} \right)}. \quad (4.17)$$

4.3.2.3.2 Example and Verification

The long SSMA 1200S162-68 member evaluated in Section 4.2.7.3.2 as a column is now evaluated as a beam with a uniform moment along the member to compare prediction methods to ABAQUS results. The ABAQUS boundary conditions and applied loading are described in Figure 4.77. The beam ends are modeled as warping-free and the cross-section at the longitudinal midline is warping-fixed. Warping at the member ends is visible in Figure 4.77 for this lateral-torsional buckling mode.

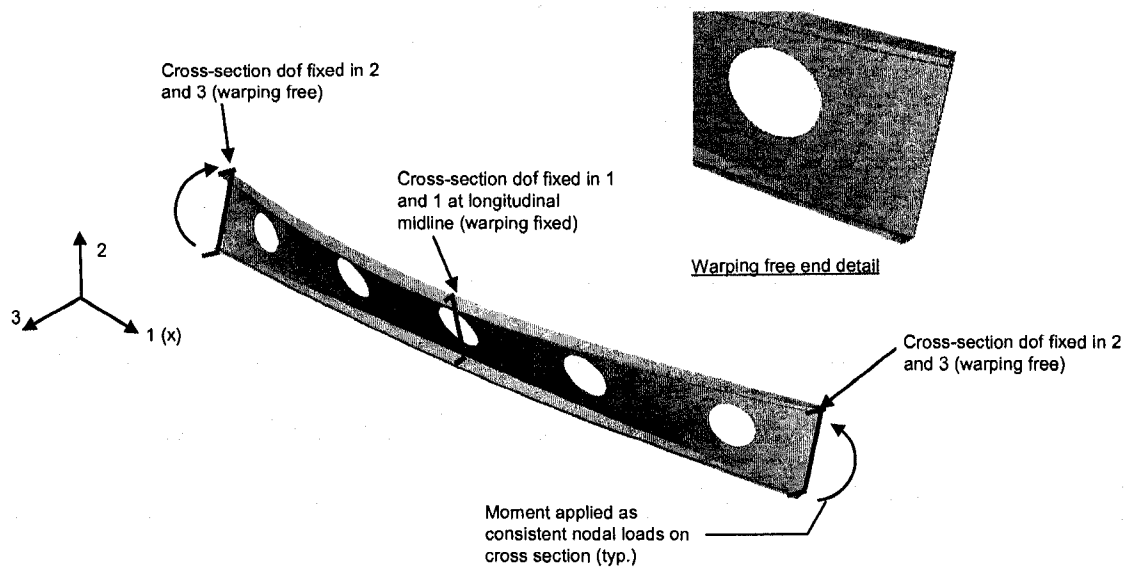


Figure 4.77 ABAQUS boundary conditions and applied loading for an SSMA 1200S162-68 beam with holes ($h_{hole}/h=0.50$ shown).

Figure 4.78 demonstrates that both the “weighted stiffness” and “weighted properties” models are accurate predictors of M_{cre} for $h_{hole}/h \leq 0.50$ in this particular case. For $h_{hole}/h > 0.50$, the reduction in prediction accuracy occurs because the weighted average approximations for C_w are not consistent with the actual physical behavior (J was shown to be consistent with the “weight properties” method for calculating section properties in Section). If a designer does not know $C_{w,avg}$, then using the net section properties (calculated with CUFSM, see Figure 4.37) or the “weighted properties” prediction with $C_{w,net}=0$ are both viable options for conservatively predicting M_{cre} .

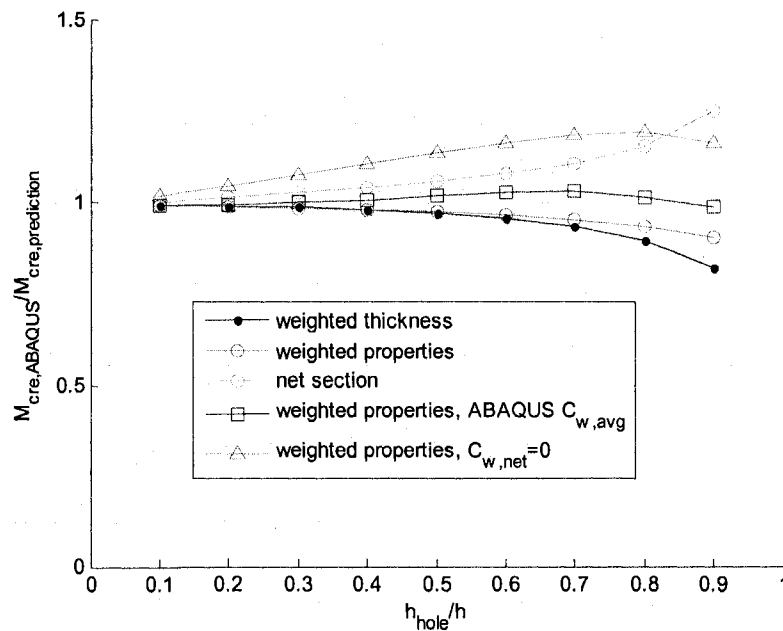


Figure 4.78 Comparison of “weighted thickness” and “weighted properties” prediction methods for the SSMA 1200S162-68 lateral-torsional beam buckling mode. Predictions using net section properties are also plotted as a conservative benchmark.

Chapter 5

Experiments on cold-formed steel columns with holes

The elastic buckling modes discussed in Chapter 4 and their influence on the load-deformation response of cold-formed steel columns can be readily observed and quantified with experiments. In this study, 24 cold-formed steel lipped C-section columns with and without slotted web holes are tested to failure. The column lengths and cross-section dimensions are specifically chosen to explore the connection between local, distortional, and global elastic buckling modes, ultimate strength, and the resulting failure mechanisms. The elastic buckling behavior is evaluated for each specimen with a finite element eigenbuckling analysis, taking care to accurately simulate the tested boundary conditions and measured specimen dimensions. These elastic buckling results are used to provide a means of understanding the varied deformation response under load. The columns are tested with friction-bearing boundary conditions where the ends of each specimen are milled flat and parallel, and bear directly against

steel platens. Recommendations are made to advise other researchers on the viability of the friction-bearing boundary conditions when testing short and intermediate length columns.

5.1 Acknowledgements



The cold-formed steel column tests described in this chapter were completed with a team effort from the individuals below:

Eric Harden	Latrobe Hall Machine Shop
Walter Krug	Maryland Hall Machine Shop
Michael Franckowiak	Maryland Hall Machine Shop
Dr. Rachel Sangree	Johns Hopkins Postdoctoral Researcher
Jack Spangler	Senior Mechanical Engineer – Structures Lab
Nickolay Logvinosky	Structures Lab Technician
Mario Fasano	Johns Hopkins Senior
Rebecca Pierce	Johns Hopkins Freshman
Dawneshia Sanders	Baltimore Polytechnic Institute Senior
Alexander Pei	High School Intern

Clark Western Building Systems in Dundalk, MD graciously donated the structural studs.

5.2 Testing Program

Twenty-four cold-formed steel lipped C-section columns with and without pre-punched slotted web holes were tested to failure. The primary experimental parameters are column cross-section, column length, and the presence or absence of slotted web holes. The specimen naming convention, as it relates to the testing parameters, is defined in Figure 5.1.

	No Holes	Holes	
SSMA 362S162-33 	362-1-24-NH	362-1-24-H	Short Column
	362-2-24-NH	362-2-24-H	
	362-3-24-NH	362-3-24-H	
	362-1-48-NH	362-1-48-H	Intermediate Column
	362-2-48-NH	362-2-48-H	
	362-3-48-NH	362-3-48-H	
SSMA 600S162-33 	600-1-24-NH	600-1-24-H	Short Column
	600-2-24-NH	600-2-24-H	
	600-3-24-NH	600-3-24-H	
	600-1-48-NH	600-1-48-H	Intermediate Column
	600-2-48-NH	600-2-48-H	
	600-3-48-NH	600-3-48-H	

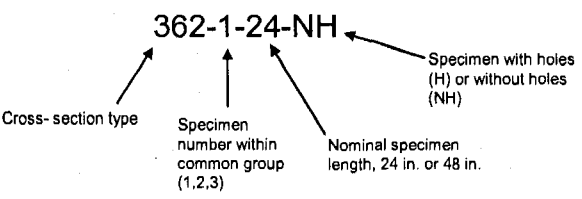


Figure 5.1 Column testing parameters and naming convention

5.2.1 Rationale for selecting specimen dimensions

5.2.1.1 Cross-section types

Two industry standard cross-sections from the Steel Stud Manufacturers Association (SSMA 2001), 362S162-33 and 600S162-33, were evaluated in this study. The 362S162-33 cross-section has a nominal web width of 3.62 in., while the 600S162-33 web is wider at 6.00 in. Both sections have a 1.62 in. flange and nominal sheet thickness of 0.0346 in. Specific measured dimensions are provided in Section 5.2.4.

The buckling half-wavelengths that form along the length of the specimens are cross-section dependent, and can be calculated with the semi-analytical finite strip method (FSM) (Schafer and Adány 2006). FSM assumes simply supported boundary conditions, and therefore the local and distortional half-wavelengths for the cross-sections studied here, as provided in Table 5.1, are only a guide as to the expected half-wavelength in the fixed-fixed tests. The FSM half-wavelengths are still a useful reference when deciding on specimen lengths (see Section 5.2.1.2) and identifying buckling modes (see Section 5.3.2), especially as specimen length increases and local and distortional buckling half-

wavelengths converge to the fundamental (simply supported) half-wavelengths reported in Table 5.1.

Table 5.1 FSM local and distortional buckling half-wavelengths for nominal 362S162-33 and 600S162-33 cross-sections

Cross-section	Elastic buckling half-wavelength	
	Local (L) in.	Distortional (D) in.
362	2.8	15.4
600	4.7	12.2

5.2.1.2 Column lengths

More than 80% of the tested specimens with holes available in the literature are stub columns, as depicted in the specimen length histogram of tested specimens provided in Figure 5.2. (The histogram is constructed with the specimens from the elastic buckling database in Section 4.2.6.) Stub columns accommodate local buckling half-waves, but due to their short length, distortional buckling is typically restrained from forming at relevant stress levels. The specimen lengths selected in this study, a 24 in. short column and a 48 in. intermediate length column, ensure that at least one distortional half-wave and multiple local half-waves can form along the length of the column (see Table 5.1). Further, at least for North American practice, the selected lengths are more typical of the unbraced length of actual cold-formed steel columns in an “all-steel” design with bridging in place to brace the studs.

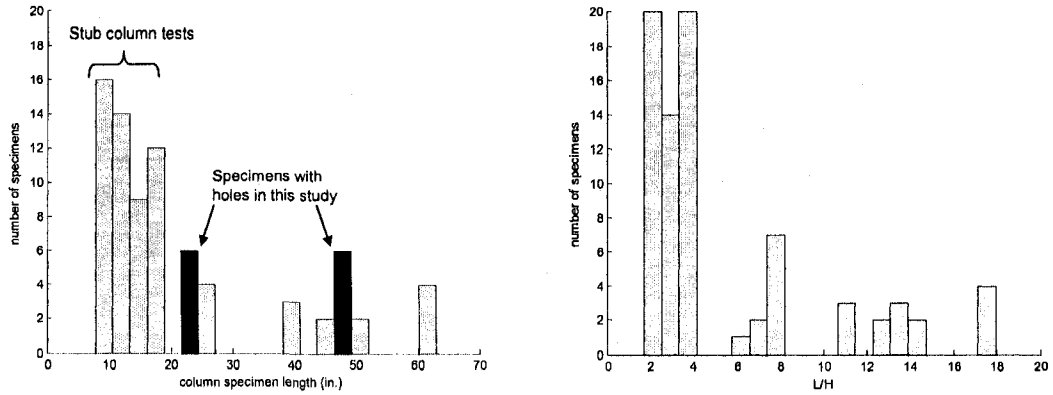


Figure 5.2 Tested lengths of cold-formed steel columns with holes as a function of (a) column length L and (b) L versus out-to-out column width H

5.2.1.3 Hole type and location

One slotted web hole is located at the mid-height of the short column to evaluate its influence at the mid-length of one distortional buckling half-wave. Two slotted web holes are oriented in the intermediate length columns with an industry standard spacing of 24 in. (SSMA 2001). The holes also coincide with the locations where distortional buckling half-waves are expected to have their maximum displacement under load. A typical short column and intermediate length column specimen with slotted holes is provided in Figure 5.3.

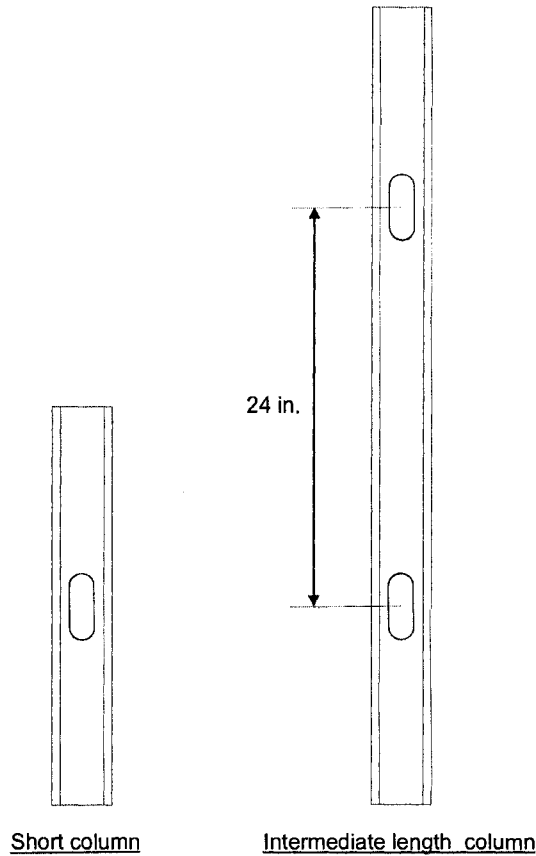


Figure 5.3 Typical column specimens with slotted holes

5.2.2 Column test setup

The column tests were performed with the 100 kip capacity two-post MTS machine shown in Figure 5.4. The upper crosshead and lower actuator are fitted with 12 in. x 12 in. x 1 in. thick chrome-moly 4140 steel platens ground flat and parallel. The column specimens bear directly on the steel platens as they are compressed. Friction between the column ends and the steel platens are the only lateral forces that restrain the column cross-section under load. An MTS load cell (model number 661-23A-02) measured the applied compressive force on each specimen, and an internal MTS length-voltage displacement transducer (LVDT) reported actuator displacement.

All column specimens were loaded in displacement control at a constant rate of 0.004 inches per minute. This rate was selected to ensure that the 3 ksi axial stress per minute upper limit in the Specification for stub column testing would not be exceeded (AISI-TS-2-02 2001). An MTS 407 controller was used to operate the hydraulic actuator during the compression tests.

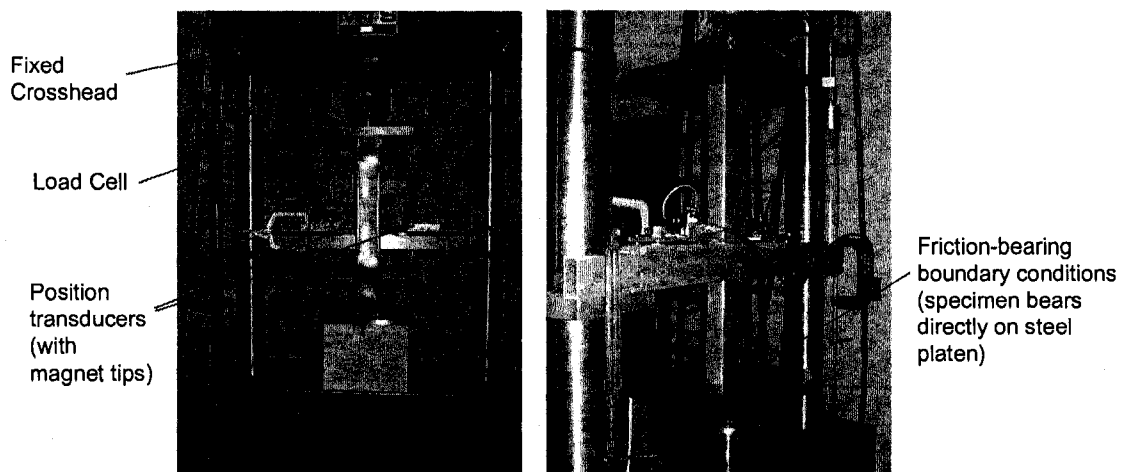


Figure 5.4 Column test setup and instrumentation

Two Novotechnik T Series position transducers fitted with ball-jointed magnet tips measured the east-west displacements of the specimen flange-lip intersections at column mid-height. Each transducer has a stroke of six inches and is powered by one 9-volt battery. The battery strengths were checked periodically to ensure that a drop in battery charge did not influence the transducer readings. The load cell and transducer readings are transmitted as voltage to a PC fitted with a National Instruments data acquisition card. The voltages are then converted to forces and displacements with the conversion factors summarized in Table 5.2. All displacement conversion factors were

determined by the author with a voltmeter and digital calipers. The data is plotted to the PC screen and recorded in a text file with a custom LabVIEW program (Labview 2005).

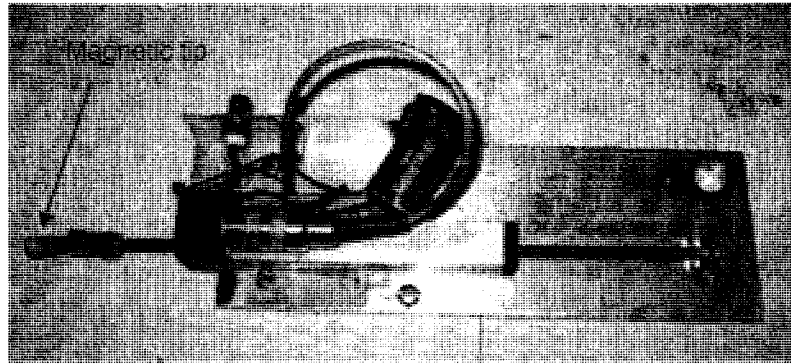


Figure 5.5 Novotechnik position transducer with ball-jointed magnetic tip

Table 5.2 Voltage conversion factors for column test instrumentation

Measurement	Source	Conversion
Tensile Force	MTS Load Cell	1 Volt = 1000 lbf
Actuator Displacement	MTS Internal LVDT	1 Volt = 0.300 in.
West Flange Displacement	Novotechnik Position Transducer	1 Volt = 0.678 in.
East Flange Displacement	Novotechnik Position Transducer	1 Volt = 0.678 in.

5.2.3 Column specimen preparation

All column specimens were cut from 8 ft. structural studs using the Central Machinery 4 ½ inch metal cutting band saw shown in Figure 5.15. For short columns without holes, the whole series of specimens (for example 362-1-24-NH, 362-2-24-NH, and 362-2-24-NH) was cut from a single 8 ft. structural stud. For all other specimen types, each specimen was cut from its own individual stud. Tensile coupons for materials testing were obtained from the leftover stud lengths.

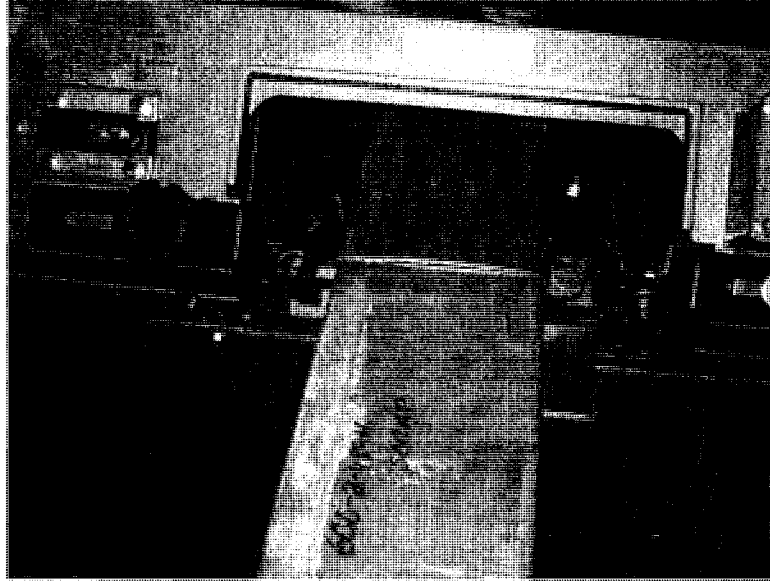


Figure 5.6 Central Machinery metal band saw used to rough cut column specimens

The specimen ends were milled to ensure flat and parallel bearing surfaces for testing. The flatness tolerance across the specimen end is recommended as ± 0.001 inches for stub columns and was adopted as the goal for this study (Galambos 1998a). The short columns were side-milled with a Fadel computer numerically-controlled (CNC) vertical milling machine. The intermediate length columns were too long for the CNC machine, and were instead side-milled with a Bridgeport manual milling machine. During initial trials the milling process caused troublesome vibrations of the specimen. The large clamping forces required to dampen the vibration also tended to modify the shape of the C-section during the milling process. Unsatisfactory flatness results were obtained in these trials, with flatness variations of up to ± 0.010 inches.

The milling procedure was improved by encasing the specimen ends in bismuth diaphragms before milling as demonstrated in Figure 5.7. The diaphragms preserved the undeformed shape of the specimens, dampened vibration during the milling

process, and reduced the clamping force required to hold the specimens in place. Bismuth is a chemical element that is relatively soft compared to steel at room temperature and melts at 158 degrees Fahrenheit.

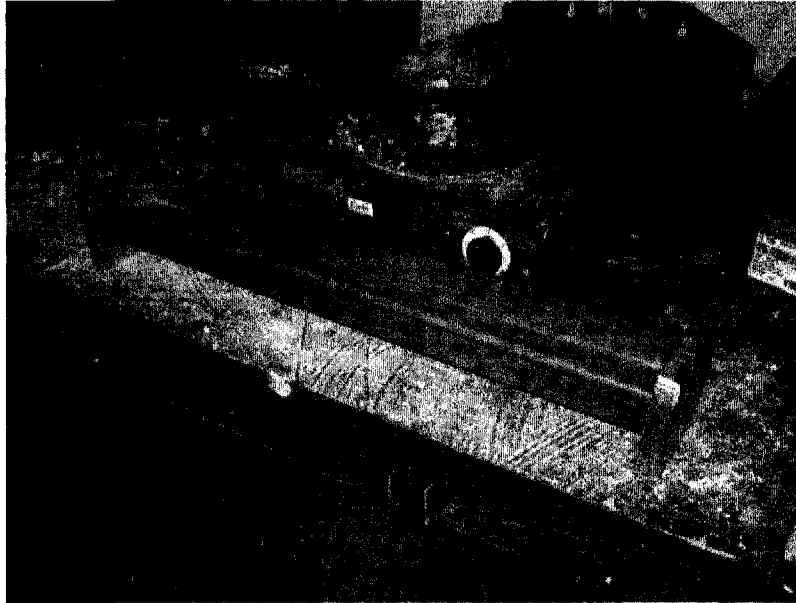


Figure 5.7 362S162-33 short column specimen with bismuth end diaphragms

Liquid bismuth was poured into custom wood forms at the specimen ends. Once the bismuth was set, the specimen (with bismuth end diaphragms) was positioned in the milling machine (Figure 5.8 through Figure 5.11). Several passes were made until the steel cross-section and bismuth diaphragm were flush. Both column ends were milled without removing the specimen from the milling table to reduce the chances of unparallel bearing ends. The bismuth diaphragms were removed from the specimen with a few taps of a wooden mallet and then melted down for use with the next specimen. The flatness tolerance of ± 0.001 inches was achieved for all but four specimens (see Section 5.2.4.4, the maximum out-of-flatness was +0.003 in.).

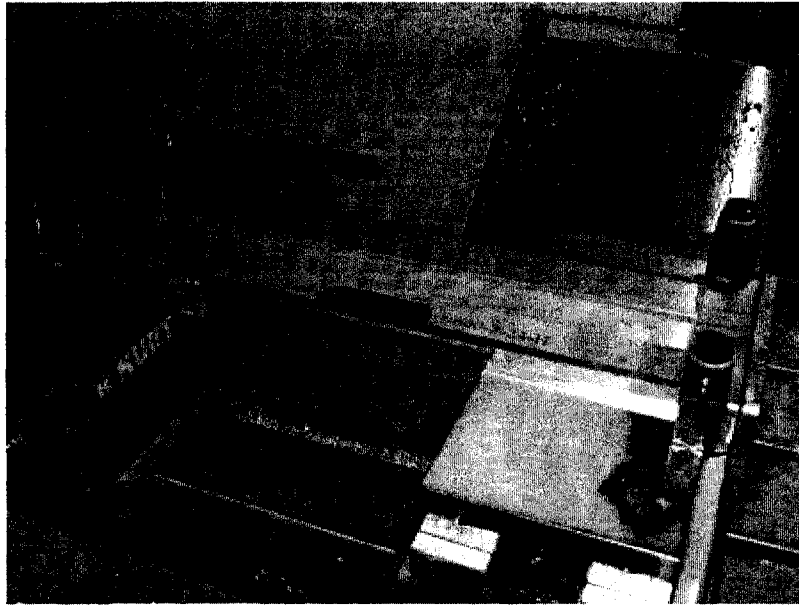


Figure 5.8 600S162-33 short column specimen oriented in CNC machine



Figure 5.9 An end mill is used to prepare the column specimens

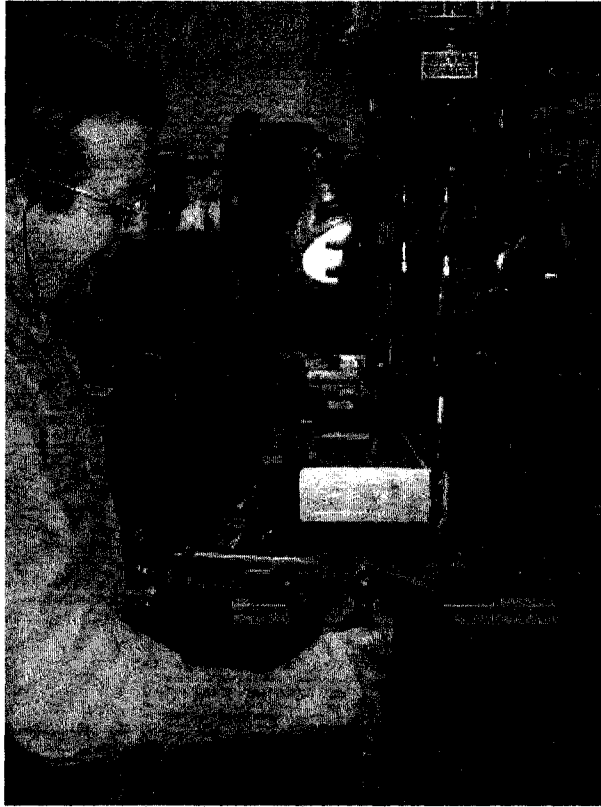


Figure 5.10 The intermediate length specimens were end-milled in a manual milling machine

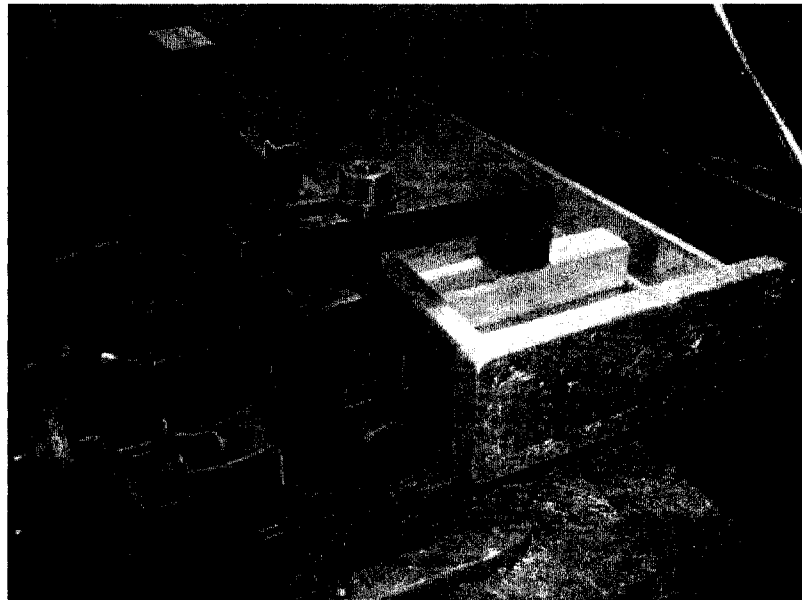


Figure 5.11 The specimens are clamped at the webs only to avoid distortion of the cross-section

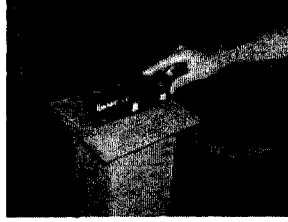
5.2.4 Column specimen measurements and dimensions

5.2.4.1 Specimen reference system and dimension notation

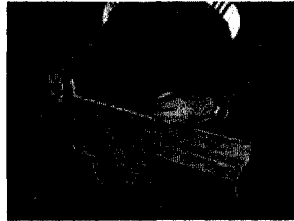
All column dimensions are measured with reference to the orientation of the specimen in the testing machine. The assumed reference system and specimen dimension notation are provided in Figure 5.15.

5.2.4.2 Cross-section measurements

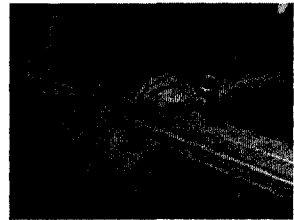
The out-to-out dimensions of the web, flanges, and lip stiffeners were measured with digital calipers and aluminum reference plates at the midlength of the specimens. The measurement procedure for a typical cross-section is summarized in Figure 5.12 (specimen setup) and Figure 5.13 (cross section dimensions). The outside corner radii were measured using a set of radius gauges with 1/32 in. increments. The cross-section dimensions, based on the average of three independent measurements, are provided for each specimen in Table 5.3.



Check levelness of measuring platform with the angle indicator. The slope perpendicular to the length of the specimen should be as close to zero as possible.



Find and mark the longitudinal midline of the specimen.

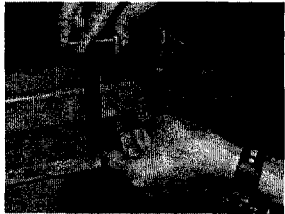


Clamp the specimen to the measuring platform.

Figure 5.12 Setup procedure for measuring specimen cross section dimensions



Clamp a beveled aluminum plate to the flange. Use the veneer caliper to measure the distance between the edge of the lip and the outside face of the beveled plate. The true dimension (D_1 or D_2) is then found by subtracting the thickness of the beveled plate from the veneer caliper reading.



Clamp beveled aluminum plates to the lip and web, offsetting them longitudinally by about 1/2 inch. Make sure that the beveled faces are oriented so that they are touching the channel.



Use the extension on the veneer caliper to measure the distance between the outside face of the lip plate and the inside face of the web plate. Make sure that the extension is flush with the flange surface. The true dimension (B_1 or B_2) is found by subtracting the thickness of the beveled plate from the veneer caliper reading.



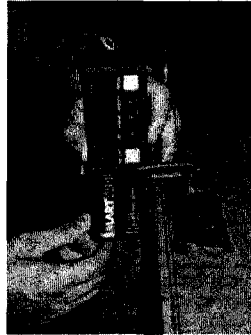
Clamp beveled aluminum plates to each flange, offsetting them longitudinally by about 1/2 inch. Make sure that the beveled faces are oriented so that they are touching the channel.

Use the extension on the veneer caliper to measure the distance between the outside face of one flange plate and the inside face of the other flange plate. Make sure that the extension is flush with the web surface. The true dimension H is found by subtracting the thickness of the beveled plate from the veneer caliper reading.

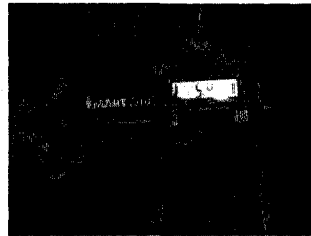
Figure 5.13 Procedure for measuring specimen cross-section dimensions



Clamp beveled aluminum plate to flange.



Measure the flange angle with the angle indicator (F_1 and F_2).



Clamp the beveled aluminum plate to the stiffener lip. Measure the flange angle using the angle indicator (S_1 and S_2).

Figure 5.14 Procedure for measuring flange-lip and flange-web angles

The four corner angles of each C-section are measured with a digital angle indicator as demonstrated in Figure 5.14. The angle indicator has a precision of 0.1 degrees. The flange-lip angles S_1 and S_2 are measured at the midlength of the specimens; the web-flange angles F_1 and F_2 are measured at multiple points along the specimen as denoted in Table 5.4. The C-section corner angle magnitudes, based on the average of two independent measurements, are provided for each specimen in Table 5.4.

Table 5.3 Summary of measured cross section dimensions

Specimen	H	B ₁	B ₂	D ₁	D ₂	RT ₁	RT ₂	RB ₁	RB ₂
	<i>in.</i>	<i>in.</i>	<i>in.</i>	<i>in.</i>	<i>in.</i>	<i>in.</i>	<i>in.</i>	<i>in.</i>	<i>in.</i>
362-1-24-NH	3.654	1.550	1.621	0.411	0.431	0.188	0.188	0.172	0.188
362-2-24-NH	3.712	1.586	1.585	0.416	0.422	0.172	0.203	0.266	0.281
362-3-24-NH	3.623	1.677	1.679	0.425	0.399	0.188	0.172	0.281	0.281
362-1-24-H	3.583	1.650	1.595	0.430	0.437	0.188	0.203	0.281	0.281
362-2-24-H	3.645	1.627	1.593	0.440	0.391	0.188	0.188	0.281	0.281
362-3-24-H	3.672	1.674	1.698	0.418	0.426	0.188	0.188	0.266	0.266
362-1-48-NH	3.624	1.611	1.605	0.413	0.426	0.172	0.172	0.281	0.281
362-2-48-NH	3.624	1.609	1.585	0.407	0.421	0.188	0.172	0.297	0.281
362-3-48-NH	3.614	1.604	1.599	0.425	0.401	0.188	0.188	0.266	0.266
362-1-48-H	3.622	1.602	1.595	0.420	0.412	0.172	0.172	0.281	0.281
362-2-48-H	3.623	1.594	1.610	0.425	0.403	0.172	0.172	0.281	0.281
362-3-48-H	3.633	1.604	1.610	0.395	0.432	0.172	0.172	0.281	0.250
600-1-24-NH	6.037	1.599	1.631	0.488	0.365	0.172	0.156	0.250	0.203
600-2-24-NH	6.070	1.582	1.614	0.472	0.380	0.203	0.203	0.266	0.266
600-3-24-NH	6.030	1.601	1.591	0.369	0.483	0.156	0.172	0.266	0.219
600-1-24-H	6.040	1.594	1.606	0.484	0.359	0.172	0.172	0.250	0.219
600-2-24-H	6.011	1.608	1.602	0.369	0.500	0.172	0.172	0.203	0.234
600-3-24-H	6.032	1.606	1.577	0.360	0.478	0.172	0.172	0.250	0.203
600-1-48-NH	6.018	1.621	1.609	0.486	0.374	0.172	0.172	0.234	0.219
600-2-48-NH	6.017	1.596	1.601	0.482	0.357	0.172	0.172	0.234	0.234
600-3-48-NH	6.026	1.585	1.627	0.489	0.338	0.172	0.172	0.266	0.219
600-1-48-H	6.010	1.598	1.625	0.480	0.388	0.188	0.156	0.250	0.219
600-2-48-H	6.017	1.589	1.607	0.476	0.356	0.172	0.172	0.234	0.234
600-3-48-H	6.062	1.632	1.588	0.366	0.480	0.172	0.172	0.219	0.250

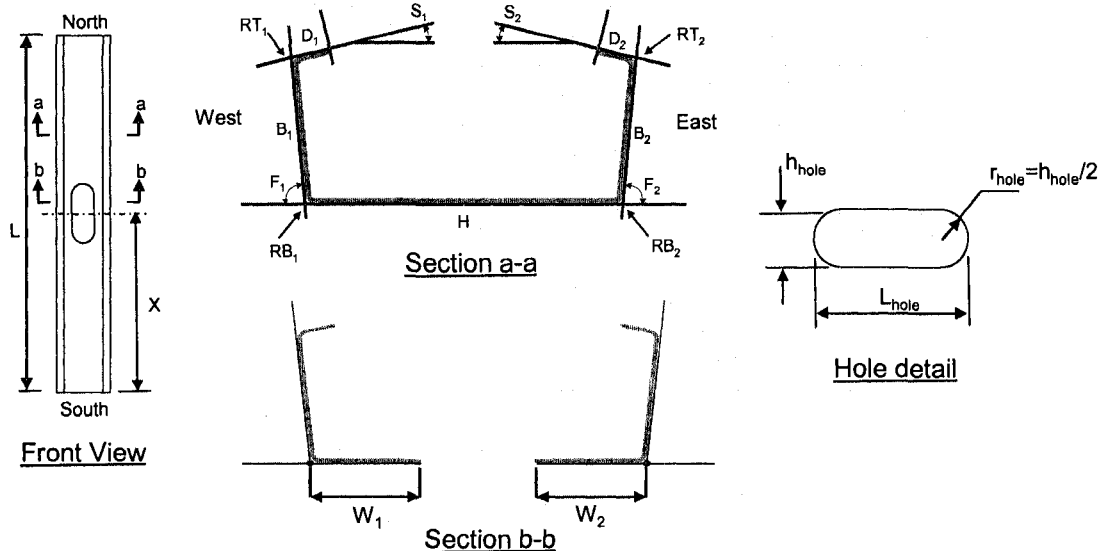


Figure 5.15 Specimen measurement nomenclature

Table 5.4 Summary of measured lip-flange and flange-web cross section angles

Specimen	X S ₁		S ₂		X F ₁		F ₂		X F ₁		F ₂		X F ₁		F ₂		X F ₁		F ₂		
	in.	degrees	degrees	degrees	in.	degrees	degrees	degrees	in.	degrees	degrees	degrees	in.	degrees	degrees	degrees	in.	degrees	degrees	degrees	degrees
362-1-24-NH	12	12.767	8.367	82.600	84.500	12	86.033	86.833	18	84.533	87.000										
362-2-24-NH	12	11.367	11.567	86.800	84.800	12	87.600	85.467	18	86.400	83.700										
362-3-24-NH	12	9.567	9.433	85.700	85.000	12	86.300	85.400	18	85.600	83.000										
362-1-24-H	12	11.130	10.930	83.200	83.970	12	87.600	85.600	18	84.330	86.430										
362-2-24-H	12	4.367	10.267	86.000	85.133	12	86.333	85.167	18	84.400	84.500										
362-3-24-H	12	10.533	10.833	85.200	86.333	12	87.700	86.133	18	87.667	89.033										
362-1-48-NH	12	7.800	10.100	85.100	85.600	18	84.300	85.000	24	85.000	85.600	30	84.000	85.200	36	85.300	85.700				
362-2-48-NH	12	8.000	10.800	85.500	84.900	18	84.800	85.100	24	84.200	84.600	30	84.800	85.300	36	85.200	84.900				
362-3-48-NH	12	9.100	12.200	86.900	84.000	18	85.800	83.900	24	85.300	84.100	30	86.400	83.400	36	86.100	83.700				
362-1-48-H	12	8.500	9.800	86.500	84.800	18	86.600	85.000	24	85.600	84.200	30	85.500	85.100	36	86.400	84.400				
362-2-48-H	12	8.300	11.200	86.800	84.800	18	86.500	84.200	24	85.600	83.800	30	85.500	84.100	36	86.700	83.800				
362-3-48-H	12	9.700	7.300	85.300	85.200	18	84.700	86.100	24	84.100	85.300	30	84.400	84.700	36	85.200	85.000				
600-1-24-NH	24	1.567	2.133	90.567	92.033	12	92.467	93.733	18	91.433	93.767										
600-2-24-NH	24	1.733	2.333	91.000	92.033	12	91.167	94.067	18	91.467	93.333										
600-3-24-NH	24	-2.167	3.500	93.700	89.767	12	94.067	91.033	18	92.733	89.667										
600-1-24-H	24	0.967	2.033	89.000	91.000	12	90.400	92.267	18	91.200	92.600										
600-2-24-H	24	1.800	1.100	94.433	90.900	12	93.233	88.733	18	91.967	89.000										
600-3-24-H	24	0.100	4.100	93.500	90.000	12	93.300	89.300	18	90.100	86.300										
600-1-48-NH	24	0.167	1.400	91.033	92.933	18	90.833	92.700	24	90.600	92.800	30	91.333	92.900	36	91.667	93.200				
600-2-48-NH	24	2.000	2.367	90.767	91.900	18	90.233	92.300	24	89.900	91.867	30	90.967	92.000	36	91.467	92.767				
600-3-48-NH	24	2.600	2.300	90.000	92.100	18	89.200	91.900	24	90.000	92.100	30	90.700	92.600	36	90.900	92.500				
600-1-48-H	24	2.533	2.100	90.933	92.167	18	91.000	92.767	24	90.000	92.633	30	91.000	92.000	36	91.100	92.967				
600-2-48-H	24	2.400	1.000	89.000	90.700	18	89.200	91.000	24	88.900	91.200	30	89.600	91.600	36	90.200	92.200				
600-3-48-H	24	0.667	3.633	93.067	89.400	18	93.000	89.500	24	92.300	89.433	30	93.467	89.900	36	93.467	89.600				

NOTE: X is the longitudinal distance from the south end of the specimen

5.2.4.3 Specimen thickness

All structural studs were delivered by the manufacturer with a zinc outer coating applied for galvanic corrosion protection. The total zinc thickness (i.e., summation of the zinc coating thicknesses applied to each side of the steel sheet) and the base metal thickness (sheet thickness with total zinc coating removed) defined in Figure 5.16 were measured for each specimen. The total zinc thickness was used to calculate the centerline cross-section dimensions from the out-to-out measurements (see Section 5.2.4.2), which were then input along with the base metal thickness into the nonlinear finite element models discussed in Chapter 7. The base metal thickness was also used to calculate the steel yield stress provided in Section 5.2.5.

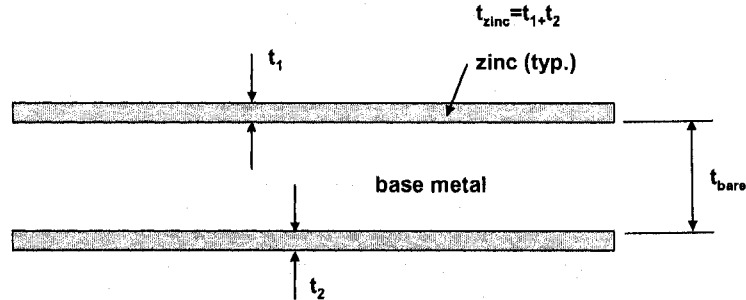


Figure 5.16 Base metal and zinc thickness definitions

Total zinc thickness and base metal thickness were measured for each specimen from tensile coupons cut from the west flange, east flange, and web of an untested section of structural stud. The thickness measurements were made to a precision of 0.0001 inches with a digital micrometer fitted with a thimble friction clutch. The thickness was determined by averaging five measurements taken within the gauge

length of the tensile coupon (see Figure 5.27 for the definition of gauge length). The base sheet metal thicknesses $t_{bare,w}$ (web), $t_{bare,fl}$ (west flange), $t_{bare,fz}$ (east flange) and corresponding total zinc coating thicknesses $t_{zinc,w}$, $t_{zinc,fl}$, and $t_{zinc,fz}$ are summarized for each specimen in Table 5.5.

Table 5.5 Specimen bare steel and zinc coating thicknesses

Specimen	Web		West Flange		East Flange	
	$t_{bare,w}$ in.	$t_{zinc,w}$ in.	$t_{bare,fl}$ in.	$t_{zinc,fl}$ in.	$t_{bare,fz}$ in.	$t_{zinc,fz}$ in.
362-1-24-NH						
362-2-24-NH	0.0368	N/M	0.0415	N/M	0.0372	N/M
362-3-24-NH						
362-1-24-H	0.0390	0.0030	0.0391	0.0034	0.0391	0.0028
362-2-24-H	0.0368	0.0057	0.0390	0.0023	0.0391	0.0034
362-3-24-H	0.0394	0.0027	0.0394	0.0018	0.0394	0.0026
362-1-48-NH	0.0392	0.0025	0.0393	0.0020	0.0392	0.0020
362-2-48-NH	0.0393	0.0025	0.0394	0.0022	0.0393	0.0026
362-3-48-NH	0.0389	0.0013	0.0391	0.0009	0.0390	0.0017
362-1-48-H	0.0391	0.0019	0.0393	0.0017	0.0394	0.0017
362-2-48-H	0.0390	N/M	0.0391	N/M	0.0391	N/M
362-3-48-H	0.0401	0.0000	0.0400	0.0000	0.0397	0.0010
600-1-24-NH						
600-2-24-NH	0.0438	N/M	0.0432	N/M	0.0438	N/M
600-3-24-NH						
600-1-24-H	0.0414	0.0042	0.0422	0.0044	0.0428	0.0030
600-2-24-H	0.0427	0.0039	0.0384	0.0084	0.0424	0.0042
600-3-24-H	0.0429	0.0031	0.0431	0.0026	0.0430	0.0036
600-1-48-NH	0.0434	0.0026	0.0436	0.0024	0.0434	0.0028
600-2-48-NH	0.0435	0.0017	0.0430	0.0024	0.0430	0.0023
600-3-48-NH	0.0436	0.0015	0.0432	0.0021	0.0433	0.0020
600-1-48-H	0.0429	0.0022	0.0426	0.0023	0.0429	0.0021
600-2-48-H	0.0429	N/M	0.0428	N/M	0.0431	N/M
600-3-48-H	0.0430	N/M	0.0434	N/M	0.0430	N/M

NOTE: N/M Not measured

The zinc coating was removed by immersing the tensile coupons in a ferric chloride bath for 100 minutes. The immersion time was determined with a study of coupon thickness variation over time for the 362-2-24-H web and the 600-2-24-H west flange tensile coupons. The coupons were removed from the ferric chloride bath every 10 minutes, cleaned, and then measured. Figure 5.17 demonstrates that the coupon thickness converges to a constant value, the base metal thickness, at approximately 100 minutes.

The average zinc coating thickness (i.e., average of t_{zinc} , $t_{zinc,f1}$, and $t_{zinc,f2}$) for all specimens was 0.0026 inches using the ferric chloride method described above. Specimen coating thickness measurements were also made with a Positest DFT digital thickness gauge (www.defelsko.com) which produced an average coating thickness for all specimens of 0.0016 in. At the microscopic level, the bonding of the zinc to the steel substrate results in a gradient from pure zinc to a mixture of steel and zinc (Porter 1991). This gradient complicates the identification of the non-structural thickness of the galvanic coating. The base thickness and coating thickness determined with the ferric chloride method (as reported in Table 5.5) are used throughout this thesis. Accurate identification of the non-structural and structural contributions of the galvanic coating is warranted as a topic of future research, especially since the load-deformation response and ultimate strength are sensitive to base metal thickness.

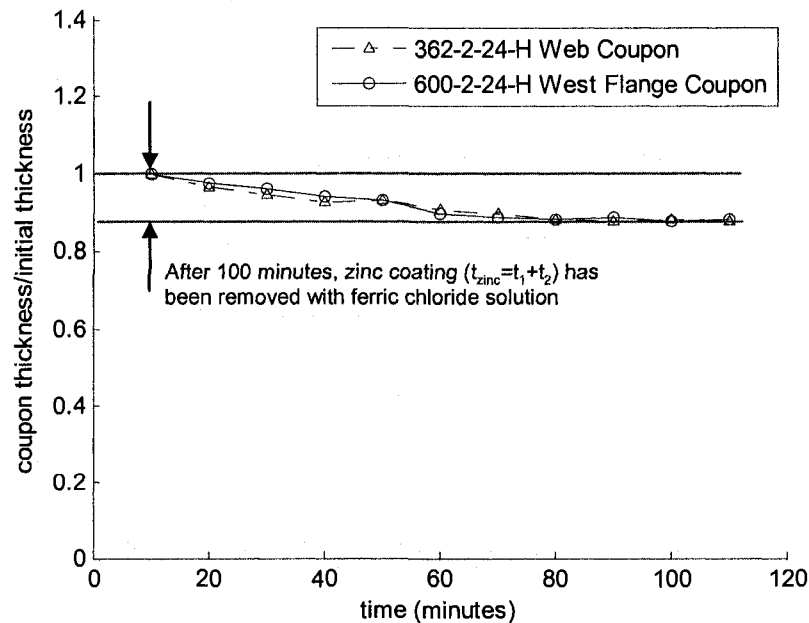


Figure 5.17 Removal of tensile coupon zinc coating as a function of time

5.2.4.4 Specimen end flatness and length

After each specimen was saw cut and milled flat, the vertical height gauge (with a precision of 0.001 inches) shown in Figure 5.18 was used to measure the specimen length and flatness. For each specimen, two independent length measurements were taken at each rounded corner location described in Figure 5.19. The height gauge and specimen are placed on the same steel table to ensure that all measurements are made in the same reference plane. The steel table was checked for flatness with a dial gauge and precision stand before measurements proceeded. Lengths LRT_1 , LRT_2 , LRB_1 , and LRB_2 as well as the average length L are provided for each specimen in Table 5.6. The specimen flatness, defined as the difference between LRT_1 , LRT_2 , LRB_1 , and LRB_2 and the average length L , is reported in Table 5.7. All but four specimens met the flatness tolerance of ± 0.001 inches, with intermediate length column 362-2-48-H having the maximum deviation of $+0.003$ inches at LRT_2 .

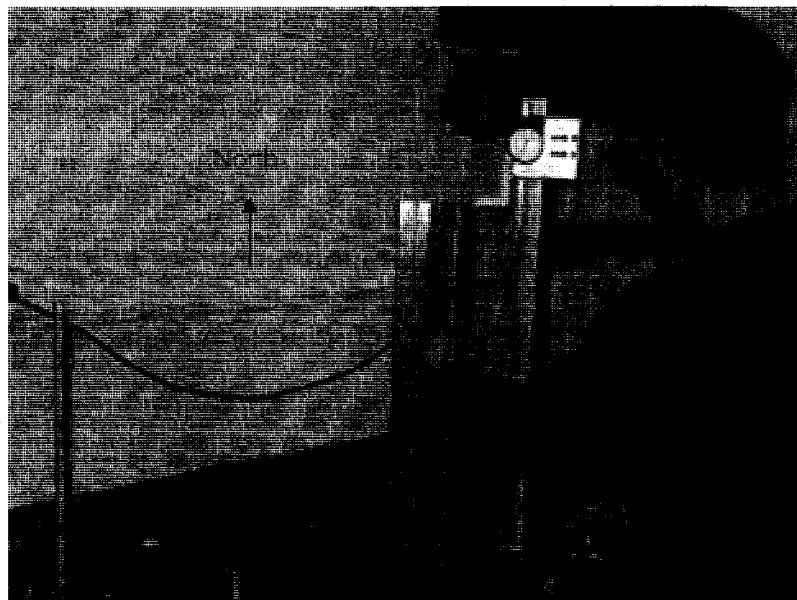


Figure 5.18 A height gauge is used to measure specimen length

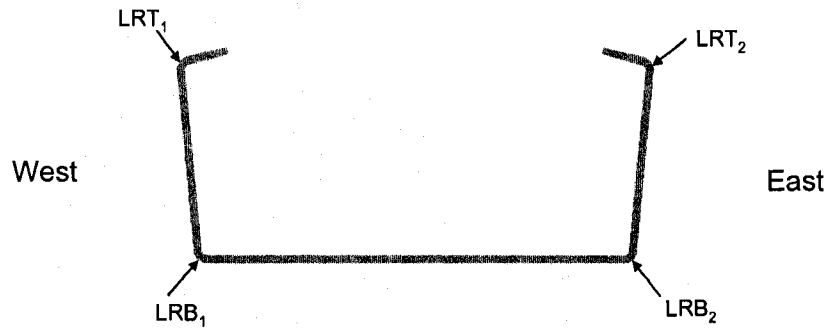


Figure 5.19 Lengths are measured at the four corners of the C-section column

Table 5.6 Measured column specimen length

Specimen	LRT1 <i>in.</i>	LRT2 <i>in.</i>	LRB1 <i>in.</i>	LRB2 <i>in.</i>	L (avg.) <i>in.</i>
362-1-24-NH	24.100	24.100	24.098	24.099	24.099
362-2-24-NH	24.097	24.098	24.099	24.099	24.098
362-3-24-NH	24.097	24.098	24.098	24.099	24.098
362-1-24-H	24.100	24.099	24.098	24.100	24.099
362-2-24-H	24.097	24.099	24.099	24.100	24.099
362-3-24-H	24.099	24.099	24.099	24.100	24.099
362-1-48-NH	48.214	48.214	48.214	48.214	48.214
362-2-48-NH	48.303	48.300	48.301	48.298	48.301
362-3-48-NH	48.192	48.19	48.191	48.189	48.191
362-1-48-H	48.217	48.216	48.216	48.216	48.216
362-2-48-H	48.232	48.232	48.231	48.231	48.232
362-3-48-H	48.196	48.200	48.195	48.198	48.197
600-1-24-NH	24.100	24.101	24.099	24.099	24.100
600-2-24-NH	24.102	24.104	24.102	24.103	24.103
600-3-24-NH	24.100	24.098	24.099	24.099	24.099
600-1-24-H	24.102	24.100	24.100	24.101	24.101
600-2-24-H	24.098	24.099	24.100	24.100	24.099
600-3-24-H	24.101	24.101	24.101	24.100	24.101
600-1-48-NH	48.255	48.255	48.255	48.255	48.255
600-2-48-NH	48.250	48.250	48.250	48.251	48.250
600-3-48-NH	48.295	48.294	48.295	48.294	48.295
600-1-48-H	48.089	48.088	48.089	48.088	48.089
600-2-48-H	48.253	48.251	48.253	48.253	48.253
600-3-48-H	48.061	48.061	48.059	48.059	48.060

Table 5.7 Specimen end flatness

Specimen	Flatness (Deviation from Average Length)			
	LRT1 <i>in.</i>	LRT2 <i>in.</i>	LRB1 <i>in.</i>	LRB2 <i>in.</i>
362-1-24-NH	0.001	0.001	-0.001	0.000
362-2-24-NH	-0.001	0.000	0.001	0.001
362-3-24-NH	-0.001	0.000	0.000	0.001
362-1-24-H	0.001	0.000	-0.001	0.001
362-2-24-H	-0.002	0.000	0.000	0.001
362-3-24-H	0.000	0.000	0.000	0.001
362-1-48-NH	0.000	0.000	0.000	0.000
362-2-48-NH	0.002	-0.001	0.001	-0.002
362-3-48-NH	0.002	-0.001	0.001	-0.002
362-1-48-H	0.001	0.000	0.000	0.000
362-2-48-H	0.001	0.001	0.000	0.000
362-3-48-H	-0.001	0.003	-0.002	0.001
600-1-24-NH	0.000	0.001	-0.001	-0.001
600-2-24-NH	-0.001	0.001	-0.001	0.000
600-3-24-NH	0.001	-0.001	0.000	0.000
600-1-24-H	0.001	-0.001	-0.001	0.000
600-2-24-H	-0.001	0.000	0.001	0.001
600-3-24-H	0.000	0.000	0.000	-0.001
600-1-48-NH	0.000	0.000	0.000	0.000
600-2-48-NH	0.000	0.000	0.000	0.001
600-3-48-NH	0.001	-0.001	0.001	-0.001
600-1-48-H	0.001	0.000	0.001	0.000
600-2-48-H	0.001	-0.001	0.001	0.001
600-3-48-H	0.001	0.001	-0.001	-0.001

5.2.4.5 Location and dimensions of slotted holes

The length and width of the slotted holes, L_{hole} and h_{hole} , were measured to a precision of 0.001 inches with digital calipers. The east-west locations of the holes, W_1 and W_2 , were measured by clamping aluminum plates to the outside surface of the flanges and then using the caliper extension to measure the distance from the edge of the hole to the aluminum plate. (This process is similar to the cross-section measurement procedures described in Figure 5.13.) The hole size and web location dimensions, based on the average of three independent measurements, are provided for each specimen in Table 5.8.

Table 5.8 Measured slotted hole dimensions and locations

Specimen	X <i>in.</i>	W ₁ <i>in.</i>	W ₂ <i>in.</i>	L _{hole} <i>in.</i>	h _{hole} <i>in.</i>	X <i>in.</i>	W ₁ <i>in.</i>	W ₂ <i>in.</i>	L _{hole} <i>in.</i>	h _{hole} <i>in.</i>
362-1-24-H	L/2	0.946	1.141	4.003	1.492					
362-2-24-H	L/2	1.146	0.967	4.000	1.502					
362-3-24-H	L/2	0.935	1.114	4.005	1.493					
362-1-48-H	(L-24)/2	1.252	0.974	3.999	1.500	(L+24)/2	1.198	0.952	4.001	1.494
362-2-48-H	(L-24)/2	1.126	1.016	4.001	1.496	(L+24)/2	1.171	0.973	4.003	1.494
362-3-48-H	(L-24)/2	0.982	1.112	4.000	1.493	(L+24)/2	0.967	1.133	4.003	1.491
600-1-24-H	L/2	2.147	2.361	4.002	1.498					
600-2-24-H	L/2	2.365	2.155	4.001	1.491					
600-3-24-H	L/2	2.347	2.166	4.001	1.493					
600-1-48-H	(L-24)/2	2.161	2.375	4.002	1.494	(L+24)/2	2.162	2.383	3.998	1.497
600-2-48-H	(L-24)/2	2.166	2.351	4.001	1.499	(L+24)/2	2.176	2.360	4.002	1.498
600-3-48-H	(L-24)/2	2.371	2.162	3.999	1.497	(L+24)/2	2.365	2.156	4.003	1.494

5.2.4.6 Web imperfections

Variations in the specimen webs were measured to provide a basis for the local buckling initial imperfection magnitudes in the specimen nonlinear finite element models constructed in Section 7.2. The measurement setup shown in Figure 5.20 uses a dial gauge with a precision of 0.001 inches mounted to a laboratory stand in contact with a flat steel table. The specimen was supported horizontally at both ends by a matching pair of steel bars that were ground flat and parallel. The bars were also in contact with the steel table, ensuring that the specimen and the dial gauge were in the same horizontal reference plane. Each specimen web was marked with a grid of measurement points shown in Figure 5.21. The stand and dial gauge were shifted from grid point to grid point and elevation measurements were recorded. The variations from the average elevation of the specimen web, based on an average of two measurements per grid point, are provided for each specimen in Table 5.9.

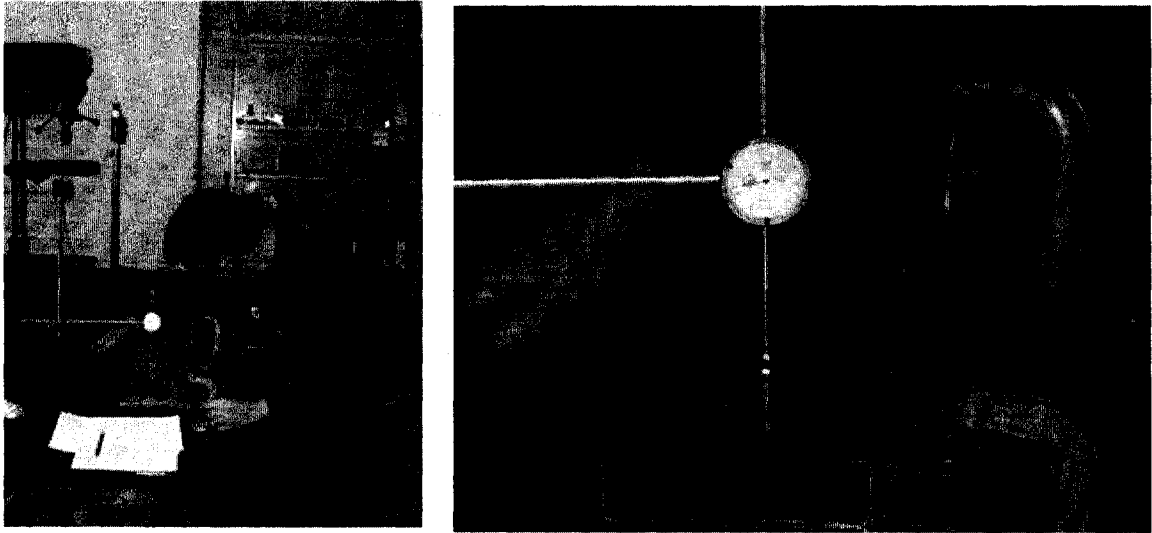


Figure 5.20 A dial gauge and precision stand are used to measure initial web imperfections

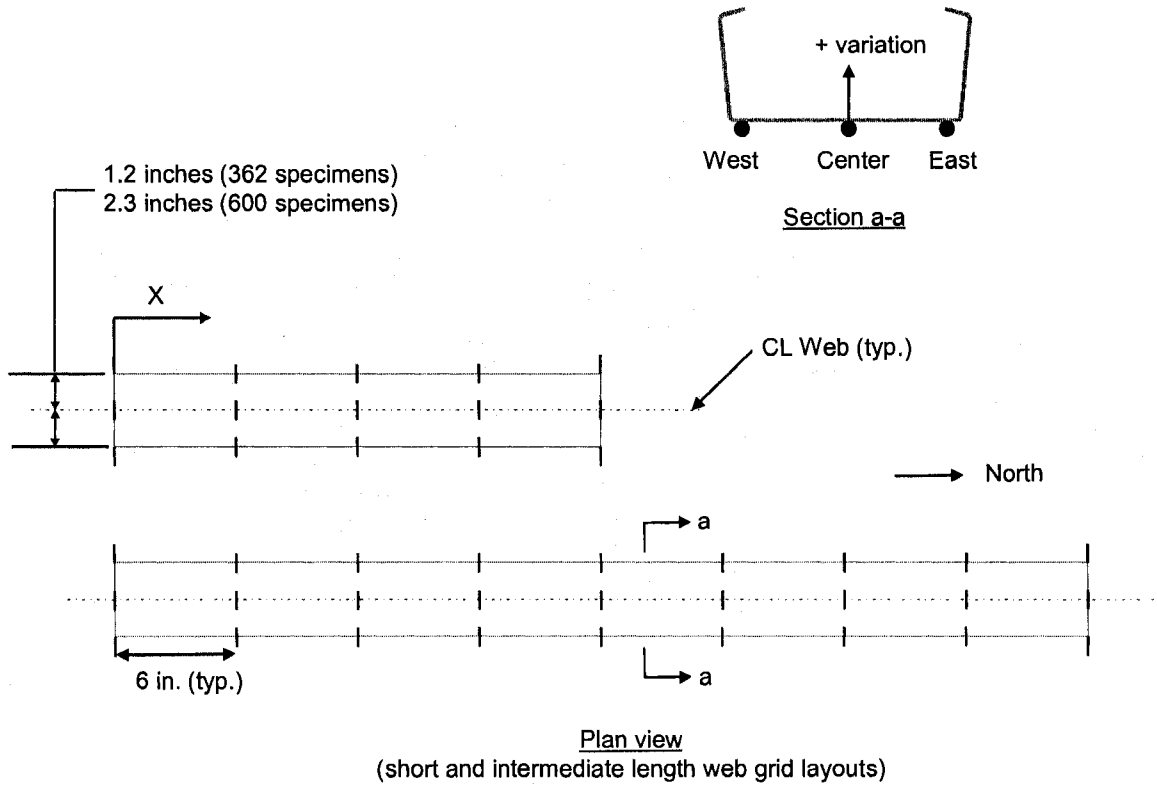


Figure 5.21 Web imperfection measurement grid and coordinate system

5.2.4.7 Specimen orientation in the testing machine

When placing the specimen in the testing machine, the southern end of the specimen was oriented at the bottom platen such that the center of the compressive force was applied through the gross centroid of the C-section. The centerline of the web is positioned in line with the centerline of the bottom platen and offset towards the back of the testing machine as described in Figure 5.22. The centroid locations were calculated using the centerline dimensions of a nominal SSMA 362S162-33 and 600S162-33 cross section.

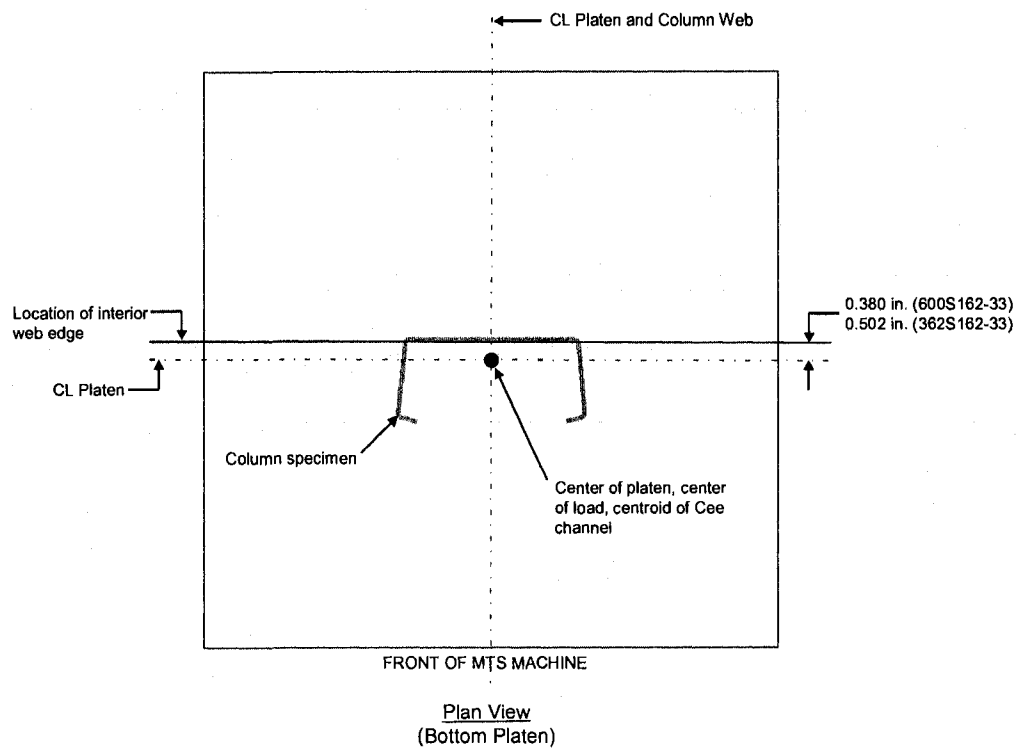


Figure 5.22 Column specimen alignment schematic

The actual cross section and thickness measurements produced centroid offsets slightly different from the nominal offsets considered in the column tests. The difference between the nominal and measured offsets, defined here as ΔCG , are provided in Table 5.10. ΔCG produces end moments in the specimens that are several orders of magnitude smaller than the applied loads in this study. For example, the end moments created by a ΔCG of 0.059 inches for specimen 600-3-24-NH are calculated as 2.0×10^{-6} kip-inches at peak load ($P_{test}=12.24$ kips) using the structural analysis program MASTAN (Ziemian and McGuire 2005). The assumed MASTAN structural system in Figure 5.23 demonstrates that relatively stiff compression platens and fixed-fixed end conditions effectively eliminate end moments from small load eccentricities.

Table 5.10 Specimen gross centroid and offset from applied load during tests

Specimen	Specimen Measurements		Centroid Shift		ΔCS in.
	x_{cg}	t_z	$x_{cg} - t_z$	used in tests	
	in.	in.	in.	in.	
362-1-24-NH	0.482	0.038	0.463	0.502	0.039
362-2-24-NH	0.471	0.038	0.452	0.502	0.050
362-3-24-NH	0.504	0.038	0.485	0.502	0.017
362-1-24-H	0.511	0.042	0.489	0.502	0.013
362-2-24-H	0.490	0.042	0.469	0.502	0.033
362-3-24-H	0.524	0.042	0.503	0.502	-0.001
362-1-48-NH	0.475	0.041	0.454	0.502	0.048
362-2-48-NH	0.468	0.042	0.447	0.502	0.055
362-3-48-NH	0.475	0.040	0.455	0.502	0.047
362-1-48-H	0.470	0.041	0.449	0.502	0.053
362-2-48-H	0.470	0.042	0.449	0.502	0.053
362-3-48-H	0.486	0.040	0.466	0.502	0.036
600-1-24-NH	0.354	0.047	0.330	0.380	0.050
600-2-24-NH	0.347	0.047	0.323	0.380	0.057
600-3-24-NH	0.344	0.047	0.321	0.380	0.059
600-1-24-H	0.363	0.046	0.340	0.380	0.040
600-2-24-H	0.368	0.047	0.344	0.380	0.036
600-3-24-H	0.361	0.046	0.338	0.380	0.042
600-1-48-NH	0.362	0.046	0.339	0.380	0.041
600-2-48-NH	0.355	0.045	0.333	0.380	0.047
600-3-48-NH	0.353	0.045	0.330	0.380	0.050
600-1-48-H	0.362	0.045	0.340	0.380	0.040
600-2-48-H	0.352	0.046	0.329	0.380	0.051
600-3-48-H	0.356	0.046	0.333	0.380	0.047

t_z sheet thickness with zinc coating

ΔCS difference measured and as tested centroid offsets

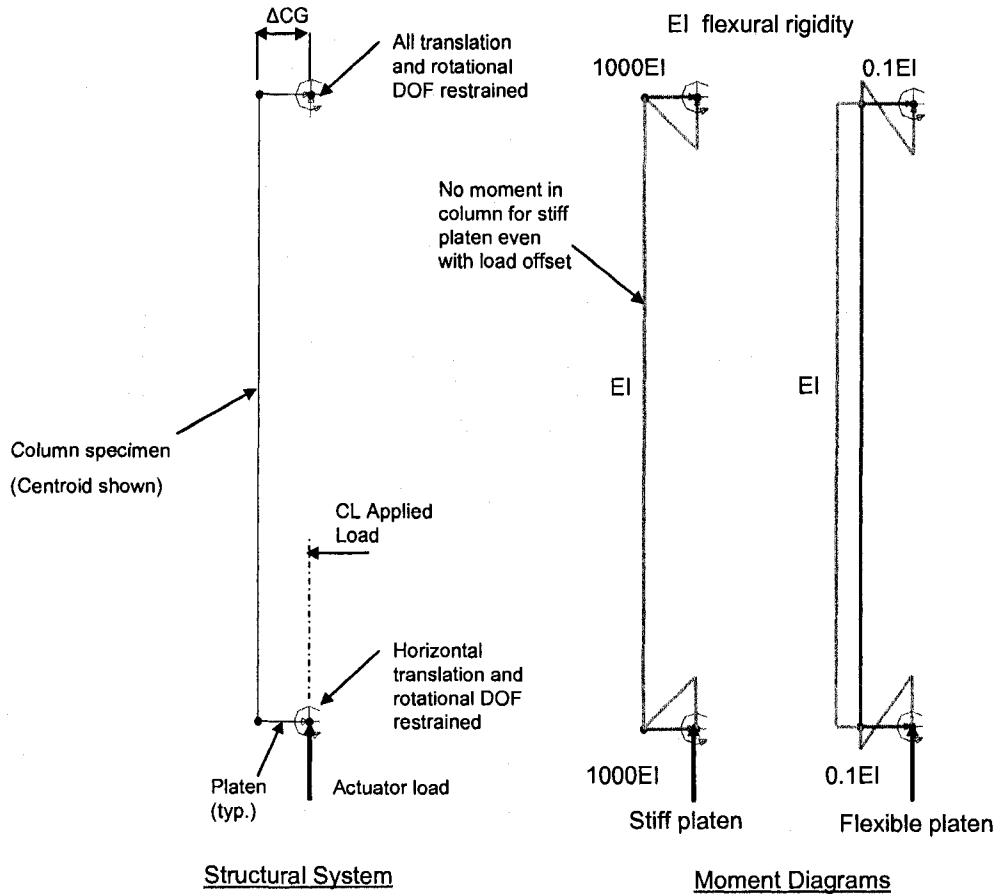


Figure 5.23 Influence of platen bending stiffness on end moments for a fixed-fixed eccentric column

Once the specimen is aligned on the bottom platen, 500 lbs of compressive force was applied to the column and weak-axis out of straightness measurements were taken. The distance from the front of the top and bottom platens to the interior web edge is denoted as S_{top} and S_{bottom} in Figure 5.24. S_{top} and S_{bottom} are obtained as the average of three independent measurements with digital calipers as shown in Figure 5.25 and then corrected for a systematic platen offset (see Figure 5.24) and the initial web imperfections in Table 5.9. The initial out-of-straightness ΔS provided in Table 5.11 is

calculated from S_{top} and S_{bottom} and implemented as an initial geometric imperfection into the nonlinear finite element models in 7.2.

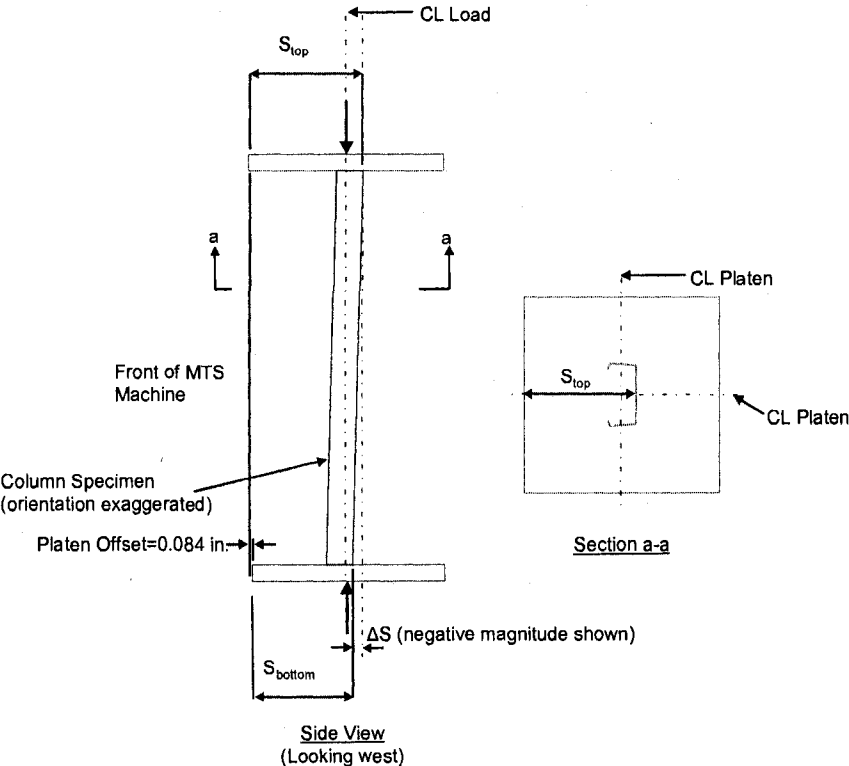


Figure 5.24 Column specimen weak axis out-of-straightness schematic

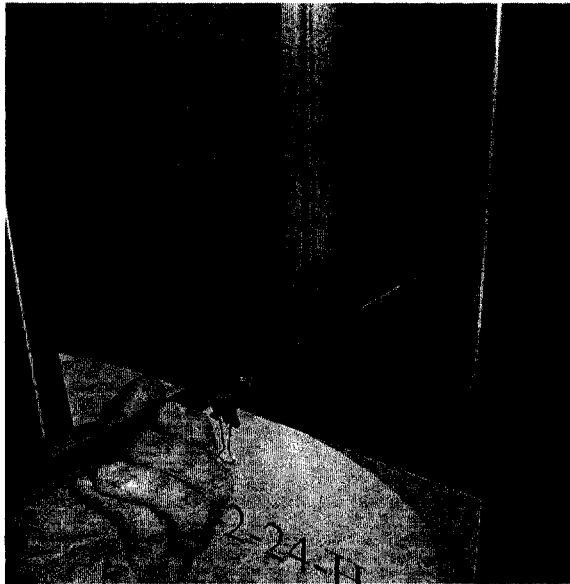


Figure 5.25 Digital calipers are used to measure the distance from the column web to platen edge

Table 5.11 Summary of out-of-straightness calculations

Specimen	S _{bottom}	S _{top}	Platen Offset	S _{bottom}	Correction	S _{bottom}	Correction	S _{top}	ΔS
	As measured	As measured	Top platen edge is offset from bottom platen Edge	Corrected for top platen offset	Web Imperfection @ X=0	Corrected for Web Imperfection @ X=0	Web Imperfection @ X=L	Corrected for Web Imperfection @ X=L	Initial out of straightness
	in.	in.	in.	in.	in.	in.	in.	in.	in.
362-1-24-NH	6.507	6.622	0.084	6.591	0.015	6.577	0.022	6.600	-0.024
362-2-24-NH	6.523	6.612	0.084	6.607	0.015	6.593	0.024	6.588	0.004
362-3-24-NH	6.531	6.585	0.084	6.615	0.017	6.598	0.025	6.560	0.038
362-1-24-H	6.524	6.613	0.084	6.608	0.016	6.592	0.009	6.604	-0.012
362-2-24-H	6.532	6.578	0.084	6.616	0.014	6.602	0.010	6.568	0.034
362-3-24-H	6.529	6.629	0.084	6.613	0.021	6.592	0.015	6.615	-0.023
362-1-48-NH	6.352	6.393	0.084	6.436	0.009	6.427	0.013	6.380	0.047
362-2-48-NH	6.535	6.649	0.084	6.619	-0.004	6.623	-0.002	6.651	-0.028
362-3-48-NH	6.537	6.614	0.084	6.621	-0.001	6.622	0.004	6.610	0.012
362-1-48-H	6.530	6.554	0.084	6.614	-0.015	6.629	-0.009	6.563	0.066
362-2-48-H	6.534	6.617	0.084	6.618	0.011	6.607	0.022	6.594	0.013
362-3-48-H	6.532	6.616	0.084	6.616	0.019	6.598	0.015	6.601	-0.003
600-1-24-NH	6.352	6.472	0.084	6.436	0.055	6.381	0.027	6.444	-0.063
600-2-24-NH	6.365	6.560	0.084	6.449	0.061	6.388	0.031	6.529	-0.141
600-3-24-NH	6.451	6.494	0.084	6.535	0.034	6.501	0.057	6.437	0.063
600-1-24-H	6.356	6.486	0.084	6.440	0.052	6.388	0.021	6.466	-0.078
600-2-24-H	6.360	6.399	0.084	6.444	0.020	6.424	0.051	6.348	0.076
600-3-24-H	6.355	6.403	0.084	6.439	0.007	6.432	0.040	6.363	0.069
600-1-48-NH	6.346	6.436	0.084	6.430	0.060	6.370	0.030	6.406	-0.036
600-2-48-NH	6.354	6.488	0.084	6.438	0.060	6.377	0.023	6.465	-0.087
600-3-48-NH	6.354	6.463	0.084	6.438	0.055	6.383	0.031	6.432	-0.049
600-1-48-H	6.311	6.458	0.084	6.395	0.059	6.336	0.024	6.433	-0.098
600-2-48-H	6.352	6.422	0.084	6.436	-0.033	6.469	0.025	6.396	0.072
600-3-48-H	6.348	6.430	0.084	6.432	0.028	6.404	0.046	6.384	0.020

5.2.5 Materials testing

Tensile coupon tests were performed to obtain the steel stress-strain curve and yield stress for the web, west flange, and east flange of each specimen in this study. The tests were conducted in accordance with ASTM specification E 8M-04, "Standard Test Methods for Tension Testing of Metallic Materials (Metric)" (ASTM 2004).

5.2.5.1 Tensile coupon preparation

Tensile coupons were always obtained from the same 8 ft. structural stud which produced the column specimen. Flat portions of the web and flanges were first rough cut with a metal band saw as shown in Figure 5.26, and then finished to the dimensions in Figure 5.27 with a CNC milling machine. The special jig in Figure 5.27 allowed for three tensile coupons to be produced at once. The tensile coupons were stripped of their zinc coating (see Section 5.2.4.3 for procedure) and then measured within the gauge length for bare metal thickness, t , and minimum width, w_{min} . The minimum width is determined by taking the minimum of five independent measurements within the gauge length of the specimen with digital calipers.

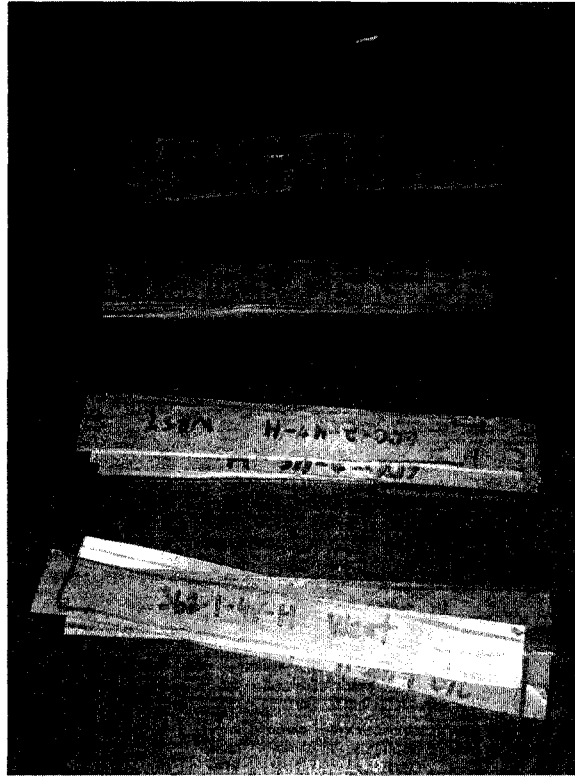
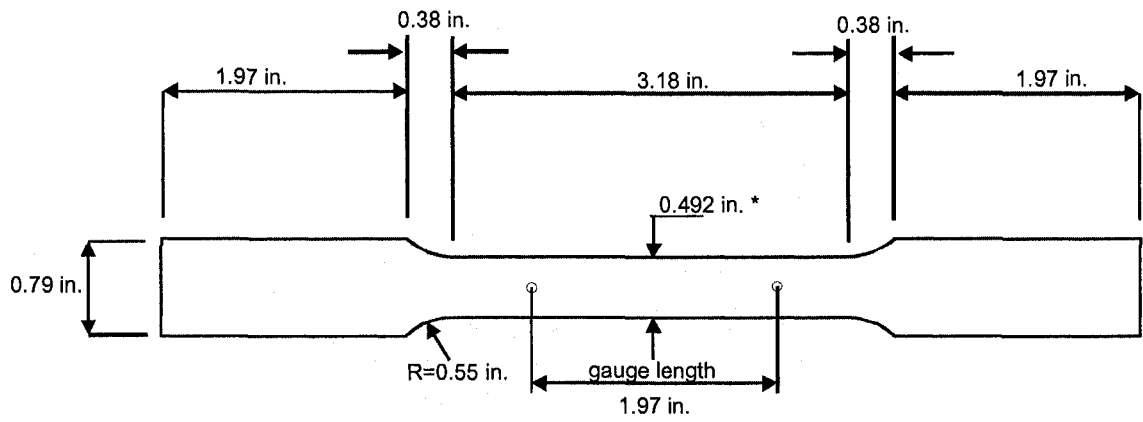


Figure 5.26 Tensile coupons are first rough cut with a metal ban saw



*nominal, actual dimension will vary slightly

Figure 5.27 Tensile coupon dimensions as entered in the CNC milling machine computer



Figure 5.28 A custom jig allows three tensile coupons to be milled at once in the CNC machine

5.2.5.2 Tensile test setup

A screw-driven ATS 900 testing machine with a maximum capacity of 10 kips was used to apply the tensile load. Tensile coupons were positioned in the machine with friction grips as shown in Figure 5.29. A bubble level with a short, straight edge was used to ensure that each specimen was aligned vertically between the grips. An MTS 634.11D-54 extensometer measured engineering strain and an MTS load cell measured force on the specimen. The extensometer was placed at the vertical midlength of the specimen, centered within the gauge length. The raw voltage data from the extensometer and load cell were sent to a PC containing a National Instruments data acquisition card. The voltage data was converted to tensile force and engineering strain using the conversion factors provided in Table 5.12. The data was plotted on the screen and recorded to a file with a custom LabVIEW program (Labview 2005).

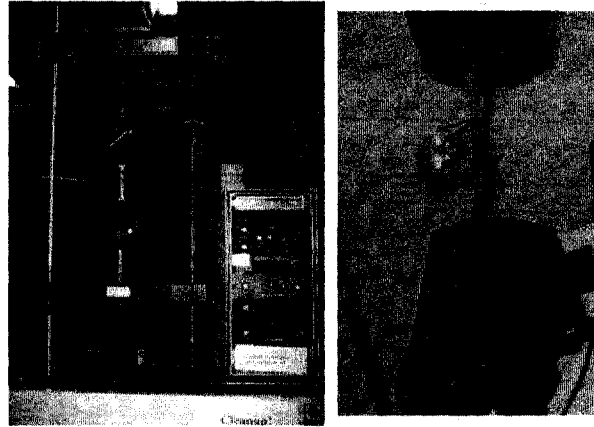


Figure 5.29 ATS machine used to test tensile coupons

Table 5.12 Voltage conversion factors for tensile coupon testing

Tensile Coupon Testing		
Measurement	Source	Conversion
Tensile Force	MTS Load Cell	1 Volt = 1000 lbf
Engineering Strain	MTS Extensometer	1 Volt = 3.96×10^{-5} strain (in./in.)

5.2.5.3 Tensile test results

Two distinct steel stress-strain curves were observed in this study. Tensile coupons from the 362S162-33 structural studs demonstrate gradual yielding behavior, while the tensile coupons from the 600S162-33 studs demonstrated a sharp yielding plateau. The yield stress, F_y , for the gradually yielding specimens was determined with the 0.2% strain offset method. The stress-strain curve for specimen 362-3-48-NH (East Flange) demonstrates the offset method in Figure 5.30. The yield stress for the sharply yielding specimens was determined by averaging the stresses in the yield plateau. ASTM does not provide specific guidelines on how to average the plateau stresses. For this autographic method, the averaging range is determined by using two strain offset lines, one at 0.4% strain offset and the other at 0.8% offset as shown for specimen 600-24-

NH (West Flange) in Figure 5.31. The steel modulus of elasticity, E , was assumed as 29500 ksi for all specimens when determining the yield stress. The tensile coupon yield stresses and cross section dimensions are summarized in Table 5.13. The mean and standard deviation for all 362S162-33 and 600S162-33 tensile coupons tested are provided in Table 5.14.

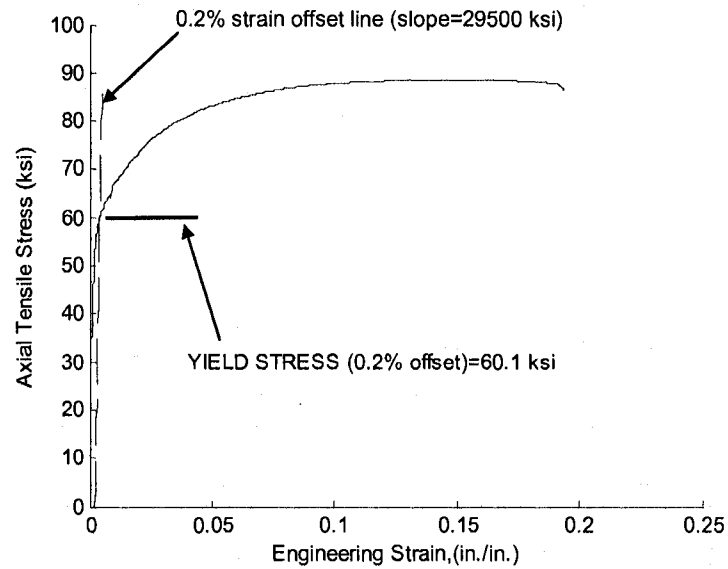


Figure 5.30 Gradually yielding stress-strain curve with 0.2% strain offset method

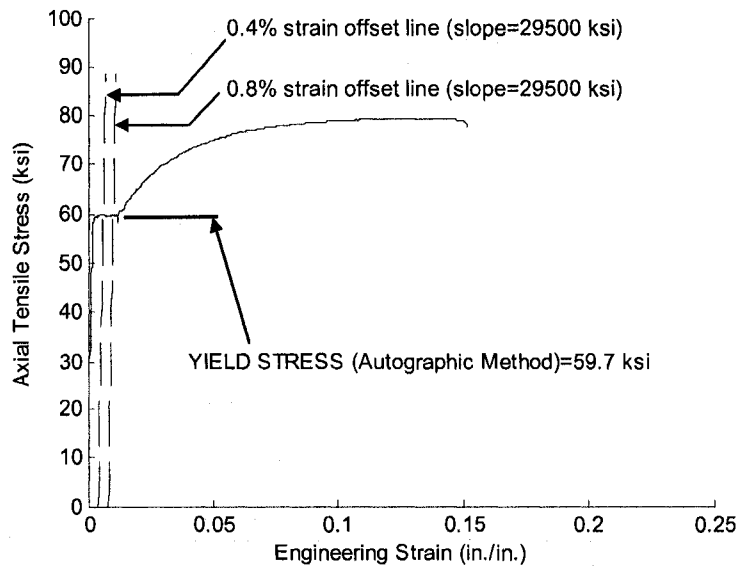


Figure 5.31 Sharp-yielding stress strain curve using an autographic method for determining F_y

Table 5.13 Summary of column specimen steel yield stress

Specimen	Web			West Flange			East Flange		
	$t_{base,w}$ in.	W_{min} in.	F_y ksi	$t_{base,f1}$ in.	W_{min} in.	F_y ksi	$t_{base,f2}$ in.	W_{min} in.	F_y ksi
362-1-24-NH									
362-2-24-NH	0.0368	0.4985	53.3	0.0415	0.4975	54.7	0.0372	0.4955	57.4
362-3-24-NH									
362-1-24-H	0.0390	0.4945	55.9	0.0391	0.4963	59.3	0.0391	0.4968	58.5
362-2-24-H	0.0368	0.4886	52.9	0.0390	0.4950	58.8	0.0391	0.4945	59.5
362-3-24-H	0.0394	0.4945	55.6	0.0394	0.4927	N/C	0.0394	0.4947	56.4
362-1-48-NH	0.0392	0.4985	59.4	0.0393	0.4965	59.7	0.0392	0.4975	59.9
362-2-48-NH	0.0393	0.4990	59.2	0.0394	0.4975	59.3	0.0393	0.4970	59.2
362-3-48-NH	0.0389	0.4930	58.0	0.0391	0.5000	58.9	0.0390	0.4930	60.1
362-1-48-H	0.0391	0.4998	59.5	0.0393	0.4985	58.2	0.0394	0.4991	58.1
362-2-48-H	0.0390	0.4992	58.8	0.0391	0.4961	60.6	0.0391	0.4975	59.8
362-3-48-H	0.0401	0.4990	57.8	0.0400	0.4957	58.0	0.0397	0.4978	59.1
600-1-24-NH									
600-2-24-NH	0.0438	0.4950	60.6	0.0432	0.4950	59.7	0.0438	0.5000	55.9
600-3-24-NH									
600-1-24-H	0.0414	0.4899	61.9	0.0422	0.4940	63.6	0.0428	0.4964	60.3
600-2-24-H	0.0427	0.4964	57.8	0.0384	0.4874	55.6	0.0424	0.4938	61.8
600-3-24-H	0.0429	0.4966	59.7	0.0431	0.4954	58.0	0.0430	0.4960	62.6
600-1-48-NH	0.0434	0.4985	58.7	0.0436	0.4955	62.3	0.0434	0.4965	59.3
600-2-48-NH	0.0435	0.4985	N/C	0.0430	0.4970	63.4	0.0430	0.4970	63.3
600-3-48-NH	0.0436	0.4995	60.4	0.0432	0.4955	N/C	0.0433	0.4965	61.9
600-1-48-H	0.0429	0.4970	60.3	0.0426	0.4980	63.0	0.0429	0.4970	60.8
600-2-48-H	0.0429	0.4994	61.8	0.0428	0.4962	62.1	0.0431	0.4977	62.2
600-3-48-H	0.0430	0.4992	60.7	0.0434	0.4961	59.7	0.0430	0.4977	64.0

NOTE: N/C Tests results were not obtained

Table 5.14 Column specimen steel yield stress statistics

Stud Type	yield stress, F_y	
	mean ksi	STDV ksi
362S162-33	58.1	2.0
600S162-33	61.0	2.0

5.3 Elastic buckling calculations

Elastic buckling provides a means to categorize and potentially better understand the load-deformation response and ultimate strength of the thin-walled columns in this study. The local, distortional, and global elastic buckling modes and their associated critical elastic buckling loads ($P_{cr,l}$, $P_{cr,d}$, $P_{cr,g}$) are presented here for each specimen. Calculations are performed with a shell finite element eigenbuckling analysis as opposed to an analysis using FSM (Schafer and Adány 2006) to capture the influence of the slotted web holes and the tested (fixed-fixed) boundary conditions.

5.3.1 Finite element modeling assumptions

Eigenbuckling analysis in ABAQUS is performed for the 24 column specimens (ABAQUS 2007a). All columns are modeled with S9R5 reduced integration nine-node thin shell elements. Cold-formed steel material properties are assumed as $E=29500$ ksi and $\nu=0.30$. The centerline C-section dimensions input into ABAQUS are calculated using the out-to-out dimensions and flange and lip angles at the mid-height of each column specimen as provided in Table 5.3 and Table 5.4. Each column specimen is loaded with a set of consistent nodal loads in ABAQUS to simulate a constant pressure across the bearing edge of the specimen. The nodes on the loaded column face are coupled together in the direction of loading with an ABAQUS “pinned” rigid body constraint (see Figure 4.12).

5.3.2 Elastic buckling results

5.3.2.1 Buckled shapes / eigenmodes

The first (lowest buckling load) local (L) and distortional (D) buckled shapes for specimens with and without slotted holes are compared in Figure 5.32 and Figure 5.33. The L and D modes for each specimen were identified visually by manually searching through the elastic buckling modes produced in the eigenbuckling analysis. The nominal cross-section half-wavelengths in Table 5.1 were compared to the half-wavelengths in the finite element model to assist in the categorization. The local and distortional modes that most resembled the FSM results for L and D modes were selected. This method of modal identification is neither exact nor ideal, especially when both local and

distortional buckling are present in the same eigenmode. Formal modal identification has recently been developed in the context of the finite strip method (Schafer and Adány 2006) and future work is ongoing to extend this method to finite element analyses and to problems such as the ones encountered here.

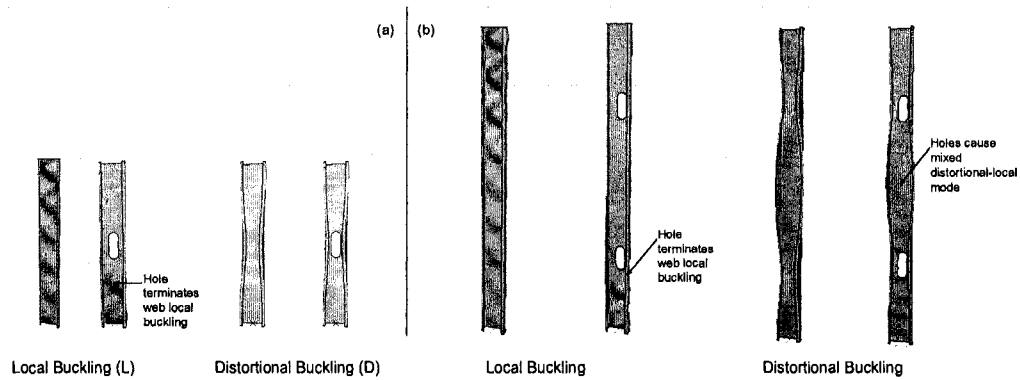


Figure 5.32 (a) Local and distortional elastic buckled mode shapes for (a) short ($L=48$ in.) 362S162-33 specimens and (b) intermediate length ($L=48$ in.) 362S162-33 specimens.

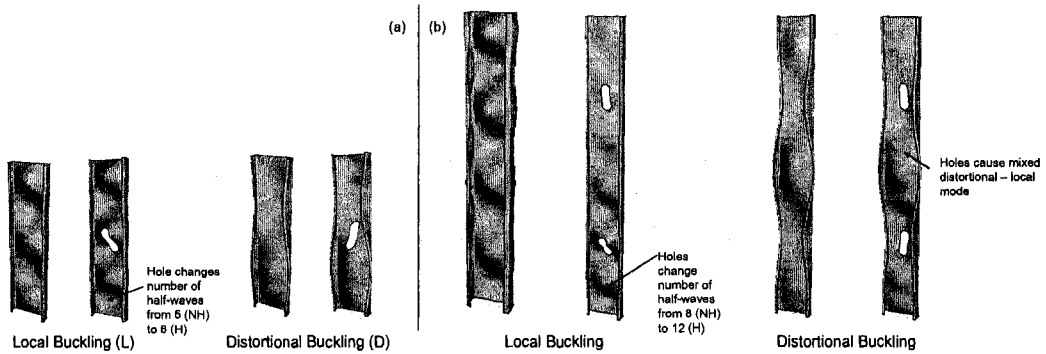


Figure 5.33 Local and distortional elastic buckled mode shapes for (a) short ($L=48$ in.) 600S162-33 specimens and (b) intermediate length ($L=48$ in.) 600S162-33 specimens.

5.3.2.2 Buckling loads / eigenvalues

The primary goal of this research program is to extend the Direct Strength Method to cold-formed steel structural members with holes. The Direct Strength Method (DSM), a design method for cold-formed steel structural members, predicts column ultimate strength by predicting the column failure mode and ultimate strength through

knowledge of the local (L), distortional (D), or global (G) elastic buckling modes. This connection is made using the critical elastic buckling load, P_{cr} , and the slenderness, defined with the ratio of column squash load P_{yg} to P_{cr} for the L, D, and G modes. Table 5.15 summarizes P_{cr} and P_{yg} for the specimens evaluated in this study. The squash load P_{yg} is calculated with the gross cross-sectional area, and P_{cr} includes the effects of the holes and the tested (fixed-fixed) boundary conditions. (Note, the implications of using P_{yg} as opposed to $P_{y,net}$ at the net section are discussed in Chapter 8.)

The influence of holes on P_{cr} is of interest in the context of DSM because elastic buckling loads and slenderness are used to predict ultimate strength. To isolate the influence of holes on P_{cr} , additional eigenbuckling analyses of the specimens with holes (specimens labeled with an H) were performed, but with the holes removed (the boundary and loading conditions were not modified and the mesh used in the models was identical except for the removed elements at the hole location). The comparison of P_{cr} for specimens with holes (H) and then with holes removed (noH) is also summarized in Table 5.15.

Table 5.15 Critical elastic buckling loads, influence of holes on elastic buckling

Specimen Name	P_{y0} kips	ELASTIC BUCKLING			HOLE INFLUENCE*		
		P_{cre} kips	$P_{cr'}$ kips	P_{crd} kips	P_{cre}/P_{cre}^{noH}	$P_{cr'}/P_{cr'}^{noH}$	P_{crd}/P_{crd}^{noH}
362-1-24-NH	15.5	109.4	4.9	10.6			
362-2-24-NH	15.6	112.5	4.8	10.2		N/A	
362-3-24-NH	15.7	112.2	5.0	10.7			
362-1-24-H	16.4	119.3	5.9	13.5	0.98	1.03	1.12
362-2-24-H	15.7	112.8	5.4	12.4	0.98	1.02	1.13
362-3-24-H	16.4	130.6	5.7	12.9	0.99	1.02	1.12
362-1-48-NH	16.9	30.5	5.2	9.7			
362-2-48-NH	16.7	29.5	5.2	9.6		N/A	
362-3-48-NH	16.6	29.6	5.1	9.5			
362-1-48-H	16.6	30.0	5.3	9.4	0.94	1.03	0.98
362-2-48-H	16.8	29.7	5.2	9.3	0.94	1.03	0.98
362-3-48-H	16.8	36.2	5.7	9.6	0.95	1.03	0.98
600-1-24-NH	24.7	244.5	3.4	6.8			
600-2-24-NH	24.5	234.9	3.4	6.7		N/A	
600-3-24-NH	24.5	218.4	3.4	6.6			
600-1-24-H	25.0	239.3	3.3	7.0	1.01	1.02	1.09
600-2-24-H	23.1	238.4	3.2	6.7	1.01	1.01	1.08
600-3-24-H	24.7	242.6	3.5	7.3	1.02	1.01	1.08
600-1-48-NH	25.1	61.8	3.5	5.2			
600-2-48-NH	26.2	59.6	3.4	5.7		N/A	
600-3-48-NH	25.4	60.2	3.4	5.7			
600-1-48-H	25.2	56.3	3.4	5.1	0.87	1.02	1.02
600-2-48-H	25.5	53.0	3.4	5.0	0.87	1.02	1.02
600-3-48-H	25.6	55.8	3.4	5.0	0.86	1.02	1.02

* For specimens with holes (H), the holes are removed and elastic buckling calculated (noH). The hole (H) and no hole (noH) finite element models are otherwise identical, isolating the influence of the holes.

5.3.2.3 Modal interaction at ultimate strength

An additional reason for the selection of these specimen cross-sections, at these lengths, beyond the reasons discussed in Section 5.2.1, is that the specimens provide much needed experimental data on cross-sections with potential modal interaction at ultimate strength both with and without holes. Typically modal interaction is understood to be a concern when the elastic buckling loads of multiple modes are at or near the same value, and the ratio of any two elastic buckling loads (e.g., P_{crd}/P_{crd}) is considered a useful parameter for study. However, for modes with different post-buckling strength and where material yielding is considered, a more pressing concern may be the situation when both failure modes predict similar capacities. Which mode does the column fail in if the predicted capacity in local (P_{nl}) and distortional (P_{nd}) are at or near the same level? What impact does a hole have on the failure mode that is

triggered? In the specimens selected here, the ratio of P_{crd}/P_{crd} varies from a min of 0.44 to a max of 0.68, but is never near 1.0. Therefore, by this traditional measure no meaningful interaction would be anticipated. However, if the DSM methodology is used to predict the capacities, as illustrated in Figure 5.34, the predictions for the ratio of the two limit states P_n/P_{nd} ranges from a min of 0.86 to a max of 0.90 in the 362S162-33 short columns and from a min of 1.0 to a max of 1.05 in the 600S162-33 short columns (the ratios are similar for the long column specimens). Thus, these cross-sections provide a means to examine the potential for local-distortional modal interaction at ultimate strength, and offer valuable data for determining any necessary modification to the DSM methodology when holes are present.

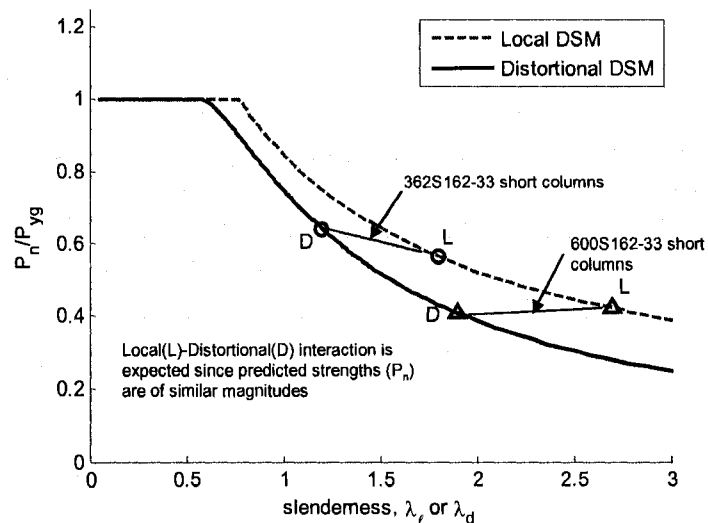


Figure 5.34 Local (L) and distortional (D) DSM strength predictions are similar in magnitude for both 362S162-33 and 600S162-33 cross-sections, indicating that L-D modal interaction will occur during the tested response of the columns.

5.3.3 Discussion of elastic buckling results

5.3.3.1 Local buckling

Boundary conditions have little influence on the local buckling mode shapes (compared with FSM L modes), but the presence of the slotted web holes can change the shape, half-wavelength, and buckling load of the first (lowest) local buckling mode observed. In the 362S162-33 specimens the web holes terminate local buckling in the vicinity of the holes, see Figure 5.32. In the 600S162-33 specimens the web holes cause an increased number of half-waves along the length to occur in the lowest local mode, see Figure 5.33. The presence of holes causes a slight increase in P_{cr} (see Table 5.15) which is consistent with the increased number of observed local buckling half-waves. The more extensive elastic buckling studies Chapter 3 and Chapter 4 demonstrate that a hole can increase or decrease the number of buckled half-waves (and the critical elastic buckling load) of rectangular plates and cold-formed steel structural studs.

5.3.3.2 Distortional buckling

Boundary conditions and the presence of holes have an influence on the observed distortional buckling mode shapes (compared with FSM D modes) and buckling loads. The boundary conditions (fixed-fixed) allow a smaller number of half-waves to form than predicted using the simply supported FSM D modes of Table 5.1. For example, observe the restrained shape of the buckled distortional half-wave near the member ends in Figure 5.32a. In longer specimens (see Figure 5.32b and Figure 5.33b), the influence of the boundary conditions lessens and the half-wavelength of distortional

buckling at mid-height approaches that of the FSM D mode of Table 5.1. (Section 4.2.6.2 explores the influence of fixed-fixed boundary conditions on P_{crit} using the column experiment database.) The presence of the web holes complicates the predicted D modes, see Figure 5.32 and Figure 5.33. Local buckling now appears within the D mode itself. The half-wavelength of these interacting L modes is significantly shorter than the lowest L modes observed. Further, and rather unintuitively, the buckling load, P_{crit} , actually increases with the presence of holes in the short column specimens (as much as 13%). However, this increase is lost at the longer specimen length where the maximum change in the buckling load is +/- 2%. This result suggests that in the shorter specimens the removal of the material most susceptible to out-of-plane bending, at the mid-depth of the web, actually serves to stiffen the column (a localized increase in the transverse bending stiffness of plates with holes has been observed, see Figure 4.30). This influence does not persist in the longer specimens suggesting that the increased stiffness is only relevant when the D mode is at a restrained half-wavelength. Thus, if the D mode is free to form (over a long enough unbraced length) the holes do not increase the elastic buckling load.

5.3.3.3 Global buckling

The global (Euler) buckled shapes for the intermediate 362S162-33 and 600S162-33 columns in Figure 5.35 occur as flexural-torsional buckling, although local and distortional deformation are both present in the mode shape for specimens with and without holes, which is an unexpected result. The interaction between the global, local,

and distortional modes makes the identification of the global mode difficult. The Euler buckling load and mode shape predicted with classical methods (in CUTWP), which do not allow cross-section distortion and ignore holes, were used to determine the range of buckling loads (eigenvalues) to be visually searched. The reported modes in Figure 5.35 are the ones closest to the expected buckling load exhibiting significant global deformations. Additional eigenbuckling analyses of the 362S162-33 and 600S162-33 cross-sections were performed at a longer column length (8 ft.) and these analyses show no local or distortional interaction with the global modes. Therefore, the observed interaction is length dependent and not a fundamental feature of global buckling in these cross-sections. An alternative hypothesis for the “unusual” mode shapes in Figure 5.35 is that several buckling mode shapes exist near the global critical elastic buckling load, which causes the eigensolver to misreport the global mode as a linear combination of buckled shapes.

As for the global buckling loads, the slotted holes have a small influence on the global buckling load for the intermediate length 362S162-33 specimens, reducing P_{cre} by a maximum of 6%. However, P_{cre} for the intermediate length 600S162-33 columns decreases by a maximum of 14% with the presence of the two slotted holes, which is an unexpected result attributed to the local and distortional modes mixing with global buckling (i.e., Figure 5.35). Additional research work is ongoing to determine under what conditions holes influence the global critical elastic buckling load.

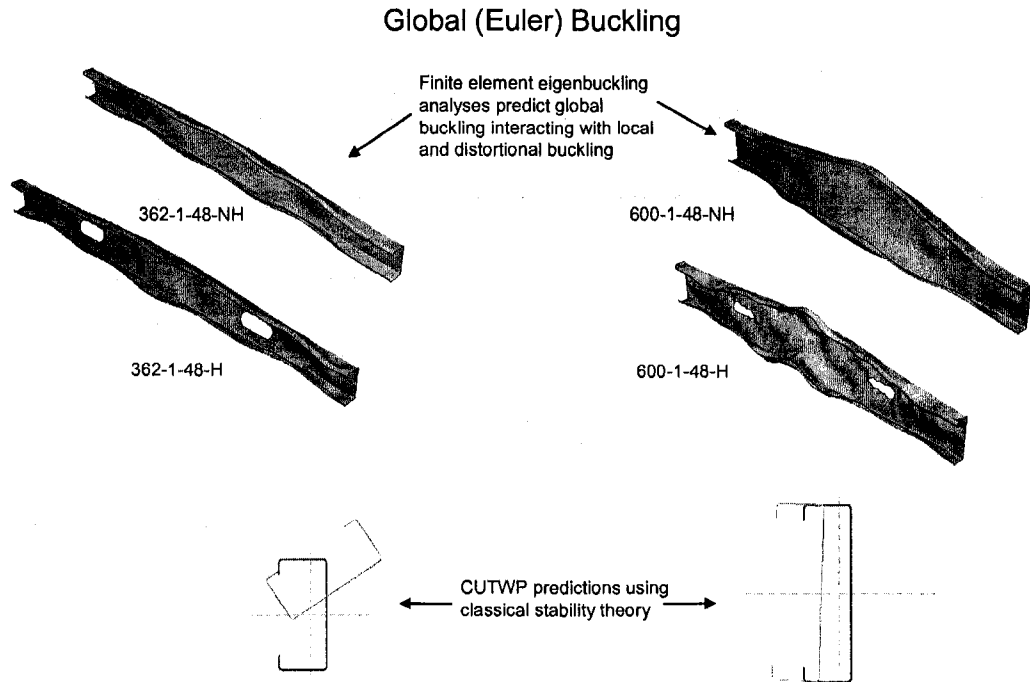


Figure 5.35 Comparison of global mode shapes for intermediate length 362S162-33 and 600S162-33 specimens.

5.4 Experiment results

5.4.1 Ultimate strength

The peak tested compressive load for all column specimens and an average peak load for each test group are provided in Table 5.16. The slotted holes are shown to have only a small influence on compressive strength in this study, with the largest reduction being 2.7% for the 362S162-33 short columns.

Table 5.16 Specimen ultimate strength results

Specimen	P_{test} kips	Mean kips	Std. Dev. kips
362-1-24-NH	10.48		
362-2-24-NH	10.51	10.4	0.2
362-3-24-NH	10.15		
362-1-24-H	10.00		
362-2-24-H	10.38	10.1	0.2
362-3-24-H	9.94		
362-1-48-NH	9.09		
362-2-48-NH	9.49	9.4	0.2
362-3-48-NH	9.48		
362-1-48-H	8.95		
362-2-48-H	9.18	9.2	0.2
362-3-48-H	9.37		
600-1-24-NH	11.93		
600-2-24-NH	11.95	12.0	0.2
600-3-24-NH	12.24		
600-1-24-H	12.14		
600-2-24-H	11.62	11.9	0.3
600-3-24-H	11.79		
600-1-48-NH	11.15		
600-2-48-NH	11.44	11.3	0.1
600-3-48-NH	11.29		
600-1-48-H	11.16		
600-2-48-H	11.70	11.3	0.3
600-3-48-H	11.16		

5.4.2 Failure modes and post-peak ductility

5.4.2.1 Short columns

The loading progression for the 362162S-33 short columns is depicted in Figure 5.36 (without a hole) and Figure 5.37 (with a hole). Both columns exhibit local buckling of the web near the supports combined with one distortional half-wave along the length. This distortional buckling pattern is consistent with that predicted by the elastic buckling mode shapes of Figure 5.32a. For the column with the hole, localized hole deformation (Figure 5.37, rightmost picture) initiates at a load of approximately $0.4P_{test}$ and increases in magnitude as the test progresses. This observed deformation behavior is visually consistent with the “unstiffened strip” approach discussed in **Error! Reference source**

not found, where the strip of web on either side of the hole is assumed to behave as an unstiffened element.

The inward flange deformation concentrates at the hole after peak load in the short 362S162-33 specimens with holes. It is hypothesized that the slotted hole reduces the post-peak resistance of the web, causing the flanges and lips to carry more of the column load. This reduction in post peak resistance is quantified by observing the reduction in area under the load-displacement curve for the column with the slotted hole, as shown in Figure 5.38.

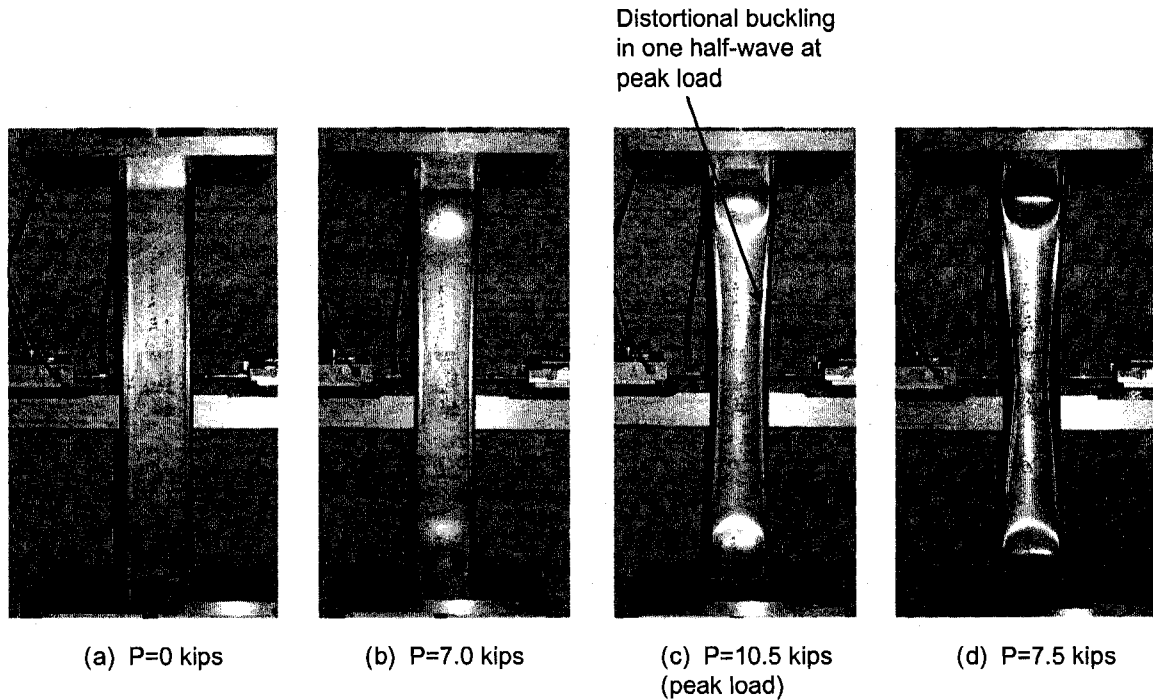


Figure 5.36 Load-displacement progression for short column specimen 362-2-24-NH

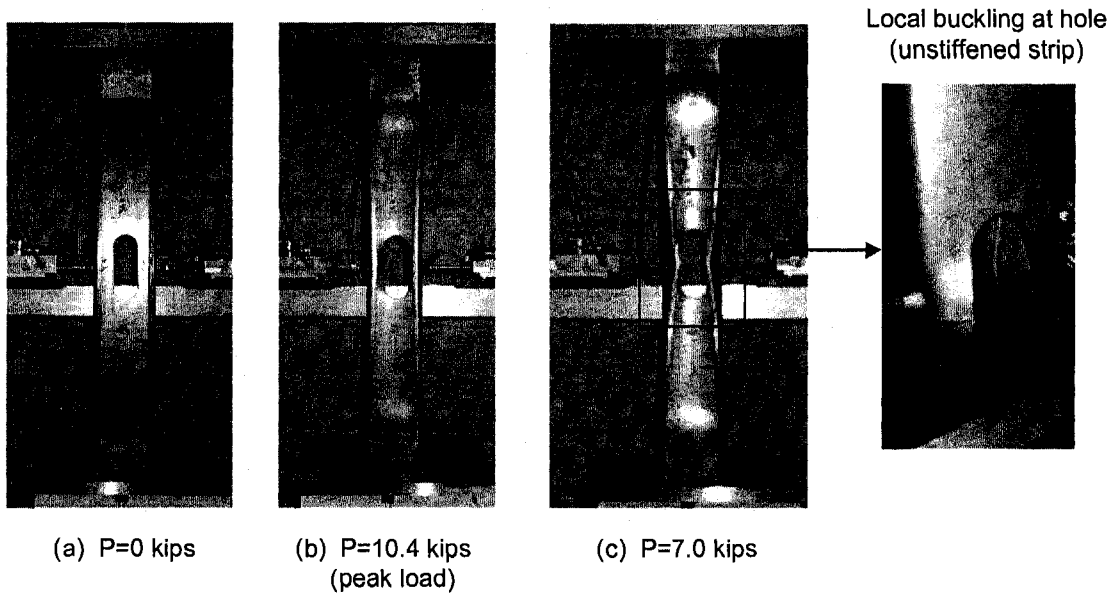


Figure 5.37 Load-displacement progression for short column specimen 362-2-24-H

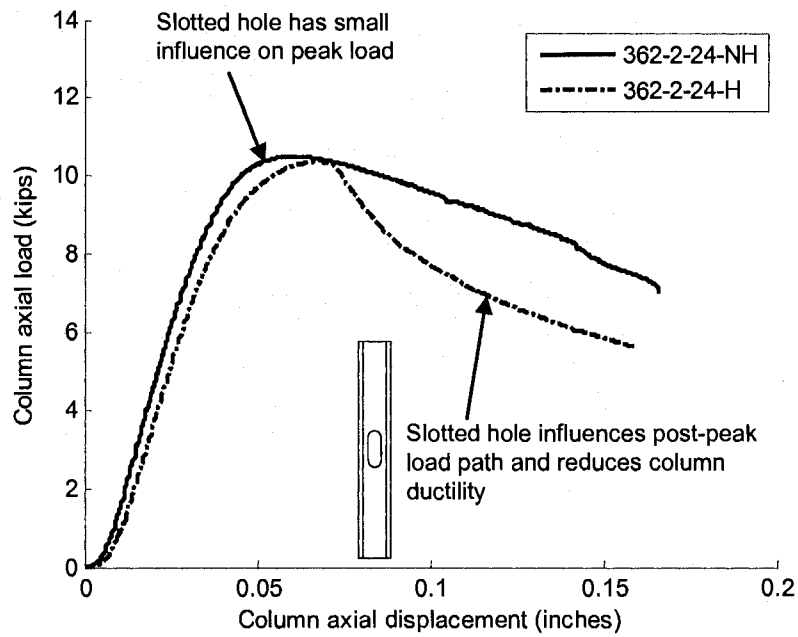


Figure 5.38 Load-displacement curve for a 362S162-33 short column with, without a slotted hole

Position transducers placed at the mid-height of the short column specimens capture the rate of lateral flange displacement associated with distortional buckling, δ_b , as shown in Figure 5.39. Figure 5.39 demonstrates that the initiation of web local buckling does not influence the axial stiffness of specimen 362-2-24-NH, but rather that a softening of the load-axial deformation curve coincides with the increased rate of lateral flange movement (distortional buckling). This observation suggests that the loss in axial stiffness associated with distortional buckling plays a larger role than web local buckling in the peak load response of the 362S162-33 short columns. The influence of the slotted hole on lateral flange displacement is provided in Figure 5.40, where the post-peak flange displacement rates are significantly higher for the 362S162-33 short column with holes. The results of Figure 5.40 indicate that holes potentially have a significant impact on the collapse mechanisms triggered from distortional buckling. Lateral flange displacement plots are provided for all specimens in Appendix F.

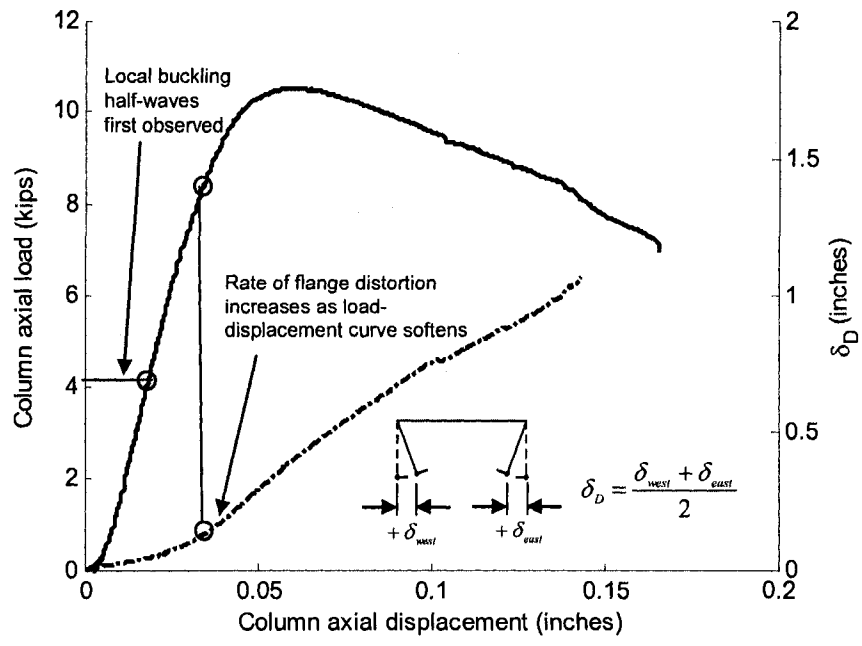


Figure 5.39 Comparison of load-deformation response and lateral flange displacements for specimen 362-2-24-NH

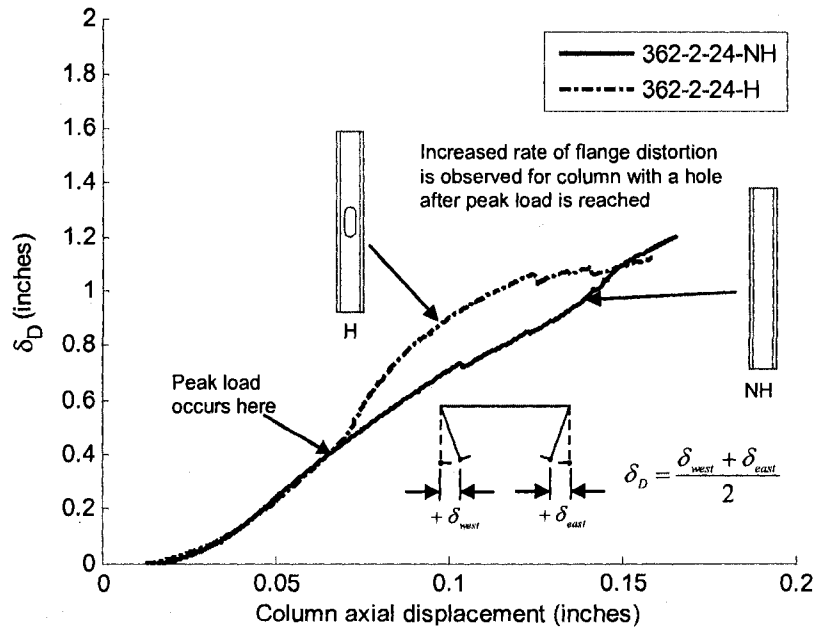


Figure 5.40 Influence of a slotted hole on 362S162-33 short column lateral flange displacement

Figure 5.41 and Figure 5.42 depict the deformation response of the 600S162-33 short columns with and without a slotted hole. In both cases, local buckling at the loaded ends combines with one distortional half-wave along the column length. The distortional buckling pattern for these specimens is not wholly consistent with the elastic buckling predictions of Figure 5.33a, which shows two distortional half-waves; however, specimens 600-2-24-H and 600-3-24-H did buckle in two half-waves, see Appendix F for pictures. These results suggest that geometric imperfections also have a role to play in the details of the buckling mode initiated in the loaded response. The deformation response of the member with and without the hole is similar through the test progression, suggesting that the hole has a small influence on compressive strength and post-peak ductility for the hole width to web width ratios considered here. Figure 5.43 confirms that the slotted hole has a minimal effect on the post-peak load response of the column.

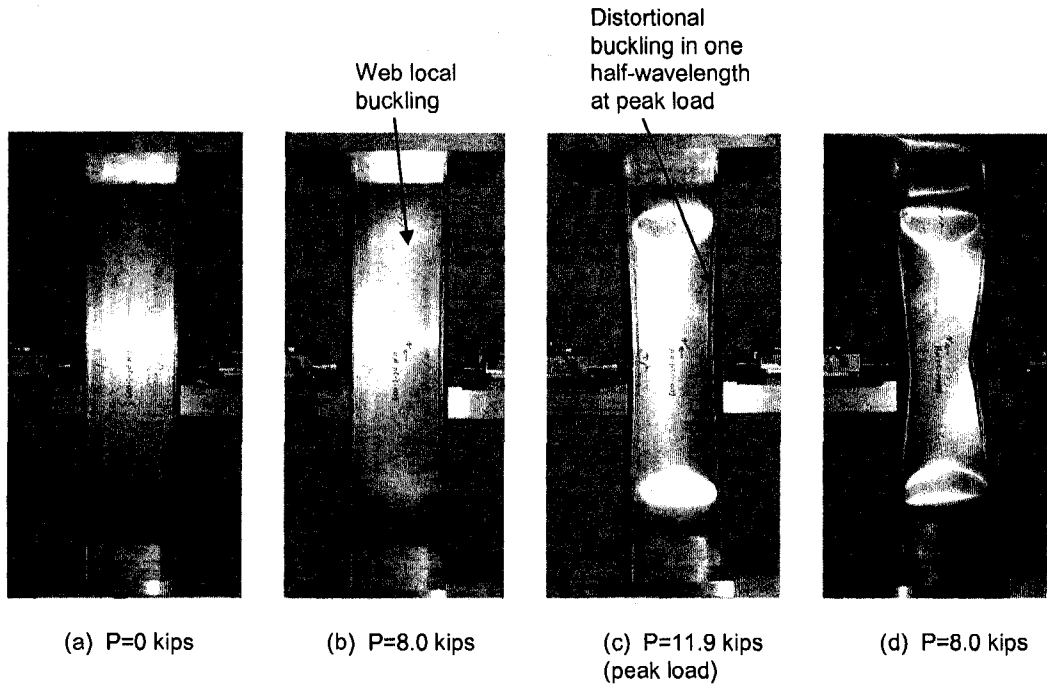


Figure 5.41 Load-displacement progression for short column specimen 600-1-24-NH

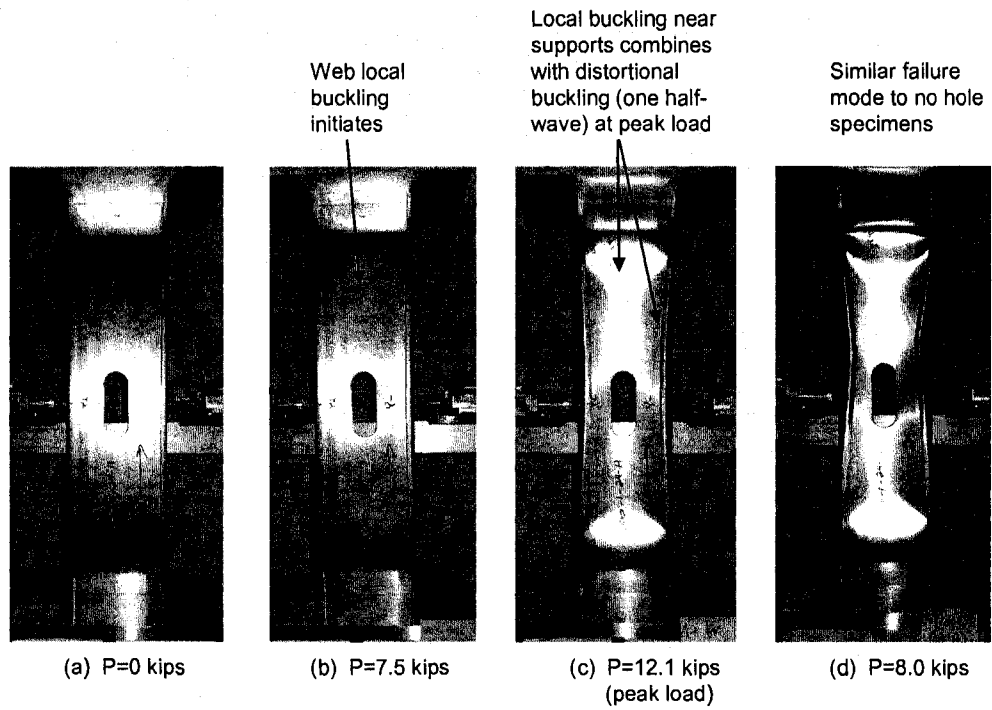


Figure 5.42 Load-displacement progression for short column specimen 600-1-24-H

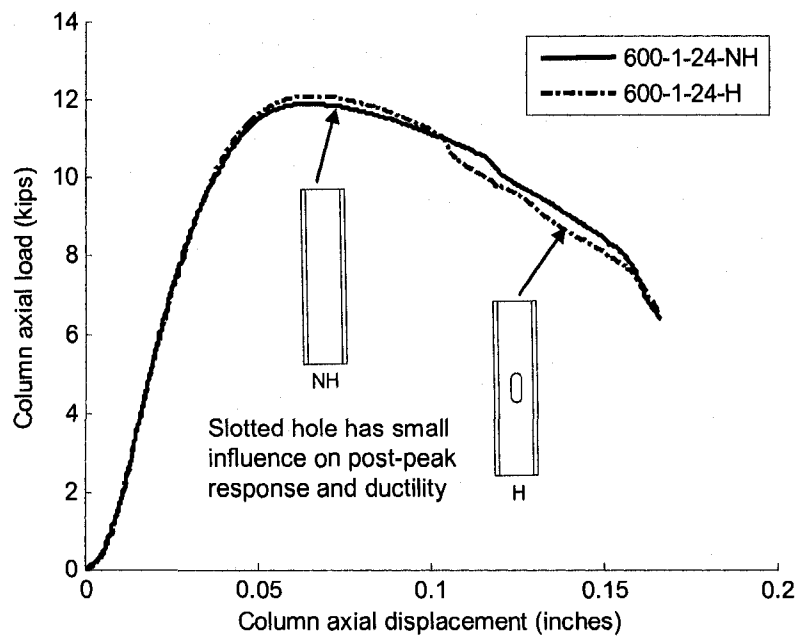


Figure 5.43 Comparison of load-displacement response for short 600S162-33 column specimens with and without holes

5.4.2.2 Intermediate length columns

Figure 5.44 and Figure 5.45 summarize the deformation response of the 362S162-33 intermediate length columns with and without holes. In both cases, local web buckling is first observed at approximately $0.45P_{test}$ which is lower than, but the same order of magnitude as, the calculated local critical elastic buckling load P_{cr} . Note in Figure 5.45 that the local buckling half-waves are dampened in the vicinity of the holes, similar to the elastic buckling prediction of Figure 5.32b. Further, the observed local buckling waves are at half-wavelengths consistent with the local buckling mode in Figure 5.32b, not those shown interacting with distortional buckling. (This observation supports the idea that the fundamental elastic buckling modes L, D, and G are representative of the physical behavior of the column and that the mixed modes observed in an eigenbuckling analysis only exist numerically.) Three distortional buckling half-waves become well-

formed at approximately $0.70P_{test}$, overcoming the local half-waves in the web except at the mid-height of the column. This distortional buckling pattern is consistent with the elastic buckling prediction in Figure 5.32b. Figure 5.46 demonstrates that the presence of slotted holes has only a minimal influence on load-axial displacement response.

All of the 362S162-33 intermediate length columns failed soon after the peak load with a sudden loss in load-carrying capacity caused by global flexural-torsional buckling. Yielding of the column flanges reduces the torsional stiffness of the section, and the friction end conditions could not restrain the twisting of the column. The twisting of specimen 362-3-48-NH is quantified in Figure 5.47 as the difference between the west and east mid-height flange displacements, δ_t , captured by the position transducers. The lateral displacement of the flange tips due to distortional buckling (δ_b), also shown in Figure 5.47, is separated from the twisting effect by averaging the west and east mid-height flange displacements. Figure 5.47 shows that the cross-section is both 'opening' and 'twisting', but it is the abrupt increase in δ_t occurring well past peak load that leads to the collapse of the member in the test.

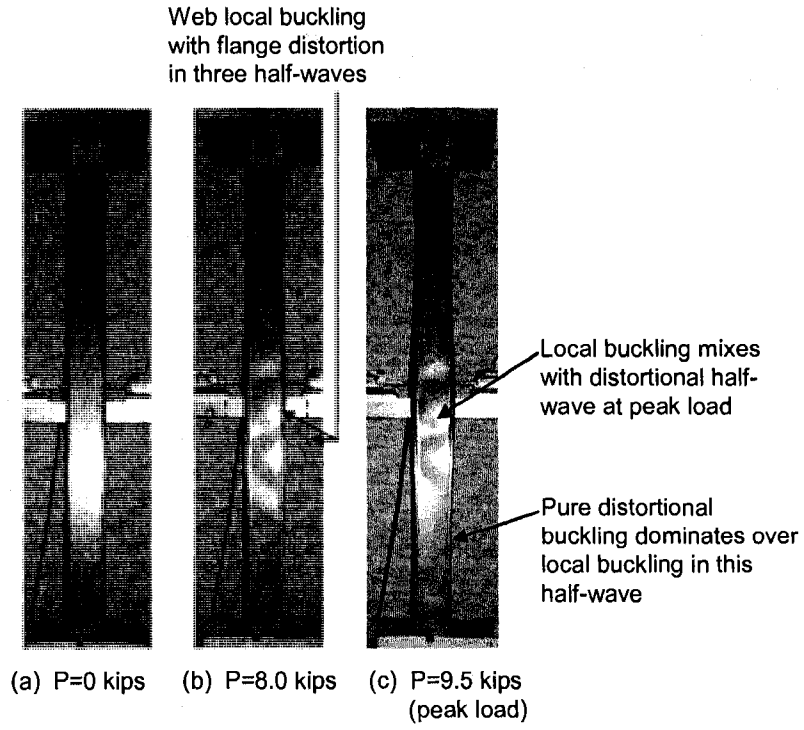


Figure 5.44 Load-displacement progression, intermediate length column specimen 362-3-48-NH

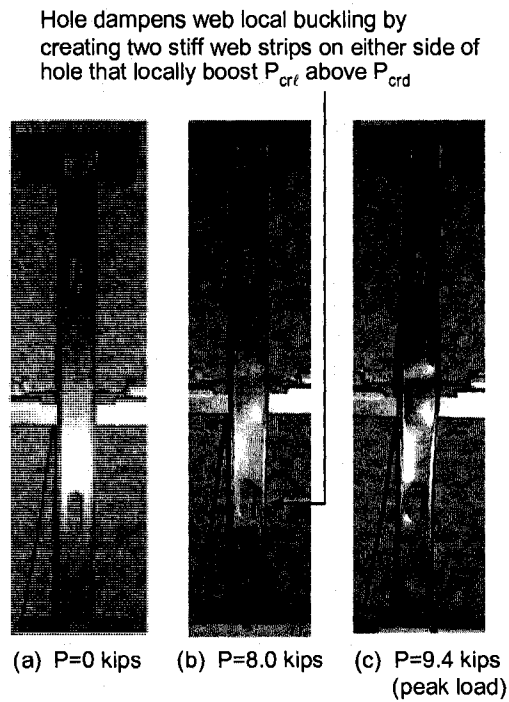


Figure 5.45 Load-displacement progression for intermediate length column specimen 362-3-48-H

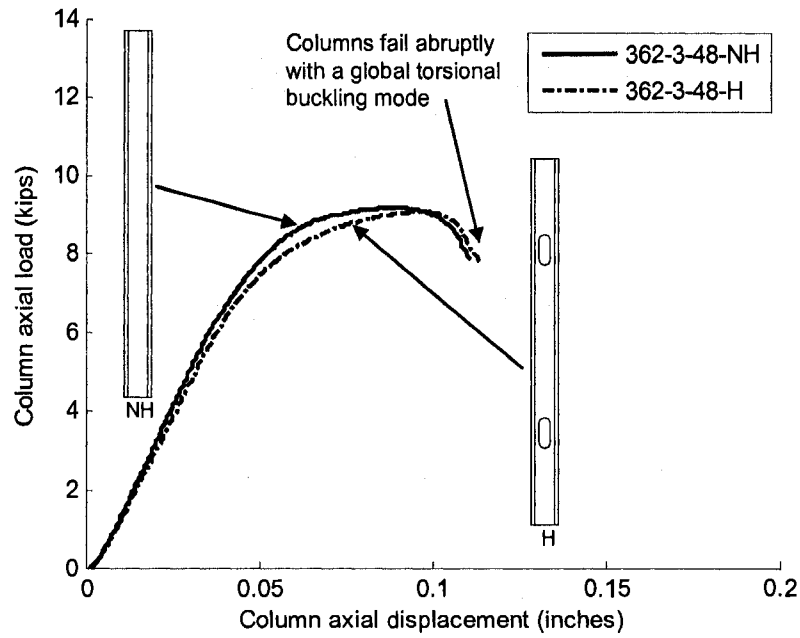


Figure 5.46 Load-displacement curve, 362S162-33 intermediate column with and without a hole

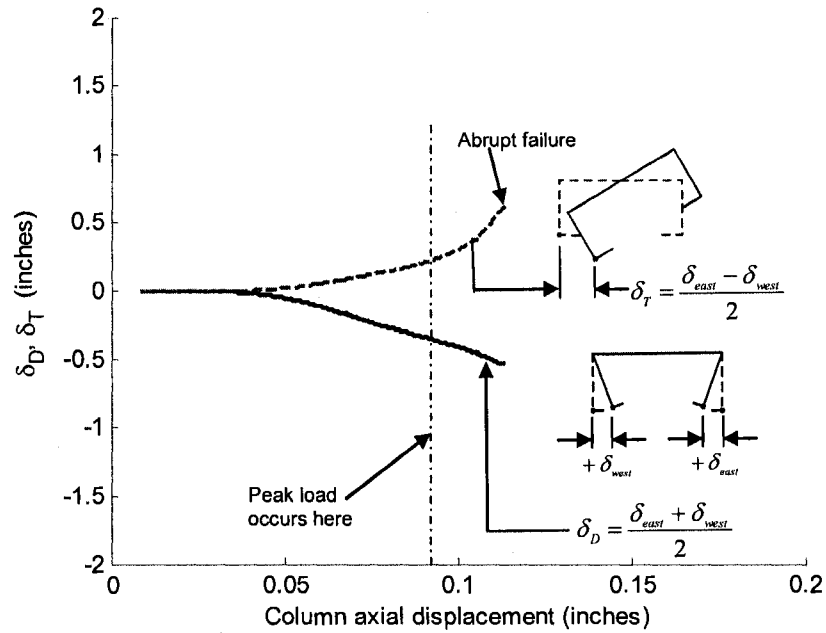


Figure 5.47 362S162-33 long column mid-height flange displacements show the global torsional failure mode

The load-displacement response for the intermediate length 600S162-33 columns with and without slotted holes is depicted in Figure 5.48 and Figure 5.49. Local buckling is observed at approximately $0.45P_{test}$ for both sections. The holes do not restrict the local buckling half-waves as was the case in the 362S162-33 intermediate length columns. This local buckling behavior is consistent with that observed in the elastic buckling analysis, see Figure 5.33b. Three distortional half-waves form as the columns (all 3 of the 600S162-33 intermediate length specimens) approach peak load. Two loud sounds resonate from the columns near peak load as the local web buckling half-waves at the two column ends abruptly snap into one distortional half-wave per end. The change from local-dominated to distortional-dominated web buckling is reflected as two drops in the load-displacement response near peak load for the 600S162-33 column without holes, as shown in Figure 5.50. The 600S162-33 column with slotted holes is not affected by this abrupt mode switching, as it maintains web local buckling well beyond peak load. The observations suggest that in this case the holes are beneficial because they maintain the local buckling half-waves through peak load, allowing the column to rely more on the post-peak strength provided by the buckled web. This mode switching is a difficult challenge for numerical models and these results, repeated in 3 tests, provides an important and challenging experimental benchmark for the numerical modeling of these members Section 7.2.

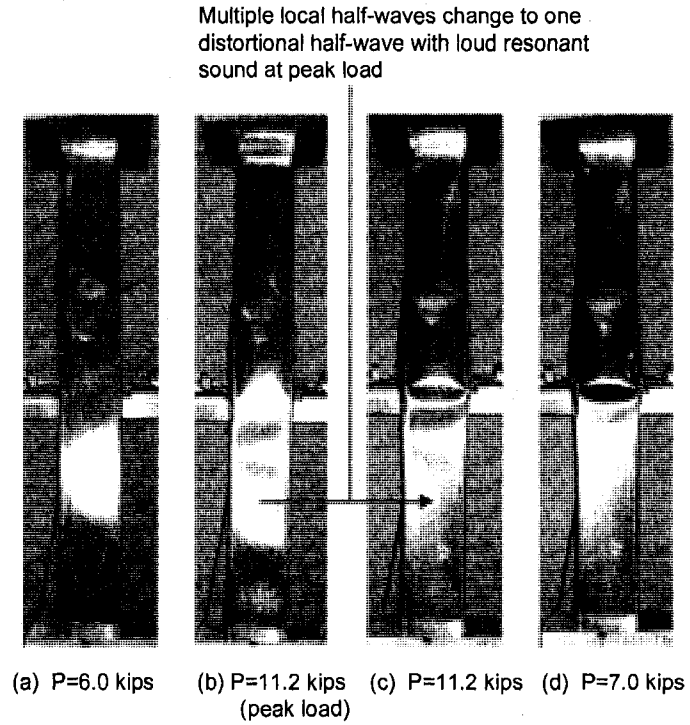


Figure 5.48 Load-displacement progression, intermediate length column specimen 600-1-48-NH

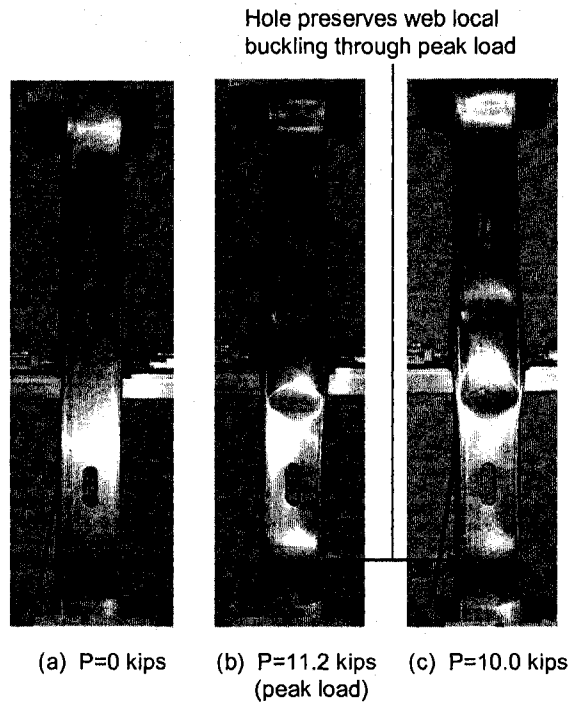


Figure 5.49 Load-displacement progression, intermediate length column specimen 600-1-48-NH

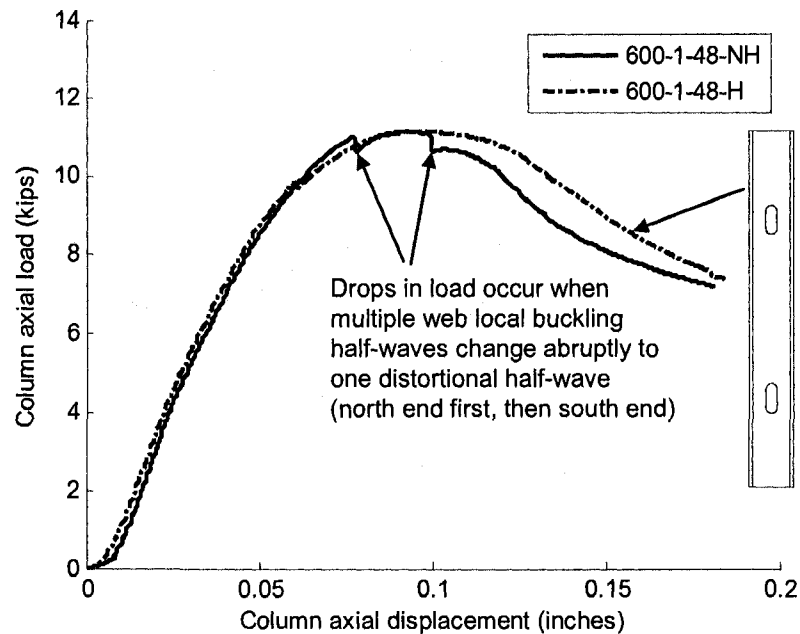


Figure 5.50 Load-displacement comparison of intermediate length 600S162-33 specimens with and without holes

5.4.3 Discussion of hole influence on elastic buckling and tested response

Both local and distortional elastic buckling were observed in the tested response of the specimens and contributed in different ways to the failure modes of the columns. Local buckling initiated plastic folding in the web at peak load, and distortional buckling was reflected as either opening ($-\delta_b$) or closing ($+\delta_b$) of the cross-section and yielding of the flanges and lip stiffeners. All three of the short 362S162-33 columns with holes exhibited a 'closed' distortional buckling failure ($+\delta_b$), where the presence of the slotted hole concentrated the plastic deformation in the flanges and lips adjacent to the hole. This result was different from the short 362S162-33 columns without holes where mixed local-distortional failures were observed. The slotted holes also changed the

buckling influence at peak load in the intermediate length 600S162-33 specimens, where the holes prevented local web buckling from switching to distortional buckling in all three specimen tests. The deformation at peak load for the intermediate length 362S162-33 and short 600S162-33 specimens was less sensitive to the presence of slotted holes, exhibiting mixed local-distortional failure modes consistent with DSM predictions (L and D of similar magnitudes) as discussed in Section 5.3.2.3.

The visual observations in this study highlight the complex relationship between elastic buckling and column failure and the sensitivity of their interaction to the choice of cross-section and column length. In the cases of the short 362S162-33 and intermediate length 600S162-33 specimens, it is clearly demonstrated that holes can influence column deformation and ductility by changing how elastic buckling modes, local and distortional in this case, affect the axial stiffness and plastic deformation of the column under load. This data is important in the context of the Direct Strength Method, especially for this current effort to extend DSM to members with holes, since elastic buckling is used to predict the failure mode (local, distortional, or global) and ultimate strength.

5.4.4 Discussion of friction-bearing boundary conditions

The friction-bearing end conditions used in this testing are advantageous because specimen alignment and preparation can be performed without welding or the use of grout or hydrostone. The specimens were aligned by hand in the testing machine without special equipment. However, preparing the specimen ends with a milling

machine can be time consuming. Further, small deviations in flatness may significantly impact the tested results and failure modes; real care must be taken in the specimen end preparation. Finally, lack of a positive connection between specimen and platen makes it difficult to exactly know the boundary conditions.

In this study, friction between the column ends and the platens prevented a change in shape of the cross-section up to peak load in all specimens, but slipping of the cross-section was observed after peak load. This slipping was signaled by loud metal-on-metal “popping” sounds associated with observable changes in the cross-section ($-\delta_b$ of the flanges, see Figure 5.47 for definition) at the column ends. Also, uplift warping deformations like those shown in Figure 5.51 occurred in the post-peak range for the short 600S162-33 columns experiencing distortional type failures. Distortional buckling modes are anticipated to be sensitive to this uplift since they are highly sensitive to warping deformations. The intermediate length 362S162-33 columns experienced a sudden global flexural-torsional failure shortly after reaching peak load as the twisting of the columns overcame the friction between the column ends and the platens. The friction-bearing end conditions did not allow a detailed study of the global flexural-torsional post-peak response for the intermediate length 362S162-33 columns and likely decreased their ultimate strengths.

Overall, for short and intermediate length column testing focused on local and distortional buckling modes, the advantages of the simple friction-bearing boundary conditions outweighed the disadvantages. Proper care must be taken to insure the ends are milled flat and the platens are level and parallel. For longer column tests, where

large torsional rotations must be restrained, the bearing conditions employed here are not recommended for use.

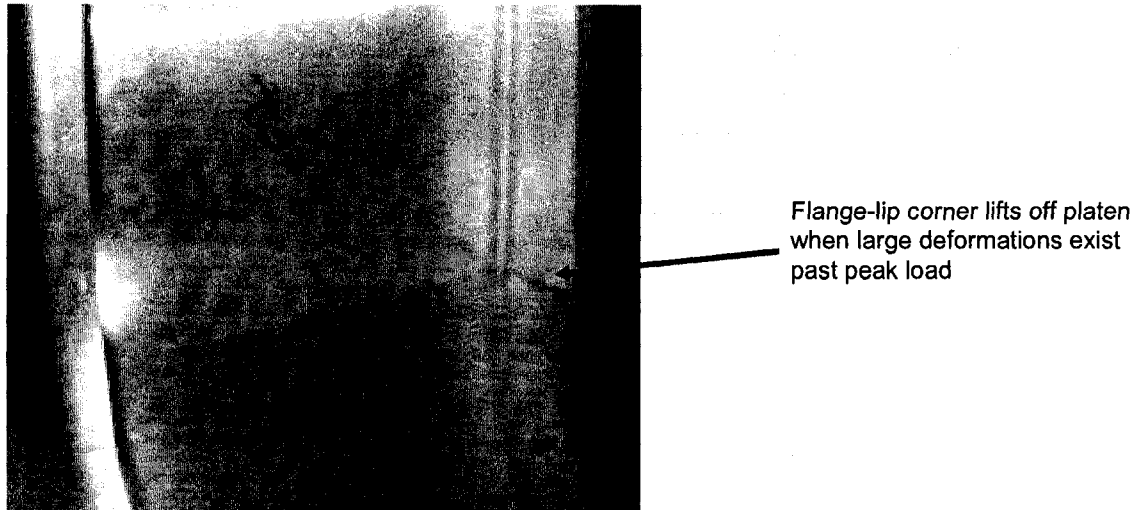


Figure 5.51 Short 600S162-33 column flange-lip corner lifts off platen during post-peak portion of test

Chapter 6

Predicting residual stresses and plastic strains in cold-formed steel members

Thin cold-formed steel members begin as thick, molten, hot steel slabs. Each slab is typically hot-rolled, cold-reduced, and annealed before coiling and shipping the thin steel sheet to roll-forming producers (US Steel 1985). Once at a plant, the sheet is unwound through a production line and plastically folded to form the final shape of a structural member, as shown in Figure 6.1. This manufacturing process imparts residual stresses and plastic strains through the sheet thickness. These residual stresses and strains influence the load-displacement response and ultimate strength of cold-formed steel members.

In previous work a statistical approach was employed to draw conclusions on the magnitude and distribution of longitudinal residual stresses using a data set of surface strain measurements collected by researchers between 1975 and 1997 (Schafer and Peköz 1998). The measured surface strains are converted to residual stresses using Hooke's

Law and then distributed through the thickness as membrane (constant) and bending (linear variation) components. These residual stress distributions are a convenient way to express the measured residual surface strains, and are convenient as well for use in nonlinear finite element analyses, but they are not necessarily consistent with the underlying mechanics.

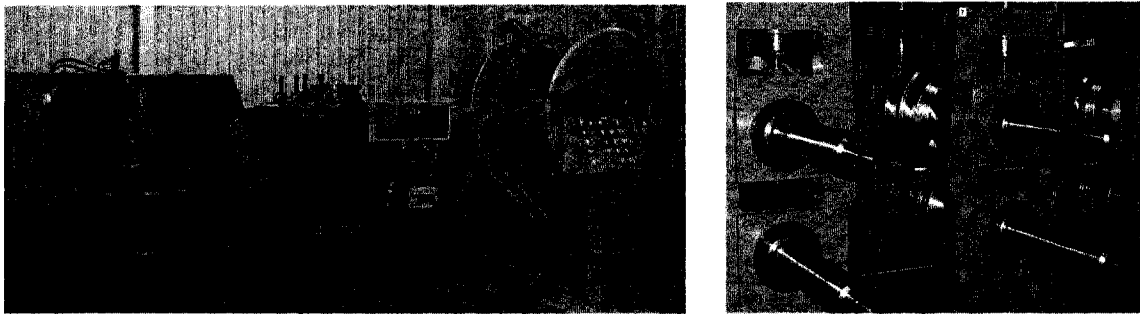


Figure 6.1 Cold-formed steel roll-forming: (left) Sheet coil enters roll-forming line, (right) steel sheet is cold-formed into C-shape cross-section (photos courtesy of Bradbury Group).

Plastic bending, followed by elastic springback, creates a nonlinear through-thickness residual stress distribution, in the direction of bending, as shown in Figure 6.2 (Shanley 1957). The presence of nonlinear residual stress distributions in cold-formed steel members has been confirmed in experiments (Key and Hancock 1993) and in nonlinear finite element modeling of press-braking steel sheets (Quach et al. 2006). A closed-form analytical prediction method for residual stresses and equivalent plastic strains from coiling, uncoiling, and mechanical flattening of sheet steel has also been proposed (Quach et al. 2004). The same plastic bending that creates these residual stresses also initiates the cold-work of forming effect, where plastic strains increase the apparent yield stress in the steel sheet (and ultimate strength in some cases) (Yu 2000).

Together, these residual stresses and plastic strains comprise the initial material state of a cold-formed steel member.

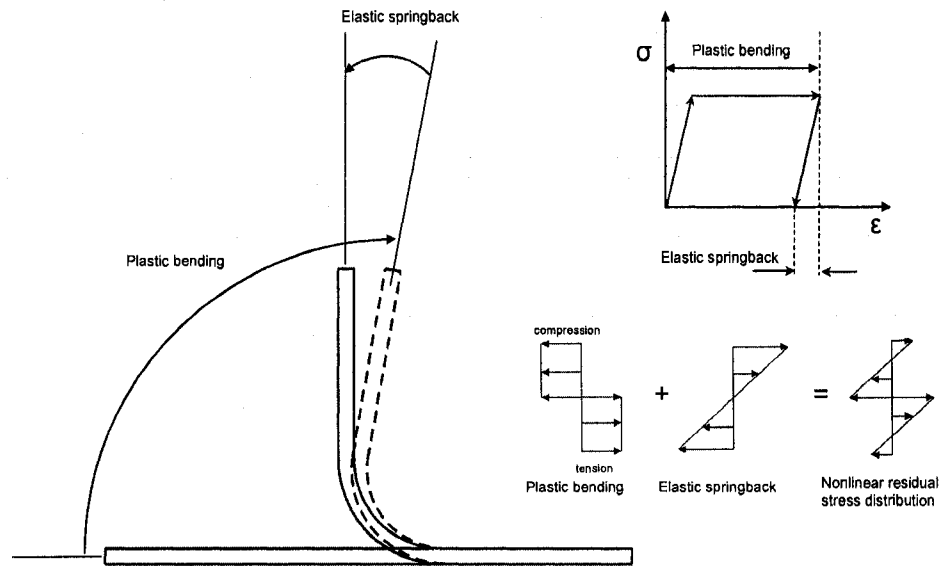


Figure 6.2 Forming a bend: plastic bending and elastic springback of thin sheets results in a nonlinear through-thickness residual stress distribution.

A general method for predicting the manufacturing residual stresses and plastic strains in cold-formed steel members is proposed here. The procedure is founded on common industry manufacturing practices and basic physical assumptions. The primary motivation for the development of this method is to define the initial state of a cold-formed steel member for use in a subsequent nonlinear finite element analysis. The derivation of the prediction method is provided for each manufacturing step, and the predictions are evaluated with measured residual strains from existing experiments. The end result of the method is intended to be accessible to a wide audience including manufacturers, design engineers, and the academic community. This method also has the potential to compliment and improve Chapter A7.1.2 of the existing Specification (AISI-S100 2007), which currently allows for an increase in member strength from the

cold-work of forming effect at cross-section corners, but does not directly account for the influence of the nonlinear through-thickness corner residual stresses or the influence of plastic strains and residual stresses from coiling, uncoiling, and flattening of the sheet steel.

6.1 Stress-strain coordinate system and notation

The stress-strain coordinate system and geometric notation used in the forthcoming derivations are defined in Figure 6.3. The x -axis is referred to as the transverse direction and the z -axis as the longitudinal direction of a structural member. Cross-section elements are referred to as either "corners" or "flats". The sign convention for stress and strain is positive for tension and negative for compression.

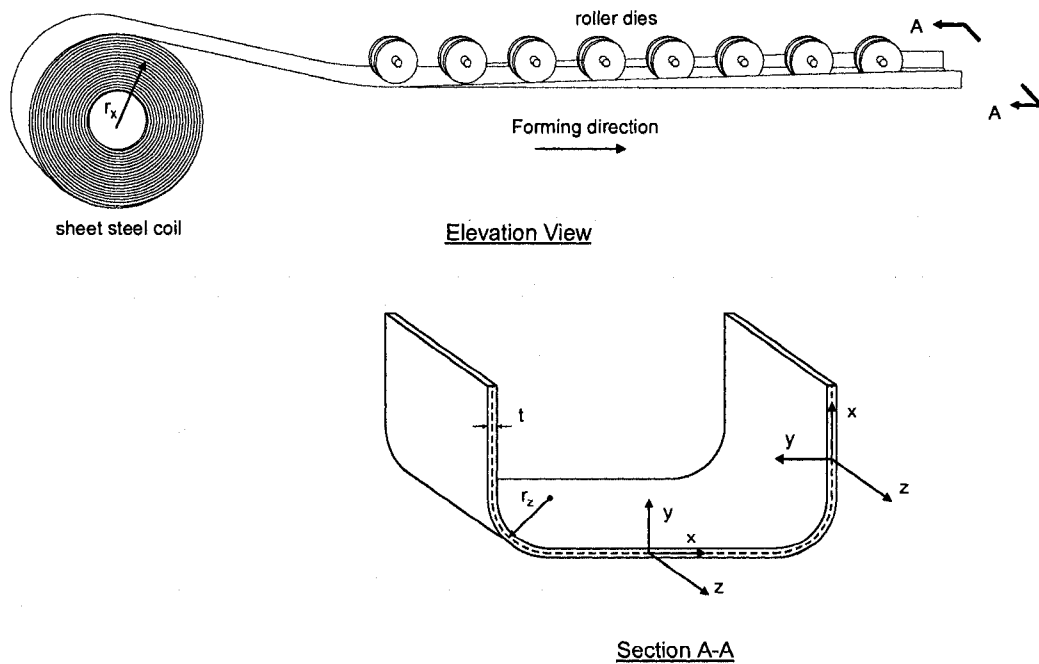


Figure 6.3 Stress-strain coordinate system as related to the coiling and cold-forming processes.

6.2 Prediction method assumptions

The following assumptions are employed to develop this prediction method:

- a. Plane sections remain plane before and after cold-forming of the sheet steel. This assumption permits the use of beam mechanics to derive prediction equations.

- b. The sheet thickness t remains constant before and after cold-forming of the sheet steel. A constant sheet thickness is expected after cold-bending if the bending is performed without applied tension (Hill 1950). Cross-section measurements demonstrate modest sheet thinning at the corners, where t in the corners is typically five percent less than in the flange and web (Dat 1980). This thinning is ignored here to simplify the derivations, although a reduced thickness based on the plastic strain calculations in Section 6.4 could be used if a higher level of accuracy is required.

- c. The sheet neutral axis remains constant before and after cross-section cold-forming. Theoretical models used in metal forming theory do predict a small shift in the through-thickness neutral axis towards the inside of the corner as the sheet plastifies (Hill 1950). This shift is calculated as six percent of the sheet thickness, t , when assuming a centerline corner radius, r_c , of $2.5t$. A neutral axis shift of similar magnitude has been observed in the nonlinear finite element model results for thin press-braked steel sheets (Quach et al. 2006). This small shift is ignored here to simplify the derivations.

d. The steel stress-strain curve is assumed as elastic-perfectly plastic when calculating residual stresses. More detailed stress-strain models that include hardening are obviously possible, but a basic model is chosen to simplify the derivations. The implication of this assumption is that the residual stresses may be underestimated, especially in corner regions where the sheet has yielded completely through the thickness.

e. Plane strain behavior is assumed to exist during coiling, uncoiling, and flattening ($\epsilon_x=0$) and during cross-section cold-forming ($\epsilon_z=0$).

f. The steel sheet is fed from the top of the coil into the roll-forming bed as shown in Figure 6.4a. This assumption is consistent with measured bending residual stress data (see Section 6.6) and manufacturing setups suggested by roll-forming equipment suppliers (Figure 6.1). The author did observe the alternative setup in Figure 6.4b (sheet steel unrolling from the bottom of the coil) at a roll-forming plant, suggesting that the direction of uncoiling is a source of variability in measured residual stress data.

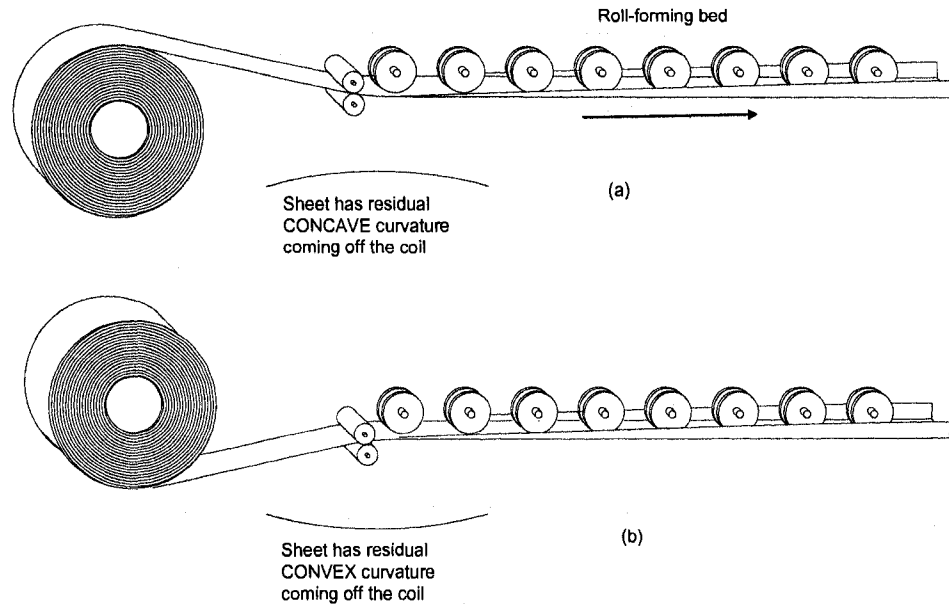


Figure 6.4 Roll-forming setup with sheet coil fed from the (a) top of the coil and (b) bottom of coil. The orientation of the coil with reference to the roll-forming bed influences the direction of the coiling residual stresses.

g. Membrane residual stresses are zero. Membrane residual stresses have been measured by several researchers (Ingvarsson 1975; Dat 1980; Weng and Peköz 1990; De Batista and Rodrigues 1992; Kwon 1992; Bernard 1993; Key and Hancock 1993), although the magnitudes are small relative to bending residual stresses (see Table 6.1). Membrane residual stresses are experimentally determined by averaging the measured surface strains on the two faces of a thin steel sheet. Given the variability inherent in these measurements it is difficult to know if the resulting membrane stresses (strains) are real or simply unavoidable experimental error.

6.3 Derivation of the residual stress prediction method

The prediction method proposed here assumes that two manufacturing processes contribute to the through-thickness residual stresses in cold-formed steel members: (1) sheet coiling, uncoiling, and flattening, and (2) cross-section roll-forming. Algebraic equations for predicting the through-thickness residual stress and effective plastic strains in corners and flats are derived here and then summarized in flowcharts in Figure 6.13 and Figure 6.17.

6.3.1 Residual stresses from sheet coiling, uncoiling, and flattening

Coiling the sheet steel after annealing and galvanizing, but prior to shipment, may yield the steel if the virgin yield strain, ϵ_{yield} , is exceeded. If plastic deformation does occur, a residual curvature will exist in the sheet as it is uncoiled. This residual curvature is locked into a structural member resulting in longitudinal residual stresses as the sheet is flattened by the roll-formers. This process of coiling, uncoiling with residual curvature, and flattening is described in Figure 6.5.

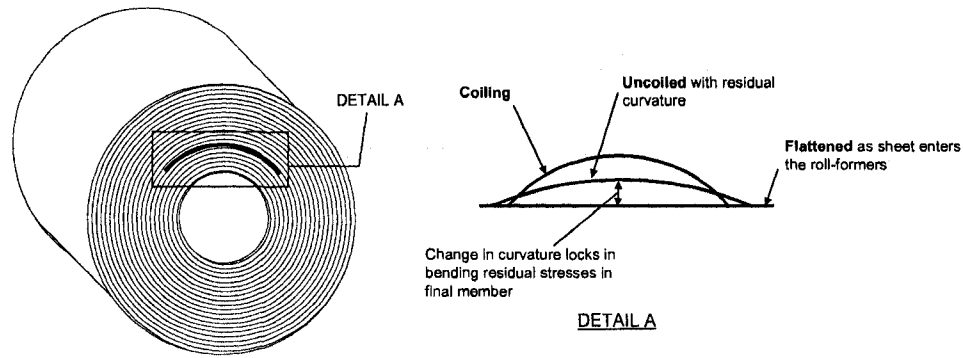


Figure 6.5 Coiling of the steel sheet may result in residual curvature which results in bending residual stresses as the sheet is flattened.

6.3.1.1 Coiling

The through-thickness strain induced from coiling is related to the radial location of the sheet in the coil r_x , with the well known relationship from beam mechanics:

$$\frac{\epsilon_z}{y} = \frac{1}{r_x} \quad (6.1)$$

ϵ_z is the engineering strain through the thickness y in the coiling (longitudinal) direction z . y varies from $-t/2$ to $t/2$, where t is the sheet thickness. The radius associated with the elastic-plastic threshold initiating through-thickness yielding from coiling, r_{ep} , is derived by substituting $\epsilon_z = \epsilon_{yield}$ and $y = t/2$ (outer fiber strain) into Eq. (6.1):

$$r_{ep} = \frac{t}{2\epsilon_{yield}} \quad (6.2)$$

When the coil radius r_x is greater than r_{ep} the sheet steel experiences only elastic deformation on the coil. For sheet steel rolled to a coil radius r_x less than r_{ep} , through-thickness yielding will occur as shown in Figure 6.6.

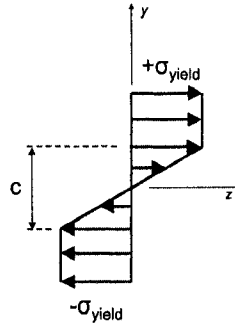


Figure 6.6 Longitudinal residual stress distribution from coiling.

When $r_x < r_{ep}$, the depth of the elastic core c is defined as:

$$c = 2r_x \varepsilon_{yield} \leq t. \quad (6.3)$$

6.3.1.2 Uncoiling

As the yielded sheet is uncoiled in preparation for the roll-forming line, the sheet steel springs back elastically resulting in a change in the through-thickness stress. This stress distribution is determined by first calculating the plastic coiling moment

$$M_x^{coil} = \sigma_{yield} \left[\left(\frac{t}{2} \right)^2 - \frac{1}{3} (r_x \varepsilon_{yield})^2 \right], \quad (6.4)$$

and then applying an opposing moment elastically to simulate the removal of the imposed radial displacement

$$\sigma_z^{uncoil} = \frac{-12M_x^{coil} y}{t^3}. \quad (6.5)$$

6.3.1.3 Flattening

After the sheet has been unrolled, a permanent radius of curvature will still exist if r_x was less than r_{ep} on the coil. This permanent radius is

$$r_x^{uncoil} = \frac{1}{\frac{1}{r_x} - \frac{M_x^{coil}}{EI}} \quad (6.6)$$

Steel sheet with permanent curvature from coiling is pressed flat as the sheet enters the roll-forming line. The longitudinal stresses resulting from flattening the sheet are simply

$$\sigma_z^{flatten} = -E \frac{y}{r_x^{uncoil}} \quad (6.7)$$

6.3.1.4 Residual stress distribution

The total through-thickness longitudinal residual stress distribution due to coiling, uncoiling, and flattening is presented in Figure 6.7.

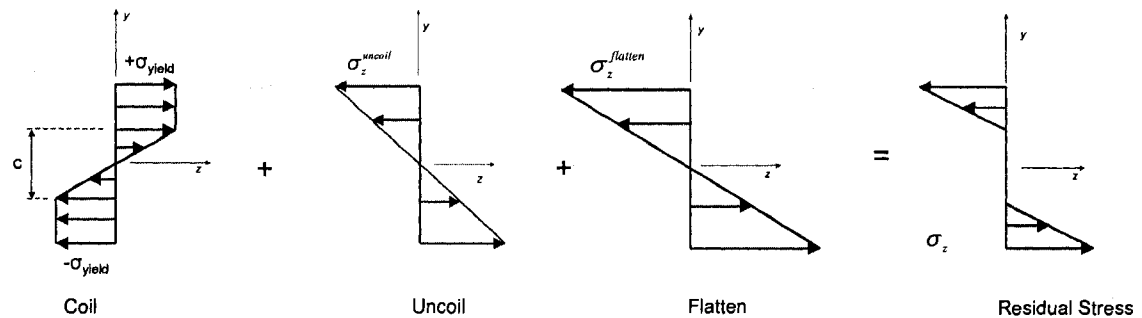


Figure 6.7 Predicted longitudinal residual stress distribution from coiling, uncoiling, and flattening of a steel sheet.

The resulting residual stress, σ_z , is self-equilibrating for axial force through the thickness but causes a residual longitudinal moment. Section 6.6 compares the stresses caused by this moment with surface strains (stresses) measured in experiments.

The longitudinal residual stresses also will create transverse stresses across the width of the coil, assuming plane strain conditions for an infinitely wide sheet.

Supporting the plane strain assumption is the observation that while the actual width of the sheet is finite, it remains several orders of magnitude greater than the sheet thickness. Under this assumption, and further assuming only elastic stresses, the transverse stresses are:

$$\sigma_x = \nu(\sigma_z^{coil} + \sigma_z^{uncoil} + \sigma_z^{flatten}). \quad (6.8)$$

Poisson's ratio, ν , is assumed here as 0.30 for steel deformed elastically. The through-thickness deformation from the uncoiling and flattening components will occur elastically, and the coiling component will be at least partially elastic through the thickness for the range of sheet thicknesses common in industry.

6.3.2 Residual stresses from cross-section roll-forming

A set of algebraic equations is derived here to predict the transverse and longitudinal residual stresses created by roll-forming a cross-section. Roll-forming residual stresses are cumulative with the coiling residual stresses derived in Section 6.3.1 and provide a complete prediction of the initial stress state of the member cross-section. The roll-forming residual stresses are assumed to exist only at the location of the formed corners, between the roller die reactions, as shown in Figure 6.8. Some yielding is expected to occur outside of the roller reactions as the stress distribution transitions from fully plastic to fully elastic; however, this transition area is not considered here to simplify the derivation.

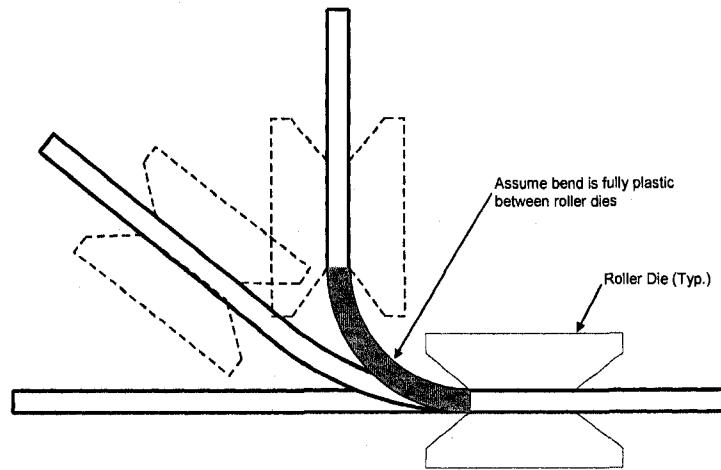


Figure 6.8 Cold-forming of a steel sheet.

The engineering strain in the steel sheet, ϵ_x , and the bend radius, r_z , are related for both small and large deformations with the strain-curvature relationship

$$\frac{1}{r_z} = \frac{\epsilon_x}{y} \quad (6.9)$$

This geometric relationship is valid for elastic and plastic bending of the steel sheet. For the small bend radii common in the cold-formed steel industry ($r_z = 2t$ to $8t$), the steel sheet yields through its thickness during the cold-forming process. The steel sheet will reach the fully plastic stress state shown in Figure 6.9 as the corner approaches its final manufactured radius.

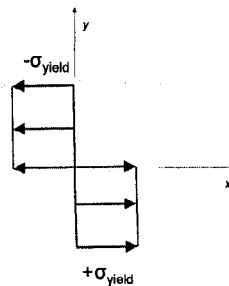


Figure 6.9 Fully plastic transverse stress state from cold-forming.

After the sheet becomes fully plastic through its thickness, the engineering strain continues to increase as the radius decreases. When the final bend radius is reached and the imposed radial displacement is removed, an elastic springback occurs that elastically unloads the corner (see Figure 6.2). The change in stress through the thickness from this elastic rebound is derived with the plastic moment force couple shown in Figure 6.10.

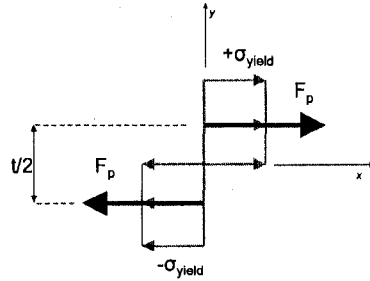


Figure 6.10 Force couple ($F_p \cdot t/2$) applied to simulate the elastic springback of the steel sheet after the imposed radial deformation is removed.

The plastic moment is calculated with the equation

$$M_z^{bend} = F_p \frac{t}{2} = \frac{\sigma_{yield} \cdot 1 \cdot t}{2} \frac{t}{2} = \frac{\sigma_{yield} t^2}{4}, \quad (6.10)$$

which is then applied elastically through the thickness to simulate the stress distribution from elastic rebound of the sheet steel:

$$\sigma_x^{rebound} = \frac{M_z^{bend} y}{I} = \frac{\left(\frac{\sigma_{yield} t^2}{4} \right) y}{\frac{1}{12} \cdot 1 \cdot t^3} = \frac{3\sigma_{yield} y}{t}. \quad (6.11)$$

The final transverse stress state is the summation of the fully plastic stress distribution through the thickness and the unloading stress from the elastic springback of the corner as shown in Figure 6.11, where σ_x is the transverse residual stress through

the thickness from the cold-forming of the corner. This stress is nonlinear through the thickness and is self-equilibrating, meaning that axial and bending sectional forces are absent in the x -direction after forming.

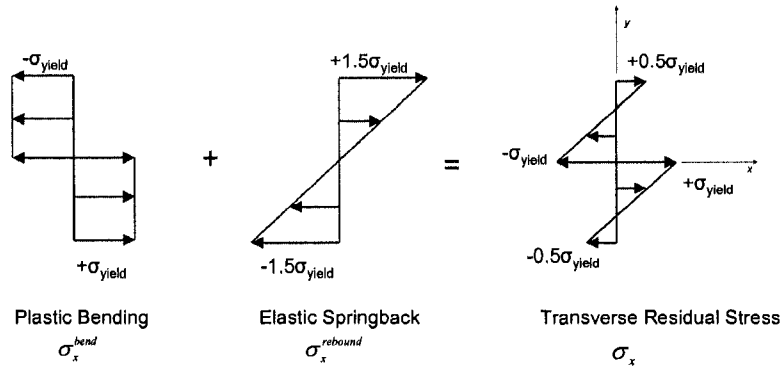


Figure 6.11 Cold-forming of a steel sheet occurs as plastic bending and elastic springback, resulting in a self-equilibrating transverse residual stress.

The transverse residual stresses will create stress in the longitudinal direction due to the assumed plane strain conditions (see Section 6.2):

$$\sigma_z = \nu \sigma_x. \quad (6.12)$$

The Poisson's ratio, ν , is assumed as 0.30 for steel deformed elastically and 0.50 for fully plastic deformation. The longitudinal residual stresses through the thickness, σ_z , are determined based on these assumptions as shown in Figure 6.12. Longitudinal residual stress, σ_z , is self-equilibrating for axial force through the thickness but causes a residual longitudinal moment. This moment is hypothesized to contribute to the observed longitudinal residual strains measured in experiments (refer to Section 6.6 for a comparison of this prediction to actual measurements).

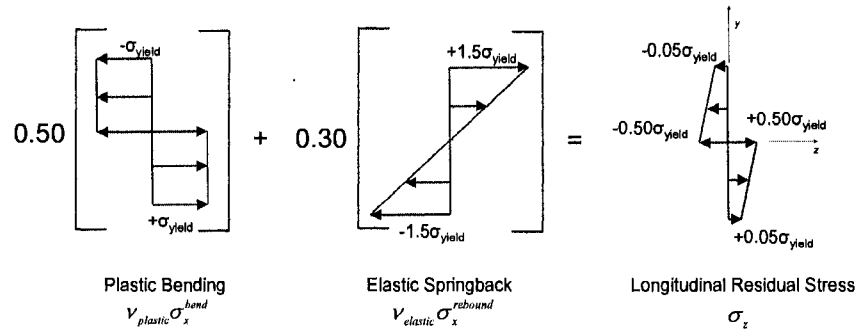


Figure 6.12 Plastic bending and elastic springback from cold-forming in the transverse direction result in longitudinal residual stresses because of the plane strain conditions.

A flowchart summarizing the proposed prediction method for residual stresses in roll-formed members is provided in Figure 6.13. Figure 6.13 explicitly demonstrates how coiling, uncoiling, flattening, and roll-forming contribute to the residual stresses locked into the cross-section during manufacturing.

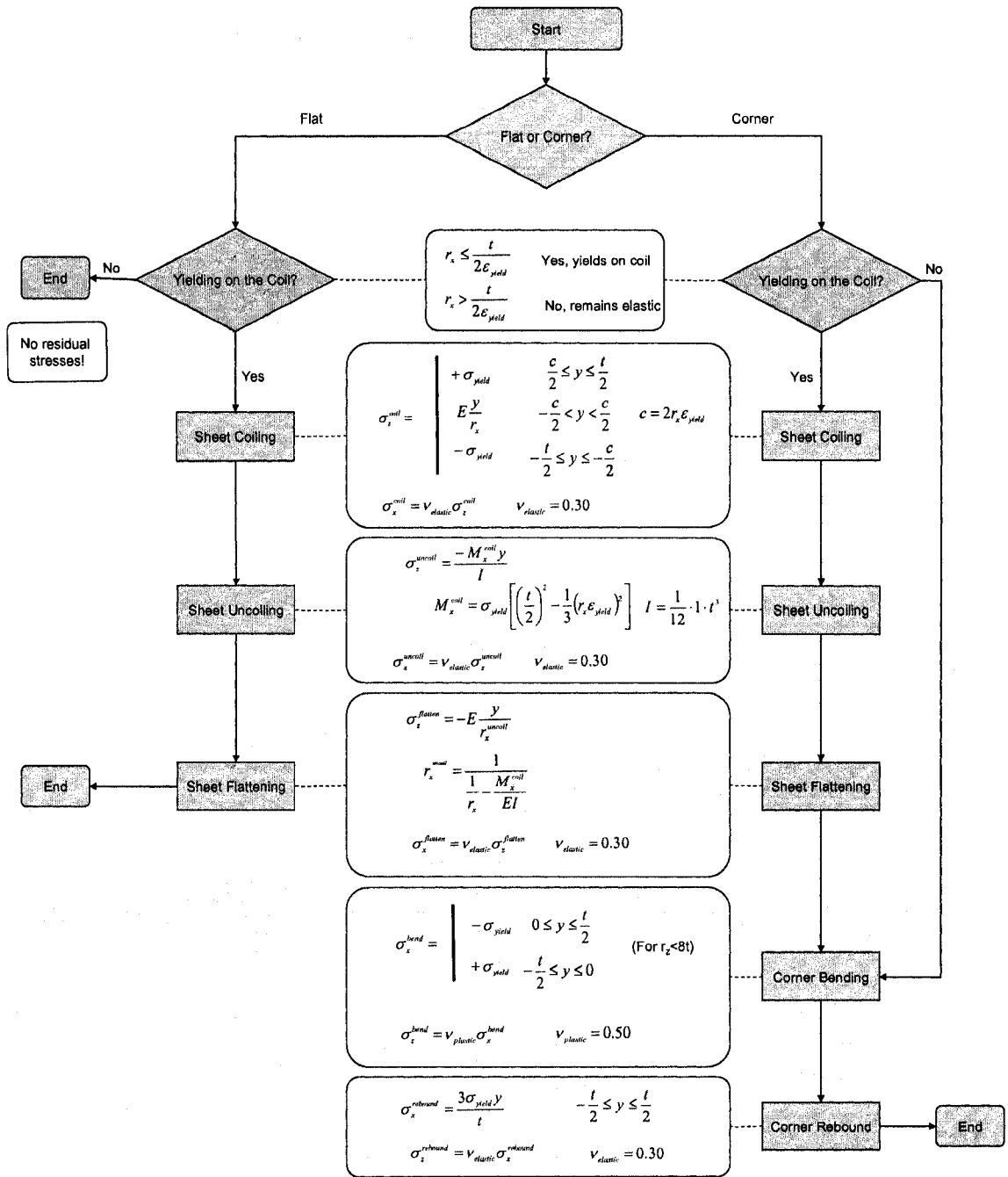


Figure 6.13 Flowchart summarizing the prediction method for residual stresses in roll-formed members.

6.4 Derivation of effective plastic strain prediction method

In the method proposed here, plastic strains occur from sheet coiling and cold-forming, and together with residual stresses describe the initial material state of the member. The general state of plastic strain at a point can be quantified by using the von Mises yield criterion extended to plastic deformations (Chen and Han 1988):

$$\varepsilon_p = \sqrt{\frac{2}{3}(\varepsilon_1^2 + \varepsilon_2^2 + \varepsilon_3^2)} \quad (6.13)$$

where ε_p is the effective plastic strain, and ε_1 , ε_2 and ε_3 are the principal strains. All of the strains are “true” strains, which may be calculated from the engineering strains via:

$$\varepsilon_1 = \ln(1 + \varepsilon_x), \varepsilon_2 = \ln(1 + \varepsilon_y), \varepsilon_3 = \ln(1 + \varepsilon_z), \quad (6.14)$$

where ε_x , ε_y , ε_z are in the Cartesian coordinate system (Figure 6.3) and x,y,z is coincident with the principal directions. True strains are employed instead of engineering strains to accommodate the large deformations from plastic bending. Also, from a practical standpoint, nonlinear FE codes such as ABAQUS (ABAQUS 2007a) require the engineer to provide true stress, true strain information (as large deformation theory is employed). The steel sheet is assumed to remain incompressible while experiencing plastic deformations, therefore when calculating ε_p

$$\varepsilon_1 + \varepsilon_2 + \varepsilon_3 = 0. \quad (6.15)$$

6.4.1 Effective plastic strain from sheet coiling

Engineering plastic strains, as shown in Figure 6.14, accumulate during the coiling of sheet steel if the coiling radius r_x is less than the elastic-plastic threshold r_{ep} .

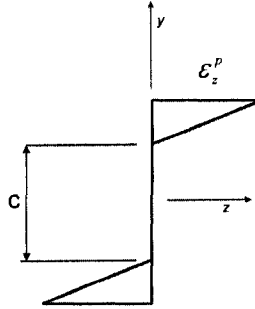


Figure 6.14 Plastic strain distribution from sheet coiling with a radius less than elastic-plastic threshold r_{ep} .

The engineering plastic strain distribution from coiling is:

$$\begin{aligned}\varepsilon_z^p &= \frac{y}{r_x} - \varepsilon_{yield}, \quad y \geq \frac{c}{2} \\ \varepsilon_z^p &= \left| \frac{y}{r_x} \right| - \varepsilon_{yield}, \quad y \leq -\frac{c}{2} \\ \varepsilon_z^p &= 0 \quad \text{otherwise,}\end{aligned}\tag{6.16}$$

where the elastic core, c , is defined in Eq. (6.3). Plane strain conditions result in $\varepsilon_1=0$, and $\varepsilon_2=-\varepsilon_3$ via the incompressibility assumption of Eq. (6.15). Further, the Cartesian coordinate system is coincident with the principal axes, resulting in the following true principal plastic strains:

$$\varepsilon_1 = 0, \quad \varepsilon_2 = -\ln(1 + \varepsilon_z^p), \quad \varepsilon_3 = \ln(1 + \varepsilon_z^p).\tag{6.17}$$

Substituting the principal strains into Eq. (6.13) and simplifying leads to the through-thickness effective plastic strain from coiling

$$\epsilon_p^{coiling} = \frac{2}{\sqrt{3}} \ln(1 + |\epsilon_z^p|). \quad (6.18)$$

This plastic strain distribution, depicted in Figure 6.15, will exist at all locations in the cross-section (corners and flats) when r_x is less than the elastic-plastic threshold r_{ep} .

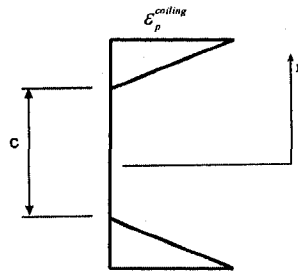


Figure 6.15 Effective plastic strain in a cold-formed steel member from sheet coiling when the radius r_x is less than the elastic-plastic threshold r_{ep} .

The plastic strain from coiling, $\epsilon_p^{coiling}$, will generally be much smaller in magnitude than the plastic strain from cross-section cold-forming, ϵ_p^{bend} , as discussed in following section.

6.4.2 Effective plastic strain from cross-section cold-forming

Large transverse plastic strains occur through the thickness of a thin steel sheet when the sheet is permanently bent. The engineering plastic strain distribution from cold-forming is described via

$$\epsilon_x^p = -\frac{y}{r_z}, \quad (6.19)$$

which assumes that the elastic core at the center of the sheet is infinitesimally small.

This assumption is consistent with the small bend radii common in industry (see 6.3.2).

Plane strain conditions and Eq. (6.15) result in $\varepsilon_3=0$, $\varepsilon_2=-\varepsilon_1$. Physically these conditions imply that the sheet will experience some thinning at the location of cold-forming (see Section 6.2), but the tendency to plastically shorten longitudinally will be resisted by the adjacent undeformed portion of the cross-section. As before, the Cartesian coordinate system is coincident with the principal axes, resulting in the following plastic principal strains:

$$\varepsilon_1 = \ln(1 + \varepsilon_x^p), \varepsilon_2 = -\ln(1 + \varepsilon_x^p), \varepsilon_3 = 0. \quad (6.20)$$

Substituting for the principal strains and simplifying, the effective plastic strain at a cold-formed corner is:

$$\varepsilon_p^{bend} = \frac{2}{\sqrt{3}} \ln(1 + |\varepsilon_x^p|) \quad (6.21)$$

This effective plastic strain distribution is shown in Figure 6.16. The distribution exists only at the cold-bent locations in a cross-section and should be added to the coiling plastic strain distribution in Figure 6.15.

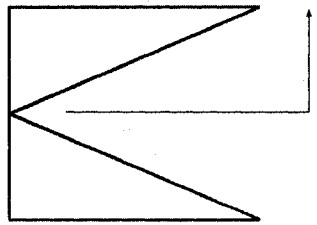


Figure 6.16 Effective von Mises true plastic strain at the location of cold-forming of a steel sheet.

A flowchart summarizing the prediction method for effective plastic strains in roll-formed members is provided in Figure 6.17.

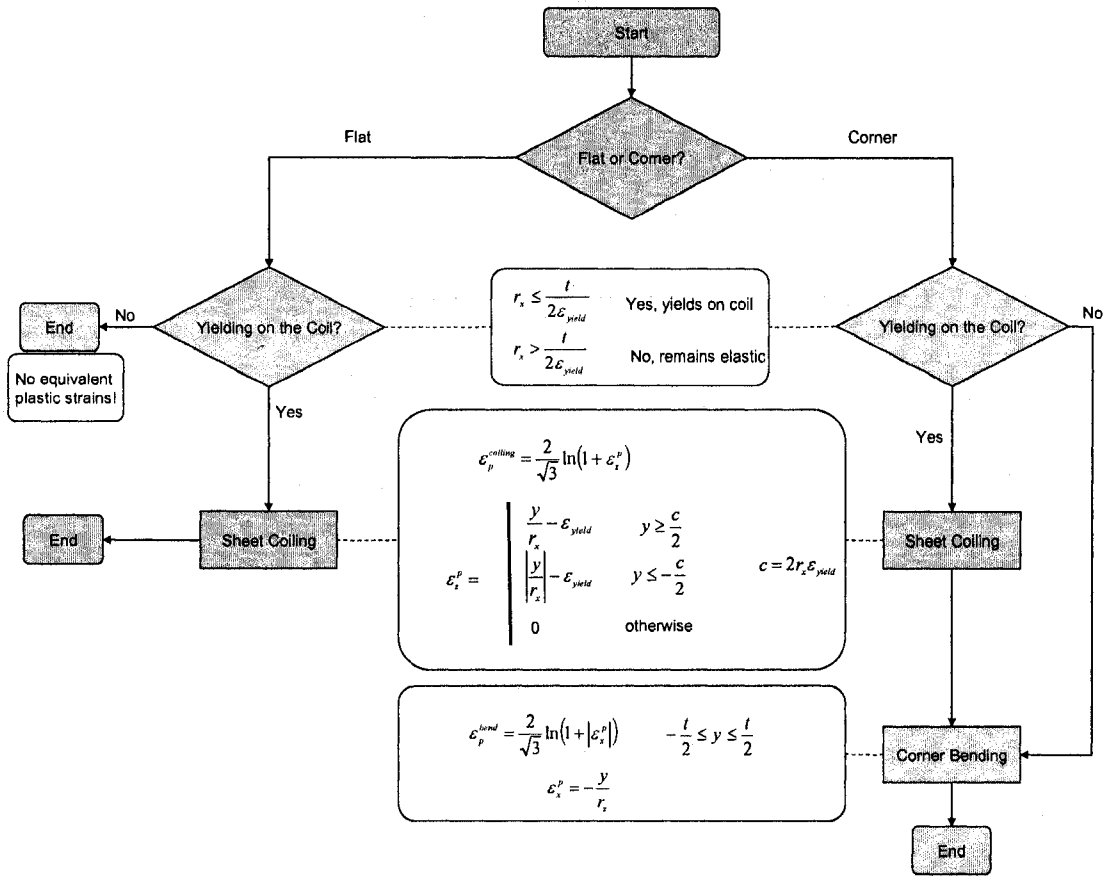


Figure 6.17 Flowchart summarizing the prediction method for effective plastic strains in roll-formed members

6.5 Employing the prediction method in practice: quantifying the coil radius influence

The residual stress and plastic strain distributions derived for cross-section cold-forming (Sections 6.3.2 and 6.4.2) are straight-forward to calculate if the yield stress, σ_{yield} , and thickness, t , of the sheet steel are known. The coiling residual stresses and plastic strains are more difficult to calculate because the coil radius coinciding with the as-formed member, i.e., the radial location of the sheet, r_x , is almost always unknown in

practice. However, r_x can be derived in an average sense though, since the range of inner and outer coil radii are known and the probability that a structural member will be manufactured from a certain r_x can be quantified.

The relationship between coil radius, r_x , and corresponding linear location S of the sheet within the coil can be described using Archimedes spiral (CRC 2003)

$$S = \frac{\pi}{t} (r_x^2 - r_{inner}^2). \quad (6.22)$$

The spiral maintains a constant pitch with varying radii, where the pitch is the thickness of the steel sheet, t , as shown in Figure 6.18, L is the total length of sheet in the coil, and r_{inner} and r_{outer} are the inside and outside coil radius, respectively. As-shipped outer coil radii range from 24 in. to 36 in. and inner coil radii range from 10 in. to 12 in. These ranges were determined by the author during a visit to a local roll-forming plant.

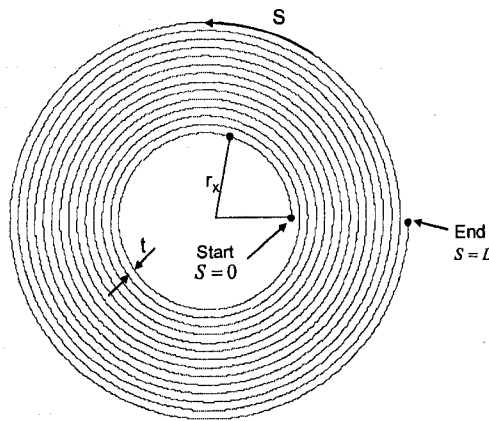


Figure 6.18 Coil coordinate system and notation.

Archimedes spiral is used to describe the probability that the steel sheet will come from a certain range of radial locations in the coil. The cumulative distribution function

(CDF), $F_R(r_x)$ = probability that the radius is less than r_x , is obtained by normalizing S by L

$$\frac{S}{L} = F_R(r_x) = \frac{r_x^2 - r_{inner}^2}{r_{outer}^2 - r_{inner}^2}. \quad (6.23)$$

The probability density function (PDF) of r_x is calculated by taking the derivative of $F_R(r_x)$

$$f_R(r_x) = \frac{dF_R(r_x)}{dr_x} = \frac{2r_x}{r_{outer}^2 - r_{inner}^2}. \quad (6.24)$$

The mean value of the radial location for a given inner and outer coil radii is

$$\bar{r}_x = \int_{r_{inner}}^{r_{outer}} f_R(r_x) r_x dr_x = \frac{2}{3} \left(r_{inner} + r_{outer} - \frac{r_{inner} r_{outer}}{r_{inner} + r_{outer}} \right). \quad (6.25)$$

The variance of the radial location is

$$s_R^2 = \int_{r_{inner}}^{r_{outer}} f_R(r_x) (r_x - \bar{r}_x)^2 dr_x = \frac{1}{18} \left(r_{outer}^2 + 4r_{outer}r_{inner} + r_{inner}^2 \right) \frac{(r_{outer} - r_{inner})^2}{(r_{outer} + r_{inner})^2}. \quad (6.26)$$

These statistics for r_x can then be used with the prediction method for coiling, uncoiling, and flattening residual stresses and plastic strains described in Sections 6.3.1 and 6.4.1.

Figure 6.19 summarizes the influence of sheet thickness and virgin yield stress on the longitudinal residual stress distributions in flats and corners. (The method proposed in this chapter provides residual stresses and strains for the entire member, only the longitudinal residual stresses are shown in Figure 6.19.) The solid lines in Figure 6.19 are calculated using the mean value, $\bar{r}_x=18.7$ in, from Eq. (6.25) assuming $r_{inner}=12$ in. and $r_{outer}=24$ in. The distributions with the dashed lines are calculated with $\bar{r}_x \pm s_R$, where $s_R=3.4$ in. is calculated with Eq. (6.26). The residual stresses are nonlinear through the thickness and have different shapes for flats and corners. The stress magnitudes at the

outer fibers increase for thicker sheets and lower yield stresses. The accuracy of the linear bending residual stress model commonly employed in finite element analyses is perhaps sufficient when yield stress is low and thickness is high (relatively), but for typical thicknesses (0.0346 in. to 0.0713 in.) and yield stress (50 ksi) the assumption of a linear longitudinal stress distribution is not consistent with the mechanics-based predictions in Figure 6.19.

Longitudinal Residual Stresses

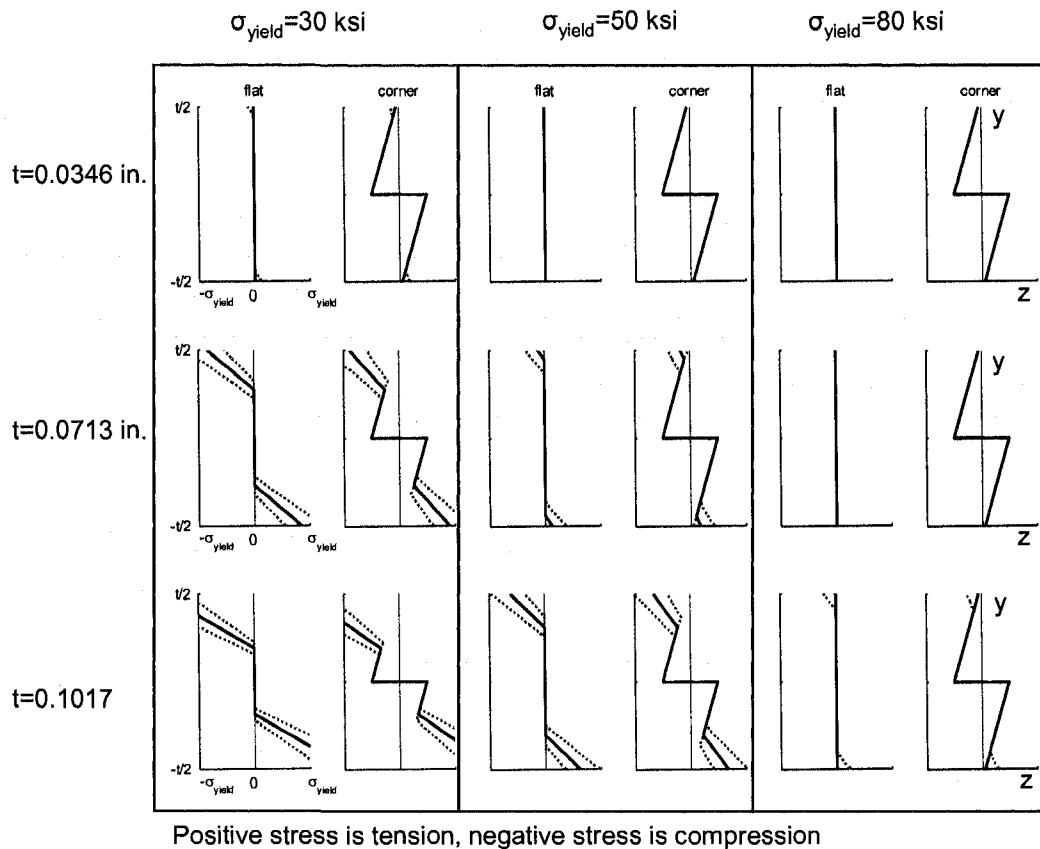


Figure 6.19 Influence of sheet thickness and yield stress on through-thickness longitudinal residual stresses (z-direction, solid lines are predictions for mean coil radius, dashed lines for mean radius +/- one standard deviation).

6.6 Comparison of prediction method to measured residual stresses

The flat and corner residual surface strain measurements from 18 roll-formed specimens are used to evaluate the proposed residual stress prediction method. The prediction method provides the complete through-thickness longitudinal strain (stress) distribution if the radial location in the coil from which the specimen originated in the coil, r_x , is known. Since the radial coil location of the 18 specimens is unknown, r_x is statistically estimated for each specimen using the coil radius that best fits the predicted surface strains to the measured surface strains from a specimen cross-section (for both corners and flats). Once the best fit radial locations have been calculated, they are examined to determine if their magnitude is rational when compared to typical inner and outer dimensions of a sheet coil. Although this comparison only provides a partial evaluation of the prediction method, it is as far as one can go with the available data. Qualitatively the prediction method is consistent with the more detailed through thickness findings (Key and Hancock 1993; Quach et al. 2006).

6.6.1 Measurement statistics

The mean and standard deviation of the residual stresses for the 18 roll-formed specimens used in this comparison are provided in Table 6.1. Positive membrane stresses are tensile stresses and positive bending stresses cause tension at $y=-t/2$ (see Figure 6.3 for coordinate system). The statistics demonstrate that both membrane and bending residual stress measurements are highly variable and that the membrane

stresses are small relative to the steel yield stresses. Details on the residual stress measurements for each of the 18 specimens are described in a previous research progress report (Moen and Schafer 2007b).

Table 6.1 Statistics of the residual stresses in roll-formed members

Element	Residual stress as % σ_{yield}				No. of Samples
	Membrane		Bending		
	Mean	STDEV	Mean	STDEV	
Corners	5.7	10.1	32.0	23.8	23
Flats	1.8	10.7	25.2	20.7	120

6.6.2 Mean-squared error (MSE) estimate of radial location

To explore the validity of the prediction method, the flat and corner residual stress measurements from the 18 specimens are used to estimate the radial location r_x from which each specimen originated. These estimated radial locations are then used to calculate the difference between the predicted and measured longitudinal residual stresses.

6.6.2.1 MSE minimization

The location of the specimen in the coil, r_x , is estimated by minimizing the sum of the mean-squared errors (MSE) for the $p=1,2,\dots,n_q$ measurements taken around the cross-section of the $q=1,2,\dots,18$ specimens

$$\hat{r}_{x,q} = \arg \min \sum_{p=1}^{n_q} \left(\frac{\sigma_{pq}^{measured} - \sigma_{pq}^{predicted}}{\sigma_{yield,pq}} \right)^2. \quad (6.27)$$

Both corner and flat measurements are included in the minimization.

6.6.2.2 Bending component of longitudinal residual stress distribution

The bending component of the predicted residual stress distribution must be isolated to compare with the measured values. The total predicted longitudinal residual stress distribution in the flats and corners of each cross-section is integrated to calculate the sectional moment through the thickness

$$M_x = \int_{-\frac{t}{2}}^{\frac{t}{2}} \sigma_z y dy . \quad (6.28)$$

M_x is then converted into a predicted outer fiber bending residual stress which can then be directly compared to the measurements

$$\sigma_{pq}^{predicted} = \frac{M_x \left(\frac{t}{2} \right)}{I} . \quad (6.29)$$

6.6.2.3 Estimated coil radii using MSE

Figure 6.20 demonstrates the mean-squared error results for de M. Batista and Rodrigues Specimen CP1 (De Batista and Rodrigues 1992). The radial location that minimizes the prediction error is $1.60r_{inner}$ in this case, and is summarized in Table 6.2 for all 18 roll-formed specimens considered. The estimated radial locations fall within the range of inner and outer coil radii assumed in the prediction (r_{inner} to $2.40r_{inner}$) except for Dat RFC13 which is slightly outside the range at $2.45r_{inner}$. The MSE radial location cannot be determined in the three Bernard specimens (Bernard 1993) since the bending residual stresses in the flats are predicted to be zero. These three specimens are cold-

formed steel decking with a thin sheet thickness t ranging from 0.022 in. to 0.0400 in. and a relatively high yield stress σ_{yield} ranging from 87 ksi to 94 ksi. In this case, the coiling and uncoiling of the steel sheet will occur elastically as demonstrated in Figure 6.19. Measured bending residual stress magnitudes in the flats of the Bernard specimens are on average $0.03\sigma_{yield}$ which is consistent with the prediction method.

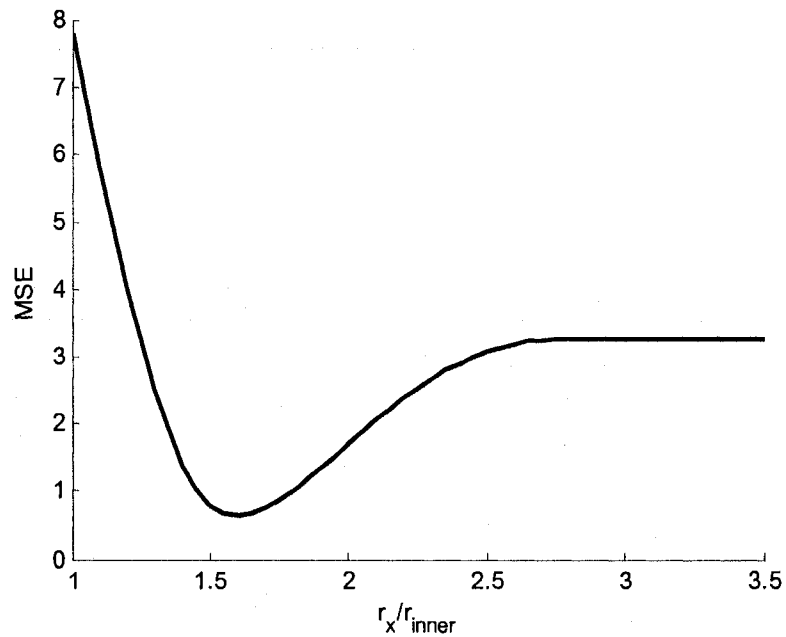


Figure 6.20 The mean-squared error of the predicted and measured bending residual stresses for de M. Batista and Rodrigues (De Batista and Rodrigues 1992), Specimen CP1 is minimized when $r_x=1.60r_{inner}$.

Table 6.2 Radial location in the coil that minimizes the sum of the mean square prediction error for roll-formed members

Researcher	Specimen	r_x estimate in.
de M. Batista and Rodrigues (1992)	CP2	12.0
de M. Batista and Rodrigues (1992)	CP1	16.0
Weng and Peköz (1990)	RFC13	18.0
Weng and Peköz (1990)	RFC14	11.0
Weng and Peköz (1990)	R13	14.5
Weng and Peköz (1990)	R14	13.0
Weng and Peköz (1990)	P3300	19.5
Weng and Peköz (1990)	P4100	15.0
Weng and Peköz (1990)	DC-12	23.0
Weng and Peköz (1990)	DC-14	16.0
Dat (1980)	RFC14	20.0
Dat (1980)	RFC13	24.5
Bernard (1993)	Bondek 1	N/A
Bernard (1993)	Bondek 2	N/A
Bernard (1993)	Condeck HP	N/A
Abdel-Rahman and Siva (1997)	Type A - Spec 1	16
Abdel-Rahman and Siva (1997)	Type A - Spec 2	16
Abdel-Rahman and Siva (1997)	Type B - Spec 1	13

$r_{inner}=10$ in., $r_{outer}=24$ in.

N/A coiling residual stresses are predicted as zero

6.6.3 Statistical variations between measurements and predictions

The predicted radial locations in Table 6.2 are now used to calculate the statistical variations between the experiments and predictions. The bending residual stresses in the 18 roll-formed members are calculated using the MSE-predicted radial location r_x with the residual stress prediction method summarized in Figure 6.13. The bending component of the residual stress prediction is then obtained with Eq. (6.29). The difference between the predicted and measured residual bending stresses, e_{pq} , for the $p=1,2,\dots,n$ measurements taken around the cross-section of the $q=1,2,\dots,18$ specimens is calculated as

$$e_{pq} = \frac{\sigma_{pq}^{measured} - \sigma_{pq}^{predicted}}{\sigma_{yield,pq}} \quad (6.30)$$

The error histogram for the flat cross-sectional elements in Figure 6.21a demonstrates that the mean difference μ_e is near zero with a standard deviation $s_e=0.15\sigma_{yield}$. The scattergram in Figure 6.21b demonstrates the strength of the correlation between the measurements and predictions in the flats; the solid regression line passes nearly through zero (y -intercept= $0.05\sigma_{yield}$) and has nearly a unit slope ($m=0.92$). Also, the majority of the data lies within \pm one standard deviation of the estimate, denoted as the dashed lines in the figure. It is concluded that the prediction method is consistent with the measured data in the flats.

The corner element error histogram in Figure 6.22a shows a negative bias of $\mu_e=-0.16\sigma_{yield}$ meaning that the predicted residual stresses are generally higher than the measured values. The standard deviation of the error is large ($s_e=0.19\sigma_{yield}$) but is less than the standard deviation of the corner residual stress measurements in Table 6.1 ($s_m=0.24\sigma_{yield}$). This demonstrates a greater match between the measurements and predictions, although more corner residual stress measurements are needed to improve the strength of this comparison. The scattergram in Figure 6.22b highlights the variability in the measured corner data, especially in the region corresponding to $\sigma_{predicted}=0.4\sigma_{yield}$, where bending residual stresses (strains) vary from 0 to $0.7\sigma_{yield}$.

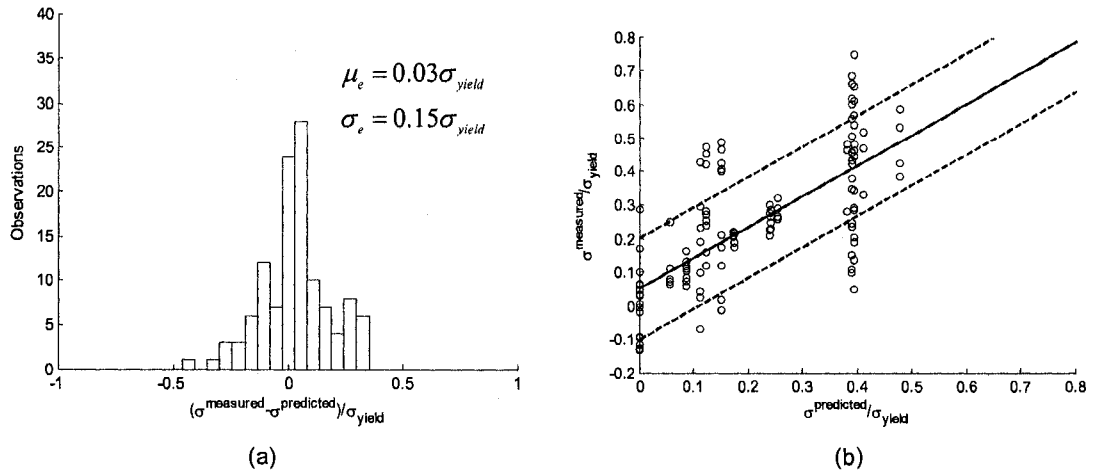


Figure 6.21 (a) Histogram and (b) scattergram of bending residual stress prediction error (flat cross-sectional elements) for 18 roll-formed specimens.

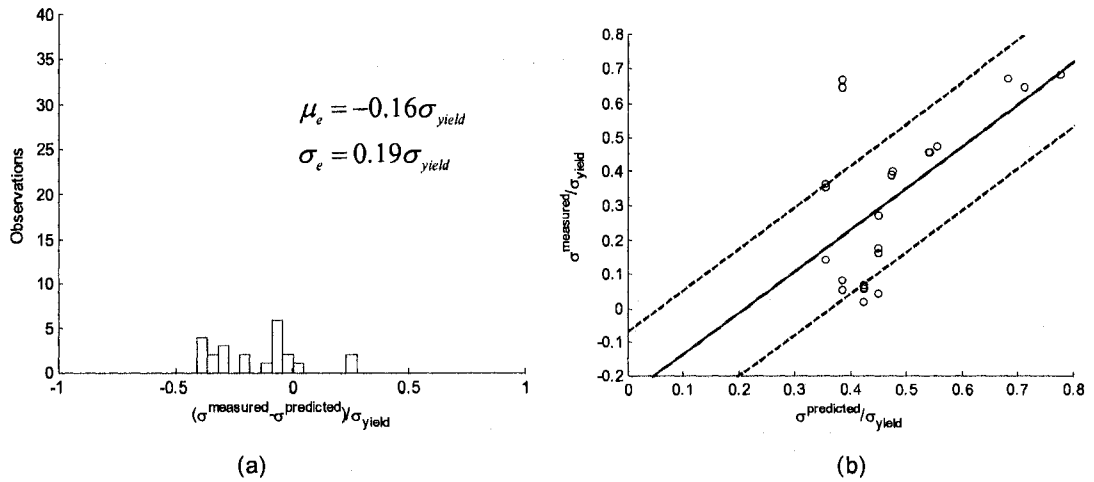


Figure 6.22 (a) Histogram and (b) scattergram of bending residual stress prediction error (corner cross-sectional elements) for 18 roll-formed specimens.

6.7 Discussion

The residual stresses and strains predicted with this method (Section 6.3 for stress, Section 6.4 for strain) form the initial material state in the cross-section. In design, this initial material state is sometimes considered through the so-called cold-work of forming effect, where the yield stress of the material is increased above the virgin yield stress,

σ_{yield} , to account for the 'working of the corners'. For one-dimensional stress-strain this concept is expressed as shown in Figure 6.23, where 'working the corners' results in a residual plastic strain, ϵ_p , such that when the section is re-loaded the stress at which yielding re-initiates, σ_{ry} , is greater than the virgin yield stress, σ_{yield} . If no residual stresses existed the apparent increase in the yield stress from σ_{yield} to σ_{ry} can be significant. However, as Figure 6.19 illustrates, 'working the corners' also contributes to residual stresses, σ_{rs} , and these residual stresses may decrease the apparent yield stress.

The prediction method presented herein provides a more nuanced understanding of the cold-work of forming effects. The residual plastic strains may increase the apparent yield stress, but those strains vary through the thickness and have contributions from both transverse and longitudinal strains. Further, residual stresses follow their own relatively complicated distribution through the thickness. In a multi-axial stress state using the von Mises yield criterion, Figure 6.23 is enforced for the effective stress – effective strain pair for every point in the cross-section. As a result, the apparent yield stress upon loading varies through the thickness and is influenced by both the residual stresses and strains. Even under simple loading conditions (e.g., compression) a cold-formed member undergoes plate bending well in advance of collapse, so the strains demanded of the material also vary through the thickness and around the cross-section. While it is indeed possible to model such effects in a finite element analysis, assuming these effects can be collapsed into a generic increase in the yield stress for the entire section as is currently done in design would seem to be an oversimplification.

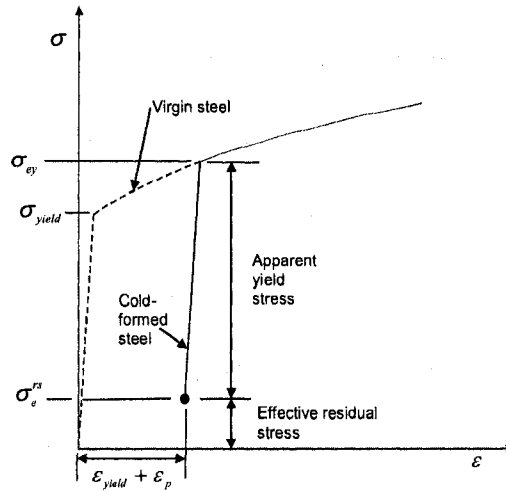


Figure 6.23 Definition of apparent yield stress, effective residual stress, and effective plastic strain as related to a uniaxial tensile coupon test.

Implementation of the residual stresses and initial plastic strains into a commercial finite element program such as ABAQUS, where the member is modeled using shell elements, is relatively straightforward. The number of through-thickness section (integration) points must be increased to resolve the nonlinear through-thickness residual stress and strain distributions. The residual stresses and strains predicted herein can be relatively large. Further, conventional loading (e.g., compression, major-axis bending) may cause loading or unloading of these initial stresses at a given point in the cross-section. As a result, the hardening rule: isotropic, kinematic, or mixed can have practical differences in the observed response even when the applied loads themselves are not reversing.

For this situation, kinematic hardening, which approximates the Bauschinger effect, provides a more conservative model of the anticipated material behavior than isotropic hardening. However, to model kinematic hardening the location of the center of the yield surface in stress space (also known as the backstress) must be determined for each

point in the cross-section at the end of the manufacturing process. This location is a function of the extent of yielding, in the example of Figure 6.23, the backstress would be the $\Delta\sigma_1, \Delta\sigma_2, \Delta\sigma_3$ triad that results in the effective stress increasing from σ_{yield} to σ_{ey} . Unfortunately, the elastic-perfectly plastic assumption used to predict residual stresses herein does not directly allow for the calculation of the backstress. However, the effective plastic strain may be used to approximate the backstress as provided in Appendix G. Further examination of the predicted residual stress and strains and their impact on the peak strength and collapse response of cold-formed steel members in nonlinear finite element analysis is currently underway, including the work presented in Section 7.2.

6.8 Acknowledgements

The development of this residual stress prediction method would not have been possible without accurate information about the manufacturing process of sheet steel coils and cold-formed steel members. Thanks to Clark Western Building Systems, Mittal Steel USA, and the Cold-Formed Steel Engineers Institute (CFSEI) for their important contributions to this research, especially Bill Craig, Ken Curtis, Tom Lemler, Joe Wellinghoff, Ezio Defrancesco, Jean Fraser, Narayan Pottore, and Don Allen.

Chapter 7

Nonlinear finite element modeling of cold-formed steel structural members

Commercial finite element programs provide a means for realistic collapse simulation of cold-formed steel structural members. Thin shell finite element formulations provided in ABAQUS (e.g., the S9R5 element discussed in Chapter 2) are designed to capture the sharp folds and through-thickness yielding characteristic of cold-formed steel beams and columns at their ultimate limit state. Robust solution algorithms are available to predict unstable, geometrically nonlinear collapse. The ability to define the initial state of a member, including geometric imperfections and the effects of residual stresses and initial plastic strains from the manufacturing process, is also feasible. Care must be taken though with computational results since they are often sensitive to modeling inputs and assumptions. It is prudent to study these sensitivities and validate a specific modeling protocol with known experiment results before trusting the protocol to consistently produce physically realistic results.

This chapter begins with preliminary nonlinear finite element studies of stiffened elements (i.e., a simply supported plate, see Figure 3.1 for definition) with and without holes, which are designed to gain experience with available ABAQUS nonlinear finite element solution methods. The influence of imperfections on stiffened elements is also evaluated, and the through-thickness yielding patterns of a stiffened element (i.e., “effective width”) with and without a hole are compared. The conclusions reached from this preliminary work are used to guide the development and validation of a nonlinear finite element modeling protocol which is needed in Chapter 8 to explore the Direct Strength Method for members with holes.

7.1 Preliminary nonlinear FE studies

Exploratory nonlinear finite element studies are conducted in this section to gain experience with ABAQUS input parameters and solution controls. All studies are focused on the simulation of a stiffened element loaded uniaxially to collapse, and specific attention is paid to the modeling of a stiffened element with a hole. Experience gained from solving this highly nonlinear problem will be valuable when implementing the larger simulation studies on full cold-formed steel members with holes in Section 7.2.

7.1.1 Finite element modeling definitions

The stiffened element is modeled with ABAQUS S9R5 thin shell finite elements, where the plate dimensions are $h=3.4$ in. and $L=27.2$ in. (see Figure 3.2 for plate dimension definitions) and the plate thickness t is 0.0346 in. (These dimensions are

specifically chosen to be consistent with the flat web width and thickness of an SSMA 362S162-33 structural stud.) Cold-formed steel material properties are assumed as $E=29500$ ksi and $\nu=0.30$. Material nonlinearity is simulated in ABAQUS with classical metal plasticity theory, including the assumption of a von Mises yield surface and isotropic hardening behavior. The nonlinear plastic portion of the true stress-strain curve shown in Figure 7.1 was obtained from a tensile coupon test (Yu 2005) and input into ABAQUS to define the limits of the von Mises yield surface as a function of plastic strain.

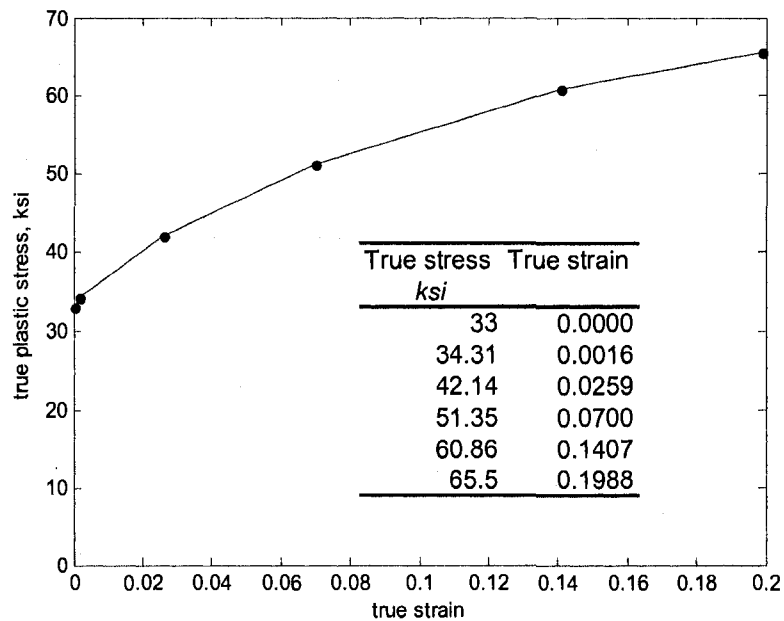


Figure 7.1 True stress-strain curve derived from a tensile coupon test (Yu 2005)

The boundary conditions of the stiffened element are summarized in Figure 7.2. The plate is simply-supported around the perimeter with sides free to wave. The nodes at the loaded edges of the plate are coupled to displace together longitudinally (in the 1

direction), which prevents local failure modes of the plate at the loaded edges. The nodal coupling is provided with an equation constraint in ABAQUS.

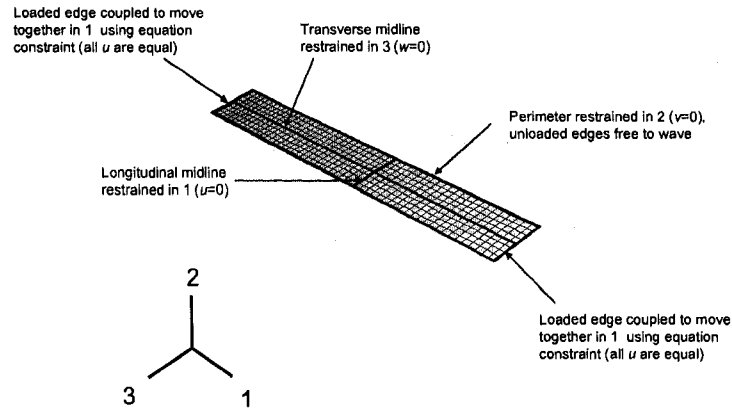


Figure 7.2 Simply supported boundary conditions with equation constraint coupling at loaded edges

Two types of loading conditions, uniform load and uniform displacement, are considered as shown in Figure 7.3. The uniform compressive load is applied as consistent nodal loads on the plate edge. The magnitude of the uniform load is represented by the parameter λ , which is an accumulation of load steps $\Delta\lambda$ automatically determined by ABAQUS. $\Delta\lambda$ is large when the Newton-Raphson algorithm converges quickly (along the linear branch of the load-displacement curve) and adjusts to smaller increments as equilibrium becomes more difficult to achieve (near the peak of the load-displacement curve). For the uniform displacement case, the total displacement δ of the plate edges is applied over 100 steps, where the maximum displacement increment at each step is set to $\Delta\delta=0.0145t$.

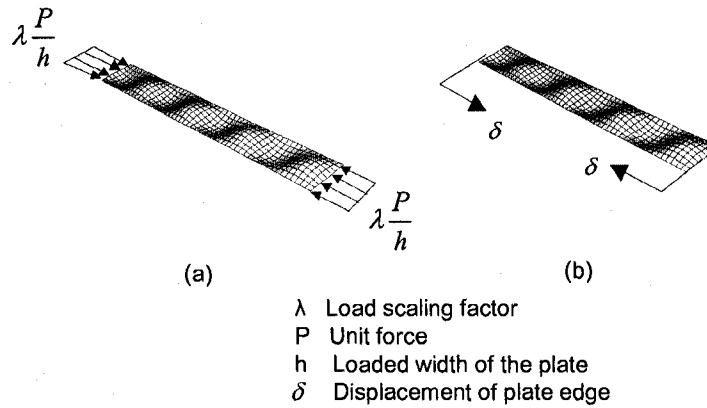


Figure 7.3 Application of (a) uniform load and (b) uniform displacement to a stiffened element

Initial geometric imperfections are imposed based on the fundamental elastic buckling mode of the stiffened element (see buckled shape in Figure 7.3). The magnitude of the imperfections is chosen based on a probabilistic treatment developed for cold-formed steel members (Schafer and Peköz 1998). Since the stiffened element considered here is chosen to be consistent with the web of a structural stud, a Type 1 (local buckling) imperfection is assumed as shown in Figure 7.4. The maximum magnitude of the imperfection field is selected such that there is a 50 percent chance that a randomly occurring imperfection in the plate, Δ , will have a magnitude less than d_1 , i.e., $P(\Delta < d_1) = 0.50$. For this probability of occurrence, the initial imperfection field of the stiffened element is scaled to $d_1/t = 0.34$.

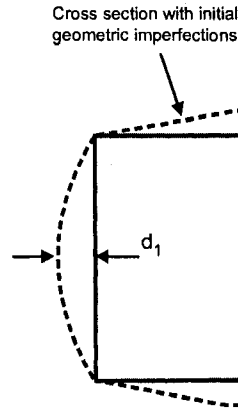


Figure 7.4 Type 1 imperfection (Schafer and Peköz 1998)

7.1.2 ABAQUS nonlinear solution methods

Two nonlinear solution methods, the modified Riks method and a Newton-Raphson technique with artificial damping, are available in ABAQUS to solve difficult nonlinear problems. The modified Riks Method (i.e., *STATIC, RIKS in ABAQUS), was developed in the early 1980's and enforces an arc length constraint on the Newton-Raphson incremental solution to assist in the identification of the equilibrium path at highly nonlinear points along the load-deflection curve. This method is discussed extensively in several publications (Crisfield 1981; Powell and Simons 1981; Ramm 1981; Schafer 1997; ABAQUS 2007a). Another solution option is a Newton-Raphson technique (i.e., *STATIC, STABILIZE in ABAQUS) which adds artificial mass proportional damping as local instabilities develop (that is, when changes in nodal displacements increase rapidly over a solution increment) to maintain equilibrium (Yu 2005; ABAQUS 2007a). Local instabilities near peak load are common in cold-formed steel members, such as when a thin plate develops at a fold line prior to collapse.

In this study, the stiffened element described in Section 7.1.1 is loaded to collapse in ABAQUS employing the modified Riks method with uniform loads applied uniaxially (see Figure 7.3a) and then with the artificial damping solution method employing uniform displacements (see Figure 7.3b). (Either method is capable of solving problems with applied loads or applied displacements.) The goal of this preliminary study is to gain experience with the solution controls for each method. Additional background information pertaining to the ABAQUS implementation of the artificial damping method is also discussed to provide specific guidance (and raise future research questions) on its proper use.

7.1.2.1 Modified Riks solution

The load-displacement curves and deformed shapes (at peak load) of the stiffened element solved with the modified Riks method are provided in Figure 7.5. Different post-peak equilibrium paths were obtained by varying $\Delta\lambda_{max}$, the maximum load increment limit for the ABAQUS automatic step selection algorithm. The existence of multiple solutions is consistent with a plate containing periodic geometric imperfections, since each half-wavelength has an equal chance of deforming locally into a plastic failure zone.

Although there were several different post-peak paths observed depending upon the choice of $\Delta\lambda_{max}$, the primary failure mechanism for the plate was a sharp yield-line fold occurring transversely across the plate. Figure 7.6 demonstrates that this folding occurs at the crest of the buckled half-wave of the initial geometric imperfection field; in

this case the failure mechanism of the plate is linked to the initial imperfection shape. The quantity and location of the plastic folds influenced the overall ductility of the stiffened element (i.e., the area under the load-displacement curve). As the number of folds increase, the post-peak strength and ductility of the plate increase. The peak compressive load of the stiffened element was not sensitive to changes in $\Delta\lambda_{max}$.

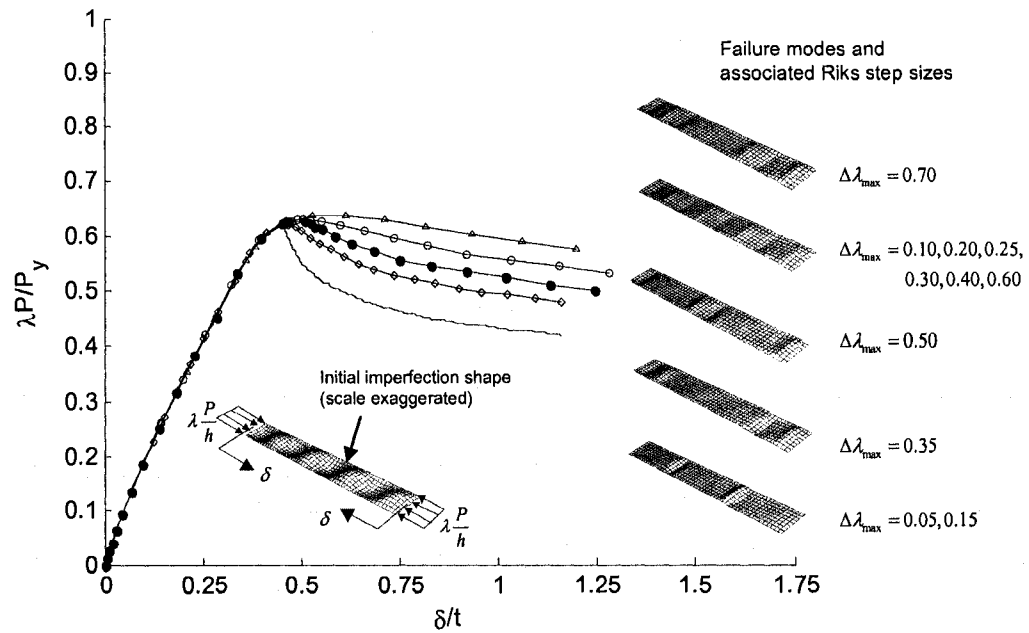


Figure 7.5 Modified Riks method load-displacement solutions and failure modes

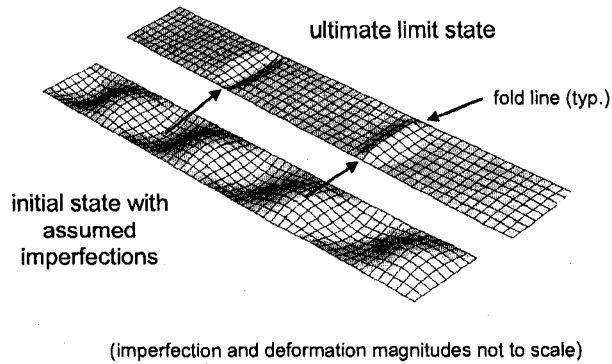


Figure 7.6 Correlation between initial imperfection shape and fold line locations at failure

7.1.2.2 Artificial damping solution

7.1.2.2.1 Background on artificial damping solution method

Artificial mass proportional damping is employed in ABAQUS to alleviate local instabilities in the *STATIC, STABILIZE solution method. The global equilibrium equations at each displacement step can be written as:

$$\mathbf{P} - \mathbf{F} - \mathbf{D} = 0 \quad (7.1)$$

where \mathbf{P} is the vector of applied external forces, \mathbf{F} is the vector of calculated internal forces, and \mathbf{D} is the vector of viscous damping forces. The damping force vector \mathbf{D} is calculated at each step based on the following relationship:

$$\mathbf{D} = (c\mathbf{M})\mathbf{v} \quad (7.2)$$

where c is the damping ratio, \mathbf{M} is an artificial mass matrix calculated with a unit material density, and \mathbf{v} represents the change in nodal displacements divided by the size of the "time" step selected by ABAQUS. \mathbf{v} is called the "nodal velocity" in ABAQUS since the dimensions are length/"time", which makes \mathbf{v} sensitive to the definition of "time". In this study, the total "time" is selected as one unit and the maximum "time" step allowed is 0.01 units. If the total "time" is chosen as 100 units and the maximum "time" step as 1 unit, it seems that the magnitude of the damping forces \mathbf{D} would change. Following the same argument, the magnitude of \mathbf{v} is impacted by the choice of units for the problem (feet, inches, meters, mm) since \mathbf{v} has dimensions of length/"time" units. Future work is needed to evaluate the influence of "time" and length units on the calculation of the "nodal velocity" \mathbf{v} . The evaluation of the artificial damping solution

sensitivity to the magnitude and distribution of mass in a member is also another future research topic.

When the solution is stable, changes in nodal displacements are small and viscous damping is negligible. When large changes in displacements occur between two consecutive load steps (as in the case of a local instability), damping forces are applied to help make up the difference between \mathbf{P} and \mathbf{F} . v may only be high for certain locations in the member, and therefore damping will only be applied there. ABAQUS provides both automatic and manual options for selection the damping factor c ; if c is chosen manually, ABAQUS recommends that it should be chosen as a small number since large damping forces can add too much artificial stiffness to the system, producing an unreasonable solution. When the automatic option is selected, ABAQUS finds c such that the dissipated energy to total strain energy ratio after the first load step is equal to 2.0×10^{-4} .

7.1.2.3 Artificial damping results

The artificial damping solutions for the stiffened element are presented in Figure 7.7. Load-deformation results pertaining to both manually and ABAQUS-selected damping factors are plotted, demonstrating that the magnitude of the damping parameter c influences the post-peak response and causes the prediction of several different load paths (in a similar way to how $\Delta\lambda_{max}$ affected the modified Riks solutions). Peak load is not sensitive to the quantity of damping in this case, and is consistent with the magnitude predicted with the modified Riks method.

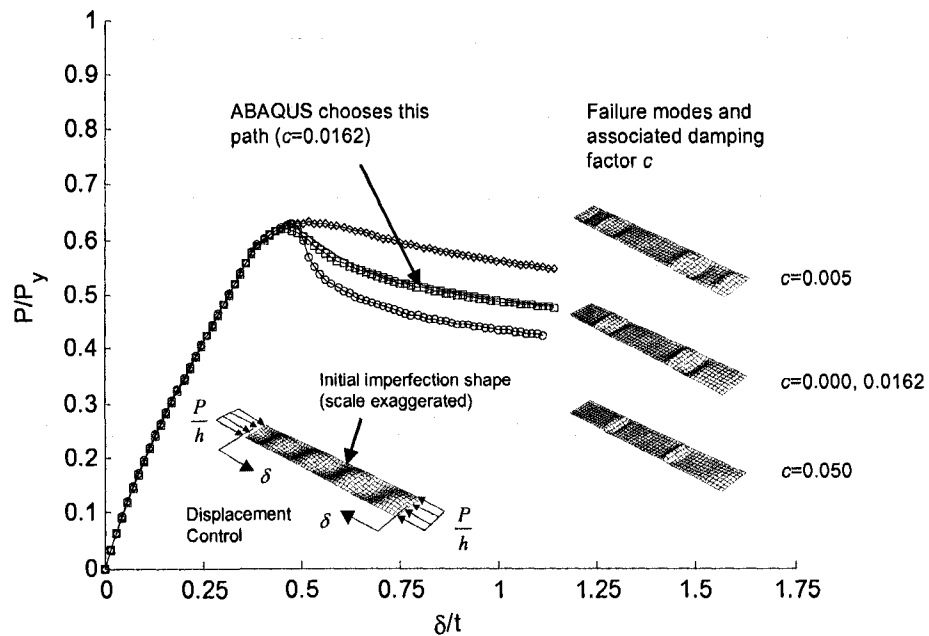


Figure 7.7 Artificial damping load-displacement solutions and failure modes

7.1.3 ABAQUS nonlinear solution controls

Section 7.1.2 summarizes the preliminary experiences gained using ABAQUS nonlinear solution methods to determine the ultimate strength of stiffened elements. Equilibrium paths and failure modes can be sensitive to solution controls, although the peak resisting load of the plate was consistently predicted. The nonlinear solution of a stiffened element with a slotted hole is attempted with the modified Riks method (*STATIC, RIKS), the default Newton-Raphson solution algorithm (*STATIC), and Newton-Raphson with artificial damping (*STATIC, STABILIZE) solution methods available in ABAQUS. The goal of the study is to determine a set of solutions controls

(load step size, damping factor, convergence limits) that is capable of capturing the post-peak load-displacement response of a stiffened element with a hole.

7.1.3.1 Problem description

The stiffened element described in Section 7.1.1 is considered in this study. A single slotted hole is placed at the midlength of the plate and centered between the unloaded edges. The slotted hole has dimensions of $h_{hole}=1.5$ in., $L_{hole}=4$ in., and $r_{hole}=0.75$ in. (see Figure 3.2 for hole dimension definitions).

The boundary conditions of the stiffened element were initially assumed to be simply-supported with both transverse and longitudinal plate midlines restrained and the loaded edge nodes coupled with constraint equations as described in Figure 7.2. It was often observed that the constraints used to enforce uniform displacements in 1 (u) at the loaded edges and the transverse midline restraint in 2 ($w=0$) were contributing to solution convergence problems, and therefore an alternative set of boundary conditions was developed as shown in Figure 7.8.

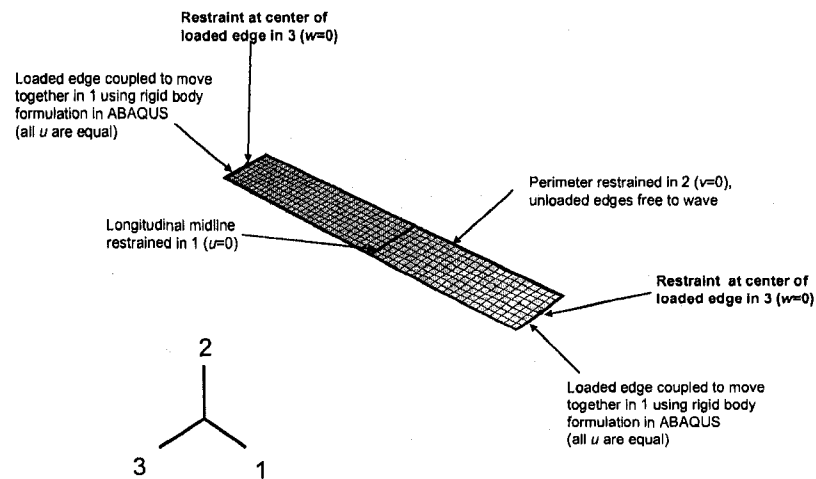


Figure 7.8 Stiffened element boundary conditions with rigid body coupling at loaded edges

A comparison of the geometric imperfections assumed for the stiffened element with and without the hole is provided in Figure 7.9. $d_1/t=0.34$ is used to scale the initial imperfection field of the plate. This magnitude corresponds to a probability of occurrence of $P(\Delta < d_1)=0.50$ (see Section 7.1.1 for details). The peak load of the stiffened element is sensitive to initial geometric imperfections, and therefore it is important to consider the same imperfection shape when comparing the load-displacement responses of the stiffened element with and without a hole. The imperfection shape is imposed on the stiffened element with the slotted hole by mapping the buckled mode shape to nodal coordinates using custom MATLAB code (Mathworks 2006).

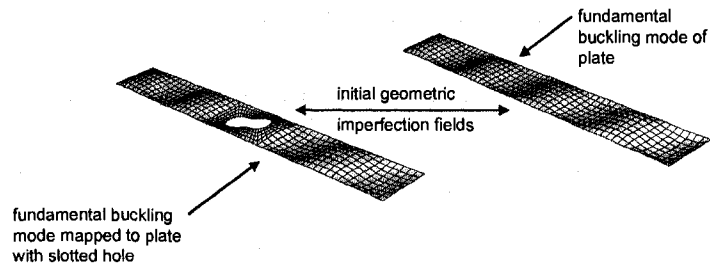


Figure 7.9 Initial geometric imperfection field used for the stiffened element with and without a hole

Eight exploratory ABAQUS models are evaluated in this study, each solving the same nonlinear problem of a stiffened element with a slotted hole compressed uniaxially until failure as shown in Figure 7.10. Each model employs a different combination of ABAQUS solution controls and boundary conditions as summarized in Table 7.1.

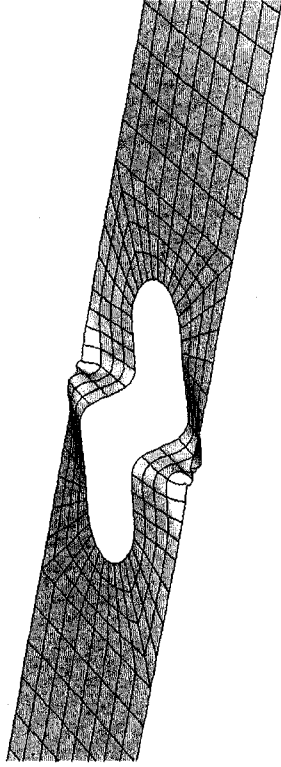


Figure 7.10 Deformation at ultimate load of a stiffened element with a hole loaded in compression. The common failure mechanism is material yielding adjacent to the hole followed by plate folding.

Table 7.1 Summary of nonlinear finite element models and associated solution controls

Model	ABAQUS Method	*STATIC				*STATIC, RIKS				Solution Controls				Loading Type and Boundary Conditions
		initial step size	total time	min step size	max step size	initial step size	max step size	iteration limits	residual limits	damping factor	line search			
RIKS1	*STATIC, RIKS	---	---	---	---	0.05	0.2	4 (D)	8 (D)	16 (D)	0.005 (D)	---	NO	uniform load, equation constraint
RIKS2	*STATIC, RIKS	---	---	---	---	(D)	(D)	4 (D)	8 (D)	16 (D)	0.005 (D)	---	NO	uniform load, equation constraint
RIKS3	*STATIC, RIKS	---	---	---	---	0.05	0.05	8	16	33	0.005 (D)	---	NO	imposed displacement, rigid body constraint
STATIC1	*STATIC	0.01	1	1.00E-20	0.01	---	---	8	16	33	0.005 (D)	---	NO	uniform load, equation constraint
STATIC2	*STATIC	0.01	1	1.00E-20	0.01	---	---	8	16	33	0.005 (D)	0.0162	YES	uniform load, equation constraint
STAB1	*STATIC, STABILIZE	0.01	1	1.00E-20	0.01	---	---	8	16	33	0.005 (D)	0.0162	NO	imposed displacement, rigid body constraint
STAB2	*STATIC, STABILIZE	0.01	1	1.00E-20	0.01	---	---	8	16	33	0.1	---	NO	imposed displacement, rigid body constraint
STAB3	*STATIC, STABILIZE	0.01	1	1.00E-20	0.01	---	---	8	16	33	0.005 (D)	0.0162	NO	uniform load, rigid body constraint

7.1.3.2 Modified Riks method solution controls

The RIKS1 and RIKS2 finite element models are loaded with a uniformly distributed load at both ends as shown in Figure 7.3(a), where equation constraints couple the loaded edge nodes (see Figure 7.2). The initial and maximum load step magnitudes are defined for RIKS1 based on experience gained from the study in Section 7.1.2.1. The RIKS2 model allows ABAQUS to select all load stepping parameters automatically.

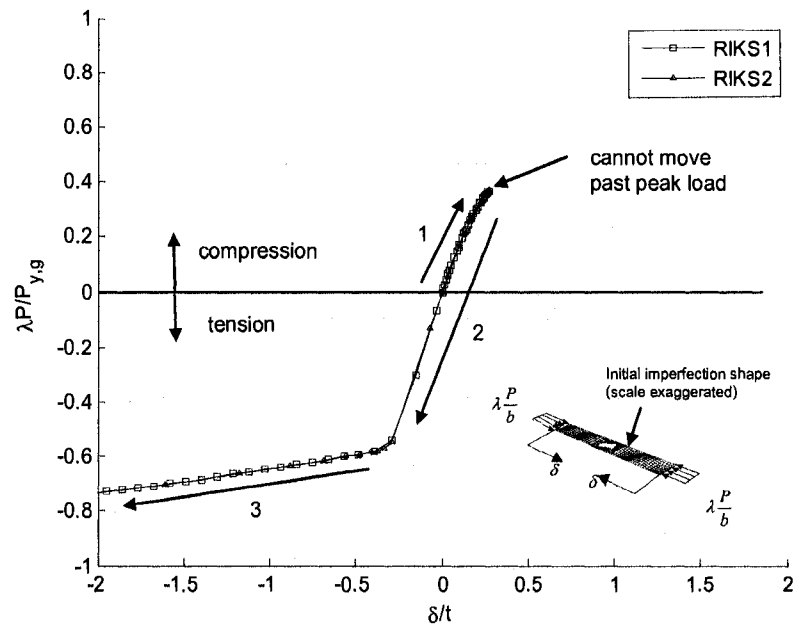


Figure 7.11 Load-displacement curve for the RIKS1 and RIKS2 models showing direction reversal along load path

The load-displacement responses from the RIKS1 and RIKS2 models are compared in Figure 7.11. For both models, ABAQUS does not capture the peak load and reverts back along the equilibrium path until the plate is loaded to failure in tension! The ABAQUS Theory Manual states that this type of direction switch is possible when

the equilibrium path exhibits very high curvature (ABAQUS 2007a). The ABAQUS message files (.msg) for these models report that the moment residuals are too high at the loaded edge nodes and at nodes along the transverse midline of the plate, suggesting that these boundary conditions are contributing to the convergence difficulties for the solution.

The RIKS3 model is loaded with imposed displacements at both ends as shown in Figure 7.3 (b), where the midline constraint is removed and the loaded edge nodes are coupled with a rigid body constraint instead of an equation constraint in ABAQUS (see Figure 7.8). According to the ABAQUS Analysis User's Manual, only the reference node governing the motion of the rigid body is involved in element level calculations. This improves computational efficiency and releases the solution algorithm from the force and moment residual minimization constraints for all nodes in the rigid body except the reference node.

The solution results from the stiffened elements loaded with consistent nodal loads (RIKS1, RIKS2) and imposed displacements (RIKS3) are compared in Figure 7.12. Before yielding occurs, the three models produce nearly identical load-displacement results. As yielding initiates, the RIKS3 model predicts a peak load and post-peak response for the stiffened element. This comparison demonstrates that imposed displacements and rigid body constraints (in contrast to applied loads and equation constraints) improve the chances for convergence in this case.

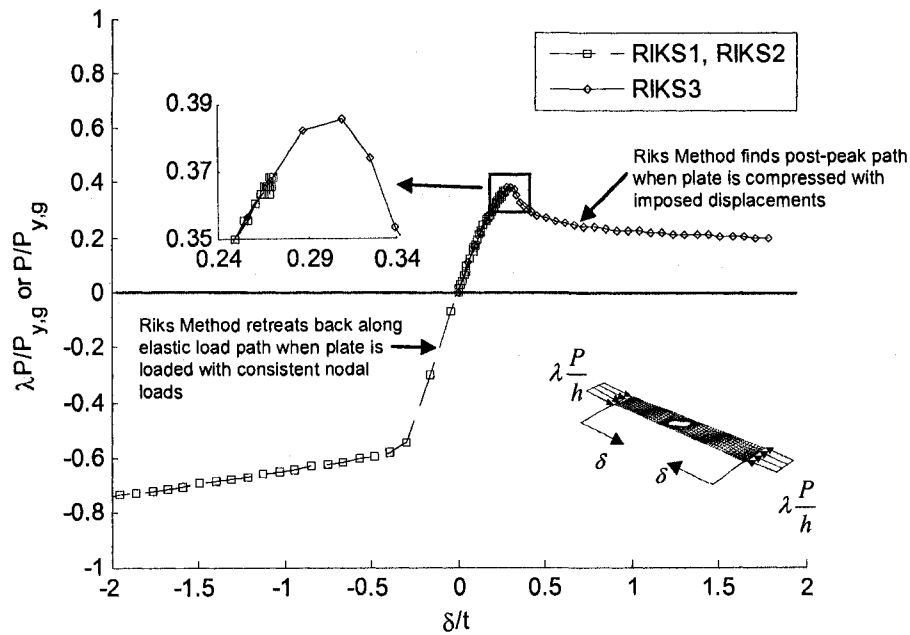


Figure 7.12 RIKS1 and RIKS2 models experience convergence problems and return along the loading path, the RIKS3 model successfully predicts a peak load and finds a post-peak load path

7.1.3.3 Newton-Raphson method

The STATIC1 and STATIC2 models employ the Newton-Raphson algorithm with uniform displacements at the loaded edges imposed with equation constraints (see Figure 7.2). The stepping parameters are chosen to ensure at least 100 increments are achieved before completion of the simulation. The number of convergence criteria iterations is also modified by doubling the ABAQUS parameters I_o , I_r , and I_c from their default values (see Table 7.1). I_o represents the number of equilibrium iterations before a check is performed to ensure that the magnitudes of the moment and force residual vectors are decreasing. After I_o iterations, if the residuals are not decreasing between two consecutive equilibrium iterations then the length of the increment step is reduced and the equilibrium search is restarted. I_r represents the number of equilibrium

iterations after which the logarithmic rate of convergence check begins. I_c represents the maximum number of equilibrium iterations within a time increment step. A line search algorithm is also employed in the STATIC2 model to improve the convergence of the Newton-Raphson algorithm when nodal force and moment residuals are large. This algorithm finds the solution correction vector which minimizes the out-of-balance forces in the structural system (ABAQUS 2007a).

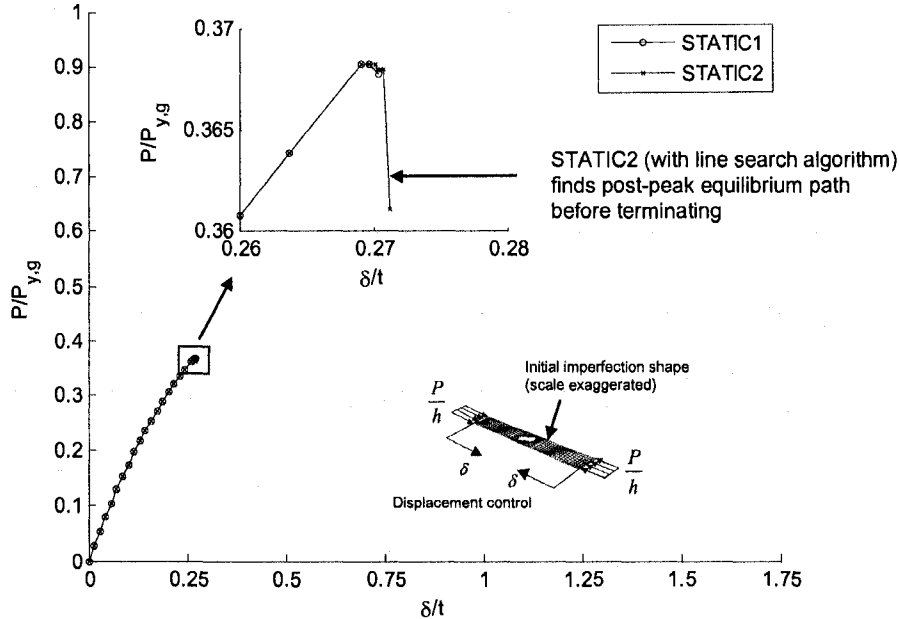


Figure 7.13 STATIC1 and STATIC2 load-displacement curves demonstrate convergence difficulties near the peak load.

Figure 7.13 compares the STATIC1 and STATIC2 load-displacement curves. The STATIC1 model finds the peak load but then terminates due to moment residual convergence issues as it attempts to predict the first step of the post-peak response. The ABAQUS message (.msg) file for this model states that the moment residuals at nodes along the loaded edges, along the transverse midline of the plate, and at some nodes

near the hole are increasing and convergence is judged unlikely. The solution is terminated after the automatic time stepping procedure requires a smaller time step than the minimum set in this model (1×10^{-20}). The STATIC2 model with the line search algorithm also finds the peak load of the stiffened element and is able to track onto a post-peak equilibrium path before terminating from the same convergence problems experienced by the STATIC1 model. The success of the line search algorithm in identifying a post-peak equilibrium path highlights its potential for solving nonlinear problems, although a significant increase in computational effort (almost twice the wallclock time) was also noted.

7.1.3.4 Newton-Raphson with artificial damping

The STAB1 and STAB2 models solve the stiffened element problem using a displacement control Newton Raphson algorithm coupled with the automatic artificial damping discussed in Section 7.1.2.2. The boundary conditions are modified to those summarized in Figure 7.8 because of the convergence issues observed with the constraint equations and transverse midline restraints. As in the case of STATIC1 and STATIC2, the convergence iteration limits I_b , I_r , and I_c are doubled from their default values. In an attempt to alleviate the moment residual convergence issues from previous runs, the Newton Raphson parameter R_n^α is modified to relax the residual requirements when the solution approaches the peak load. R_n^α is the allowable limit on the ratio of the largest residual force or moment at a node (r_{max}^α) to the largest change in force or moment at a node averaged over each time step increment that has been

completed (q^α). The α superscript indicates that R_n^α can be defined for either a displacement field u or a rotation field Φ . The convergence limit can be written mathematically as:

$$r_{\max}^\alpha \leq R_n^\alpha q^\alpha. \quad (7.3)$$

The default for R_n^α of 0.005 is used in STAB1 for both u and Φ fields, whereas in STAB2 $R_n^u=0.005$ and $R_n^\Phi=0.100$.

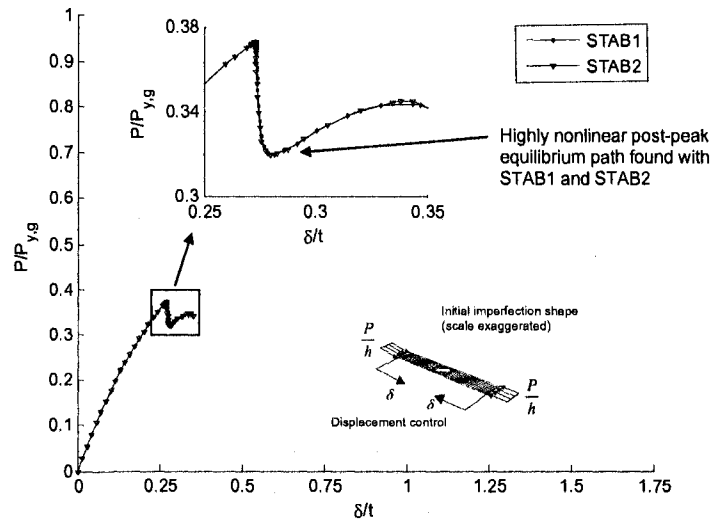


Figure 7.14 STAB1 and STAB2 load-displacement curves demonstrate a highly nonlinear post-peak equilibrium path

The ABAQUS solutions from models STAB1 and STAB2 in Figure 7.14 demonstrate a highly nonlinear post-peak equilibrium path. Both models are able to successfully predict the peak load and then move to a secondary load path. The solution terminates because the maximum number of Newton-Raphson iterations is reached. The modification of the moment residual limit R_n^Φ from 0.005 to 0.100 did not influence the solution results.

The STAB3 finite element model employs a uniform loading with the Newton-Raphson algorithm and artificial damping to determine the nonlinear response of the stiffened element with a slotted hole. The STAB3 boundary conditions are the same as those for the STAB1 and STAB2 models, where the plate edges are constrained to move together as rigid bodies (see Figure 7.8). Figure 7.15 compares the STAB1 and STAB2 (displacement control) to the STAB3 (load control) results and shows that, prior to yielding, the three models predict the same response. Differences in the load paths are observed after yielding though, especially in the STAB3 model, which reaches peak load and then carries this load with zero stiffness over a large deformation range. This unstable post-peak behavior results from a complete loss of stiffness as the hole collapses under load control. The peak loads predicted for the stiffened element by the displacement control STAB3 model is seven percent higher than the STAB1 and STAB2 load control solutions, demonstrating that the peak load is sensitive to the loading method (uniform load or uniform displacements) in this case.

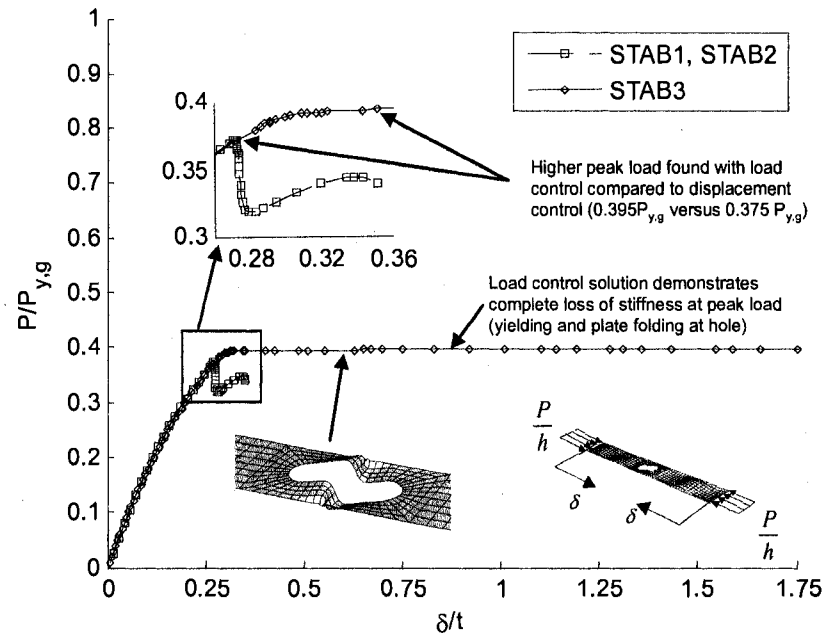


Figure 7.15 The STAB1 and STAB2 models (artificial damping, displacement control) exhibit a sharp drop in load as folding of the plate initiates near the hole. The STAB3 model (artificial damping, load control) finds the compressive load at which a complete loss of stiffness occurs.

7.1.4 Influence of a slotted hole on the ultimate strength of a stiffened element (without geometric imperfections)

The solution controls from the previous section resulting in successful simulations are now implemented to evaluate the influence of a slotted hole on the ultimate strength and failure mode of a stiffened element. The loading and boundary conditions, dimensions, material properties, and solution controls are the same as those used for the STAB2 model described in Section 7.1.3.4 and Table 7.1. Initial geometric imperfections are not considered.

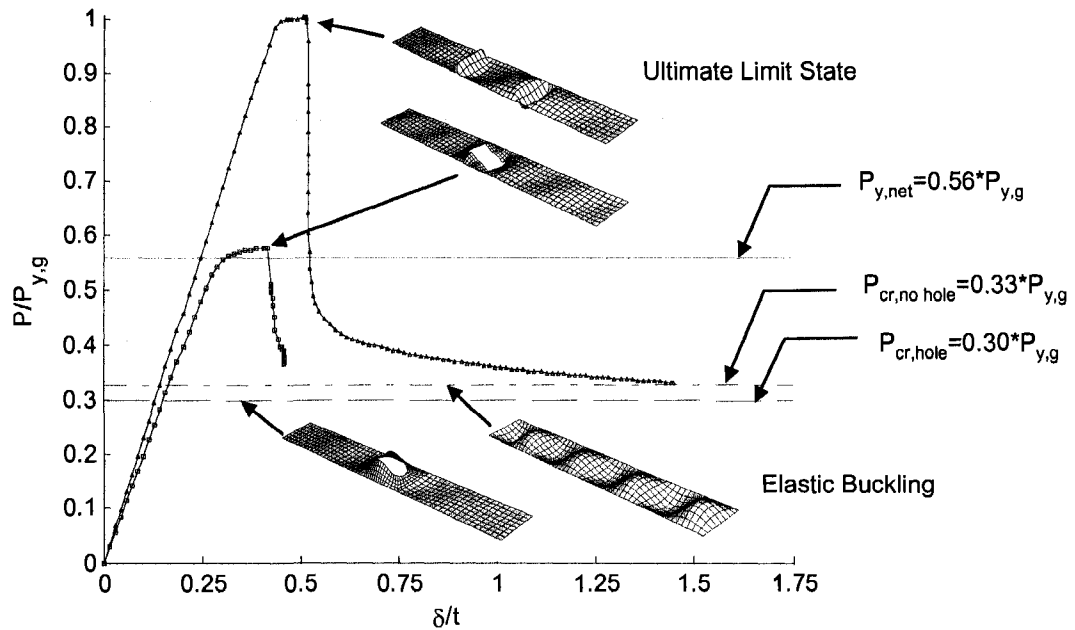


Figure 7.16 Comparison of ultimate limit state and elastic buckling plate behavior, initial imperfections are not considered in these results

Figure 7.16 demonstrates that the slotted hole reduces the strength of the stiffened element from $1.0 P_{y,g}$ to $0.58 P_{y,g}$, where $P_{y,g}$ is the resultant compressive force on the stiffened element to cause yielding calculated with the gross cross-sectional area of the plate. The predicted peak load of the stiffened element with the hole is consistent with the load at yielding of the net section, $P_{y,net} = 0.56 P_{y,g}$. This observation, that the strength of the stiffened element with the hole is limited to $P_{y,net}$, highlights an important consideration in the development of the Direct Strength Method in Chapter 8. The hole also reduces the axial stiffness of the stiffened element in this case, as demonstrated by the change in slope of the linear portion of the load-displacement curve in Figure 7.16.

7.1.5 Influence of geometric imperfection magnitudes on the ultimate strength of a stiffened element with and without a slotted hole

The ultimate strength of cold-formed steel members is sensitive to initial geometric imperfections. In this study the influence of imperfection magnitude on the ultimate strength of stiffened elements with and without a slotted hole is evaluated. The loading and boundary conditions, dimensions, material properties, and solution controls are the same as those used for the STAB2 model discussed in Section 7.1.3.4 and summarized in Table 7.1. The imperfection field is assumed as the fundamental elastic buckling mode pictured in Figure 7.9. Local buckling (Type 1) imperfection magnitudes corresponding to $P(\Delta < d_i) = 0.25, 0.50, 0.75, 0.95,$ and 0.99 from the CDF in Figure 7.32 are considered.

Figure 7.17 and Figure 7.18 present the load-displacement results for the stiffened element without and with the hole and demonstrate that increasing imperfection magnitudes reduces peak load and change post-peak response. The elastic stiffness is also softened, which can be observed by comparing the imperfection results to the linear slope of the load-displacement curve without imperfections. This softening results from the initial out-of-plane deformations which engage more of the bending stiffness of the plate and less of the axial stiffness as the plate is compressed. Out-of-plane deformations (such as initial imperfections) increase the magnitude of the geometric stiffness matrix which negates the initial elastic stiffness of the undeformed system. Imperfections are observed to decrease strength but increase ductility of the stiffened

element with and without a hole. The load-displacement results also highlight that the hole reduces the ductility of the stiffened element, which is consistent with the column experiment results in Chapter 5.

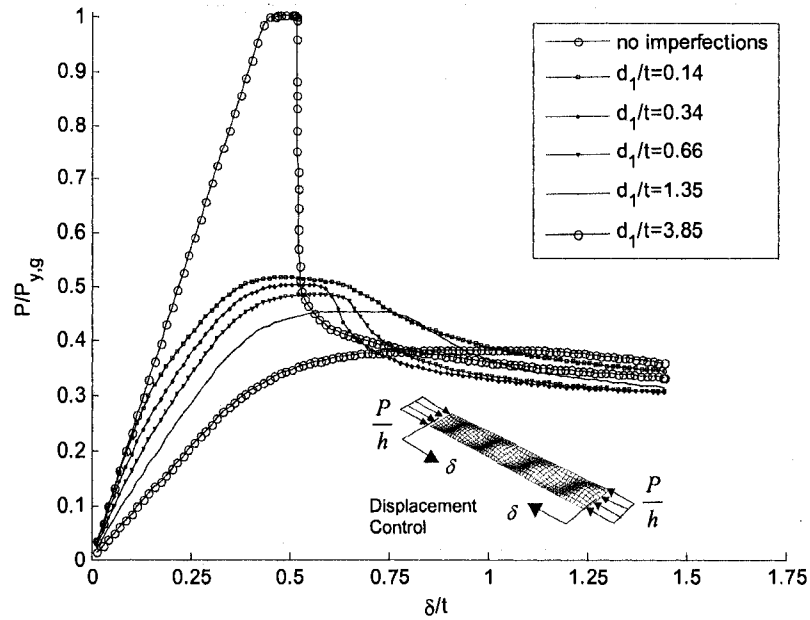


Figure 7.17 Load-displacement sensitivity to imperfection magnitude for a plate without a hole

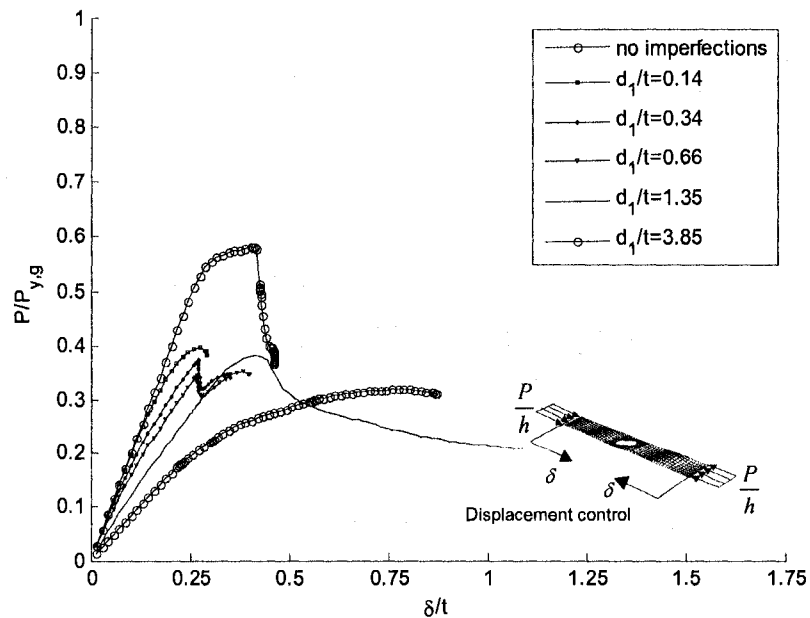


Figure 7.18 Load-displacement sensitivity to imperfection magnitude for a plate with a slotted hole

7.1.6 Determination of unstiffened element “effective width” using nonlinear finite element modeling

The “effective width” method provides an approximation to the complex non-uniform stress distribution in a thin buckled plate under compression. Initially presented in the 1930’s by von Karman and extended to cold-formed steel members by Winter in the 1940’s, the method accounts for the reduction in load-carrying capacity of a stiffened element (von Karman et al. 1932; Winter 1947). The inability of the center of the plate to carry compressive load is caused by out-of-plane deformations in the shape of the fundamental elastic buckling mode. These deformations reduce the axial stiffness, concentrating the compressive force at the edges of a plate. The ultimate load is reached when these edge stresses, carried by the “effective width”, exceed the yield stress of the plate material. The “effective width” concept is the basis of most cold-formed steel design codes around the world today.

In this study, a nonlinear finite element model is employed to calculate the longitudinal stress distribution at failure for a stiffened element with and without a slotted hole. The distribution of stresses for both cases is compared, and the variation in effective width along the length of the stiffened element is determined. The stiffened element is modeled with the same loading and boundary conditions, dimensions, material properties, and solution controls as those used for the STAB2 model discussed in Section 7.1.3.4 and described in Table 7.1. The initial imperfection geometry corresponds to the fundamental elastic buckling mode of the plate without the hole as described in Figure 7.9. $d_1/t=0.34$ is used to scale the initial imperfection field of the

plate, which corresponds to a probability of occurrence of $P(\Delta < d_i) = 0.50$ as discussed in Section 7.1.1. The effective width is calculated by first integrating the longitudinal (S_{11}) membrane stresses at cross-sections along the length of the stiffened element and then dividing the resulting areas by the yield stress of the steel as shown in Figure 7.19. The membrane stresses are the longitudinal (S_{11}) stresses that occur at the midplane of the stiffened element as defined in Figure 7.20.

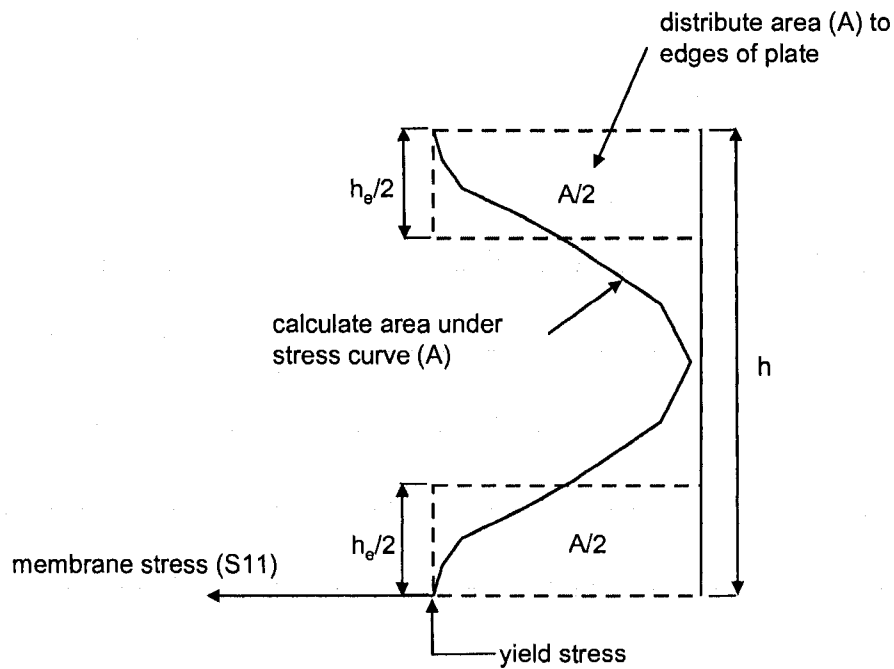


Figure 7.19 Calculation of "effective width" at a cross-section along a stiffened element

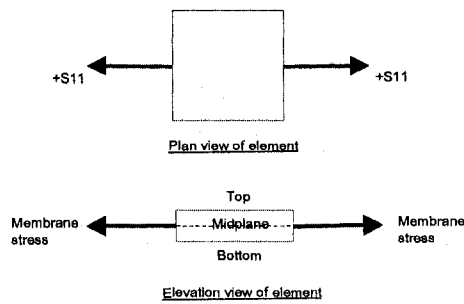


Figure 7.20 Definition of longitudinal (S_{11}) membrane stress

Figure 7.21(a) highlights the variation in membrane longitudinal stress (S11) occurring at the failure load of the stiffened element. The highest stresses accumulate along the edges of the plate and decrease toward the center of the plate. The largest edge stresses occur at the crests of the half-waves where the grey stress contours indicate yielding of the plate. The corresponding effective width is presented in Figure 7.21(b). The maximum effective width of $0.51 h_c/h$ occurs at the inflection point between half-waves, while the minimum effective width of $0.48 h_c/h$ occurs at the wave crests. The predicted effective width for this plate using Section B2.1 of the AISI specification is $0.50 h_c/h$ (AISI-S100 2007).

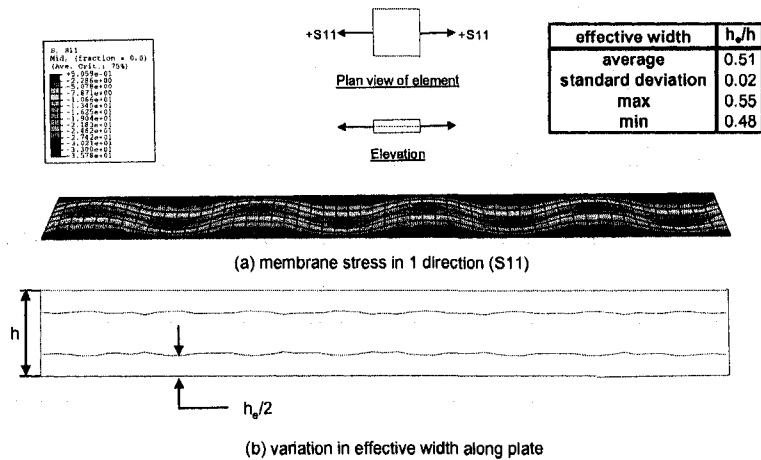


Figure 7.21 (a) longitudinal membrane stresses and (b) effective width of a stiffened element at failure

The failure mode of the stiffened element with the slotted hole is fundamentally different than without the hole. The stresses in Figure 7.22(a) demonstrate that yielding occurs only at the location of the hole when the peak load is reached. Compressive stresses are highest at the edge of the plate and then transition to tensile stresses at the

face of the hole. The effective width of the yielded portion of the plate in Figure 7.22(b) is less than that for the plate without the hole, even with the beneficial tensile stresses at the face. The average effective width is $0.38 h_e/h$, which is 25 percent less than that of the stiffened element without the hole. The predicted effective width using Section B2.2 of the AISI Specification is $0.30 h_e/h$. The effective widths of the stiffened element with and without a slotted hole are compared together in Figure 7.23.

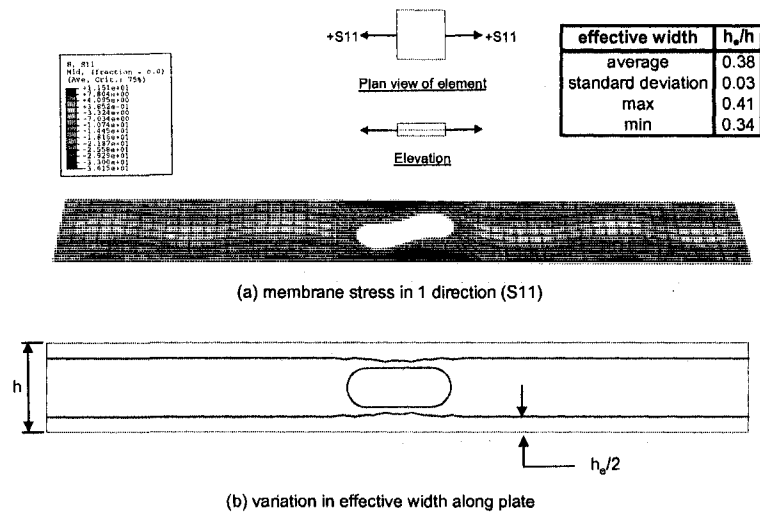


Figure 7.22 (a) longitudinal membrane stresses and (b) effective width of a stiffened element with a slotted hole at failure

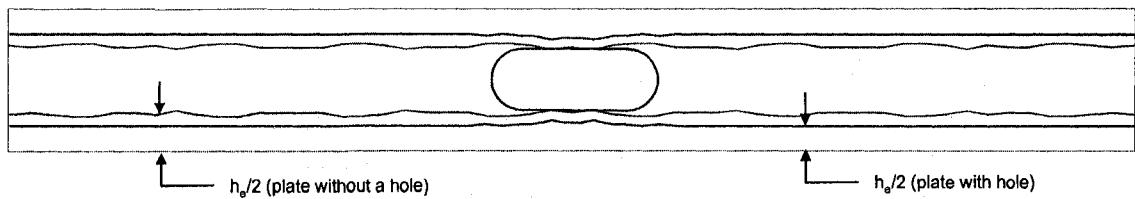


Figure 7.23 Effective width comparison for a plate with and without a slotted hole

The longitudinal stresses (S11) in the top and bottom fibers of the stiffened element at failure are different from the membrane stresses at the midplane, suggesting

that the effective width of a stiffened element actually varies through its thickness. Figure 7.24 and Figure 7.25 provide a comparison of this variation for a stiffened element with and without a slotted hole. It is observed that a plate is more effective on the surface where the out-of-plane deformation causes compression. The effective width is reduced when tensile and compressive stresses negate each other, as shown in the 2D plot of extreme fiber and membrane stresses at a representative cross-section in Figure 7.26.

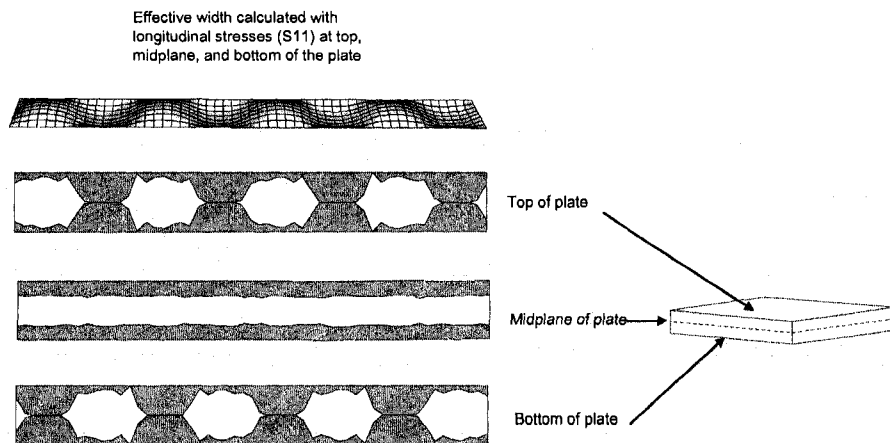


Figure 7.24 Through the thickness variation of effective width of a plate without a hole

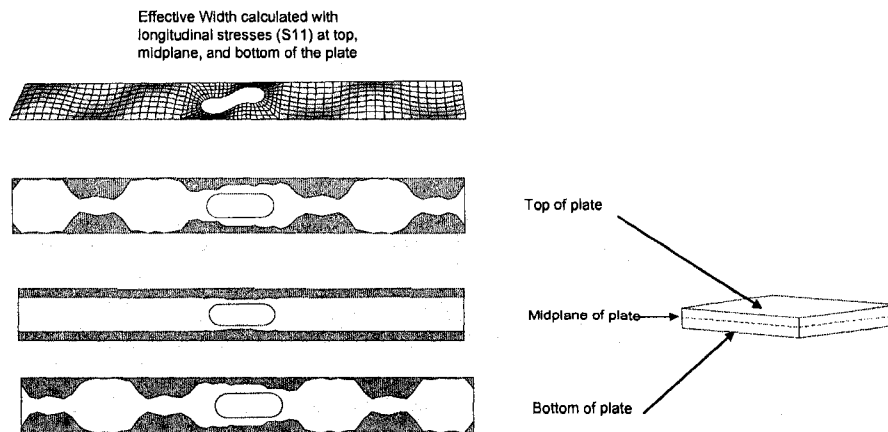


Figure 7.25 Through the thickness variation of effective width of a plate with a slotted hole

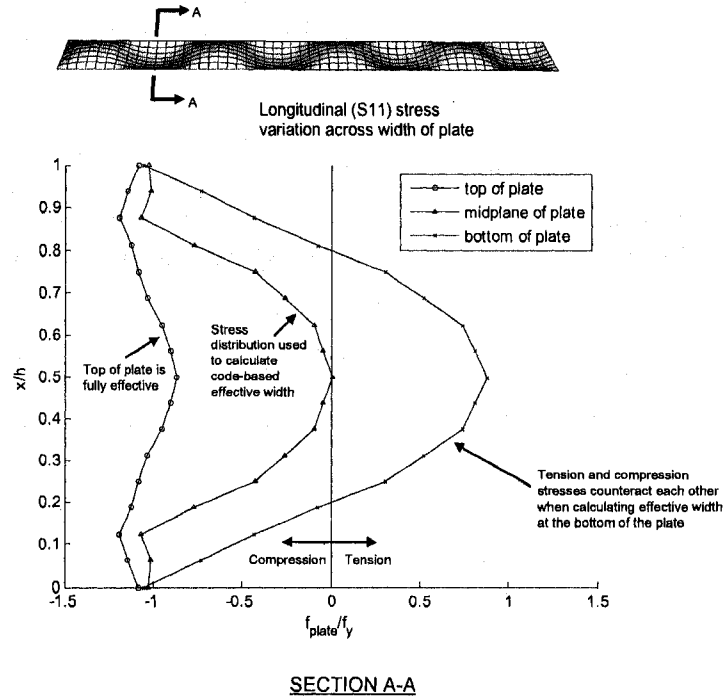


Figure 7.26 Through thickness variation in longitudinal (S11) stresses in a plate at failure

7.2 Nonlinear finite element modeling of columns with holes

A more extensive study of ABAQUS nonlinear finite element capabilities of cold-formed steel columns with holes is now presented. Simulation to collapse of the 24 column experiments described in Chapter 5 is performed, considering solution sensitivity to specific modeling parameters including initial imperfections, residual stresses and the cold-work of forming, nonlinear material modeling, and column boundary conditions. A modeling protocol is developed which produces results consistent with column experiments. This modeling tool is employed to explore the

validity of proposed Direct Strength Method equations for cold-formed steel members with holes presented in Chapter 8.

7.2.1 Modeling protocol development

7.2.1.1 Model dimensions and finite element meshing

The collapse behavior of the 24 column specimens is simulated with the general purpose finite element program ABAQUS (ABAQUS 2007a). All columns are modeled with S9R5 reduced integration nine-node thin shell elements (see Section 2.1 for details on the S9R5 element). The finite element mesh for each specimen is created with custom Matlab code developed by the author (see Appendix A); the mesh is consistent with S9R5 meshing guidelines summarized in Section 2.4. The centerline C-section dimensions input into ABAQUS are calculated using the out-to-out dimensions of each column specimen provided in Table 5.3. The cross-section corner angles are assumed as right angles (even though they were measured to be off of 90 degrees, see Table 5.4) since the distortional imperfection magnitudes obtained in Section 7.2.1.5 are derived based on a nominal cross-section with 90 degree corners*. The average base metal thickness for each specimen (i.e., the average of $t_{bare,w}$, $t_{bare,f1}$, and $t_{bare,f2}$ from Table 5.5) and column length L from Table 5.6 are used to construct the ABAQUS models, as are the location of the slotted web holes relative to the centerline of the web provided in Table 5.8.

* The measured flange-web and web-lip angles were not considered because of initial difficulties matching the experiment results to the simulations. To resolve these difficulties, a simplified model with nominal dimensions was implemented. (Modeling with plasticity at the proportional limit was found to be the true cause of the discrepancies, see Section 7.2.1.4.) Consideration of the actual cross-section dimensions, including the flared web-flange corners measured in the experiments, is warranted and is an important point of future study.

7.2.1.2 Boundary conditions and application of loading

The specimen boundary conditions in ABAQUS are defined to simulate the experiment boundary conditions as shown in Figure 7.27. The nodes on the loaded column face are coupled together in the direction of loading (1 direction) with an ABAQUS "pinned" rigid body constraint. This constraint ensures that all nodes on the loaded face of the column translate together, while the rotational degrees of freedom remain independent (as in the case of platen bearing). A total imposed displacement of 0.20 inches is applied to the reference node of the ABAQUS rigid body over a series of steps (see Section 7.2.1.3) to simulate the displacement control loading applied by the bottom platen during the experiment. Friction-contact boundary conditions were also evaluated in ABAQUS as described in Appendix J although their influence on the ultimate strength of the column specimens was determined to be minimal.

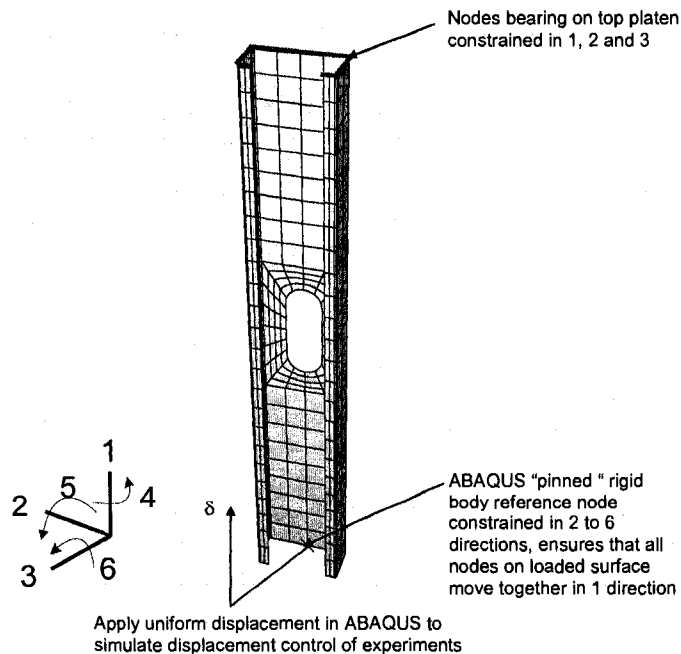


Figure 7.27 ABAQUS boundary conditions simulating column experiments

7.2.1.3 Nonlinear solution method

The modified Riks method (*STATIC, RIKS) is employed as the solution algorithm in this study. The preliminary nonlinear finite element studies on stiffened elements demonstrated that the modified Riks method was able to capture the complete load-deformation response when imposed displacements are used to load the member (see Figure 7.12). ABAQUS automatic time stepping was enabled, with the suggested initial step size set to 0.005, the maximum step size limited to 0.01, and the maximum number of increments equal to 300 all input by the user.

7.2.1.4 Material modeling

Steel yielding and plasticity is simulated in ABAQUS using a classical metal plasticity approach with isotropic hardening. A Mises yield surface is defined with the true stress and true plastic strain obtained from uniaxial tensile coupon tests for each specimen. Three stress-strain curves (west flange, east flange, and web) were obtained for each specimen (see Section 5.2.5). The experimentally obtained engineering stress-strain curves are converted to true stress and strain and then averaged point-by-point to produce a yield stress, proportional limit, and true stress-strain curve for each specimen. (The true plastic strains and associated stresses are input into ABAQUS with the *PLASTIC command.) For Mises stresses below the yield stress, linear elastic material behavior is assumed where $E=29500$ ksi and $\nu=0.3$.

Preliminary nonlinear modeling efforts for this study determined that including plastic strains starting at the proportional limit resulted in ABAQUS simulation predictions that were as much as 25% lower than the column tested strengths. An example of the average true stress-strain curves with plasticity starting at the proportional limit are provided in Figure 7.28a for specimen 362-1-24-NH and Figure 7.29a for specimen 600-1-24-NH (average true stress-strain curves are provided for all 24 column specimens in Appendix H). Other researchers have obtained simulation results consistent with experiments by assuming that plastic strains initiate only after the yield stress (determined with the 0.2% offset method) is reached (Schafer 1997; Yu 2005; Schafer et al. 2006) - a material modeling approach that proved to be successful at predicting the column experiment peak loads for this study also. The true stress-strain curves in Appendix H were therefore modified to ensure that plasticity initiates in ABAQUS only after the yield stress is reached for the gradually yielding stress-strain curves (362S162-33 specimens, see Figure 7.28b) and at the initiation of the yield plateau for the sharp-yielding curves (600S162-33 specimens, see Figure 7.29b). Figure 7.30 demonstrates the disparity between the experiment and FE simulation load-deformation response for column specimen 600-1-24-NH when plasticity initiates at the proportional limit. The reasons for this disparity are unclear and warrant future study. Additional research work is planned to study the details of metal plasticity in ABAQUS by loading a single finite element to failure in tension.

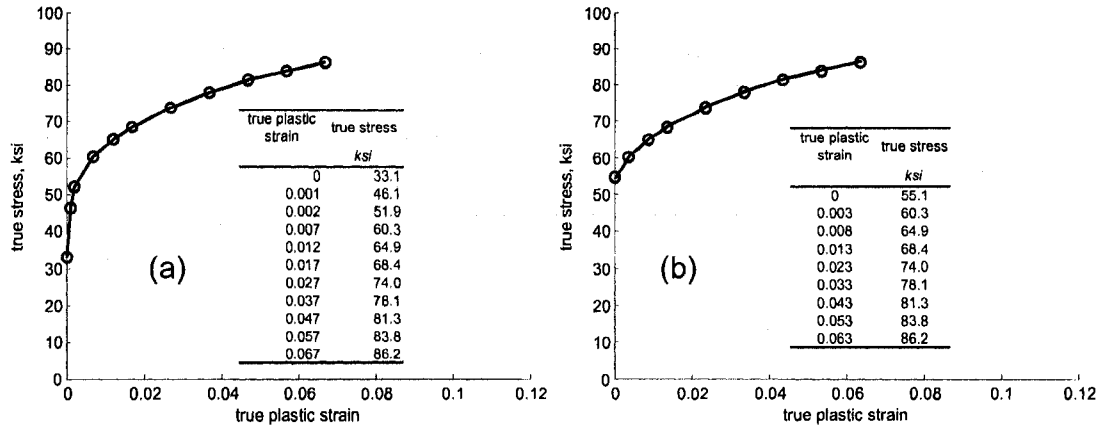


Figure 7.28 ABAQUS plastic strain curve for specimen 362-1-24-NH assuming (a) plasticity initiates at the proportional limit and (b) plasticity initiates at 0.2% offset yield stress

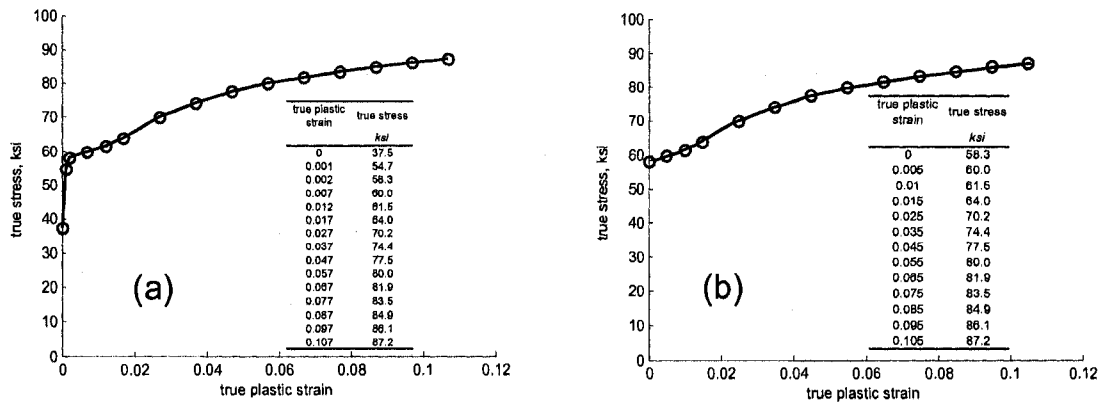


Figure 7.29 ABAQUS plastic strain curve for specimen 600-1-24-NH assuming (a) plasticity initiates at the proportional limit and (b) plasticity initiates at the beginning of the yield plateau (refer to Appendix H for the details on the development of this curve).

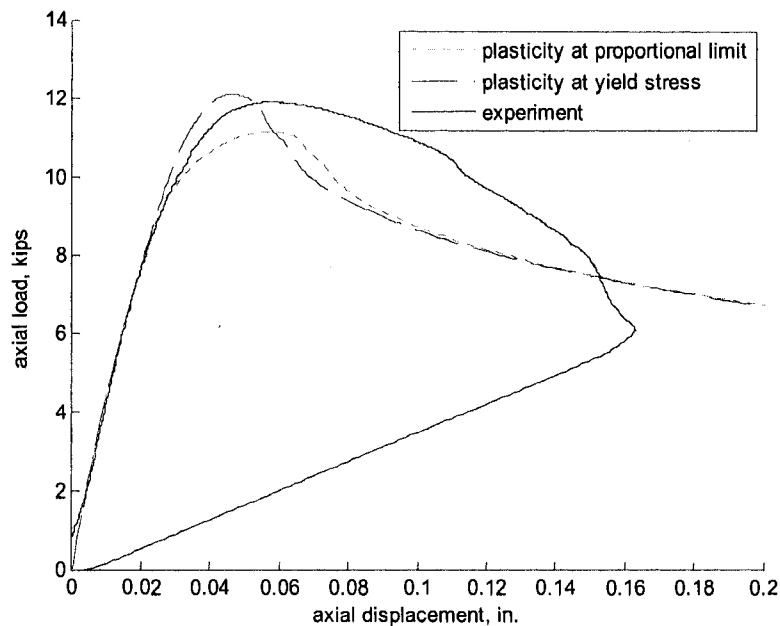


Figure 7.30 Influence of ABAQUS material model on the load-deformation response of specimen 600-1-24-NH (work this figure with Figure 7.29)

7.2.1.5 Initial geometric imperfections

The ultimate strength and failure mechanisms of cold-formed steel columns are sensitive to initial geometric imperfections, as demonstrated in the preliminary studies on stiffened elements in Section 7.1.5. In this study, the sympathetic local (L) and distortional (D) elastic buckling modes are obtained with eigenbuckling analyses for each column specimen and imposed on the nominal geometry in each finite element model. (An ABAQUS .fil file is created for each eigenbuckling analysis which is then called from the nonlinear .inp file with the *IMPERFECTION command). The boundary conditions at both specimen ends are assumed to be warping free when obtaining the imperfection shapes (see Figure 4.2 for definition) to ensure consistency with CUFSM boundary conditions. Specimens with and without holes are modeled with the same elastic buckling imperfection shapes by filling the holes with additional finite elements

as shown in Figure 7.31. This procedure ensures that the load-displacement behavior of both the hole and no hole specimens are compared on equivalent basis (both will have the no hole L and D imperfection shapes). Filling in the holes is necessary (instead of eliminating them completely) because it preserves the nodal numbering and geometry of the specimens with holes, making it convenient to superimpose the L and D modes onto the initial nodal geometry in ABAQUS.

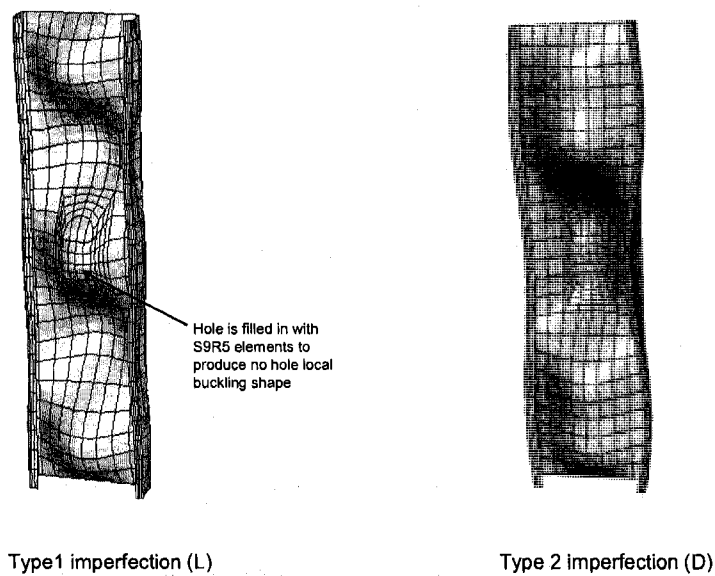


Figure 7.31 Slotted holes are filled with S9R5 elements to obtain no hole imperfection shapes

The magnitudes of the L and D imperfections are determined with the same probabilistic treatment used for the stiffened element studies in Section 7.1 (Schafer and Peköz 1998). Finite element simulations with L and D imperfection magnitudes corresponding to the 25th and 75th percentiles of the CDF in Figure 7.32 are performed for each specimen to obtain a range of simulated load-displacement responses to compare to experiment results. FE simulations are also performed using the L and D elastic

buckling mode shapes and imperfection magnitudes measured directly from the column specimens. In this case the local imperfection magnitude for each specimen is taken as the maximum deviation from the average web elevation as reported in Table 5.9. The distortional imperfection magnitude for each specimen is determined by finding the largest measured angular deviation from 90 degrees along each specimen and calculating the associated flange-lip displacement as shown in Figure 7.33. The Type 1 imperfection magnitudes measured in the experiments are often 2 to 3 times larger than the 75th percentile CDF magnitudes as shown in Table 7.2. The Type 2 imperfection magnitudes for the 362S162-33 specimens also are 2 to 3 times larger than the 75th percentile CDF magnitudes, primarily because these specimens tended to open up at the sawn ends (i.e., flange-web angles increased above 90 degrees) when they were saw-cut from full stud lengths. Other researchers have studied this observed change in cross-section after saw-cutting (Wang et al. 2006). The 600S162-33 specimens were less sensitive to this saw-cutting effect, resulting in measured distortional imperfection magnitudes consistent with the 75th percentile of the imperfection CDF.

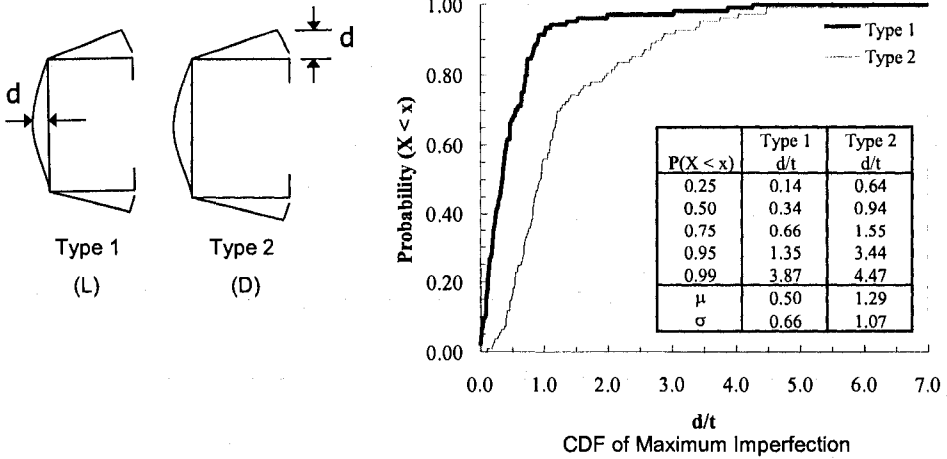


Figure 7.32 L and D imperfection magnitudes described with a CDF (Schafer and Peköz 1998)

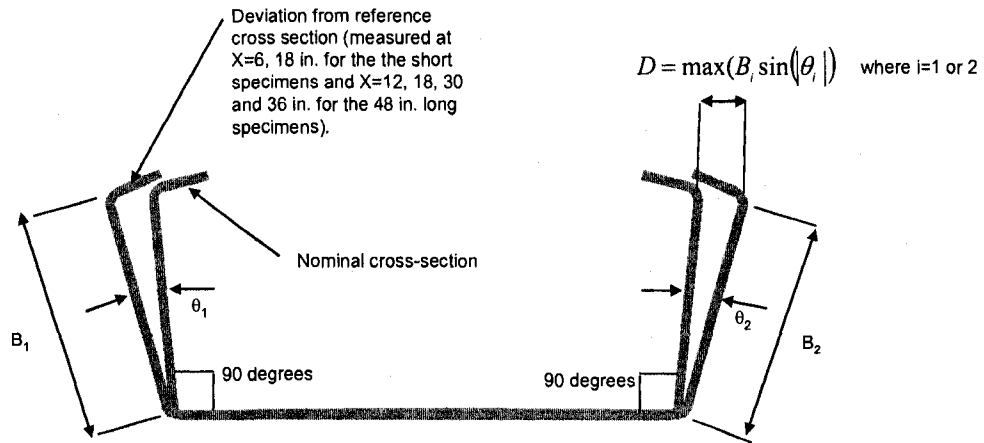


Figure 7.33 Method for measuring distortional imperfection magnitudes from experiments

Table 7.2 Local and distortional imperfection magnitudes

Specimen	Type 1 Imperfection Magnitude (L)			Type 2 Imperfection Magnitude (D)		
	25% CDF	75% CDF	Measured	25% CDF	75% CDF	Measured
362-1-24-NH	0.005	0.025	0.038	0.025	0.060	0.200
362-2-24-NH	0.005	0.025	0.054	0.025	0.060	0.174
362-3-24-NH	0.005	0.025	0.036	0.025	0.060	0.205
362-1-24-H	0.005	0.026	0.052	0.025	0.061	0.195
362-2-24-H	0.005	0.025	0.058	0.025	0.059	0.159
362-3-24-H	0.006	0.026	0.044	0.025	0.061	0.140
362-1-48-NH	0.005	0.026	0.071	0.025	0.061	0.168
362-2-48-NH	0.006	0.026	0.080	0.025	0.061	0.163
362-3-48-NH	0.005	0.026	0.057	0.025	0.060	0.184
362-1-48-H	0.005	0.026	0.084	0.025	0.061	0.161
362-2-48-H	0.005	0.026	0.066	0.025	0.061	0.174
362-3-48-H	0.006	0.026	0.050	0.026	0.062	0.156
600-1-24-NH	0.006	0.029	0.061	0.028	0.068	0.106
600-2-24-NH	0.006	0.029	0.075	0.028	0.068	0.114
600-3-24-NH	0.006	0.029	0.096	0.028	0.068	0.114
600-1-24-H	0.006	0.028	0.062	0.027	0.065	0.064
600-2-24-H	0.006	0.027	0.089	0.026	0.064	0.124
600-3-24-H	0.006	0.028	0.087	0.028	0.067	0.102
600-1-48-NH	0.006	0.029	0.071	0.028	0.067	0.090
600-2-48-NH	0.006	0.028	0.077	0.028	0.067	0.077
600-3-48-NH	0.006	0.029	0.073	0.028	0.067	0.074
600-1-48-H	0.006	0.028	0.095	0.027	0.066	0.084
600-2-48-H	0.006	0.028	0.049	0.027	0.067	0.062
600-3-48-H	0.006	0.028	0.068	0.028	0.067	0.099

The initial out-of-straightness of each column specimen was measured in the MTS machine under a small preload before the start of each test. This global imperfection is also superimposed on the nodal geometry for each specimen finite element model as

shown in Figure 7.34. The magnitude of the global imperfection, Δ_g , is provided in Table 7.3.

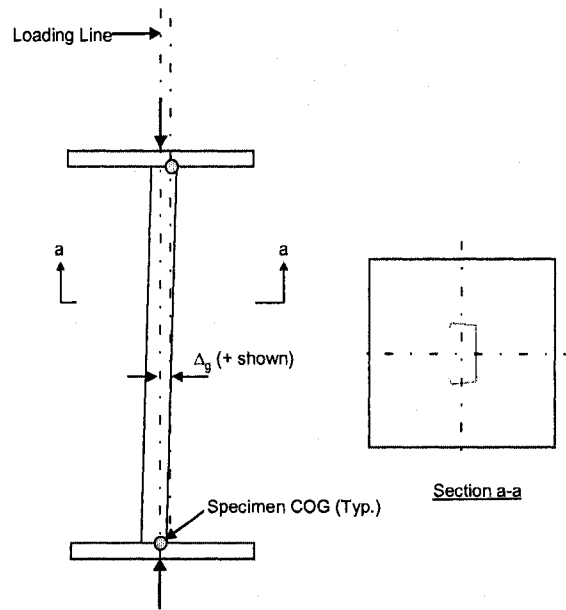


Figure 7.34 Definition of out-of-straightness imperfections implemented in ABAQUS

Table 7.3 Out-of-straightness imperfection magnitudes

Specimen	Δ_g in.
362-1-24-NH	-0.024
362-2-24-NH	0.004
362-3-24-NH	0.038
362-1-24-H	-0.012
362-2-24-H	0.034
362-3-24-H	-0.023
362-1-48-NH	0.047
362-2-48-NH	-0.028
362-3-48-NH	0.012
362-1-48-H	0.066
362-2-48-H	0.013
362-3-48-H	-0.003
600-1-24-NH	-0.063
600-2-24-NH	-0.141
600-3-24-NH	0.063
600-1-24-H	-0.078
600-2-24-H	0.076
600-3-24-H	0.069
600-1-48-NH	-0.036
600-2-48-NH	-0.087
600-3-48-NH	-0.049
600-1-48-H	-0.098
600-2-48-H	0.072
600-3-48-H	0.020

7.2.1.6 Residual stresses and equivalent plastic strains

Chapter 6 describes a general method for predicting the through thickness residual stresses and strains in cold-formed steel members which can then be readily input into ABAQUS. The prediction method assumes that residual stresses and plastic strains occur over the full cross-section from coiling, uncoiling, and flattening of the sheet coil. The coiling residual stresses are largest when the sheet thickness t is large (>0.068 in.) and the yield stress is low (<40 ksi). The predicted coiling, uncoiling, and flattening residual stresses (and plastic strains) are zero in this study because the column specimens have a relatively low sheet thickness (~ 0.040 in.) and high yield stress (~ 60 ksi).

Residual stresses and plastic strains from the roll-forming of the cross-section are considered in this study. These stresses are applied in ABAQUS with the element local coordinate system shown in Figure 7.35 starting from section point 1 (SNEG). The transverse residual stress distribution (2-direction) is provided in Figure 7.36 and the longitudinal distribution (1-direction) in Figure 7.37 as a function of yield stress σ_{yield} (σ_{yield} is listed in Table 5.13 for each specimen). Plastic strains are input into ABAQUS in von Mises space and therefore only plastic strain magnitudes are required, not a specific direction. The highest initial strains occur at the inner and outer surfaces of the corners as shown in Figure 7.38. ε_p is approximated using the procedure outlined in Figure 6.17.

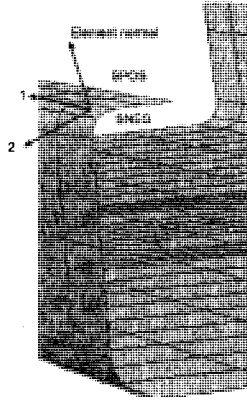


Figure 7.35 ABAQUS element local coordinate system for use with residual stress definitions

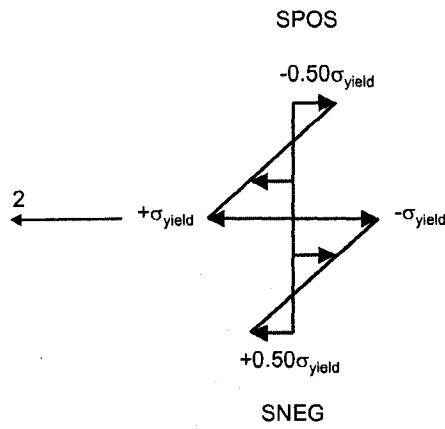


Figure 7.36 Transverse residual stress distribution applied at the corners of the cross-section

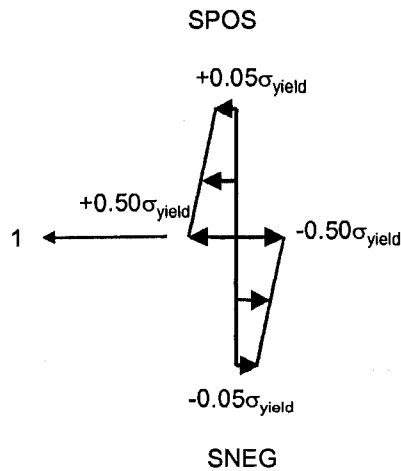


Figure 7.37 Longitudinal residual stress distribution applied at the corners of the cross-section

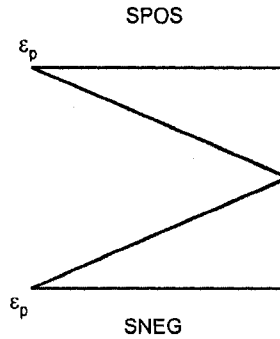


Figure 7.38 Equivalent plastic strain distribution at the corners of the cross-section

The transverse residual stress distribution has the special property that it is self-equilibrating for both moment and axial force, i.e. the total force and moment through the thickness is zero. This self-equilibrating characteristic ensures that no deformation (or redistribution of stress) will occur in ABAQUS in the initial state. The longitudinal stress distribution is self-equilibrating for axial force but not for moment. The deformations associated with this out-of-balance bending moment are infinitesimal and very small redistributions in stress are observed (± 0.1 ksi) in the initial state.

The number of element section points through the thickness dictates the accuracy of the residual stress distribution. If only a small number of section points are used, the discontinuity in stress at the middle thickness cannot be modeled accurately and excessive transverse deformations of the cross-section will occur. Figure 7.39 demonstrates the decrease in unbalanced through-thickness transverse moment, M_{UB} , as the number of section points increase (sheet thickness is assumed as $t=0.040$ in. and $\sigma_{yield}=60$ ksi). As the number of section points decrease, the residual stress approaches $0.50M_y$, where M_y is the yield moment of the sheet steel per unit width defined as:

$$M_y = \frac{t^2}{6} \sigma_{yield} \quad (7.4)$$

55 section points are used in the specimen finite element models for this study as a compromise between model accuracy and computational cost. ABAQUS limits the maximum number of section points to 250 for the S9R5 element (ABAQUS 2007b).

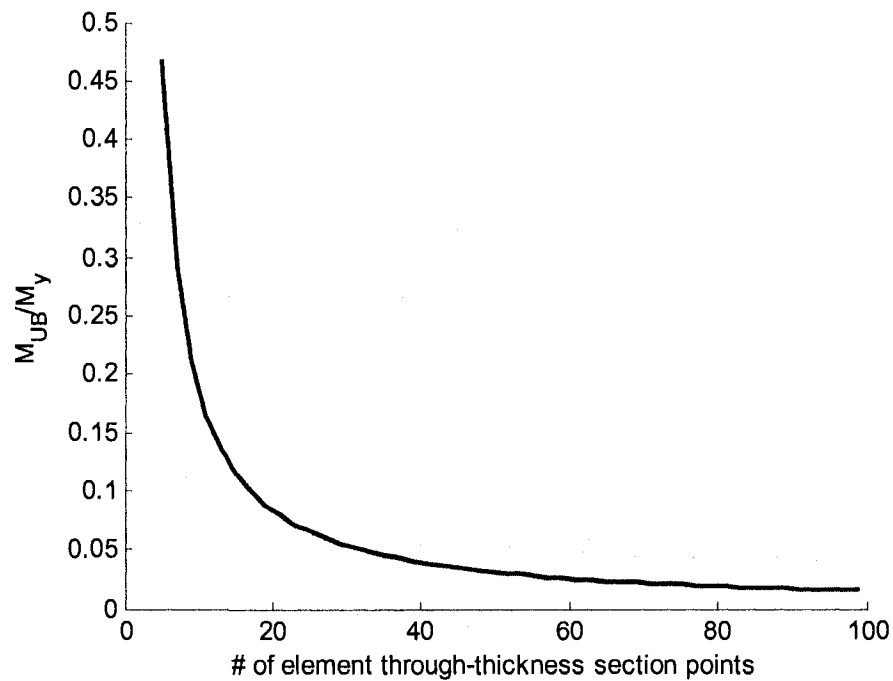


Figure 7.39 Influence of section points on the unbalanced moment (accuracy) of the transverse residual stress distribution as implemented in ABAQUS

7.2.2 Modeling protocol validation

7.2.2.1 Ultimate strength and failure mechanisms

The nonlinear finite element protocol presented in Section 7.2.1 is demonstrated to be a viable, conservative predictor of peak load when compared to the experiment results in Table 7.4. The mean of the experimental peak load P_{test} to ABAQUS peak load

P_{ABAQUS} ratios are 1.03 (25th percentile imperfection CDF), 1.05 (75th percentile imperfection CDF), and 1.11 (measured imperfections). In a few cases (and always with specimens with holes), ABAQUS was not able to obtain the peak load, either because the modified Riks solution algorithm reversed the direction of the applied load (similar to that observed in Figure 7.12 for stiffened elements) or because the ABAQUS could not find equilibrium and terminated the simulation. As imperfection magnitudes increased, the modified Riks solution algorithm was more successful at reaching peak load. This trend is hypothesized to occur because for small imperfection magnitudes a specific deformation pattern is not established and many equilibrium paths exist near peak load, whereas for larger imperfection magnitudes a dominate deformation shape and equilibrium path are defined early in the simulation. Nonlinear FE load-displacement behavior is provided for a representative sample of specimens in Figure 7.40 to Figure 7.47, including the load-displacement curves and deformed shape at collapse (compare these simulated shapes to the pictures of experiments in Appendix F). FE simulation load-displacement curves are provided for all specimens in Appendix I.

Table 7.4 Comparison of nonlinear FE simulation peak loads to experiments

Specimen	P _{test}	25th percentile imperfection CDF		75th percentile imperfection CDF		Measured imperfections	
		P _{ABAQUS}	P _{test} /P _{ABAQUS}	P _{ABAQUS}	P _{test} /P _{ABAQUS}	P _{ABAQUS}	P _{test} /P _{ABAQUS}
		kips	kips	kips		kips	
362-1-24-NH	10.48	10.26	1.02	9.88	1.06	8.72	1.20
362-2-24-NH	10.51	10.13	1.04	9.70	1.08	8.82	1.19
362-3-24-NH	10.15	10.21	0.99	9.85	1.03	8.69	1.17
362-1-24-H	10.00	9.22	1.09	9.08	1.10	8.48	1.18
362-2-24-H	10.38	8.83	1.18	8.70	1.19	8.27	1.26
362-3-24-H	9.94	9.19	1.08	9.11	1.09	8.78	1.13
362-1-48-NH	9.09	9.48	0.96	9.34	0.97	7.76	1.17
362-2-48-NH	9.49	9.40	1.01	9.27	1.02	8.36	1.14
362-3-48-NH	9.48	9.26	1.02	8.89	1.07	7.44	1.28
362-1-48-H	8.95	8.97	1.00	8.73	1.02	8.30	1.08
362-2-48-H	9.18	8.91	1.03	8.63	1.06	8.26	1.11
362-3-48-H	9.37	8.58	1.09	DNC	---	ED	---
600-1-24-NH	11.93	12.14	0.98	12.03	0.99	11.83	1.01
600-2-24-NH	11.95	12.10	0.99	12.01	1.00	11.74	1.02
600-3-24-NH	12.24	12.10	1.01	11.99	1.02	11.64	1.05
600-1-24-H	12.14	DNC	---	11.63	1.04	11.45	1.06
600-2-24-H	11.62	11.10	1.05	11.08	1.05	10.82	1.07
600-3-24-H	11.79	DNC	---	11.76	1.00	11.49	1.03
600-1-48-NH	11.15	11.27	0.99	11.14	1.00	11.32	0.98
600-2-48-NH	11.44	11.27	1.02	11.39	1.00	11.30	1.01
600-3-48-NH	11.29	11.37	0.99	11.18	1.01	11.04	1.02
600-1-48-H	11.16	DNC	---	10.22	1.09	ED	---
600-2-48-H	11.70	DNC	---	DNC	---	10.17	1.15
600-3-48-H	11.16	DNC	---	10.35	1.078	10.30	1.08
Average			1.03		1.05		1.11
Standard deviation			0.05		0.05		0.08

DNC Did Not Complete, Abaqus terminated before finding the peak load
ED Excessive distortion - Abaqus error, imperfection magnitude causes element distortional

The initial elastic slope of the 25% CDF and 75% CDF FE load-displacement curves are consistent with experimental results as shown in Figure 7.40 to Figure 7.47, demonstrating that the elastic material modeling assumptions and specimen dimensions are consistent with the experiments. The initial slope of the load-displacement curve is also sensitive to imperfection magnitudes, and therefore the similarities between experiment and the FE results confirm the assumption that the 25th and 75th percentile imperfection magnitudes in the FE simulations produce physically realistic results. This is contrary to the FE simulations with measured imperfections for the 362S162-33 specimens (for example, see Figure 7.40), where the initial load-displacement slope and peak load are 15% to 30% less than the experimental results (see Table 7.4 and Figure 7.40). The FE simulations for the 600S162-33 specimens are much less sensitive to imperfection magnitudes (for example, see Figure 7.44). The maximum difference in test to predicted ratio between the three imperfection levels (25% CDF, 75% CDF, and measured) in Table 7.4 for the 600S162-33 specimens is 3%.

The post-peak ductility of the column specimens is often underpredicted in the ABAQUS nonlinear finite element models. The collapse mechanism of a column dictates its ductility and in some cases its peak load. For example, outward distortional buckling has been shown to produce lower column strengths than inward distortional buckling (Silvestre and Camotim 2005). This observation could explain why the FE simulations of the 362S162-33 specimens with holes (which exhibit outward distortional buckling) have a lower peak load and ductility than the experiment results (all three specimens exhibit inward distortional buckling, see Appendix F). Another factor influencing column ductility may be the ABAQUS material modeling effect discussed in Section 7.2.1.4. When plasticity is considered at the proportional limit (see Figure 7.30) the peak of the load-displacement curve is flattened which is more consistent with experiment results. These hypotheses motivate important future work to better understand metal plasticity and material modeling in ABAQUS and also the influence of imperfection shapes on FE column ductility and strength predictions.

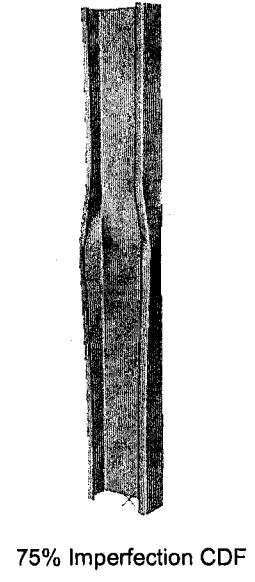
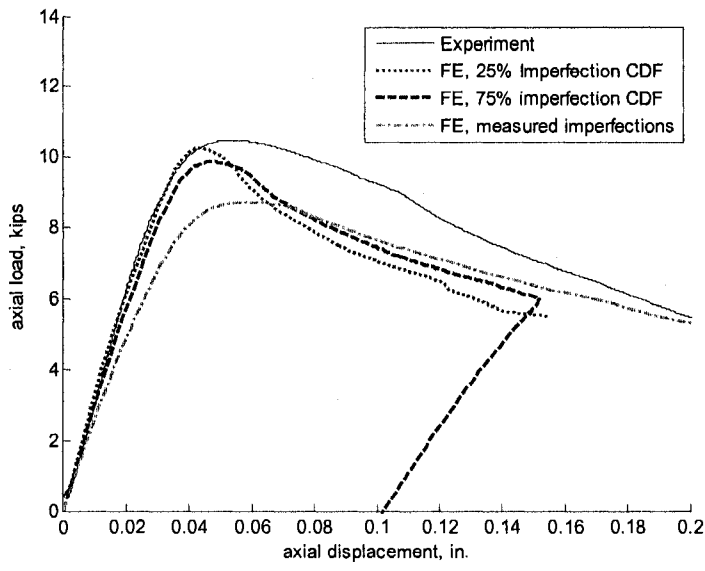


Figure 7.40 Load-displacement response of specimen 362-1-24-NH

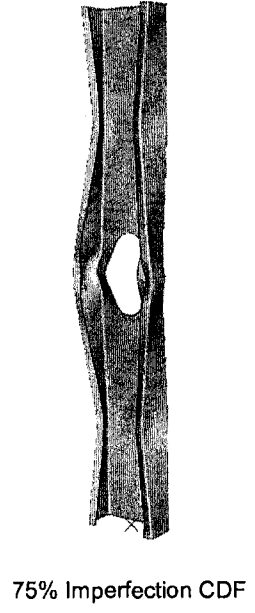
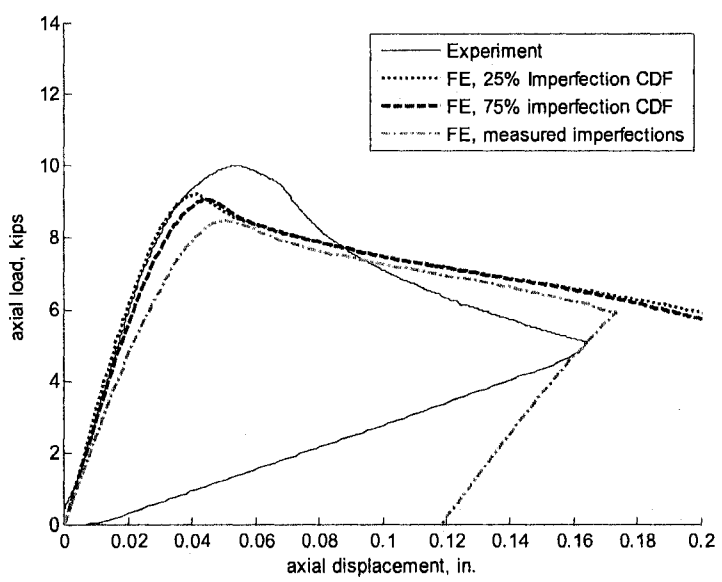


Figure 7.41 Load-displacement response of specimen 362-1-24-H

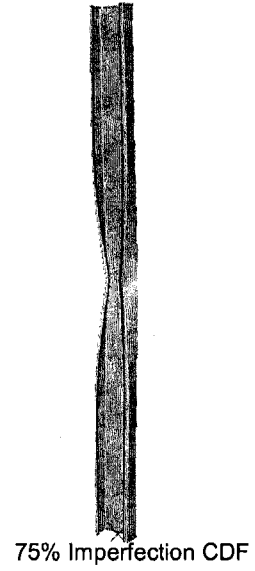
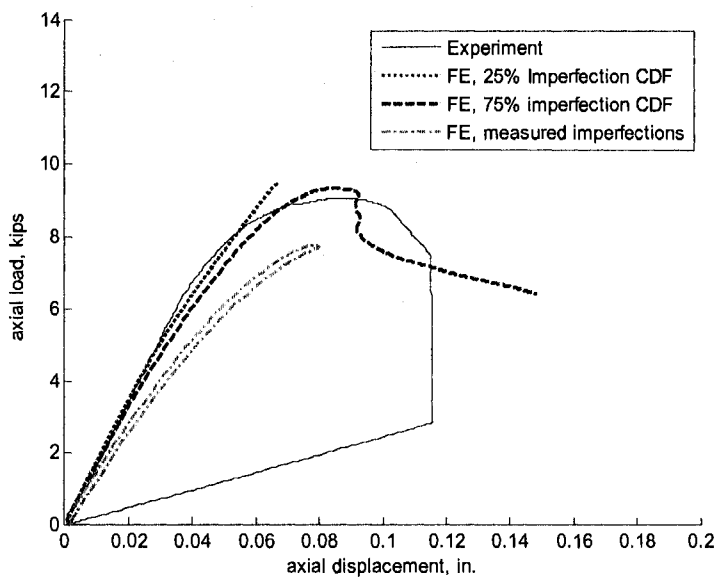


Figure 7.42 Load-displacement response of specimen 362-1-48-NH

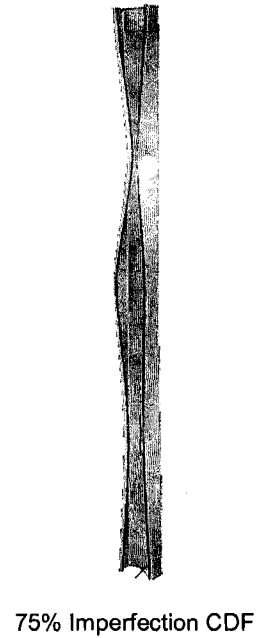
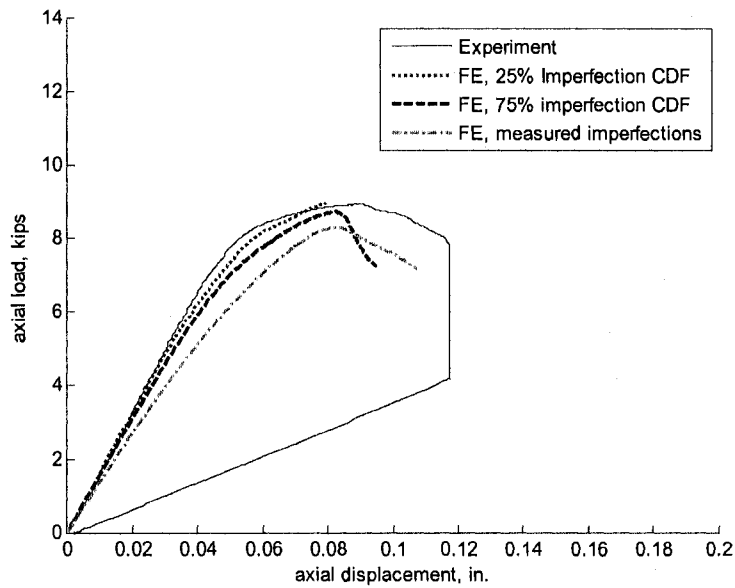


Figure 7.43 Load-displacement response of specimen 362-1-48-H

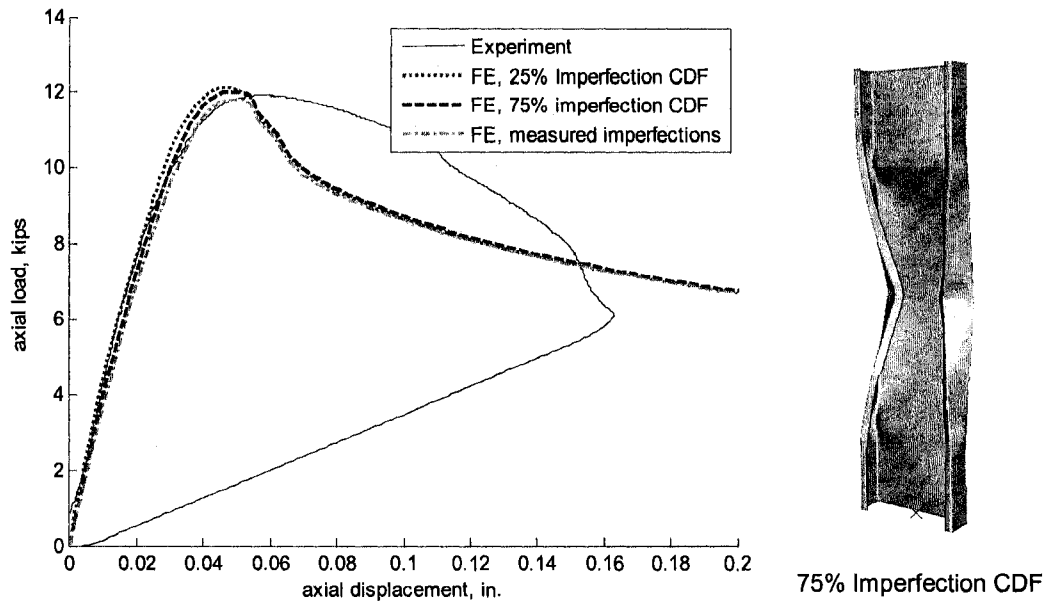


Figure 7.44 Load-displacement response of specimen 600-1-24-NH

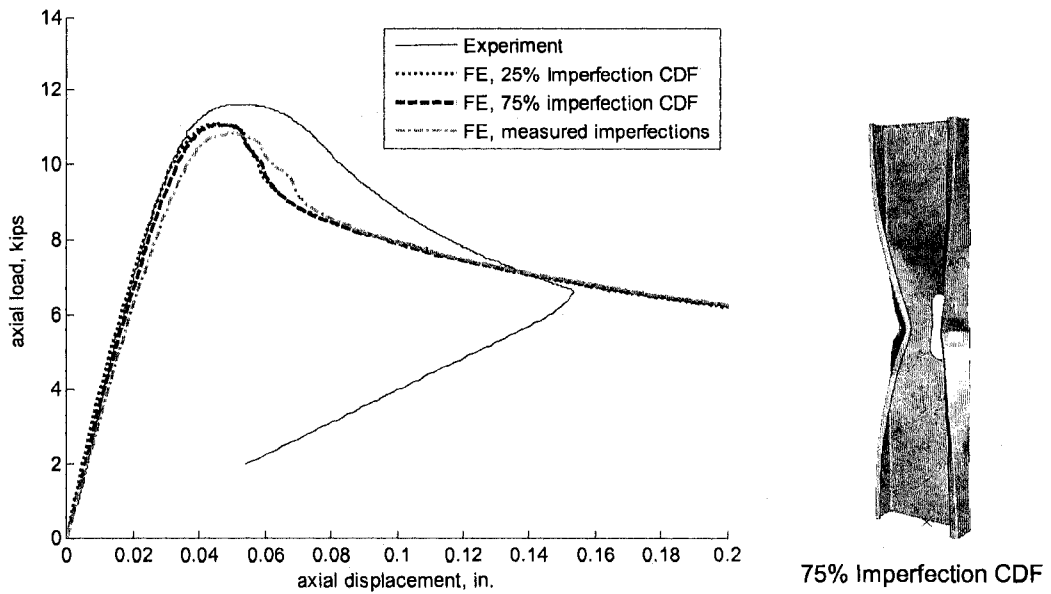


Figure 7.45 Load-displacement response of specimen 600-2-24-H

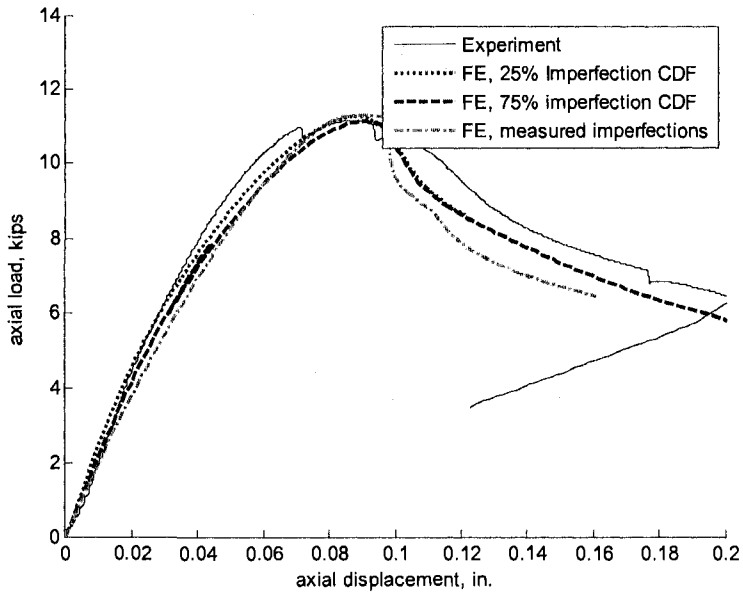


Figure 7.46 Load-displacement response of specimen 600-1-48-NH

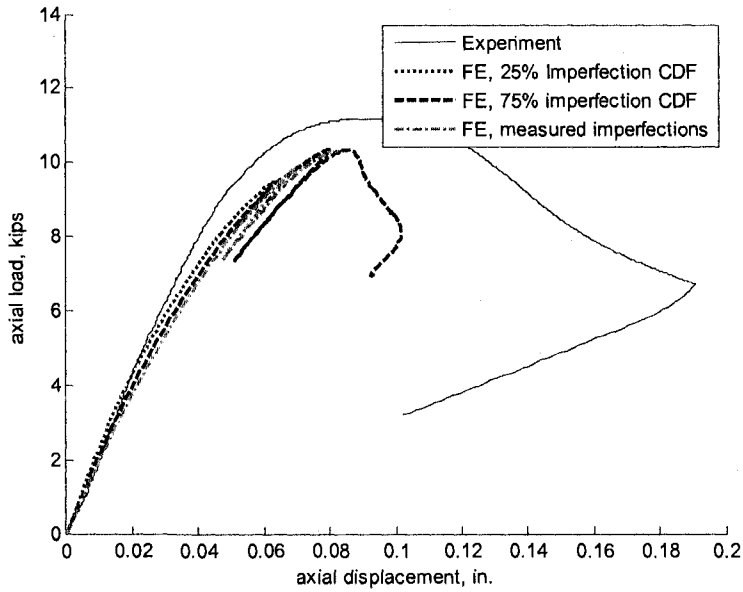


Figure 7.47 Load-displacement response of specimen 600-3-48-H

7.2.2.2 Influence of residual stresses and initial plastic strains

Residual stresses (RS) and initial plastic strains (PS) from the manufacturing process are approximated with the prediction method in Chapter 6 and then input into ABAQUS as discussed in Section 7.2.1.6. Figure 7.48 highlights their effect on the load-deformation response of specimen 600-1-24-NH. A small increase in peak load (approximately 2%) is observed when just initial plastic strains are considered at the corners, which simulates the increase in apparent yield stress from strain hardening. The increase in strength is minimal because the influence of the stiffened corners is offset by the large proportion of unformed steel (i.e., flats) in the cross-section. The transverse and longitudinal residual stresses created by cold-bending of the cross-section also have a minimal impact on the load-deformation response for this specimen, primarily because the plastic strains at the corners are high (ϵ_p is predicted to be large as 0.20 at the corner outer fibers) which increases the apparent yield stress in ABAQUS and prevents a loss in stiffness at the corners, even with the presence of the through-thickness residual stresses in the column. Similar load-displacement trends are also observed for specimen 362-1-24-NH as shown in Figure 7.49.

Residual stresses and plastic strains are expected to have a larger influence on the ultimate strength of members with cross-sections made from thicker sheet steel, since coiling and uncoiling of the sheet steel will impart residual stresses and plastic strains around the entire cross-sections (see Figure 6.19). Future research is planned to study the influence of through-thickness residual stresses and plastic strains on yielding

patterns and failure modes of cold-formed steel members. The ABAQUS metal plasticity model with isotropic versus kinematic hardening also needs further study to determine if one is better than the other when considering the influence of residual stresses and strains (see Section 6.7 for a more detailed discussion).

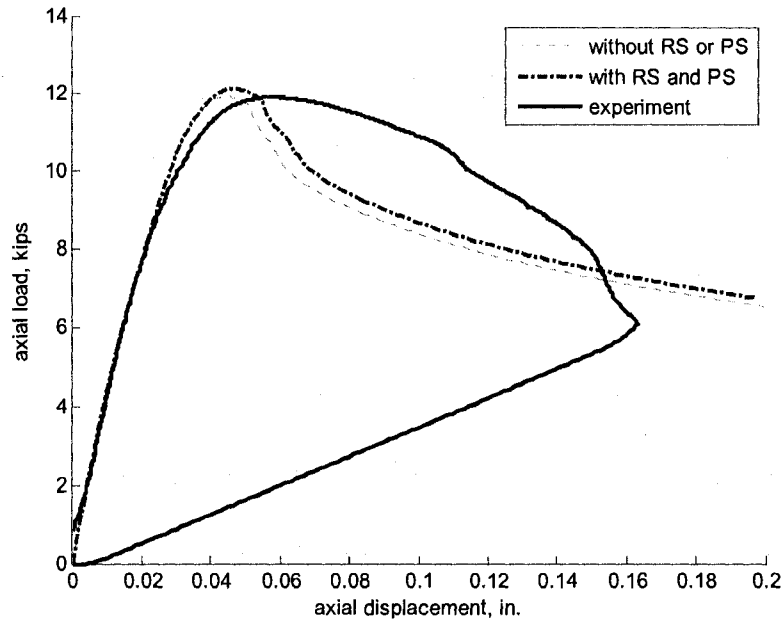


Figure 7.48 Influence of residual stresses (RS) and plastic strains (PS) on the FE load-displacement response of specimen 600-1-24-NH

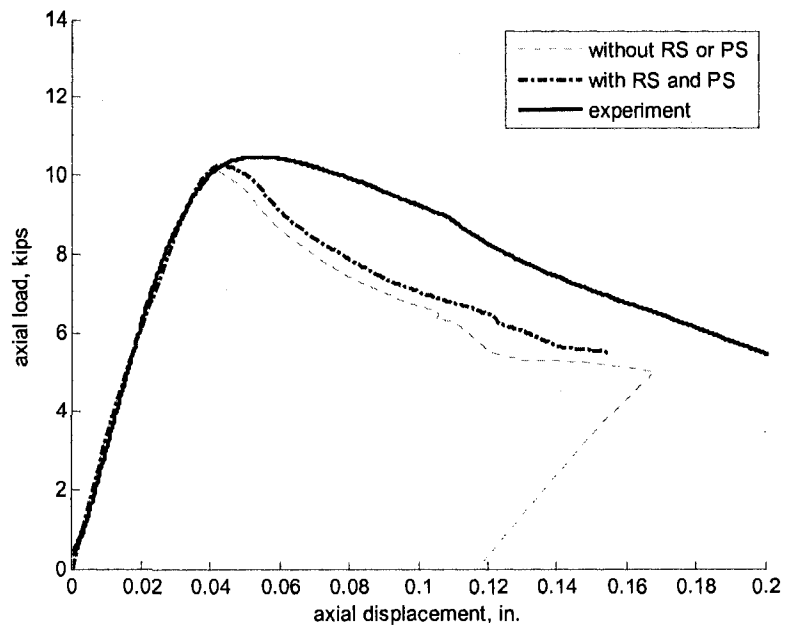


Figure 7.49 Influence of residual stresses (RS) and plastic strains (PS) on the FE load-displacement response of specimen 362-1-24-NH.

Chapter 8

The Direct Strength Method for cold-formed steel members with holes

The nonlinear finite element capability developed in Chapter 7 is now employed to evaluate proposed Direct Strength Method (DSM) formulations for cold-formed steel members with holes. Several hundred cold-formed steel columns and beams with standard SSMA structural stud cross-sections (SSMA 2001) and with varying web hole sizes, shapes, and spacings are simulated to collapse in ABAQUS. The elastic buckling properties of these members (P_{crf} , P_{crd} , and P_{cre} for columns and M_{crf} , M_{crd} , and M_{cre} for beams), including the presence of the holes, are approximated with the CUFSM elastic buckling prediction methods developed in Chapter 4. The corresponding ultimate strengths (obtained from the ABAQUS simulations) are merged with the elastic buckling information into a simulated experiments database which is utilized to identify potential modifications to the existing DSM local, distortional, and global failure prediction curves. Specific DSM options are proposed from these comparisons, which are then

compared to the experiment elastic buckling and tested strength databases in Chapter 4 to formalize the final proposed DSM recommendations for cold-formed steel members with holes.

8.1 DSM for columns with holes

8.1.1 Database of simulated column experiments

Simulated experiments were conducted on 211 C-section columns with evenly-spaced slotted or circular web holes in ABAQUS. Column lengths and cross-sections were specifically selected with custom Matlab code employing the existing DSM design curves to identify columns predisposed to local, distortional, and global buckling type failures. The cross-sections were chosen from a catalog of 99 industry standard C-sections published by the Steel Stud Manufacturers Association (SSMA 2001). The nominal out-to-out dimensions provided in the SSMA catalog were converted to centerline dimensions and then constructed in ABAQUS with the meshing procedure described in Section 7.2.1.1. Evenly spaced circular or slotted web holes were placed in the columns with hole spacing S (defined in Figure 3.2) varying between 12 and 22 inches. The holes were centered transversely in the web and their depth, h_{hole} , was varied such that the ratio of the net cross-sectional area, A_{net} , to the gross cross-sectional area, A_g , ranged between 0.60 and 1.0.

The ABAQUS boundary conditions and application of loading, described in Figure 8.1, are implemented to be consistent with CUFSM, i.e. pinned-pinned and free-to-warp with a uniform stress applied at the member ends. These boundary conditions were

specifically chosen to permit the use of CUFSM simplified elastic buckling methods when predicting the elastic buckling behavior of columns with holes. (If pinned-pinned warping-fixed end conditions or fixed-fixed end conditions were used the elastic buckling predictions would have required modifications factors, see Eq. (4.8) for an example). CUFSM boundary conditions represent a lower bound on member strength are therefore considered conservative in design. Consistent nodal loads are applied to simulate the uniform compressive stress at the column ends (see Section 7.2.1.2 for information on S9R5 consistent nodal loads). The loads (a reference load of 1 kip was applied at each end in ABAQUS) are distributed over the first two sets of cross-section nodes to avoid localized failures at the loaded edges.

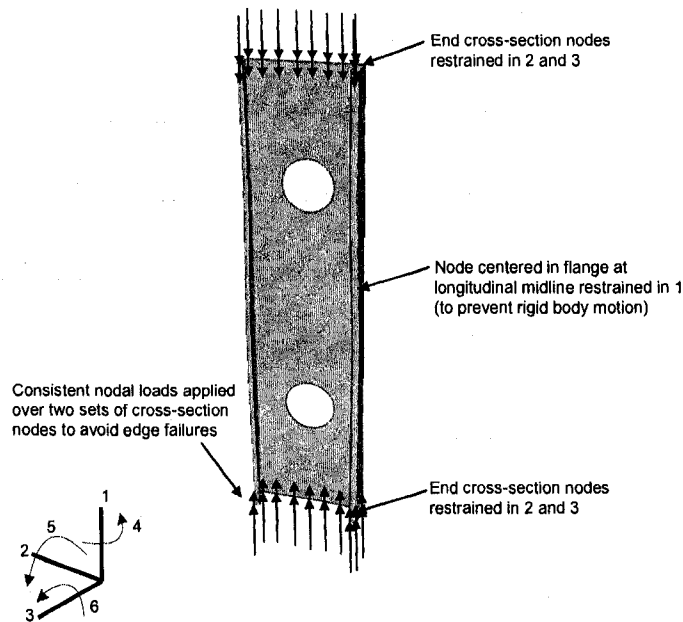


Figure 8.1 ABAQUS simulated column experiments boundary conditions and application of loading

The ABAQUS simulations were performed with the modified Riks nonlinear solution algorithm. Automatic time stepping was enabled with a suggested initial arc

length step of 0.25 (the Riks method increments in units of energy, in this case kip·in.), a maximum step size of 0.75, and the maximum number of solution increments set at 300. Metal plasticity was simulated with the material modeling procedure described in Section 7.2.1.4. The plastic true stress-strain curve for specimen 362-1-48-H in Appendix H was assumed for all column models (but modified so that plasticity starts at the yield stress, see Section 7.2.1.4), where the steel yield stress $F_y=58.6$ ksi. Residual stresses and initial plastic strains, as discussed in Section 7.2.1.6, were not considered in the ABAQUS models because their implementation requires further validation and they were not observed to markedly influence column ultimate strength (see Figure 7.48 and Figure 7.49).

Imperfections were imposed on the initial column geometry in ABAQUS with custom Matlab code which combines the local, distortional buckling, and global cross-section mode shapes from CUFSM along the column length. Two simulations were performed for each column, one model with 25% CDF local and distortional imperfection magnitudes and $L/2000$ global imperfections (where L is the length of the column) and the other model with 75% CDF local and distortional imperfection magnitudes and a global imperfection magnitude of $L/1000$ (see Section 7.2.1.5 for local and distortional imperfection definitions).

The global imperfection magnitude assumptions are based on hot-rolled column out-of-straightness measurements (Galambos 1998b) because no formal guidelines are currently available for cold-formed steel columns. The use of hot-rolled steel column imperfection magnitudes is consistent with the DSM approach for global buckling

controlled failures. DSM employs the same global design curve as that specified by the Structural Stability Research Council (SSRC) for hot-rolled steel (Galambos 1998b), thereby indirectly assuming that the influence of hot-rolled steel global imperfection magnitudes also apply to cold-formed steel. The global imperfection shape of the columns in the simulation database was either weak-axis flexural buckling or flexural-torsional buckling, depending on the cross-section dimensions and length of the column. C-sections are not symmetric about their weak bending axis, and therefore the direction of the global imperfection influences the predicted strength when weak-axis flexural buckling defines the global imperfection shape (e.g., web in compression from bowing or flange lips in compression from bowing). Simulations with both $\pm L/1000$ and $\pm L/2000$ imperfection magnitudes were performed to capture this strength effect for weak-axis flexural buckling mode shapes. Global imperfections were not considered for columns with $L/D \leq 18$ (i.e., stockier columns with a low sensitivity to global imperfections), where D is the out-to-out flange width of the column.

The local (P_{crf}), distortional (P_{crd}), and global (P_{cre}) critical elastic buckling loads were predicted for each column with custom Matlab code based on the CUFSM prediction methods described in Section 4.2.7. The database of simulated column experiments, including cross-section type, column and hole geometry, simulated ultimate strength (P_{test25} and P_{test75}) and critical elastic buckling loads for each column (including the presence of holes) is provided in Appendix K.

8.1.2 Distortional buckling study

A group of 20 columns from the SSMA column simulation database was chosen to evaluate the influence of the ratio A_{net}/A_g on the tested strength of columns predicted to collapse with a distortional failure mode. A_g is the gross cross-sectional area of a column and A_{net} is the cross-sectional area at the location of a hole. In this study the column length, L , is held constant at 24 in. and the column widths range from 6 in. to 12 in. The SSMA cross-sections chosen have relatively thick sheet steel (t up to 0.1017 in.) which prevents a local buckling type failure. The web of each column has two circular holes where the hole spacing $S=12$ in (see Figure 3.2 for the definition of S). The hole depth (diameter), h_{hole} , is varied for each column to produce A_{net}/A_g of 1.0 (no holes), 0.9, 0.8, 0.7, and 0.6. Refer to Appendix K, Study Type D, for specific cross-section and hole geometry information for each column. Figure 8.2 provides an example of an SSMA 600S250-97 structural stud column considered in the study.

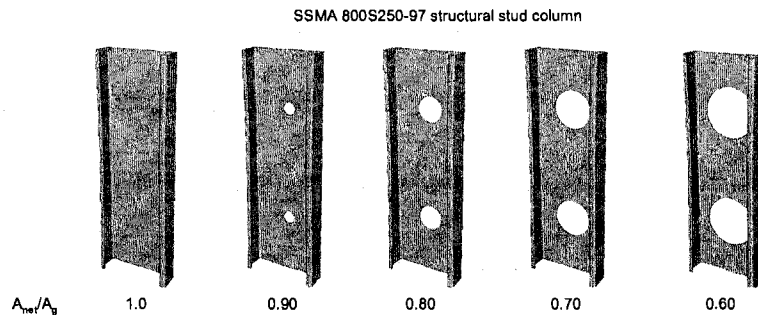


Figure 8.2 SSMA 800S250-97 structural stud with web holes considered in the DSM distortional buckling study

The simulation results for $A_{net}/A_g = 1.0, 0.9, 0.8, 0.7,$ and 0.6 are compared to the DSM distortional buckling prediction curve in Figure 8.4 to Figure 8.8. The column strengths, P_{test25} and P_{test75} , without holes ($A_{net}/A_g = 1.0$) are consistent with the DSM design curve as

shown in Figure 8.4a, confirming the viability of the nonlinear simulation protocol. The mean and standard deviation of the simulated test to predicted ratio is 1.10 and 0.10 respectively for 25% CDF local and distortional imperfections, and 1.06 and 0.13 for 75% CDF imperfections (global imperfections are not considered in these stocky columns). For the columns with holes, the simulated test strengths diverge from the DSM prediction curve as distortional slenderness, $\lambda_d = (P_{yg}/P_{crd})^{0.5}$, decreases as shown in Figure 8.5a to Figure 8.8a (P_{yg} is the squash load of the column calculated with the gross cross-sectional area A_g). This divergent trend in P_{test} with decreasing λ_d can be explained as follows. When λ_d is high (i.e. P_{crd} is low relative to P_{yg}), the column strength is lower than P_{yg} because the collapse mechanism is controlled by distortional buckling deformations. The presence of a hole may decrease P_{crd} (as predicted with the method in Section 4.2.7.2), but the distortional failure mechanism still dominates in this case. When λ_d is low, P_{crd} is much higher than P_{yg} and the column is not as sensitive to distortional deformation. Instead, the column fails by yielding of the cross-section. When a hole is added, the yielding of the cross-section occurs at the location of the hole (i.e., at the net section) resulting in the collapse of the unstiffened strips adjacent to the hole. This collapse is accompanied by distortional and global deformations caused by the reduction in stiffness at the net section. These two column failure mechanisms, a distortional buckling failure (when λ_d is high) and yielding and collapse of the net section (when λ_d is low), are compared in Figure 8.3.

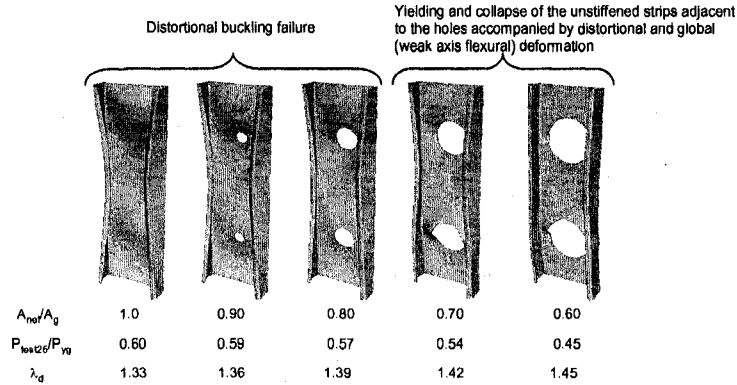


Figure 8.3 SSMA 800S250-97 structural stud failure mode transition from distortional buckling to yielding at the net section

The observations from this study are used to formulate a modified DSM distortional curve for columns with holes which captures the failure mechanism transition from yielding at the net cross-section to a distortional type failure mode and limits the strength of the column to its squash load at the net section:

Distortional Buckling

The nominal axial strength, P_{nd} , for distortional buckling shall be calculated in accordance with the following:

(a) For $\lambda_d \leq \lambda_{d1}$

$$P_{nd} = P_{y_{net}} \quad (\text{cap on column strength})$$

(b) For $\lambda_{d1} < \lambda_d \leq \lambda_{d2}$

$$P_{nd} = P_{y_{net}} - \left(\frac{P_{y_{net}} - P_{d2}}{\lambda_{d2} - \lambda_{d1}} \right) \lambda_d \quad (\text{yield control transition})$$

(c) For $\lambda_d > \lambda_{d2}$

$$P_{nd} = \left(1 - 0.25 \left(\frac{P_{crd}}{P_y} \right)^{0.6} \right) \left(\frac{P_{crd}}{P_y} \right)^{0.6} P_y \quad (\text{existing DSM distortional curve})$$

where

$$\lambda_d = \sqrt{P_y / P_{crd}}$$

$$\lambda_{d1} = 0.561 (P_{y_{net}} / P_y)$$

$$\lambda_{d2} = 0.561 (14 (P_{y_{net}} / P_y)^{-0.4} - 13)$$

$$P_{d2} = (1 - 0.25 (1/\lambda_{d2})^{1.2}) (1/\lambda_{d2})^{1.2} P_y$$

$$P_{y_{net}} = F_y A_{net} \geq 0.6 P_y$$

$$A_{net} = \text{Column cross-sectional area at the location of hole(s)}$$

$$P_{crd} = \text{Critical elastic distortional column buckling load including hole(s)}$$

The modified DSM distortional curve is added in Figure 8.5b to Figure 8.8b as A_{net}/A_g decreases, simulating the transition from the existing DSM curve to the capped column strength exhibited by the simulated test data. The linear portion of the modified prediction curve represents the unstiffened strip distortional collapse mechanism and the nonlinear portion represents a collapse mechanism driven by distortional buckling. This proposed modification to the DSM distortional prediction curve will be compared against the column experiments database developed in Section 4.2.6.1 as a part of several proposed DSM options considered later in this chapter.

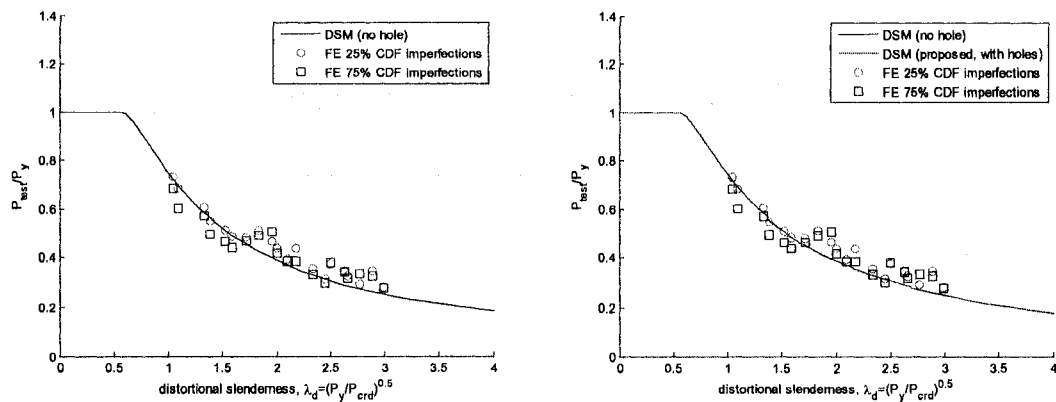


Figure 8.4 Comparison of simulated column strengths ($A_{net}/A_g=1.0$) to (a) the existing DSM distortional buckling design curve and to (b) the proposed DSM distortional buckling curve for columns with holes

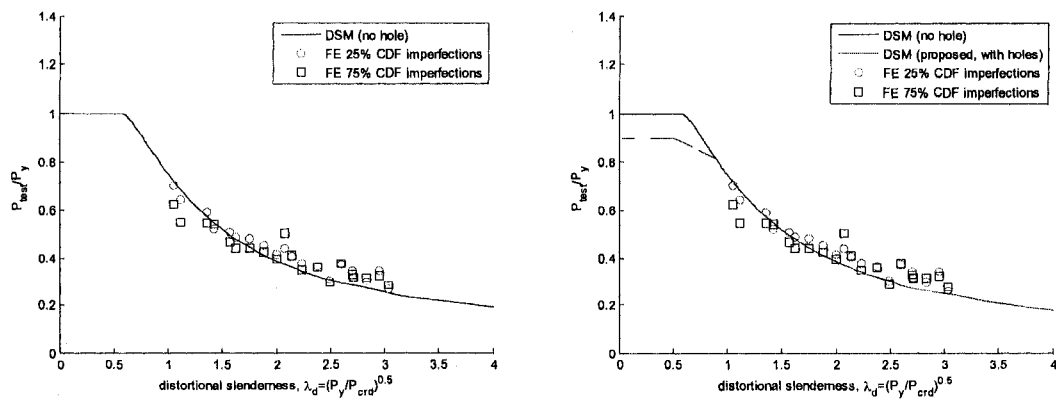


Figure 8.5 Comparison of simulated column strengths ($A_{net}/A_g=0.90$) to (a) the existing DSM distortional buckling design curve and to (b) the proposed DSM distortional buckling curve for columns with holes

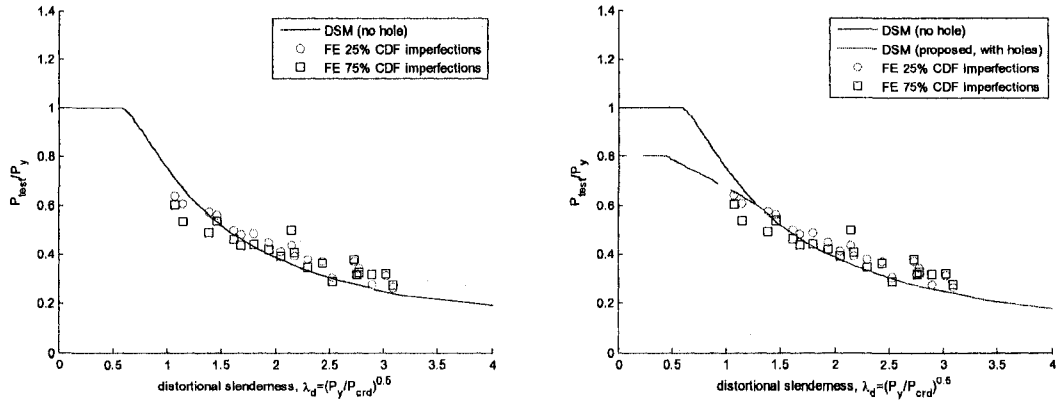


Figure 8.6 Comparison of simulated column strengths ($A_{net}/A_g=0.80$) to (a) the existing DSM distortional buckling design curve and to (b) the proposed DSM distortional buckling curve for columns with holes

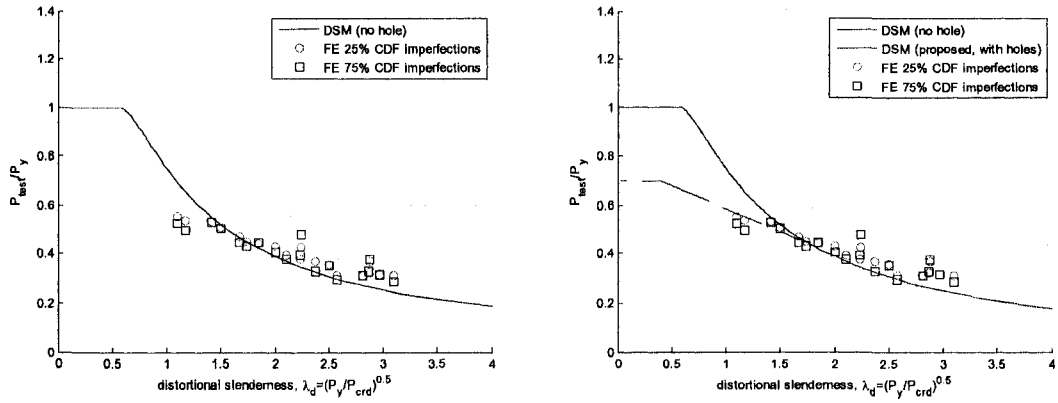


Figure 8.7 Comparison of simulated column strengths ($A_{net}/A_g=0.70$) to (a) the existing DSM distortional buckling design curve and to (b) the proposed DSM distortional buckling curve for columns with holes

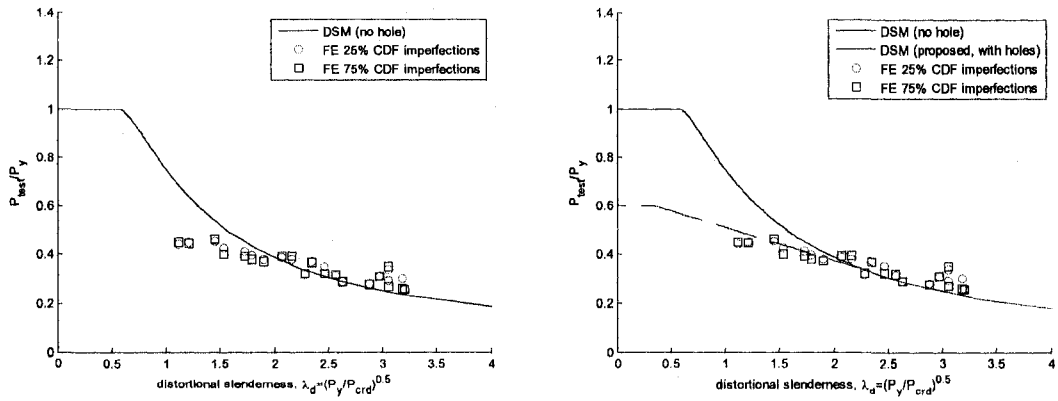


Figure 8.8 Comparison of simulated column strengths ($A_{net}/A_g=0.60$) to (a) the existing DSM distortional buckling design curve and to (b) the proposed DSM distortional buckling curve for columns with holes

8.1.3 Global buckling study

This study compares simulated strengths to DSM predictions of cold-formed steel columns with holes predicted to experience a global failure. A global failure is triggered by yielding for a stocky column and flexural or flexural-torsional buckling for slender columns. No modifications are proposed to the DSM global buckling design curve for columns with holes, as the influence of holes on short columns will be accounted for with the DSM local buckling design curve (see Section 8.1.4). For example, when $P_{nc} = P_{yg}$, P_{nt} will always be made less than or equal to P_{ynet} , and therefore the nominal column strength, P_n , will always be less than or equal to P_{ynet} .

A group of 18 columns predisposed to a global failure were selected from the SSMA column simulation database. In this study the column length, L , varied from 8 in. to 96 in. to consider a wide range of global column slenderness, $\lambda_c = (P_{yg}/P_{cre})^{0.5}$. The SSMA cross-sections are purposely selected with low local buckling slenderness (i.e., sections with thicker sheet steel up to $t=0.1017$ in. and relatively narrow flanges and webs). DSM predicts that local buckling does not influence global buckling behavior when $\lambda_c \leq 0.776$. The web of each column contains evenly spaced slotted holes where the hole spacing S varies from 8 in. to 22 in. The hole length, L_{hole} , is held constant at 4 in., while the hole depth, h_{hole} , is varied for each column to produce A_{net}/A_g of 1.0 (no holes), 0.9, and 0.8. (Refer to Appendix K, Study Type G, for specific column cross-section and hole geometry information.) The four columns with the lowest global slenderness (for example, Specimen ID # 137 to 140 in Appendix K) were modeled with circular holes instead of slotted holes because the slotted holes resulted in impractical column layouts,

with the hole extending over more than 50% of the column length. The global imperfection shape for five of the longer columns was weak-axis flexural buckling, and therefore four simulated strengths are determined for these columns (instead of the typical two): 25% CDF local and distortional imperfections with $\pm L/2000$ global imperfections and 75% CDF local and distortional imperfections with $\pm L/1000$ global imperfections.

Figure 8.9 to Figure 8.11 compare the simulated column strengths to the DSM global prediction curve as A_{net}/A_g decreases. The simulated strengths for columns without holes are consistent with the DSM global prediction curve as shown in Figure 8.9a. The mean and standard deviation of the simulated test to predicted ratio for columns without holes is 1.06 and 0.05 respectively for 25% CDF local and distortional imperfections $\pm L/2000$ global imperfection and 0.95 and 0.07 for 75% local and distortional imperfections $\pm L/1000$ global imperfection.

Figure 8.10a and Figure 8.11a demonstrate that for columns with holes, the predicted strengths are consistent with the DSM global design curve when global slenderness λ_c is greater than 2. Most of the columns in this region fail by weak-axis flexural buckling. When λ_c is between 1 and 2, all of the columns fail by flexural-torsional buckling and the simulated column strengths (with 25% CDF imperfections) are 20% higher than the DSM predictions. This conservative trend is caused by the simplified prediction method developed in Section 4.3.2.3, which is known to be a conservative predictor of P_{cr} when torsional buckling influences the global buckling mode. When P_{cr} is underpredicted, the global slenderness increases, which shifts the tested data off of the DSM design curve;

the shift is especially clear in Figure 8.11a. This observation further motivates the future work to study the influence of holes on the warping torsion constant, C_w .

Simulated column strengths diverge below the DSM prediction curve when λ_c decreases and A_{net}/A_g increases as shown in Figure 8.10a and Figure 8.11a. These columns are short, ranging in length from 8 in. to 26 in., and exhibit a yielding failure mode at the net section, similar to that observed in the distortional failure study in Figure 8.3. This observation supports the proposed modification to the DSM distortional buckling curve, which accurately predicts the strengths of these columns as shown in Figure 8.9b and Figure 8.11b, where the diverging data points are plotted against the modified DSM distortional prediction curve. This observation reiterates the conclusion drawn in the distortional buckling study, that yielding and collapse of the unstiffened strips adjacent to a hole influence both distortional and global failure modes as slenderness decreases.

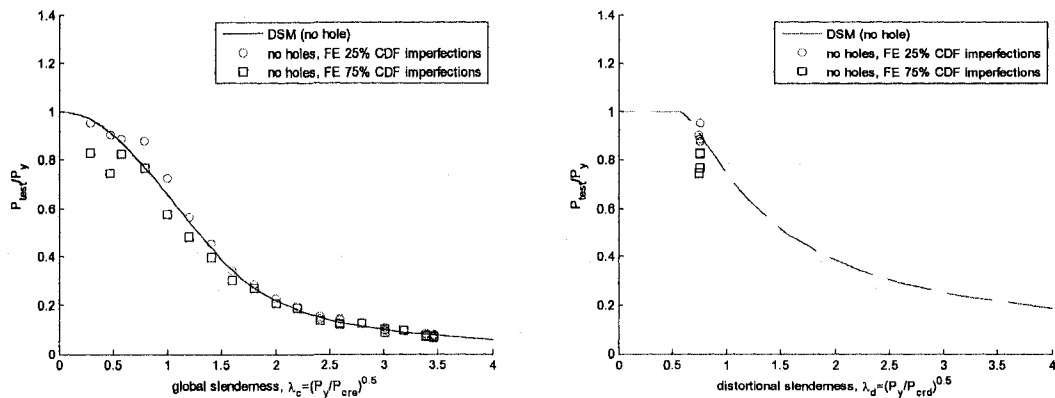


Figure 8.9 Comparison of simulated column strengths ($A_{net}/A_g=1.00$) to (a) the existing DSM global buckling design curve and to (b) the proposed DSM distortional buckling curve for columns with holes

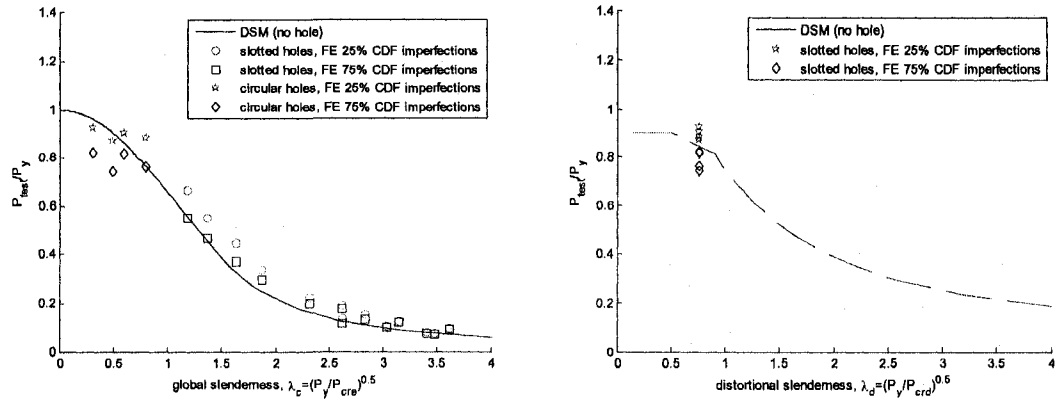


Figure 8.10 Comparison of simulated column strengths ($A_{net}/A_g=0.90$) to (a) the existing DSM global buckling design curve and to (b) the proposed DSM distortional buckling curve for columns with holes

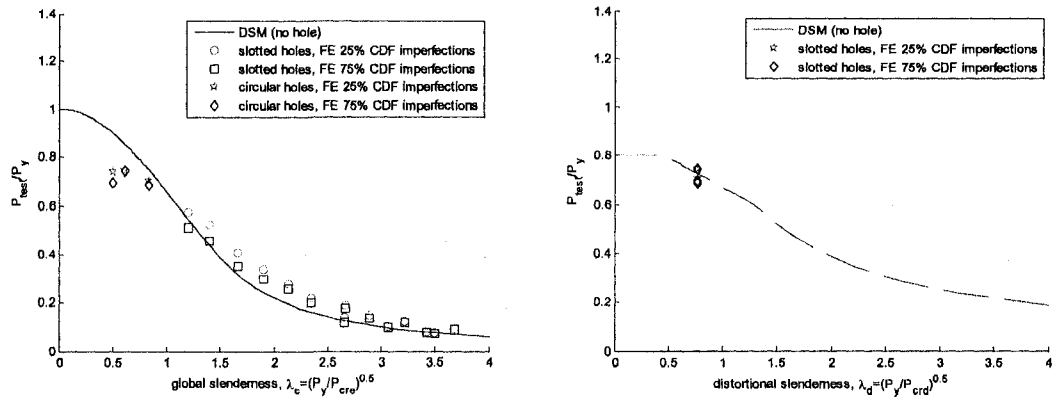


Figure 8.11 Comparison of simulated column strengths ($A_{net}/A_g=0.80$) to (a) the existing DSM global buckling design curve and to (b) the proposed DSM distortional buckling curve for columns with holes

8.1.4 Local buckling study

The distortional buckling failure study in Section 8.1.2 and the global buckling failure study in Section 8.1.3 demonstrated that the presence of holes decreases ultimate strength when cold-formed steel columns fail by yielding and collapse of the unstiffened strips adjacent to a hole at the net cross-section. Holes were observed to have a minimal influence on ultimate strength when the column failure mode was dictated by elastic buckling. The goal of this study is to determine if this trend is consistent for columns with holes experiencing local-global buckling interaction at failure.

Eleven columns from the simulation database in Appendix K were chosen for this study. The columns have SSMA cross-sections and lengths which result in a local buckling slenderness, λ_e , ranging from 0.8 to 3.0. The column length, L , varies from 24 in. to 88 in. and column widths range from 3.5 in. to 12 in. The web of each column contains evenly spaced circular holes where the hole spacing S varies from 12 in. to 17 in. The hole depth (diameter), h_{hole} , is varied for each column to produce A_{net}/A_g of 1.0 (no holes), 0.80, and 0.65. Refer to Appendix K, Study Type L, for specific column cross-section and hole geometry information.

The simulated ultimate strengths of the 11 columns without holes, P_{test} , are compared to the DSM local buckling strength prediction, P_{net} , in Figure 8.12. The simulated test to predicted ratios are more variable than those observed in the distortional and global failure studies but on average are close to unity, with a trend towards increasingly conservative predictions with increasing λ_e as shown in Figure 8.12a. The mean and standard deviation of the simulated test to prediction ratio is 1.05 and 0.14 respectively for 25% CDF local and distortional imperfections $\pm L/2000$ global imperfections and 1.03 and 0.15 for 75% local and distortional imperfections $\pm L/1000$ global imperfections.

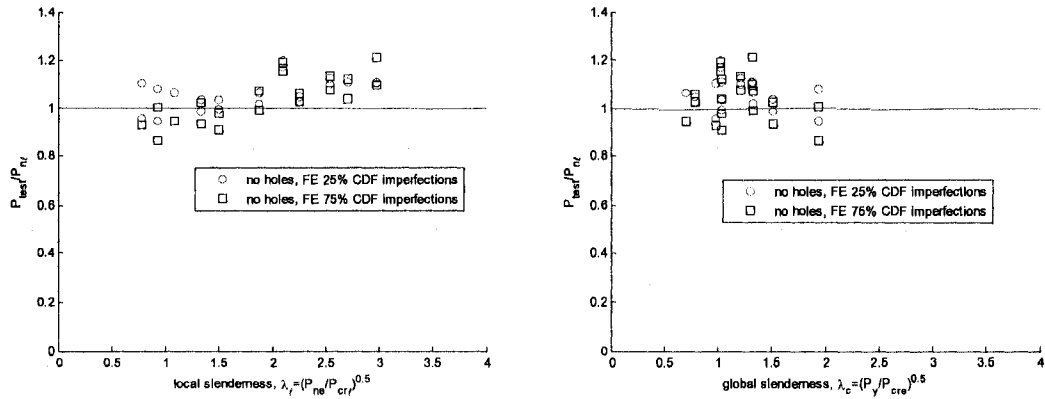


Figure 8.12 Comparison of column test-to-prediction ratios for columns ($A_{net}/A_g=1.0$) failing by local-global buckling interaction as a function of (a) local slenderness (b) global slenderness

Figure 8.13 and Figure 8.14 compare the simulated strengths of the 11 columns to the predicted strength, P_{nl} , as A_{net}/A_g decreases from 1.0 (no hole), to 0.80, to 0.65. (In Figure 8.13 and Figure 8.14 the test strengths are those associated with $P_{test25+}$ in Appendix K, i.e. the 25% CDF local and distortional imperfection magnitudes and +L/2000 global imperfection magnitudes.) Figure 8.13a compares the simulated strengths $P_{test25+}$ to P_{nl} without the influence of holes. (The local-global buckling interaction complicates the comparison because P_{nl} and λ_l are both a function of P_{ne} . By initially assuming that P_{ne} is not influenced by the hole, the effect of hole size on simulated strength is more clearly observed.) As local slenderness (λ_l) decreases in Figure 8.13a (i.e., the influence of local buckling on member strength decreases) the tested strength becomes more sensitive to increasing hole size (i.e., decreasing A_{net}/A_g), diverging below the prediction P_{nl} by as much as 40% when $\lambda_l=0.75$.

Figure 8.14a demonstrates that the sensitivity of column strength to a decrease in A_{net}/A_g is related to the ratio of P_{ynet} to P_{ne} . When P_{ynet}/P_{ne} is high, the strength sensitivity to A_{net}/A_g

is low because global buckling initiates the column failure. As P_{nc}/P_{ynet} approaches unity, column failure is initiated by unstiffened strip buckling and yielding at the net cross-section and therefore the sensitivity of column strength to A_{net}/A_g increases. A column with the largest drop in strength with increasing hole size is the SSMA 350S162-68 column with $L=34$ in. and $S=17$ in. shown in Figure 8.15. In this case a large hole ($A_{net}/A_g=0.65$) causes the collapse of the net section resulting in an unfavorable and sudden weak-axis flexural failure and a 42% strength reduction when compared to the same column without holes. The SSMA 350S162-68 column with smaller holes ($A_{net}/A_g=0.80$) fails in a combination of distortional and flexural-torsional buckling with a 12% strength reduction.

Figure 8.13b plots the same information as Figure 8.14a, except now P_{nc} is calculated using P_{cre} including the influence of holes. For 8 out of the 11 columns, the prediction P_{nc} shifts from unconservative to slightly conservative, even for large holes. One exception is the SSMA 800S250-43 column with $L=74$ in. and $S=12$ in. shown in Figure 8.16, where the strength prediction becomes overly conservative as A_{net}/A_g increases. P_{cre} is predicted to decrease by 45% when $A_{net}/A_g=0.65$, although the tested strength decreases by only 10%. Figure 8.16 demonstrates that the C-section web is susceptible to local buckling, and that the presence of holes does not adversely affect the failure mode in this case. The strength predictions for the SSMA 350S162-68 column (Figure 8.15) and the SSMA 350S162-54 column with $L=24$ in. and $S=12$ in. are viable when $A_{net}/A_g=0.80$, but are underestimated by 20% with Option 4 (5) when $A_{net}/A_g=0.65$ because of the introduction of an unstable weak-axis flexural failure mode triggered by the collapse of

the net section. A hinge forms at the location of the net section, and the global slenderness is high enough that the column becomes susceptible to a flexural buckling mode. These “hinge” failures are not observed in the distortional buckling study (see Section 8.1.2) because the global slenderness of the columns is lower (i.e. the weak axis flexural stiffness is higher), avoiding a global buckling failure. Option 6 accurately predicts the strength of the SSMA 350S162-68 column and the SSMA 350S162-54 columns because the method assumes that the global strength, P_{ne} , is reduced by P_{ynet}/P_y .

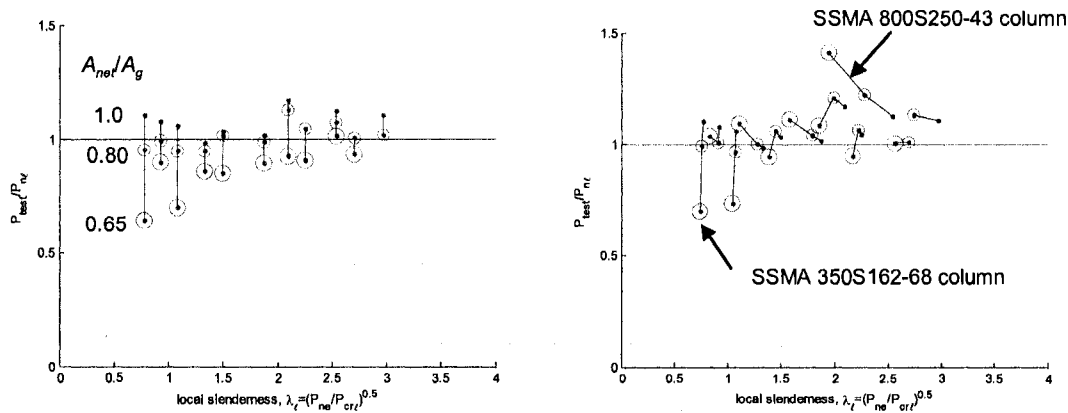


Figure 8.13 Comparison of column test-to-prediction ratios for columns failing by local-global buckling interaction with P_{ne} calculated (a) without the influence of holes (b) and with the influence of holes

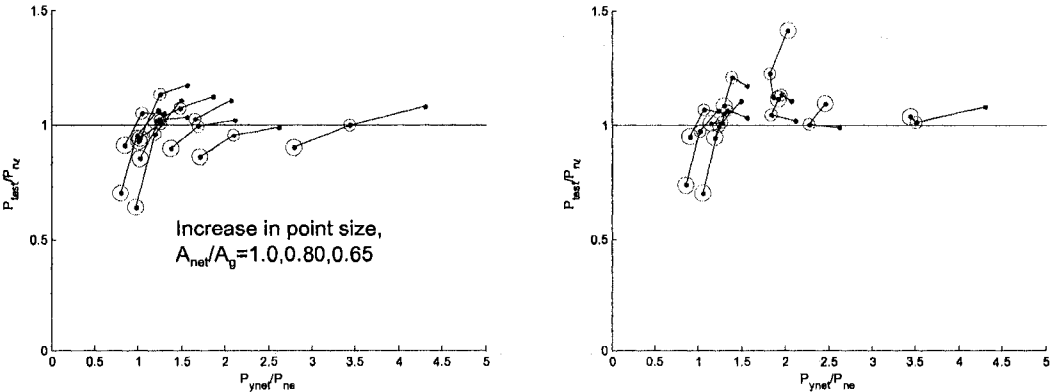


Figure 8.14 Comparison of column test-to-prediction ratios for columns failing by local-global buckling interaction as a function of P_{ynet}/P_{ne} where P_{ne} is calculated (a) without the influence of holes (b) and with the influence of holes

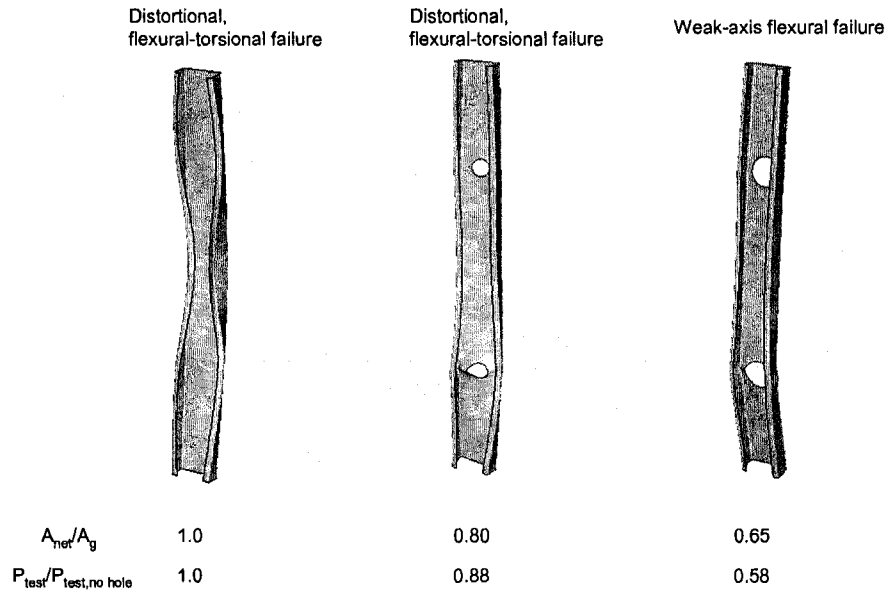


Figure 8.15 SSMA 350S162-68 column failure mode changes from distortional-flexural torsional buckling failure to weak axis flexure as hole size increases ($L=34$ in.)

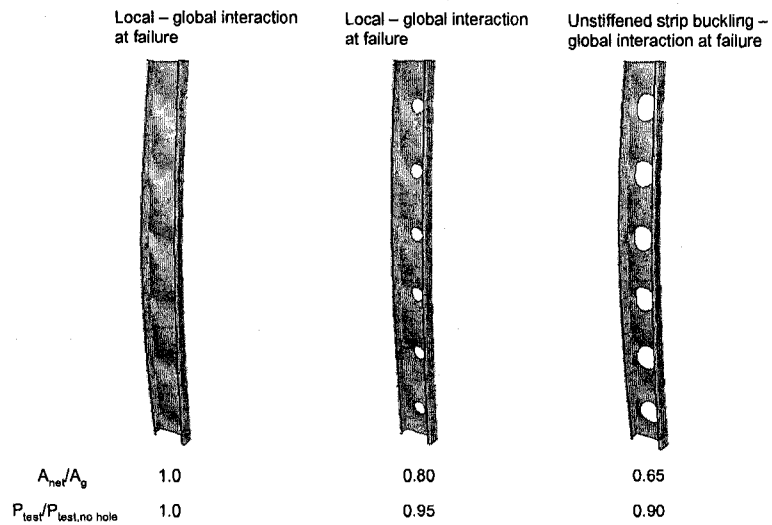


Figure 8.16 SSMA 800S250-43 ($L=74$ in.) column web local buckling changes to unstiffened strip buckling at peak load as hole size increases

The observations from this study are now employed to propose two options for the DSM local buckling design curve for columns with holes. The presence of holes

influenced the tested strength of the cold-formed steel columns over the full range of local slenderness considered. This result was different from the distortional and global failure studies, where holes were observed to reduce strength only from the collapse and yielding at the net section as slenderness decreased. The strength reduction from the holes was predicted in DSM for 8 out of the 11 columns, when P_{nl} was calculated with P_{ne} included the influence of holes (compare Figure 8.13a to Figure 8.13b). A transition similar to that proposed for the DSM distortional design curve is still justified though, especially when $P_{ynet}/P_{ne} \leq 1$ (see Figure 8.14b), to capture the yielding and collapse at the net section observed in columns with low local and global slenderness. The strength of two columns with large holes were underpredicted because of unstable global collapse initiated by yielding at the net-section, motivating the implementation of a limit on hole size (i.e., A_{net}/A_g) to ensure the viability of the DSM approach. Two modification options are proposed for the DSM local design curve based on these conclusions:

Local Buckling (Option A)

The nominal axial strength, P_{nl} , for local buckling shall be calculated in accordance with the following:

- (a) For $\lambda_\ell \leq \lambda_{\ell 1}$
 $P_{nl} = P_{ne} \leq P_{ynet}$ (cap on column strength)
- (b) For $\lambda_{\ell 1} < \lambda_\ell \leq \lambda_{\ell 2}$

$$P_{nl} = P_{ynet} - \left(\frac{P_{ynet} - P_{\ell 2}}{\lambda_{\ell 2} - \lambda_{\ell 1}} \right) (\lambda_\ell - \lambda_{\ell 1})$$
 (yield transition when $P_{ynet}/P_{ne} \leq 1$)
- (c) For $\lambda_\ell > \lambda_{\ell 2}$

$$P_{nl} = \left(1 - 0.15 \left(\frac{P_{crf}}{P_{ne}} \right)^{0.4} \right) \left(\frac{P_{crf}}{P_{ne}} \right)^{0.4} P_{ne}$$
 (DSM local buckling curve, unchanged)

where

$$\begin{aligned} \lambda_\ell &= \sqrt{P_{ne}/P_{crf}} \\ \lambda_{\ell 1} &= 0.776(P_{ynet}/P_{ne}) \leq 0.776 \\ \lambda_{\ell 2} &= 0.776(1.7(P_{ynet}/P_{ne})^{1.6} - 0.7), P_{ynet}/P_{ne} \leq 1 \\ &= 0.776, P_{ynet}/P_{ne} > 1 \quad \text{(no transition when } P_{ynet}/P_{ne} > 1 \text{)} \\ P_{\ell 2} &= (1 - 0.15(1/\lambda_{\ell 2})^{0.8})(1/\lambda_{\ell 2})^{0.8} P_{ne} \end{aligned}$$

$$P_{ynet} = F_y A_{net} \geq 0.6 P_y \quad (\text{limit reduction of the net section to } 0.6 P_y)$$

$$A_{net} = \text{Column cross-sectional area at the location of hole(s)}$$

$$P_{crl} = \text{Critical elastic local column buckling load including hole(s)}$$

Local Buckling (Option B)

The nominal axial strength, $P_{n\ell}$, for local buckling shall be calculated in accordance with the following:

(a) For $\lambda_\ell \leq \lambda_{\ell 1}$

$$P_{n\ell} = P_{ynet} (P_{ne} / P_y) \quad (\text{cap on column strength})$$

(b) For $\lambda_{\ell 1} < \lambda_\ell \leq \lambda_{\ell 2}$

$$P_{n\ell} = P_{ynet} \left(\frac{P_{ne}}{P_y} \right) - \left(\frac{P_{ynet} (P_{ne} / P_y) - P_{\ell 2}}{\lambda_{\ell 2} - \lambda_{\ell 1}} \right) (\lambda_\ell - \lambda_{\ell 1}) \quad (\text{yield transition when } P_{ynet}/P_{ne} \leq 1)$$

(c) For $\lambda_\ell > \lambda_{\ell 2}$

$$P_{n\ell} = \left(1 - 0.15 \left(\frac{P_{crl}}{P_{ne}} \right)^{0.4} \right) \left(\frac{P_{crl}}{P_{ne}} \right)^{0.4} P_{ne} \quad (\text{DSM local buckling curve, unchanged})$$

where

$$\lambda_\ell = \sqrt{P_{ne} / P_{crl}}$$

$$\lambda_{\ell 1} = 0.776 (P_{ynet} / P_y)$$

$$\lambda_{\ell 2} = 0.776 (1.7 (P_{ynet} / P_y)^{-1.6} - 0.7)$$

$$P_{\ell 2} = (1 - 0.15 (1 / \lambda_{\ell 2})^{0.8}) (1 / \lambda_{\ell 2})^{0.8} P_{ne}$$

$$P_{ynet} = F_y A_{net} \geq 0.6 P_y \quad (\text{limit reduction of the net section to } 0.6 P_y)$$

A_{net} = Column cross-sectional area at the location of hole(s)

P_{crl} = Critical elastic local column buckling load including hole(s)

Option A imposes a transition from the DSM local buckling curve to column strength at the net section, P_{ynet} , when $P_{ynet} < P_{ne}$ as shown in Figure 8.17a for the case when $P_{ne} = P_y$ (i.e., stub columns) and $P_{ynet} = 0.8 P_{yg}$. When $P_{ynet} > P_{ne}$, Option A assumes that holes influence only the critical elastic buckling loads (P_{crl} , P_{cre}) and otherwise do not change the failure mode of the column; this case is demonstrated in Figure 8.17c when $P_{cre} = P_{yg}$. Option B also imposes a transition to the net column strength from the DSM local failure curve, although the transition is assumed to occur for all values of P_{ynet}/P_{ne} . In essence, the Option B curve for stub columns shown in Figure 8.17a is scaled down based on the ratio P_{ynet}/P_y . The result is an additional reduction in predicted strength for global

column failures without local buckling interaction that is not captured by Option A. This difference between Option A and Option B is highlighted in Figure 8.17b, where $P_{ynet}=0.8P_{yg}$ and $P_{cre} = 5P_{yg}$. The validity of both options are evaluated in the following section against the simulation database and the experiment database assembled in Chapter 4.

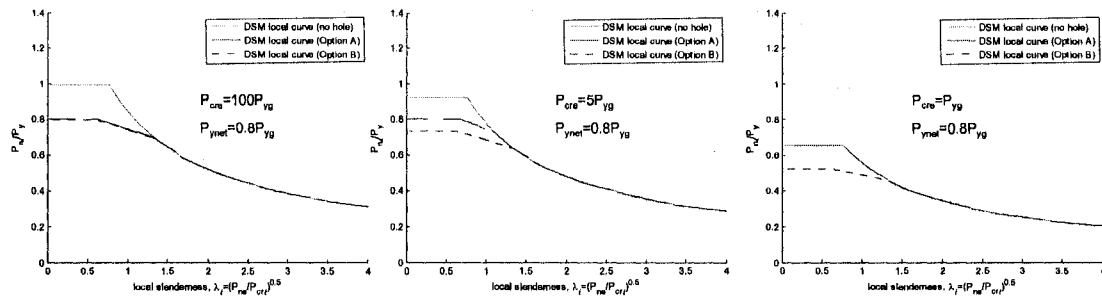


Figure 8.17 Comparison of DSM local buckling design curve options when $P_{ynet}=0.80 P_{yg}$ and (a) $P_{cre}=100P_{yg}$, (b) $P_{cre}=5P_{yg}$ and (c) $P_{cre}=P_{yg}$

8.1.5 Presentation and evaluation of DSM options

Six options for extending DSM to columns with holes are evaluated in this section. The options range from simple substitutions in the existing code to more involved modifications, including the incorporation of the design curve transitions discussed in Section 8.1.2 and Section 8.1.4 for distortional and local buckling.

8.1.5.1 Description of DSM options

Option 1: Include hole(s) in P_{cr} determinations, ignore hole otherwise
 This method, in presentation, appears identical to currently available DSM expressions

Flexural, Torsional, or Torsional-Flexural Buckling

The nominal axial strength, P_{ne} , for flexural, ... or torsional- flexural buckling is

$$\text{for } \lambda_c \leq 1.5 \quad P_{ne} = (0.658^{\lambda_c^2}) P_y$$

$$\text{for } \lambda_c > 1.5 \quad P_{ne} = \left(\frac{0.877}{\lambda_c} \right) P_y = 0.877 P_{cre}$$

where $\lambda_c = \sqrt{P_y / P_{cre}}$

$$P_y = A_g F_y$$

P_{cre} = Critical elastic global column buckling load ... (including hole(s))

A_g = gross area of the column

Local Buckling

The nominal axial strength, P_{nl} , for local buckling is

$$\text{for } \lambda_\ell \leq 0.776 \quad P_{nl} = P_{ne}$$

$$\text{for } \lambda_\ell > 0.776 \quad P_{nl} = \left[1 - 0.15 \left(\frac{P_{crl}}{P_{ne}} \right)^{0.4} \right] \left(\frac{P_{crl}}{P_{ne}} \right)^{0.4} P_{ne}$$

where $\lambda_\ell = \sqrt{P_{ne} / P_{crl}}$

P_{crl} = Critical elastic local column buckling load ... (including hole(s))

P_{ne} is defined above.

Distortional Buckling

The nominal axial strength, P_{nd} , for distortional buckling is

$$\text{for } \lambda_d \leq 0.561 \quad P_{nd} = P_y$$

$$\text{for } \lambda_d > 0.561 \quad P_{nd} = \left(1 - 0.25 \left(\frac{P_{crd}}{P_y} \right)^{0.6} \right) \left(\frac{P_{crd}}{P_y} \right)^{0.6} P_y$$

where $\lambda_d = \sqrt{P_y / P_{crd}}$

P_{crd} = Critical elastic distortional column buckling load ... (including hole(s))

Option 2: Include hole(s) in P_{cr} determinations, Use P_{ynet} everywhere
 The only change in this method is to replace P_y with P_{ynet}

Flexural, Torsional, or Torsional-Flexural Buckling

The nominal axial strength, P_{ne} , for flexural, ... or torsional- flexural buckling is

$$\text{for } \lambda_{cnet} \leq 1.5 \quad P_{ne} = (0.658^{\lambda_{cnet}^2}) P_{ynet}$$

$$\text{for } \lambda_{cnet} > 1.5 \quad P_{ne} = \left(\frac{0.877}{\lambda_{cnet}^2} \right) P_{ynet} = 0.877 P_{cre}$$

where

$$\lambda_{cnet} = \sqrt{P_{ynet}/P_{cre}}$$

$$P_{ynet} = A_{net} F_y$$

P_{cre} = Critical elastic global column buckling load ... (including hole(s))

A_{net} = net area of the column

Local Buckling

The nominal axial strength, P_{nl} , for local buckling is

$$\text{for } \lambda_\ell \leq 0.776 \quad P_{nl} = P_{ne}$$

$$\text{for } \lambda_\ell > 0.776 \quad P_{nl} = \left[1 - 0.15 \left(\frac{P_{crl}}{P_{ne}} \right)^{0.4} \right] \left(\frac{P_{crl}}{P_{ne}} \right)^{0.4} P_{ne}$$

where

$$\lambda_\ell = \sqrt{P_{ne}/P_{crl}}$$

P_{crl} = Critical elastic local column buckling load ... (including hole(s))

P_{ne} is defined above

Distortional Buckling

The nominal axial strength, P_{nd} , for distortional buckling is

$$\text{for } \lambda_{dnet} \leq 0.561 \quad P_{nd} = P_{ynet}$$

$$\text{for } \lambda_{dnet} > 0.561 \quad P_{nd} = \left(1 - 0.25 \left(\frac{P_{crd}}{P_{ynet}} \right)^{0.6} \right) \left(\frac{P_{crd}}{P_{ynet}} \right)^{0.6} P_{ynet}$$

where

$$\lambda_{dnet} = \sqrt{P_{ynet}/P_{crd}}$$

P_{crd} = Critical elastic distortional column buckling load ... (including hole(s))

Option 3: Cap P_{ne} and P_{nd} , otherwise no strength change, include hole(s) in P_{cr}
This method puts bounds in place and assumes local-global interaction happens at full P_{ne}

Flexural, Torsional, or Torsional-Flexural Buckling

The nominal axial strength, P_{ne} , for flexural, ... or torsional- flexural buckling is

$$\text{for } \lambda_c \leq 1.5 \quad P_{ne} = \left(0.658 \lambda_c^2 \right) P_y$$

$$\text{for } \lambda_c > 1.5 \quad P_{ne} = \left(\frac{0.877}{\lambda_c^2} \right) P_y = 0.877 P_{cre}$$

where $\lambda_c = \sqrt{P_y / P_{cre}}$

P_{cre} = Critical elastic global column buckling load ... (including hole(s))

$P_y = A_g F_y$

A_g = gross area of the column

Local Buckling

The nominal axial strength, P_{nl} , for local buckling is

$$\text{for } \lambda_\ell \leq 0.776 \quad P_{nl} = P_{ne} \leq P_{ynet}$$

$$\text{for } \lambda_\ell > 0.776 \quad P_{nl} = \left[1 - 0.15 \left(\frac{P_{crl}}{P_{ne}} \right)^{0.4} \right] \left(\frac{P_{crl}}{P_{ne}} \right)^{0.4} P_{ne} \leq P_{ynet}$$

where $\lambda_\ell = \sqrt{P_{ne} / P_{crl}}$

P_{crl} = Critical elastic local column buckling load ... (including hole(s))

P_{ne} is defined in Section above.

$P_{ynet} = A_{net} F_y$

A_{net} = net area of the column

Distortional Buckling

The nominal axial strength, P_{nd} , for distortional buckling is

$$\text{for } \lambda_d \leq 0.561 \quad P_{nd} = P_y \leq P_{ynet}$$

$$\text{for } \lambda_d > 0.561 \quad P_{nd} = \left(1 - 0.25 \left(\frac{P_{crd}}{P_y} \right)^{0.6} \right) \left(\frac{P_{crd}}{P_y} \right)^{0.6} P_y \leq P_{ynet}$$

where $\lambda_d = \sqrt{P_y / P_{crd}}$

P_{crd} = Critical elastic distortional column buckling load ... (including hole(s))

Option 4: Cap P_{ne} , transition P_{nd} , include hole(s) in P_{cr} determinations
 This method puts bounds and transition in place, assumes local-global interaction at full P_{ne}

Flexural, Torsional, or Torsional-Flexural Buckling

The nominal axial strength, P_{ne} , for flexural, ... or torsional- flexural buckling is

$$\text{for } \lambda_c \leq 1.5 \quad P_{ne} = \left(0.658^{\lambda_c^2}\right) P_y$$

$$\text{for } \lambda_c > 1.5 \quad P_{ne} = \left(\frac{0.877}{\lambda_c^2}\right) P_y = 0.877 P_{cre}$$

where $\lambda_c = \sqrt{P_y/P_{cre}}$

P_{cre} = Critical elastic global column buckling load ... (including hole(s))

$P_y = A_g F_y$

A_g = gross area of the column

Local Buckling

The nominal axial strength, P_{nl} , for local buckling is

$$\text{for } \lambda_\ell \leq 0.776 \quad P_{nl} = P_{ne} \leq P_{ynet}$$

$$\text{for } \lambda_\ell > 0.776 \quad P_{nl} = \left[1 - 0.15 \left(\frac{P_{crl}}{P_{ne}}\right)^{0.4}\right] \left(\frac{P_{crl}}{P_{ne}}\right)^{0.4} P_{ne} \leq P_{ynet}$$

where $\lambda_\ell = \sqrt{P_{ne}/P_{crl}}$

P_{crl} = Critical elastic local column buckling load ... (including hole(s))

P_{ne} is defined in Section above.

$P_{ynet} = A_{net} F_y$

A_{net} = net area of the column

Distortional Buckling

The nominal axial strength, P_{nd} , for distortional buckling shall be calculated in accordance with the following:

(a) For $\lambda_d \leq \lambda_{d1}$

$$P_{nd} = P_{ynet}$$

(b) For $\lambda_{d1} < \lambda_d \leq \lambda_{d2}$

$$P_{nd} = P_{ynet} - \left(\frac{P_{ynet} - P_{d2}}{\lambda_{d2} - \lambda_{d1}}\right) \lambda_d$$

(c) For $\lambda_d > \lambda_{d2}$

$$P_{nd} = \left(1 - 0.25 \left(\frac{P_{crl}}{P_y}\right)^{0.6}\right) \left(\frac{P_{crl}}{P_y}\right)^{0.6} P_y$$

where

$$\lambda_d = \sqrt{P_y/P_{crl}}$$

$$\lambda_{d1} = 0.561(P_{ynet}/P_y)$$

$$\lambda_{d2} = 0.561(14(P_{ynet}/P_y)^{0.4} - 13)$$

$$P_{d2} = (1 - 0.25(1/\lambda_{d2})^{1.2})(1/\lambda_{d2})^{1.2} P_y$$

$$P_{ynet} = F_y A_{net} \geq 0.6 P_y$$

A_{net} = Column cross-sectional area at the location of hole(s)

P_{crl} = Critical elastic distortional column buckling load including hole(s)

Option 5: Transition P_{ne} (Option A), transition P_{nd} , include hole(s) in P_{cr} determinations
 This method puts bounds and transition in place, assumes local-global interaction at full P_{ne}

Flexural, Torsional, or Torsional-Flexural Buckling

The nominal axial strength, P_{ne} , for flexural, ... or torsional- flexural buckling is

$$\text{for } \lambda_c \leq 1.5 \quad P_{ne} = \left(0.658^{\lambda_c^2} \right) P_y$$

$$\text{for } \lambda_c > 1.5 \quad P_{ne} = \left(\frac{0.877}{\lambda_c^2} \right) P_y = 0.877 P_{cre}$$

where $\lambda_c = \sqrt{P_y/P_{cre}}$

P_{cre} = Critical elastic global column buckling load ... (including hole(s))

$P_y = A_g F_y$

A_g = gross area of the column

Local Buckling

The nominal axial strength, $P_{ne\ell}$, for local buckling shall be calculated in accordance with the following:

(a) For $\lambda_\ell \leq \lambda_{\ell 1}$

$$P_{ne\ell} = P_{ne} \leq P_{ynet} \quad \text{(cap on column strength)}$$

(b) For $\lambda_{\ell 1} < \lambda_\ell \leq \lambda_{\ell 2}$

$$P_{ne\ell} = P_{ynet} - \left(\frac{P_{ynet} - P_{\ell 2}}{\lambda_{\ell 2} - \lambda_{\ell 1}} \right) (\lambda_\ell - \lambda_{\ell 1}) \quad \text{(yield transition when } P_{ynet}/P_{ne} \leq 1)$$

(c) For $\lambda_\ell > \lambda_{\ell 2}$

$$P_{ne\ell} = \left(1 - 0.15 \left(\frac{P_{cr\ell}}{P_{ne}} \right)^{0.4} \right) \left(\frac{P_{cr\ell}}{P_{ne}} \right)^{0.4} P_{ne} \quad \text{(DSM local buckling curve, unchanged)}$$

where

$$\lambda_\ell = \sqrt{P_{ne}/P_{cr\ell}}$$

$$\lambda_{\ell 1} = 0.776 (P_{ynet}/P_{ne}) \leq 0.776$$

$$\lambda_{\ell 2} = 0.776 (1.7 (P_{ynet}/P_{ne})^{1.6} - 0.7), \quad P_{ynet}/P_{ne} \leq 1$$

$$= 0.776, \quad P_{ynet}/P_{ne} > 1 \quad \text{(no transition when } P_{ynet}/P_{ne} > 1)$$

$$P_{\ell 2} = (1 - 0.15 (1/\lambda_{\ell 2})^{0.8}) (1/\lambda_{\ell 2})^{0.8} P_{ne}$$

$$P_{ynet} = F_y A_{net} \geq 0.6 P_y \quad \text{(limit reduction of the net section to } 0.6 P_y)$$

A_{net} = Column cross-sectional area at the location of hole(s)

$P_{cr\ell}$ = Critical elastic local column buckling load including hole(s)

Distortional Buckling

Same as Option 4

Option 6: Transition P_{nr} (Option B), transition P_{nd} , include hole(s) in P_{cr} determinations
 This method puts bounds and transition in place, assumes local-global interaction at full P_{ne}

Flexural, Torsional, or Torsional-Flexural Buckling

The nominal axial strength, P_{ne} , for flexural, ... or torsional- flexural buckling is

$$\text{for } \lambda_c \leq 1.5 \quad P_{ne} = \left(0.658\lambda_c^2\right)P_y$$

$$\text{for } \lambda_c > 1.5 \quad P_{ne} = \left(\frac{0.877}{\lambda_c^2}\right)P_y = 0.877P_{cre}$$

where $\lambda_c = \sqrt{P_y/P_{cre}}$

P_{cre} = Critical elastic global column buckling load ... (including hole(s))

$P_y = A_g F_y$

A_g = gross area of the column

Local Buckling

The nominal axial strength, P_{nl} , for local buckling shall be calculated in accordance with the following:

(a) For $\lambda_\ell \leq \lambda_{\ell 1}$

$$P_{nl} = P_{ynet} (P_{ne} / P_y) \quad \text{(cap on column strength)}$$

(b) For $\lambda_{\ell 1} < \lambda_\ell \leq \lambda_{\ell 2}$

$$P_{nl} = P_{ynet} \left(\frac{P_{ne}}{P_y}\right) - \left(\frac{P_{ynet} (P_{ne}/P_y) - P_{\ell 2}}{\lambda_{\ell 2} - \lambda_{\ell 1}}\right) (\lambda_\ell - \lambda_{\ell 1}) \quad \text{(yield transition when } P_{ynet}/P_{ne} \leq 1)$$

(c) For $\lambda_\ell > \lambda_{\ell 2}$

$$P_{nl} = \left(1 - 0.15 \left(\frac{P_{cr\ell}}{P_{ne}}\right)^{0.4}\right) \left(\frac{P_{cr\ell}}{P_{ne}}\right)^{0.4} P_{ne} \quad \text{(DSM local buckling curve, unchanged)}$$

where

$$\lambda_\ell = \sqrt{P_{ne}/P_{cr\ell}}$$

$$\lambda_{\ell 1} = 0.776(P_{ynet}/P_y)$$

$$\lambda_{\ell 2} = 0.776(1.7(P_{ynet}/P_y)^{-1.6} - 0.7)$$

$$P_{\ell 2} = (1 - 0.15(1/\lambda_{\ell 2})^{0.8}) (1/\lambda_{\ell 2})^{0.8} P_{ne}$$

$$P_{ynet} = F_y A_{net} \geq 0.6P_y \quad \text{(limit reduction of the net section to } 0.6P_y)$$

A_{net} = Column cross-sectional area at the location of hole(s)

$P_{cr\ell}$ = Critical elastic local column buckling load including hole(s)

Distortional Buckling

Same as Option 4

8.1.6 DSM comparison to column test simulation database

The six DSM prediction options for cold-formed steel columns with holes are evaluated with the simulated column experiment database developed in Section 8.1.1 and summarized in Appendix K. (Tested strengths with and without global imperfections are provided in Appendix K. The simulated strengths considered in this study contain global imperfections, except for stocky columns with $L/D < 18$ where D is the column flange width). The simulated data is compared against DSM predictions while evaluating data trends against member slenderness, hole size (A_{net}/A_g), and column dimensions L/h , where h is the flat web width of a column.

Figure 8.18 to Figure 8.21 compare the simulated test data to predictions for local, distortional, and global buckling controlled column failures. Option 1 is identical to the existing DSM approach for columns without holes, except the critical elastic buckling loads ($P_{cr\ell}$, P_{crd} , and P_{cr}) are determined with the influence of holes. Option 1 is observed to be an accurate predictor of strength when λ_ℓ , λ_d , and λ_c are high, but results in unconservative predictions (by as much as 30 % for distortional buckling controlled specimens, see Figure 8.20) as λ_ℓ , λ_d , and λ_c decreases below 1.5. The unconservative predictions occur because Option 1 does not account for the column strength limit P_{ynet} , nor does it account for a transition from an elastic buckling controlled failure to a yield-controlled failure at the net section discussed in Section 8.1.2 and Section 8.1.3.

Option 2 is observed to be a conservative predictor in Figure 8.18 to Figure 8.21 for high λ_ℓ , λ_d , and λ_c and demonstrates improved accuracy over Option 1 when slenderness decreases and hole size increases (see Figure 8.20). Option 2 replaces P_{ynet} everywhere

within the existing DSM formulation, which has the effect of increasing λ_e , λ_d , and λ_c and decreasing predicted strength. Option 3 test-to-predicted trends are similar to Option 1 with increasingly unconservative predictions as slenderness decreases, demonstrating that the P_{ynet} limit on P_{ne} and P_{nd} in Option 3 are not fully effective at capturing the yield transition to the net section. Option 4 is identical to Option 3 except the yield transition on the DSM distortional curve developed in Section 8.1.2 is employed to provide a more accurate prediction of the net-section yielding influence. Option 4 demonstrates an improvement in accuracy over Option 3, although it overpredicts the strength of the two columns discussed in Section 8.1.4 (SSMA 350S162-68 and SSMA 350S162-54 columns), where large holes caused a sudden weak-axis flexural buckling failure. Option 5 includes both local and distortional yield transitions, although the predictions are identical to Option 4 because the distortional transition always predicts lower strengths than the local transition for the columns considered. Option 6 deviates from the other approaches and accounts for the presence of holes by reducing P_{ne} by the ratio P_{ynet}/P_y when λ_e is less than 0.776; this option also always including a local buckling transition (Option 5 imposes a transition on the DSM local buckling design curve only when $P_{ynet} < P_{ne}$, see Figure 8.17). The reduction in P_{ne} shifts the global buckling-controlled specimens in Options 1 through 5 to the DSM local buckling curve in Option 6, resulting in conservative predictions with decreasing λ_e .

Table 8.1 summarizes the test-to-predicted ratio statistics for the six DSM options. The standard deviation (SD) is useful when comparing the methods, because it provides a metric for how well the trends in strength are following the prediction curves. (The

mean is also an important statistic but can hide unconservative prediction trends in some columns with overconservative predictions in other columns). A low standard deviation is appealing because it enables higher strength reduction factors in a design code. The strength reduction factor ϕ is also provided for each option. ϕ is calculated with the following equation from Chapter F of the Specification (AISI-S100 2007):

$$\phi = C_{\phi} (M_m F_m P_m) e^{-\beta_o \sqrt{V_M^2 + V_F^2 + C_p V_P^2 + V_Q^2}}, \quad (8.1)$$

where the calibration coefficient $C_{\phi}=1.52$ for LRFD, the mean value of the material factor $M_m=1.10$ for concentrically loaded compression members, the mean value of the fabrication factor $F_m=1.0$, the mean value of the professional factor $P_m=1.0$, the coefficient of variation (COV) of the material factor $V_m=0.10$, the COV of the fabrication factor $V_f=0.05$, the COV of the load effect $V_q=0.21$ for LRFD, and the correction factor $C_p=1$. The COV of the test results, V_p , is calculated as the ratio of the standard deviation to the mean of the test-to-predicted statistics in Table 8.1.

No one option stands out above the rest when studying the table, although Option 2, 3, and 4 (5) have the most evenly distributed statistics between local and distortional buckling column groups. The observations from this comparison will be combined with the DSM comparison to the experimental database in the next section.

Table 8.1 DSM test-to-predicted statistics for column simulations

Option	Description	Local buckling				Distortional buckling				Global buckling			
		Mean	SD	ϕ	# of tests	Mean	SD	ϕ	# of tests	Mean	SD	ϕ	# of tests
1	P_y everywhere	1.06	0.15	0.83	93	1.07	0.17	0.82	178	1.11	0.21	0.78	114
2	$P_{y_{net}}$ everywhere	1.06	0.15	0.83	93	1.08	0.16	0.83	176	1.11	0.22	0.77	116
3	Cap P_{nc} , P_{nd}	1.06	0.15	0.83	93	1.09	0.17	0.82	186	1.13	0.21	0.79	106
4	Transition P_{nd} , Cap P_{nc}	1.08	0.14	0.85	89	1.04	0.19	0.79	200	1.16	0.19	0.82	96
5	Transition P_{nd} and P_{nc} (Option A)	1.08	0.14	0.85	89	1.04	0.19	0.79	200	1.16	0.19	0.82	96
6	Transition P_{nd} and P_{nc} (Option B)	1.07	0.20	0.78	221	1.10	0.15	0.85	164	---	---	---	0

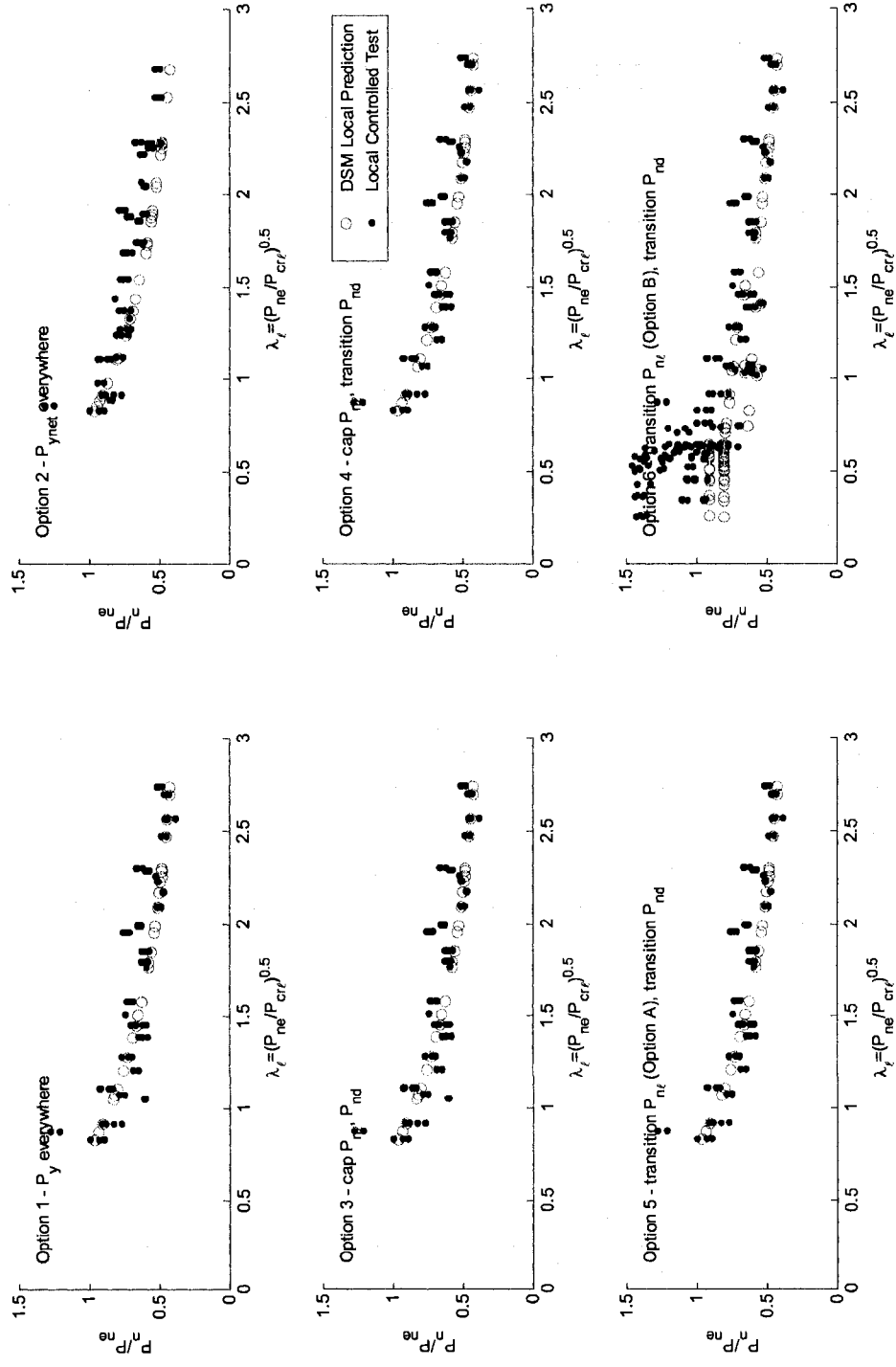


Figure 8.18 Comparison of simulated test strengths to predictions for columns with local buckling-controlled failures as a function of local slenderness (tested strength is normalized by P_{ne})

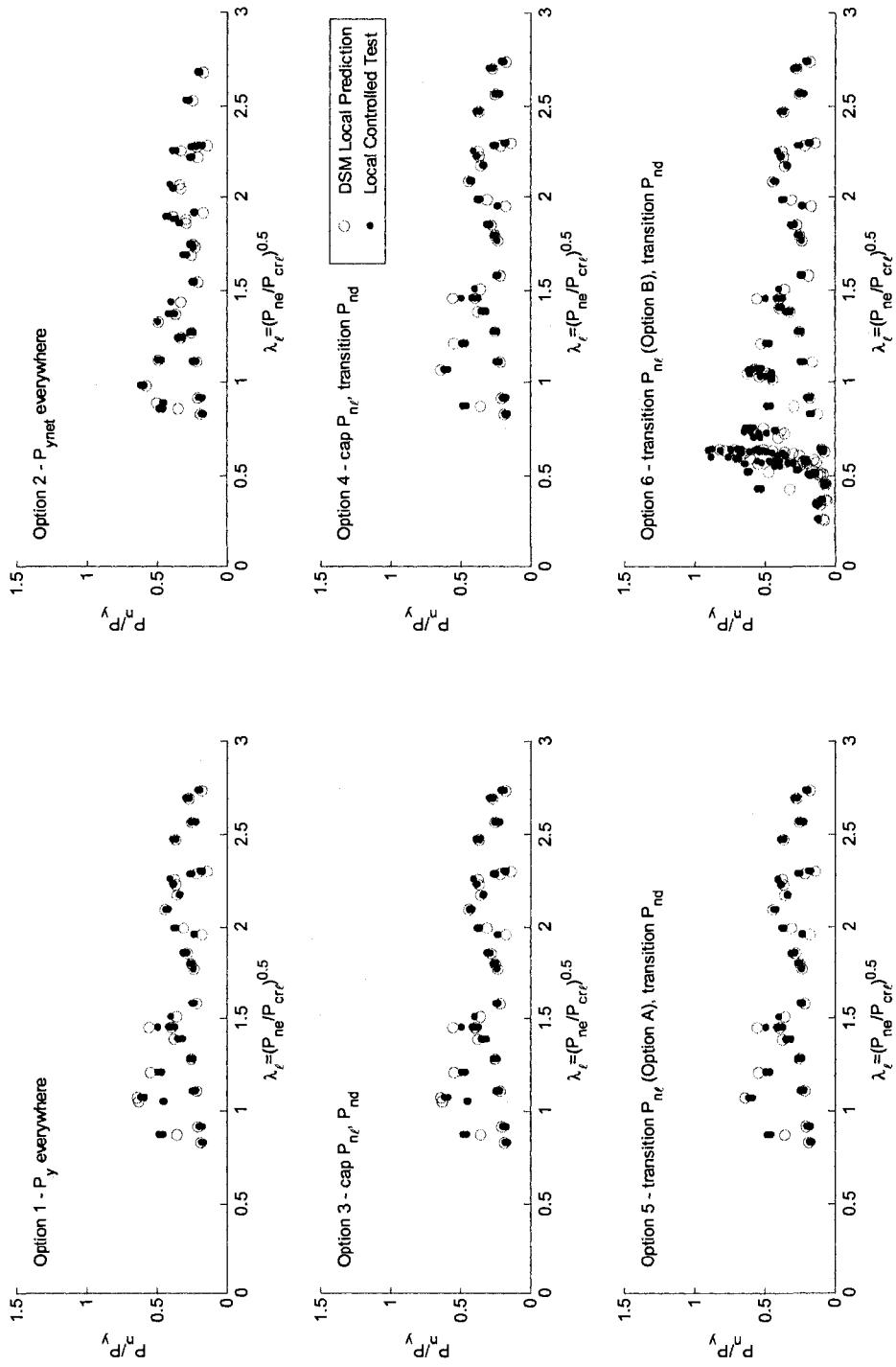


Figure 8.19 Comparison of simulated test strengths to predictions for columns with local buckling-controlled failures as a function of local slenderness (tested strength is normalized by P_{yg})

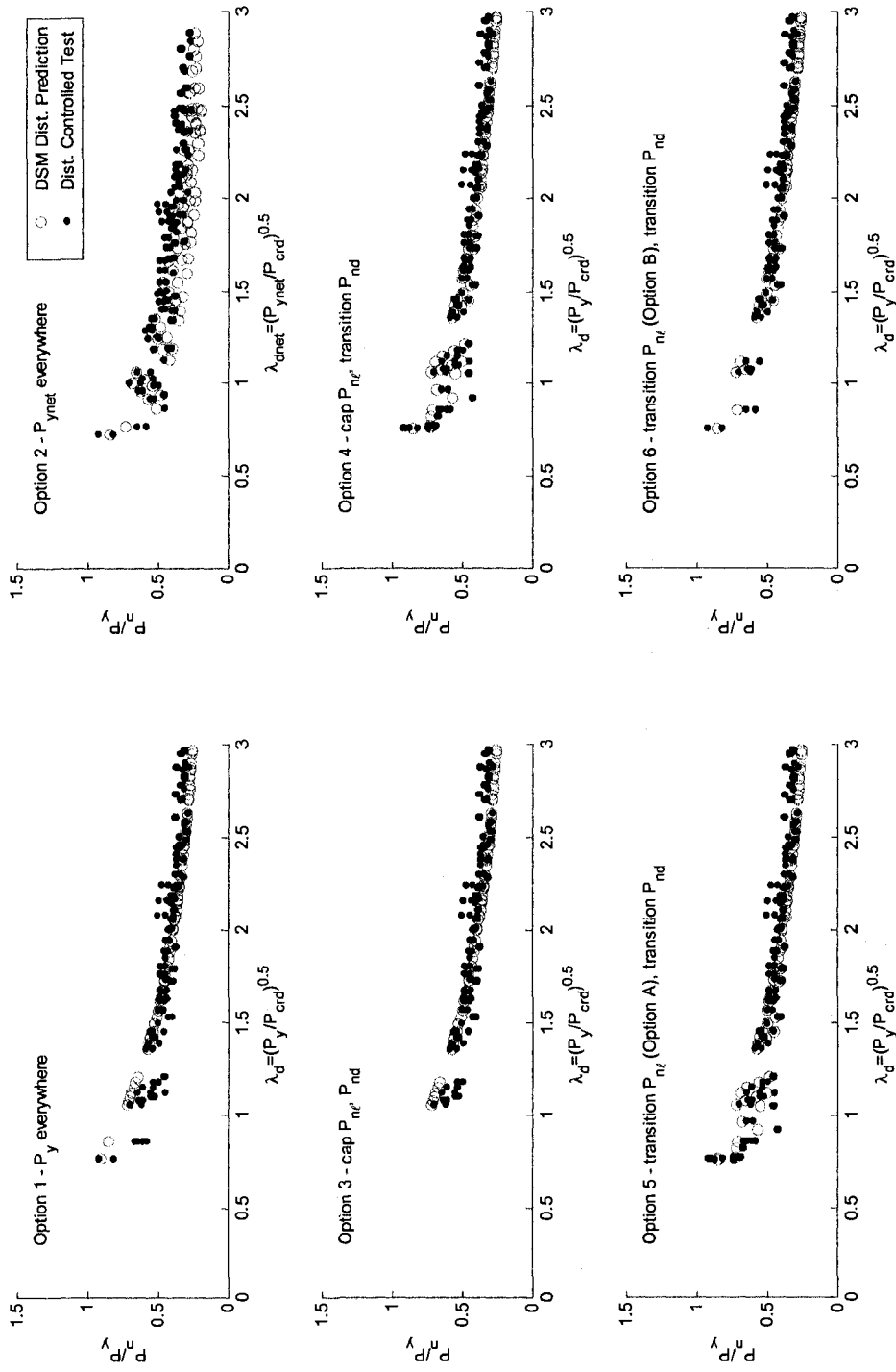


Figure 8.20 Comparison of simulated test strengths to predictions for columns with distortional buckling-controlled failures as a function of distortional slenderness

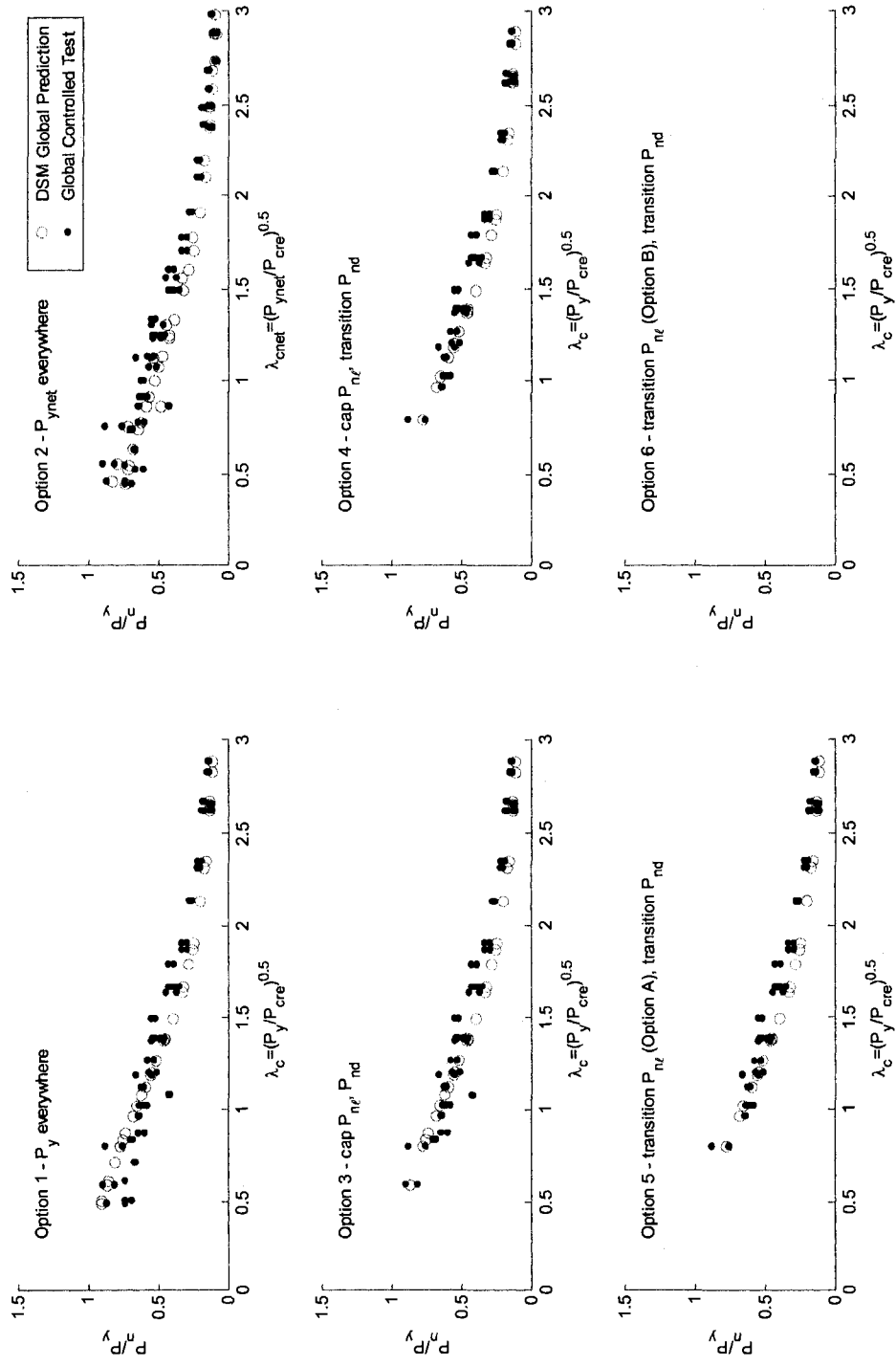


Figure 8.21 Comparison of simulated test strengths to predictions for columns with global buckling-controlled failures (i.e., no local interaction) as a function of global slenderness

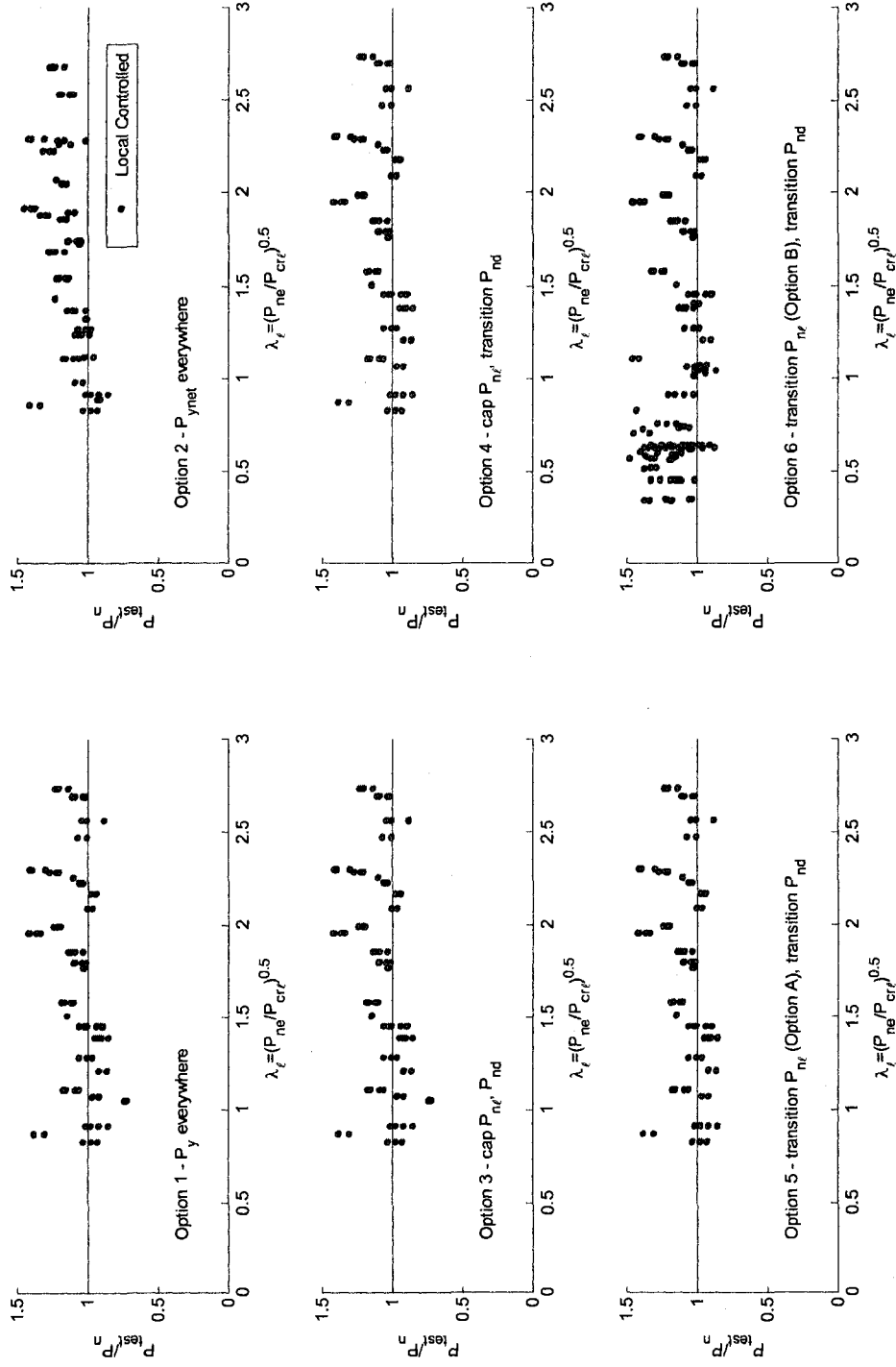


Figure 8.22 Test-to-predicted ratios for local buckling-controlled simulated column failures as a function of local slenderness

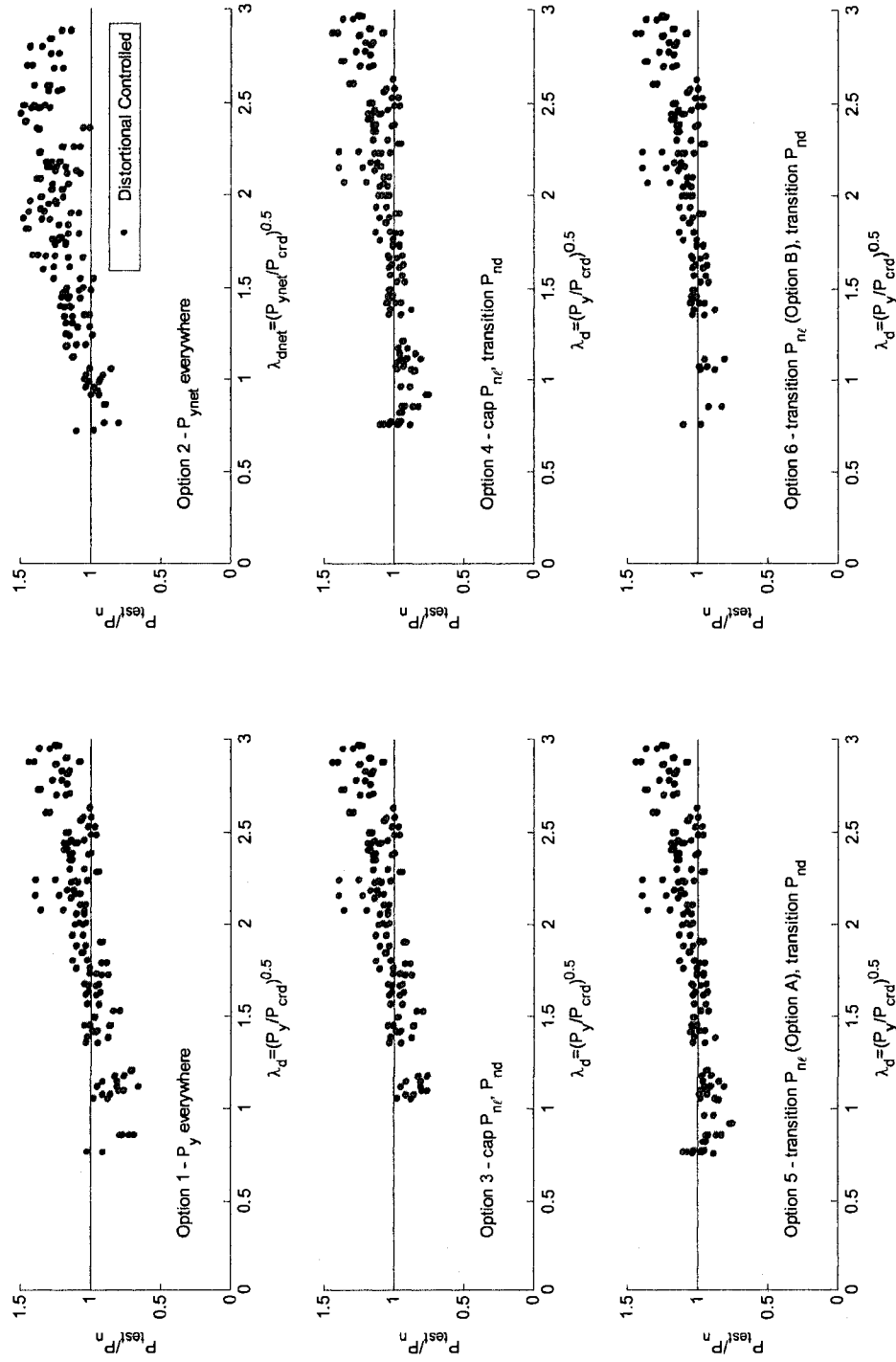


Figure 8.23 Test-to-predicted ratios for distortional buckling-controlled simulated column failures as a function of distortional slenderness

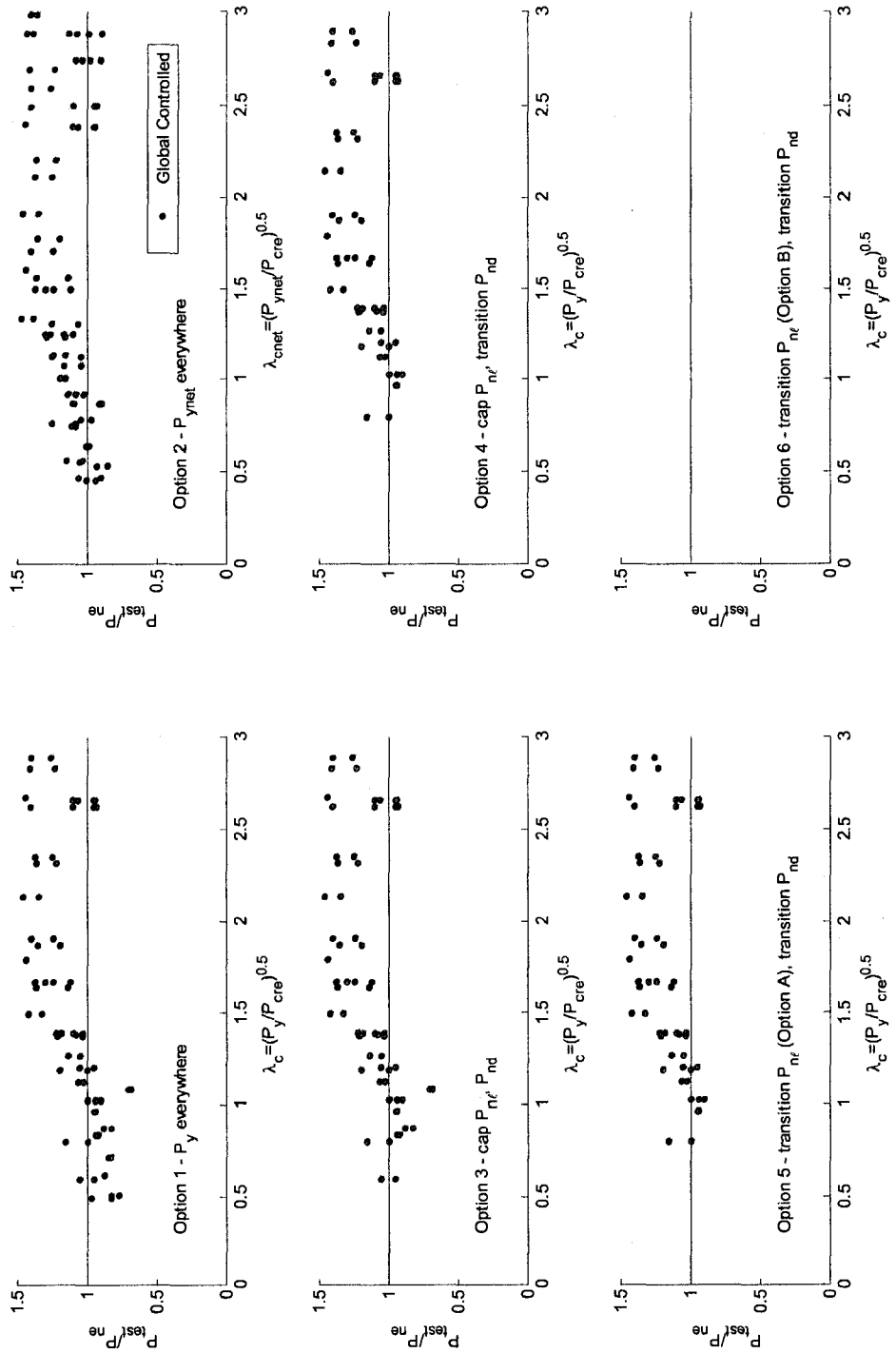


Figure 8.24 Test-to-predicted ratios for simulated global buckling-controlled column failures (i.e., no local buckling interaction) as a function of global slenderness

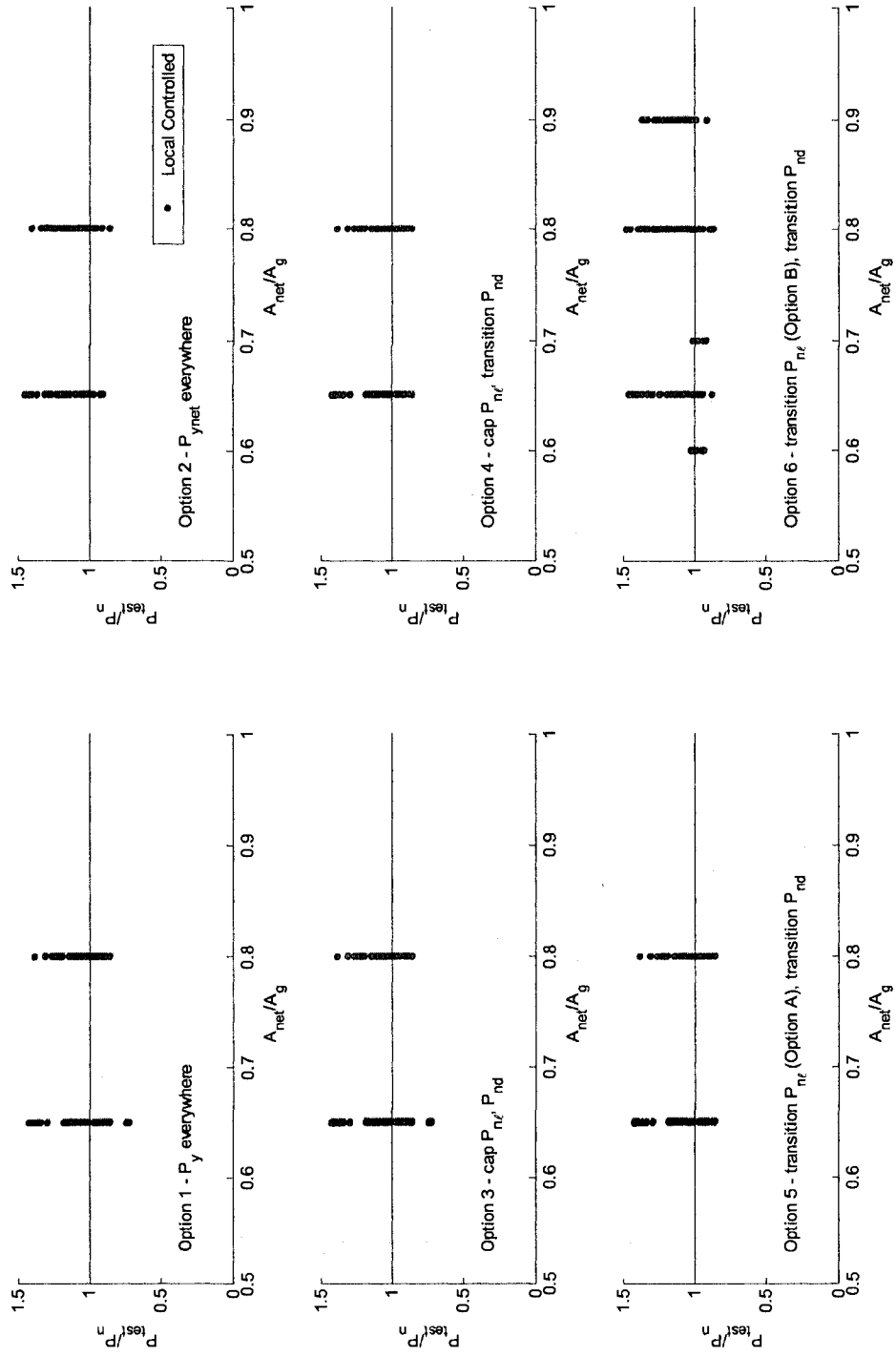


Figure 8.25 Test-to-predicted ratios for simulated local buckling-controlled column failures as a function of net cross-sectional area to gross cross-sectional area

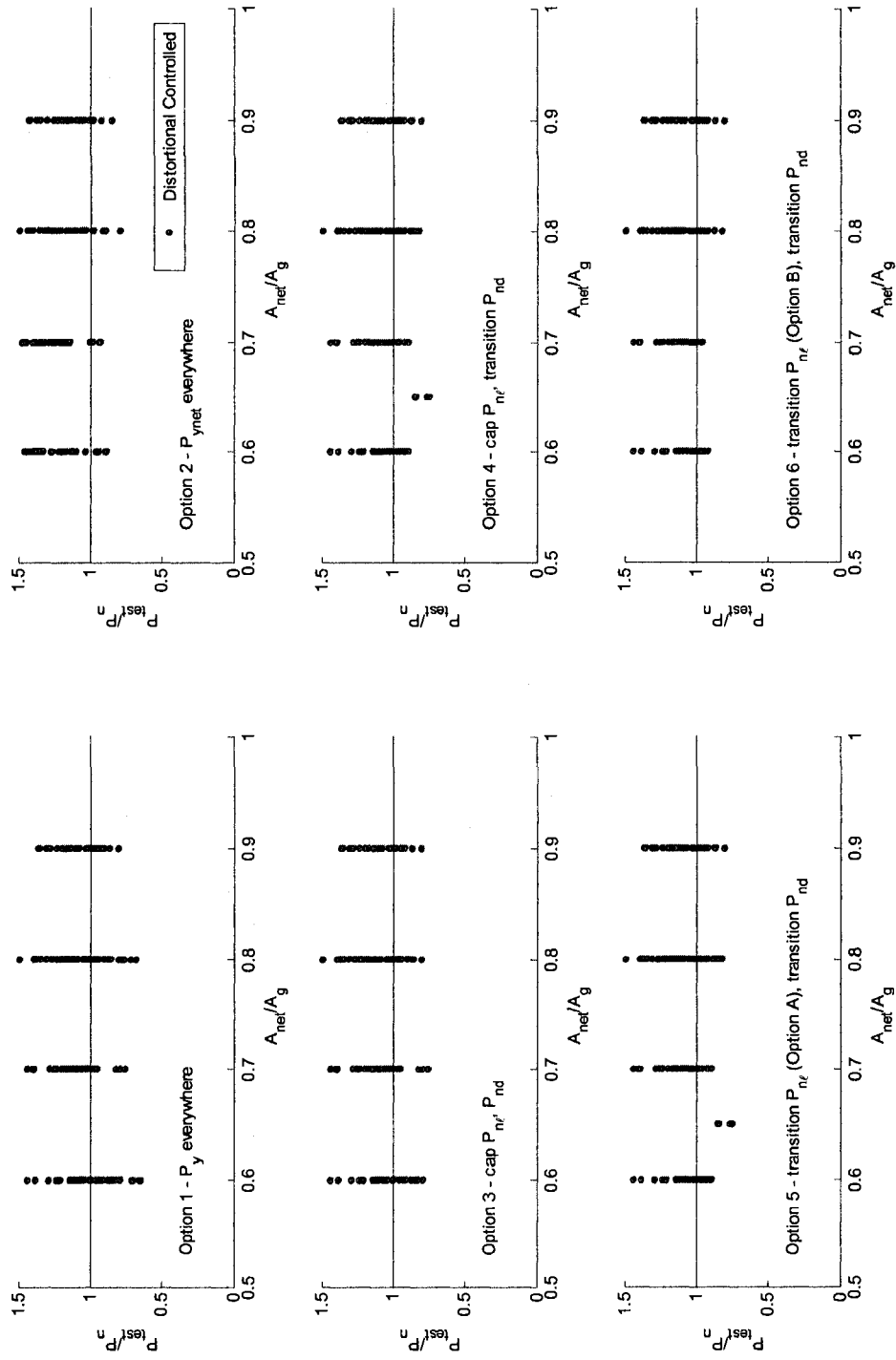


Figure 8.26 Test-to-predicted ratios for simulated distortional buckling-controlled column failures as a function of net cross-sectional area to gross cross-sectional area

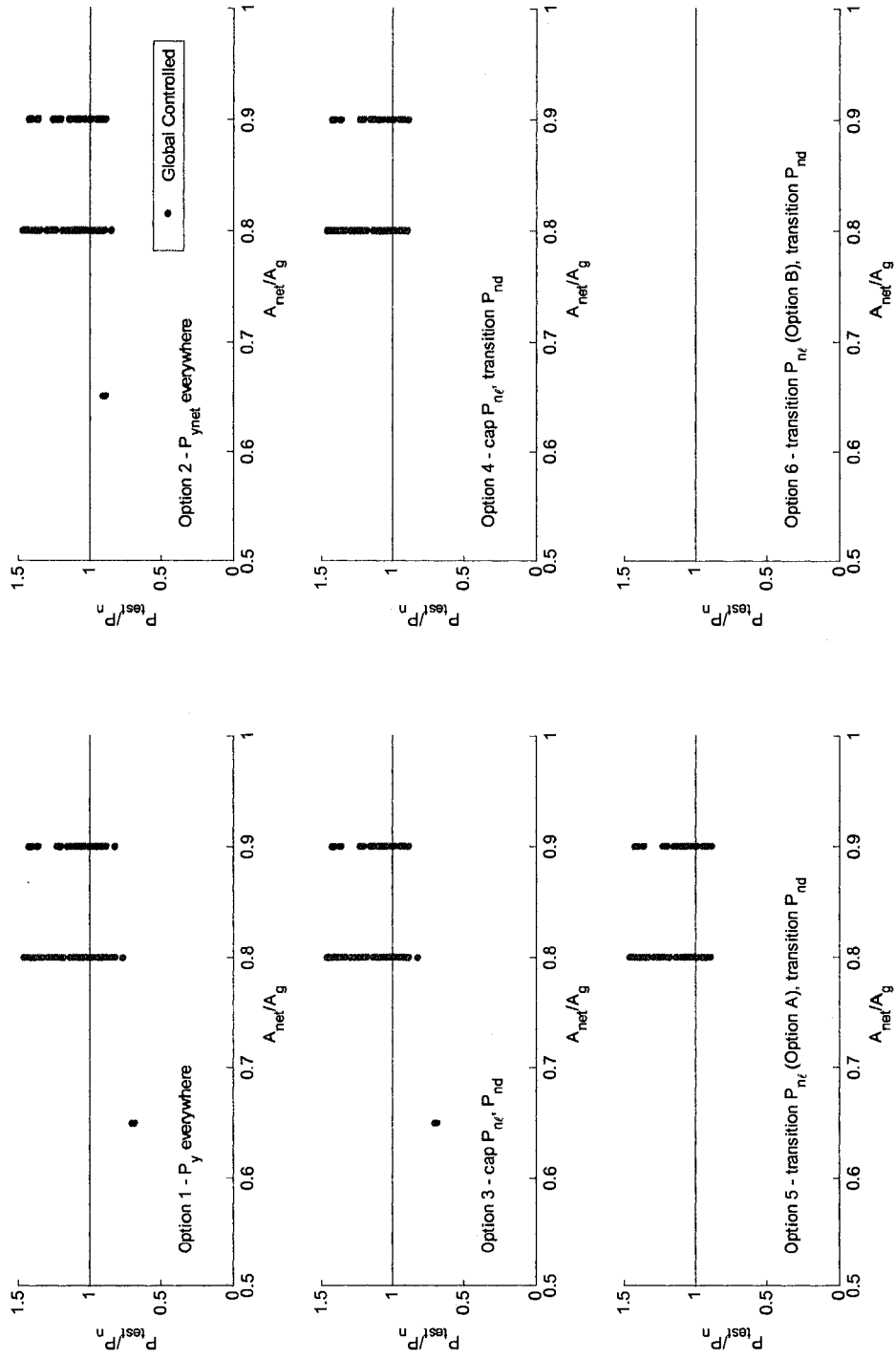


Figure 8.27 Test-to-predicted ratios for simulated global buckling-controlled column failures as a function of net cross-sectional area to gross cross-sectional area

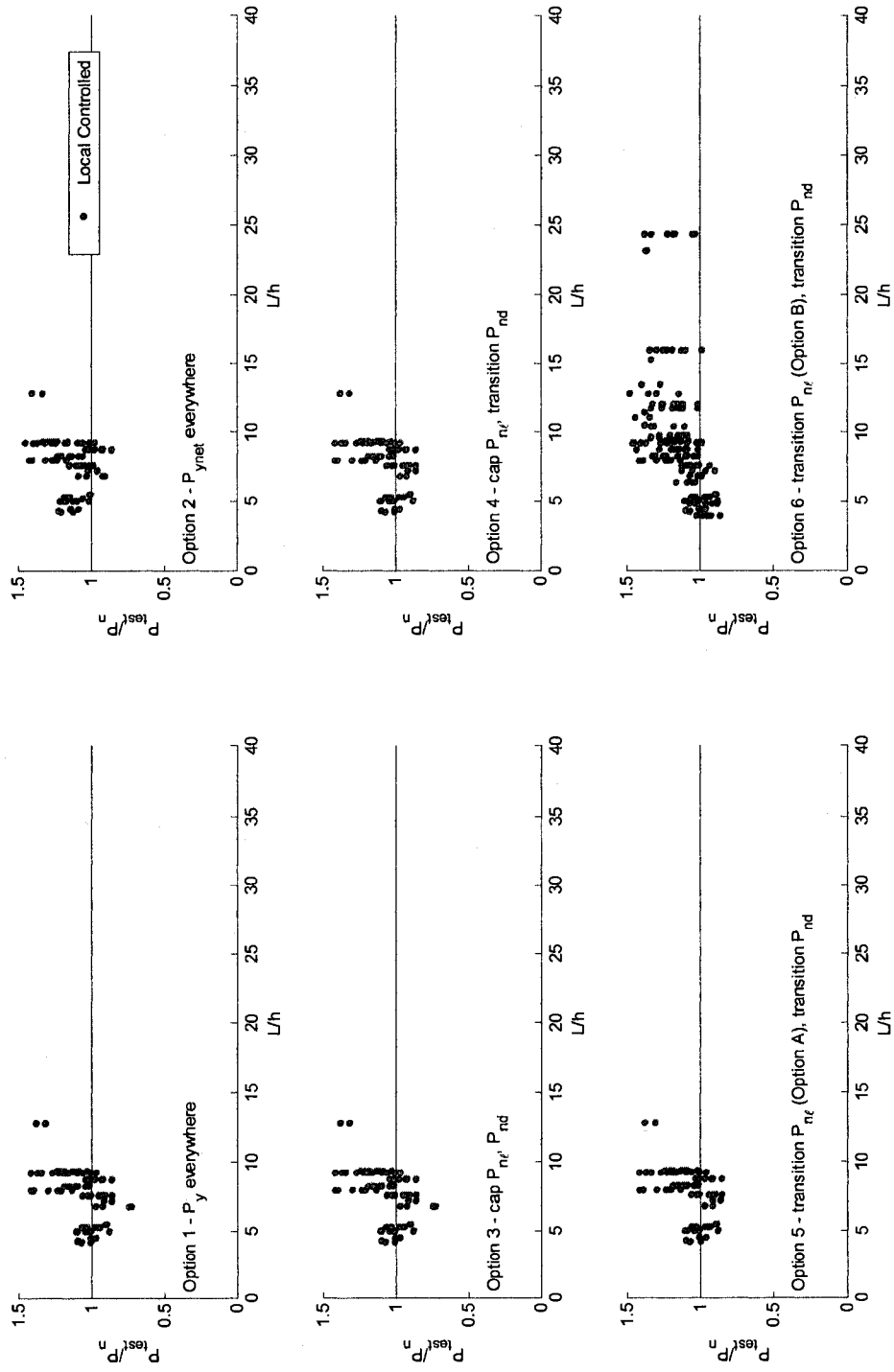


Figure 8.28 Test-to-predicted ratios for simulated local buckling-controlled column failures as a function of column length, L , to flat web width, h

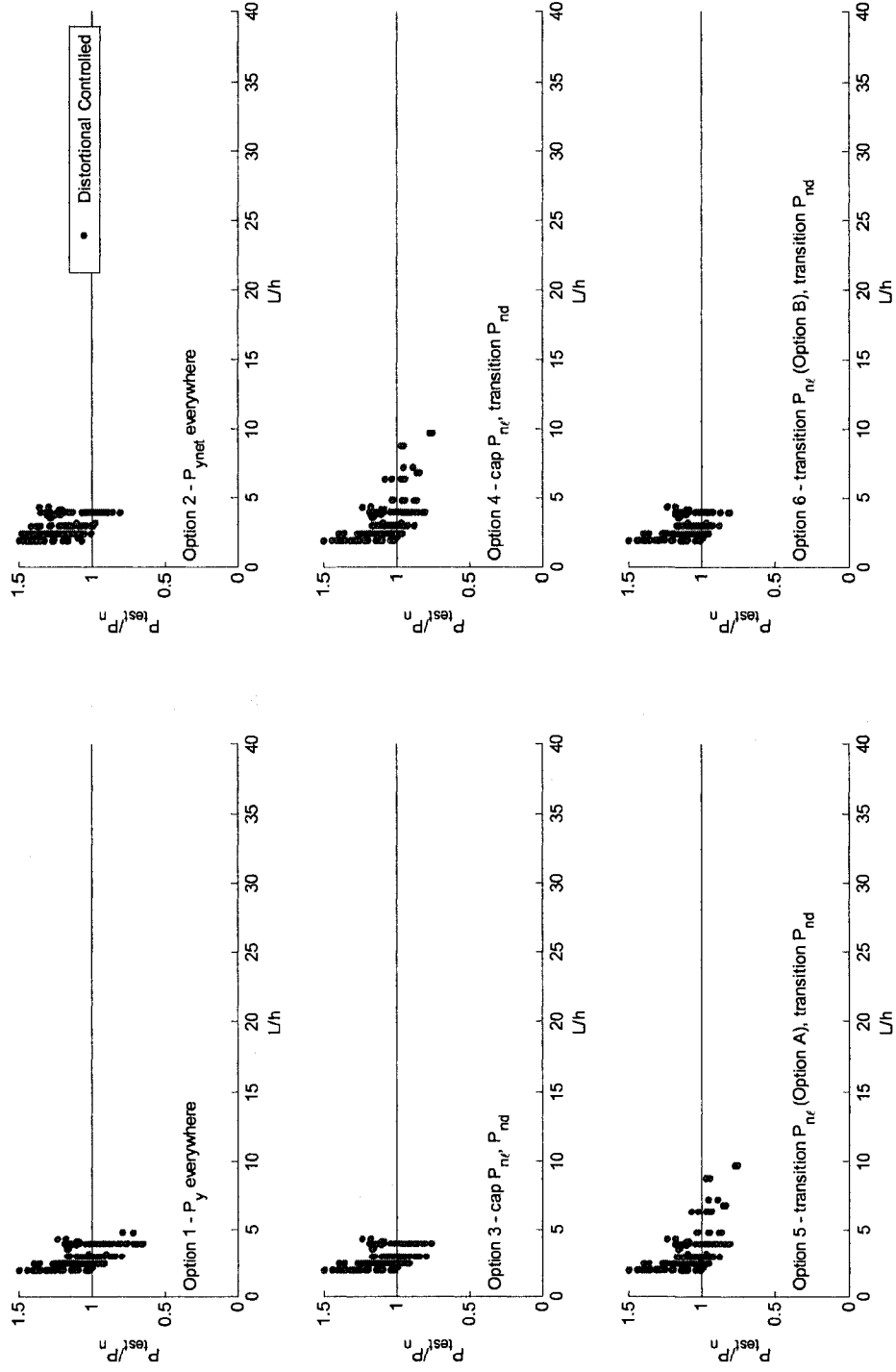


Figure 8.29 Test-to-predicted ratios for simulated distortional buckling-controlled column failures as a function of column length, L , to flat web width, h

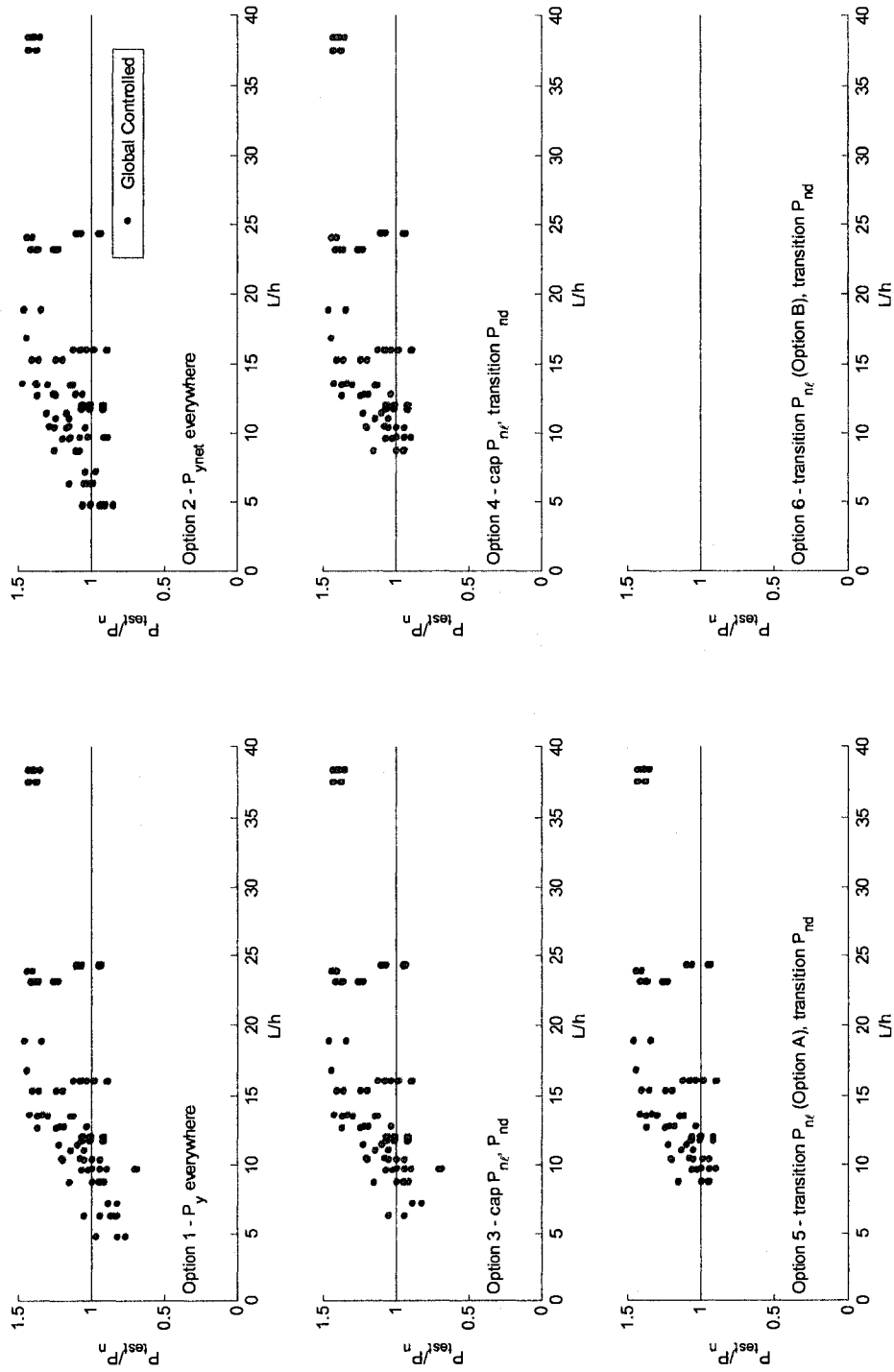


Figure 8.30 Test-to-predicted ratios for simulated global buckling-controlled column failures as a function of column length, L , to web width, h

8.1.7 DSM comparison to experimental column database

The six DSM options are now compared to the column experiment database first assembled in Section 4.2.6.2. The database contains the elastic buckling properties of each column, including the presence of holes and the influence of boundary conditions, as well as the tested strengths. Figure 8.31 through Figure 8.34 compare the experiment strengths to DSM predictions for local, distortional, and global buckling controlled column failures. Option 1 is observed to be an accurate predictor of column strength when local, distortional, and global slenderness are high, but overpredicts the tested strength as slenderness decreases. This trend is consistent with the simulated experiment comparison in Section 8.1.6 and emphasizes the need for a limit on column strength when yielding at the net section controls the failure of a column with holes. Option 2 is even more conservative in this study when compared to the simulated column study because the tested specimens considered only have one hole, and therefore employing P_{ynet} produces unrealistically high column slenderness. Option 3 shifts column specimens from the global buckling failure group to the local buckling failure group with the P_{ynet} limit on P_{nc} , resulting in improved accuracy when compared to Option 2. Four columns in the Option 3 distortional buckling failure group are still overpredicted by more than 10% though as observed in Figure 8.33. Option 4 and Option 5 improve the accuracy of the underpredicted specimen strengths in Option 3 with the addition of the distortional and local yield control transitions to the net section. Option 6 is an overly conservative predictor of columns failing by global buckling.

Table 8.2 summarizes the test-to-predicted ratio statistics for all columns in the database. Options 3, 4, and 5 are identified as the methods with the mean closest to unity and with the lowest standard deviations. The statistics for just the stub columns ($\lambda_c < 0.20$) in Table 8.3 confirm the viability of DSM Options 3, 4, and 5, and provides more direct evidence that holes limit the column strength to the net section P_{ynet} ; the mean test-to-predicted ratio is 0.84 for global (yielding) failures of stub columns employing Option 1.

Table 8.2 DSM test-to-predicted ratio statistics for column experiments

Option	Description	Local buckling				Distortional buckling				Global buckling			
		Mean	SD	ϕ	# of tests	Mean	SD	ϕ	# of tests	Mean	SD	ϕ	# of tests
1	P_y everywhere	1.03	0.11	0.87	52	1.09	0.16	0.83	15	1.06	0.17	0.82	11
2	P_{ynet} everywhere	1.17	0.09	0.89	47	1.22	0.13	0.87	15	1.17	0.15	0.85	16
3	Cap P_{nt} , P_{nd}	1.07	0.08	0.90	42	1.06	0.13	0.85	29	1.16	0.09	0.90	7
4	Transition P_{nd} , Cap P_{nt}	1.07	0.08	0.90	40	1.10	0.11	0.87	33	1.19	0.08	0.90	5
5	Transition P_{nd} and P_{nt} (Option A)	1.06	0.08	0.89	47	1.13	0.10	0.89	26	1.19	0.08	0.90	5
6	Transition P_{nd} and P_{nt} (Option B)	1.12	0.15	0.84	56	1.14	0.10	0.89	22	---	---	---	0

Table 8.3 DSM test-to-predicted ratio statistics for column experiments (stub columns only)

Option	Description	Local buckling				Distortional buckling				Global buckling			
		Mean	SD	ϕ	# of tests	Mean	SD	ϕ	# of tests	Mean	SD	ϕ	# of tests
1	P_y everywhere	0.98	0.10	0.88	33	0.83	0.01	0.92	3	0.84	0.08	0.88	3
2	P_{ynet} everywhere	1.12	0.07	0.90	28	1.03	0.06	0.91	3	1.07	0.12	0.86	8
3	Cap P_{nt} , P_{nd}	1.03	0.06	0.91	23	1.00	0.12	0.86	16	---	---	---	0
4	Transition P_{nd} , Cap P_{nt}	1.04	0.06	0.91	21	1.06	0.11	0.87	18	---	---	---	0
5	Transition P_{nd} and P_{nt} (Option A)	1.03	0.07	0.90	28	1.11	0.10	0.88	11	---	---	---	0
6	Transition P_{nd} and P_{nt} (Option B)	1.03	0.07	0.90	29	1.11	0.10	0.88	10	---	---	---	0

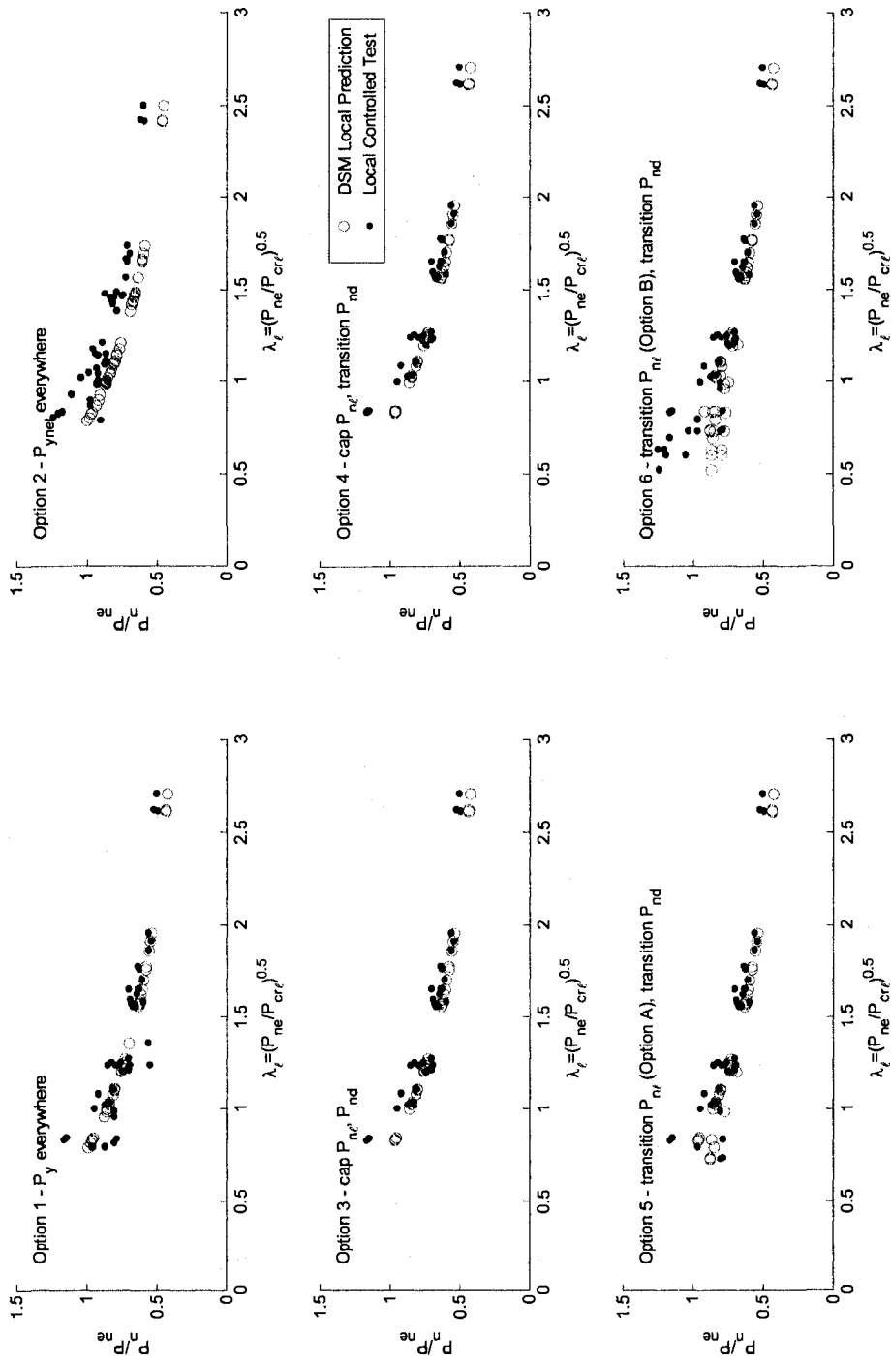


Figure 8.31 Comparison of experimental test strengths to predictions for columns with local buckling-controlled failures as a function of local slenderness (tested strength is normalized by P_{ne})

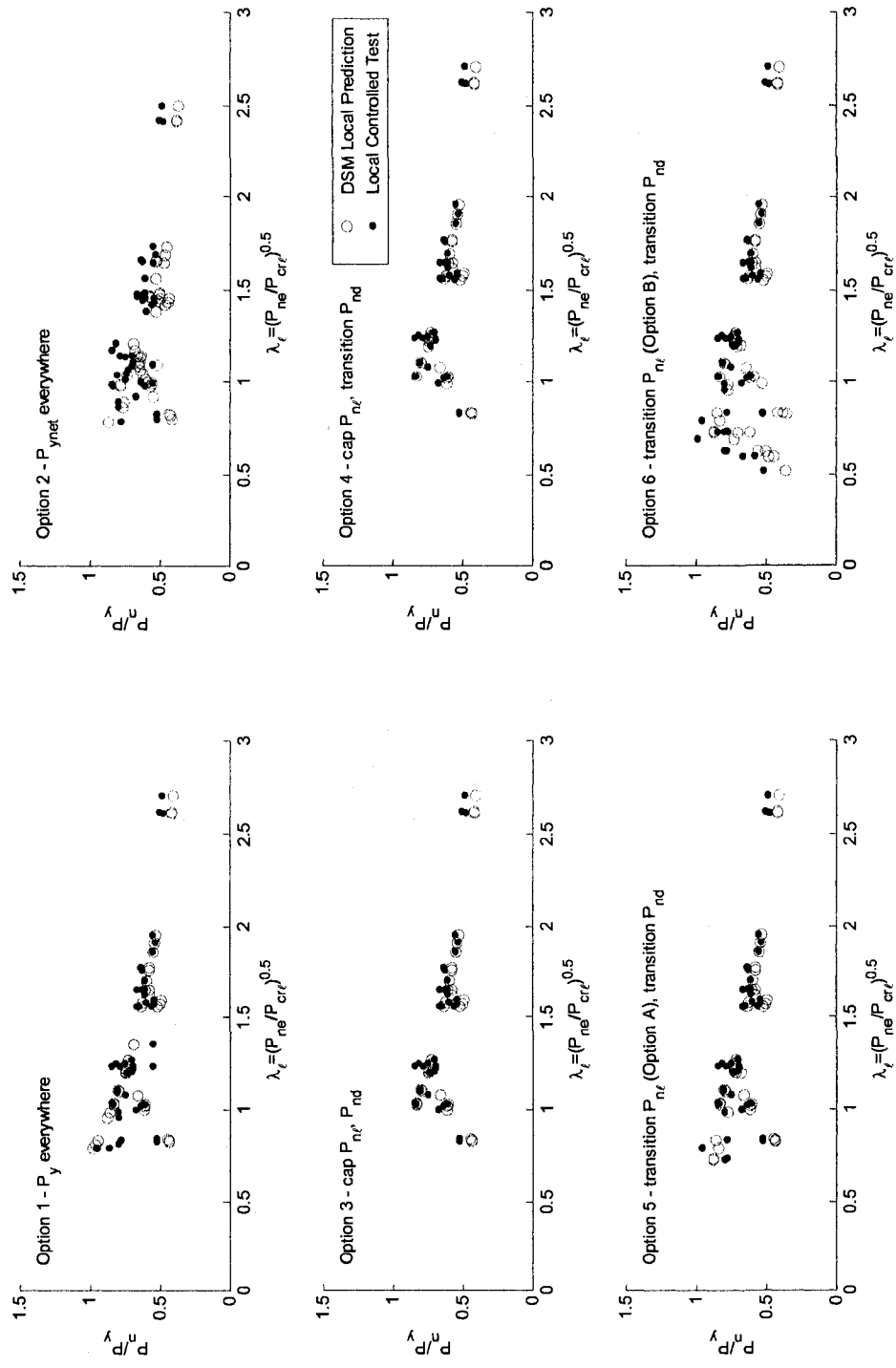


Figure 8.32 Comparison of experimental test strengths to predictions for columns with local buckling-controlled failures as a function of local slenderness (tested strength is normalized by P_y)

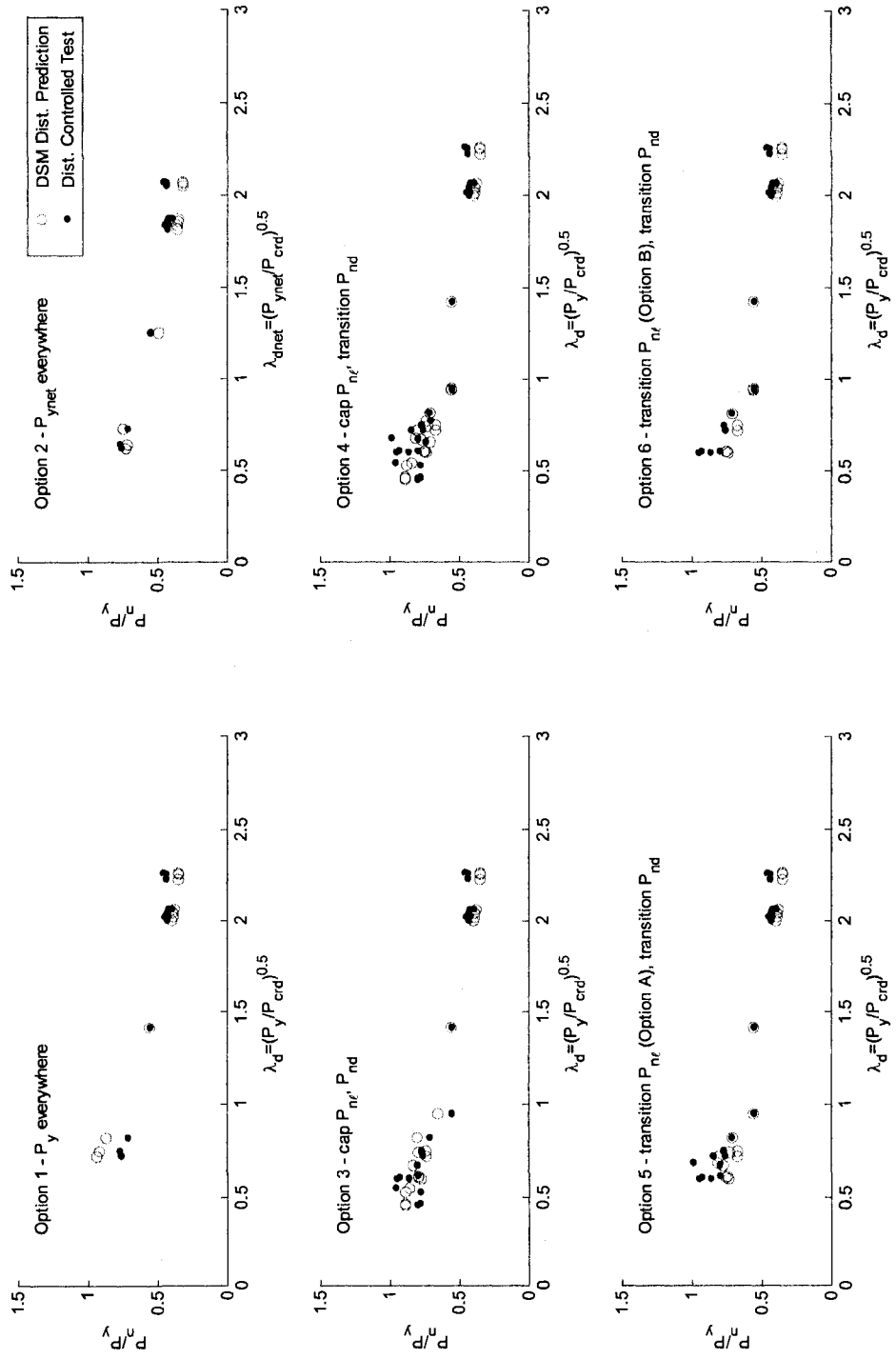


Figure 8.33 Comparison of experimental test strengths to predictions for columns with distortional buckling-controlled failures as a function of distortional slenderness

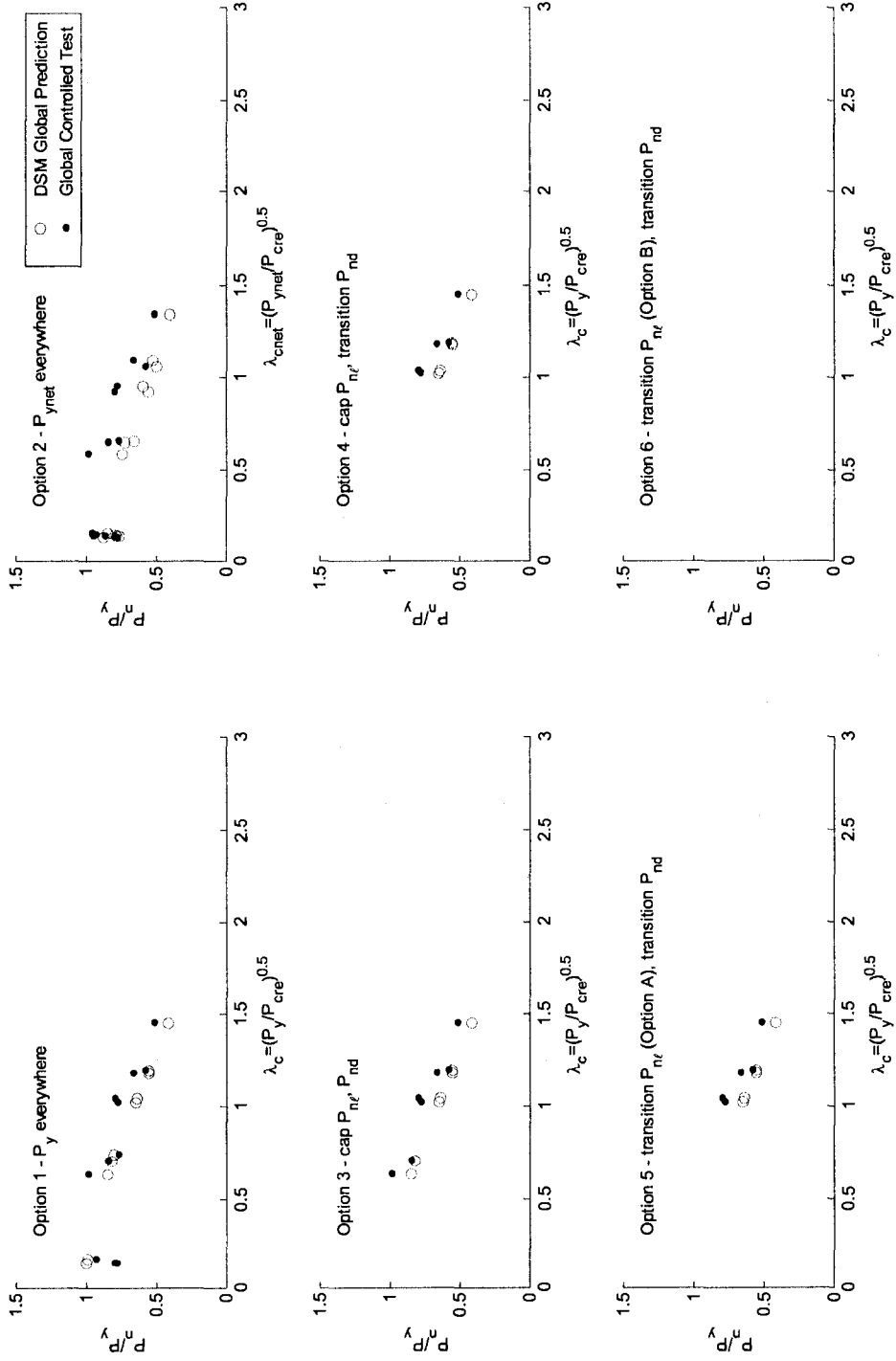


Figure 8.34 Comparison of experimental test strengths to predictions for columns with global buckling-controlled failures as a function of global slenderness

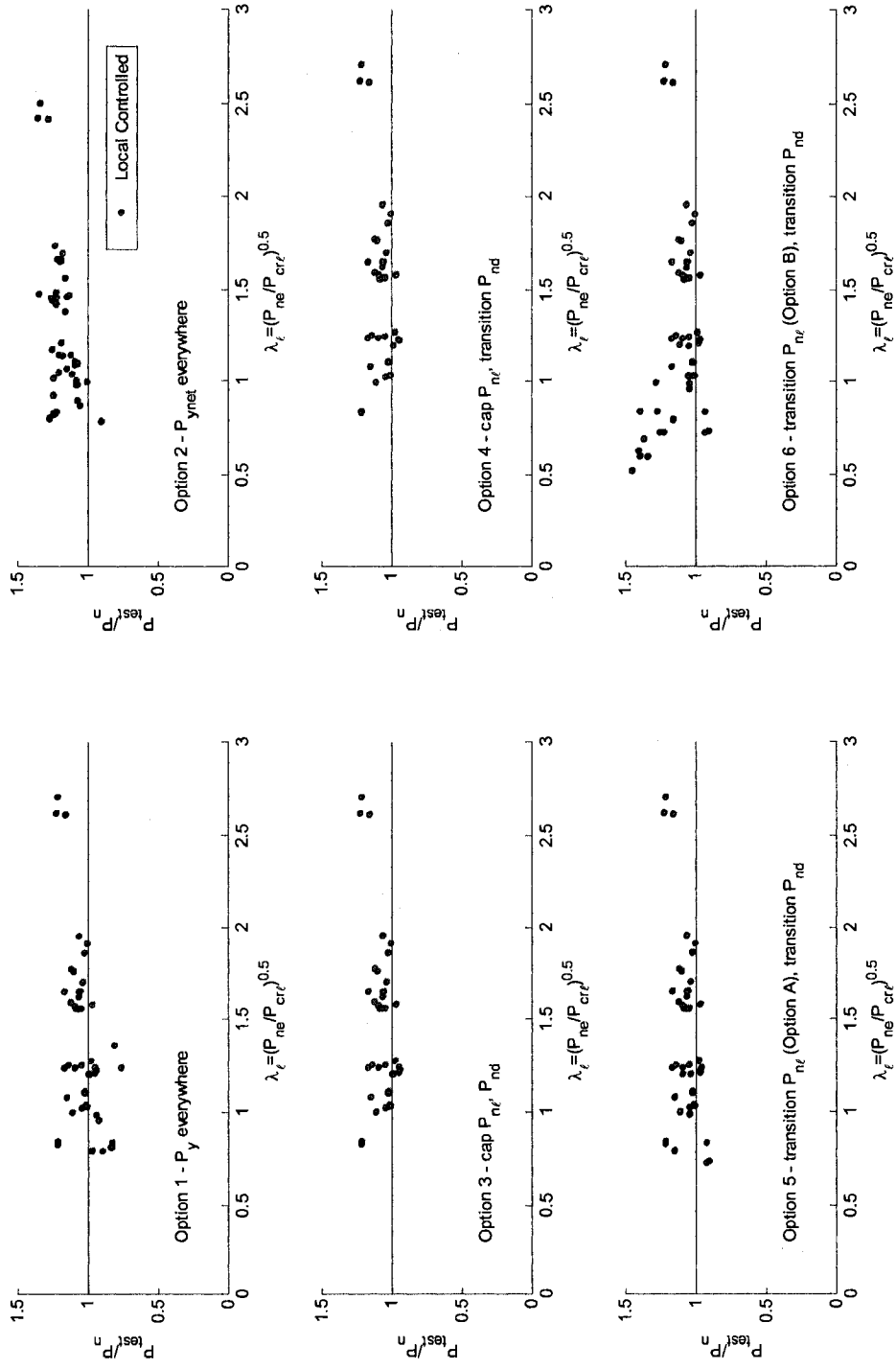


Figure 8.35 Test-to-predicted ratios for experiment local buckling-controlled column failures as a function of local slenderness.

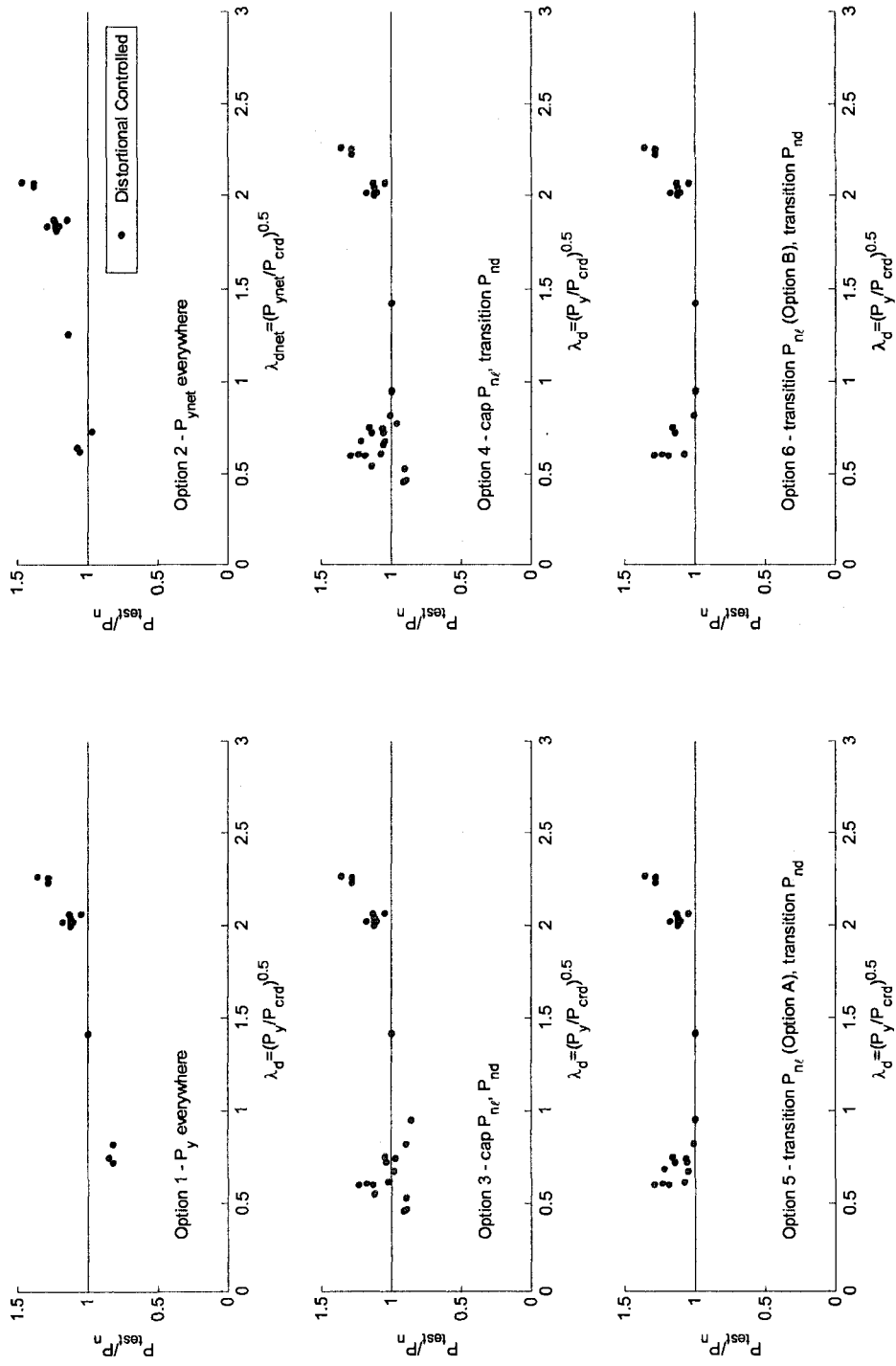


Figure 8.36 Test-to-predicted ratios for experiment distortional buckling-controlled column failures as a function of distortional slenderness

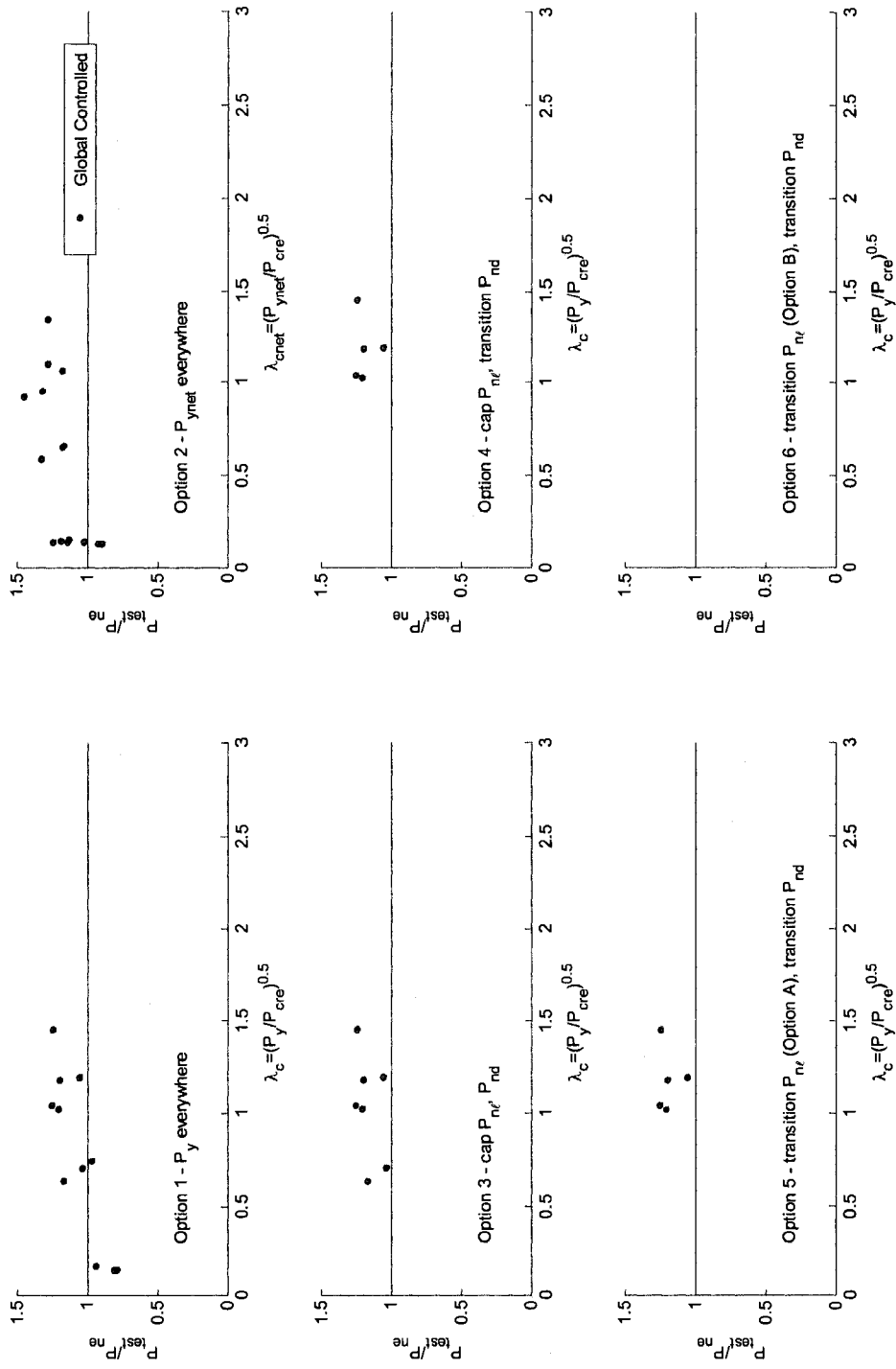


Figure 8.37 Test-to-predicted ratios for experiment global buckling-controlled column failures as a function of global slenderness

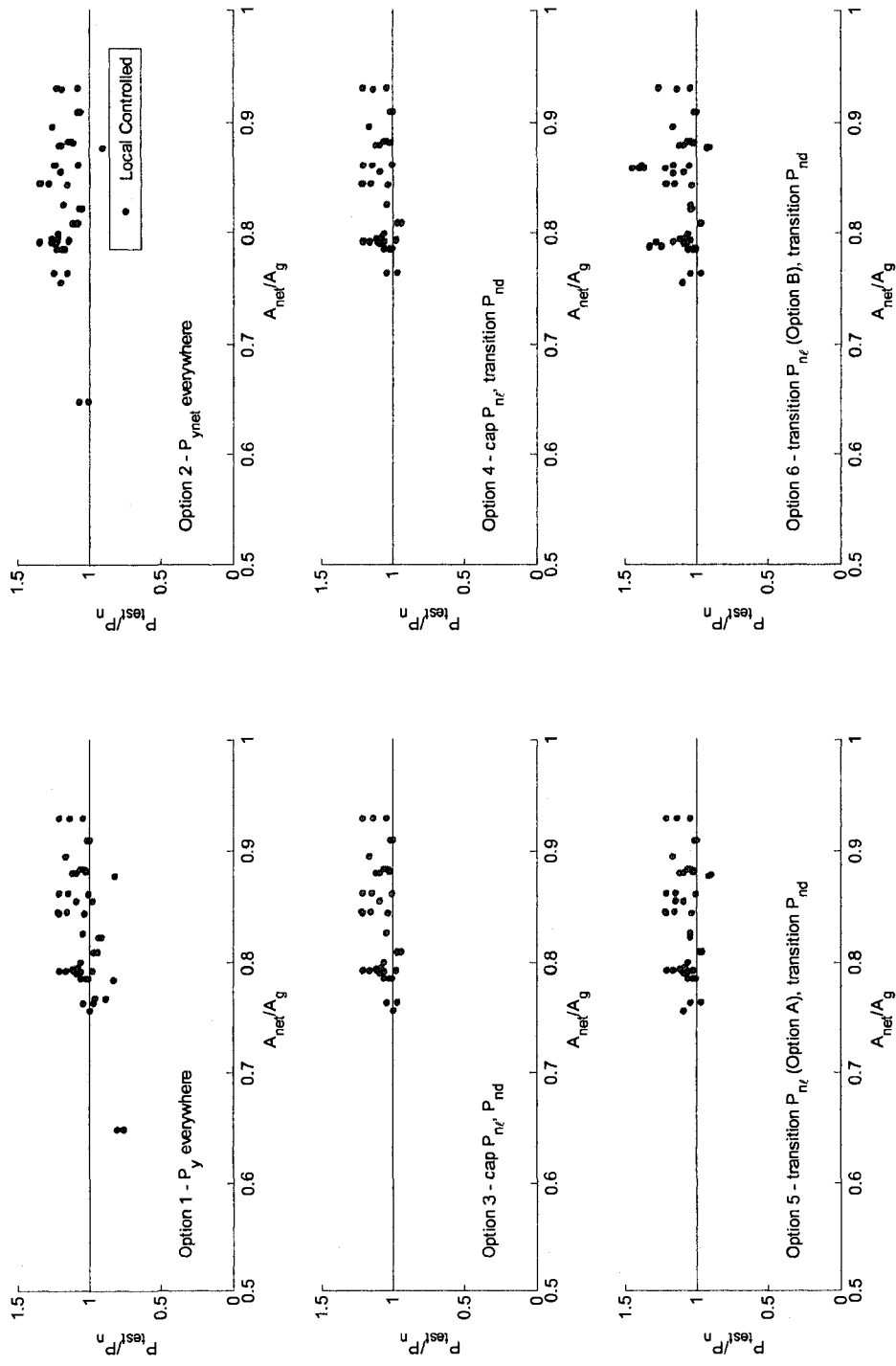


Figure 8.38 Test-to-predicted ratios for experiment local buckling-controlled column failures as a function of net cross-sectional area to gross cross-sectional area

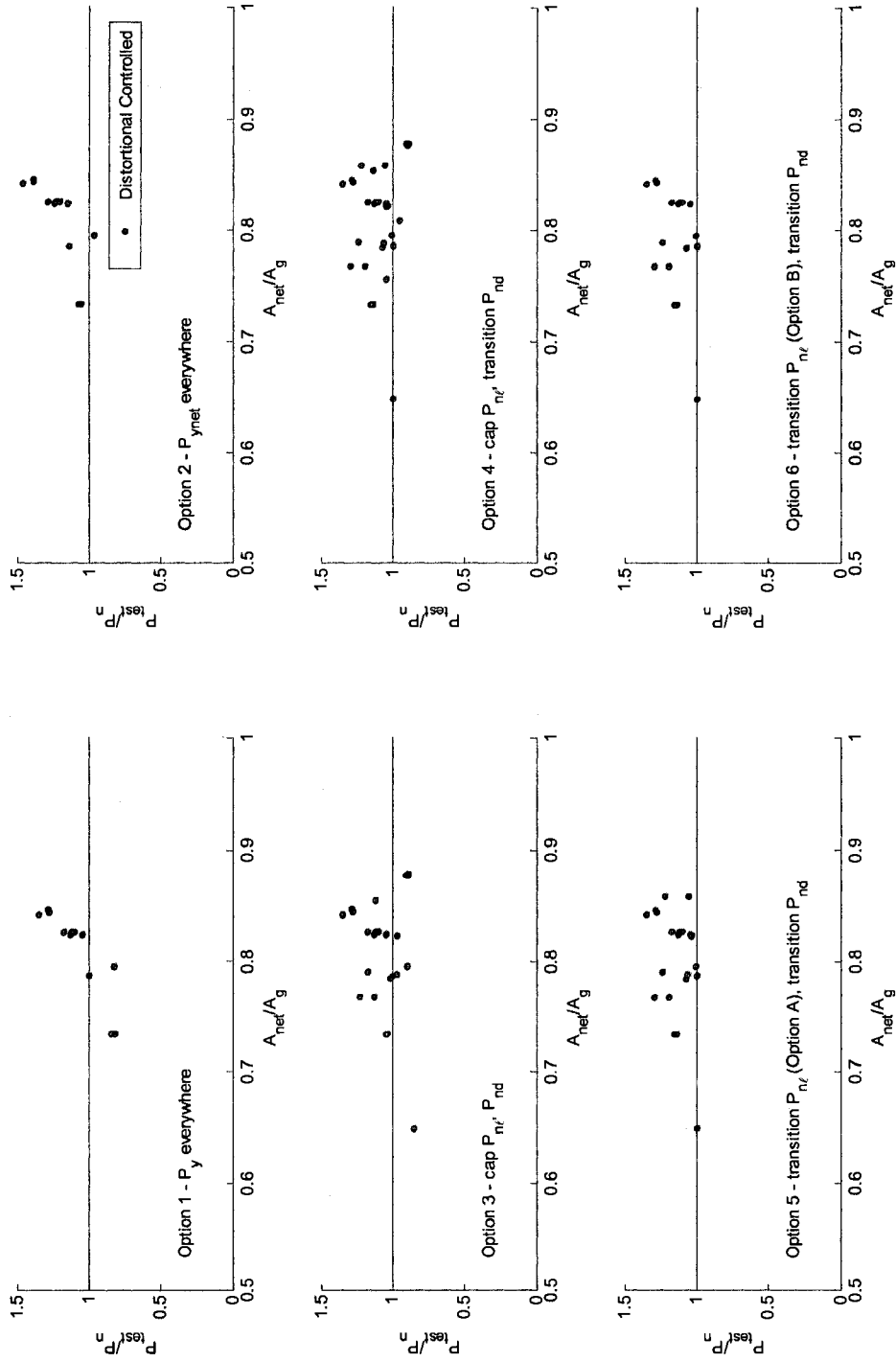


Figure 8.39 Test-to-predicted ratios for experiment distortional buckling-controlled column failures as a function of net cross-sectional area to gross cross-sectional area

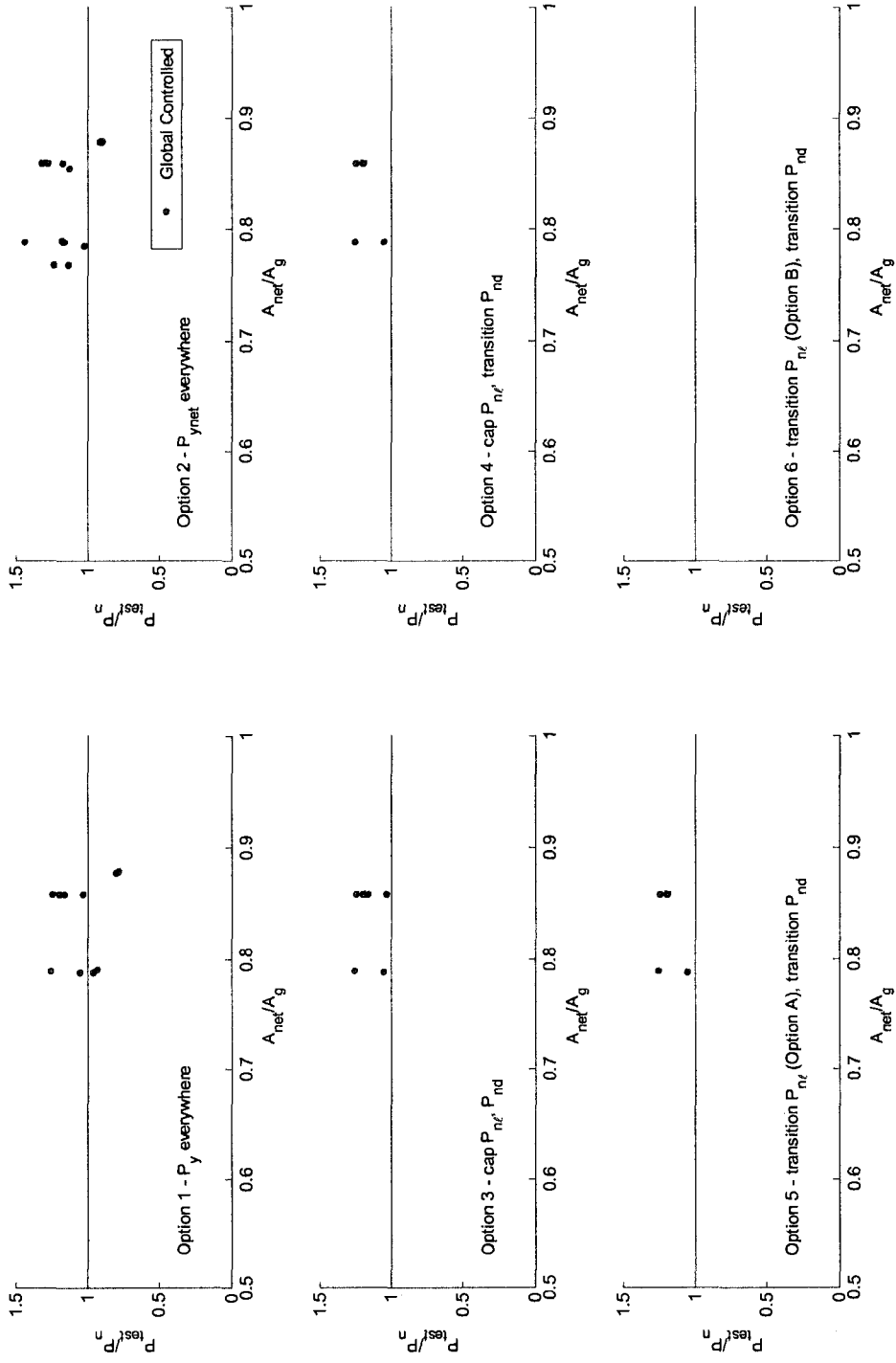


Figure 8.40 Test-to-predicted ratios for experiment global buckling-controlled column failures as a function of net cross-sectional area to gross cross-sectional area

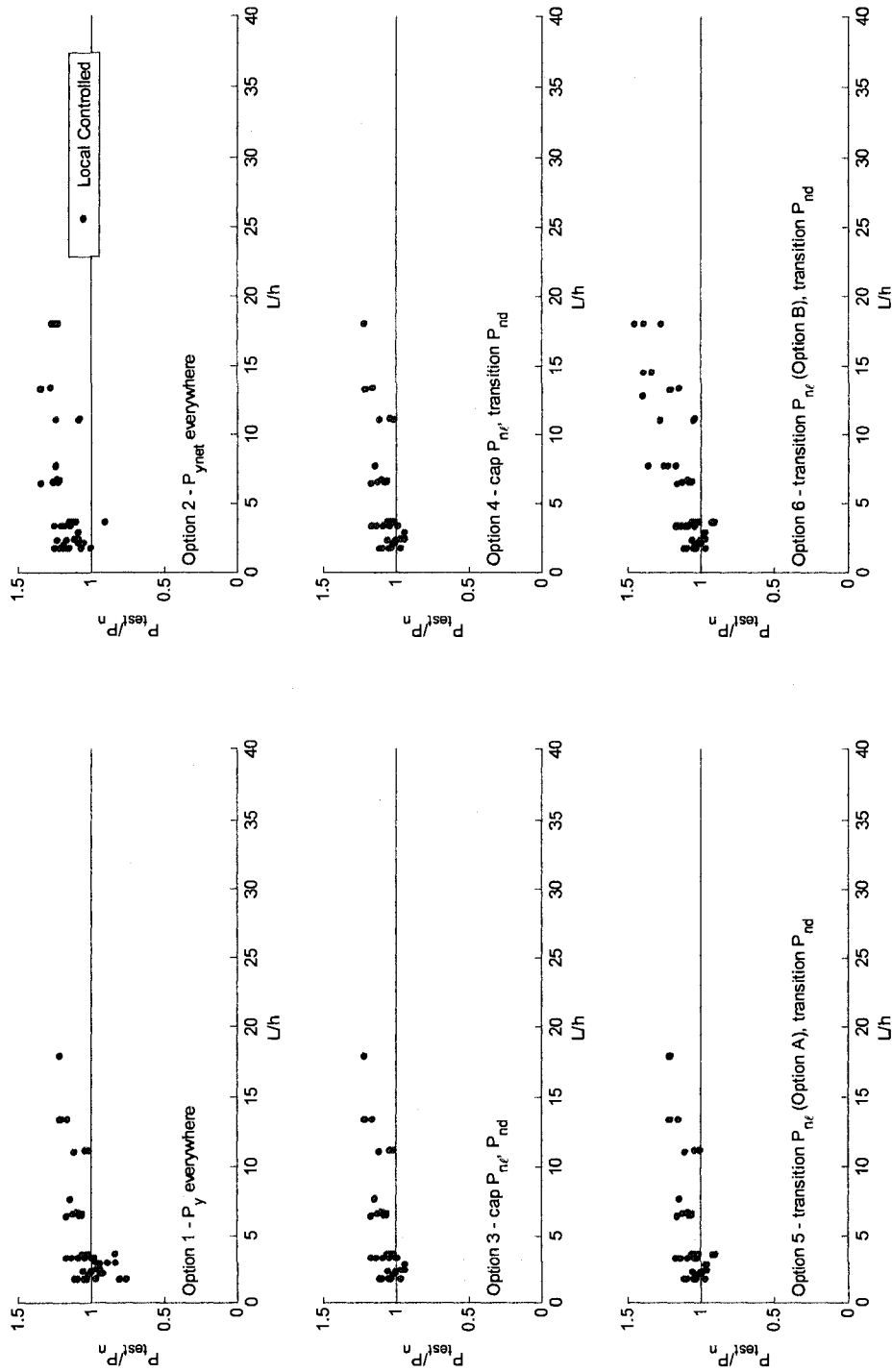


Figure 8.41 Test-to-predicted ratios for experiment local buckling-controlled column failures as a function of column length, L , to flat web width, h

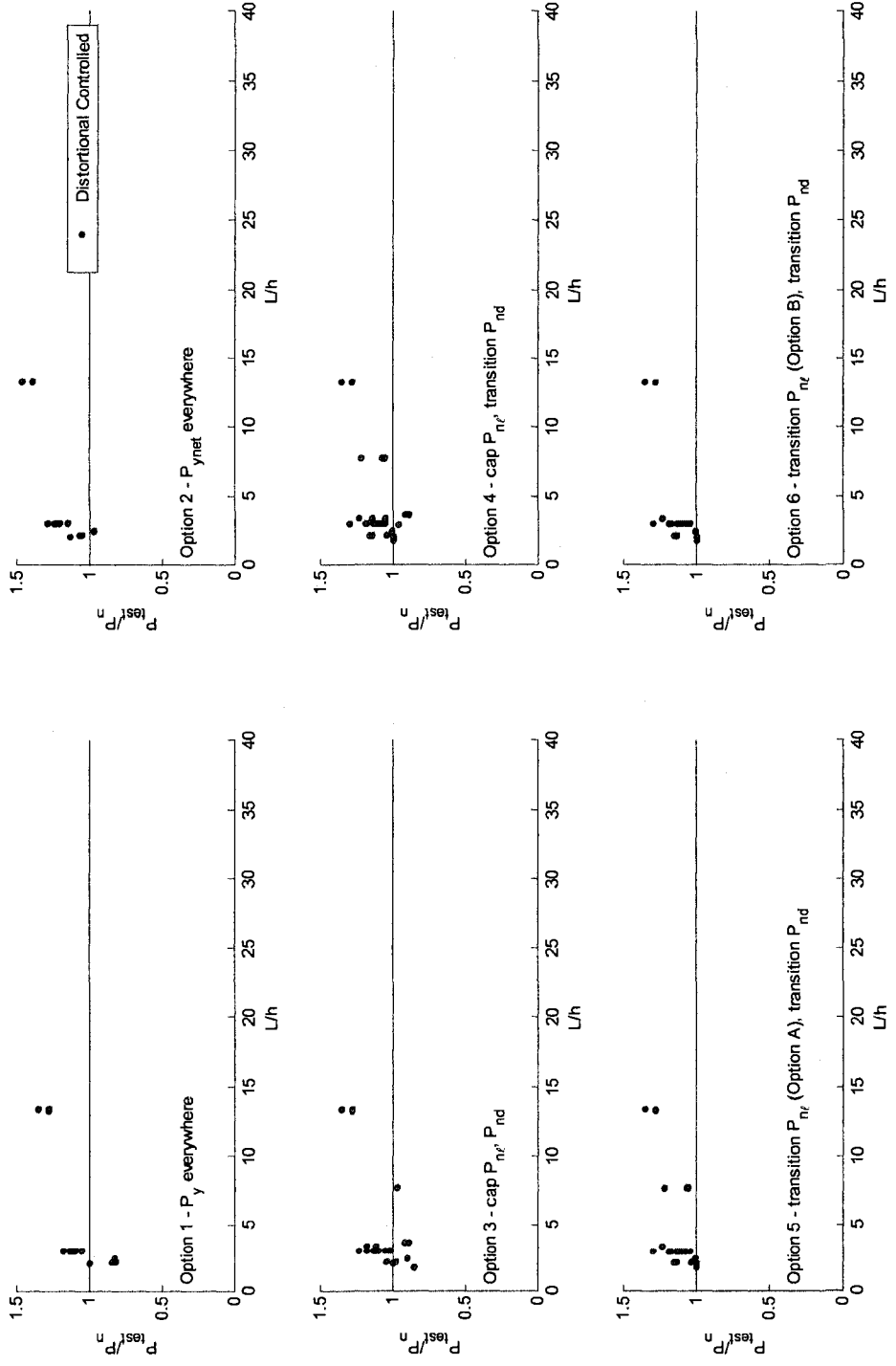


Figure 8.42 Test-to-predicted ratios for experiment distortional buckling-controlled column failures as a function of column length, L , to flat web width, h

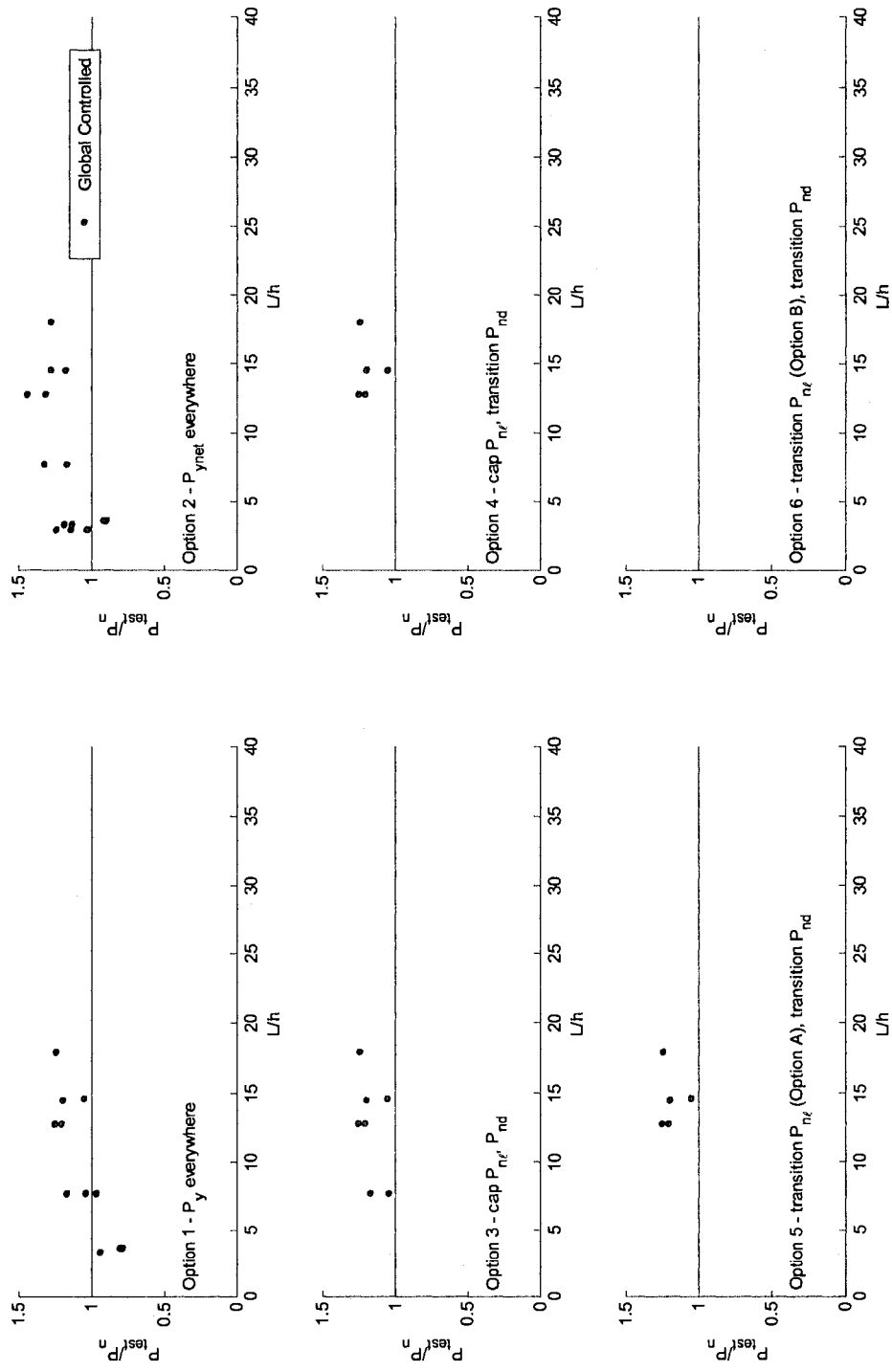


Figure 8.43 Test-to-predicted ratios for experiment global buckling-controlled column failures as a function of column length, L , to web width, h

8.1.8 Recommendations – DSM for columns with holes

Options 3, 4, and 5 are presented as viable proposals for extending DSM to columns with holes. This recommendation is based on the test-to-predicted statistics and data trends presented in Section 8.1.6 and Section 8.1.7, and also considers the effort to implement the modifications and their ease of use by design engineers. Option 3 accounts for the reduction in column strength from the presence of holes by capping P_{nc} and P_{nd} at P_{ynet} . This is a simple modification to implement in the Specification and avoids additional calculation work for a design engineer (except for that required to calculate the critical elastic buckling loads including the influence of the holes). Options 4 and 5 are refinements of Option 3, where the cap on P_{nc} and P_{nd} becomes a transition from an elastic buckling controlled failure mode to a yield controlled failure at P_{ynet} . These two methods require additional effort from the designer when compared to Option 3, but they have an important advantage. Options 4 and 5 are more closely tied to the failure mechanisms influencing column strength because they capture the yield transition to the net section in their predictions. The transitions increase the probability that strength will be accurately predicted for general column and hole geometries. Option 5 has the additional advantage of capturing the influence of a yield transition for closed cross-sections that do not experience distortional buckling. This generality is what motivates the use of the Direct Strength Method (AISI-S100 2007, Appendix 1).

8.2 DSM for laterally braced beams with holes

8.2.1 Database of simulated column experiments

Simulated experiments were conducted on 125 C-section laterally braced beams with evenly-spaced circular web holes in ABAQUS. Cross-sections were specifically selected with custom Matlab code employing the existing DSM design curves to identify beams predisposed to local and distortional buckling-controlled failures. The cross-sections were chosen from a catalog of 99 industry standard C-sections published by the Steel Stud Manufacturers Association (SSMA 2001). The nominal out-to-out dimensions provided in the SSMA catalog were converted to centerline dimensions and then constructed in ABAQUS with the meshing procedure described in Section 7.2.1.1. The beams in the database have a constant length $L=48$ in. to accommodate multiple local and distortional buckling half-waves along the beam. Evenly spaced circular web holes were placed in the columns with hole spacing S (defined in Figure 3.2) of 16 inches (i.e., three evenly spaced holes). The holes were centered transversely in the web and their depth (diameter), h_{hole} , was varied such that the ratio of the net moment of inertia, I_{net} , to the gross cross-sectional area, I_g , ranged between 0.85 and 1.0.

The ABAQUS boundary conditions and application of loading, described in Figure 8.44, are implemented to be consistent with CUFSM, i.e. pinned-pinned and free-to-warp with a uniform stress applied at the member ends. Each beam is laterally braced by restraining the compression flange at the midlength of the beam. (Initial modeling trials, where all nodes centered in the compression flange were laterally restrained,

resulted in simulated strengths 25% higher than DSM predictions for beams without holes.) Consistent nodal loads were applied to simulate the linear stress gradient at the beam ends (see Section 7.2.1.2 for information on S9R5 consistent nodal loads). The loads (a reference moment of 1 kip-in. was applied at each end in ABAQUS) were distributed over the first two sets of cross-section nodes to avoid localized failures at the loaded edges.

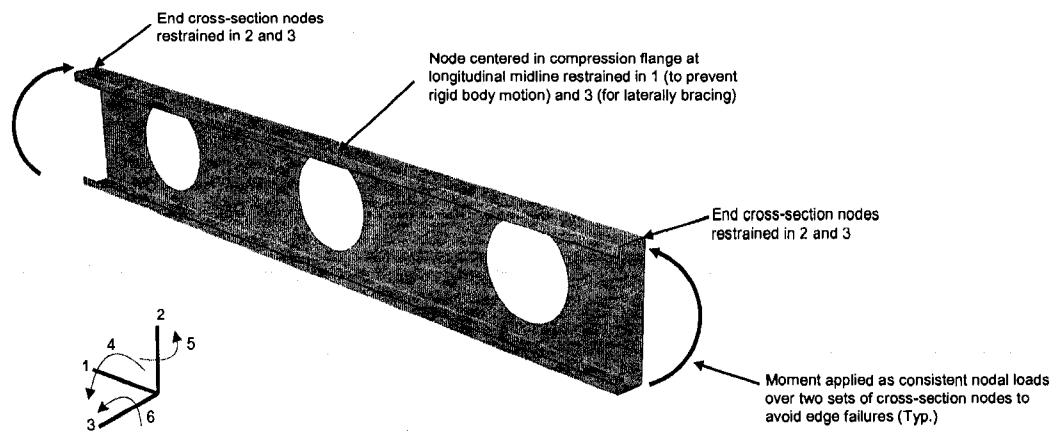


Figure 8.44 ABAQUS simulated beam experiments boundary conditions and application of loading

The ABAQUS simulations were performed with the modified Riks nonlinear solution algorithm. Automatic time stepping was enabled with a suggested initial arc length step of 1 (the Riks method increments in units of energy, in this case kip-in.), a maximum step size of 3, and the maximum number of solution increments set at 300. Metal plasticity was simulated with the material modeling procedure described in Section 7.2.1.4. The plastic true stress-strain curve for specimen 362-1-48-H in Appendix H was assumed for all column models (but modified such that plasticity starts at the yield stress, see Section 7.2.1.4), where the steel yield stress $F_y=58.6$ ksi. Residual stresses

and initial plastic strains, as discussed in Section 7.2.1.6, were not considered in the ABAQUS models because their implementation requires further validation and they were not observed to markedly influence column ultimate strength (see Figure 7.48 and Figure 7.49).

Imperfections were imposed on the initial beam geometry in ABAQUS with custom Matlab code which combines the local and distortional buckling cross-section mode shapes from CUFSM along the column length. Two simulations were performed for each beam, one model with 25% CDF local and distortional imperfection magnitudes and the other model with 75% CDF local and distortional imperfection magnitudes (see Section 7.2.1.5 for local and distortional imperfection definitions).

The local ($M_{cr,l}$) and distortional ($M_{cr,d}$) critical elastic buckling loads were predicted for each beam with custom Matlab code based on the CUFSM prediction methods described in Section 4.3. The database of simulated beam experiments, including cross-section type, column and hole geometry, simulated ultimate strength (M_{test25} and M_{test75}) and critical elastic buckling loads for each beam (including the presence of holes) is provided in Appendix L.

8.2.2 Local buckling study

Twelve beams from the simulation database in Appendix L were chosen to study the influence of web holes on the ultimate strength of laterally braced beams predisposed to a local buckling-controlled failure. The beams have SSMA cross-sections which result in a local buckling slenderness, λ_t , ranging from 1.3 to 2.0. (The slenderness

range considered here is relatively narrow because only 12 of the 99 SSMA cross-sections, when employed as laterally braced beams, are controlled by a local buckling failure. The majority of beam cross-sections are predicted to exhibit a distortional buckling-controlled failure.) The web of each beam contains three evenly spaced circular holes where the hole spacing $S=16$ in. The hole depth (diameter), h_{hole} , is varied for each beam to produce I_{net}/I_g of 1.0 (no holes), 0.95, 0.90, and 0.85. Refer to Appendix L, Study Type L, for specific beam cross-section and hole geometry information.

The simulation results for $I_{net}/I_g = 1.0, 0.95, 0.90,$ and $0.85,$ are compared to the DSM distortional buckling prediction curve in Figure 8.46 to Figure 8.49. The beam strengths, M_{test25} and M_{test75} , without holes ($I_{net}/I_g = 1.0$) are consistent with the DSM design curve as shown in Figure 8.46a, confirming that the nonlinear simulation protocol developed for columns in Section 7.2 is also viable when conducting cold-formed steel beam simulations. The mean and standard deviation of the simulated test to predicted ratio is 1.05 and 0.05 respectively for 25% CDF local and distortional imperfections, and 1.03 and 0.05 for 75% CDF local and distortional imperfections. For the beams with holes, the simulated test strengths diverge from the DSM prediction curve as local slenderness, $\lambda_c = (M_{yg}/M_{cr})^{0.5}$, decreases as shown in Figure 8.47a to Figure 8.49a (M_{yg} is the yield moment of the column calculated with the gross cross-sectional area I_g). This divergent trend in M_{test} with decreasing λ_c is consistent with the column results with holes discussed in Section 8.1, where elastic buckling controlled the failure when slenderness was high and transitioned to yielding and collapse of the net section as slenderness decreased. Figure 8.45 shows the load-deformation response at ultimate limit state for

an SSMA 800S162-43 beam considered in this study, and highlights the transition from an elastic buckling controlled-failure to a yield controlled-failure at the net section as hole size increases.

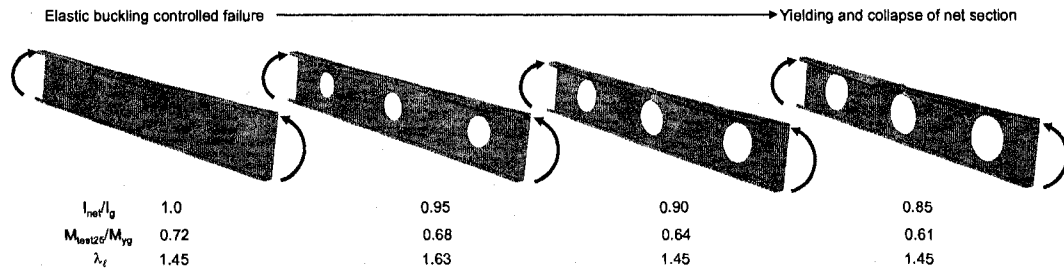


Figure 8.45 SSMA 800S162-43 beam with web holes considered in the DSM local buckling study

Two modification options are proposed for the DSM local buckling beam design curve:

Local Buckling (Option A)

The nominal flexural strength, $M_{n\ell}$, for local buckling shall be calculated in accordance with the following:

(a) For $\lambda_\ell \leq \lambda_{\ell 1}$

$$M_{n\ell} = M_{ne} \leq M_{ynet} \quad (\text{cap on beam strength})$$

(b) For $\lambda_{\ell 1} < \lambda_\ell \leq \lambda_{\ell 2}$

$$M_{n\ell} = M_{ynet} - (M_{ynet} - M_{\ell 2}) \left(\frac{\lambda_{\ell 2}}{\lambda_\ell} \right) \left(\frac{\lambda_\ell - \lambda_{\ell 1}}{\lambda_{\ell 2} - \lambda_{\ell 1}} \right) \quad (\text{nonlinear yield transition when } M_{ynet}/M_{ne} \leq 1)$$

(c) For $\lambda_\ell > \lambda_{\ell 2}$

$$M_{n\ell} = \left(1 - 0.15 \left(\frac{M_{cr\ell}}{M_{ne}} \right)^{0.4} \right) \left(\frac{M_{cr\ell}}{M_{ne}} \right)^{0.4} M_{ne} \quad (\text{DSM local buckling curve, unchanged})$$

where

$$\lambda_\ell = \sqrt{M_{ne}/M_{cr\ell}}$$

$$\lambda_{\ell 1} = 0.776(M_{ynet}/M_{ne}) \leq 0.776$$

$$\lambda_{\ell 2} = 0.776(2.4(M_{ynet}/M_{ne})^{-3.5} - 1.4), \quad M_{ynet}/M_{ne} \leq 1$$

$$= 0.776, \quad M_{ynet}/M_{ne} > 1 \quad (\text{no transition when } M_{ynet}/M_{ne} > 1)$$

$$M_{\ell 2} = (1 - 0.15(1/\lambda_{\ell 2})^{0.8}) (1/\lambda_{\ell 2})^{0.8} M_{ne}$$

$$M_{ynet} = S_{fnet} F_y \geq 0.80 M_y \quad (\text{limit reduction of the net section to } 0.80 M_y)$$

S_{fnet} = Section modulus at the hole(s) referenced to the extreme fiber at first yield

$M_{cr\ell}$ = Critical elastic local beam buckling load including hole(s)

Local Buckling (Option B)

The nominal axial strength, $M_{n\ell}$, for local buckling shall be calculated in accordance with the following:

(a) For $\lambda_\ell \leq \lambda_{\ell 1}$

$$M_{n\ell} = M_{y\text{net}} (M_{ne} / M_y) \quad (\text{cap on column strength})$$

(b) For $\lambda_{\ell 1} < \lambda_\ell \leq \lambda_{\ell 2}$

$$M_{n\ell} = M_{y\text{net}} \left(\frac{M_{ne}}{M_y} \right) - \left(M_{y\text{net}} \left(\frac{M_{ne}}{M_y} \right) - M_{\ell 2} \right) \left(\frac{\lambda_{\ell 2}}{\lambda_\ell} \right) \left(\frac{\lambda_\ell - \lambda_{\ell 1}}{\lambda_{\ell 2} - \lambda_{\ell 1}} \right) \quad (\text{nonlinear yield transition})$$

(c) For $\lambda_\ell > \lambda_{\ell 2}$

$$M_{n\ell} = \left(1 - 0.15 \left(\frac{M_{\text{cr}\ell}}{M_{ne}} \right)^{0.4} \right) \left(\frac{M_{\text{cr}\ell}}{M_{ne}} \right)^{0.4} M_{ne} \quad (\text{DSM local buckling curve, unchanged})$$

where

$$\lambda_\ell = \sqrt{M_{ne} / M_{\text{cr}\ell}}$$

$$\lambda_{\ell 1} = 0.776 (M_{y\text{net}} / M_y) \leq 0.776$$

$$\lambda_{\ell 2} = 0.776 (2.4 (M_{y\text{net}} / M_y)^{3.5} - 1.4)$$

$$M_{\ell 2} = (1 - 0.15 (1/\lambda_{\ell 2})^{0.8}) (1/\lambda_{\ell 2})^{0.8} M_{ne}$$

$$M_{y\text{net}} = S_{\text{fnet}} F_y \geq 0.80 M_y \quad (\text{limit reduction of the net section to } 0.8M_y)$$

S_{fnet} = Section modulus at the hole(s) referenced to the extreme fiber at first yield

$M_{\text{cr}\ell}$ = Critical elastic local beam buckling load including hole(s)

The framework for Option A and Option B is based on the proposed modifications to the DSM local buckling column design curve presented in Section 8.1.4. Option A imposes a transition from the DSM local buckling curve to the net section limit, $M_{y\text{net}}$, when $M_{y\text{net}} < M_{ne}$. When $M_{y\text{net}} > M_{ne}$, Option A assumes that holes influence only the critical elastic buckling loads ($M_{\text{cr}\ell}$, $M_{\text{cr}\ell}$) but otherwise do not change the failure mode of the beam. Option B also imposes a transition to the net beam strength from the DSM local failure curve, although in this case the yield transition occurs for all values of $M_{y\text{net}}/M_{ne}$. The proposed transition from the elastic buckling failure regime to the yield plateau is nonlinear for both Options A and B as demonstrated in Figure 8.47a to Figure 8.49a, in contrast to the linear transition for cold-formed steel columns with holes (see Section 8.1.4).

All beams considered in this study are laterally braced, i.e. global (lateral-torsional) buckling does not influence beam strength, and therefore Option A and B will produce the same strength predictions. The validity of both options for laterally braced beams is evaluated in the following section with the simulation database in Appendix L and the experiment database assembled in Chapter 4. Future work is planned to evaluate Option A and B for unbraced cold-formed steel beams with holes, where lateral-torsional buckling influences beam strength.

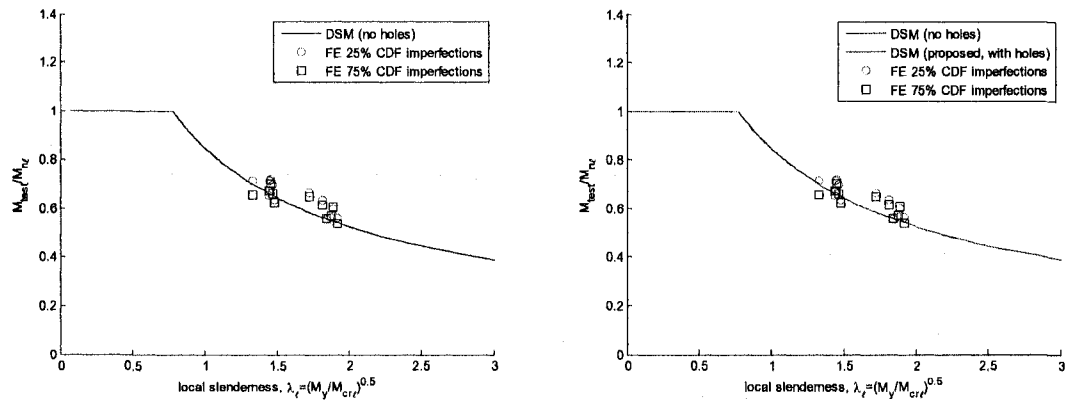


Figure 8.46 Comparison of simulated beam strengths ($I_{ncf}/I_g=1.0$, no holes) to (a) the existing DSM local buckling design curve and to (b) the proposed DSM local buckling curve for beams with holes

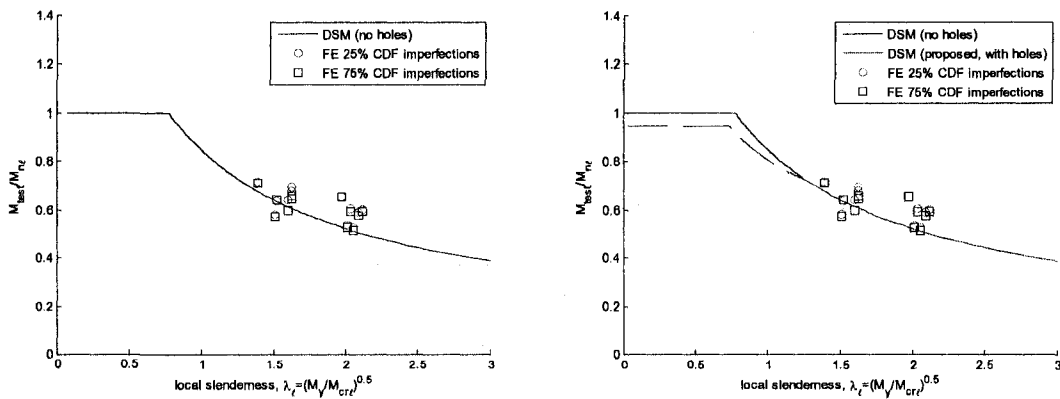


Figure 8.47 Comparison of simulated beam strengths ($I_{ncf}/I_g=0.95$) to (a) the existing DSM local buckling design curve and to (b) the proposed DSM local buckling curve for beams with holes

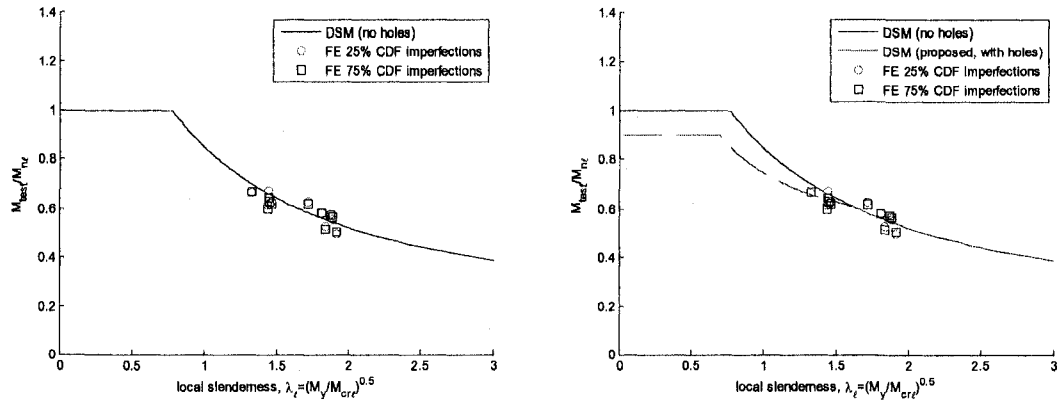


Figure 8.48 Comparison of simulated beam strengths ($I_{net}/I_g=0.90$) to (a) the existing DSM local buckling design curve and to (b) the proposed DSM local buckling curve for beams with holes

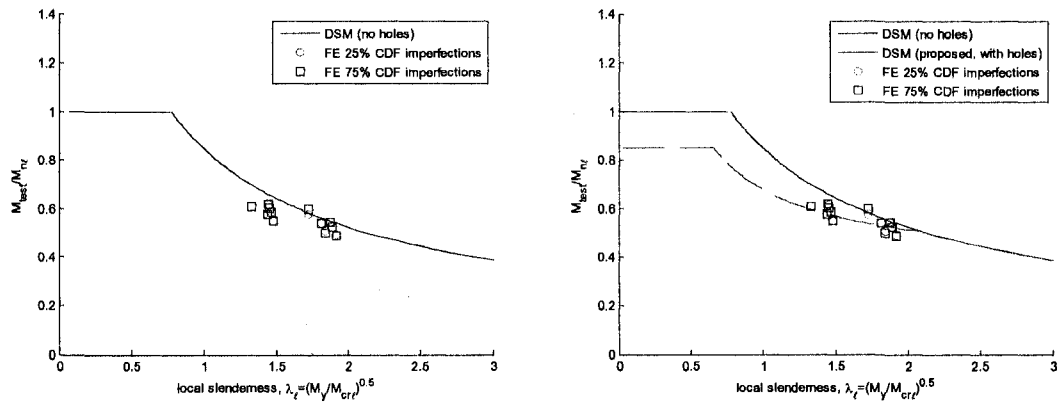


Figure 8.49 Comparison of simulated beam strengths ($I_{net}/I_g=0.85$) to (a) the existing DSM local buckling design curve and to (b) the proposed DSM local buckling curve for beams with holes

8.2.3 Distortional buckling study

A group of 11 beams from the SSMA beam simulation database was chosen to evaluate the influence of the ratio I_{net}/I_g on the tested strength of beams predicted to collapse with a distortional failure mode. (I_g is the gross moment of inertia of a beam and I_{net} is the moment of inertia at the location of a hole.) The beams have SSMA cross-sections which result in a distortional buckling slenderness, λ_d , ranging from 0.6 to 1.6. (All SSMA cross-sections, employed as beams and controlled by a distortional buckling failure, lie within this slenderness range.) In this study the beam depths range from 4 in.

to 12 in. The web of each beam has three circular holes where the hole spacing $S=16$ in (see Figure 3.2 for the definition of S). The hole depth (diameter), h_{hole} , is varied for each beam to produce I_{net}/I_g of 1.0 (no holes), 0.95, and 0.90. Refer to Appendix L, Study Type D, for specific cross-section and hole geometry information.

The simulation results for $I_{net}/I_g = 1.0, 0.95,$ and 0.90 are compared to the DSM distortional buckling prediction curve in Figure 8.51 to Figure 8.53. The beam strengths, M_{test25} and M_{test75} , without holes ($I_{net}/I_g = 1.0$) are consistent with the DSM distortional buckling design curve as shown in Figure 8.51a, with a trend of increasingly conservative predictions as distortional slenderness increases. The mean and standard deviation of the simulated test to predicted ratio is 1.08 and 0.08 respectively for 25% CDF local and distortional imperfections, and 1.02 and 0.12 for 75% CDF imperfections. For the beams with holes, the simulated test strengths demonstrate a slight divergence from the DSM prediction curve as distortional slenderness, $\lambda_d = (M_{yg}/M_{crd})^{0.5}$, decreases as shown in Figure 8.52a and Figure 8.53a (M_{yg} is the yield moment of the beam calculated with the gross cross-sectional area I_g). (Figure 8.52a and Figure 8.53a also demonstrate that M_{crd} , predicted with the simplified method in Section 4.3.2.2, increases distortional slenderness and shifts the simulated data off of the prediction curve. Future research is planned to improve the accuracy of this simplified method.) This divergent trend in M_{test} was also observed in the local buckling-controlled beam study in Section 8.2.2 and the column studies presented in Section 8.1. As λ_d decreases, the beam failure mode transitions from a distortional buckling failure to yielding and collapse of the net section. Figure 8.50 highlights this transition for the SSMA 550S162-54 beam considered

in this study by comparing the deformed shape at ultimate limit state as hole size increases.

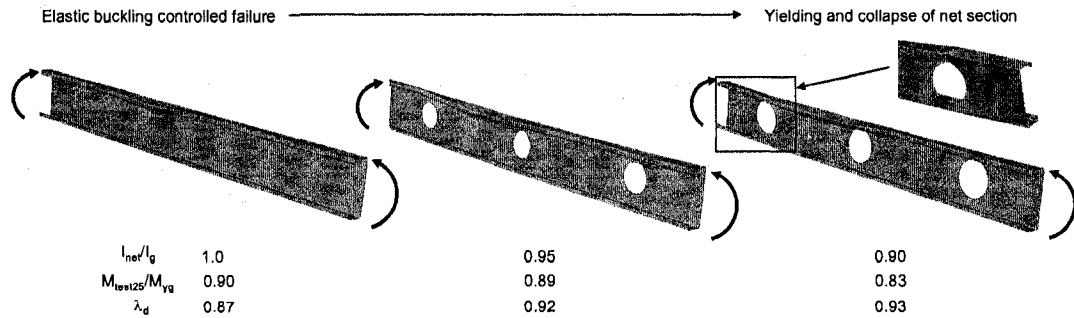


Figure 8.50 SSMA 550S162-54 structural stud failure mode transition from distortional buckling to yielding at the net section

The observations from this study are used to formulate a modified DSM distortional curve for beams with holes which captures the failure mechanism transition from yielding at the net cross-section to a distortional type failure mode and limits the strength of the beam to the yield moment at the net section:

Distortional Buckling

The nominal flexural strength, M_{nd} , for distortional buckling shall be calculated in accordance with the following:

(a) For $\lambda_d \leq \lambda_{d1}$

$$M_{nd} = M_{ynet}$$

(cap on column strength)

(b) For $\lambda_{d1} < \lambda_d \leq \lambda_{d2}$

$$M_{nd} = M_{ynet} - \left(\frac{M_{ynet} - M_{d2}}{\lambda_{d2} - \lambda_{d1}} \right) \lambda_d$$

(yield control transition)

(c) For $\lambda_d > \lambda_{d2}$

$$M_{nd} = \left(1 - 0.22 \left(\frac{M_{crd}}{M_y} \right)^{0.5} \right) \left(\frac{M_{crd}}{M_y} \right)^{0.5} M_y$$

(existing DSM distortional curve)

where

$$\lambda_d = \sqrt{M_y / M_{crd}}$$

$$\lambda_{d1} = 0.673 (M_{ynet} / M_y)$$

$$\lambda_{d2} = 0.673 (1.7 (M_{ynet} / M_y)^{-1.7} - 0.7)$$

$$M_{d2} = (1 - 0.22 (1 / \lambda_{d2})) (1 / \lambda_{d2}) M_y$$

$$M_{ynet} = S_{fnet} F_y \geq 0.80 M_y \quad (\text{limit reduction of the net section to } 0.8 M_y)$$

$$S_{fnet} = \text{Section modulus at the hole(s) referenced to the extreme fiber at first yield}$$

$$M_{crd} = \text{Critical elastic distortional beam buckling load including hole(s)}$$

The modified DSM distortional curve is added in Figure 8.51b to Figure 8.53b as I_{net}/I_g decreases, simulating the transition from the existing DSM curve to the net section strength limit exhibited by the simulated test data. The linear portion of the modified prediction curve represents the unstiffened strip distortional collapse mechanism and the nonlinear portion represents a collapse mechanism driven by distortional buckling. This proposed modification to the DSM distortional prediction curve will be compared against the beam experiments database developed in Section 4.3.1 as a part of several proposed DSM options considered later in this chapter.

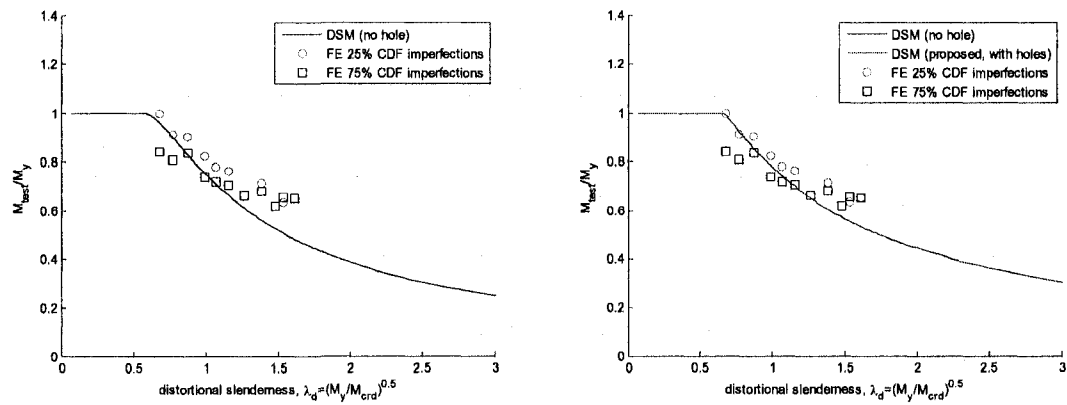


Figure 8.51 Comparison of simulated beam strengths ($I_{net}/I_g=1.0$) to (a) the existing DSM distortional buckling design curve and to (b) the proposed DSM distortional buckling curve for beams with holes

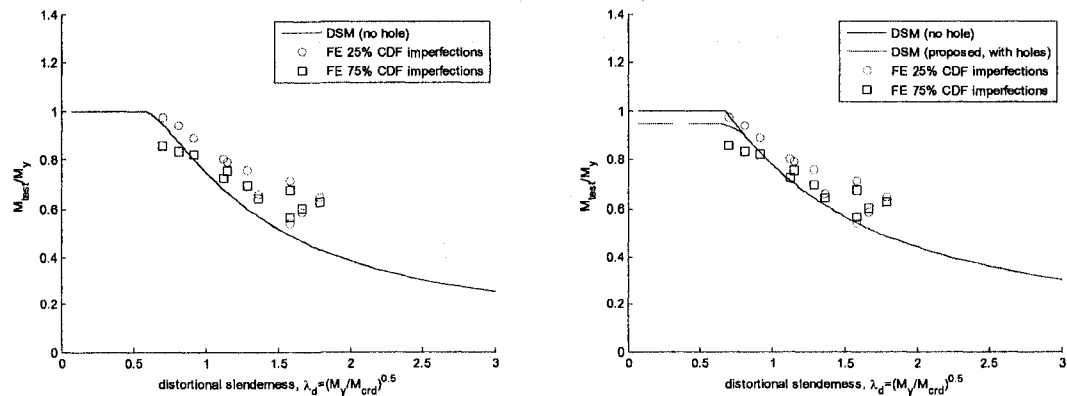


Figure 8.52 Comparison of simulated beam strengths ($I_{net}/I_g=0.95$) to (a) the existing DSM distortional buckling design curve and to (b) the proposed DSM distortional buckling curve for beams with holes

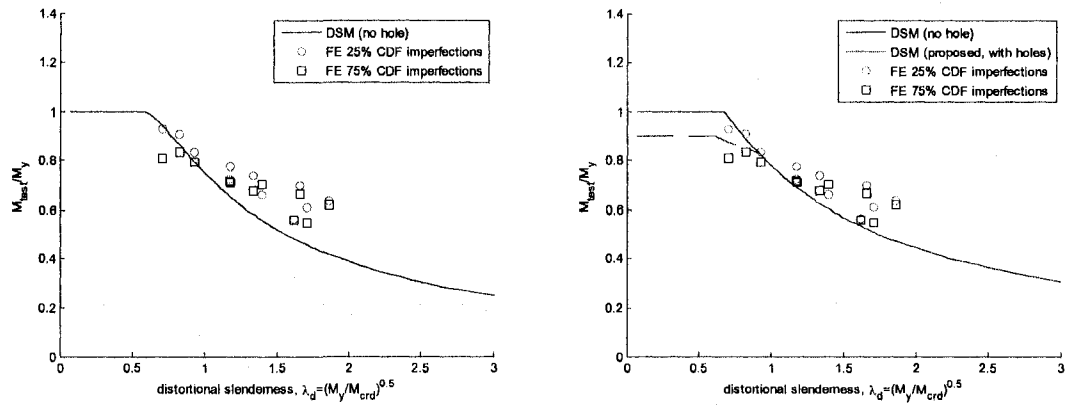


Figure 8.53 Comparison of simulated beam strengths ($I_{net}/I_g=0.90$) to (a) the existing DSM distortional buckling design curve and to (b) the proposed DSM distortional buckling curve for beams with holes

8.2.4 Presentation and evaluation of DSM options

Six options for extending DSM to laterally braced beams with holes are evaluated in this section. The options range from simple substitutions in the existing code to more involved modifications, including the incorporation of the design curve transitions discussed in Section 8.2.2 and Section 8.2.3 for local and distortional buckling.

8.2.4.1 Description of DSM options

Option 1: Include hole(s) in M_{cr} determinations, ignore hole otherwise
 This method, in presentation, appears identical to currently available DSM expressions

Lateral-Torsional Buckling

The nominal flexural strength, M_{ne} , for lateral-torsional buckling shall be calculated in accordance with the following:

- (a) for $M_{cre} < 0.56 M_y$ $M_{ne} = M_{cre}$
 (b) for $2.78M_y \geq M_{cre} \geq 0.56M_y$ $M_{ne} = \frac{10}{9} M_y \left(1 - \frac{10M_y}{36M_{cre}} \right)$
 (c) for $M_{cre} > 2.78M_y$ $M_{ne} = M_y$

where

M_{cre} = Critical elastic global beam buckling load ... (including hole(s))

Local Buckling

The nominal flexural strength, M_{nl} , for local buckling shall be calculated in accordance with the following:

- (a) For $\lambda_\ell \leq 0.776$

$$M_{nl} = M_{ne}$$

- (b) For $\lambda_\ell > 0.776$

$$M_{nl} = \left(1 - 0.15 \left(\frac{M_{crl}}{M_{ne}} \right)^{0.4} \right) \left(\frac{M_{crl}}{M_{ne}} \right)^{0.4} M_{ne}$$

where

$$\lambda_\ell = \sqrt{M_{ne}/M_{crl}}$$

M_{crl} = Critical elastic local beam buckling load including hole(s)

M_{ne} = defined in section above

Distortional Buckling

The nominal flexural strength, M_{nd} , for distortional buckling shall be calculated in accordance with the following:

- (a) For $\lambda_d \leq 0.673$

$$M_{nd} = M_y$$

- (b) For $\lambda_d > 0.673$

$$M_{nd} = \left(1 - 0.22 \left(\frac{M_{crd}}{M_y} \right)^{0.5} \right) \left(\frac{M_{crd}}{M_y} \right)^{0.5} M_y$$

where

$$\lambda_d = \sqrt{M_y/M_{crd}}$$

M_{crd} = Critical elastic distortional beam buckling load including hole(s)

Option 2: Include hole(s) in M_{cr} determinations, Use M_{ynet} everywhere
 The only change in this method is to replace M_y with M_{ynet}

Lateral-Torsional Buckling

The nominal flexural strength, M_{ne} , for lateral-torsional buckling shall be calculated in accordance with the following:

- (a) for $M_{cre} < 0.56 M_{ynet}$ $M_{ne} = M_{cre}$
 (b) for $2.78M_{ynet} \geq M_{cre} \geq 0.56M_{ynet}$ $M_{ne} = \frac{10}{9} M_{ynet} \left(1 - \frac{10M_{ynet}}{36M_{cre}} \right)$
 (c) for $M_{cre} > 2.78M_{ynet}$ $M_{ne} = M_{ynet}$

where

M_{cre} = Critical elastic global beam buckling load ... (including hole(s))

$M_{ynet} = S_{fnet} F_y \geq 0.80 M_y$

S_{fnet} = Section modulus at the hole(s) referenced to the extreme fiber at first yield

Local Buckling

The nominal flexural strength, M_{nl} , for local buckling shall be calculated in accordance with the following:

- (a) For $\lambda_\ell \leq 0.776$
 $M_{nl} = M_{ne}$
 (b) For $\lambda_\ell > 0.776$
 $M_{nl} = \left(1 - 0.15 \left(\frac{M_{crl}}{M_{ne}} \right)^{0.4} \right) \left(\frac{M_{crl}}{M_{ne}} \right)^{0.4} M_{ne}$

where

$$\lambda_\ell = \sqrt{M_{ne} / M_{crl}}$$

M_{crl} = Critical elastic local beam buckling load including hole(s)

M_{ne} = defined in section above

Distortional Buckling

The nominal flexural strength, M_{nd} , for distortional buckling shall be calculated in accordance with the following:

- (a) For $\lambda_{dnet} \leq 0.673$
 $M_{nd} = M_{ynet}$
 (b) For $\lambda_{dnet} > 0.673$
 $M_{nd} = \left(1 - 0.22 \left(\frac{M_{crd}}{M_{ynet}} \right)^{0.5} \right) \left(\frac{M_{crd}}{M_{ynet}} \right)^{0.5} M_{ynet}$

where

$$\lambda_{dnet} = \sqrt{M_{ynet} / M_{crd}}$$

M_{crd} = Critical elastic distortional beam buckling load including hole(s)

Option 3: Cap M_{nl} and M_{nd} , otherwise no strength change, include hole(s) in M_{cr}
This method puts bounds in place and assumes local-global interaction happens at full M_{ne}

Lateral-Torsional Buckling

The nominal flexural strength, M_{ne} , for lateral-torsional buckling shall be calculated in accordance with the following:

- (a) for $M_{cre} < 0.56 M_y$ $M_{ne} = M_{cre}$
 (b) for $2.78M_y \geq M_{cre} \geq 0.56M_y$ $M_{ne} = \frac{10}{9} M_y \left(1 - \frac{10M_y}{36M_{cre}} \right)$
 (c) for $M_{cre} > 2.78M_y$ $M_{ne} = M_y$

where

M_{cre} = Critical elastic global beam buckling load ... (including hole(s))

Local Buckling

The nominal flexural strength, M_{nl} , for local buckling shall be calculated in accordance with the following:

- (a) For $\lambda_\ell \leq 0.776$
 $M_{nl} = M_{ne} \leq M_{ynet}$
 (b) For $\lambda_\ell > 0.776$

$$M_{nl} = \left(1 - 0.15 \left(\frac{M_{crl}}{M_{ne}} \right)^{0.4} \right) \left(\frac{M_{crl}}{M_{ne}} \right)^{0.4} M_{ne}$$

where

$$\lambda_\ell = \sqrt{M_{ne}/M_{crl}}$$

M_{crl} = Critical elastic local beam buckling load including hole(s)

M_{ne} = defined in section above

$$M_{ynet} = S_{fnet} F_y \geq 0.80 M_y$$

S_{fnet} = Section modulus at the hole(s) referenced to the extreme fiber at first yield

Distortional Buckling

The nominal flexural strength, M_{nd} , for distortional buckling shall be calculated in accordance with the following:

- (a) For $\lambda_d \leq 0.673$
 $M_{nd} = M_y \leq M_{ynet}$
 (b) For $\lambda_d > 0.673$

$$M_{nd} = \left(1 - 0.22 \left(\frac{M_{crd}}{M_y} \right)^{0.5} \right) \left(\frac{M_{crd}}{M_y} \right)^{0.5} M_y$$

where

$$\lambda_d = \sqrt{M_y/M_{crd}}$$

M_{crd} = Critical elastic distortional beam buckling load including hole(s)

Option 4: Cap M_{ne} , transition M_{nd} , include hole(s) in M_{cr} determinations
 This method puts bounds and transition in place, assumes local-global interaction at full M_{ne}

Lateral-Torsional Buckling

The nominal flexural strength, M_{ne} , for lateral-torsional buckling shall be calculated in accordance with the following:

- (a) for $M_{cre} < 0.56 M_y$ $M_{ne} = M_{cre}$
 (b) for $2.78 M_y \geq M_{cre} \geq 0.56 M_y$ $M_{ne} = \frac{10}{9} M_y \left(1 - \frac{10 M_y}{36 M_{cre}} \right)$
 (c) for $M_{cre} > 2.78 M_y$ $M_{ne} = M_y$

where

M_{cre} = Critical elastic global beam buckling load ... (including hole(s))

Local Buckling

The nominal flexural strength, $M_{n\ell}$, for local buckling shall be calculated in accordance with the following:

- (a) For $\lambda_\ell \leq 0.776$
 $M_{n\ell} = M_{ne} \leq M_{ynet}$
 (b) For $\lambda_\ell > 0.776$

$$M_{n\ell} = \left(1 - 0.15 \left(\frac{M_{cr\ell}}{M_{ne}} \right)^{0.4} \right) \left(\frac{M_{cr\ell}}{M_{ne}} \right)^{0.4} M_{ne}$$

where

$$\lambda_\ell = \sqrt{M_{ne}/M_{cr\ell}}$$

$M_{cr\ell}$ = Critical elastic local beam buckling load including hole(s)

M_{ne} = defined in section above

$M_{ynet} = S_{fnet} F_y \geq 0.80 M_y$

S_{fnet} = Section modulus at the hole(s) referenced to the extreme fiber at first yield

Distortional Buckling

The nominal flexural strength, M_{nd} , for distortional buckling shall be calculated in with the following:

- (a) For $\lambda_d \leq \lambda_{d1}$
 $M_{nd} = M_{ynet}$ (cap on column strength)
 (b) For $\lambda_{d1} < \lambda_d \leq \lambda_{d2}$

$$M_{nd} = M_{ynet} - \left(\frac{M_{ynet} - M_{d2}}{\lambda_{d2} - \lambda_{d1}} \right) \lambda_d$$
 (yield control transition)

- (c) For $\lambda_d > \lambda_{d2}$
 $M_{nd} = \left(1 - 0.22 \left(\frac{M_{crd}}{M_y} \right)^{0.5} \right) \left(\frac{M_{crd}}{M_y} \right)^{0.5} M_y$ (existing DSM distortional curve)

where

$$\lambda_d = \sqrt{M_y/M_{crd}}$$

$$\lambda_{d1} = 0.673 (M_{ynet}/M_y)$$

$$\lambda_{d2} = 0.673 (1.7 (M_{ynet}/M_y)^{1.7} - 0.7)$$

$$M_{d2} = (1 - 0.22 (1/\lambda_{d2})) (1/\lambda_{d2}) M_y$$

$M_{ynet} = S_{fnet} F_y \geq 0.80 M_y$ (limit reduction of the net section to 0.8M_y)

S_{fnet} = Section modulus at the hole(s) referenced to the extreme fiber at first yield

M_{crd} = Critical elastic distortional beam buckling load including hole(s)

Option 5: Transition M_{ne} (Option A), transition M_{nd} , include hole(s) in M_{cr} determinations
 This method puts bounds and transition in place, assumes local-global interaction at full M_{ne}

Lateral-Torsional Buckling

The nominal flexural strength, M_{ne} , for lateral-torsional buckling shall be calculated in accordance with the following:

- (a) for $M_{cre} < 0.56 M_y$ $M_{ne} = M_{cre}$
 (b) for $2.78M_y \geq M_{cre} \geq 0.56M_y$ $M_{ne} = \frac{10}{9} M_y \left(1 - \frac{10M_y}{36M_{cre}} \right)$
 (c) for $M_{cre} > 2.78M_y$ $M_{ne} = M_y$

where

M_{cre} = Critical elastic global beam buckling load ... (including hole(s))

Local Buckling

The nominal flexural strength, M_{nl} , for local buckling shall be calculated in accordance with the following:

- (a) For $\lambda_\ell \leq \lambda_{\ell 1}$
 $M_{nl} = M_{ne} \leq M_{ynet}$ (cap on beam strength)
 (b) For $\lambda_{\ell 1} < \lambda_\ell \leq \lambda_{\ell 2}$
 $M_{nl} = M_{ynet} - (M_{ynet} - M_{\ell 2}) \left(\frac{\lambda_{\ell 2}}{\lambda_\ell} \right) \left(\frac{\lambda_\ell - \lambda_{\ell 1}}{\lambda_{\ell 2} - \lambda_{\ell 1}} \right)$ (nonlinear yield transition when $M_{ynet}/M_{ne} \leq 1$)
 (c) For $\lambda_\ell > \lambda_{\ell 2}$
 $M_{nl} = \left(1 - 0.15 \left(\frac{M_{cr\ell}}{M_{ne}} \right)^{0.4} \right) \left(\frac{M_{cr\ell}}{M_{ne}} \right)^{0.4} M_{ne}$ (DSM local buckling curve, unchanged)

where

$$\lambda_\ell = \sqrt{M_{ne}/M_{cr\ell}}$$

$$\lambda_{\ell 1} = 0.776(M_{ynet}/M_{ne}) \leq 0.776$$

$$\lambda_{\ell 2} = 0.776 \left(2.4(M_{ynet}/M_{ne})^{3.5} - 1.4 \right), M_{ynet}/M_{ne} \leq 1$$

$$= 0.776, M_{ynet}/M_{ne} > 1 \quad (\text{no transition when } M_{ynet}/M_{ne} > 1)$$

$$M_{\ell 2} = \left(1 - 0.15(1/\lambda_{\ell 2})^{0.8} \right) (1/\lambda_{\ell 2})^{0.8} M_{ne}$$

$$M_{ynet} = S_{fnet} F_y \geq 0.80 M_y \quad (\text{limit reduction of the net section to } 0.8M_y)$$

S_{fnet} = Section modulus at the hole(s) referenced to the extreme fiber at first yield

$M_{cr\ell}$ = Critical elastic local beam buckling load including hole(s)

Distortional Buckling

Same as Option 4

Option 6: Transition M_{ne} (Option B), transition M_{nd} , include hole(s) in M_{cr} determinations
 This method puts bounds and transition in place, assumes local-global interaction at full M_{ne}

Flexural, Torsional, or Torsional-Flexural Buckling

The nominal axial strength, P_{ne} , for flexural, ... or torsional- flexural buckling is

$$\text{for } \lambda_c \leq 1.5 \quad P_{ne} = \left(0.658^{\lambda_c^2}\right) P_y$$

$$\text{for } \lambda_c > 1.5 \quad P_{ne} = \left(\frac{0.877}{\lambda_c^2}\right) P_y = 0.877 P_{cre}$$

where $\lambda_c = \sqrt{P_y/P_{cre}}$
 P_{cre} = Critical elastic global column buckling load ... (including hole(s))
 $P_y = A_g F_y$
 A_g = gross area of the column

Local Buckling

The nominal axial strength, M_{ne} , for local buckling shall be calculated in accordance with the following:

- (a) For $\lambda_\ell \leq \lambda_{\ell 1}$
 $M_{ne} = M_{ynet} (M_{ne} / M_y)$ (cap on column strength)
- (b) For $\lambda_{\ell 1} < \lambda_\ell \leq \lambda_{\ell 2}$
 $M_{ne} = M_{ynet} \left(\frac{M_{ne}}{M_y}\right) - \left(M_{ynet} \left(\frac{M_{ne}}{M_y}\right) - M_{\ell 2}\right) \left(\frac{\lambda_{\ell 2}}{\lambda_\ell}\right) \left(\frac{\lambda_\ell - \lambda_{\ell 1}}{\lambda_{\ell 2} - \lambda_{\ell 1}}\right)$ (nonlinear yield transition)
- (c) For $\lambda_\ell > \lambda_{\ell 2}$
 $M_{ne} = \left(1 - 0.15 \left(\frac{M_{cr\ell}}{M_{ne}}\right)^{0.4}\right) \left(\frac{M_{cr\ell}}{M_{ne}}\right)^{0.4} M_{ne}$ (DSM local buckling curve, unchanged)

where $\lambda_\ell = \sqrt{M_{ne}/M_{cr\ell}}$
 $\lambda_{\ell 1} = 0.776(M_{ynet}/M_y) \leq 0.776$
 $\lambda_{\ell 2} = 0.776(2.4(M_{ynet}/M_y)^{3.5} - 1.4)$
 $M_{\ell 2} = (1 - 0.15(1/\lambda_{\ell 2})^{0.8})(1/\lambda_{\ell 2})^{0.8} M_{ne}$
 $M_{ynet} = S_{fnet} F_y \geq 0.80 M_y$ (limit reduction of the net section to 0.8M_y)
 S_{fnet} = Section modulus at the hole(s) referenced to the extreme fiber at first yield
 $M_{cr\ell}$ = Critical elastic local beam buckling load including hole(s)

Distortional Buckling

Same as Option 4

8.2.5 DSM comparison to beam test simulation database

The six DSM prediction options for cold-formed steel beams with holes are evaluated with the simulated laterally braced beam experiment database developed in Section 8.2.1 and summarized in Appendix L. The simulated data is compared against DSM predictions while evaluating data trends against member slenderness and hole size (I_{net}/I_g), and span to depth ratio (L/H).

Figure 8.51 and Figure 8.52 compare the simulated test data to predictions for local and distortional buckling-controlled beam failures. Option 1 is identical to the existing DSM approach for beams without holes, except the critical elastic buckling loads (M_{crf} , M_{crd} , and M_{cre}) are determined with the influence of holes. Option 1 is observed to be an accurate predictor of local buckling controlled failure strengths, although distortional predictions are conservative when λ_d is high and unconservative by as much as 20% as λ_d decreases below 1.5 (see Figure 8.52). The unconservative predictions occur because Option 1 does not account for the column strength limit M_{ynet} , nor does it account for a transition from an elastic buckling controlled failure to a yield-controlled failure at the net section.

Option 2 is observed to be a conservative predictor in Figure 8.51 and Figure 8.52 for high λ_e , and λ_d and demonstrates improved accuracy over Option 1 when slenderness decreases and hole size increases (see Figure 8.52). Option 2 replaces M_{ynet} everywhere within the existing DSM formulation, which has the effect of increasing λ_e and λ_d and decreasing predicted strength. Option 3 test-to-predicted trends are similar to Option 1 with increasingly unconservative predictions as slenderness decreases, demonstrating

that the M_{ynet} limits on M_{nc} and M_{nd} in Option 3 are not fully effective at capturing the yield transition to the net section. Option 4 is identical to Option 3 except the yield transition on the DSM distortional curve is employed to provide a more accurate prediction of the net-section yielding influence. Option 4 demonstrates an improvement in distortional buckling-controlled prediction accuracy when $\lambda_d < 1$, although the strength of 11 beams are underpredicted by up to 15% when $\lambda_d=1.3$. Option 5 accurately predicts the strength of these 11 beams with the added transition on the local buckling design curve. (Option 6 is the same as Option 5 because the beams considered are laterally-braced).

Table 8.1 summarizes the test-to-predicted ratio statistics and strength reduction factor ϕ for the six DSM options (see Eq. (8.1) for a definition of ϕ). No one option stands out above the rest when studying the table, although the observations from Figure 8.51 and Figure 8.52 support Options 3,4, and 5(6) as the methods most closely tied to underlying collapse mechanisms at ultimate limit state. The observations from this comparison will be employed along with the DSM comparison to the beam experimental database in the next section to support the recommended DSM modifications.

Table 8.4 DSM test-to-predicted statistics for laterally braced beam simulations

Option	Description	Local buckling				Distortional buckling			
		Mean	SD	ϕ	# of tests	Mean	SD	ϕ	# of tests
1	M_y everywhere	1.07	0.09	0.89	44	1.06	0.13	0.86	160
2	M_{ynet} everywhere	1.05	0.10	0.88	50	1.07	0.12	0.86	154
3	Cap M_{nc} , M_{nd}	1.07	0.09	0.89	44	1.06	0.13	0.86	160
4	Transition M_{nd} , Cap M_{nc}	1.07	0.09	0.89	44	1.06	0.13	0.86	160
5,6	Transition M_{nd} and M_{nc} (Option A, B)	1.01	0.11	0.87	72	1.09	0.12	0.87	132

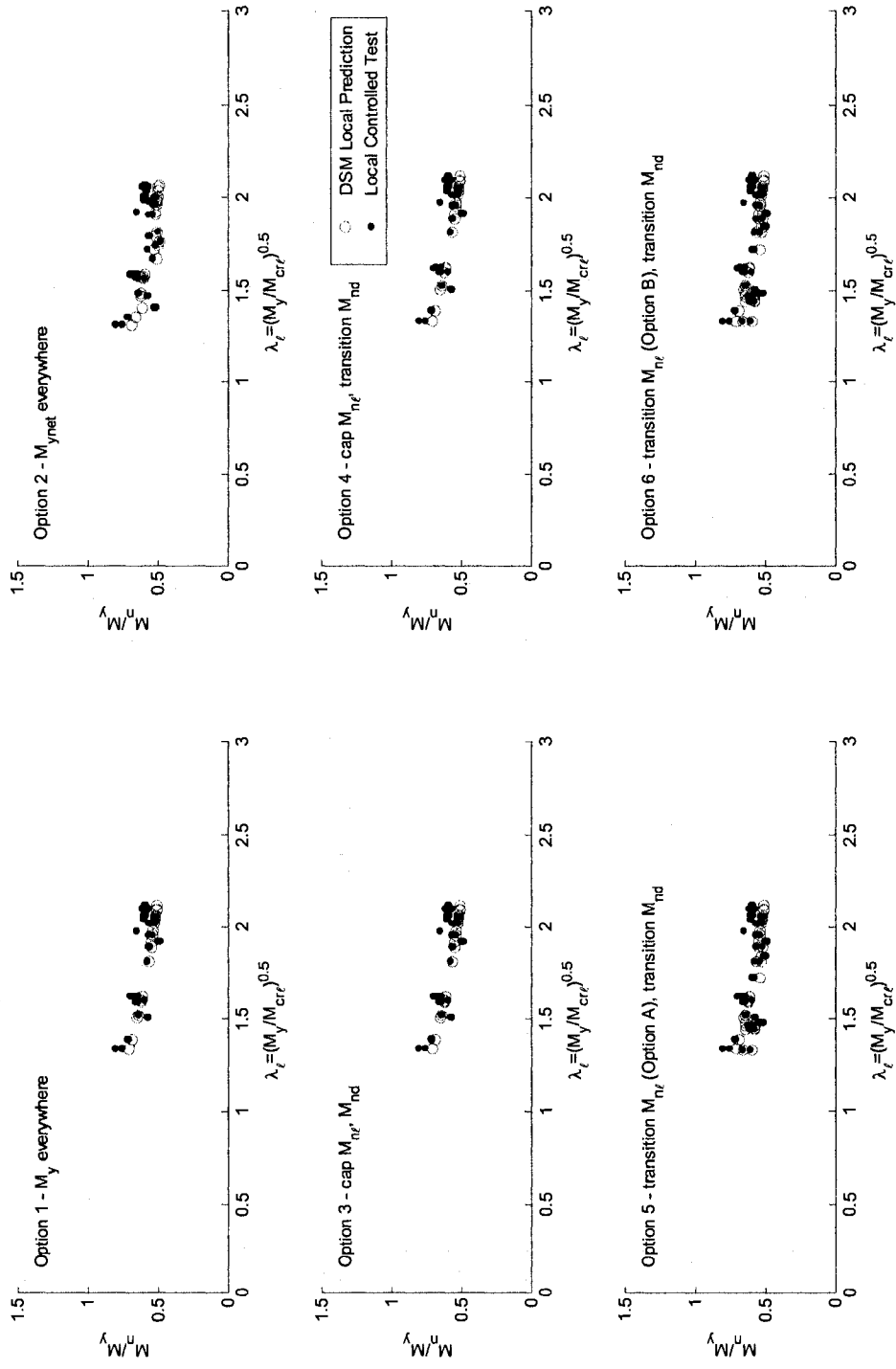


Figure 8.54 Comparison of simulated test strengths to predictions for laterally braced beams with local buckling-controlled failures as a function of local slenderness

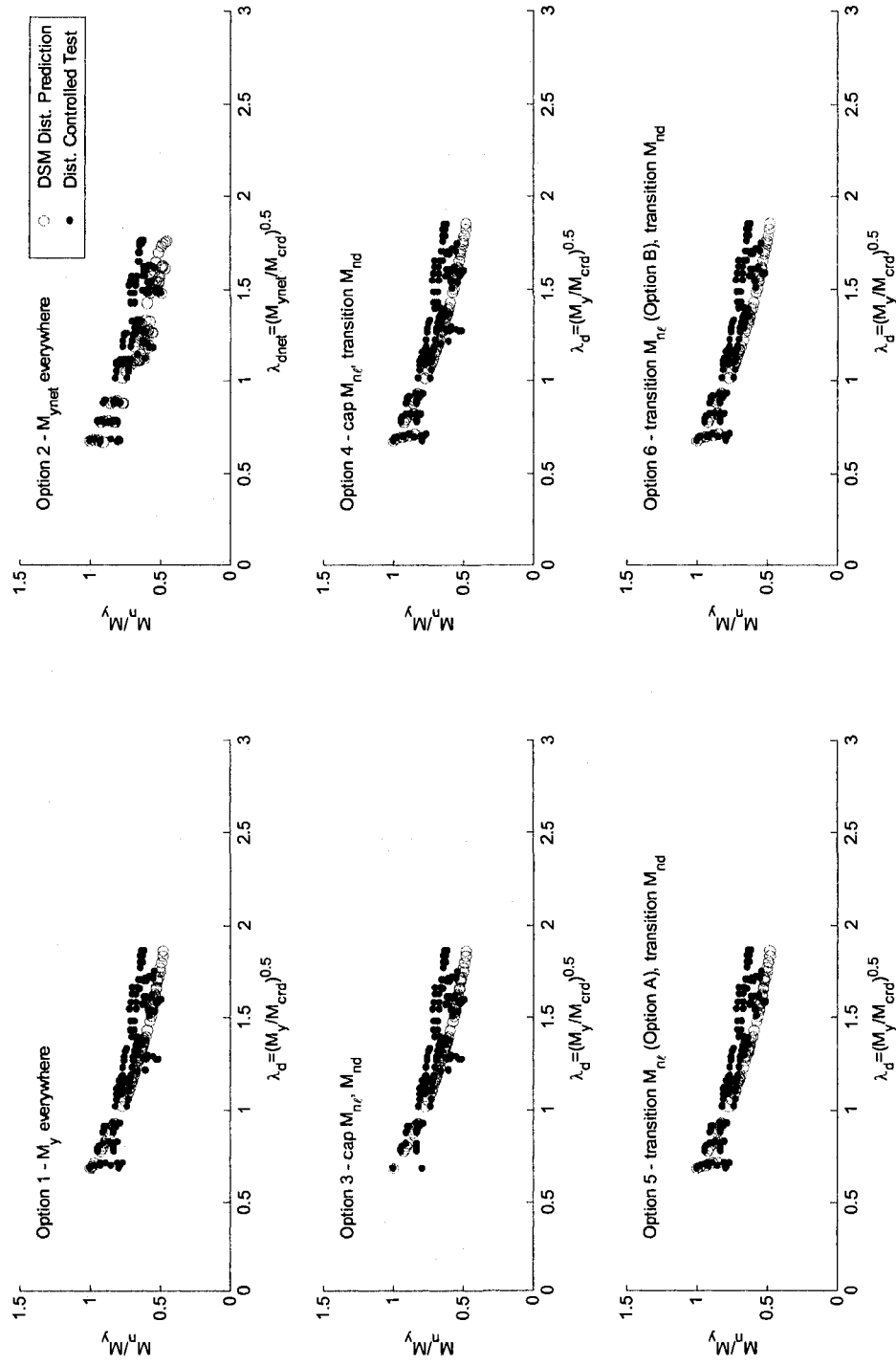


Figure 8.55 Comparison of simulated test strengths to predictions for laterally braced beams with distortional buckling-controlled failures as a function of distortional slenderness

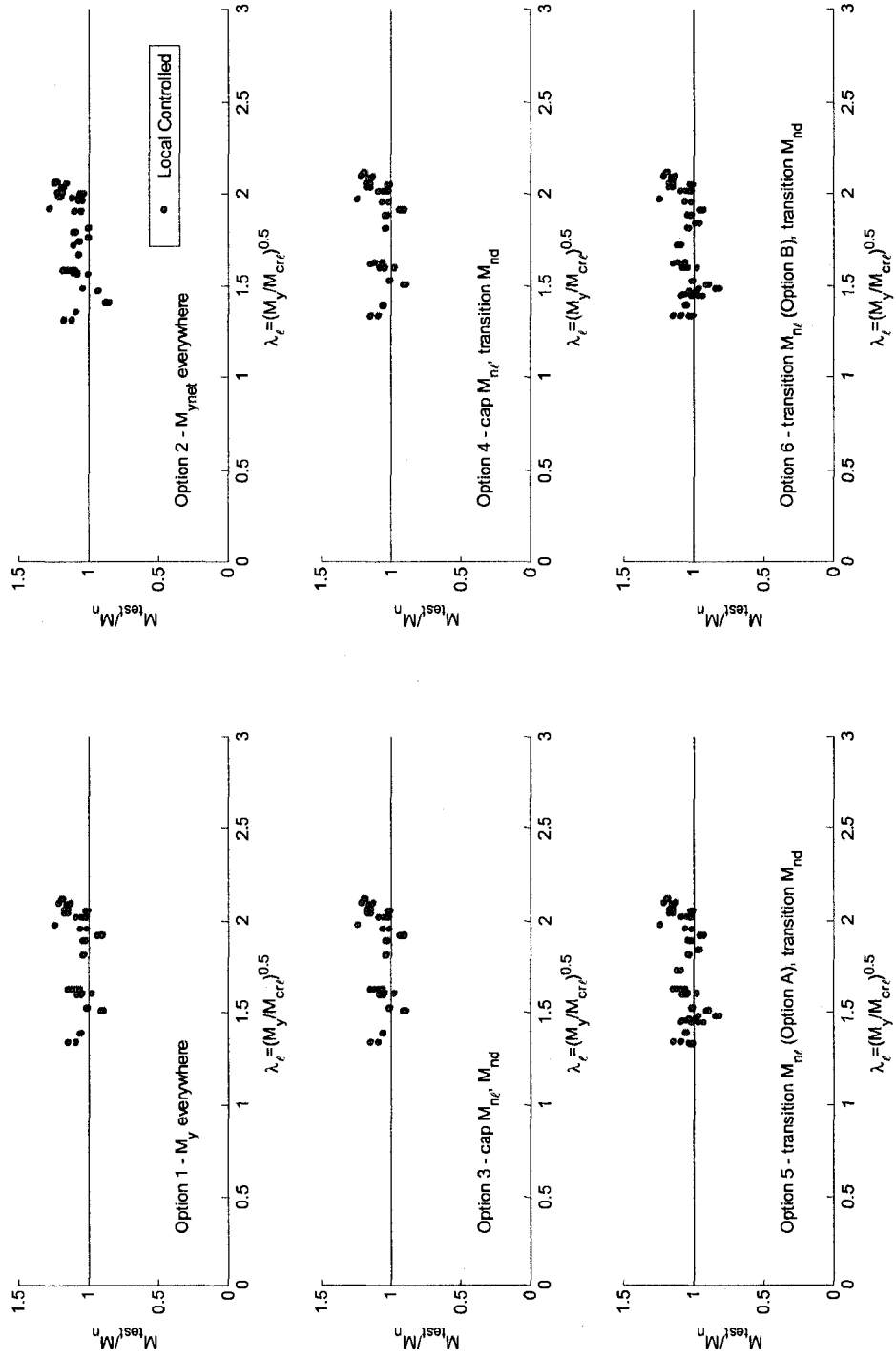


Figure 8.56 Test-to-predicted ratios for local buckling-controlled simulated laterally braced beam failures as a function of local slenderness

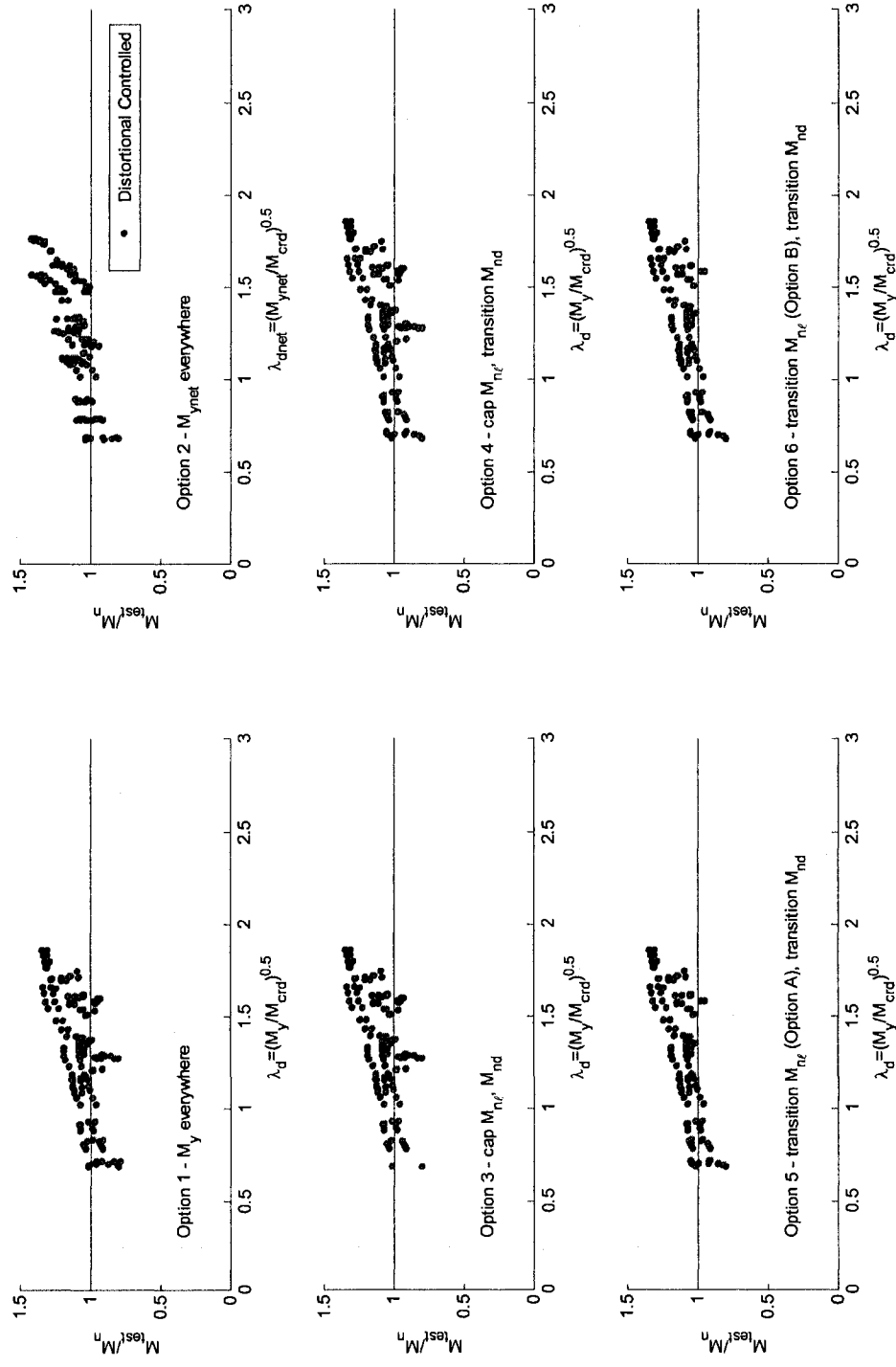


Figure 8.57 Test-to-predicted ratios for distortional buckling-controlled simulated laterally braced beam failures as a function of distortional slenderness

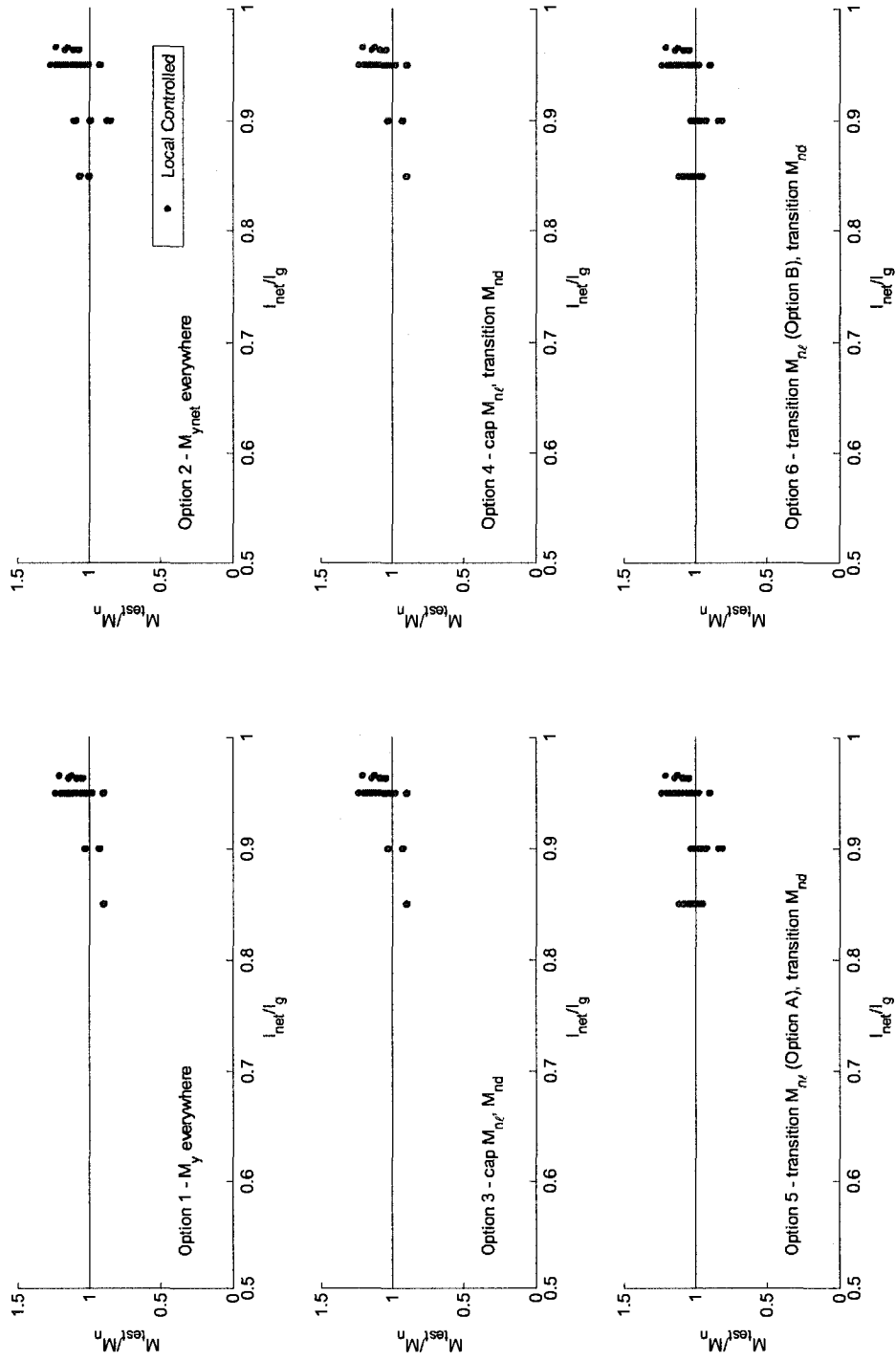


Figure 8.58 Test-to-predicted ratios for simulated local buckling-controlled laterally braced buckling-controlled laterally braced beam failures as a function of net cross-sectional moment of inertia to gross cross-sectional moment of inertia

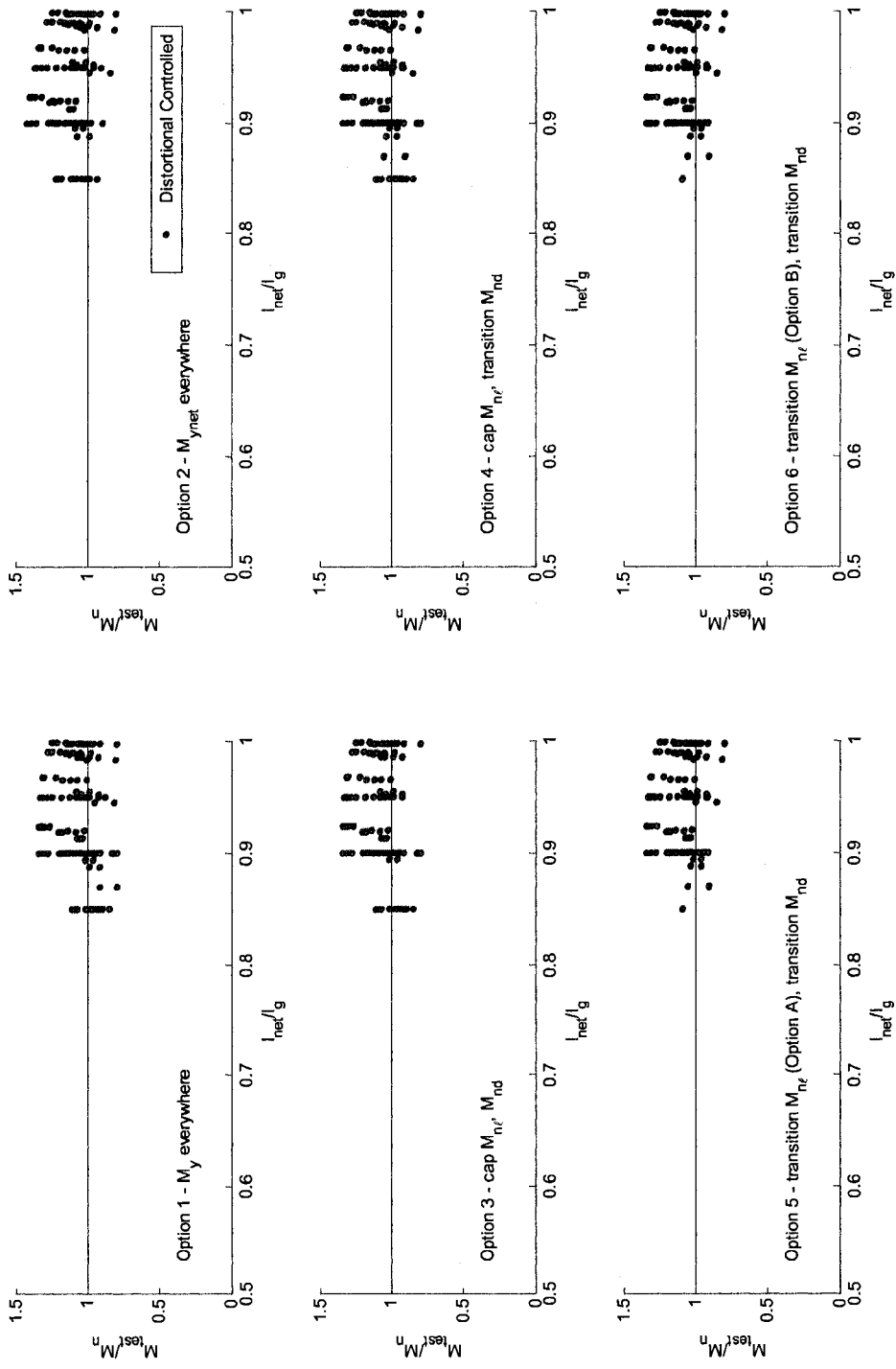


Figure 8.59 Test-to-predicted ratios for simulated distortional buckling-controlled laterally braced beam failures as a function of net cross-sectional moment of inertia to gross cross-sectional moment of inertia

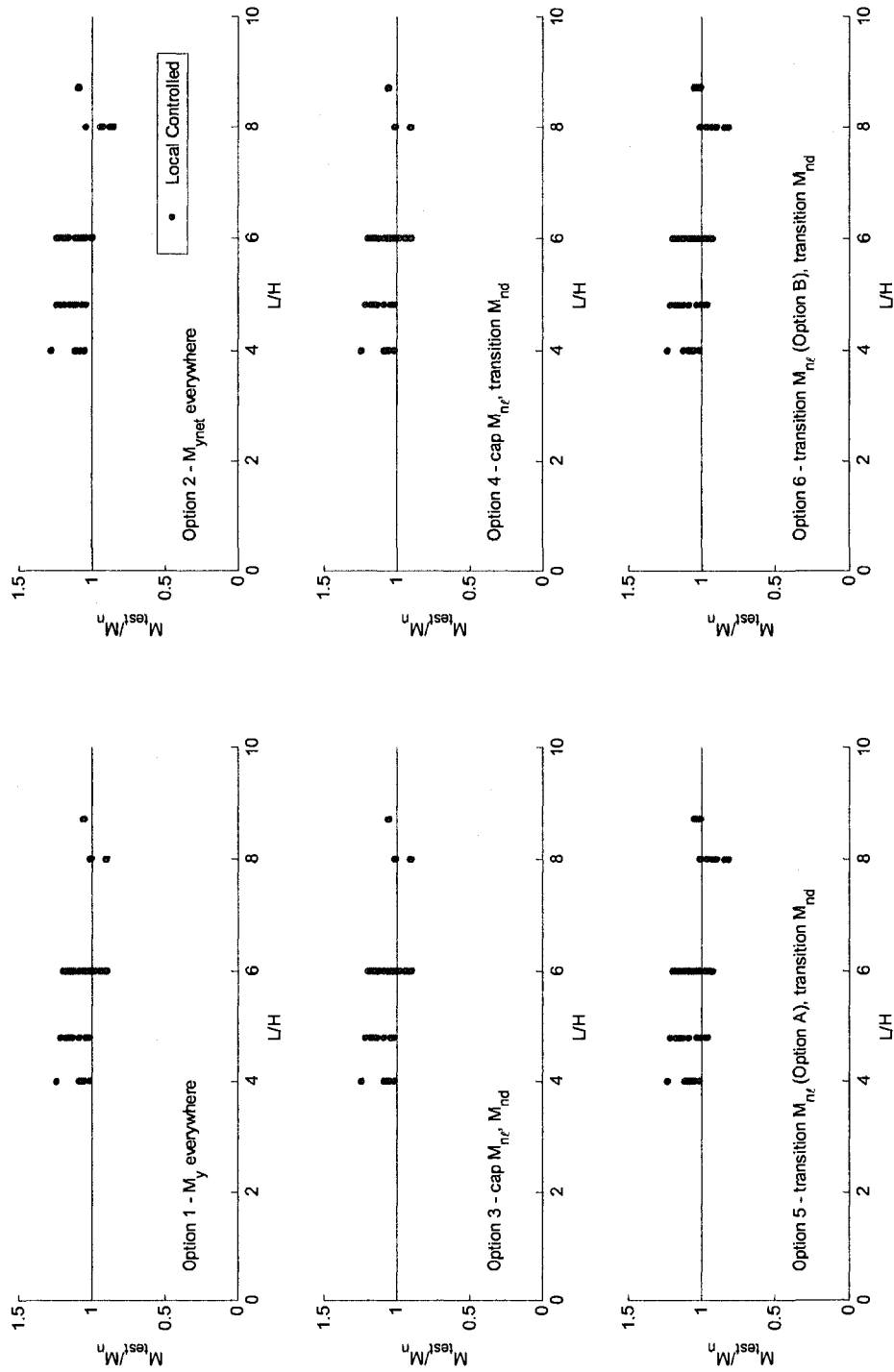


Figure 8.60 Test-to-predicted ratios for simulated local buckling-controlled laterally braced beam failures as a function of column length, L , to beam depth, H

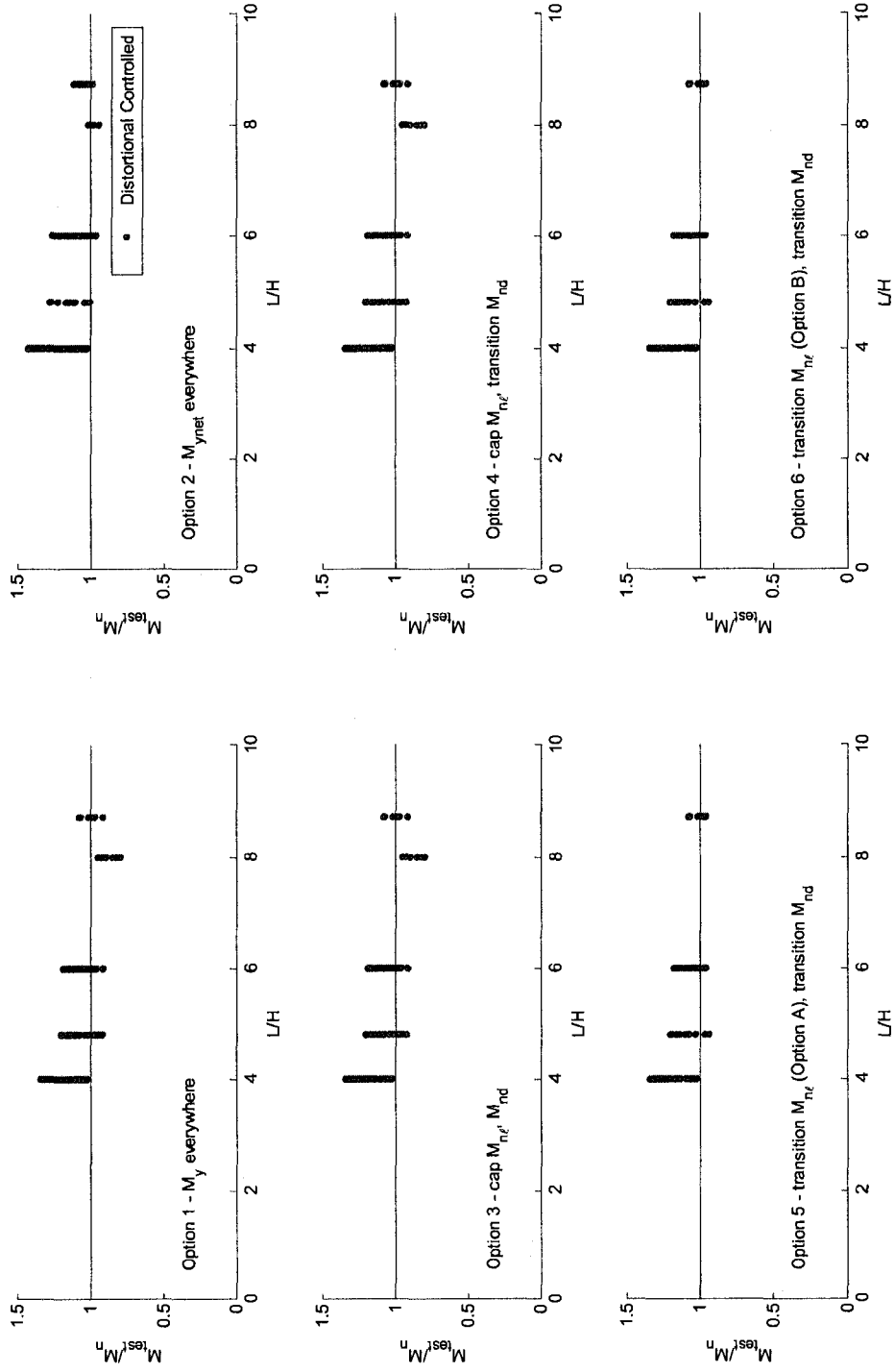


Figure 8.61 Test-to-predicted ratios for simulated distortional buckling-controlled laterally braced beam failures as a function of column length, L , to H

8.2.6 DSM comparison to experimental beam database

The six DSM options are now compared to the laterally braced beam experiment database first assembled in Section 4.3.1. The database contains the elastic buckling properties of each beam, including the presence of holes and the influence of boundary conditions, as well as the tested strengths. Figure 8.62 through Figure 8.65 compare the experiment strengths to DSM predictions for local and distortional buckling-controlled beam failures. (The local and distortional slenderness is obtained with the “pure” local and distortional elastic buckling loads L and D in this study, not the LH and DH modes described in Section 4.3). The tested strengths are lower than the predictions over a wide range of local and distortional slenderness. These trends were first observed in a preliminary DSM comparison (Moen and Schafer 2007a), and possible reasons for the difference between test and predictions were hypothesized, including experimental error, error in the determination of elastic buckling loads, and the influence of the angle straps on the calculation of the distortional critical elastic buckling load. The beams in the database have relatively small holes, with I_{net}/I_g ranging from 0.96 to 0.99 as shown in Figure 8.64 and Figure 8.65, which suggests that the presence of holes should not have a significant impact on tested strength. The test-to-predicted statistics are the same for the six DSM options as shown in Table 8.5. It is concluded that the experimental database, in its current form, cannot be used to evaluate the proposed DSM modifications. Future work is planned to investigate the differences between the DSM predictions and tested strengths for this data. In addition, more recent tests on cold-formed steel beams with

holes will be added to the database. Experiments on beams with larger holes are also needed.

Table 8.5 DSM test-to-predicted ratio statistics for column experiments

Option	Description	Local buckling				Distortional buckling			
		Mean	SD	ϕ	# of tests	Mean	SD	ϕ	# of tests
1	M_y everywhere	0.88	0.12	0.85	55	0.87	0.14	0.81	89
2	$M_{y_{met}}$ everywhere	0.88	0.12	0.85	55	0.87	0.14	0.81	89
3	Cap M_{nL} , M_{nd}	0.88	0.12	0.85	55	0.87	0.14	0.81	89
4	Transition M_{nd} , Cap M_{nL}	0.88	0.12	0.85	55	0.87	0.14	0.81	89
5,6	Transition M_{nd} and M_{nL} (Option A, B)	0.88	0.12	0.85	55	0.87	0.14	0.81	89

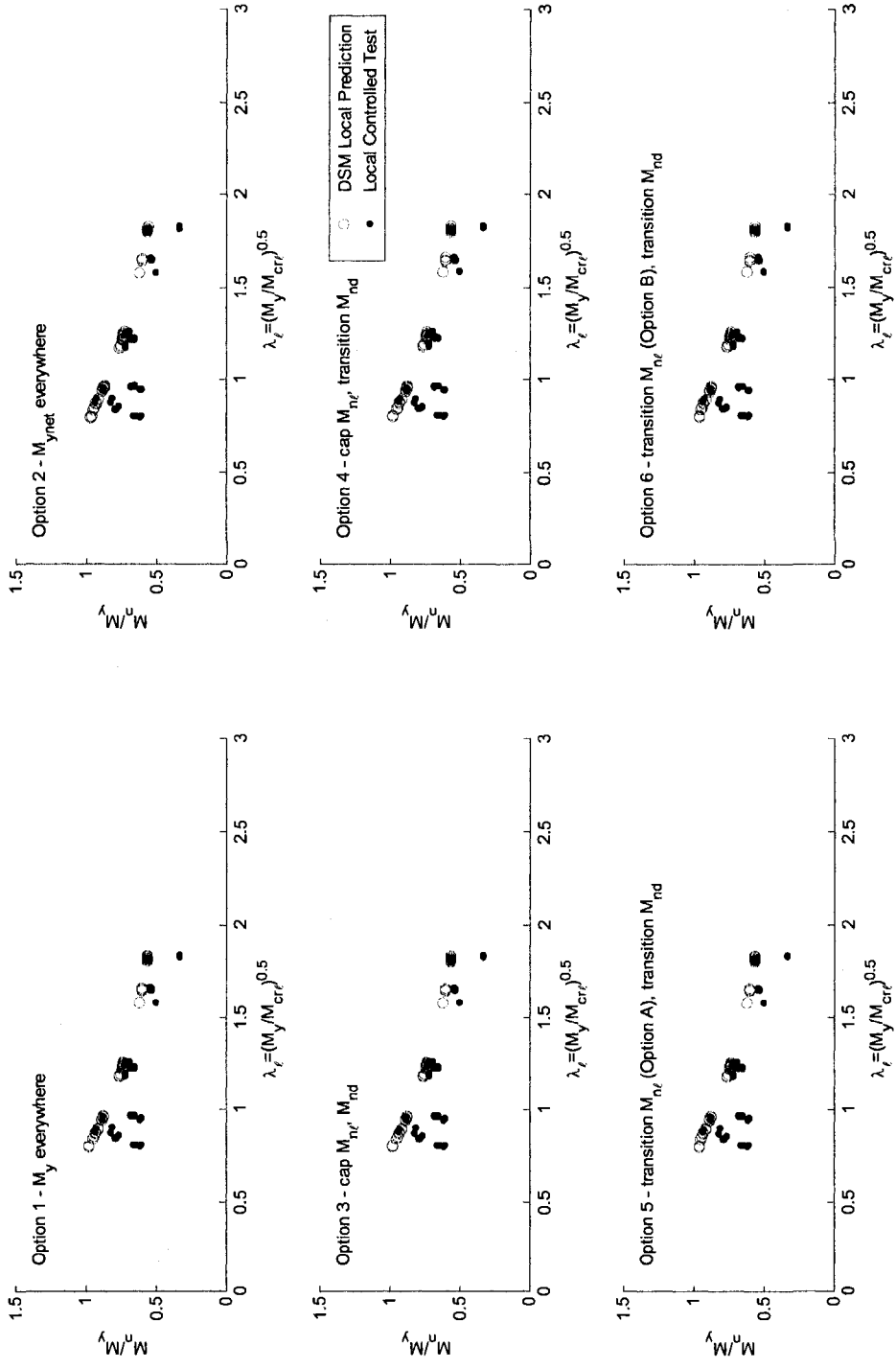


Figure 8.62 Comparison of experimental test strengths to predictions for laterally braced beams with local buckling-controlled failures as a function of local slenderness

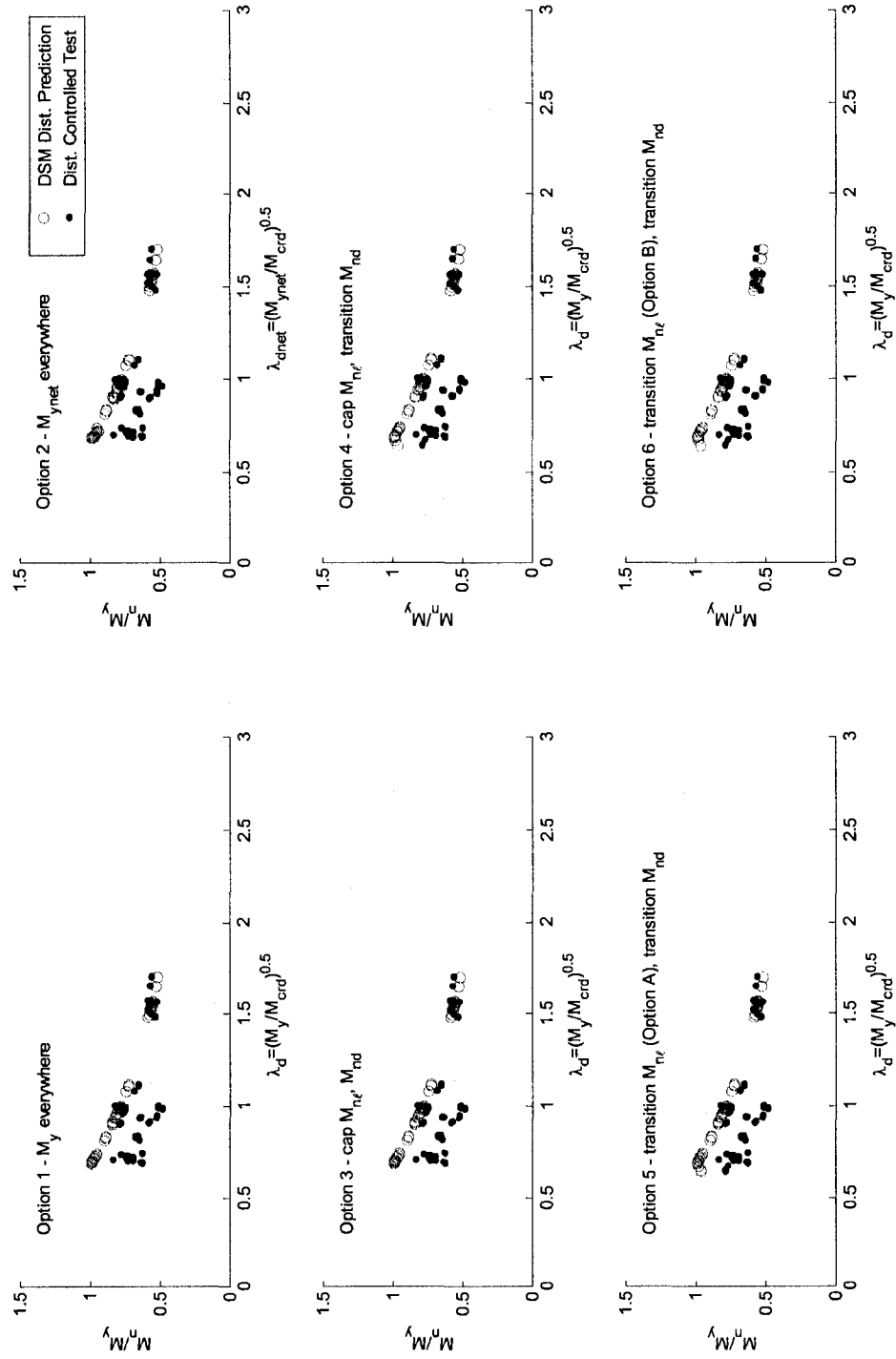


Figure 8.63 Comparison of experimental test strengths to predictions for laterally braced beams with distortional buckling-controlled failures as a function of distortional slenderness

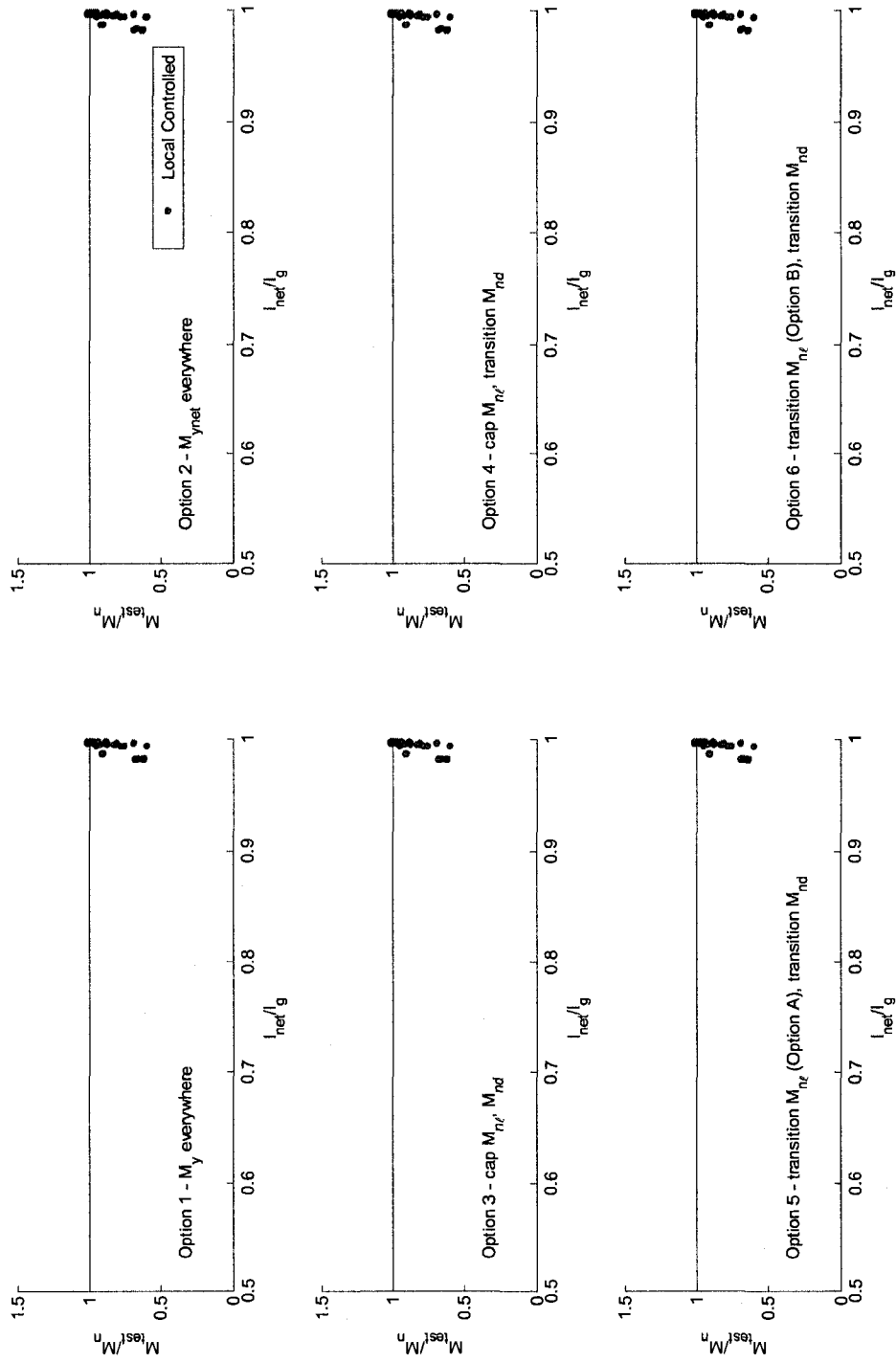


Figure 8.64 Test-to-predicted ratios for experimental local buckling-controlled laterally braced beam failures as a function of net cross-sectional moment of inertia to gross cross-sectional moment of inertia

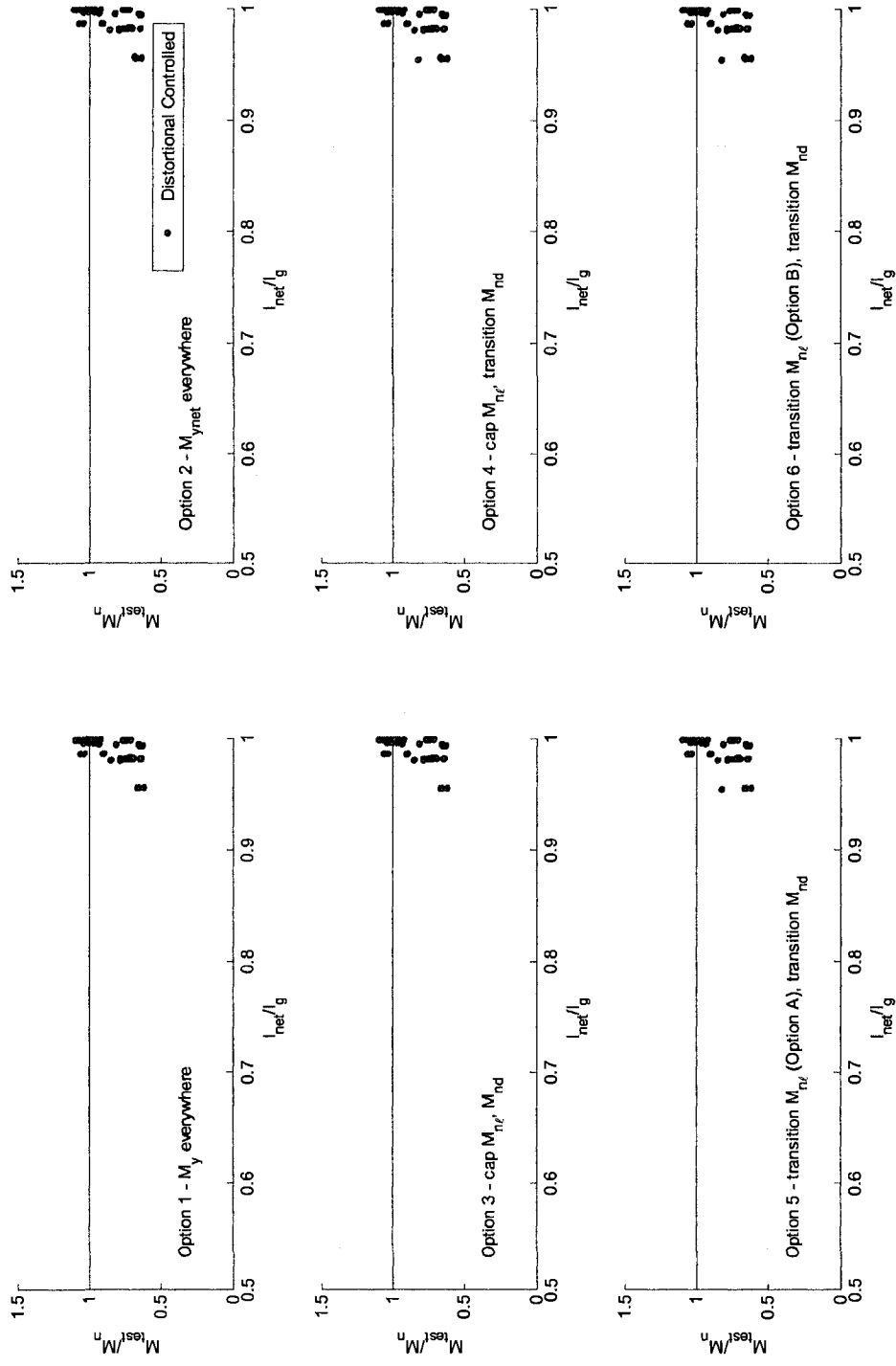


Figure 8.65 Test-to-predicted ratios for experimental distortional buckling-controlled laterally braced beam failures as a function of net cross-sectional moment of inertia to gross cross-sectional moment of inertia

8.2.7 Recommendations – DSM for beams with holes

Options 3, 4, 5, and 6 are presented as viable proposals for extending DSM to beams with holes. This recommendation is based on the test-to-predicted statistics and data trends from the simulation studies presented in Section 8.2.5, and also considers the effort to implement the modifications and their ease of use by design engineers. Option 3 accounts for the reduction in beam strength from the presence of holes by limiting M_{ne} and M_{nd} to M_{ynet} . This is a simple modification to implement in the Specification and avoids additional calculation work for a design engineer (except for that required to calculate the critical elastic buckling loads including the influence of the holes). Options 4 and 5 are refinements of Option 3, where the cap on M_{ne} and M_{nd} becomes a transition from an elastic buckling controlled failure mode to a yield controlled failure at M_{ynet} . These two methods require additional effort from the designer when compared to Option 3, but they have an important advantage. Options 4, 5, and 6 are more closely tied to the failure mechanisms influencing column strength because they capture the yield transition to the net section in their predictions. The transitions increase the probability that strength will be accurately predicted for general beam and hole geometries. Option 5 has the additional advantage of capturing the influence of a yield transition for closed cross-sections that do not experience distortional buckling. Additional nonlinear finite element simulations and experiments are needed to validate the proposed modifications to the Direct Strength Method for beams subject to lateral-torsional buckling at ultimate limit state.

Chapter 9

Conclusions and proposed future work

9.1 Conclusions

Proposed Direct Strength Method design equations are now in place for cold-formed steel members with holes. The development of the method was initiated with thin shell finite element eigenbuckling studies in ABAQUS on thin plates and full cold-formed steel members with holes. The buckling of the unstiffened strips adjacent to a hole in a thin plate influenced, and sometimes controlled, the critical elastic buckling stress of individual cross-section elements. Unstiffened strip buckling was also closely associated with distortional buckling modes at the location of the holes in C-section columns and beams. Large holes and closely-spaced holes locally stiffened thin rectangular plates and the webs of C-section columns, resulting in buckling away from the holes. The elastic buckling studies led to useful design guidelines and tools, including hole spacing limits (which prevent cumulative reductions in elastic stiffness along the length of a

member) and simplified elastic buckling prediction methods for local, distortional, and global buckling developed as an alternative to finite element eigenbuckling analysis.

The viability of the DSM framework for cold-formed steel members with holes was established early in this research using existing test results and the elastic buckling properties of cold-formed steel column and beam specimens with holes. Additional experimental work evaluated the influence of holes on the load-deformation response and failure mechanisms for short and intermediate length C-section columns. During the experiments, holes were observed to locally stiffen the web of the intermediate length C-section columns and prevented dynamic mode switching (from local buckling to distortional buckling) near peak load. Holes were also observed to decrease post-peak ductility for columns when the hole size was large relative to the web width (e.g., the 362S162-33 specimens).

Results from the experimental program were used to validate a nonlinear finite element modeling protocol. A concerted effort was made to simulate the initial state of a cold-formed steel member in the protocol, including imperfection magnitudes based on measurement statistics and residual stresses and initial plastic strains from the cold-forming process predicted with a mechanics-based approach. The nonlinear finite element modeling capability was used to construct a large database of simulated column and beam experiments with a wide range of hole sizes, spacings, and C-section dimensions. Simulation results demonstrated that as cross-section distortional or local slenderness decreased, the failure of a cold-formed steel member with holes occurred by yielding and collapse of the unstiffened strips at the net cross-section. Collapse of the

unstiffened strips sometimes triggered unstable global failure modes in columns with large holes, i.e., as hole size approached $A_{net}=0.60A_y$. (Global instabilities caused by yielding at peak load were not studied for beams with holes in this thesis, only laterally braced beams were considered.) Modifications to the local and distortional DSM curves were made to account for this unique net-section failure mechanism with a deliberate transition and cap on member strength. The final proposed DSM method for members with holes was validated with existing experimental data and the simulated experiments database.

9.2 Future work

Several interesting future research topics resulted from the elastic buckling studies, experiments, and nonlinear finite element simulations in this thesis. Future research is planned to follow up on many of these ideas and questions. The major points of future study, organized by research topic, are listed below.

Thin-shell finite element modeling in ABAQUS (Chapter 2)

The S9R5 meshing guidelines developed in this thesis were developed primary for eigenbuckling analyses. Meshing guidelines which ensure accurate results in nonlinear finite element simulations are also needed. Studies are ongoing to develop rules for determining the minimum number of through-thickness finite element integration points, the mesh density required for linear and quadratic finite element formulations, and limits on initial element distortion and curvature.

Elastic buckling of cold-formed steel cross-sectional elements with holes (Chapter 3)

1. The simplified elastic buckling prediction method presented in this thesis for unstiffened elements loaded with uniaxial compression is empirically derived. A mechanics-based unstiffened element prediction method is warranted as a topic of future research to improve the generality of the method.
2. An element-based elastic buckling prediction method which accounts for stress gradients on unstiffened elements with holes is needed to address a design case engineers may encounter in practice.
3. Elastic buckling studies are planned to develop element-based simplified methods for hole patterns found in storage racks.
4. The element-based elastic buckling prediction methods provide a convenient method to calculate F_{cr} (the critical elastic buckling stress) for general hole shapes, sizes, and spacings for use in the AISI-S100-07 effective width method. Work is planned to evaluate introduce these simplified approaches into the effective width method.

Elastic buckling of cold-formed steel members with holes (Chapter 4)

1. Yu and Davis, Ortiz-Colberg, Rhodes and MacDonald, Rhodes and Schnieder, and Pu et al. performed tests on column specimens with multiple discrete holes or hole patterns. The elastic buckling properties and tested strengths of these specimens will be added to the experiment database, in addition to tests on rack sections.
2. Automated elastic buckling modal identification tools are needed to identify local, distortional, and global buckling modes in thin-shell finite element eigenbuckling analysis. Research is ongoing to develop this capability with an implementation similar to that of the constrained finite strip method.
3. Work continues on the development and validation of the CUFSM elastic buckling approximate methods developed and the extension of these methods to members with hole patterns (e.g., storage racks). A general procedure for implementing CUFSM constraints in the local buckling prediction method is needed. Also, the current assumption that the warping torsion constant $C_w=0$ at a hole produces conservative global elastic buckling predictions for columns and beams. Additional research is needed to derive a mechanics-based approximation for C_w at a hole.

Experiments on cold-formed steel columns with holes (Chapter 5)

1. A more definitive method of measuring the base metal thickness of cold-formed steel members with a zinc galvanic coating is needed. Current standard practice is to remove the zinc coating with hydrochloric acid or a ferric chloride solution. It is difficult to know when all of the zinc has been removed though since the

zinc chemically interacts with the base metal during the initial application. Experiments are planned to determine the influence of the zinc coating on ultimate strength.

2. Research work is planned to evaluate the influence of sheet coiling on the measured yield stress in tensile coupons. It has been hypothesized by Professor Rasmussen at the University of Sydney that the same coiling curvature which causes residual stresses in cold-formed steel members also affects yield stress measurements in tensile tests.

Residual stresses and plastic strains in cold-formed steel members (Chapter 6)

1. Experimental work is planned to validate the prediction model presented in Chapter 6 relating coiling residual stresses to the coiling radius, sheet thickness, and yield stress.
2. Research is ongoing to evaluate how ABAQUS metal plasticity laws use the residual stress and initial plastic strain information and to determine if kinematic hardening or a different mixed hardening rule is required to accurately simulate the cold-work of forming effect on load-deformation response.
3. Nonlinear finite element studies are planned to identify the influence of through-thickness residual stresses and plastic strains on the load-deformation response, ultimate strength, and failure mechanisms of cold-formed steel beams and columns.
4. Hancock et al. provides a method which accounts for the cold-work of forming in the corners of cold-formed steel cross-sections when calculating ultimate strength (Hancock et al. 2001). The research in Chapter 6 provides new insight into the relationship between residual stresses and initial plastic strains from the manufacturing process. Research work is planned to revisit Hancock's cold-work of forming method to determine if it can be supplemented with this new research.
5. The current residual stress prediction method assumes an elastic-perfectly plastic material model. Research work is ongoing to introduce the effect of steel strain hardening into the prediction method.

Nonlinear finite element modeling of cold-formed steel members (Chapter 7)

1. The use of measured imperfection magnitudes instead of statistical distributions is warranted as a topic of future study, especially the use of a flared cross-section, including flange-web angles off of 90 degrees.
2. Initiating plasticity in ABAQUS at the material's proportional limit reduced the predicted strength by up to 20% when compared to experiments in Chapter 7. A study is planned to simulate a single finite element in tension to evaluate the ABAQUS implementation of metal plasticity and determine the source of the discrepancy.

The Direct Strength Method for members with holes (Chapter 8)

1. Additional validation studies are planned to compare the proposed DSM Holes methodology to the AISI-S100-07 effective width design method.
2. Nonlinear finite element studies of other DSM prequalified cross-sections (e.g., Z-sections and hat sections) as well as rack sections with hole patterns are also planned to expand the simulation database.

References

- ABAQUS. (2007a). "ABAQUS/Standard Version 6.7-1.", Dassault Systèmes, <http://www.simulia.com/>, Providence, RI.
- ABAQUS. (2007b). "Personal communication, S9R5 element section numbers." Dassault Systèmes, <http://www.simulia.com/>, Providence, RI.
- AISI-S100. (2007). *North American Specification for the Design of Cold-Formed Steel Structural Members*, American Iron and Steel Institute, Washington, D.C.
- AISI-TS-2-02. (2001). "Stub Column Test Method for Effective Area of Cold-formed Steel Columns." 2001 North American Cold Formed Steel Specification, American Iron and Steel Institute, Washington, D.C.
- AISI. (2006). *Direct Strength Method Design Guide*, American Iron and Steel Institute, Washington, D.C.
- ASTM. (2004). "E 8M-04, Standard Test Methods for Tension Testing of Metallic Materials (Metric)." ASTM International, West Conshohocken, PA.
- Batson, K.D. (1992). "Flexural Behavior of Webs with Openings," M.S. Thesis, University of Missouri-Rolla, Rolla.
- Bernard, E.S. (1993). "Flexural Behaviour of Cold-Formed Profiled Steel Decking," Ph.D. Thesis, University of Sydney, Australia, Sydney.
- Chajes, A. (1974). *Principles of Structural Stability*, Prentice Hall College Div, Englewood Cliffs, NJ.
- Chen, W.F., and Han, D.J. (1988). *Plasticity for Structural Engineers*, Springer-Verlag, New York, NY.
- Cook, R.D. (1989). *Concepts and Applications of Finite Element Analysis*, J. Wiley & Sons, New York, NY.
- CRC. (2003). *Standard Mathematical Tables and Formulae*, CRC Press, New York, NY.
- Crisfield, M.A. (1981). "A fast incremental iteration solution procedure that handles snap-through." *Computers and Structures*, 13, 55-62.
- Dat, D.T. (1980). "The Strength of Cold-Formed Steel Columns." Cornell University Department of Structural Engineering Report No. 80-4, Ithaca, NY.

- De Batista, E.M., and Rodrigues, F.C. (1992). "Residual stress measurements on cold-formed profiles." *Experimental Techniques*, 16(5), 25-29.
- Galambos, T. (1998a). "Appendix B.3, Technical Memorandum No.3: Stub Column Test Procedure." *Guide to Stability Design Criteria for Metal Structures*, 5th Edition, John Wiley & Sons, New York, NY.
- Galambos, T. (1998b). *Guide to Stability Design Criteria for Metal Structures*, 5th Edition, John Wiley & Sons, New York, NY.
- Hancock, G.J., Murray, T., and Ellifritt, D. (2001). *Cold-formed steel structures to the AISI specification*, Marcel Dekker, Inc., New York, NY.
- Hill, R. (1950). *The Mathematical Theory of Plasticity*, Oxford University Press, London, England.
- Ingvarsson, L. (1975). "Cold-forming residual stresses, effect of buckling." *Proceedings, Third Annual Specialty Conference on Cold-Formed Steel Structures*, University of Missouri-Rolla, 85-119.
- Key, P., and Hancock, G.J. (1993). "A Theoretical Investigation of the Column Behaviour of Cold-Formed Square Hollow Sections." *Thin-Walled Structures*, 16, 31-64.
- Kwon, Y.B. (1992). "Post-Buckling Behaviour of Thin-Walled Sections," Ph.D. Thesis, University of Sydney, Australia.
- Labview. (2005). "Labview, Version 8." National Instruments, www.labview.com, Austin, TX.
- Mathworks. (2007). "Matlab 7.5.0 (R2007b)." Mathworks, Inc., www.mathworks.com.
- Moen, C.D., and Schafer, B.W. (2007a). "Direct strength design for cold-formed steel members with perforations, Progress Report #3." American Iron and Steel Institute, Washington, D.C.
- Moen, C.D., and Schafer, B.W. (2007b). "Direct strength design for cold-formed steel members with perforations, Progress Report #4." American Iron and Steel Institute, Washington, D.C.
- Oden, J.T., and Martins, J.A.C. (1985). "Models and computational methods for dynamic friction phenomena." *Computer Methods in Applied Mechanics and Engineering*, 52, 527-634.
- Porter, F.C. (1991). *Zinc Handbook*, Marcel Dekker, New York, NY.
- Powell, G., and Simons, J. (1981). "Improved iterative strategy for nonlinear structures." *International Journal for Numerical Methods in Engineering*, 17, 1455-1467.
- Quach, W.M., Teng, J.G., and Chung, K.F. (2004). "Residual stresses in steel sheets due to coiling and uncoiling: a closed-form analytical solution." *Engineering Structures*, 26, 1249-1259.

- Quach, W.M., Teng, J.G., and Chung, K.F. (2006). "Finite element predictions of residual stresses in press-braked thin-walled steel sections." *Engineering Structures*, 28, 1609-1619.
- Ramm, E. (1981). "Strategies for tracing nonlinear response near limit points." *Nonlinear Finite Element Analysis in Structural Mechanics: Proceedings of the Europe-US Workshop*, 63-89.
- Schafer, B.W. (1997). "Cold-formed steel behavior and design: analytical and numerical modeling of elements and members with longitudinal stiffeners," Ph.D. Thesis, Cornell University, Ithaca, NY.
- Schafer, B.W., and Ádány, S. (2006). "Buckling analysis of cold-formed steel members using CUFSM: conventional and constrained finite strip methods." *Eighteenth International Specialty Conference on Cold-Formed Steel Structures*, Orlando, FL.
- Schafer, B.W., and Peköz, T. (1998). "Computational modeling of cold-formed steel: characterizing geometric imperfections and residual stresses." *Journal of Constructional Research*, 47, 193-210.
- Schafer, B.W., Sarawit, A., and Peköz, T. (2006). "Complex edge stiffeners for thin-walled members." *Journal of Structural Engineering*, 132(2), 212-226.
- Schuster, R.M. (1992). "Testing of Perforated C-Stud Sections in Bending." University of Waterloo, Ontario, Canada.
- Shan, M.Y., and LaBoube, R.A. (1994). "Behavior of Web Elements With Openings Subjected to Bending, Shear, and the Combination of Bending and Shear." *Civil Engineering Study 94-2, Cold-formed Steel Series*, University of Missouri-Rolla, Rolla.
- Shanley, F.R. (1957). *Strength of Materials*, McGraw-Hill Book Company, New York, NY.
- Silvestre, N., and Camotim, D. (2005). "Local-plate and distortional post-buckling behavior of cold-formed steel lipped channel columns with intermediate stiffeners." *Seventeenth International Specialty Conference on Cold-Formed Steel Structures: Recent Research and Developments in Cold-Formed Steel Design and Construction*, Orlando, FL, United States, 1-18.
- SSMA. (2001). "Product Technical Information, ICBO ER-4943P." Steel Stud Manufacturers Association, www.ssma.com.
- Timoshenko, S.P., Gere, James M. (1961). *Theory of Elastic Stability*, McGraw-Hill, New York.
- US Steel. (1985). *The Making, Shaping, and Treating of Steel, 10th Edition*, Herbick & Held, Pittsburgh, PA.
- von Karman, T., Sechler, E.E., and Donnell, L.H. (1932). "The strength of thin plates in compression." *Transactions ASME*, 54(APM 54-5).

- Wang, X.P., Lam, S.S.E., and Chung, K.F. (2006). "Cross section distortion due to cutting of cold-formed steel lipped C-section." *Thin-Walled Structures*, 44, 271-280.
- Weng, C.C., and Peköz, T. (1990). "Residual Stresses in Cold-Formed Steel Members." *ASCE Journal of Structural Engineering*, 116(6), 1611-1625.
- Western States Clay Products Association. (2004). *Design Guide for Anchored Brick Veneer over Steel Stud Systems*, [www.brick wscca.org](http://www.brick.wscca.org), Seattle, WA.
- Winter, G. (1947). "Strength of thin steel compression flanges." *Cornell University Engineering Experiment Station Reprint No. 32*.
- Yu, C. (2005). "Distortional buckling of cold-formed steel members in bending," Ph.D. Thesis, Johns Hopkins University, Baltimore.
- Yu, C., and Schafer, B.W. (2006). "Distortional buckling tests on cold-formed steel beams." *ASCE Journal of Structural Engineering*, 132(4), 515-528.
- Yu, C., and Schafer, B.W. (2007). "Effect of Longitudinal Stress Gradients on Elastic Buckling of Thin Plates." *ASCE Journal of Structural Engineering*, 133(4), 452-463.
- Yu, W.W. (2000). *Cold-Formed Steel Design*, John W. Wiley & Sons, New York, NY.
- Ziemian, R., and McGuire, W. (2005). "MASTAN version 3.0.4, www.mastan.com." Bucknell University, Lewisburg, PA.

Appendix A

ABAQUS input file generator in Matlab

The finite element models in this thesis were generated with a custom Matlab program which assembles a column or beam with any general cross-section (input in CUFSM-style format) using nine node S9R5 thin-shell finite elements. The user has the ability to add holes at specific locations in the member, dictate the boundary conditions and application of load, specify the material properties, and impose imperfection, residual stresses and plastic strains to define a member's initial state. Input files for eigenbuckling analysis and nonlinear finite element simulations can be generated. The program was used throughout this research to generate groups of ABAQUS input files for parameter studies. The program setup used to generate the nonlinear finite element models of the column experiments is provided here.


```

clear all
close all

sourceloc='C:\Documents and Settings\Cris\Desktop\cmoen\Cold Formed Steel - Holes
Research\Fall 2007\runbuck development\Rev_6NL\jhab'

%This example generates ABAQUS input files for the nonlinear
%simulation of 12 different columns with SSMA C-sections and evenly spaced
%slotted holes. The column boundary conditions are pinned-pinned warping free and the
column is
%loaded from both ends with a uniform compressive stress simulated as
%consistent nodal loads on the first two sets of cross-section nodes.
%25%CDF and 75% CDF imperfections are imposed on the member geometry with
%CUFSM local and distortional buckling mode shapes.

addpath([sourceloc '\functions\filewriting\'])
addpath([sourceloc '\functions\holes\'])
addpath([sourceloc '\functions\'])
addpath([sourceloc '\templates\'])
addpath([sourceloc '\'])

load SSMAxsections %SSMA cross section info
load SSMAnames %SSMA name list
load SSMA_wvlenghts %SSMA cFSM wavelengths for Pcr1, Pcrd
load Ag %SSMA gross cross-sectional area

%define the SSMA sections to create models for
sections=[12
86
11
73
39
95
72
56
47
75
66
87]

%define the imperfection magnitudes
imptypes=[25 75]

%define hole length (slotted holes considered here)
Lhole=4
%define rough hole spacing, will be adjusted in holes section of file
S=12

%define member lengths
Lc=[34
88
24
74
42
78
66
56
32
74
40
80]

%define hole depth such that Anet=0.70Ag
Anetfactor=0.7

count=1
for i=1:length(sections)

    section_num=sections(i)

```

```

for j=1:length(imptypes)

%MEMBER LENGTH
L=Lc(i)

%MESH ALONG LENGTH
nele=L*2;

%NUMBER OF SECTION POINTS THROUGH THE THICKNESS
sectionpoints=5

%CROSS-SECTION DIMENSIONS
%
%           Z
%
%           A
%           X
%    D2 /      I      \ D1
% RT2/_S2      S      _S1_\RT1
% B2 \        |        / B1
%           |
%    _F2\_      |      /_F1_   ABAQUS Y AXIS
%           RB2   H   RB1
%
%Dimensions are out-to-out, angles are in degrees, t is base metal +
%coating thickness, tbare is base metal thickness
%    [H      B1      B2      D1      D2      F1      F2      S1      S2      RB1
RB2    RT1      RT2      t      tbare]
dims=SSMAXsections(section_num,2:16)

%calculate hole depth
hole=Ag(section_num)*(1-Anetfactor)./dims(15)

%CROSS-SECTION MESHING
%number of elements around the cross section
%[D1  RT1  B1  RB1  H  RB2  B2  RT2  D2]
n=[2  2  2  2  16  2  2  2  2];

%CorZ=1 C-section, CorZ=2 Z-section
CorZ=1
[node,elem]=cztemplate(CorZ,dims,n)
nnodes=length(node(:,1)); %Number of FSM cross-section nodes
%Determine FE number of nodes and increment
nL=2*nele+1; %Number of FE nodes along the length
%Determine the node numbering increment along the length
if nnodes<100
    FEssection_increment=100; %so along the length the numbering goes up by 100's
else
    FEssection_increment=nnodes+1;
end

%ADD ADDITIONAL NODES
nodeadd=[]

%MATERIAL PROPERTIES
%steel
matprops(1).name='MAT100';
matprops(1).elastic=[29500 0.3];
matprops(1).plastic=[58.6, 0
    64.1517, 0.00342827
    68.2188, 0.00842827
    72.0304, 0.0134283
    77.9752, 0.0234283
    82.2224, 0.0334283
    85.7249, 0.0434283
    88.4053, 0.0534283
    90.7405, 0.0634283
    92.652, 0.0734283
    94.3657, 0.0834283
    95.8299, 0.0934283
    97.2001, 0.103428 ];

```

```

%IMPERFECTIONS
%*****IMPERFECTIONS*****
%type=0   no imperfections
%type=1   use mode shapes from ABAQUS results file
%type=2   input from file
%type 3   impose CUFEM shapes as imperfections

imperfections.type=3;
imperfections.filename=[];
imperfections.step=[];
imperfections.mode=[]

t=dims(15)
if imptypes(j)==25
    if L>24
        imperfections.magnitude=[0.14*t 0.64*t L/2000]
        imperfections.wavelength=[SSMA_wvlenghts(section_num,1)
SSMA_wvlenghts(section_num,2) L]
    else
        imperfections.magnitude=[0.14*t 0.64*t]
        imperfections.wavelength=[SSMA_wvlenghts(section_num,1)
SSMA_wvlenghts(section_num,2)]
    end

elseif imptypes(j)==75
    if L>24
        imperfections.magnitude=[0.66*t 1.55*t L/1000]
        imperfections.wavelength=[SSMA_wvlenghts(section_num,1)
SSMA_wvlenghts(section_num,2) L]
    else
        imperfections.magnitude=[0.66*t 1.55*t]
        imperfections.wavelength=[SSMA_wvlenghts(section_num,1)
SSMA_wvlenghts(section_num,2)]
    end
end
imperfections.plumb=[]
imperfections.member=[1] %1 for column, 2 for beam

%DEFINE HOLES
%Add holes to your member.
%hole.type=1   circular
%hole.type=2   rectangular
%hole.type=3   slotted w/radial ends
%hole.dimension=['width or length (ABAQUS x direction)' 'height or diameter']
%hole.location=['CUFEM cross section node (must be odd!)' 'longitudinal location'
'shift hole in direction of height']
%hole.thickness = thickness of finite elements making up hole, usually the same
as the rest of the member
%I've defined two slotted holes here in the web of the cross-section.

%number of holes
nhole=floor(L/S)

if nhole<1
    nhole=1
end

%final hole spacing
Sfinal=floor(L/nhole)
spacing=Sfinal/2:Sfinal:L-Sfinal/2
hole.type=[3*ones(nhole,1)];
%define dimensions for slotted hole
hole.dimension=[Lhole*ones(nhole,1) hhole*ones(nhole,1)];
%define location of hole in cross-section
hole.location = [(length(node)+1)/2*ones(nhole,1) spacing' zeros(nhole,1)]
hole.thickness = [dims(1,15)*ones(length(hole.type),1)]
hole.material=[100*ones(length(hole.type),1)];
hole.groups=[100000+[1:length(hole.type)]];
hole.fill=[zeros(length(hole.type),1)];
%If you don't want holes, replace above with

```

```

%hole=[ ]

%MEMBER END LOADINGS
%Loading notation is similar to CUF5M. Apply P for compression, M for
%moment, or a combination of both. Compression at both ends of
%column are
%shown here. Loads are applied as consistent nodal loads in ABAQUS.

end1load.P=1;
end1load.Mxx=0;
end1load.Mzz=0;
end1load.M11=0;
end1load.M22=0;

end2load.P=-1;
end2load.Mxx=0;
end2load.Mzz=0;
end2load.M11=0;
end2load.M22=0;

%CALCULATE CONSISTENT NODAL LOADS ON MEMBER ENDS*****
unsymm=0
[end1cload, end2cload, A,
Ixx]=consist_endloads(node,elem,end1load,end2load,unsymm, nL, FEsection_increment);

%ABAQUS NODE SETS
%Define these node sets to apply boundary conditions in ABAQUS
%      nodesetinfo=('nodeset name' [xlim1 xlim2 xint] [ylim1 ylim2 yint] [zlim1
zlim2 zint] exclude)
%where nodes are grouped based on xlim1<=x<=xlim2 and ylim1<=y<=ylim2 and
zlim1<=z<=zlim2.
%Instead of ranges, assign xint,yint,zint to something other than zero to group
nodes at specific x,y,and z
%distance intervals
%      xlim1:xint:xlim2, ylim1:yint:ylim2, ylim1:yint:ylim2.
%The exclude command can be used to exclude previously defined node sets from the
current node set.
%exclude = 0    all nodes in range are included in nodeset
%exclude = m    excludes nodeset m from current nodeset

nodesetinfo={'ENDXZERO' [0 0 0] [-1000 1000 0] [-1000 1000 0] 0;
'ENDXL' [L L 0] [-1000 1000 0] [-1000 1000 0] 0;
'DISPDOF' [L L 0] [0 0 0] [0 0 0] 0;
'MID' [L/2 L/2 0] [max(node(:,3))-0.05 max(node(:,3))+0.05 0]
[max(node(:,2))/2-0.05 max(node(:,2))/2+0.05 0] 0};

%DEFINE SPRINGS
springs=[]

%DEFINE CONTACT SURFACES, NODE SURFACES, KINEMATIC CONSTRAINTS,....
surface.type={}
surface.type=[]
surface.local=[]
surface.coord=[]
surface.coupling={};
surface.interaction=[]
surface.contact=[]
surface.aredist=[]

%ABAQUS INP FILE NAME
jobname(count)=[SSMNames(section_num) '_' num2str(i) '_' num2str(imptypes(j))];

%DEFINE ANALYSIS STEP
step(1).stepinfo={'STEP 1,' 'nlgeom,' 'INC=' [260]};
step(1).solutiontype='Static, Riks';
step(1).solutionsteps={'0.25, ,1e-10, 1'};
step(1).solutioncontrols={ };
step(1).boundarycon={'ENDXZERO' 2 3;

```

```

        'ENDXL' 2 3;
        'MID' 1 1)
step(1).coupling=[]
step(1).loads={'*Cload' end1cload(:,1) 1 end1cload(:,2)/2;
              '*Cload' end1cload(:,1)+200 1 end1cload(:,2)/2;
              '*Cload' end2cload(:,1) 1 end2cload(:,2)/2;
              '*Cload' end2cload(:,1)-200 1 end2cload(:,2)/2}
step(1).outrquest={'*Output, field, frequency=10';
                  '*Element Output';
                  '1,3,5';
                  'S,MISES';
                  '*Node Output';
                  'U';
                  '*Node Print, NSET=DISPDOF, SUMMARY=NO';
                  'UL,CF1'};

        %WRITE ABAQUS INP FILE
        %this is the important function, you can use this in for loops to generate
parameter studies
        jhabnl(L, node, elem, nele, endlload, end2load, hole, nodesetinfo, surface,
nodeadd, step, jobname(count),matprops,imperfections,springs,sectionpoints)
        count=count+1
    end

end

%CREATE BEAST BATCH FILE
%Generates a linux batch file that will submit all of the parameter study
%.inp files to the queue manager on the beast.
ABQbeastscript(jobname,ones(length(jobname),1)*4,'cdmscript')
%Run the script at the beast command line with:
% bash cdmscript

```

Appendix B

ABAQUS element-based elastic buckling results

This appendix contains the finite element plate model dimensions and ABAQUS critical elastic buckling stress results (f_{cr}) used in the Chapter 3 elastic buckling studies on stiffened and unstiffened elements.

Stiffened element in bending ($Y=0.50h$), transversely centered holes

Model number	hole type	h_{hole} in.	h in.	L_{hole} in.	S in.	L in.	t in.	ϕ_{hole} in.	Y in.	f_{cr} ksi
1	slotted	1.50	15.00	4.00	20.00	100.00	0.0346	0.00	7.50	3.26
2	slotted	1.50	15.00	6.00	20.00	100.00	0.0346	0.00	7.50	3.06
3	slotted	1.50	15.00	8.00	20.00	100.00	0.0346	0.00	7.50	2.78
4	slotted	1.50	15.00	12.00	20.00	100.00	0.0346	0.00	7.50	2.23
5	slotted	1.50	7.50	4.00	20.00	100.00	0.0346	0.00	3.75	10.63
6	slotted	1.50	7.50	6.00	20.00	100.00	0.0346	0.00	3.75	8.27
7	slotted	1.50	7.50	8.00	20.00	100.00	0.0346	0.00	3.75	6.77
8	slotted	1.50	7.50	12.00	20.00	100.00	0.0346	0.00	3.75	5.28
9	slotted	1.50	5.00	4.00	20.00	100.00	0.0346	0.00	2.50	17.97
10	slotted	1.50	5.00	6.00	20.00	100.00	0.0346	0.00	2.50	13.89
11	slotted	1.50	5.00	8.00	20.00	100.00	0.0346	0.00	2.50	11.97
12	slotted	1.50	5.00	12.00	20.00	100.00	0.0346	0.00	2.50	10.40
13	slotted	1.50	3.75	4.00	20.00	100.00	0.0346	0.00	1.88	27.16
14	slotted	1.50	3.75	6.00	20.00	100.00	0.0346	0.00	1.88	22.42
15	slotted	1.50	3.75	8.00	20.00	100.00	0.0346	0.00	1.88	20.51
16	slotted	1.50	3.75	12.00	20.00	100.00	0.0346	0.00	1.88	19.11
17	slotted	1.50	3.00	4.00	20.00	100.00	0.0346	0.00	1.50	41.14
18	slotted	1.50	3.00	6.00	20.00	100.00	0.0346	0.00	1.50	36.47
19	slotted	1.50	3.00	8.00	20.00	100.00	0.0346	0.00	1.50	34.85
20	slotted	1.50	3.00	12.00	20.00	100.00	0.0346	0.00	1.50	33.81
21	slotted	1.50	2.50	4.00	20.00	100.00	0.0346	0.00	1.25	64.42
22	slotted	1.50	2.50	6.00	20.00	100.00	0.0346	0.00	1.25	60.59
23	slotted	1.50	2.50	8.00	20.00	100.00	0.0346	0.00	1.25	59.52
24	slotted	1.50	2.50	12.00	20.00	100.00	0.0346	0.00	1.25	59.07
25	slotted	1.50	2.14	4.00	20.00	100.00	0.0346	0.00	1.07	106.30
26	slotted	1.50	2.14	6.00	20.00	100.00	0.0346	0.00	1.07	104.39
27	slotted	1.50	2.14	8.00	20.00	100.00	0.0346	0.00	1.07	104.25
28	slotted	1.50	2.14	12.00	20.00	100.00	0.0346	0.00	1.07	56.03

Appendix C

Derivation of elastic buckling coefficients for unstiffened elements

C.1 k_A for an unstiffened element in compression

The finite strip method is employed with CUFSM (Schafer and Adány 2006) to calculate the plate buckling coefficient for an unstiffened strip in compression, k_A , as a function of unstiffened strip aspect ratio (L_{hole}/h_A) and the compressive stress ratio (ψ_A). The unstiffened element model setup in CUFSM is provided in Figure C.1. The results from the CUFSM parameter study, where ψ_A is varied from 0 to 1, are presented in Figure C.2.

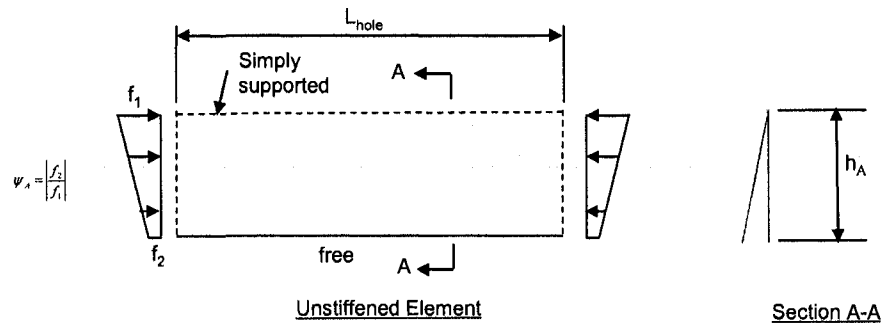


Figure C.1 CUFSM finite strip modeling definition for an unstiffened element in compression

The `fminsearch` function in Matlab (Mathworks 2007) is used to determine the variables α_1 through α_5 in the general equation form:

$$k_A = \frac{0.578}{\psi_A + 0.34} + \frac{\alpha_1 - \alpha_2\psi_A}{\alpha_3\psi_A + \alpha_4 + \left(\frac{L_{hole}}{h_A}\right)^{\alpha_5}}$$

The variables are chosen to minimize the sum of the squared errors between the CUF5M results in Figure C.2 and the fitted curve. The curve fitting results in the equation:

$$k_A = \frac{0.578}{\psi_A + 0.34} + \frac{2.70 - 1.76\psi_A}{0.024\psi_A + 0.035 + \left(\frac{L_{hole}}{h_A}\right)^2}$$

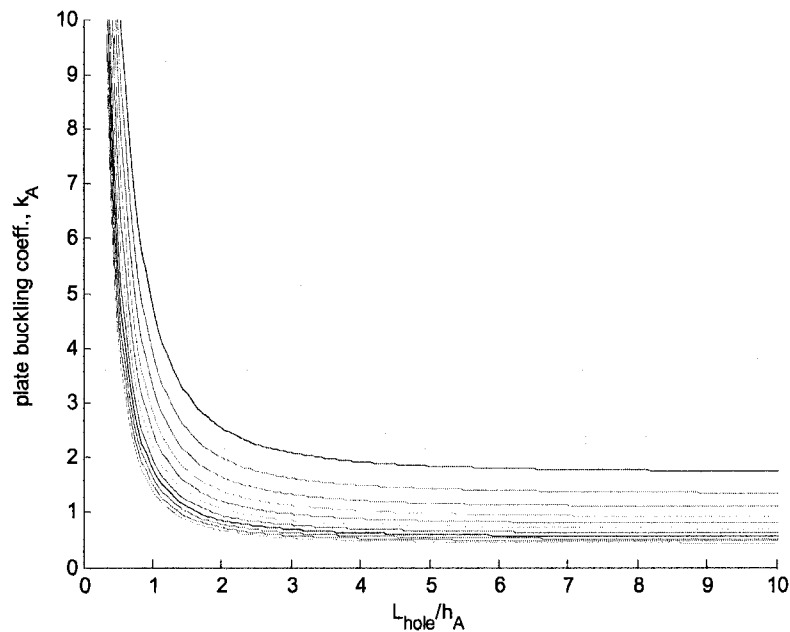


Figure C.2 The plate buckling coefficient k_A for an unstiffened element in compression (the multiple curves represent $0 \leq \psi_A \leq 1$ with a step of 0.1, 11 curves total)

The mean and standard deviation of the ABAQUS to predicted ratio when $0.1 \leq L_{hole}/y_A \leq 2$ is 1.14 and 0.61 respectively. As shown in Figure C.3, the accuracy of the prediction is often conservative within this aspect ratio range. For $2 < L_{hole}/y_A \leq 10$ the mean and standard deviation of the ABAQUS to predicted ratio are 0.99 and 0.02 respectively.

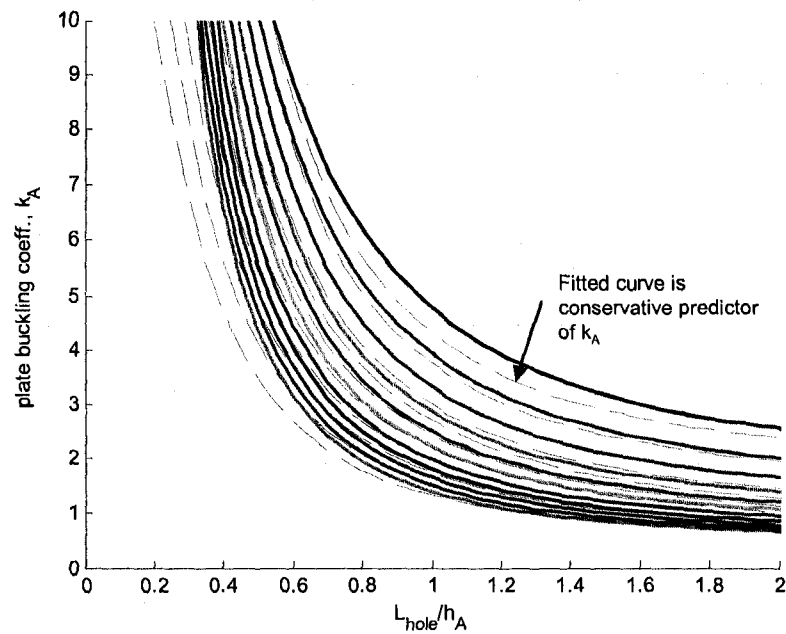


Figure C.3 The fitted curve for k_A is a conservative predictor when $L_{hole}/y_A \leq 2$

C.2 k_B for an unstiffened element with compression on the free edge

The finite strip method is employed with CUFSM (Schafer and Ádány 2006) to calculate the plate buckling coefficient for an unstiffened element with compression on the free edge and tension on the simply supported edge, k_B , as a function of unstiffened strip aspect ratio (L_{hole}/h_B) and the compressive stress ratio (ψ_B). The unstiffened element model setup in CUFSM is provided in Figure C.4.

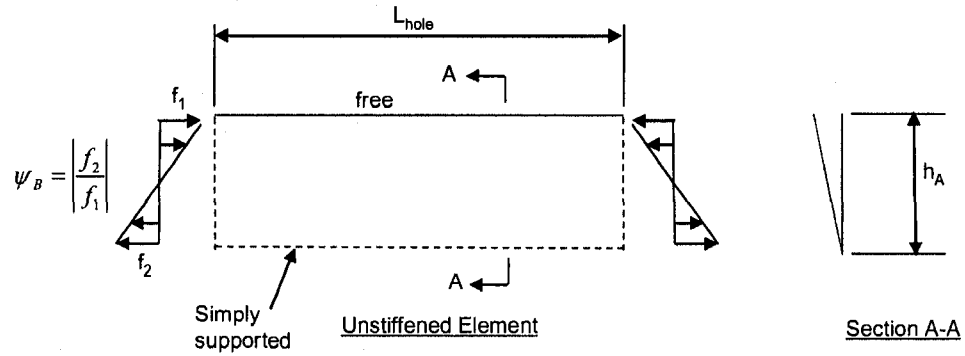


Figure C.4 CUFSM finite strip modeling definition for an unstiffened element with compression on the free edge, tension on the simply-supported edge

The results from the CUFSM parameter study, where ψ_b is varied from 0 to 10, are presented in Figure C.5C.5. As the portion of the plate that is in tension increases (i.e., ψ_b increases), the buckling mode switches from one buckled half-wave to multiple half-waves.

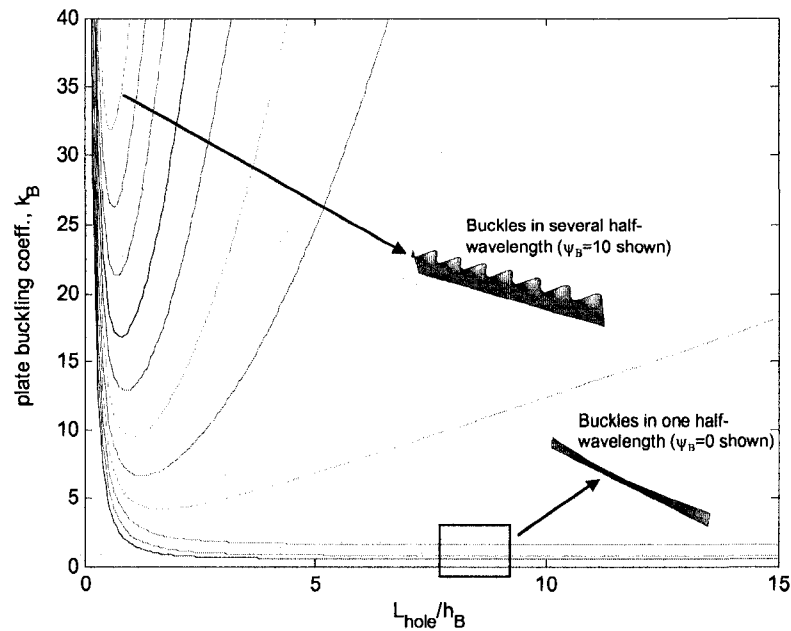


Figure C.5 Variation in plate buckling coefficient k_B for an unstiffened element with ψ_b ranging from 0 to 10

A polynomial curve is fit to the minimum k_B as shown in Figure C.6:

$$k_B = 0.340\psi_B^2 + 0.100\psi_B + 0.573.$$

The mean and standard deviation of the CUFSM minima to fitted curve prediction ratio are 1.03 and 0.11 respectively.

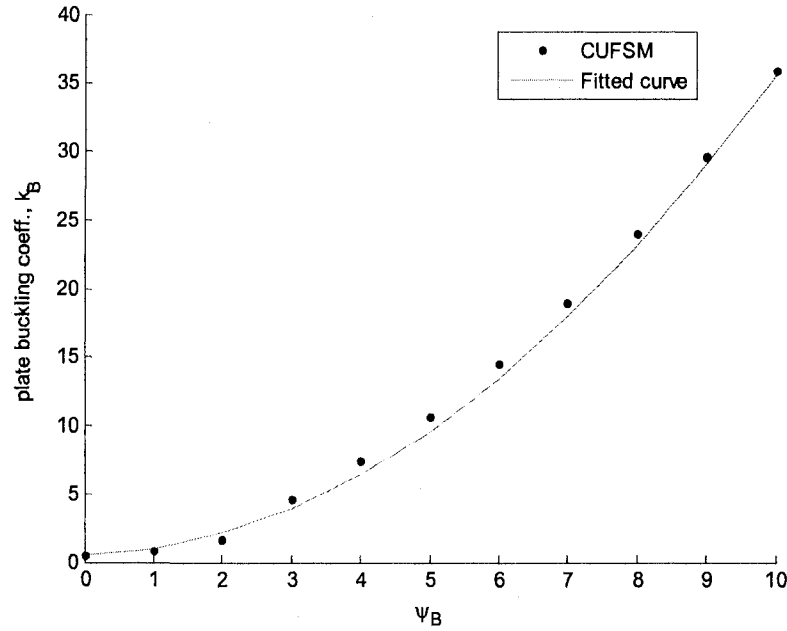


Figure C.6 Curve fit to minimum k_B for ψ_B ranging from 0 to 10

This approximation is accurate when $L_{hole}/y_B > 5$ but does not capture the boost in k_B when L_{hole}/h_B is small. Since L_{hole}/h_B may often be less than 1 when considering common plate and hole sizes, it is important to have a viable estimate of k_B to avoid overly conservative predictions. A family of curves is fit to the CUFSM predictions for the case when $0.25 \leq L_{hole}/y_B \leq 2$ and where ψ_B is varied from 0 to 10, resulting in the following equation:

$$k_B = \frac{0.38\psi_B^{1.8} + 1.6\left(\frac{h_B}{L_{hole}}\right)^2 + 0.49}{-0.20\psi_B^{0.3} + \left(\frac{h_B}{L_{hole}}\right)^{0.1} + 0.14}, \quad 0 \leq \frac{L_{hole}}{h_B} \leq 2, \quad 0 \leq \psi_B \leq 10$$

The equation provides an accurate representation of k_B as demonstrated in Figure C.7.

The mean and standard deviation of the CUFSM to predicted ratio are 0.01 and 0.03 respectively.

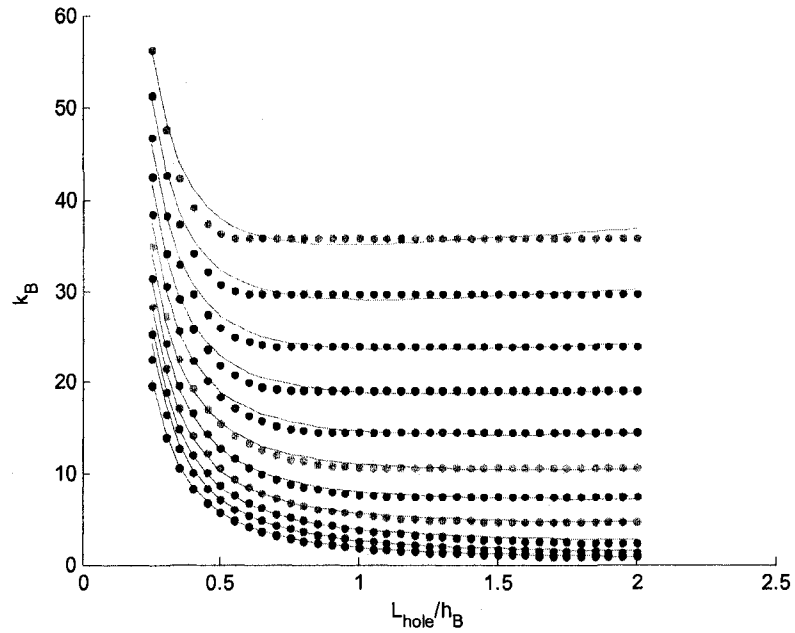


Figure C.7 Family of curves used to simulate boost in k_B when $L_{hole}/h_B \leq 2$, ψ_B ranges from 0 to 10

Appendix D

Elastic buckling prediction method of cross-sectional elements with holes

B1 Critical Elastic Buckling Stress of Elements with Perforations

B1.1 Uniformly Compressed Stiffened Element

For uniformly compressed stiffened elements with uniformly spaced perforations satisfying the limits

$$\frac{S}{h} \geq 1.5 \text{ and } \frac{S}{L_{\text{hole}}} \geq 2,$$

the critical elastic buckling stress, $f_{\text{cr}\ell}$, is

$$f_{\text{cr}\ell} = \min[f_{\text{cr}}, f_{\text{crh}}]. \quad (\text{Eq. B1.1-1})$$

The critical elastic buckling stress, f_{cr} , without the influence of perforations is

$$f_{\text{cr}} = k \frac{\pi^2 E}{12(1-\mu^2)} \left(\frac{t}{h} \right)^2, \quad (\text{Eq. B1.1-2})$$

where $k=4$ for a stiffened element with $L/h > 4$.

The critical elastic buckling stress, f_{crh} , with the influence of perforations is

$$f_{\text{crh}} = f_{\text{crh,net}} (1 - h_{\text{hole}}/h), \quad (\text{Eq. B1.1-3})$$

where the critical elastic buckling stress, $f_{\text{crh,net}}$, at the location of a perforation is

$$f_{\text{crh,net}} = \min[f_{\text{crA}}, f_{\text{crB}}]. \quad (\text{Eq. B1.1-4})$$

The critical elastic buckling stress, f_{cri} , of unstiffened strip i is

$$f_{\text{cri}} = k_i \frac{\pi^2 E}{12(1-\nu^2)} \left(\frac{t}{h_i} \right)^2 \text{ and } i = \text{A or B}, \quad (\text{Eq. B1.1-5})$$

where

$$L_{\text{hole}}/h_i \geq 1, \quad k_i = 0.425 + \frac{0.2}{(L_{\text{hole}}/h_i)^{0.95} - 0.6} \quad (\text{Eq. B1.1-6})$$

$$L_{\text{hole}}/h_i < 1, k_i = 0.925, \text{ and } i = A \text{ or } B. \quad (\text{Eq. B1.1-7})$$

B1.2 Stiffened Element Under Stress Gradient

For stiffened elements under a stress gradient with uniformly spaced perforations satisfying the limits

$$\frac{S}{h} \geq 1.5 \text{ and } \frac{S}{L_{\text{hole}}} \geq 2,$$

the critical elastic buckling stress, $f_{\text{cr}\ell}$, is

$$f_{\text{cr}\ell} = \min[f_{\text{cr}}, f_{\text{cr}h}]. \quad (\text{Eq. B1.2-1})$$

The critical elastic buckling stress, f_{cr} , without the influence of perforations is

$$f_{\text{cr}} = k \frac{\pi^2 E}{12(1-\mu^2)} \left(\frac{t}{h} \right)^2, \quad (\text{Eq. B1.2-2})$$

where

$$k = 4 + 2(1+\psi)^3 + 2(1+\psi) \quad (\text{Eq. B1.2-3})$$

and

$$\psi = |f_2/f_1| = (h-Y)/Y. \quad (\text{Eq. B1.2-4})$$

The critical elastic buckling stress, $f_{\text{cr}h}$, with the influence of perforations is

$$\text{for } h_A + h_{\text{hole}} \geq Y, f_{\text{cr}h} = f_{\text{cr}h,\text{net}} (1 + \psi_A) \frac{h_A}{Y}, \text{ and} \quad (\text{Eq. B1.2-5})$$

$$\text{for } h_A + h_{\text{hole}} < Y, f_{\text{cr}h} = f_{\text{cr}h,\text{net}} \left[1 - \frac{h_{\text{hole}}}{Y} \left(2\psi_A - \frac{h_{\text{hole}}}{Y} \right) \right], \quad (\text{Eq. B1.2-6})$$

where

$$\psi_A = \frac{Y - h_A}{Y}. \quad \text{Eq. (B1.2-7)}$$

The critical elastic buckling stress, $f_{\text{cr}h,\text{net}}$, at the location of a perforation is

$$f_{\text{cr}h,\text{net}} = \min[f_{\text{cr}A}, f_{\text{cr}B}] \quad (\text{Eq. B1.2-8})$$

Consideration of unstiffened strip "A" buckling is required only if $h_A < Y$,

$$f_{\text{cr}A} = k_A \frac{\pi^2 E}{12(1-\nu^2)} \left(\frac{t}{h_A} \right)^2 \quad (\text{Eq. B1.2-9})$$

where

$$k_A = \frac{0.578}{\psi_A + 0.34} + \frac{2.70 - 1.76\psi_A}{0.024\psi_A + 0.035 + (L_{\text{hole}}/h_A)^2} \quad (\text{Eq. B1.2-10})$$

Consideration of unstiffened strip "B" buckling is required only if $h_A + h_{\text{hole}} < Y$,

$$f_{\text{crB}} = k_B \frac{\pi^2 E}{12(1-\nu^2)} \left(\frac{t}{h_B} \right)^2 \left(\frac{Y}{Y - h_A - h_{\text{hole}}} \right), \quad (\text{Eq. B1.2-12})$$

where

for $L_{\text{hole}}/h_B > 2$

$$k_B = 0.340\psi_B^2 + 0.100\psi_B + 0.573, \quad (\text{Eq. B1.2-12})$$

for $L_{\text{hole}}/h_B \leq 2$

$$k_B = \frac{0.38\psi_B^{1.8} + 1.6 \left(\frac{h_B}{L_{\text{hole}}} \right)^2 + 0.49}{-0.20\psi_B^{0.3} + \left(\frac{h_B}{L_{\text{hole}}} \right)^{0.1} + 0.14} \quad (\text{Eq. B1.2-13})$$

and

$$\psi_B = \frac{h - Y}{Y - h_A - h_{\text{hole}}}, \quad 0 \leq \psi_B \leq 10. \quad (\text{Eq. B1.2-14})$$

B1.3 Unstiffened Element Under Uniform Compression with Perforations

For uniformly compressed unstiffened elements with uniformly spaced perforations satisfying the limits

$$\frac{L_{\text{hole}}}{h_A} \leq 10, \frac{L_{\text{hole}}}{h_B} \leq 10, \frac{h_{\text{hole}}}{h} \leq 0.50, \text{ and } \frac{S}{L_{\text{hole}}} \geq 2 \quad (\text{Eq. B1.3-1})$$

the critical elastic buckling stress, $f_{\text{cr}\ell}$, is

$$f_{\text{cr}\ell} = \min[f_{\text{cr}}, f_{\text{crh}}]. \quad (\text{Eq. B1.3-2})$$

The critical elastic buckling stress, f_{cr} , without the influence of perforations is

$$f_{\text{cr}} = k \frac{\pi^2 E}{12(1-\mu^2)} \left(\frac{t}{h}\right)^2, \quad (\text{Eq. B1.3-3})$$

where $k=0.425$ for unstiffened elements with $L/h > 4$.

The critical elastic buckling stress, f_{crh} , with the influence of perforations is

$$f_{\text{crh}} = \min \left[k \frac{\pi^2 E}{12(1-\nu^2)} \left(\frac{t}{h}\right)^2, f_{\text{crA}} \left(1 - \frac{h_{\text{hole}}}{h}\right) \right], \quad (\text{Eq. B1.3-4})$$

where

$$k = 0.425 \left(1 - 0.062 \frac{L_{\text{hole}}}{h_A}\right) \quad (\text{Eq. B1.3-5})$$

and f_{crA} is calculated with Eq. B1.1-5.

Appendix E

Derivation of global critical elastic buckling load for a column with holes

This derivation develops the equation for the flexural critical elastic buckling load of a column with two holes spaced symmetrically about the longitudinal midline of a column. The conclusions of this derivation are used as the foundation for the “weighted properties” approach for approximating P_{cre} for columns and beams with holes as described in Section 4.2.7.3.1.1. I_{NH} is the moment of inertia of the column cross section away from the hole and I_H is the moment of inertia at the hole.

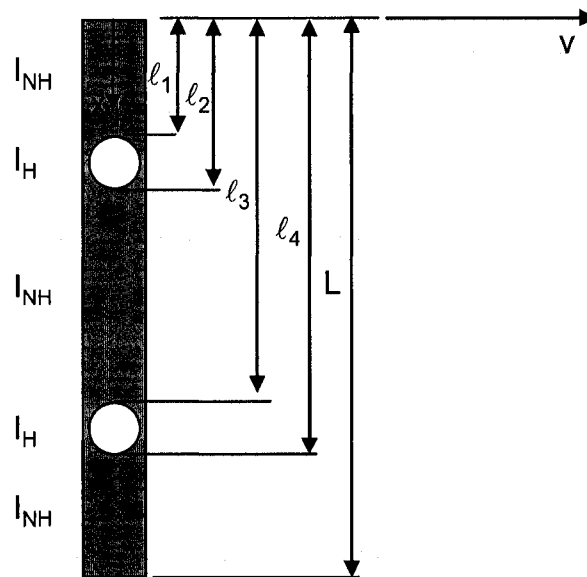


Figure E.1 Long column with two holes spaced symmetrically about the longitudinal midline.

A conservation of energy approach is employed in this derivation, and specifically the Rayleigh-Ritz Method. The derivation is founded on the fundamental principle relating the strain energy and potential energy of the column, U and W respectively:

$$\delta\Pi = \delta(U - W) = 0$$

where the column strain energy U is:

$$U = \frac{1}{2} \int EI \left(\frac{d^2 v}{dx^2} \right)^2 dx$$

and the column potential energy is

$$W = \frac{1}{2} P \int \left(\frac{dv}{dx} \right)^2 dx.$$

Applying the Raleigh-Ritz method, we assume a shape function in the deformed (buckled) configuration of the column:

$$v(x) = \alpha \sin \frac{\pi x}{L}$$

The derivatives of this function are calculated:

$$\begin{aligned} \frac{dv}{dx} &= \alpha \frac{\pi}{L} \cos \frac{\pi x}{L} \\ \frac{d^2 v}{dx^2} &= -\alpha \frac{\pi^2}{L^2} \sin \frac{\pi x}{L} \end{aligned}$$

and then substituted into the equations for U and W which are written along the length of the column as:

$$\begin{aligned} U &= \frac{EI_{NH}}{2} \int_0^L \frac{\alpha^2 \pi^4}{L^4} \sin^2 \left(\frac{\pi x}{L} \right) dx + \frac{EI_H}{2} \int_1^2 \frac{\alpha^2 \pi^4}{L^4} \sin^2 \left(\frac{\pi x}{L} \right) dx + \frac{EI_{NH}}{2} \int_2^3 \frac{\alpha^2 \pi^4}{L^4} \sin^2 \left(\frac{\pi x}{L} \right) dx \\ &+ \frac{EI_H}{2} \int_3^4 \frac{\alpha^2 \pi^4}{L^4} \sin^2 \left(\frac{\pi x}{L} \right) dx + \frac{EI_H}{2} \int_4^L \frac{\alpha^2 \pi^4}{L^4} \sin^2 \left(\frac{\pi x}{L} \right) dx \end{aligned}$$

and

$$W = \frac{1}{2} P \int_0^L \frac{\alpha^2 \pi^2}{L^2} \cos^2 \left(\frac{\pi x}{L} \right) dx = \frac{P \alpha^2 \pi^2}{4L}.$$

The derivative of U is taken with respect to the arbitrary shape function amplitude α :

$$\frac{dU}{d\delta} = \frac{EI_{NH}\alpha\pi^4}{L^4} \left[\int_0^{\ell_1} \sin^2\left(\frac{\pi x}{L}\right) dx + \int_{\ell_2}^{\ell_3} \sin^2\left(\frac{\pi x}{L}\right) dx + \int_{\ell_4}^L \sin^2\left(\frac{\pi x}{L}\right) dx \right] \\ + \frac{EI_H\alpha\pi^4}{L^4} \left[\int_{\ell_1}^{\ell_2} \sin^2\left(\frac{\pi x}{L}\right) dx + \int_{\ell_3}^{\ell_4} \sin^2\left(\frac{\pi x}{L}\right) dx \right]$$

The definite integrals inside the derivative are then solved resulting in:

$$\frac{dU}{d\delta} = \frac{EI_{NH}\alpha\pi^4}{L^4} \left[\left(\frac{\ell_1}{2} + \frac{\ell_3}{2} - \frac{\ell_2}{2} + \frac{L}{2} - \frac{\ell_4}{2} \right) + \frac{L}{4\pi} \left(-\sin \frac{2\pi\ell_1}{L} - \sin \frac{2\pi\ell_3}{L} + \sin \frac{2\pi\ell_2}{L} + \sin \frac{2\pi\ell_4}{L} \right) \right] \\ + \frac{EI_H\alpha\pi^4}{L^4} \left[\frac{L_H}{2} + \frac{L}{4\pi} \left(-\sin \frac{2\pi\ell_2}{L} + \sin \frac{2\pi\ell_1}{L} - \sin \frac{2\pi\ell_4}{L} + \sin \frac{2\pi\ell_3}{L} \right) \right]$$

The length terms from the integration sum to the length of column without a hole, L_{NH} , and the length of column with a hole, L_H . When the holes are symmetric about the longitudinal midline of the column, the trigonometric terms cancel as shown in Figure E.2 and the equation above simplifies to:

$$\frac{dU}{d\alpha} = \frac{EI_{NH}\alpha\pi^4}{L^4} \frac{L_{NH}}{2} + \frac{EI_{NH}\alpha\pi^4}{L^4} \frac{L_H}{2}$$

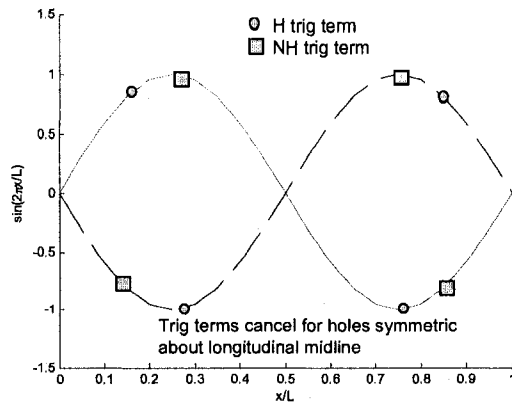


Figure E.2 Trigonometric terms in energy solution cancel when holes are symmetric about longitudinal midline of column.

The solution for the potential energy of the column is not dependent upon the moment of inertia and therefore the derivative can be solved directly as:

$$\frac{dW}{d\alpha} = \frac{P\alpha \pi^2}{2L}$$

The load P that minimizes the variation in energy is the critical elastic buckling load, P_{cre} :

$$\delta\Pi = \delta(U - W) = \frac{dU}{d\alpha} - \frac{dW}{d\alpha} = 0$$

Equating the variational energy terms:

$$\frac{EI_{NH}\alpha\pi^4}{L^4} \frac{L_{NH}}{2} + \frac{EI_H\alpha\pi^4}{L^4} \frac{L_H}{2} - \frac{P\alpha \pi^2}{2L} = 0$$

results in a solution for P_{cre} where the moment of inertia is a weighted average of the net and gross cross-section of the column.

$$P_{cre} = \frac{\pi^2 E}{L^2} \left(\frac{I_{NH}L_{NH} + I_H L_H}{L} \right)$$

P_{cre} for a column with the general case of $i=1..n$ holes can be approximated as:

$$P_{cre} = \frac{\pi^2 E}{L^2} \left(\frac{I_{NH}(L_{NH} + T_{NH}) + I_H(L_H + T_H)}{L} \right),$$

where

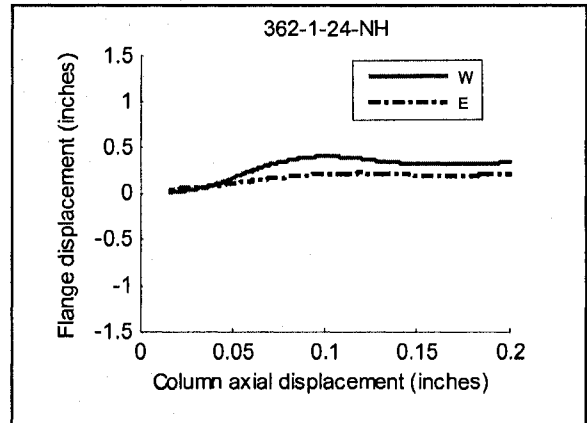
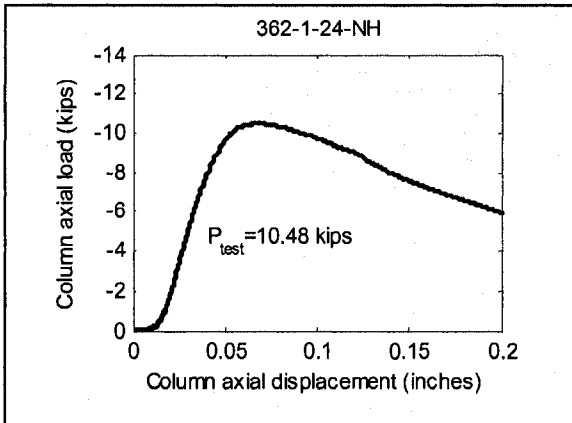
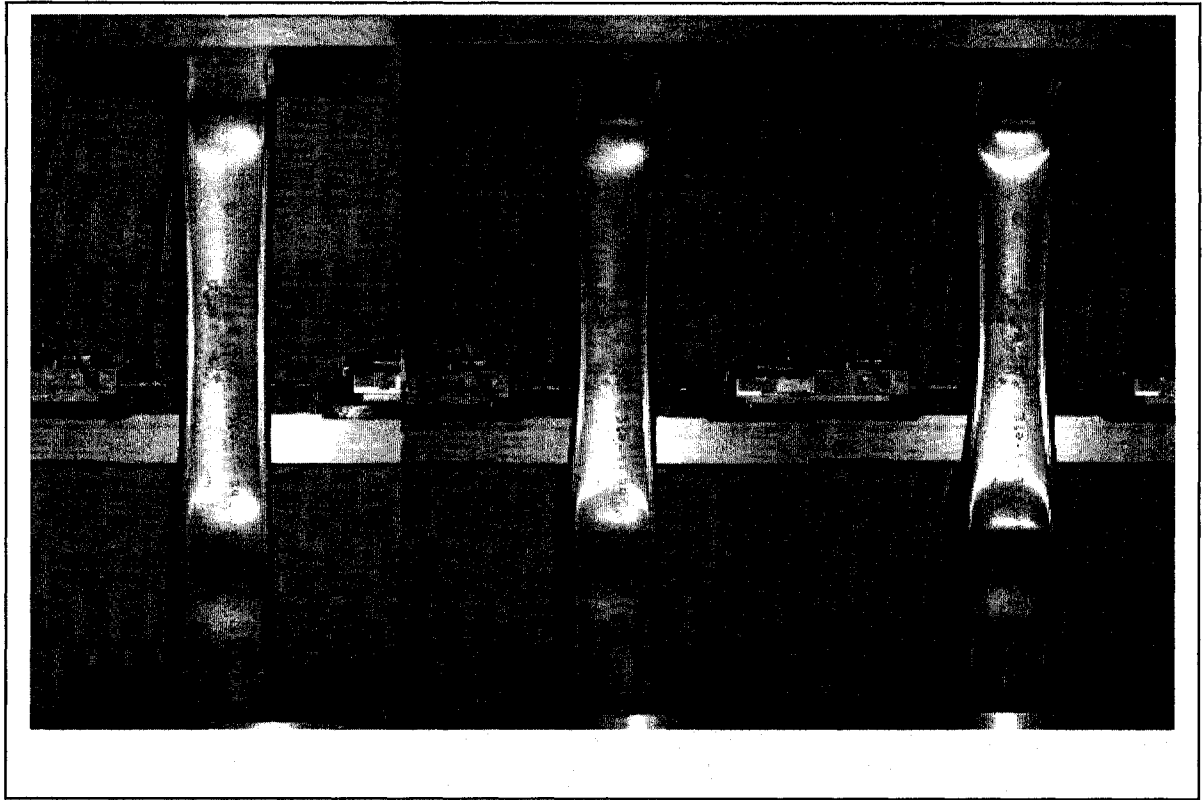
$$T_{NH} = \frac{L}{2\pi} \sum_{i=1}^n \cos\left(\frac{2\pi L_{c,i}}{L}\right) \sin\left(\frac{\pi L_{hole,i}}{L}\right), \quad T_H = -\frac{L}{2\pi} \sum_{i=1}^n \cos\left(\frac{2\pi L_{c,i}}{L}\right) \sin\left(\frac{\pi L_{hole,i}}{L}\right).$$

$L_{c,i}$ is the distance from the end of the column to the centerline of hole i and $L_{hole,i}$ is the length of hole i .

Appendix F

Column experiment results

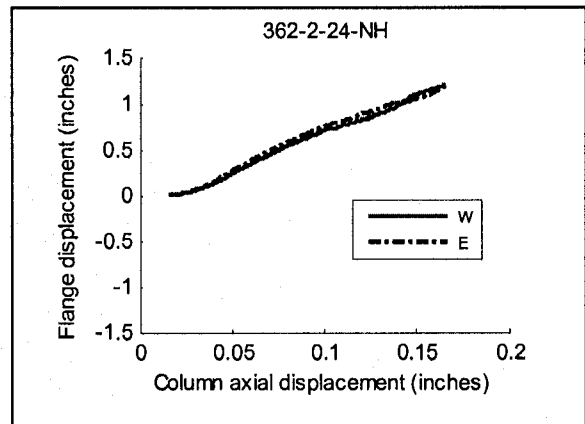
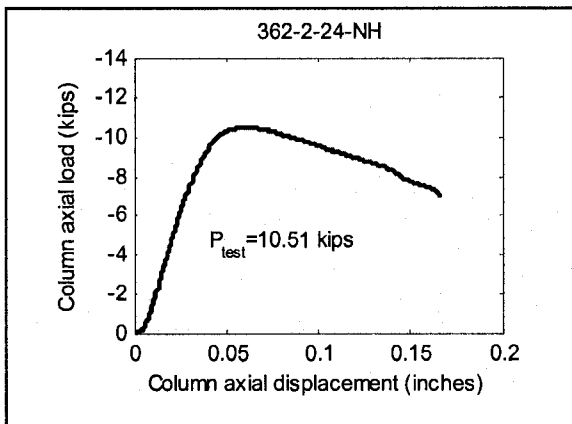
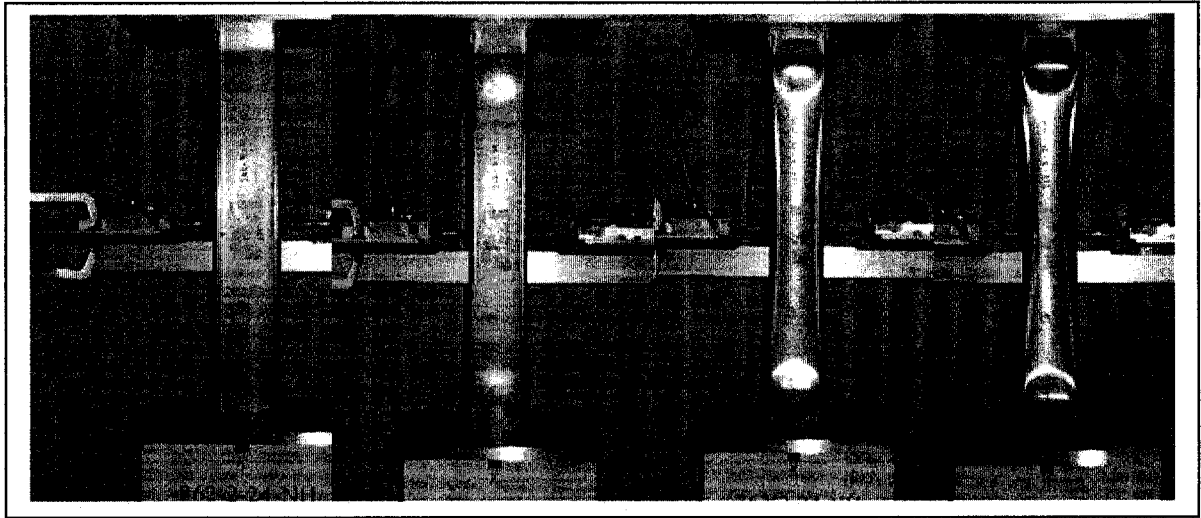
Column Specimen 362-1-24-NH



Notes:

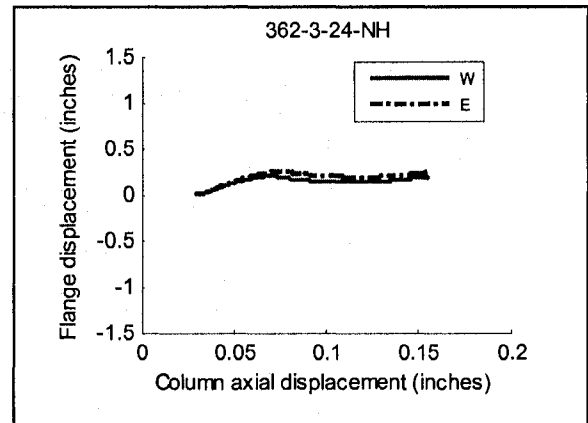
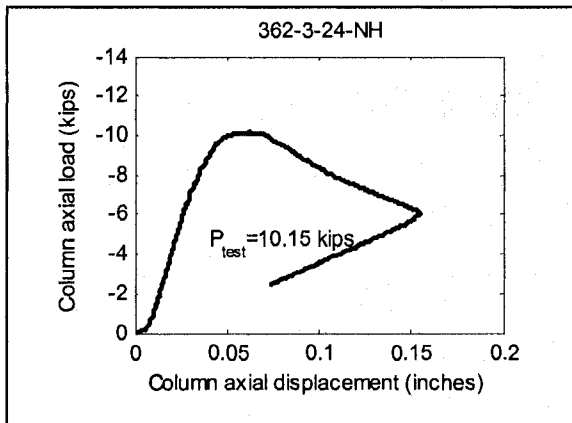
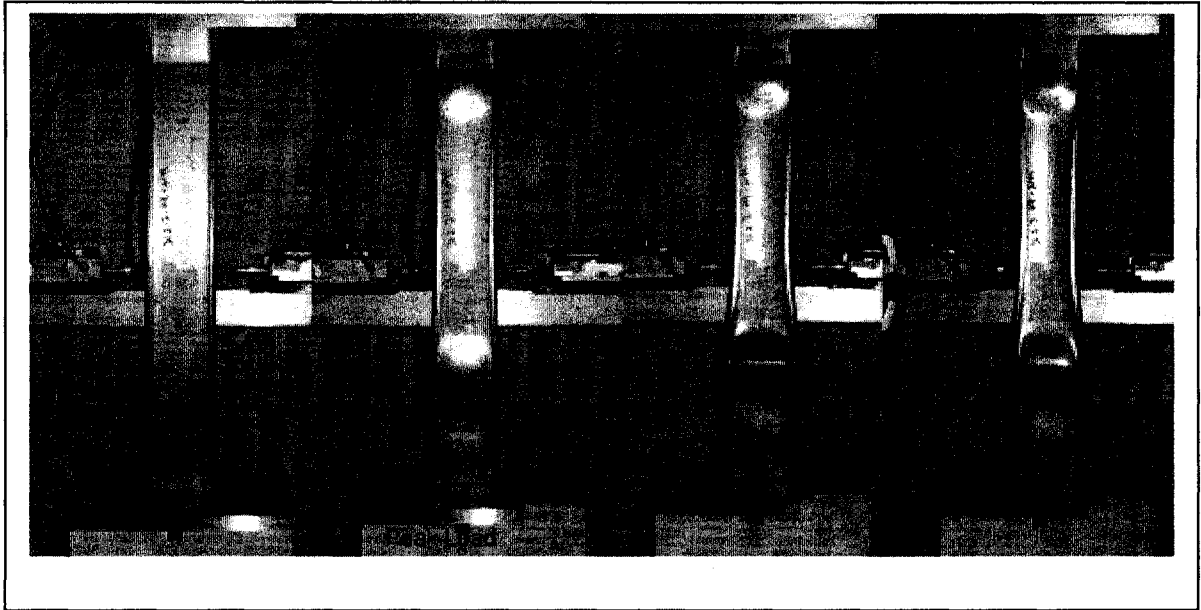
Loaded N to S instead of S to N. Adjusted all geometry measurements.
Lips rotated and not touching bottom platen after peak load.

Column Specimen 362-2-24-NH



Notes:

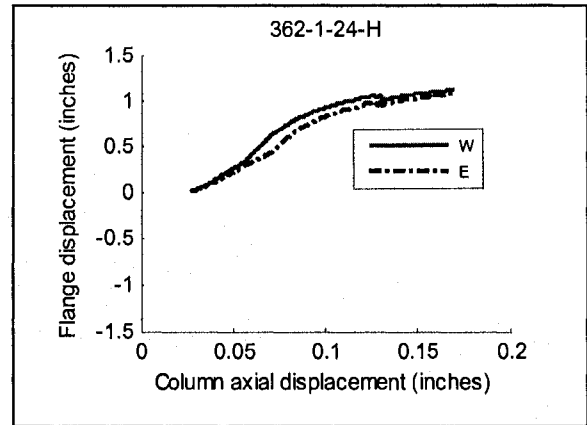
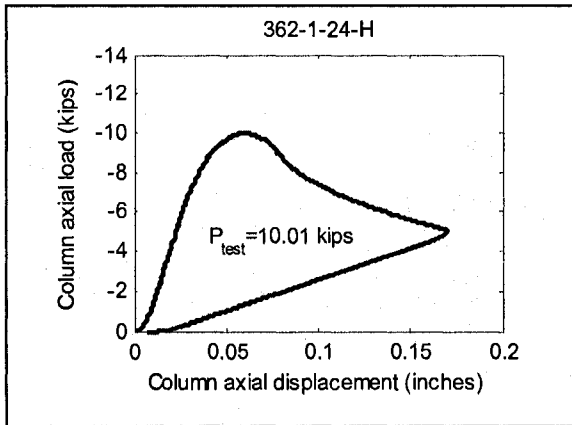
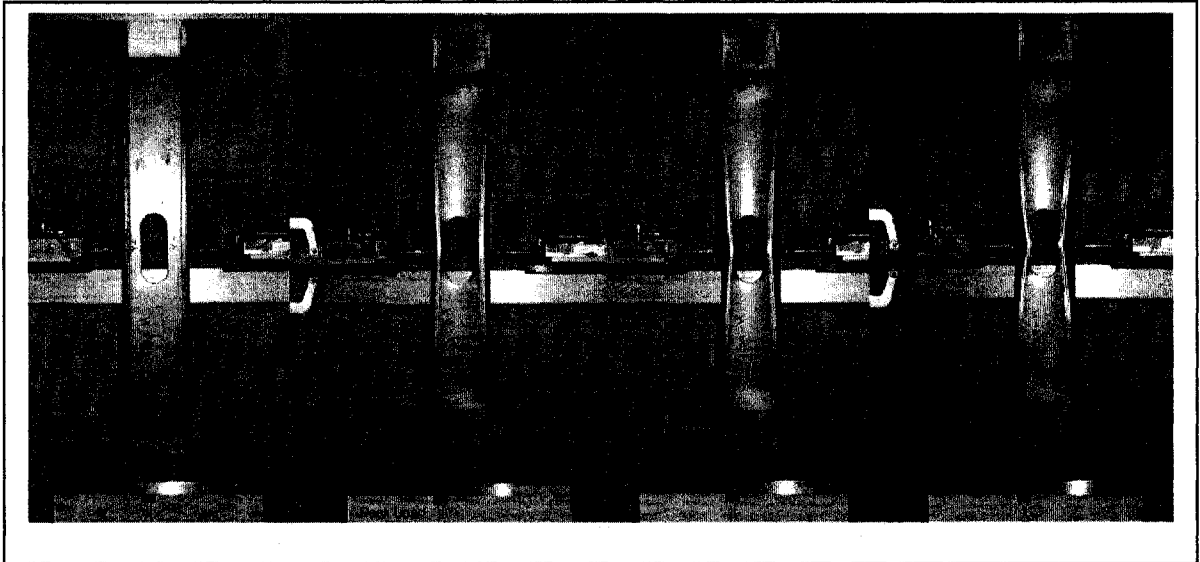
Column Specimen 362-3-24-NH



Notes:

Bottom lips rotated at 7 kips post-peak and are not bearing on platen.

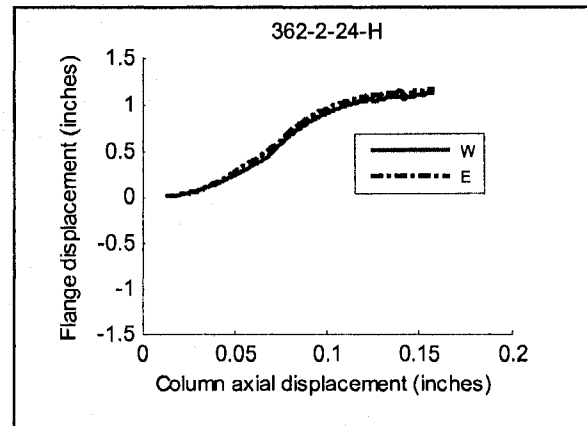
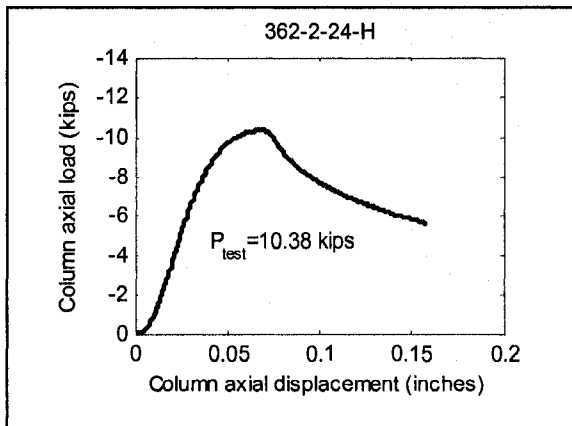
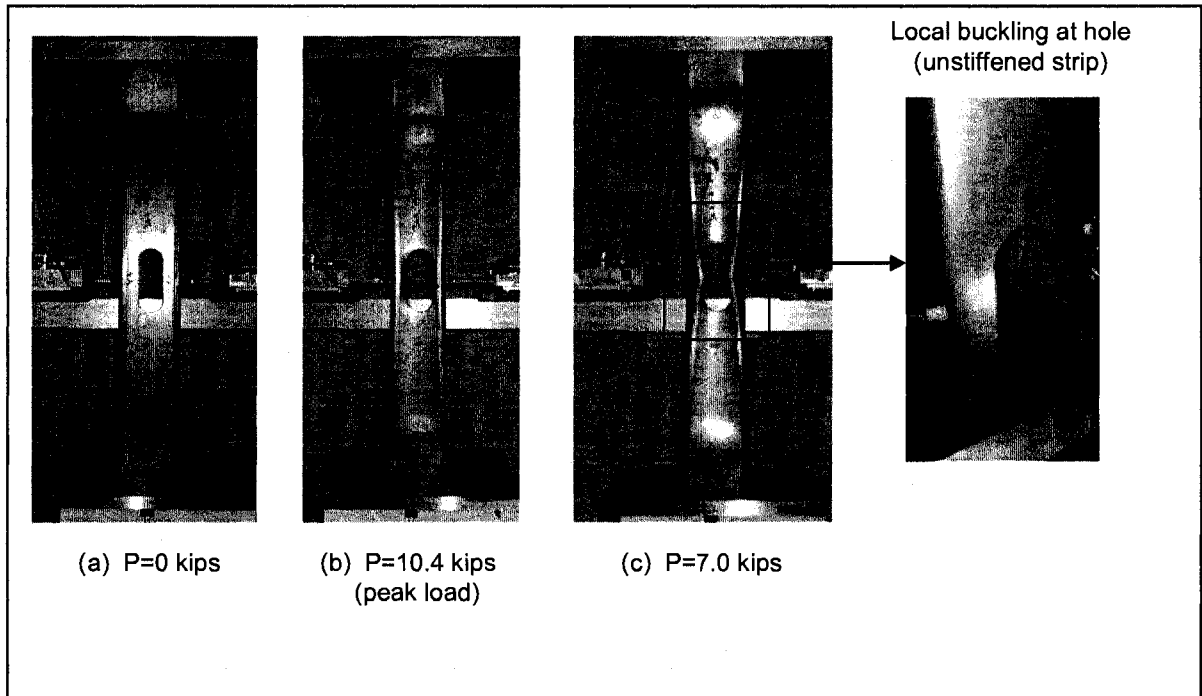
Column Specimen 362-1-24-H



Notes:

Visible buckling of web on either side of hole at 7 kips.

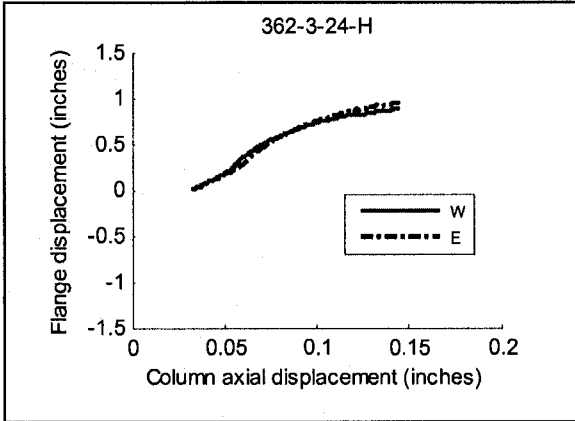
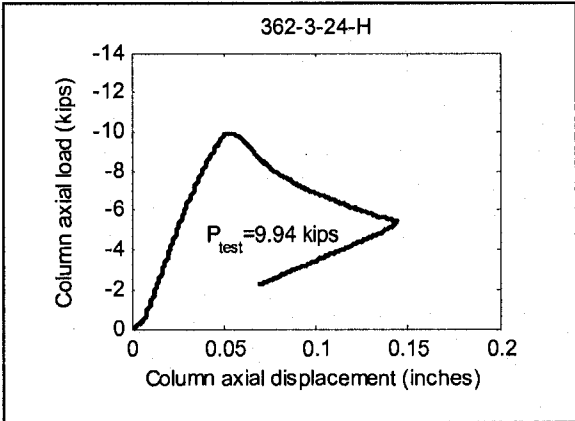
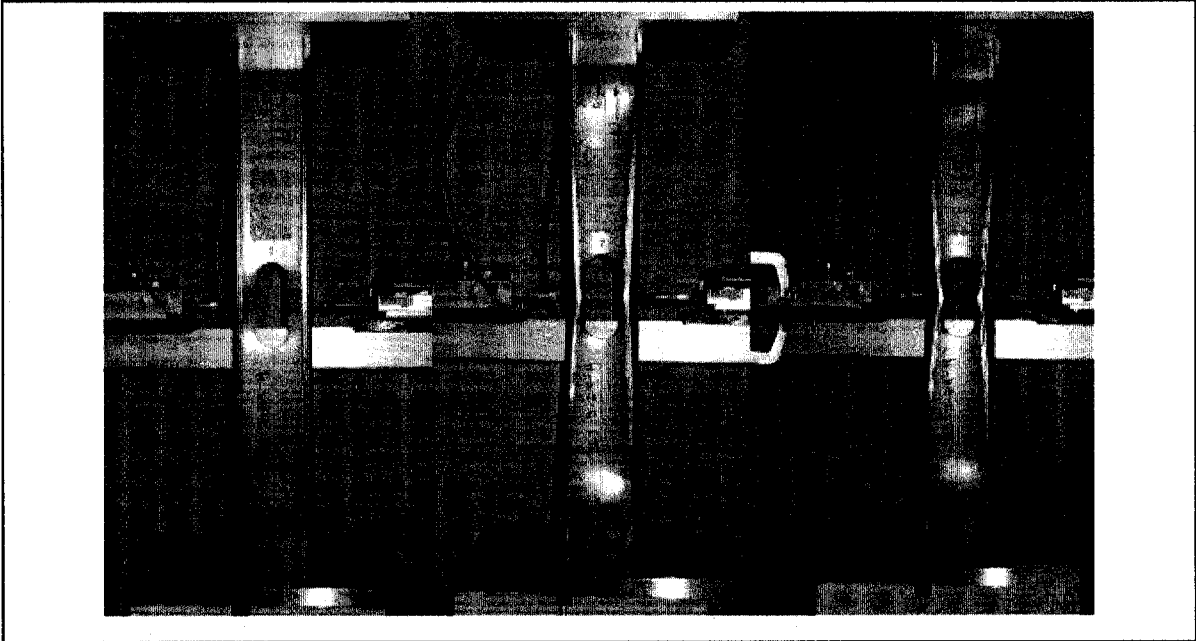
Column Specimen 362-2-24-H



Notes:

Visible buckling of web on either side of hole at 5 kips.

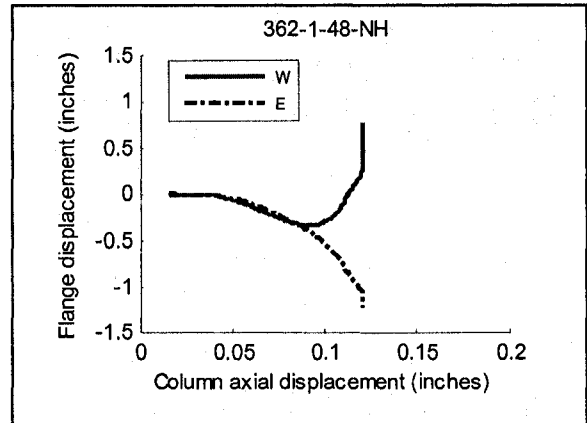
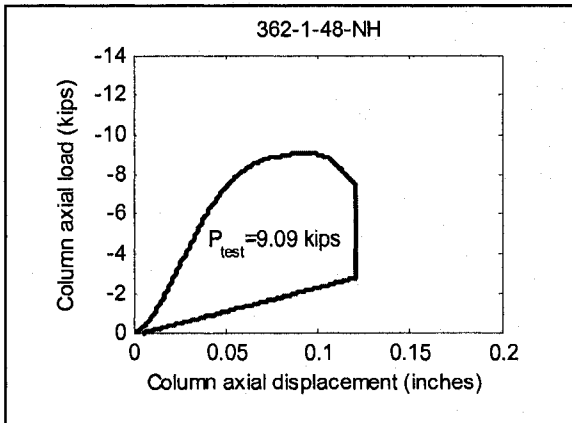
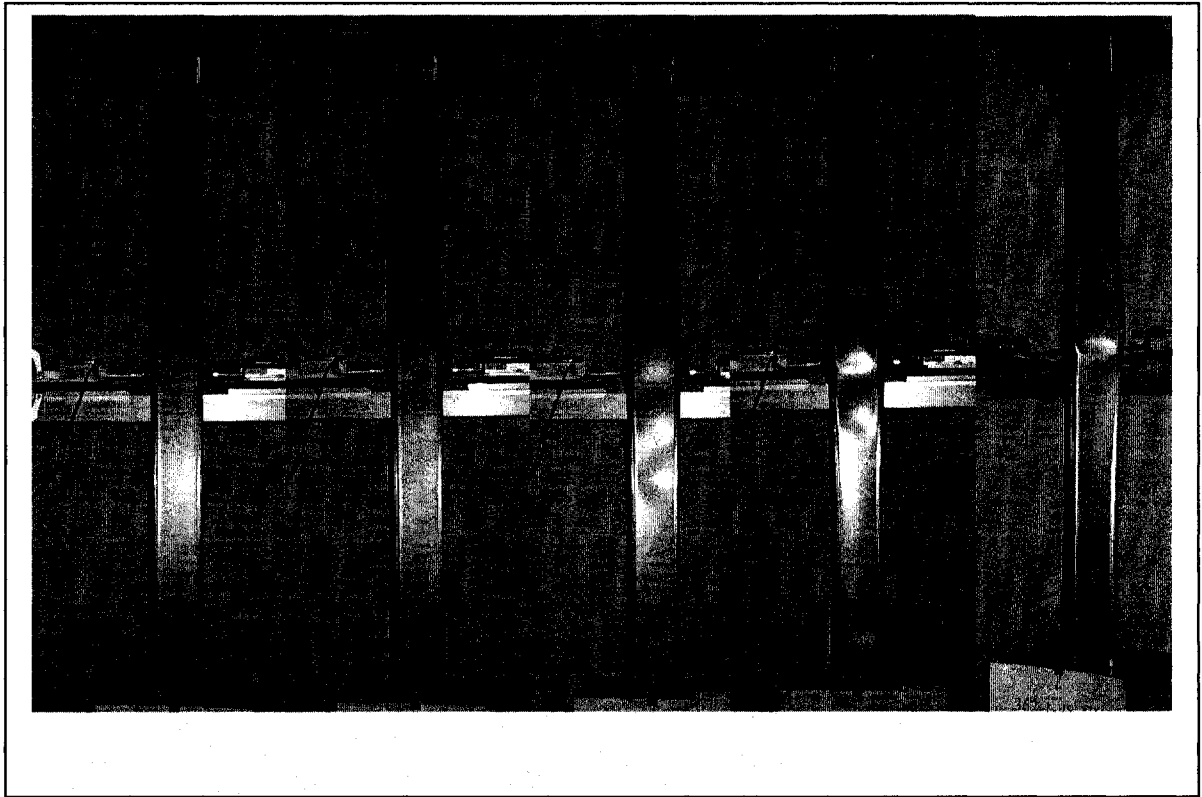
Column Specimen 362-3-24-H



Notes:

Accidental preload to 3 kips when adjusting specimen for test.

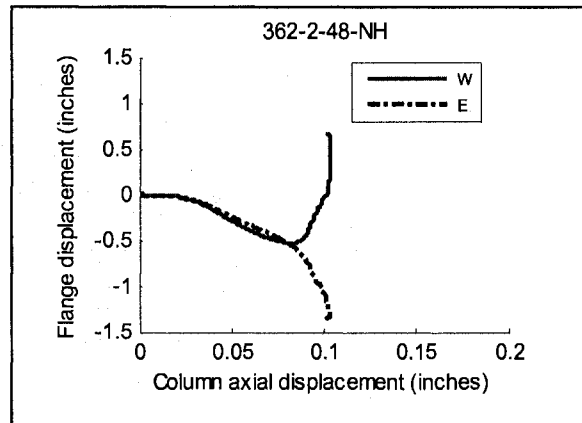
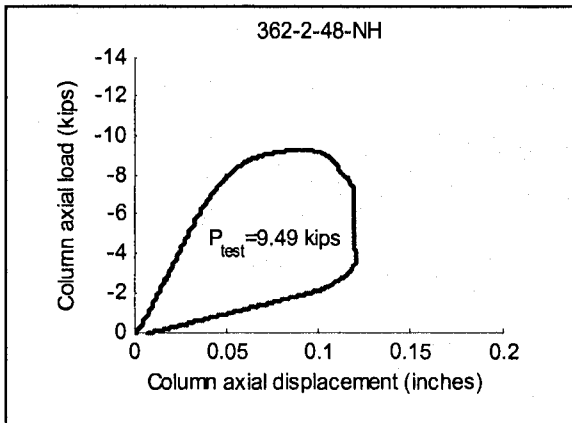
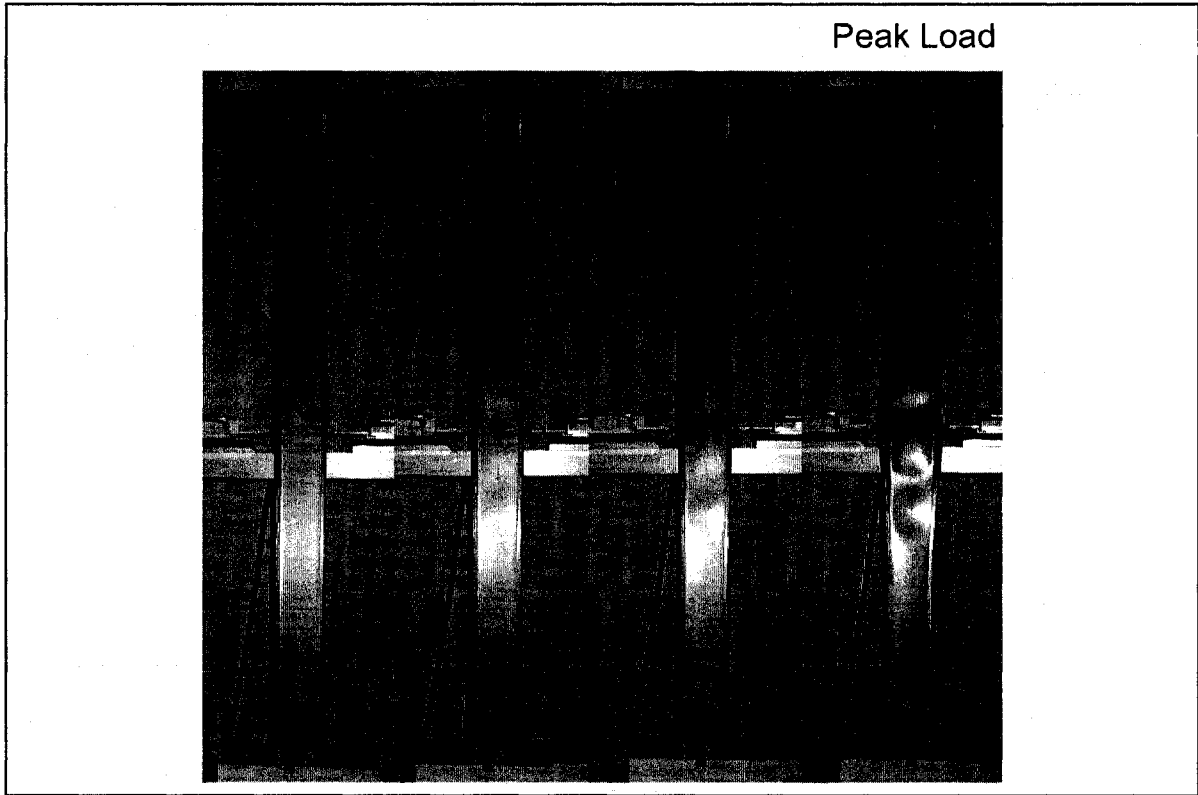
Column Specimen 362-1-48-NH



Notes:

Good end conditions – no visible gaps.
9 kips – a metallic noise – yielding of west flange and increase in local wavelengths.
Column failed by global-torsional collapse.

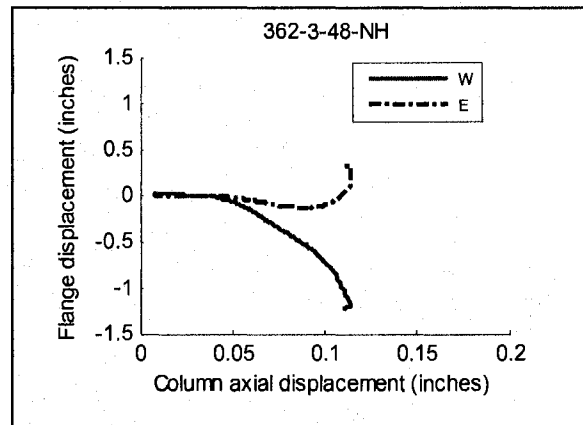
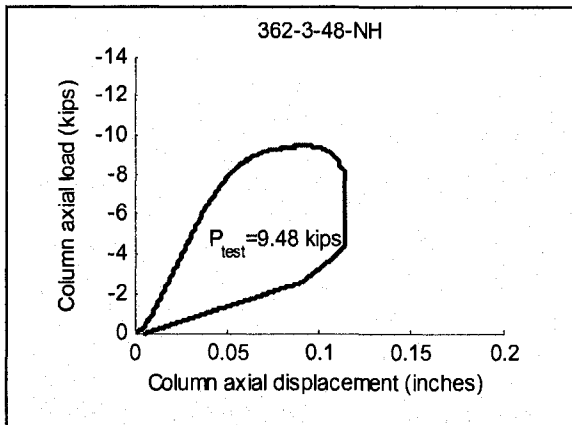
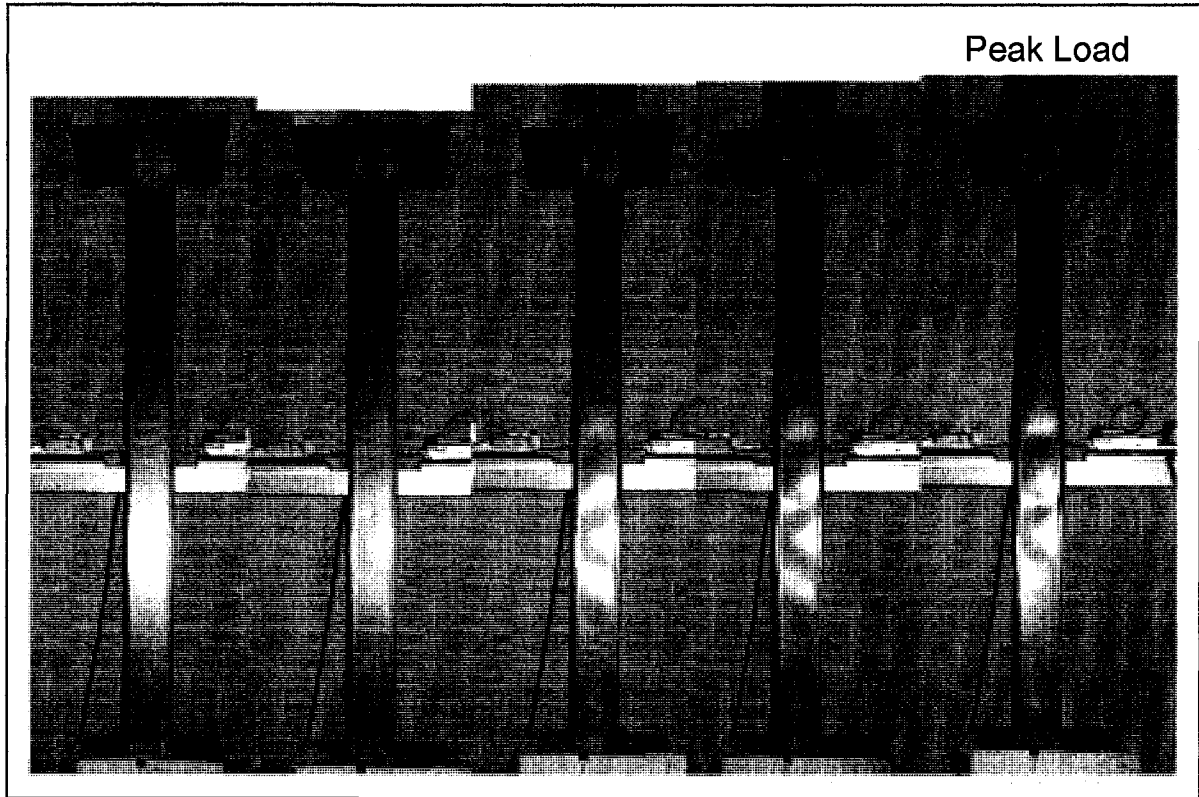
Column Specimen 362-2-48-NH



Notes:

Tight end conditions at 1.5 kips.
Local buckling at 6.5 kips .
No sounds for this test.
Column failed by global-torsional collapse.

Column Specimen 362-3-48-NH

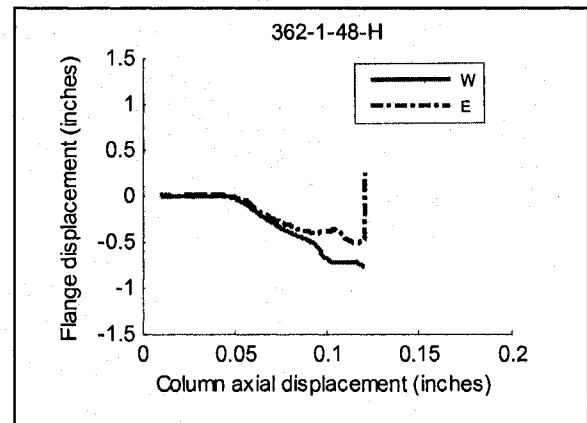
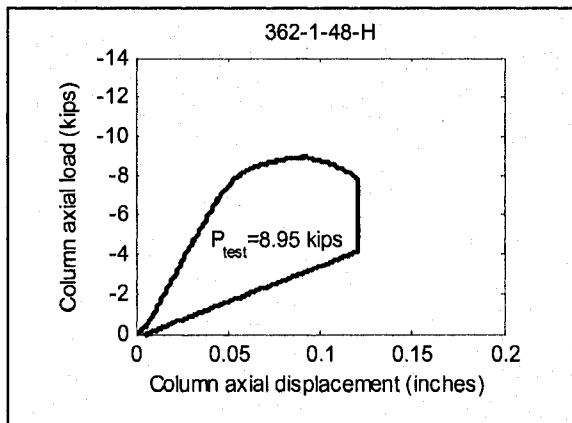
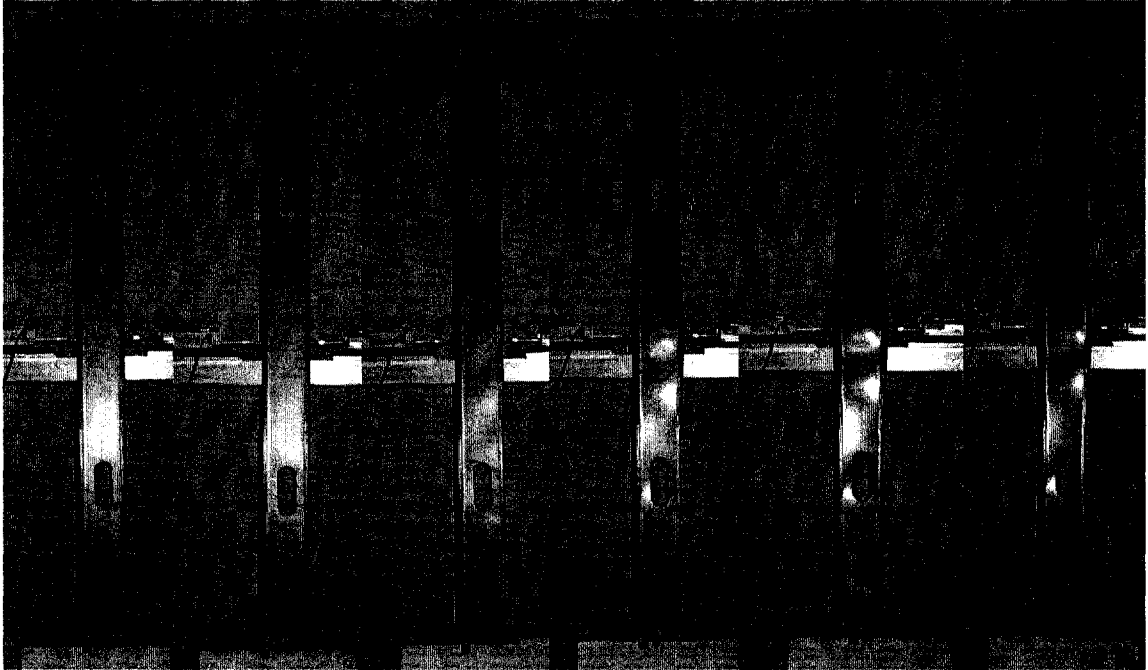


Notes:

Local buckling first observed at 6.5 kips.
Local wavelengths lengthen at 8.5 kips.
Yielding of flange lips at 9 kips (near peak).
Column failed by global-torsional collapse.

Column Specimen 362-1-48-H

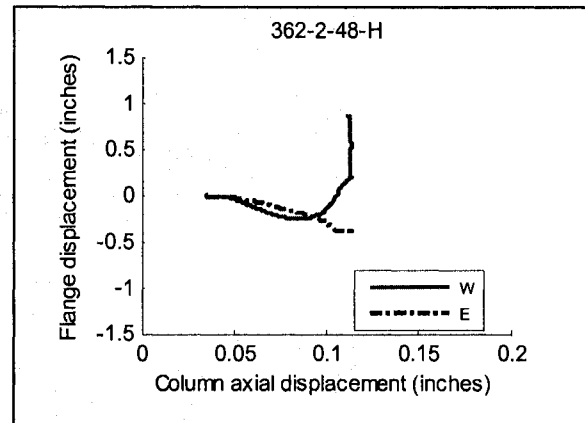
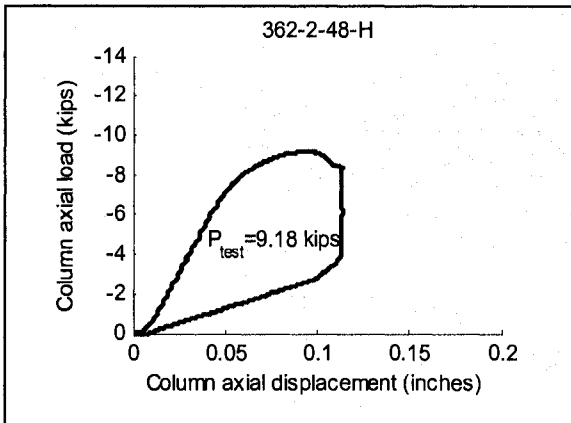
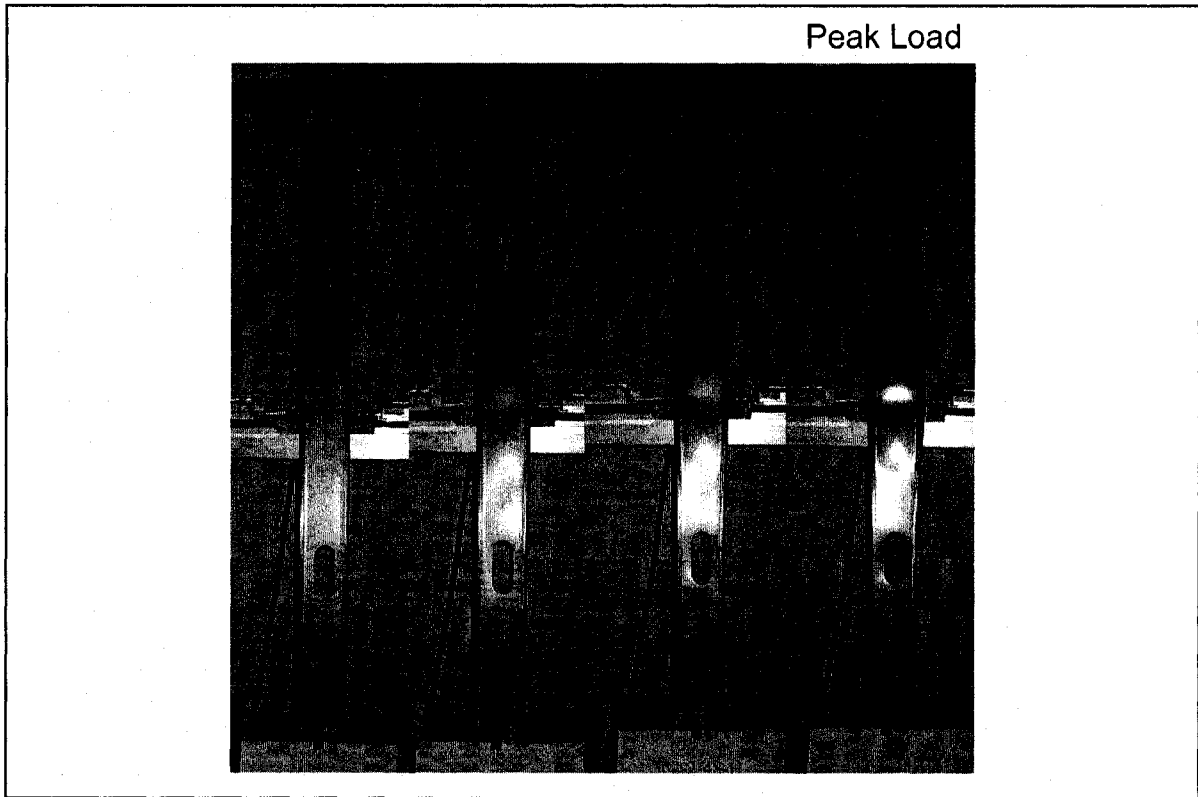
Peak Load



Notes:

- No visible gaps and ends under 1 kip.
- Local buckling is visible at 7 kips.
- Local half-waves merge at 8.5 kips.
- Bulging of web at hole occurs near peak load.
- Column failed by global-torsional collapse.

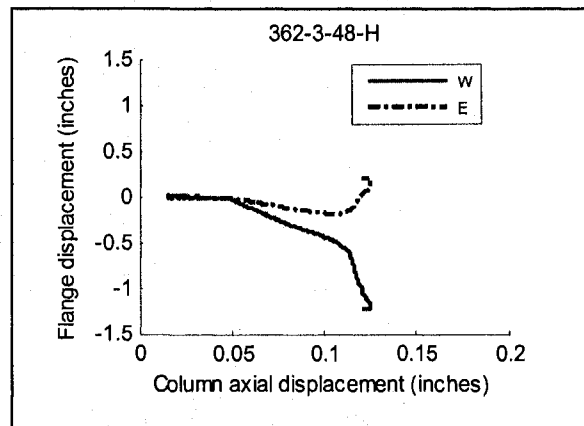
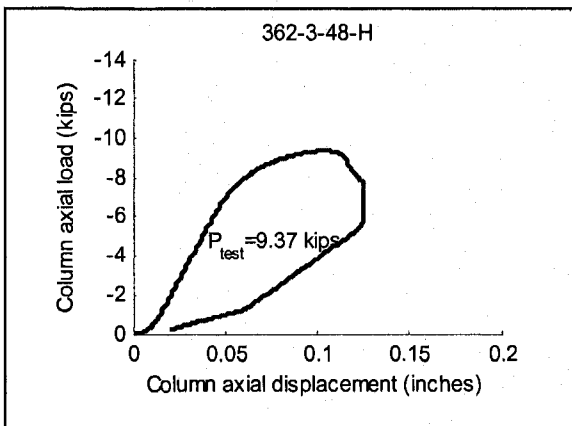
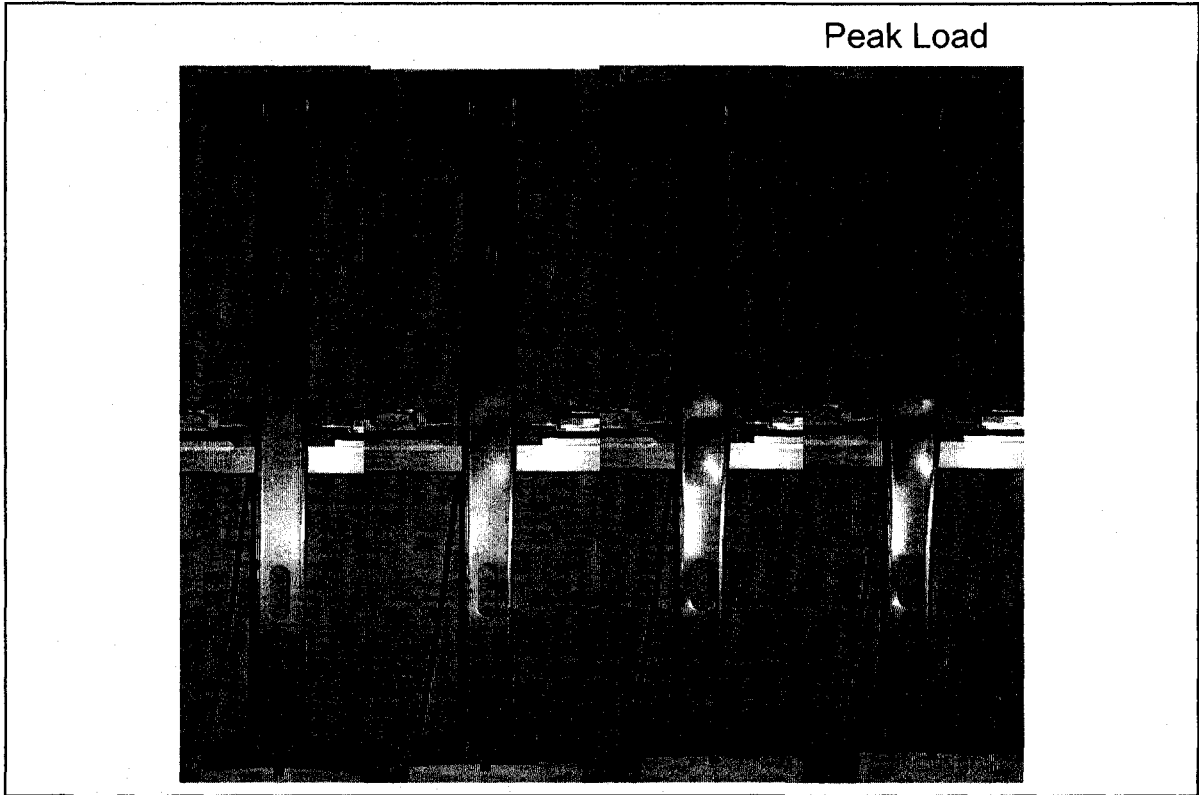
Column Specimen 362-2-48-H



Notes:

- End conditions tight at 4 kips.
- Local buckling visible at 6.5 kips.
- Distortional buckling seems to increase as load-displacement softens.
- East LVDT reaches limit of range as column starts to twist.
- Column failed by global-torsional collapse.

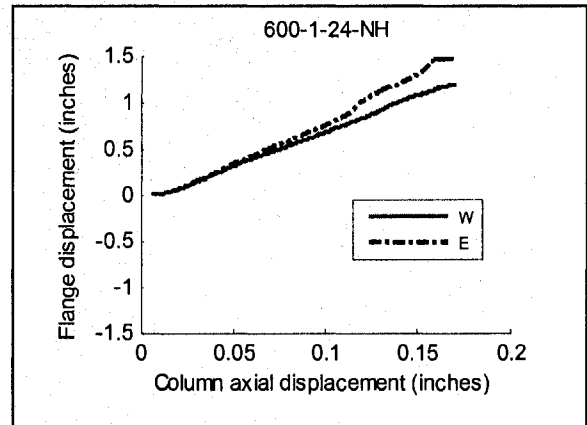
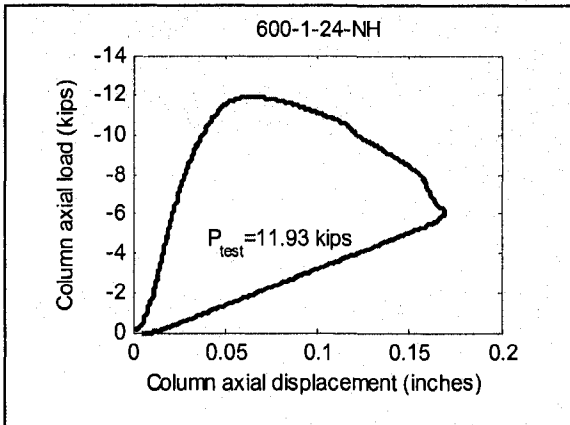
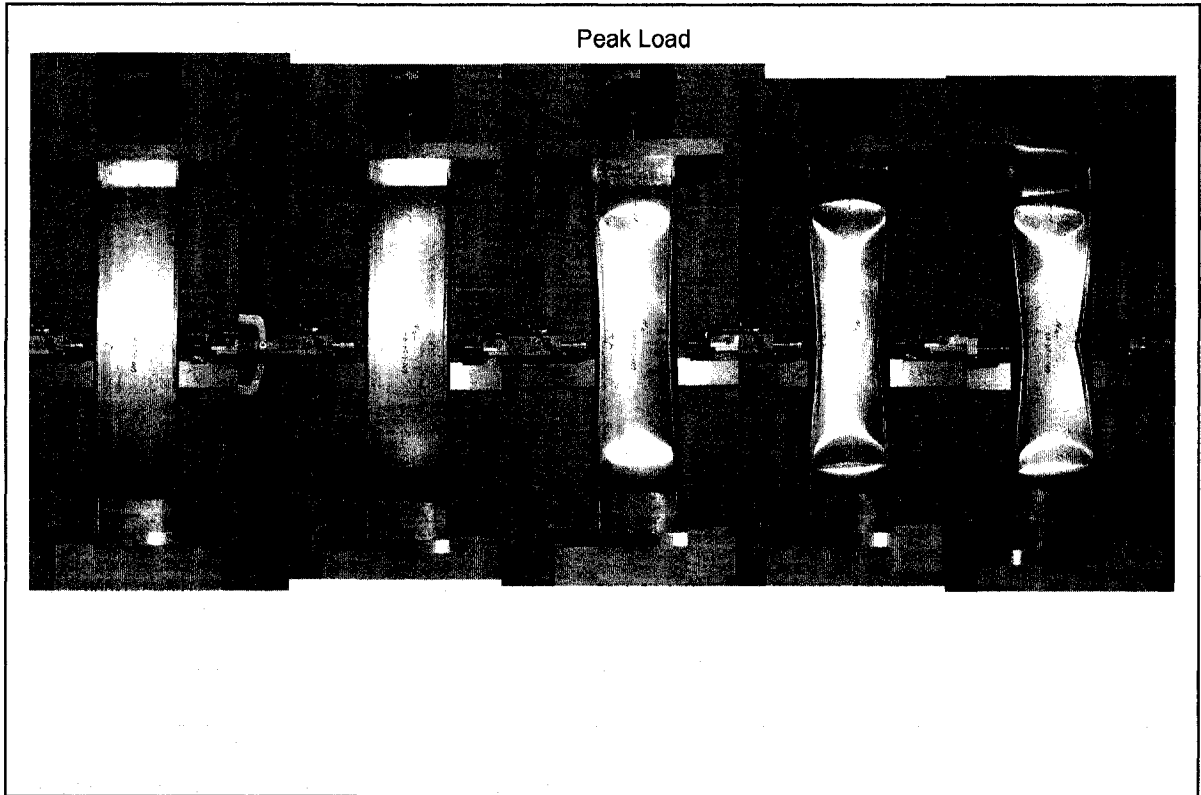
Column Specimen 362-3-48-H



Notes:

Local buckling visible at 6.5 kips.
Column failed by global-torsional collapse.

Column Specimen 600-1-24-NH

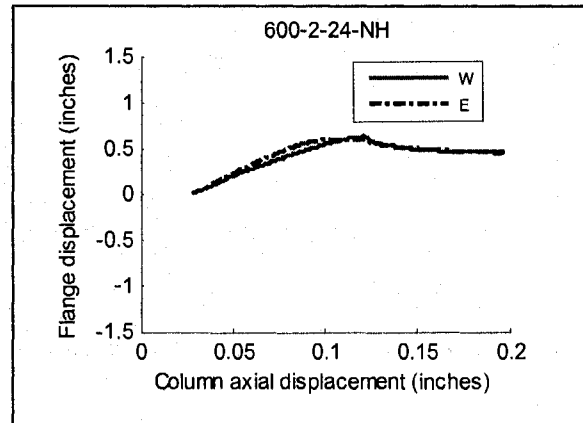
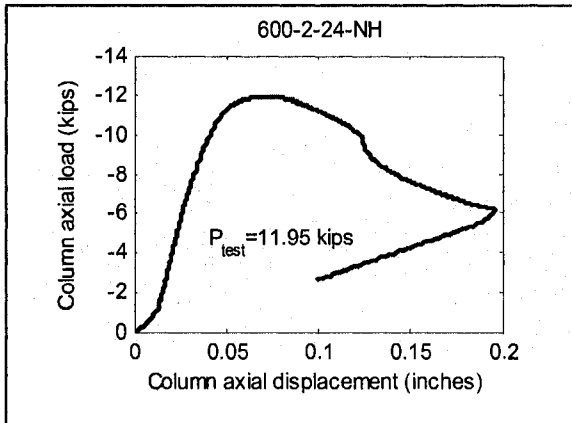


Notes:

Local and distortional waves seem to stay separate.
8 kips (post-peak) – east flange buckles.

Column Specimen 600-2-24-NH

Peak Load

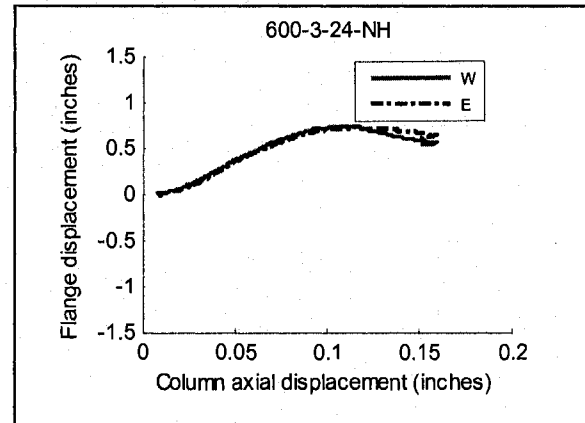
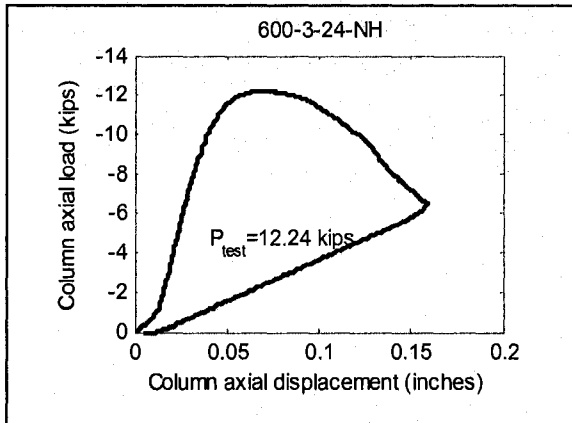
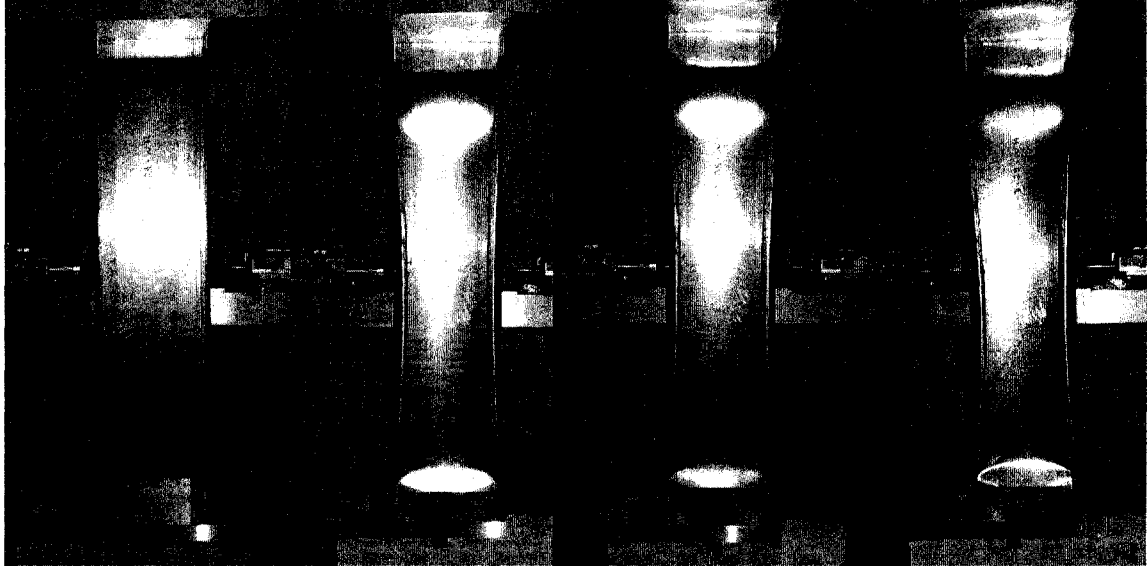


Notes:

Web has large curve when placing specimen on bottom platen.
Visible gap between platen and specimen at top west web-flange corner - 5 kips.
10 kips (post-peak)- flanges buckle and lose contact with bottom platen.

Column Specimen 600-3-24-NH

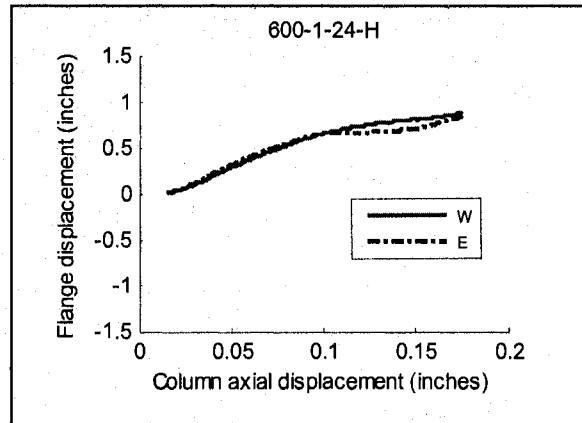
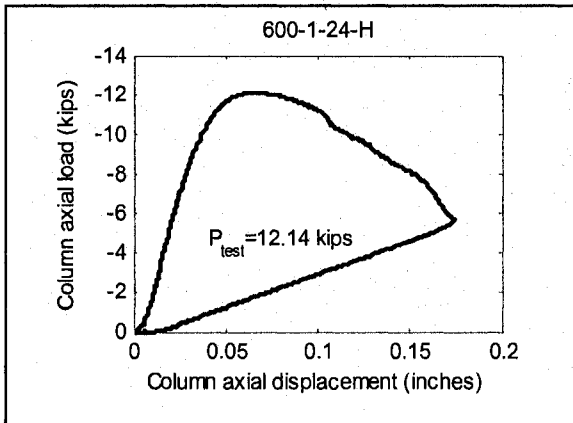
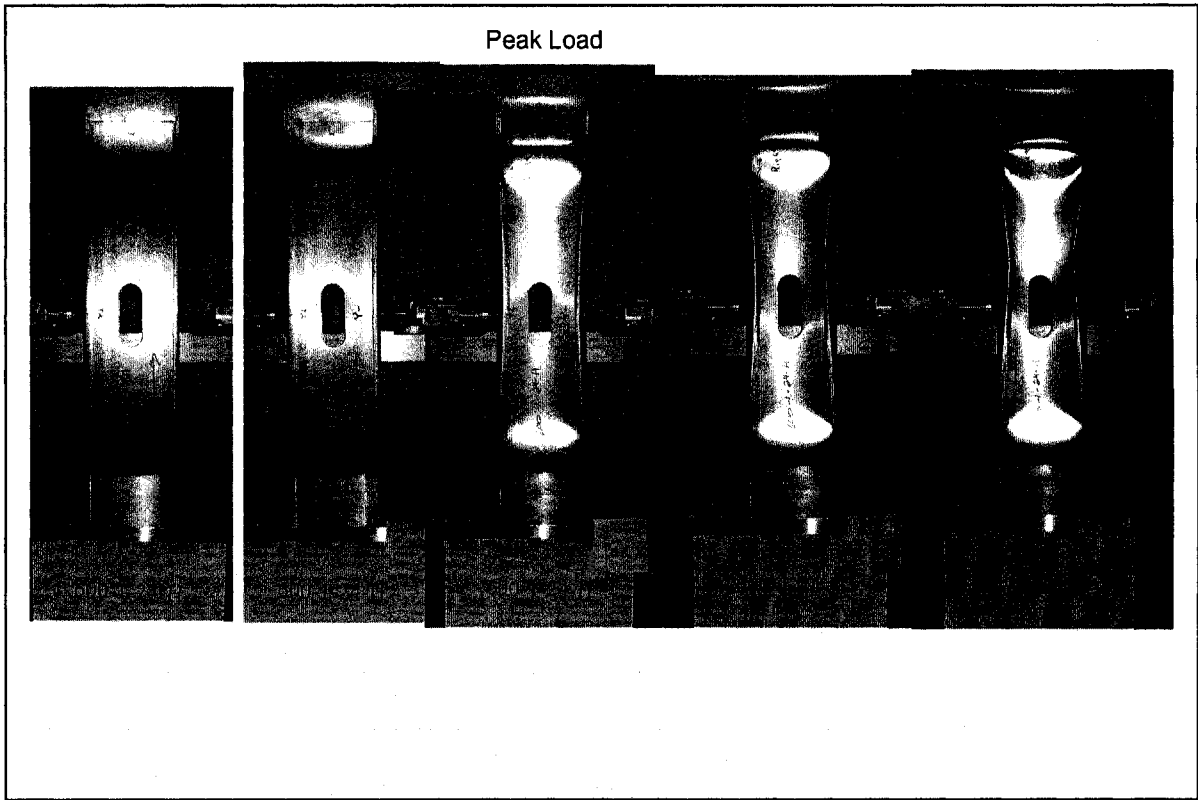
Peak Load



Notes:

Specimen failed at bottom end condition, web rolled over and was not bearing on platen.

Column Specimen 600-1-24-H

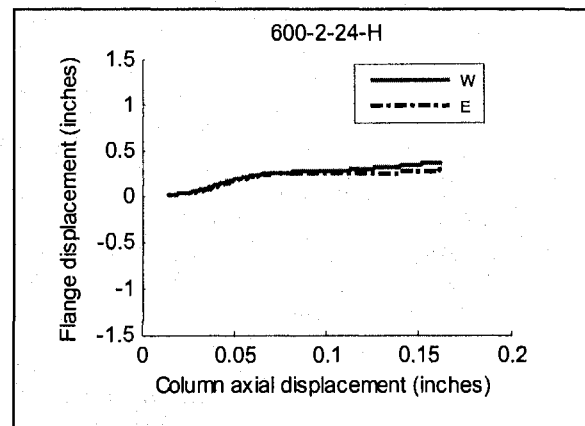
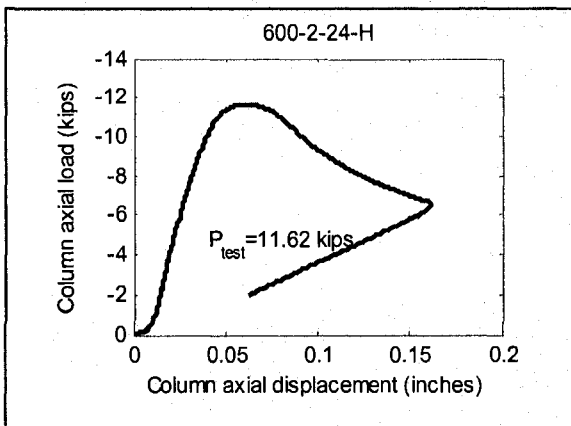
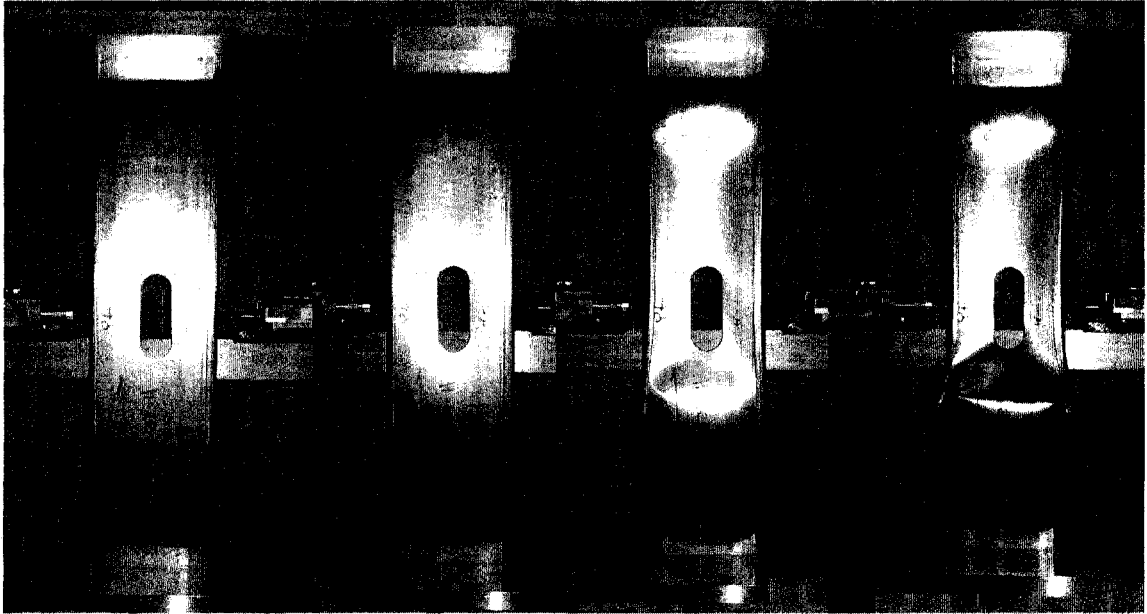


Notes:

Slight gap at east top web-flange corner - 3 kips, gap is closed at 11 kips.
 East flange gives way at 11 kips with dip in load-displ. curve, may be related to above.
 Loud popping sound at 8 kips (post-peak) and large change in load-displ. slope.

Column Specimen 600-2-24-H

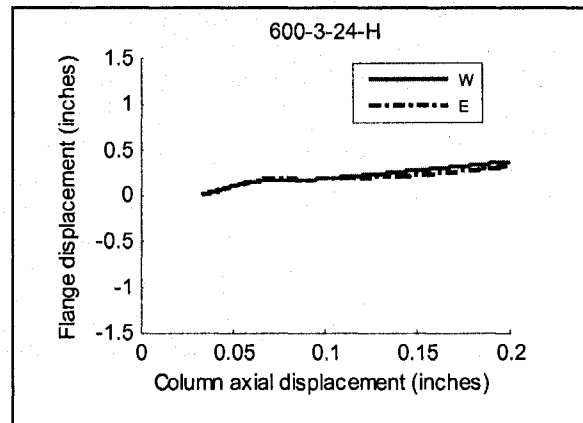
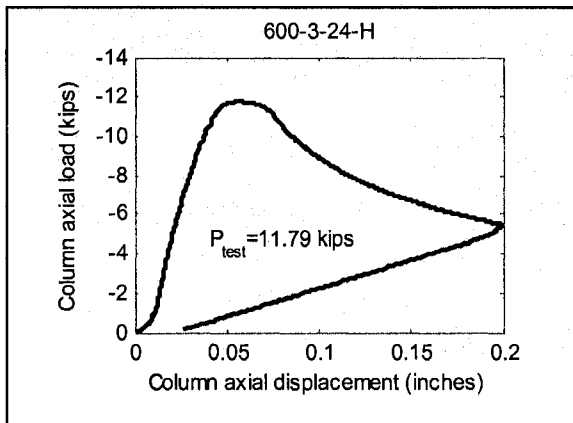
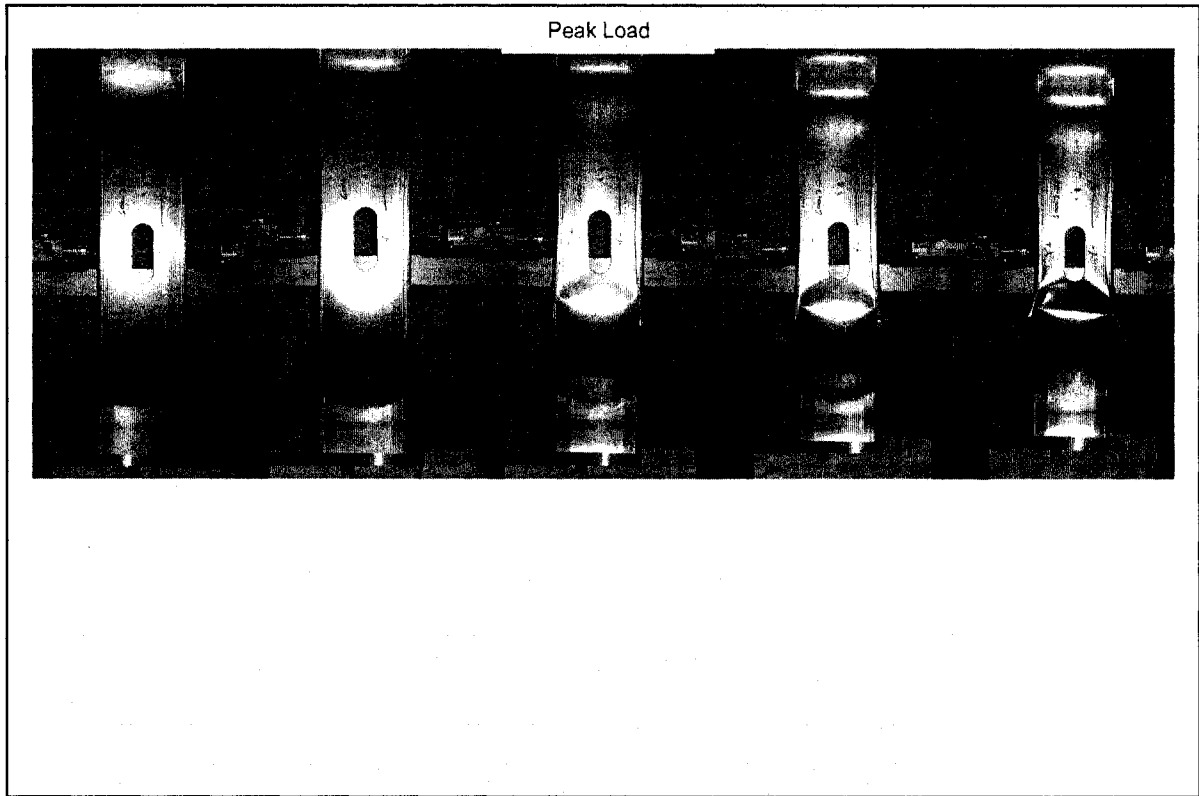
Peak Load



Notes:

Specimen failure mode similar to that of a no-hole specimen.

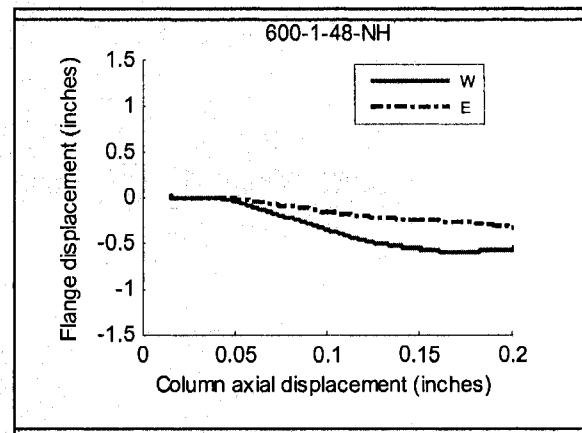
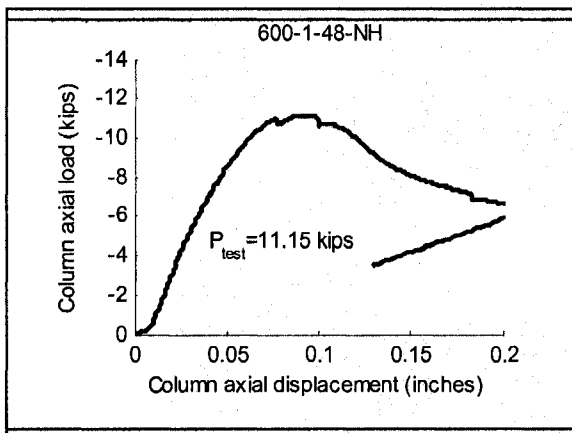
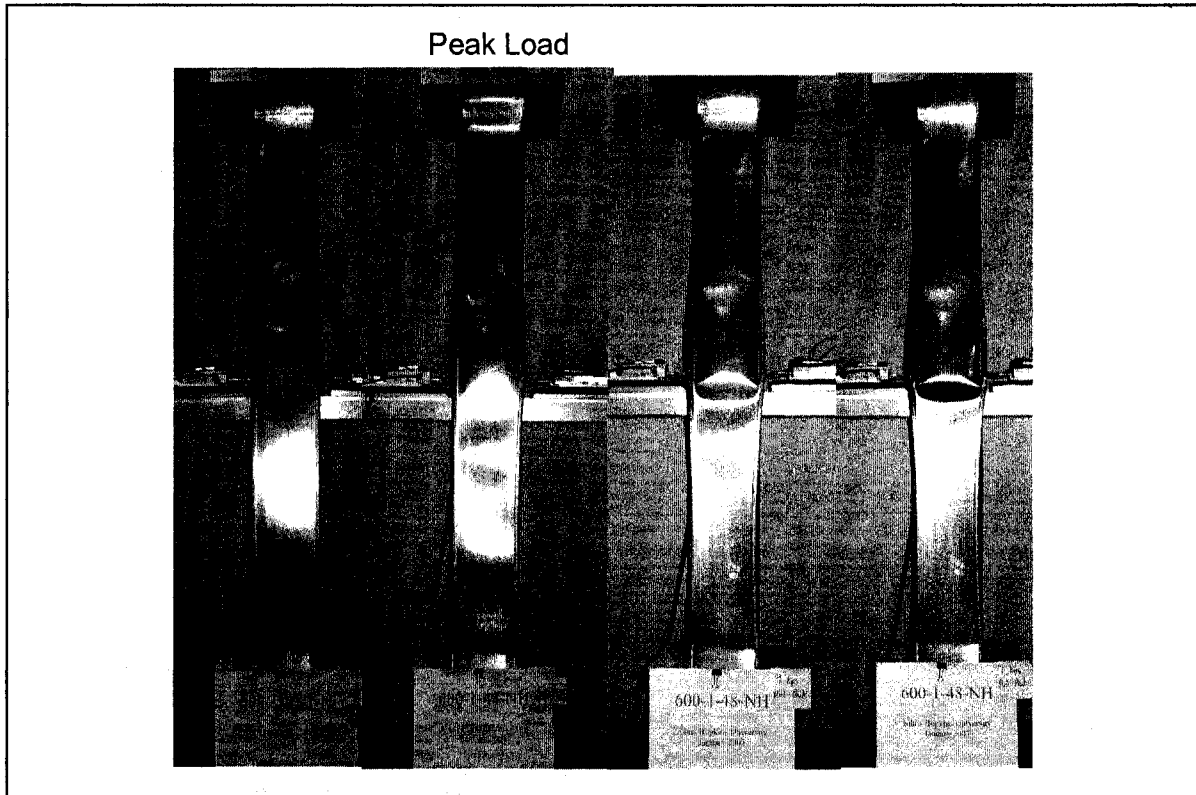
Column Specimen 600-3-24-H



Notes:

Good contact with platens.

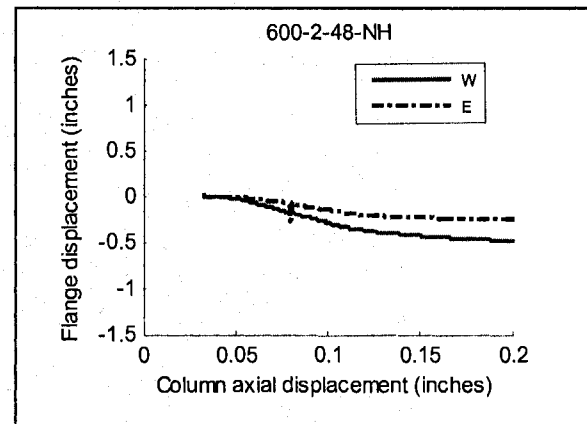
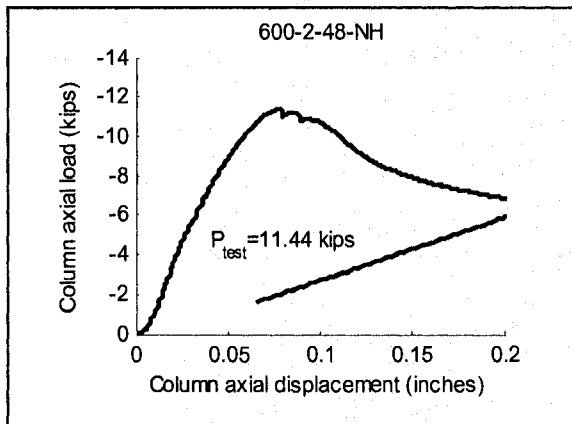
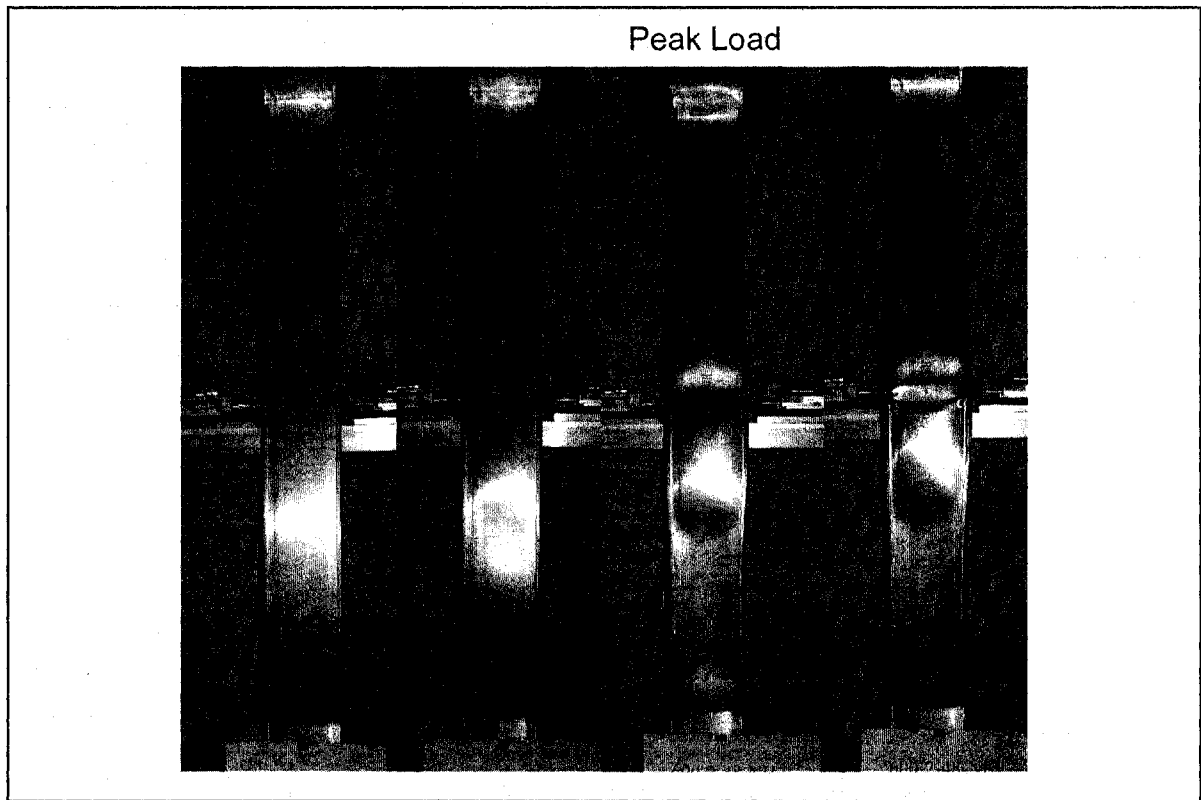
Column Specimen 600-1-48-NH



Notes:

Local buckling first observed at 4.5 kips (11 half-waves).
Distortional wave becomes prominent at 10 kips.
Loud noises 1 minute apart – L waves turn to D waves at north, then south ends.

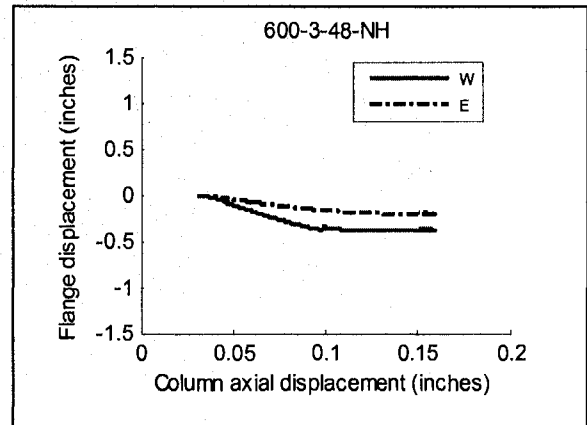
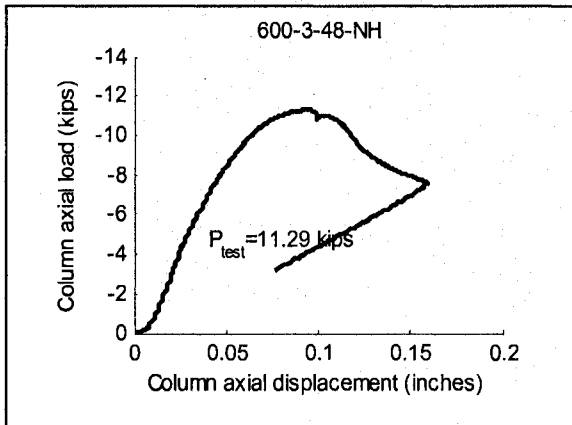
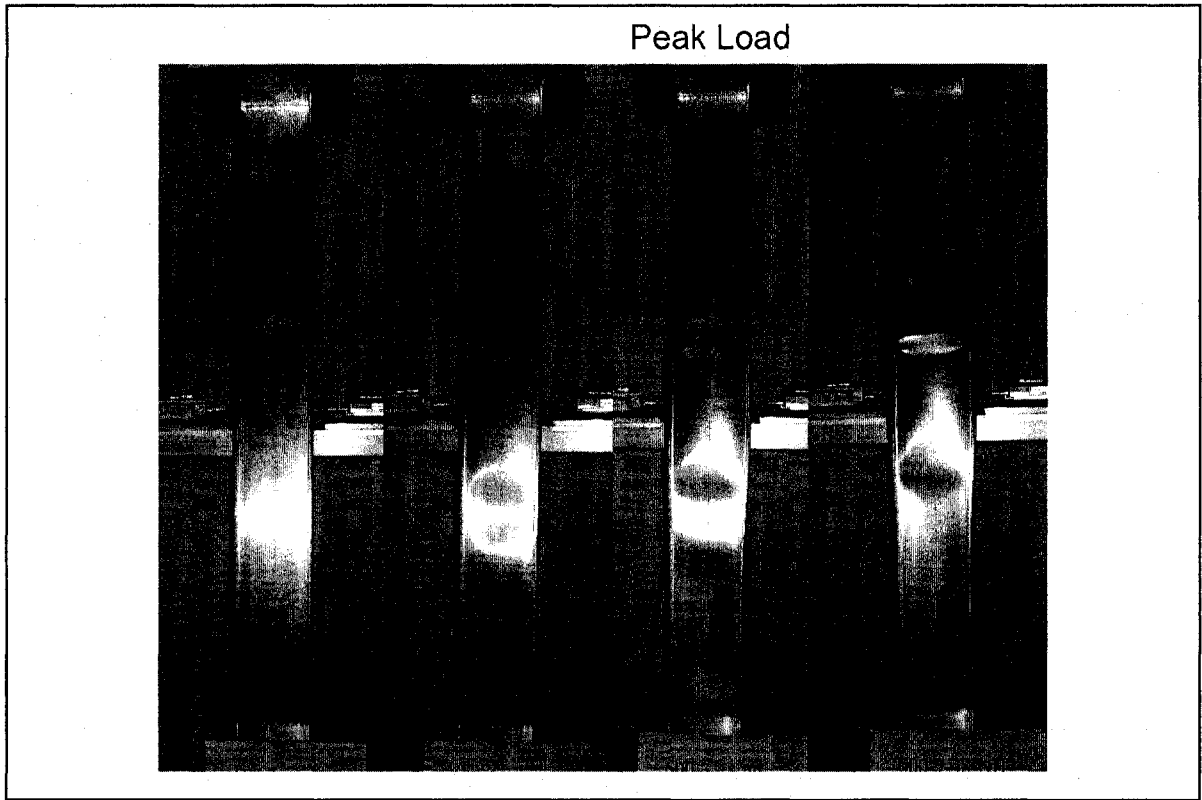
Column Specimen 600-2-48-NH



Notes:

Gap between platen and specimen at top east flange-web corner closes at 2 kips.
Can see distortional shape developing at 4.5 kips.
Local buckling visible at 5 kips.
Two loud bangs (peak load, 10.5 kips post peak) – local web waves change to D waves.
Flange distortion slows at 7 kips post-peak.

Column Specimen 600-3-48-NH

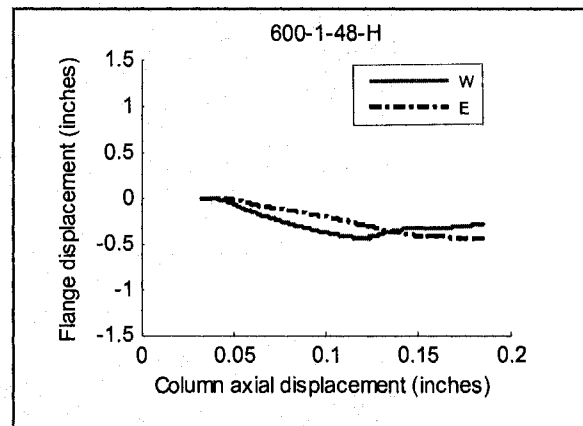
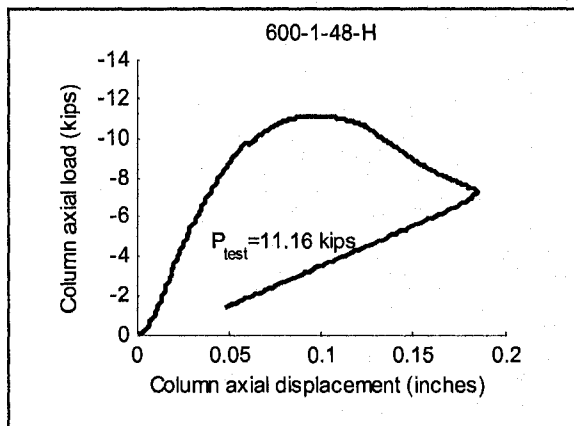
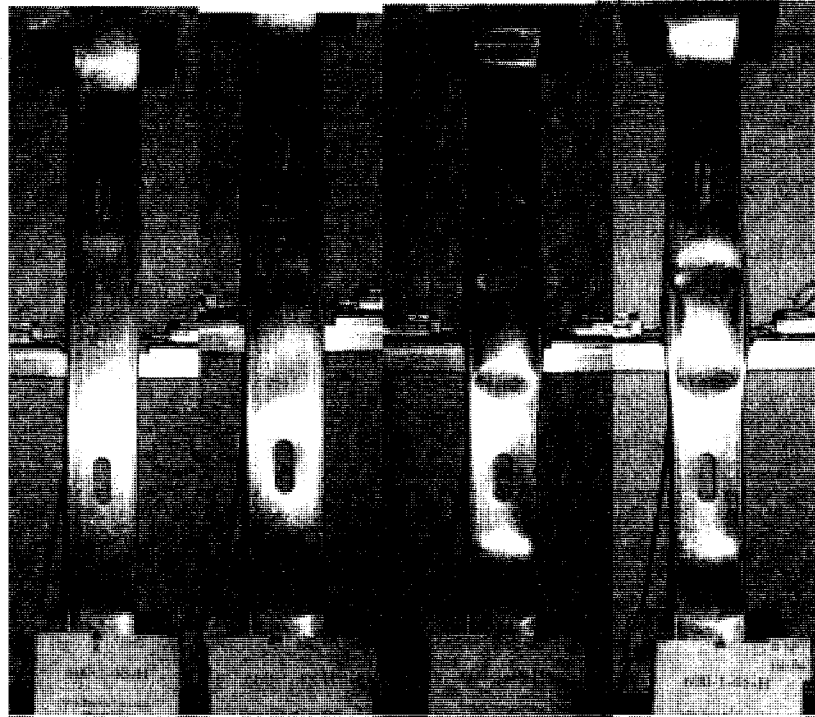


Notes:

Gap between platen and specimen at east top flange closes at 1 kip.
Loud sound at peak load – L waves change to D waves in web.

Column Specimen 600-1-48-H

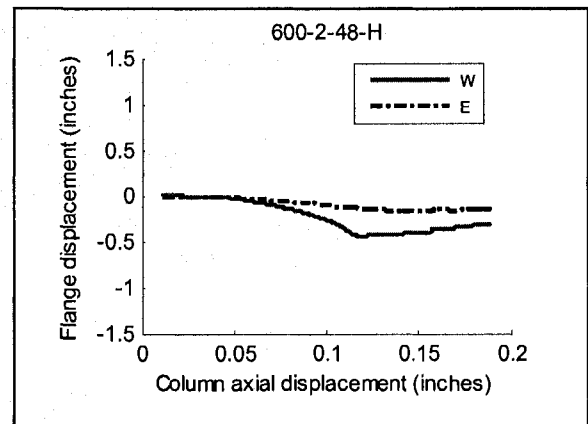
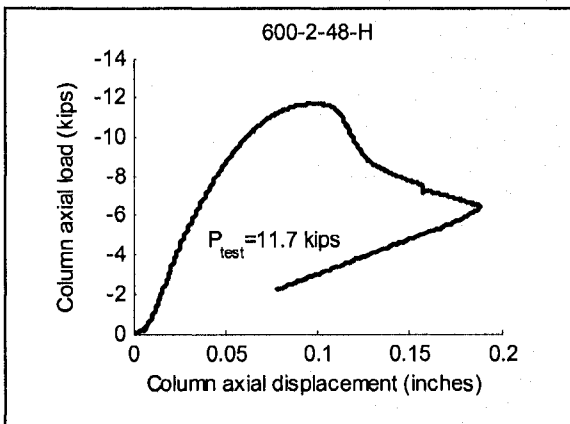
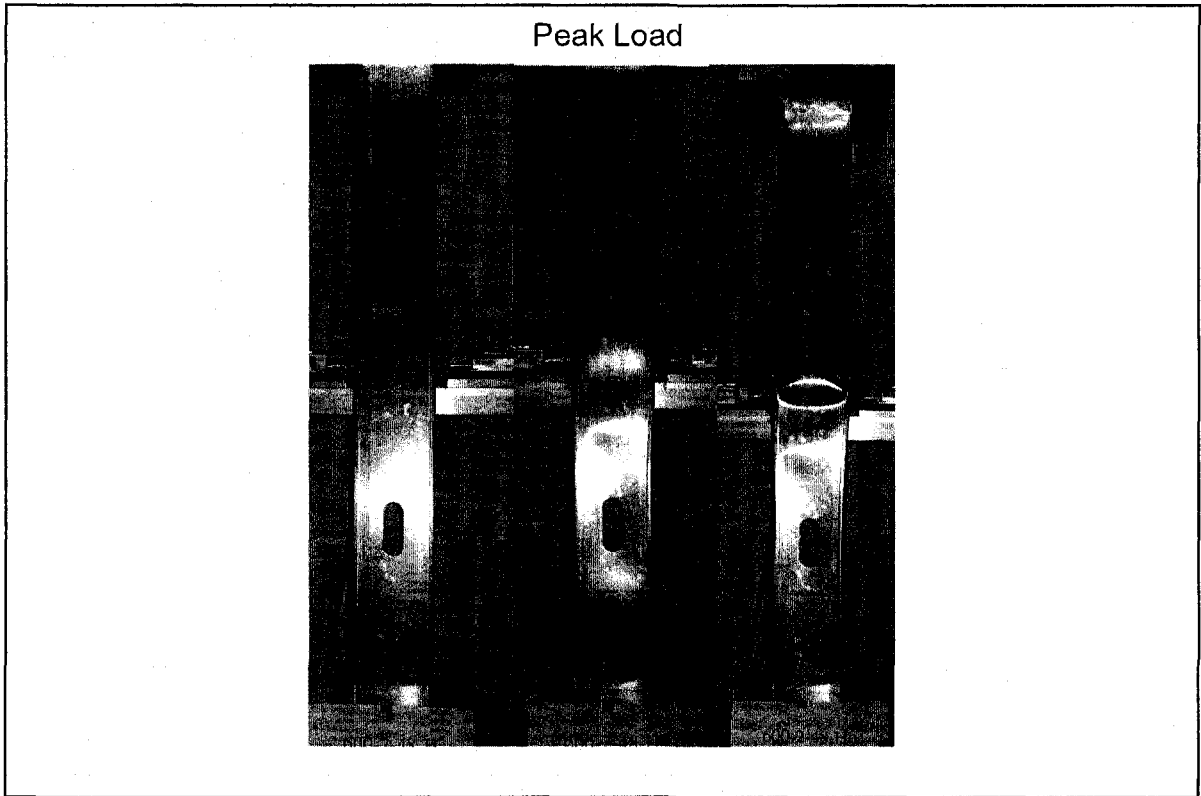
Peak Load



Notes:

Local buckling and DH mode visible at 5 kips.
Loud noise at 9.5 kips – L waves changes to D wave in web.

Column Specimen 600-2-48-H

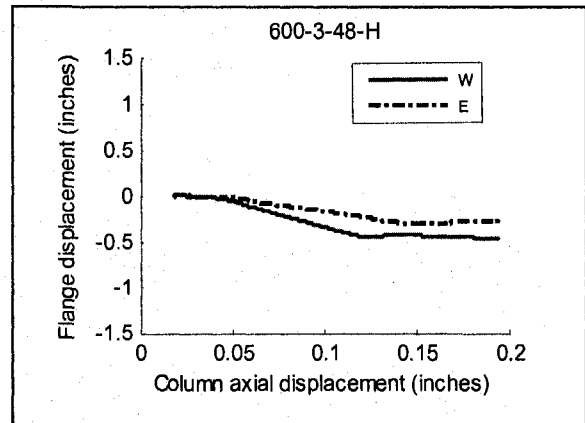
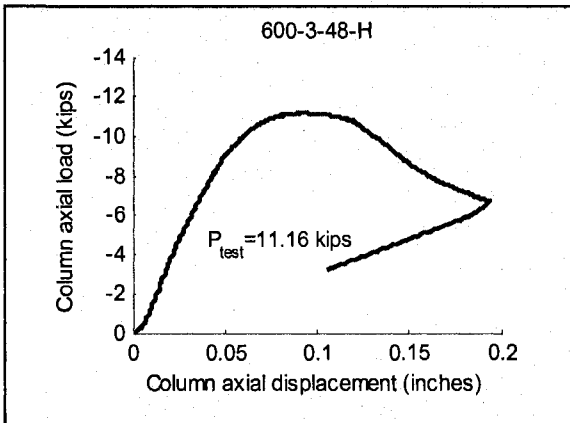
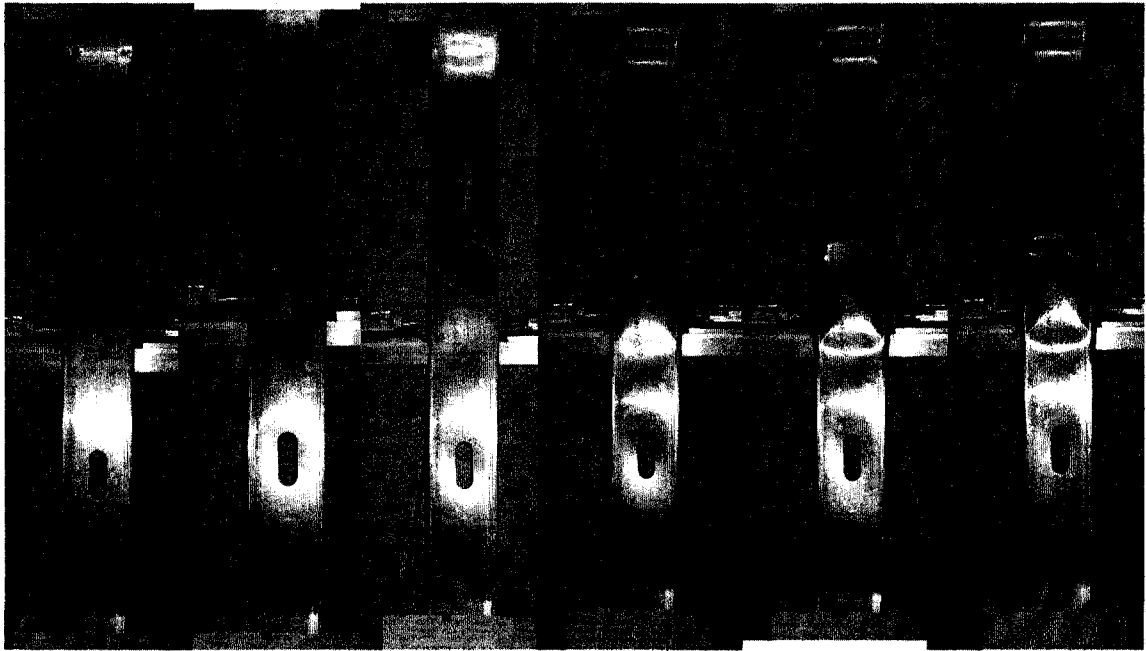


Notes:

Local buckling visible at 4 kips.
 D wave interrupted by large crease.
 L web waves change to D waves (9 kips post-peak, 7.5 kips post-peak)

Column Specimen 600-3-48-H

Peak Load



Notes:

Good platen bearing conditions.
Loud noise at 7.5 kips post-peak.
Yielding in the west flange first, then east flange.

Appendix G

Residual stresses– backstress for kinematic hardening implementation

Implementation of a kinematic hardening rule requires that the center of the yield surface, in stress space, be known for any material which has been yielded prior to the loading of interest. The coordinates of the center of the yield surface ($\Delta\sigma_1, \Delta\sigma_2, \Delta\sigma_3$), known as the backstress, cannot be directly calculated from the stresses derived herein because work hardening was ignored in the residual stress derivations. However, the plastic strains developed in the manufacturing process provide a means by which the backstress may be approximated, as provided in this appendix.

The general equation for effective stress is defined as

$$\sigma_e = \frac{1}{\sqrt{2}} \sqrt{(\sigma_1 - \sigma_2)^2 + (\sigma_2 - \sigma_3)^2 + (\sigma_3 - \sigma_1)^2}. \quad (\text{G.1})$$

Given that the through-thickness sheet stresses are zero ($\sigma_2=0$), Eq. (G.1) reduces to

$$\sigma_e = \sqrt{\sigma_1^2 - \sigma_1\sigma_3 + \sigma_3^2} \quad (\text{G.2})$$

Consider the contribution to the backstress that develops due to coiling. From Eq. (6.18) we know the plastic strain, $\epsilon_p^{coiling}$. With $\epsilon_p^{coiling}$ and knowing the material stress-strain relation (i.e., Figure 6.23) the effective stress at that plastic strain, $\sigma_{ey}^{coiling}$ may be determined. Consistent with the residual stress derivation of Eq. (6.8), we assume $\nu=0.3$ and

$$\sigma_1^{coiling} = \nu \sigma_3^{coiling} \quad (G.3)$$

Finally, substituting the preceding into Eq. (G.2) results in

$$\sigma_3^{coiling} = \frac{\sigma_{ey}^{coiling}}{\sqrt{\nu^2 - \nu + 1}} \quad (G.4)$$

Similarly for cold bending the corners, from Eq. (6.21) we know the plastic strain, ϵ_p^{bend} . With ϵ_p^{bend} and knowing the material stress-strain relation (i.e., Figure 6.23), we determine the effective stress at that plastic strain, σ_{ey}^{bend} . Consistent with the residual stress derivation of Eq. (6.12), we assume $\nu=0.5$ and

$$\sigma_3^{bend} = \nu \sigma_1^{bend} \quad (G.5)$$

and thus find

$$\sigma_1^{bend} = \frac{\sigma_{ey}^{bend}}{\sqrt{\nu^2 - \nu + 1}} \quad (G.6)$$

The backstress is then determined as:

$$\begin{aligned} \Delta\sigma_1 &= \sigma_1^{coiling} + \sigma_1^{bend} - \sigma_{yield} \\ \Delta\sigma_2 &= 0 \\ \Delta\sigma_3 &= \sigma_3^{coiling} + \sigma_3^{bend} - \sigma_{yield} \end{aligned} \quad (G.7)$$

where σ_{yield} is the virgin yield stress of the steel. This estimate assumes that the changes in material properties from coiling, uncoiling, and flattening and cold-forming do not influence one another.

Appendix H

Experiment true stress-strain curves

The average true plastic stress-strain curves are provided here for each of the 24 column tests reported in Chapter 5. For each specimen, three engineering stress-strain curves (west flange, east flange, and web) were averaged and then transformed into true stresses and strains with the following equations:

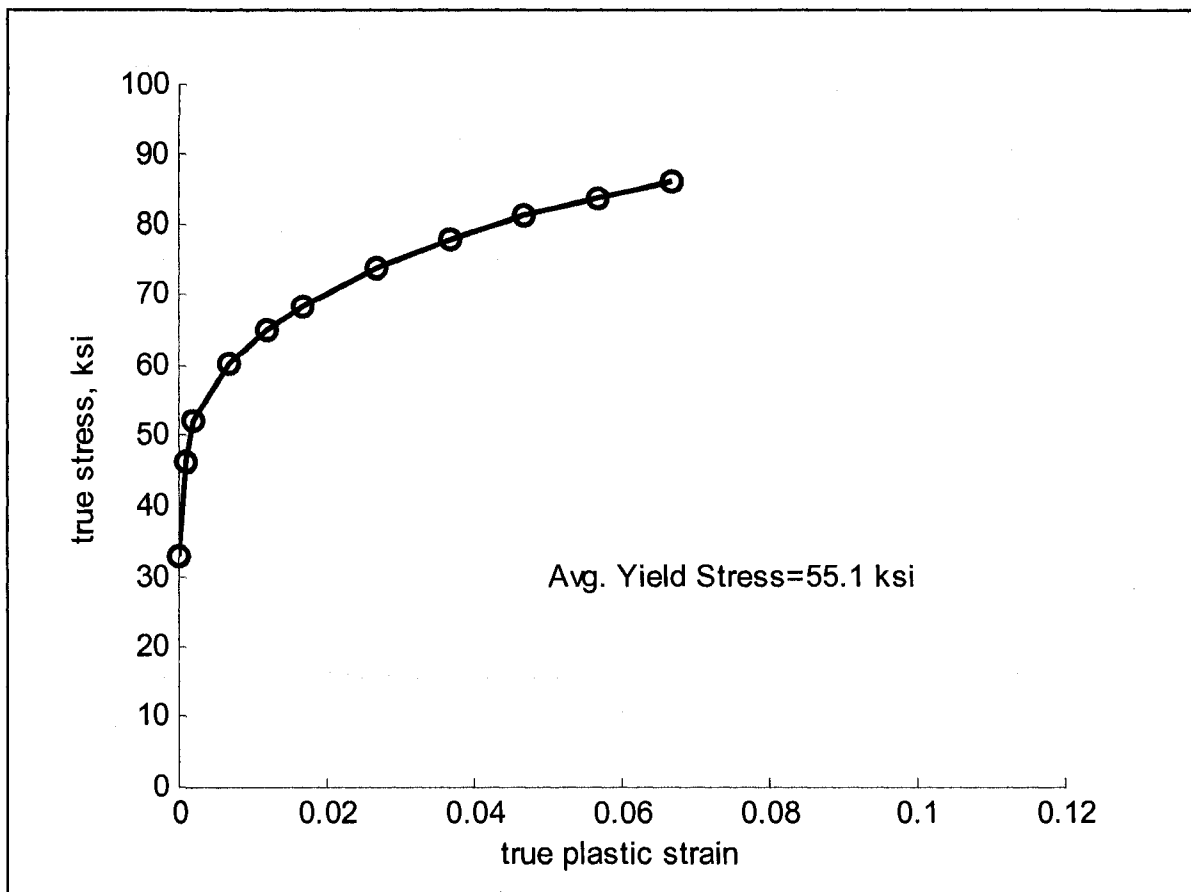
$$\begin{aligned}\varepsilon_{true} &= \ln(1 + \varepsilon_o) \\ \sigma_{true} &= \sigma_o(1 + \varepsilon_o)\end{aligned}$$

ε_{true} and σ_{true} are the true stress and strain and ε_o and σ_o are the engineering stress and strain in the above equations. The tables in this appendix provide just the plastic component of the true strain since this is what is required in ABAQUS:

$$\varepsilon_p = \varepsilon_{true} - \varepsilon_{yield}, \text{ where } \varepsilon_{yield} = \frac{\sigma_{yield}}{E}$$

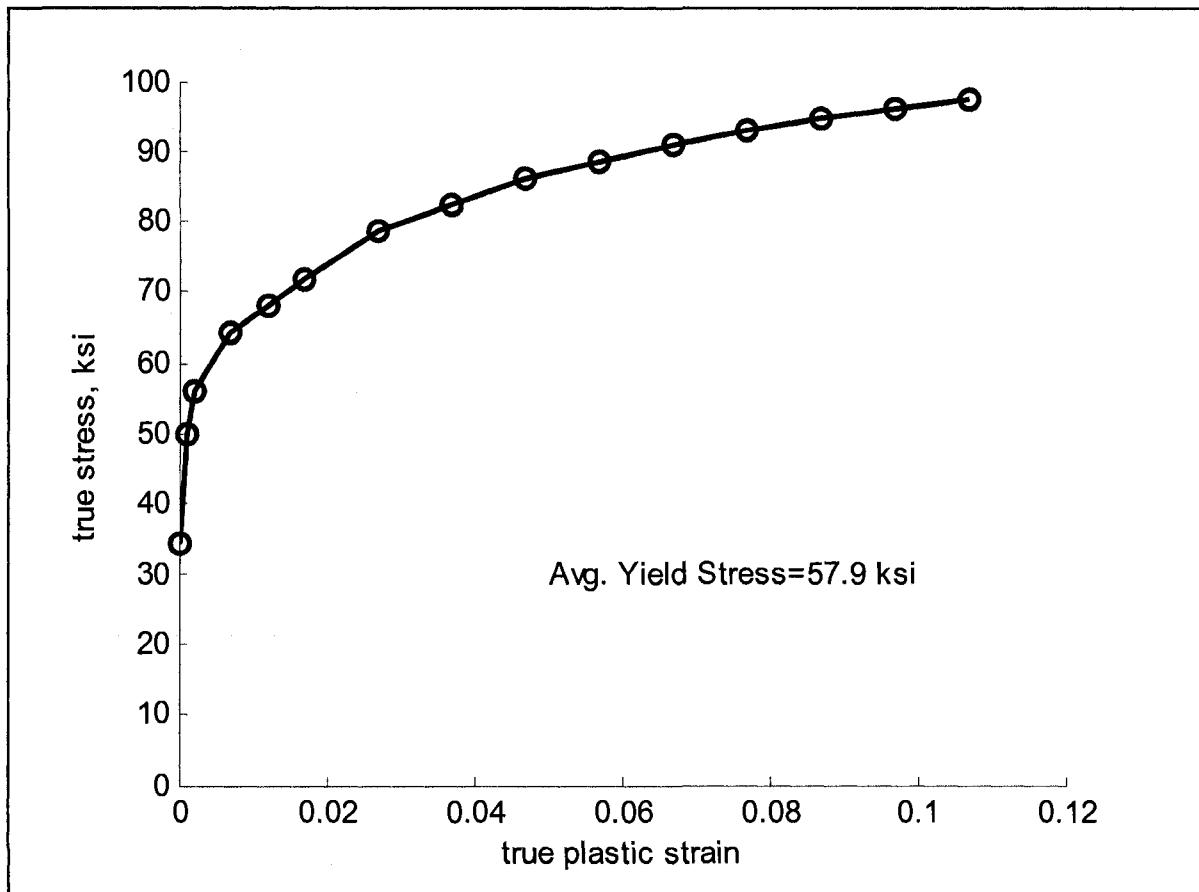
The true stress-strain curves presented here were modified prior to their implementation in ABAQUS to ensure plasticity initiated at the yield stress and not the proportional limit. Refer to Section 7.2.1.4 for details on this modeling decision.

Specimen 362-1-24-NH, 362-2-24-NH, 362-3-24-NH



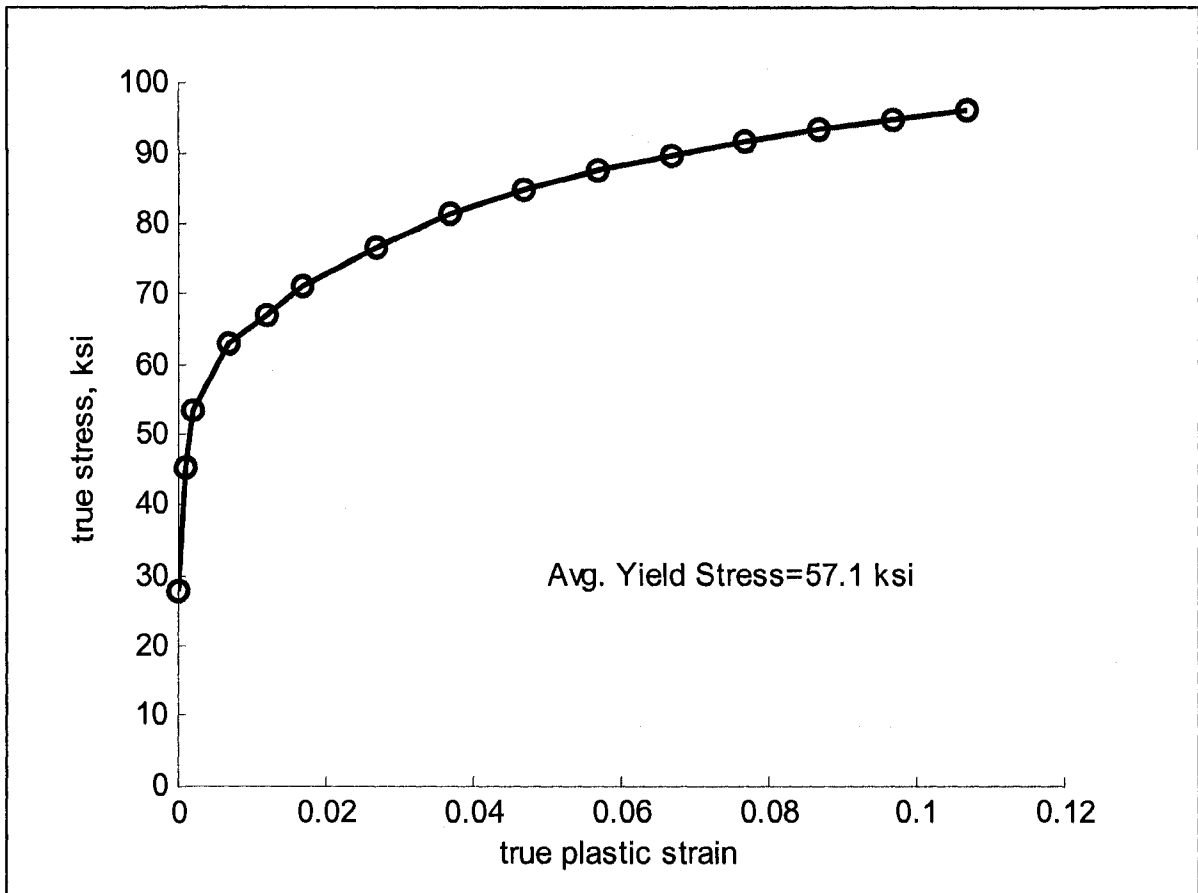
true plastic strain, ϵ_p	true stress, σ_{true} (ksi)
0	33.05
0.001	46.10
0.002	51.88
0.007	60.30
0.012	64.89
0.017	68.37
0.027	73.97
0.037	78.12
0.047	81.27
0.057	83.83
0.067	86.16

Specimen 362-1-24-H



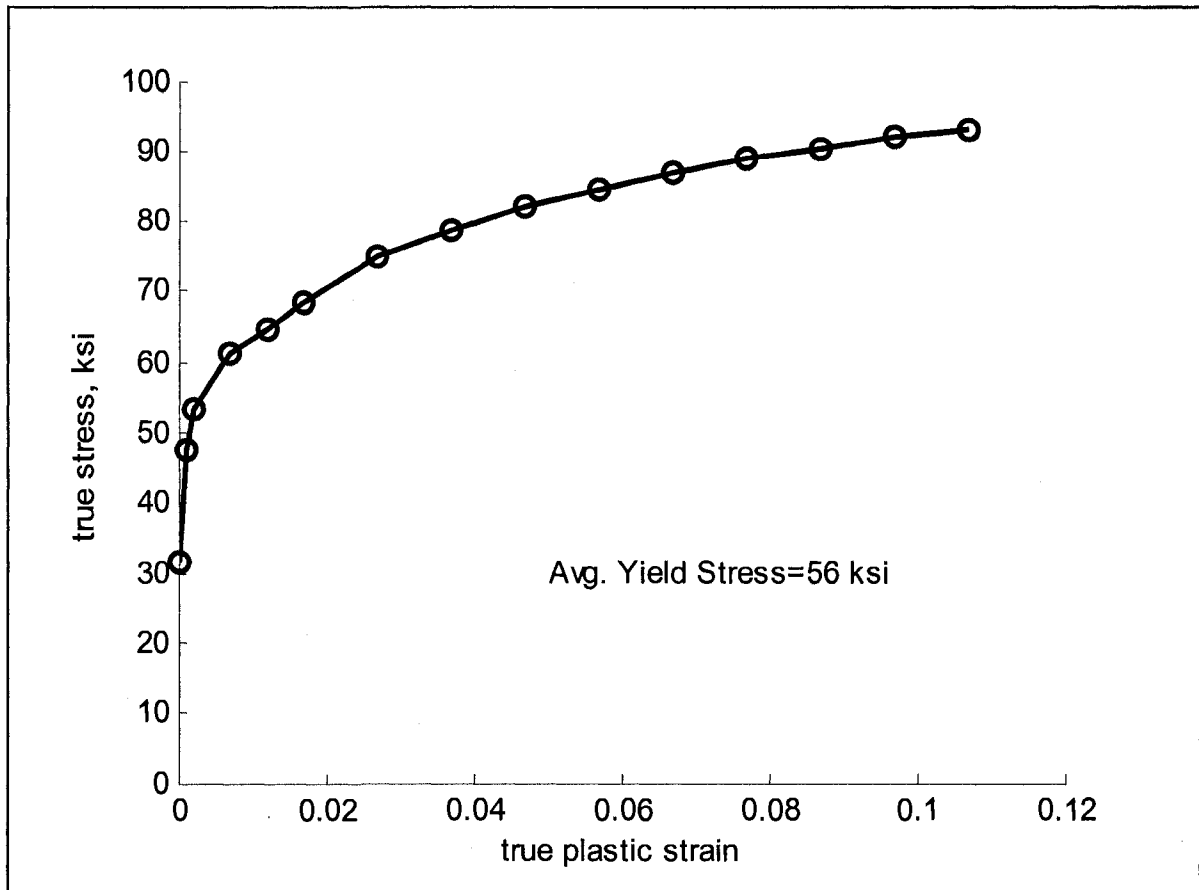
true plastic strain, ϵ_p	true stress, σ_{true} (ksi)
0	34.2
0.001	50.0
0.002	56.1
0.007	64.4
0.012	68.3
0.017	72.0
0.027	78.6
0.037	82.5
0.047	86.2
0.057	88.7
0.067	91.0
0.077	92.9
0.087	94.6
0.097	96.2
0.107	97.5

Specimen 362-2-24-H



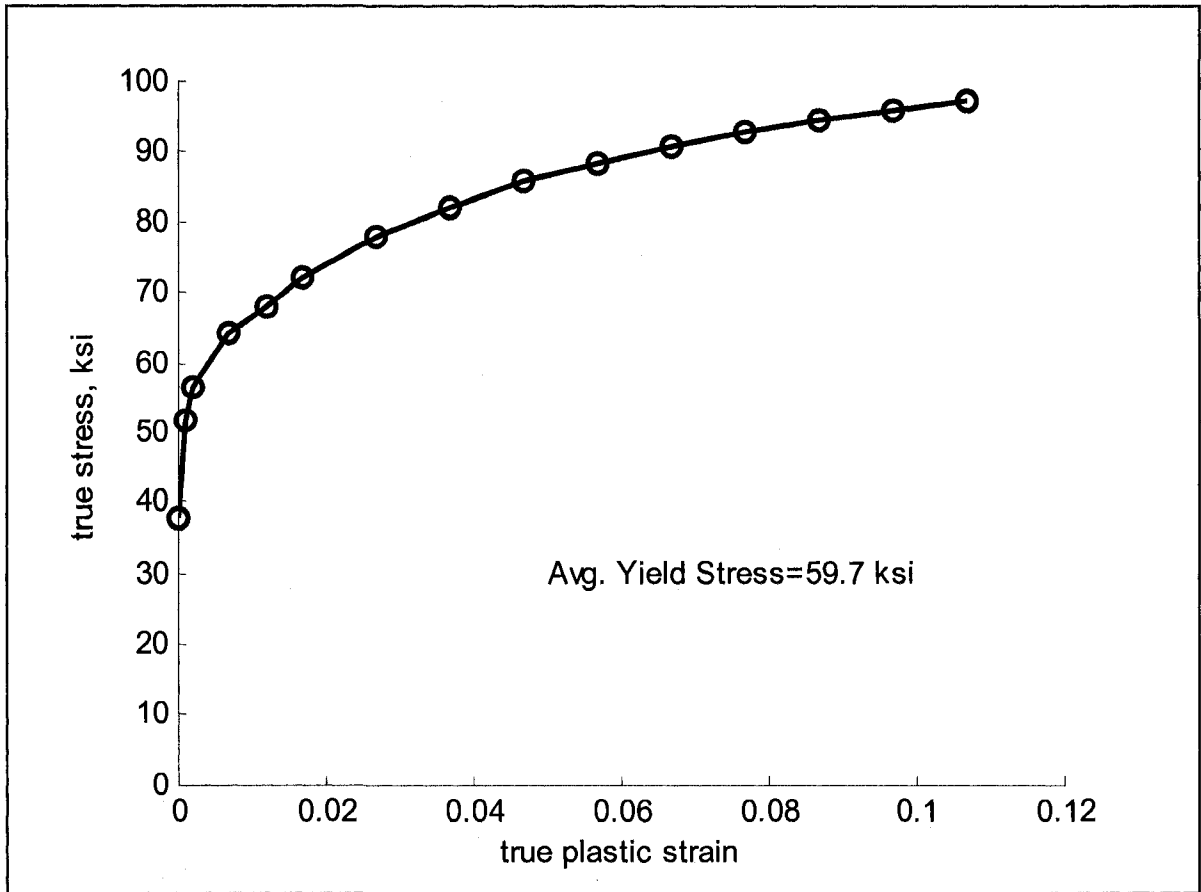
true plastic strain, ϵ_p	true stress, σ_{true} (ksi)
0	27.7
0.001	45.1
0.002	53.3
0.007	62.8
0.012	67.1
0.017	71.2
0.027	76.7
0.037	81.3
0.047	84.7
0.057	87.4
0.067	89.7
0.077	91.6
0.087	93.4
0.097	94.8
0.107	96.2

Specimen 362-3-24-H



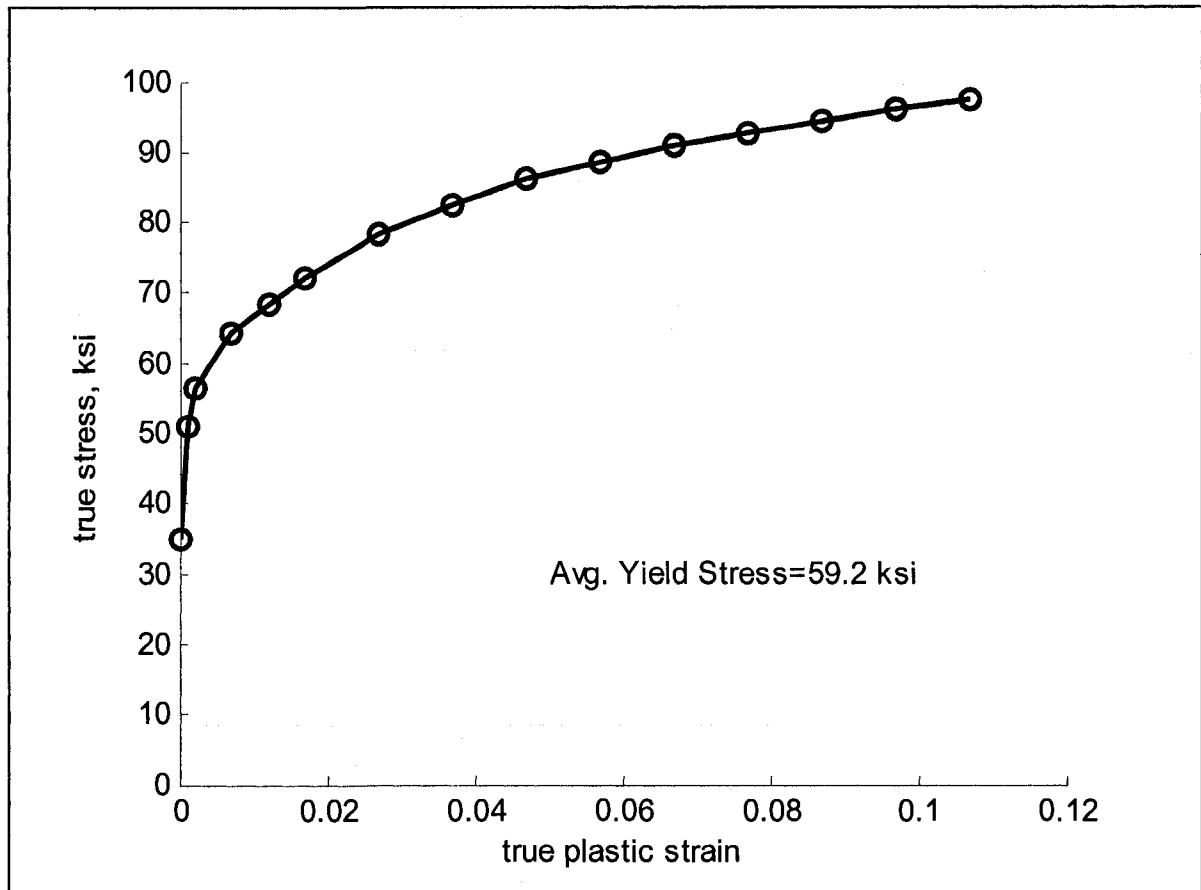
true plastic strain, ϵ_p	true stress, σ_{true} (ksi)
0	31.7
0.001	47.8
0.002	53.6
0.007	61.1
0.012	64.7
0.017	68.4
0.027	74.8
0.037	78.6
0.047	82.2
0.057	84.6
0.067	86.9
0.077	88.8
0.087	90.4
0.097	91.9
0.107	93.1

Specimen 362-1-48-NH



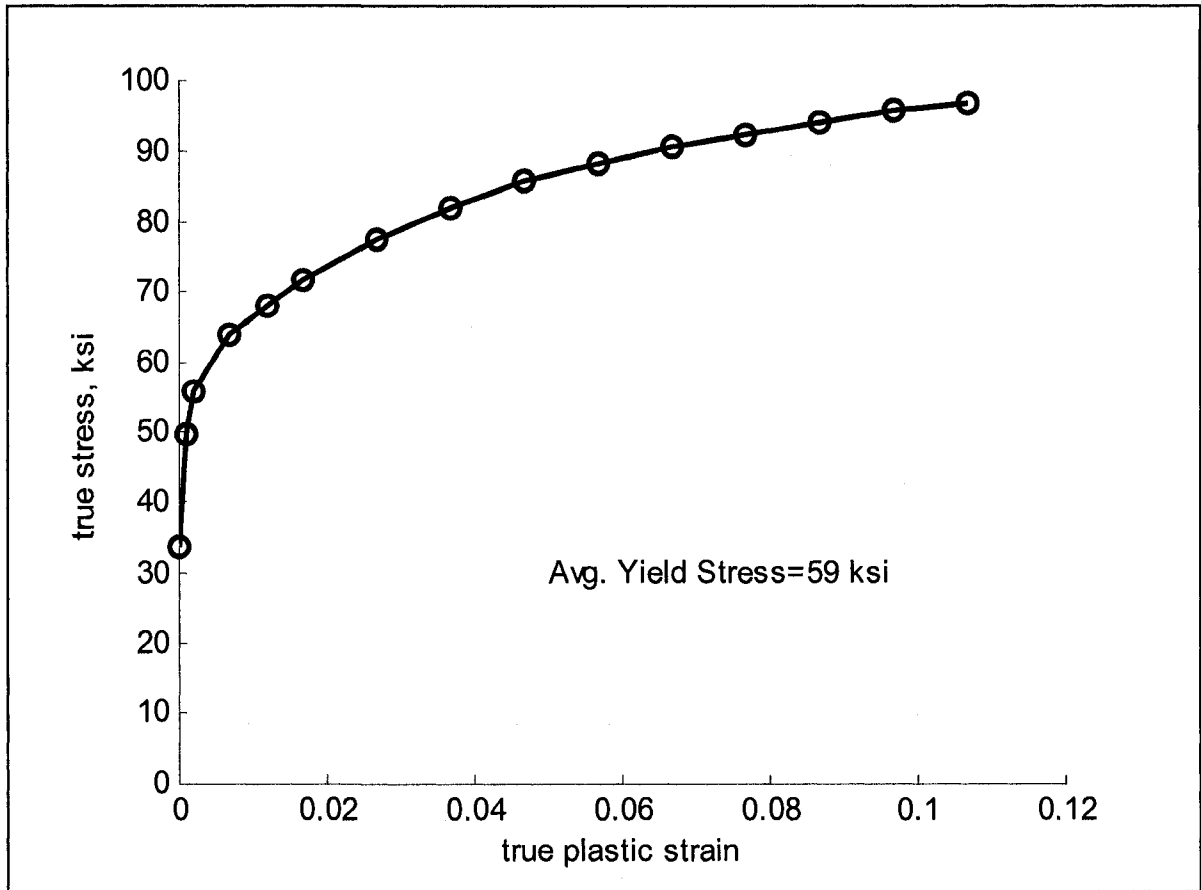
true plastic strain, ϵ_p	true stress, σ_{true} (ksi)
0	37.8
0.001	51.6
0.002	56.6
0.007	64.3
0.012	68.2
0.017	72.0
0.027	78.1
0.037	82.1
0.047	85.9
0.057	88.3
0.067	90.8
0.077	92.5
0.087	94.3
0.097	95.7
0.107	97.1

Specimen 362-2-48-NH



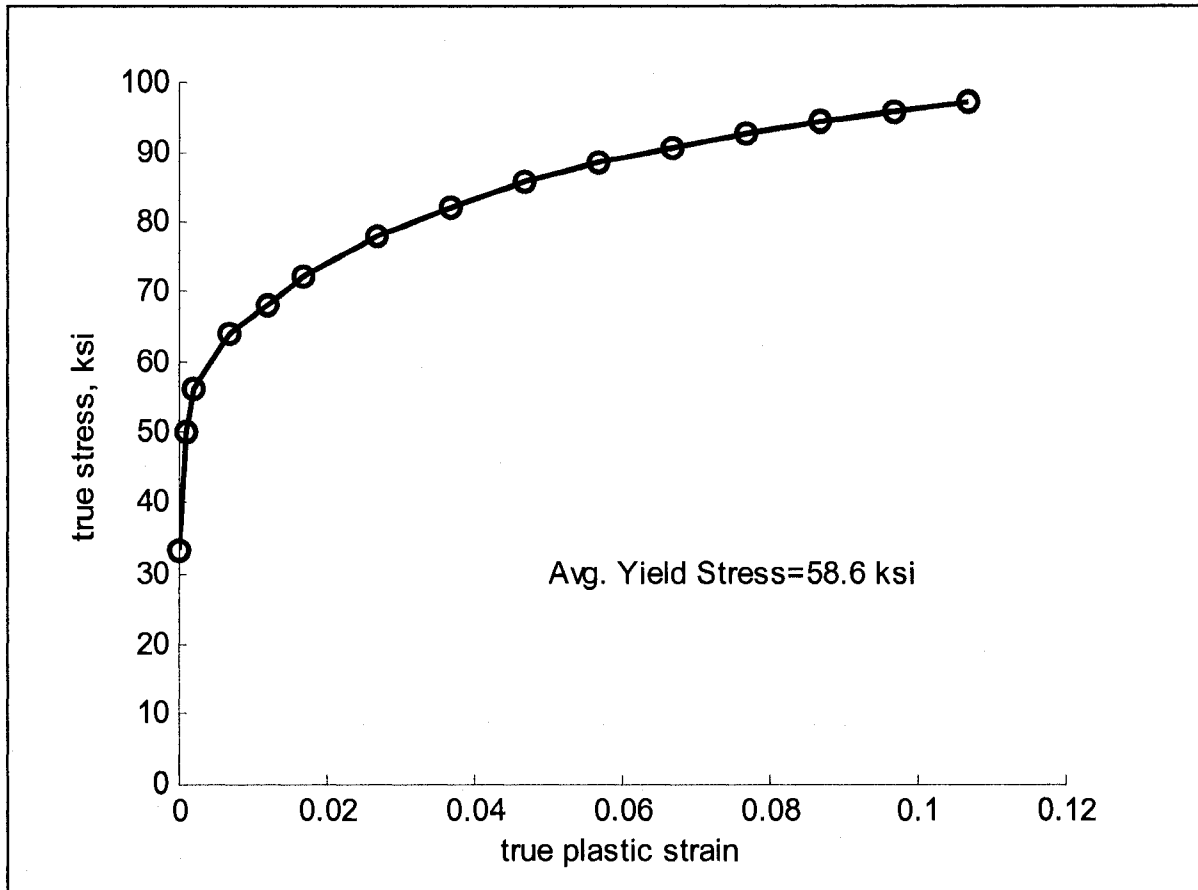
true plastic strain, ϵ_p	true stress, σ_{true} (ksi)
0	35.0
0.001	50.9
0.002	56.5
0.007	64.3
0.012	68.3
0.017	72.1
0.027	78.2
0.037	82.3
0.047	86.1
0.057	88.5
0.067	90.9
0.077	92.8
0.087	94.5
0.097	96.0
0.107	97.3

Specimen 362-3-48-NH



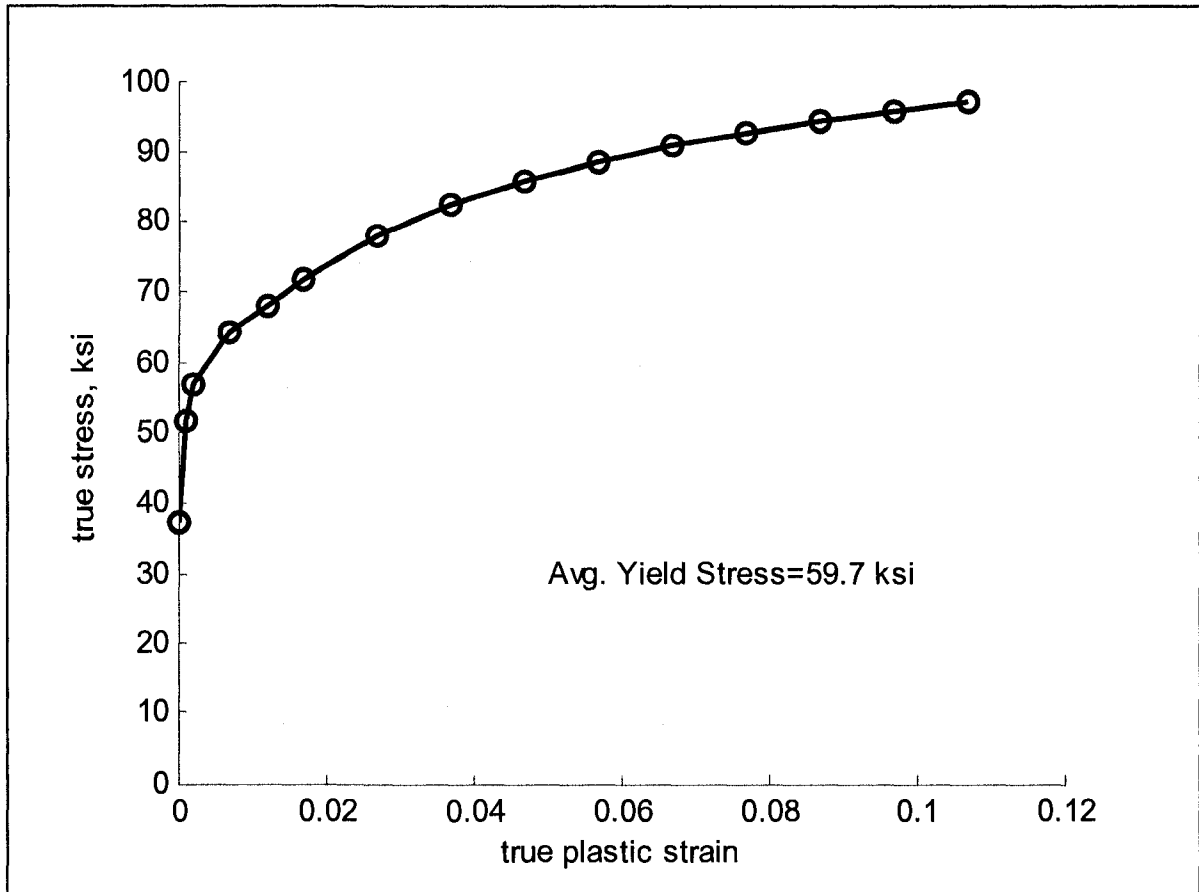
true plastic strain, ϵ_p	true stress, σ_{true} (ksi)
0	34
0.001	50
0.002	56
0.007	64
0.012	68
0.017	72
0.027	78
0.037	82
0.047	86
0.057	88
0.067	91
0.077	92
0.087	94
0.097	96
0.107	97

Specimen 362-1-48-H



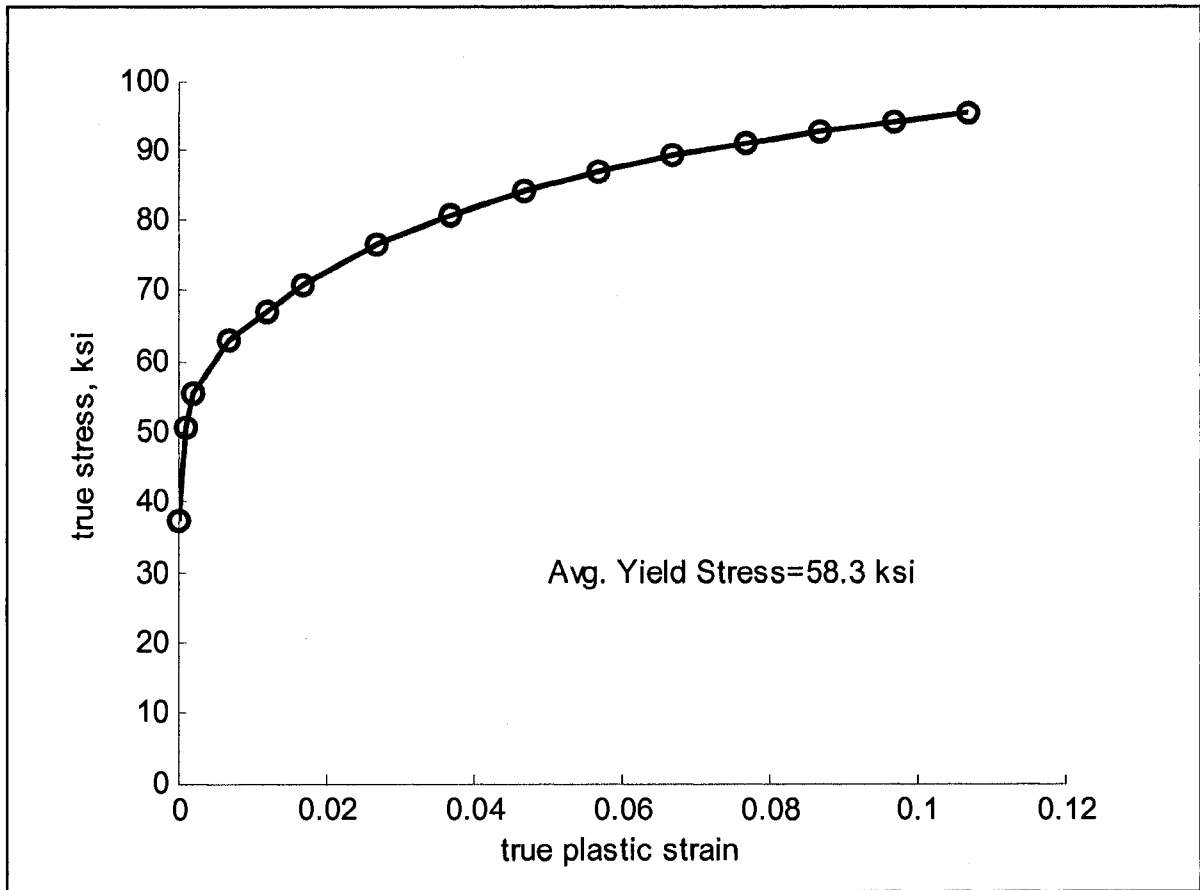
true plastic strain, ϵ_p	true stress, σ_{true} (ksi)
0	33.2
0.001	50.1
0.002	56.1
0.007	64.2
0.012	68.2
0.017	72.0
0.027	78.0
0.037	82.2
0.047	85.7
0.057	88.4
0.067	90.7
0.077	92.7
0.087	94.4
0.097	95.8
0.107	97.2

Specimen 362-2-48-H



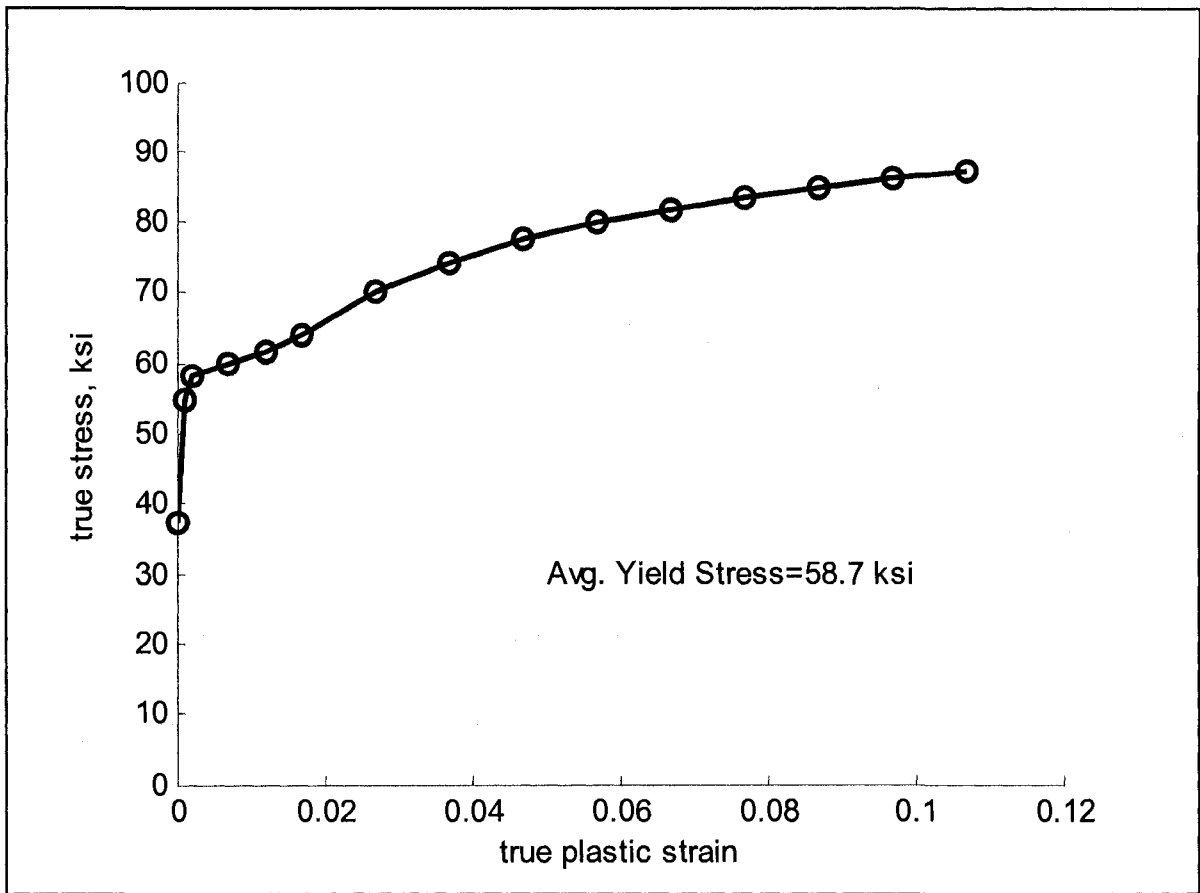
true plastic strain, ϵ_p	true stress, σ_{true} (ksi)
0	37.3
0.001	51.5
0.002	56.7
0.007	64.2
0.012	68.2
0.017	72.0
0.027	78.1
0.037	82.4
0.047	85.8
0.057	88.5
0.067	90.8
0.077	92.7
0.087	94.4
0.097	95.9
0.107	97.2

Specimen 362-3-48-H



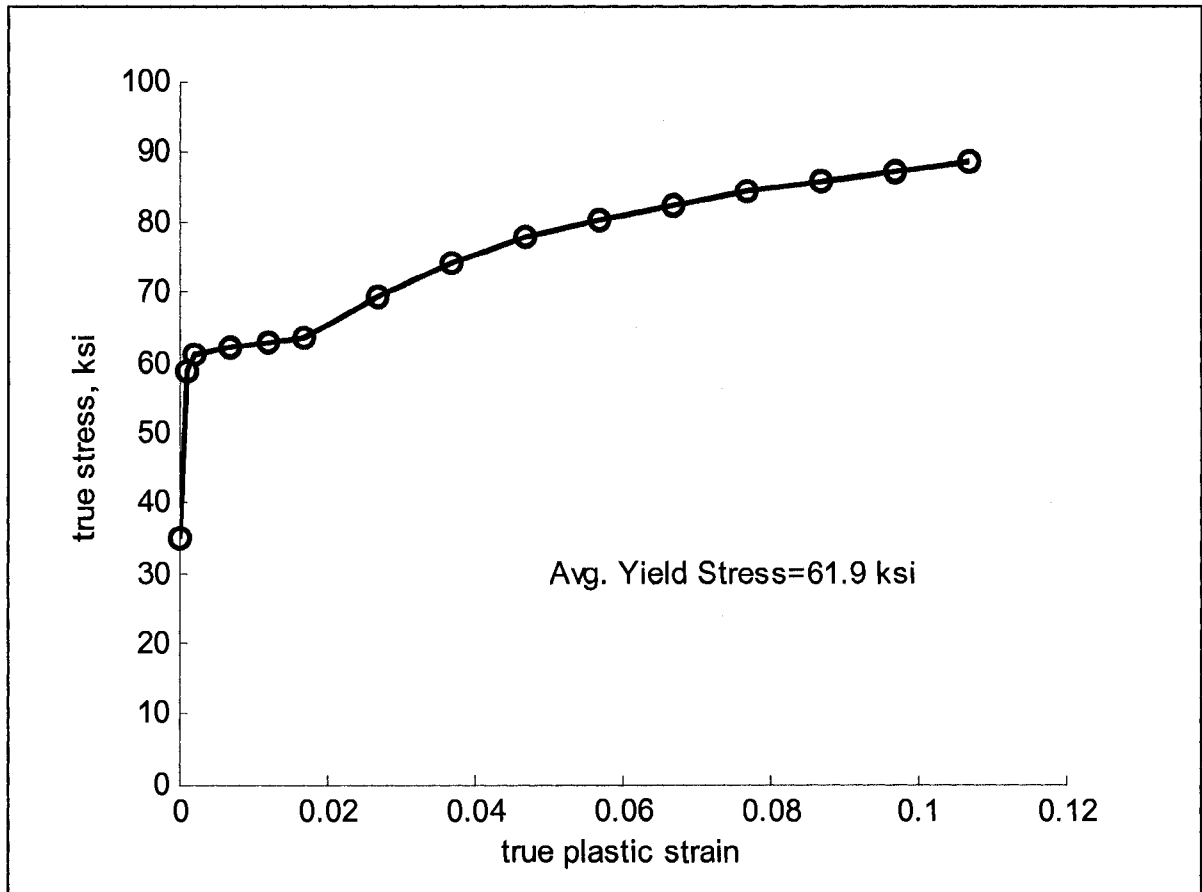
true plastic strain, ϵ_p	true stress, σ_{true} (ksi)
0	37.5
0.001	50.6
0.002	55.6
0.007	62.9
0.012	67.1
0.017	70.9
0.027	76.5
0.037	80.8
0.047	84.1
0.057	86.8
0.067	89.1
0.077	90.9
0.087	92.6
0.097	94.1
0.107	95.4

Specimen 600-1-24-NH, 600-2-24-NH, 600-3-24-NH



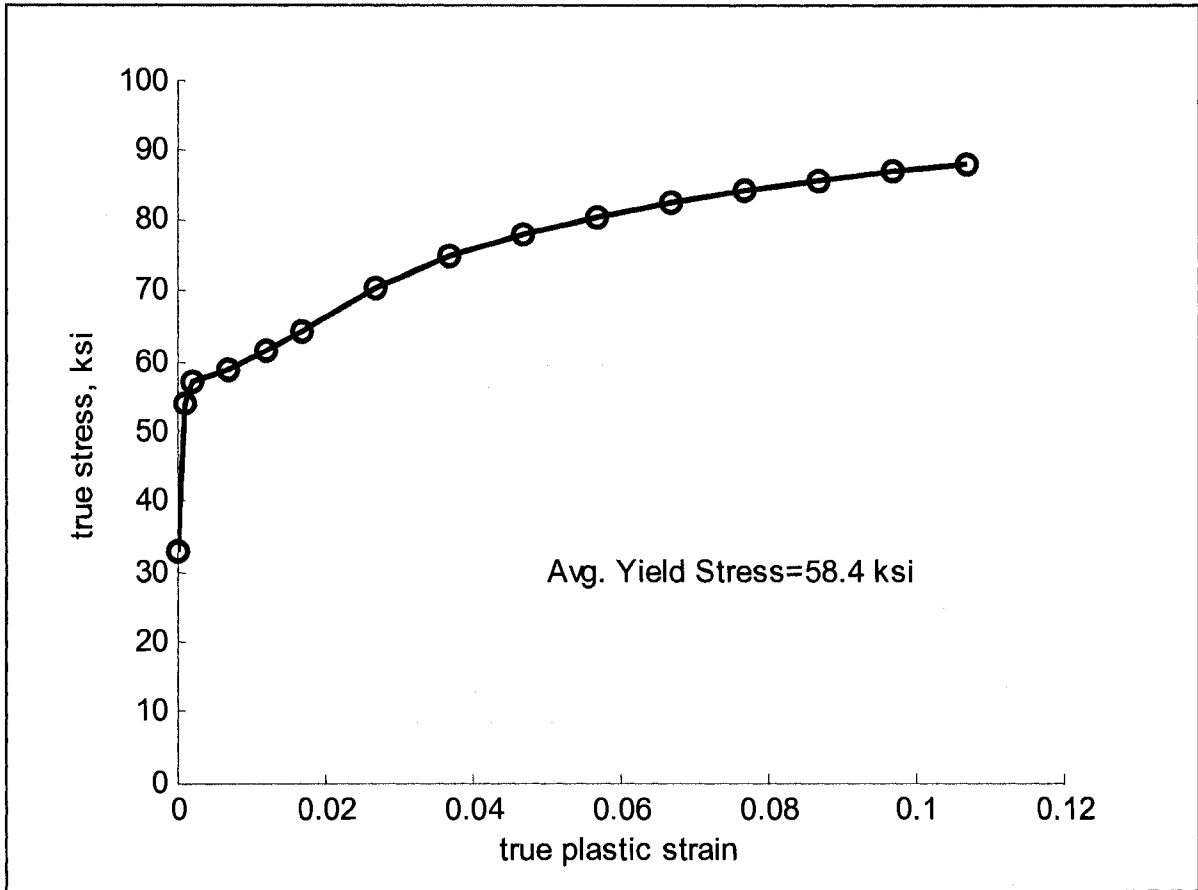
true plastic strain, ϵ_p	true stress, σ_{true} (ksi)
0	37.5
0.001	54.7
0.002	58.3
0.007	60.0
0.012	61.5
0.017	64.0
0.027	70.2
0.037	74.4
0.047	77.5
0.057	80.0
0.067	81.9
0.077	83.5
0.087	84.9
0.097	86.1
0.107	87.2

Specimen 600-1-24-H



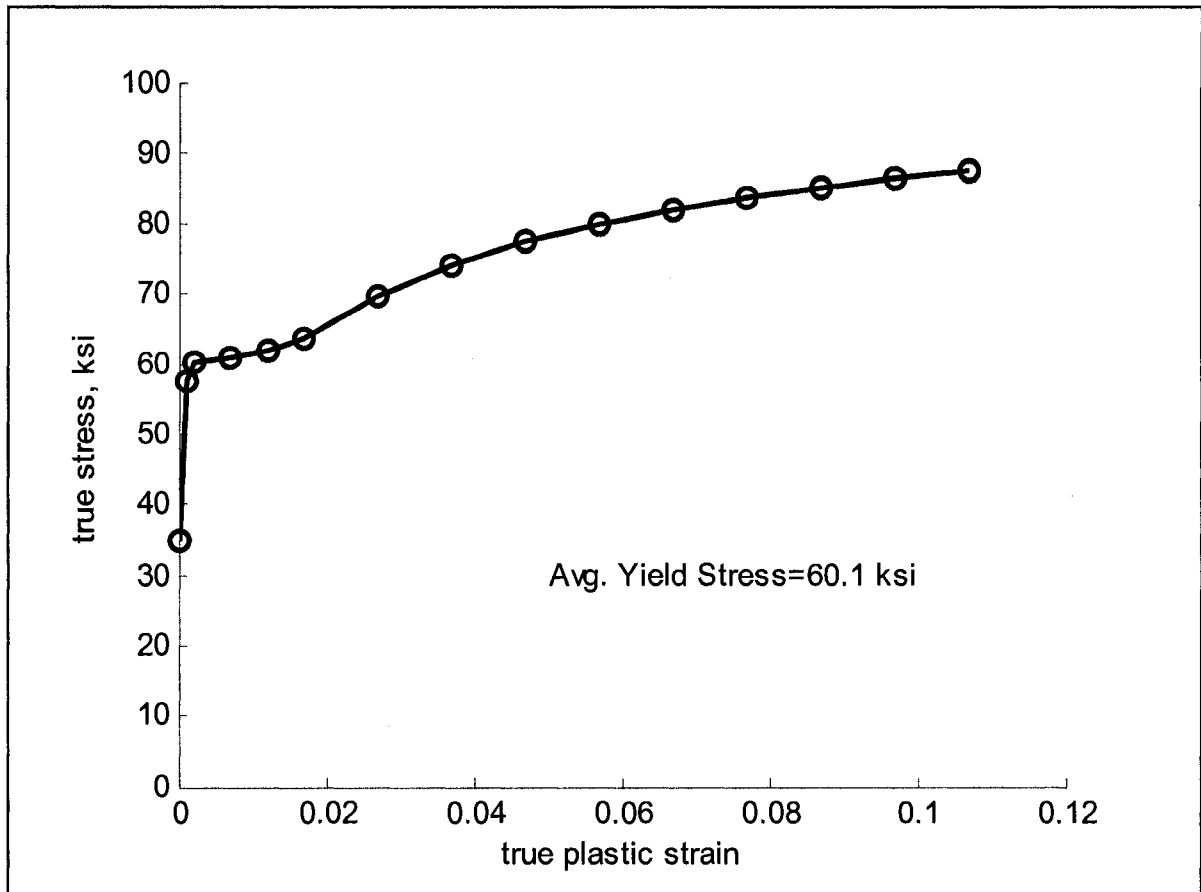
true plastic strain, ϵ_p	true stress, σ_{true} (ksi)
0	35.0
0.001	58.9
0.002	61.4
0.007	62.3
0.012	62.9
0.017	63.6
0.027	69.4
0.037	74.4
0.047	77.8
0.057	80.5
0.067	82.6
0.077	84.4
0.087	85.9
0.097	87.2
0.107	88.4

Specimen 600-2-24-H



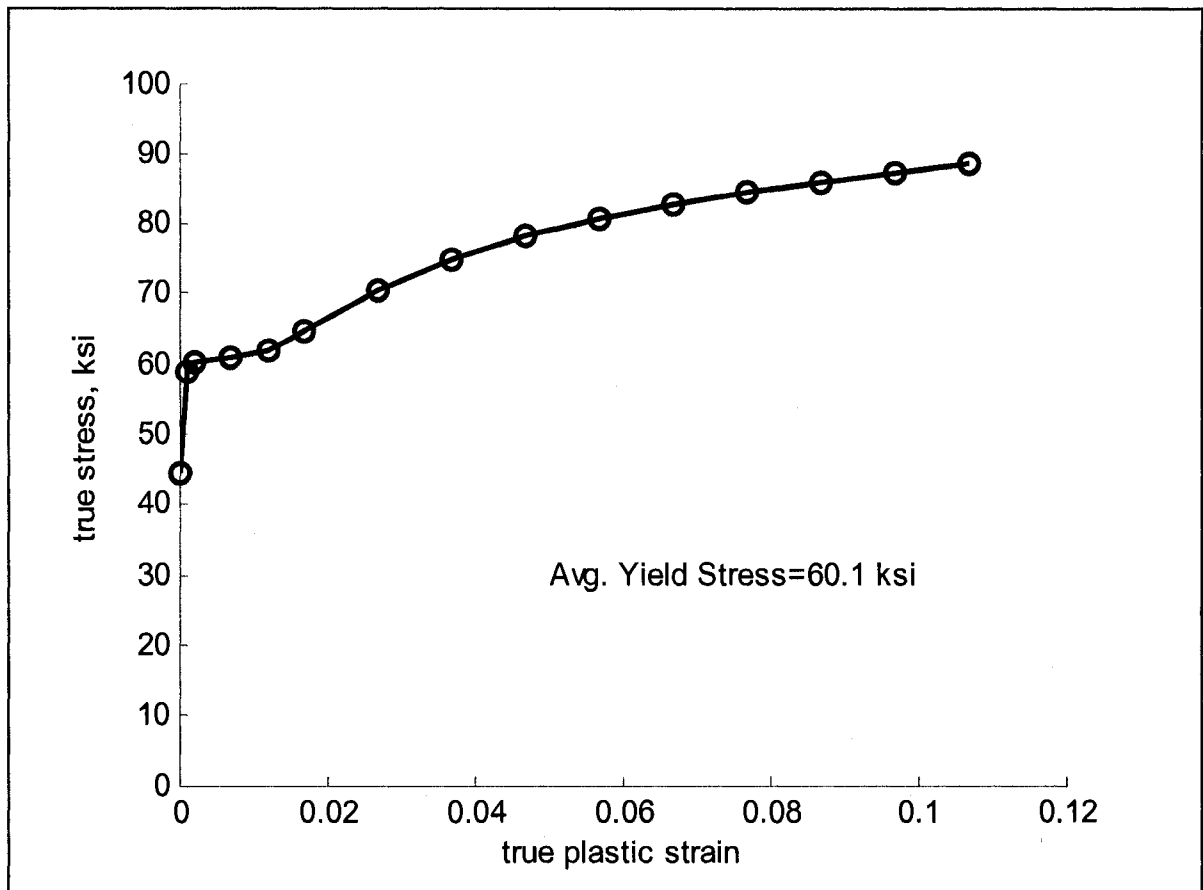
true plastic strain, ϵ_p	true stress, σ_{true} (ksi)
0	33.0
0.001	54.0
0.002	57.2
0.007	58.9
0.012	61.5
0.017	64.4
0.027	70.5
0.037	74.8
0.047	78.0
0.057	80.4
0.067	82.4
0.077	84.1
0.087	85.5
0.097	86.7
0.107	87.9

Specimen 600-3-24-H



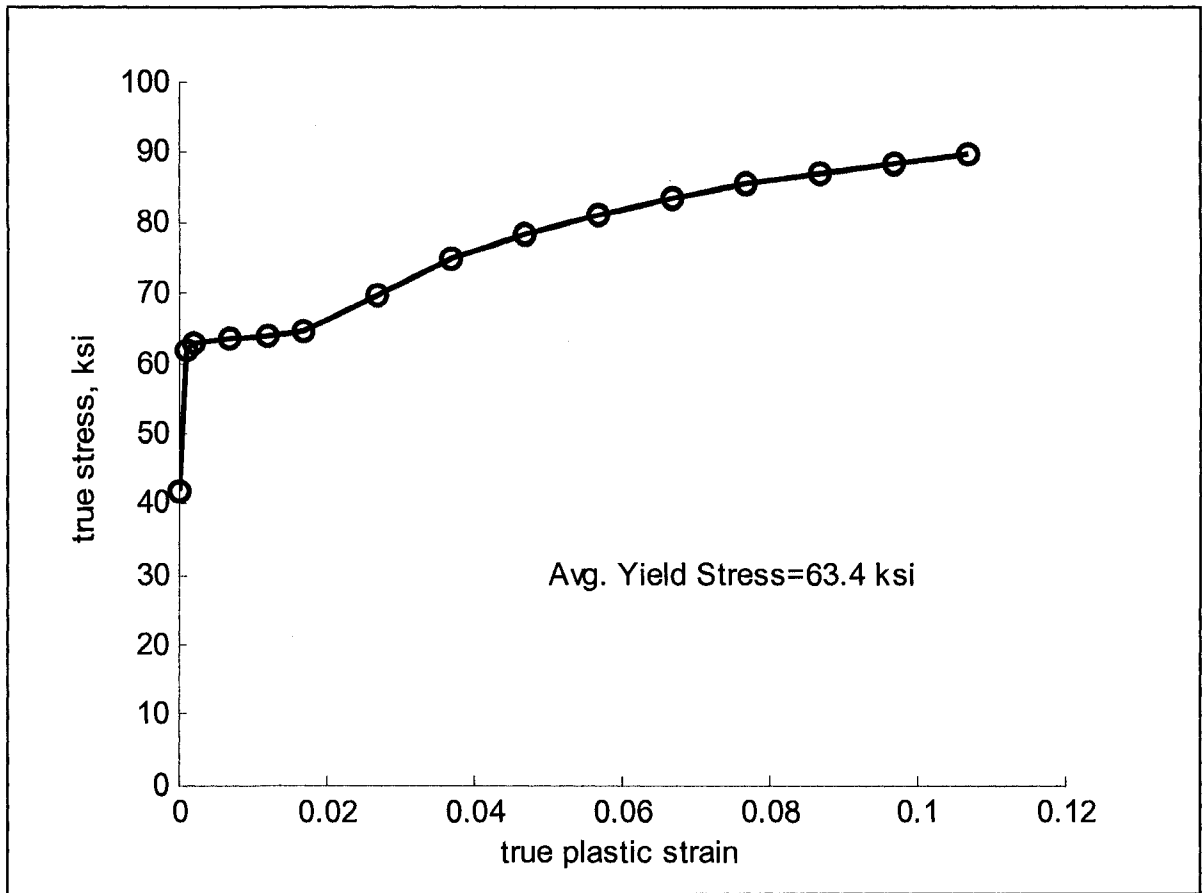
true plastic strain, ϵ_p	true stress, σ_{true} (ksi)
0	34.9
0.001	57.5
0.002	60.1
0.007	60.8
0.012	61.8
0.017	63.6
0.027	69.8
0.037	74.1
0.047	77.6
0.057	79.9
0.067	82.0
0.077	83.7
0.087	85.1
0.097	86.5
0.107	87.6

Specimen 600-1-48-NH



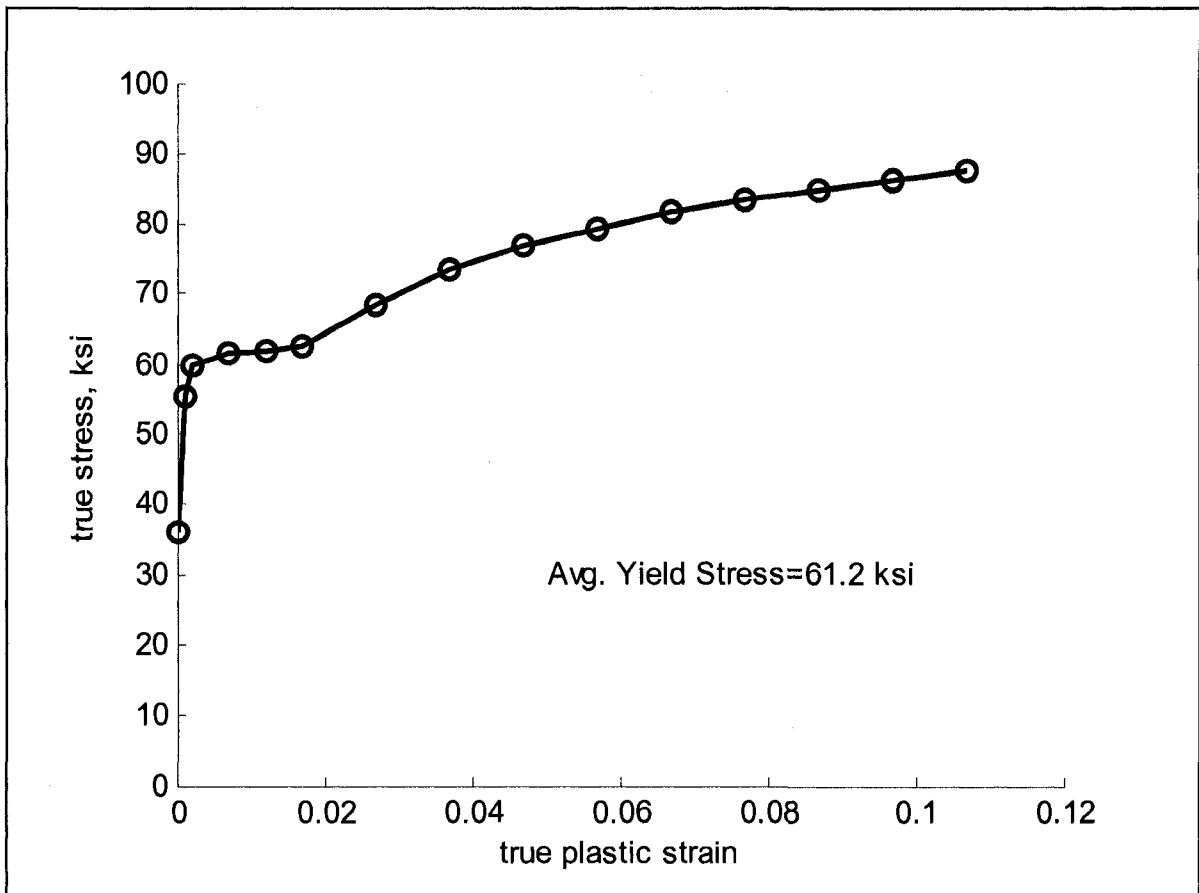
true plastic strain, ϵ_p	true stress, σ_{true} (ksi)
0	44.4
0.001	58.9
0.002	60.3
0.007	61.0
0.012	62.0
0.017	64.8
0.027	70.6
0.037	75.0
0.047	78.3
0.057	80.8
0.067	82.8
0.077	84.5
0.087	86.0
0.097	87.3
0.107	88.5

Specimen 600-2-48-NH



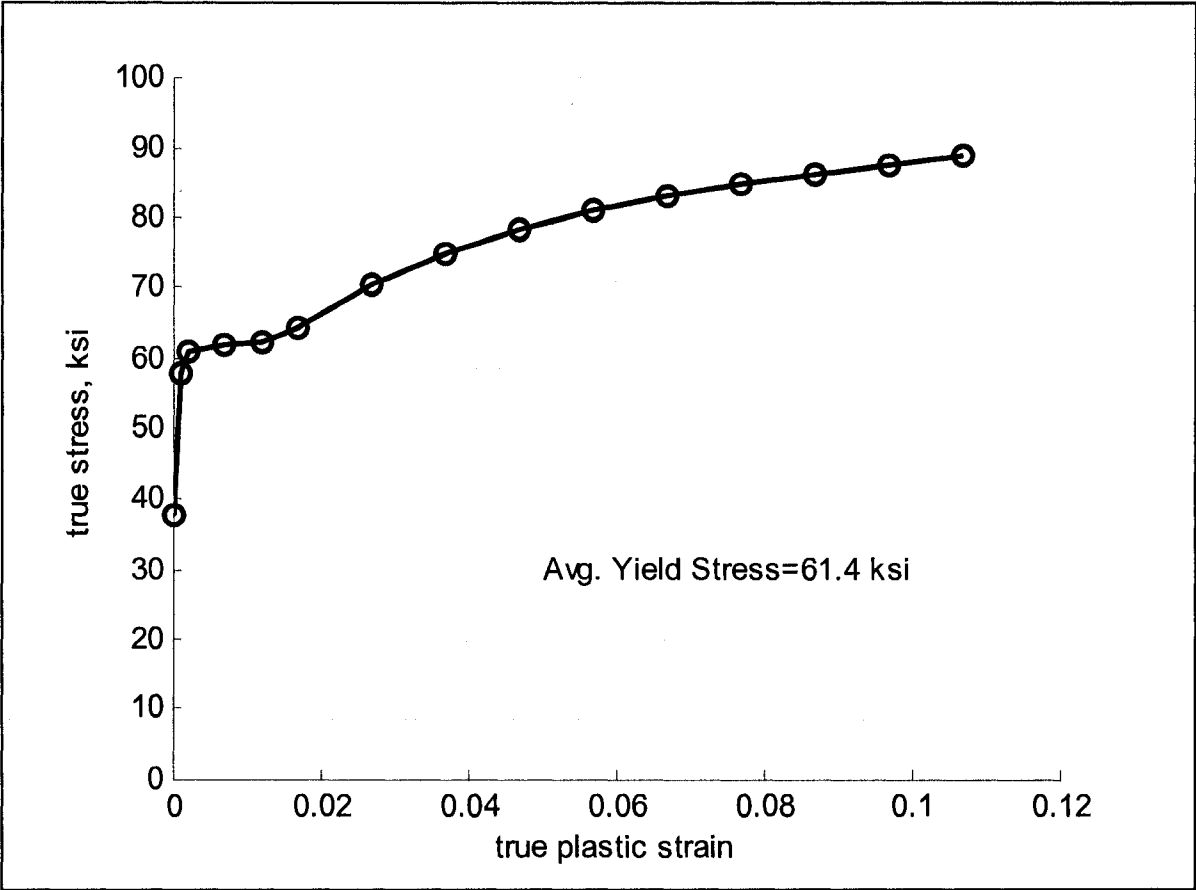
true plastic strain, ϵ_p	true stress, σ_{true} (ksi)
0	41.9
0.001	62.1
0.002	63.1
0.007	63.6
0.012	64.0
0.017	64.5
0.027	69.8
0.037	75.0
0.047	78.5
0.057	81.2
0.067	83.5
0.077	85.3
0.087	87.0
0.097	88.4
0.107	89.6

Specimen 600-3-48-NH



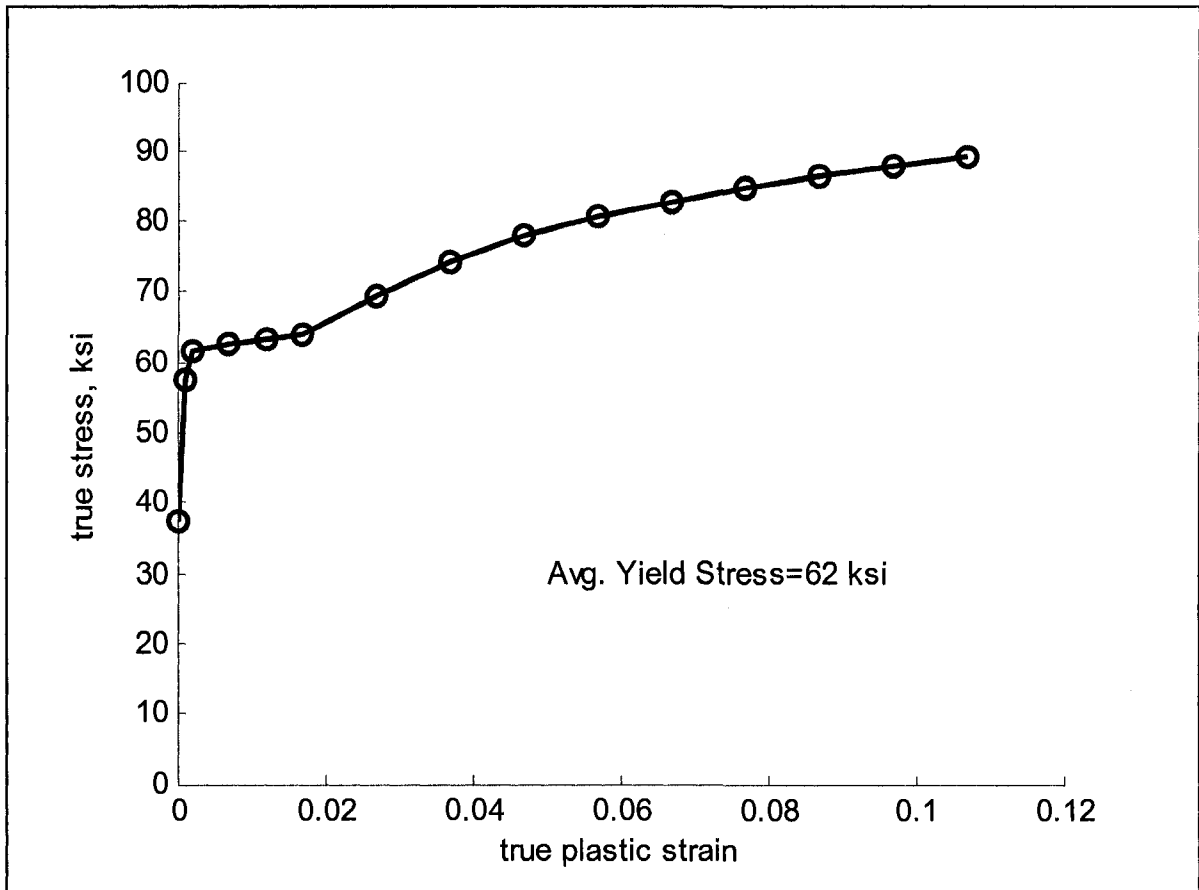
true plastic strain, ϵ_p	true stress, σ_{true} (ksi)
0	36.0
0.001	55.6
0.002	60.0
0.007	61.7
0.012	62.0
0.017	62.5
0.027	68.5
0.037	73.4
0.047	76.9
0.057	79.4
0.067	81.6
0.077	83.3
0.087	84.9
0.097	86.2
0.107	87.4

Specimen 600-1-48-H



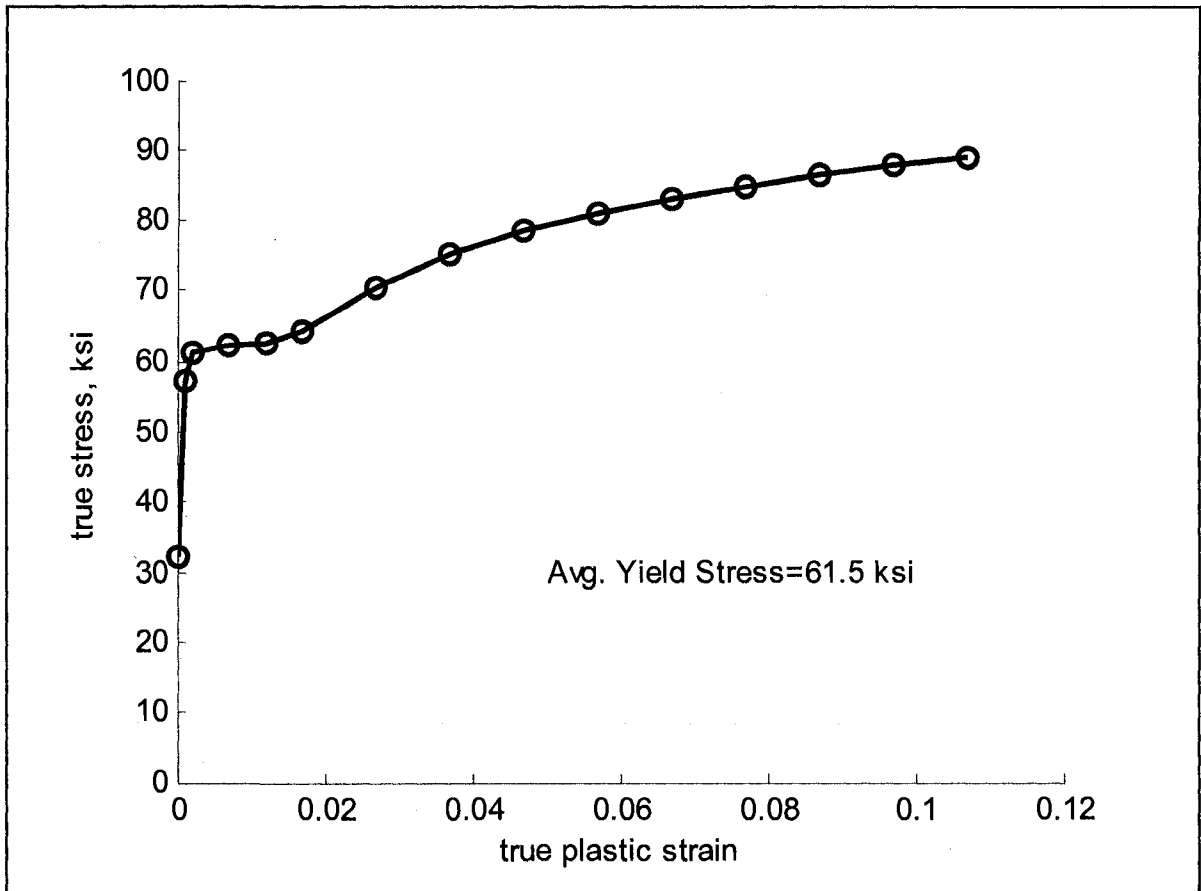
true plastic strain, ϵ_p	true stress, σ_{true} ksi
0	37.5
0.001	57.7
0.002	60.9
0.007	61.9
0.012	62.4
0.017	64.3
0.027	70.4
0.037	75.0
0.047	78.4
0.057	81.0
0.067	83.1
0.077	84.8
0.087	86.3
0.097	87.7
0.107	88.9

Specimen 600-2-48-H



true plastic strain, ϵ_p	true stress, σ_{true} ksi
0	37.4
0.001	57.6
0.002	61.6
0.007	62.6
0.012	63.3
0.017	64.1
0.027	69.4
0.037	74.2
0.047	77.8
0.057	80.6
0.067	82.9
0.077	84.8
0.087	86.4
0.097	87.8
0.107	89.1

Specimen 600-3-48-H

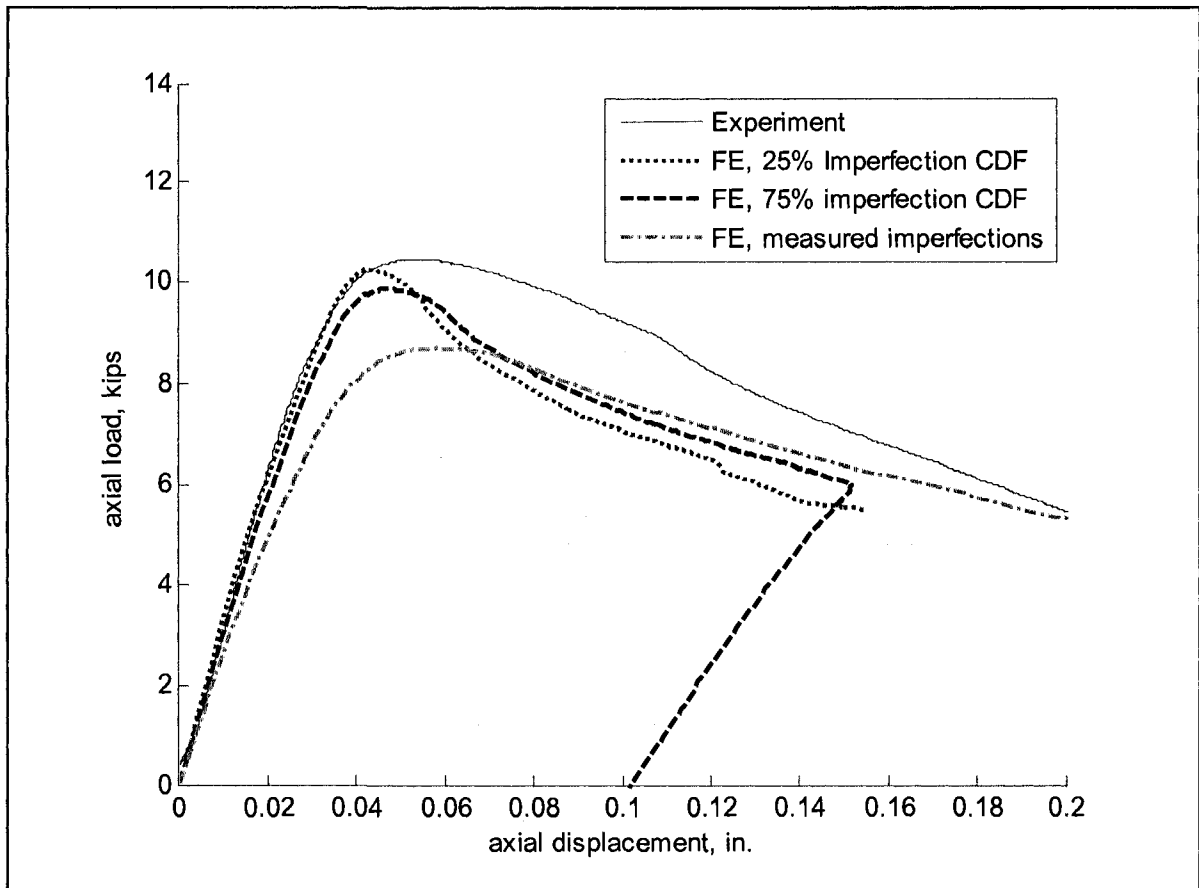


true plastic strain, ϵ_p	true stress, σ_{true} (ksi)
0	32.4
0.001	57.1
0.002	61.3
0.007	62.2
0.012	62.6
0.017	64.5
0.027	70.4
0.037	75.2
0.047	78.6
0.057	81.1
0.067	83.2
0.077	84.9
0.087	86.5
0.097	87.8
0.107	89.0

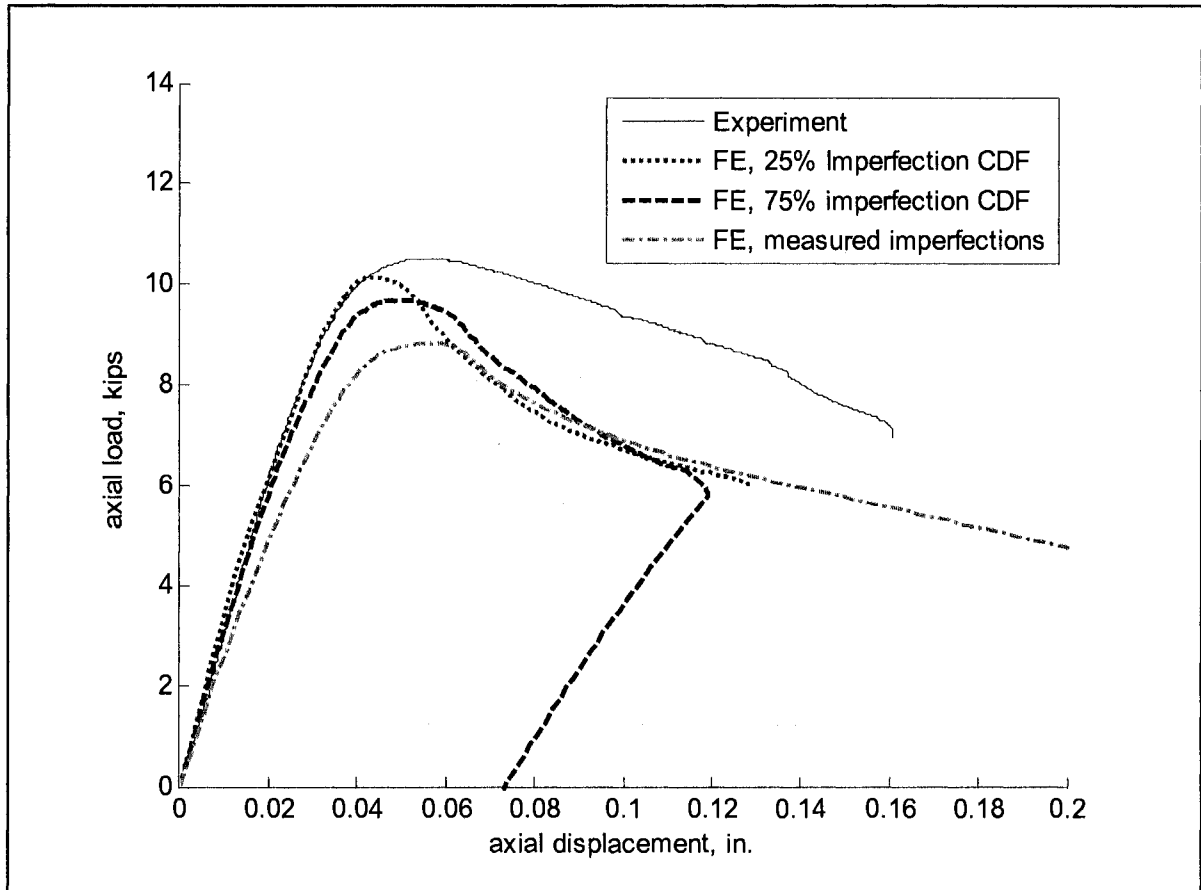
Appendix I

Column experiment nonlinear FE simulation results

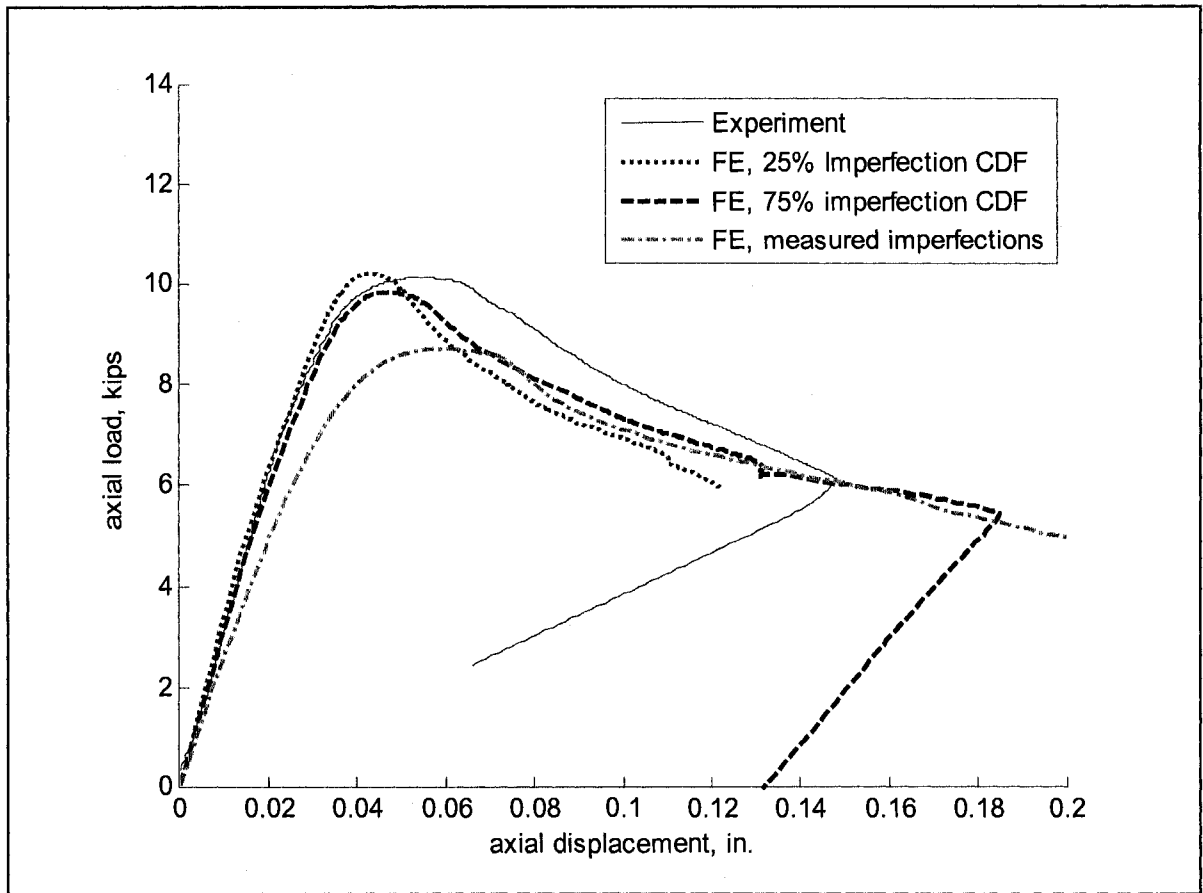
Specimen 362-1-24-NH



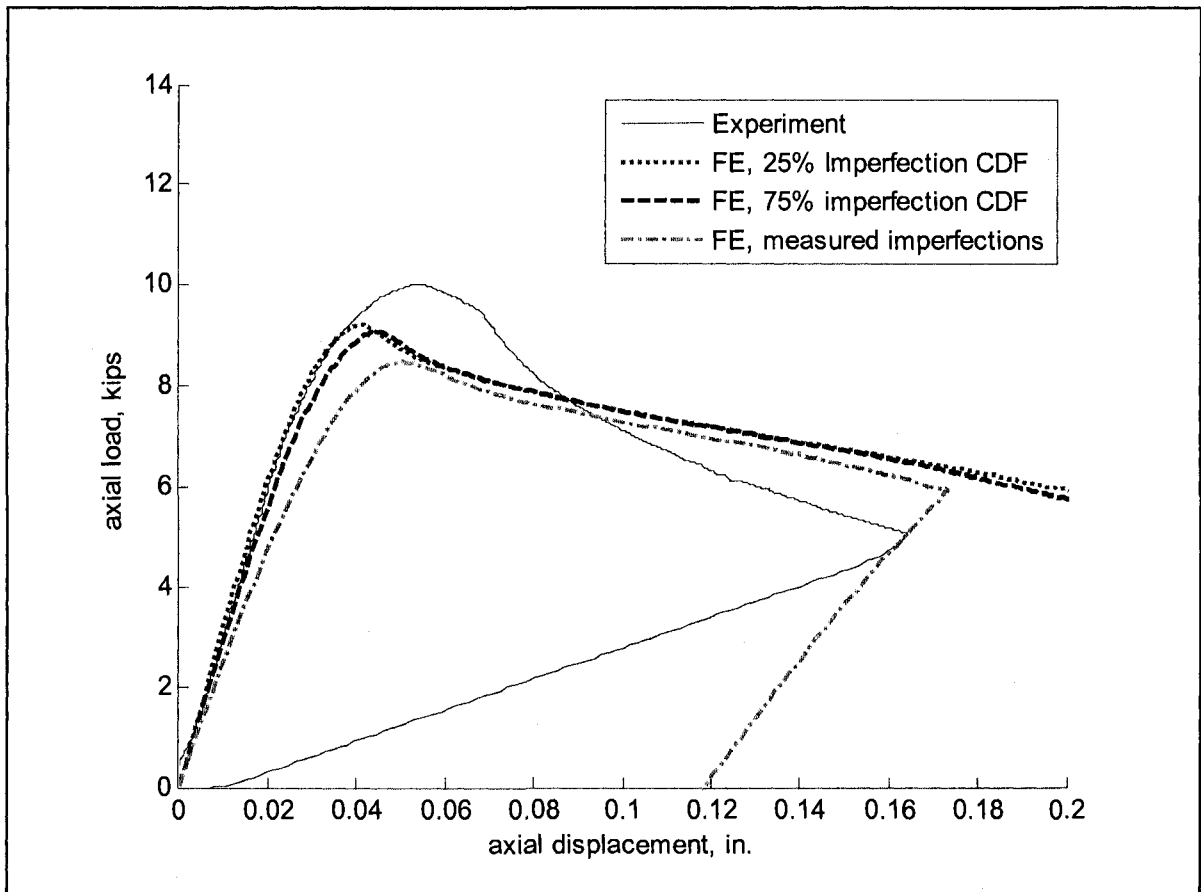
Specimen 362-2-24-NH



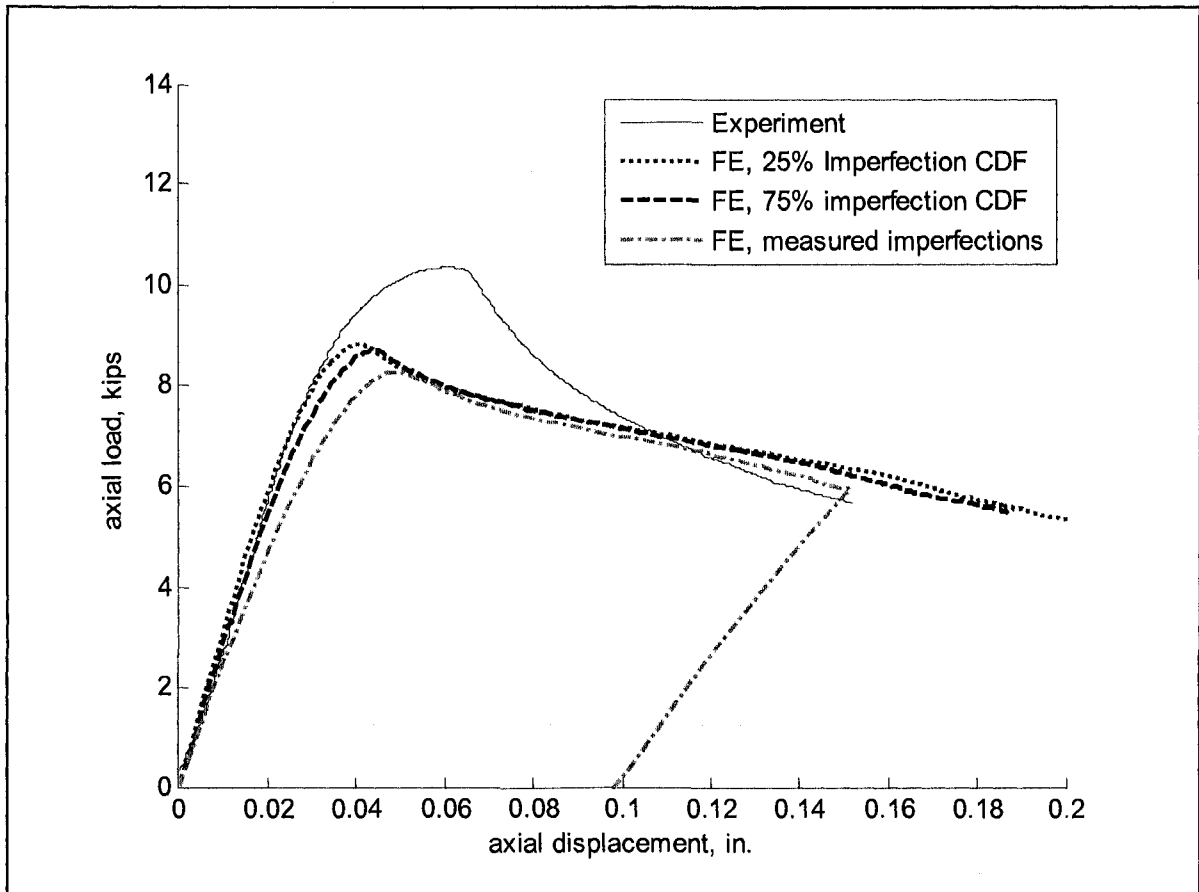
Specimen 362-3-24-NH



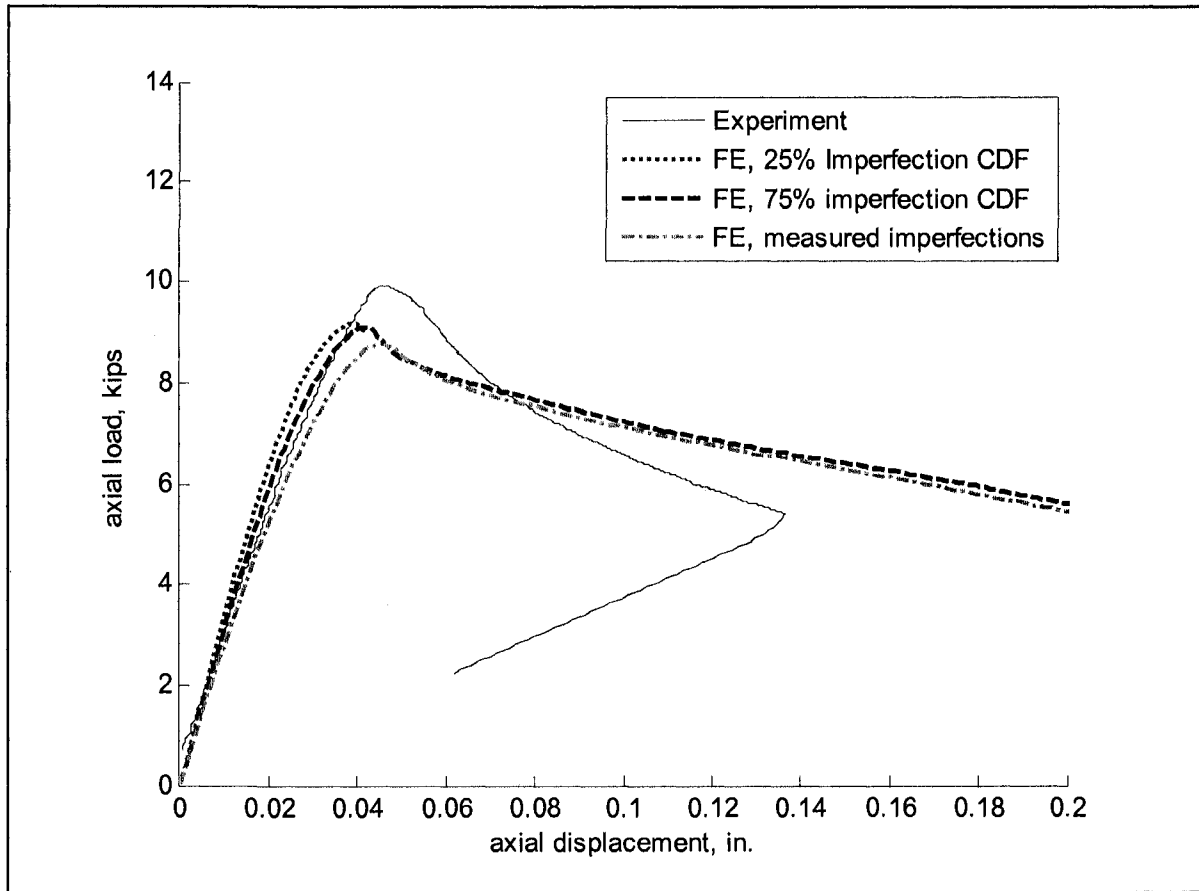
Specimen 362-1-24-H



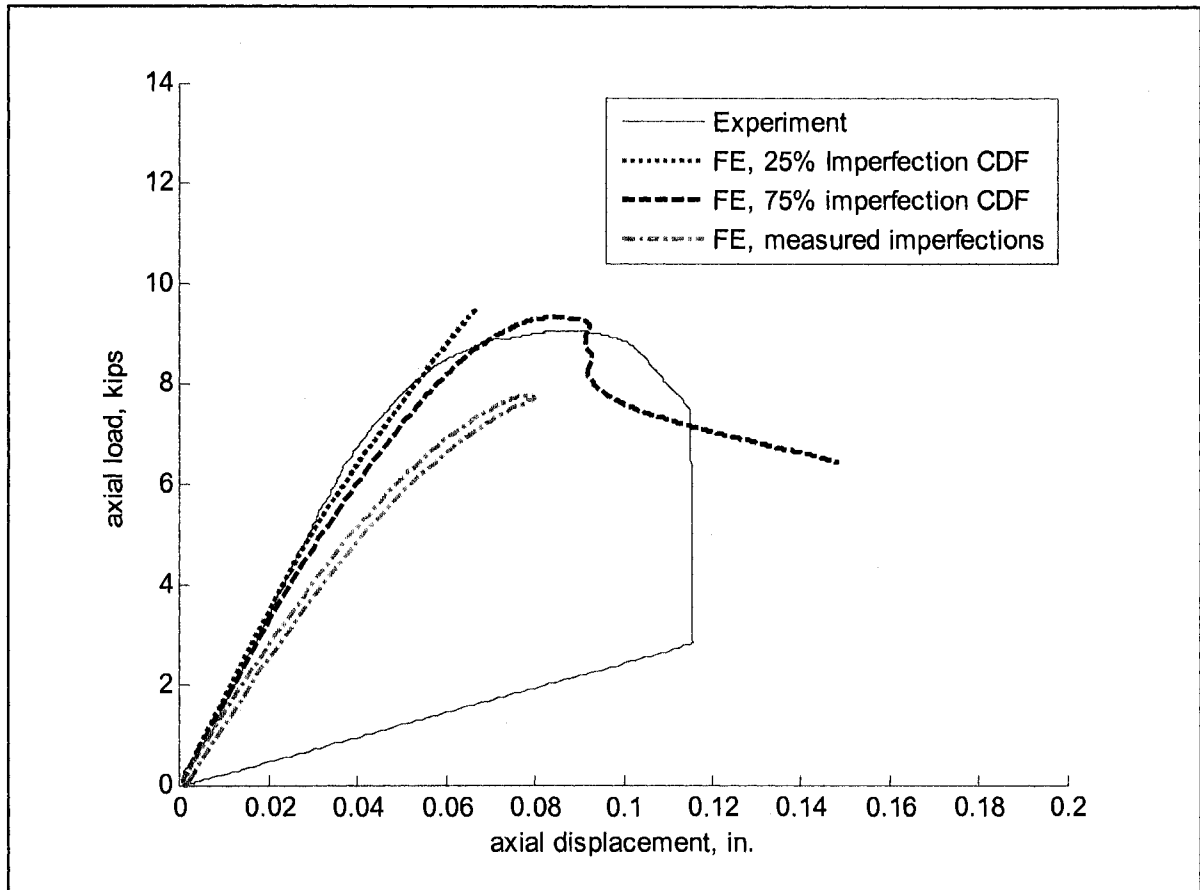
Specimen 362-2-24-H



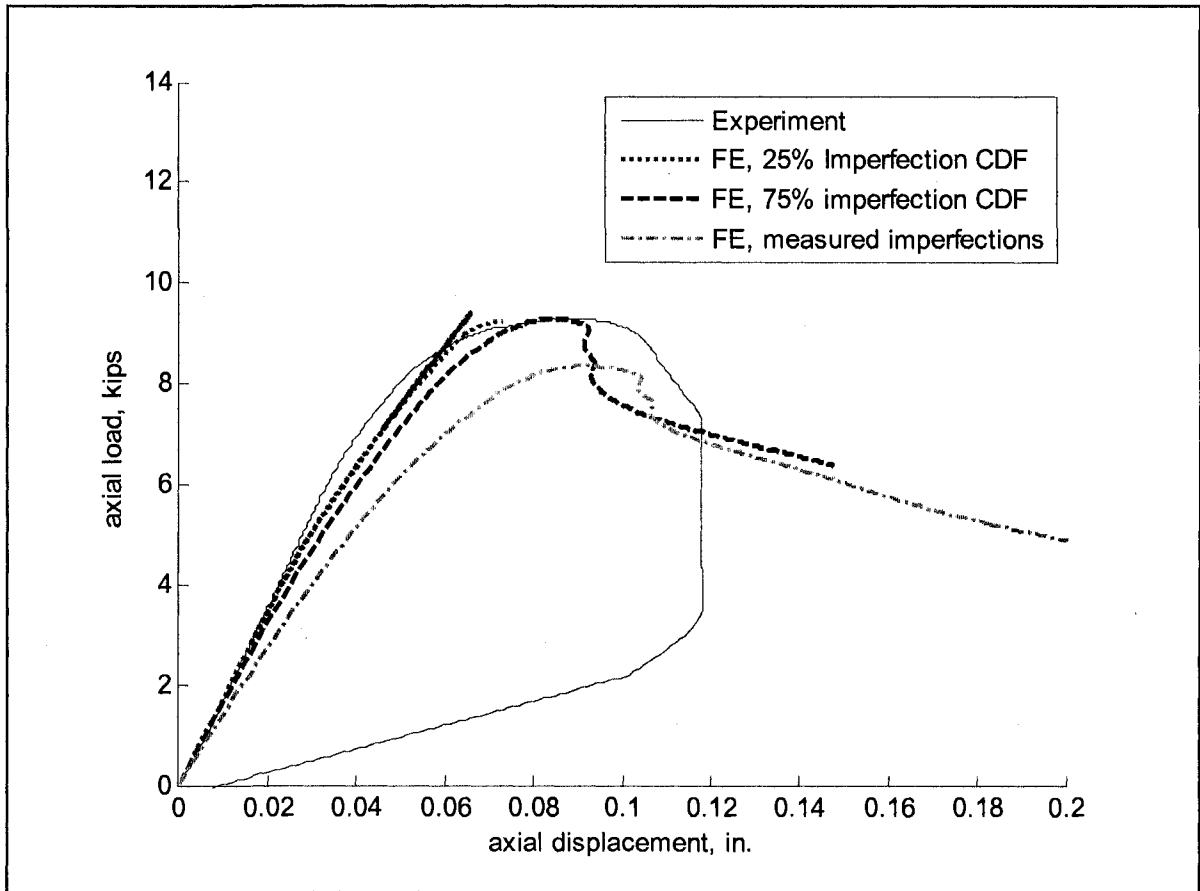
Specimen 362-3-24-H



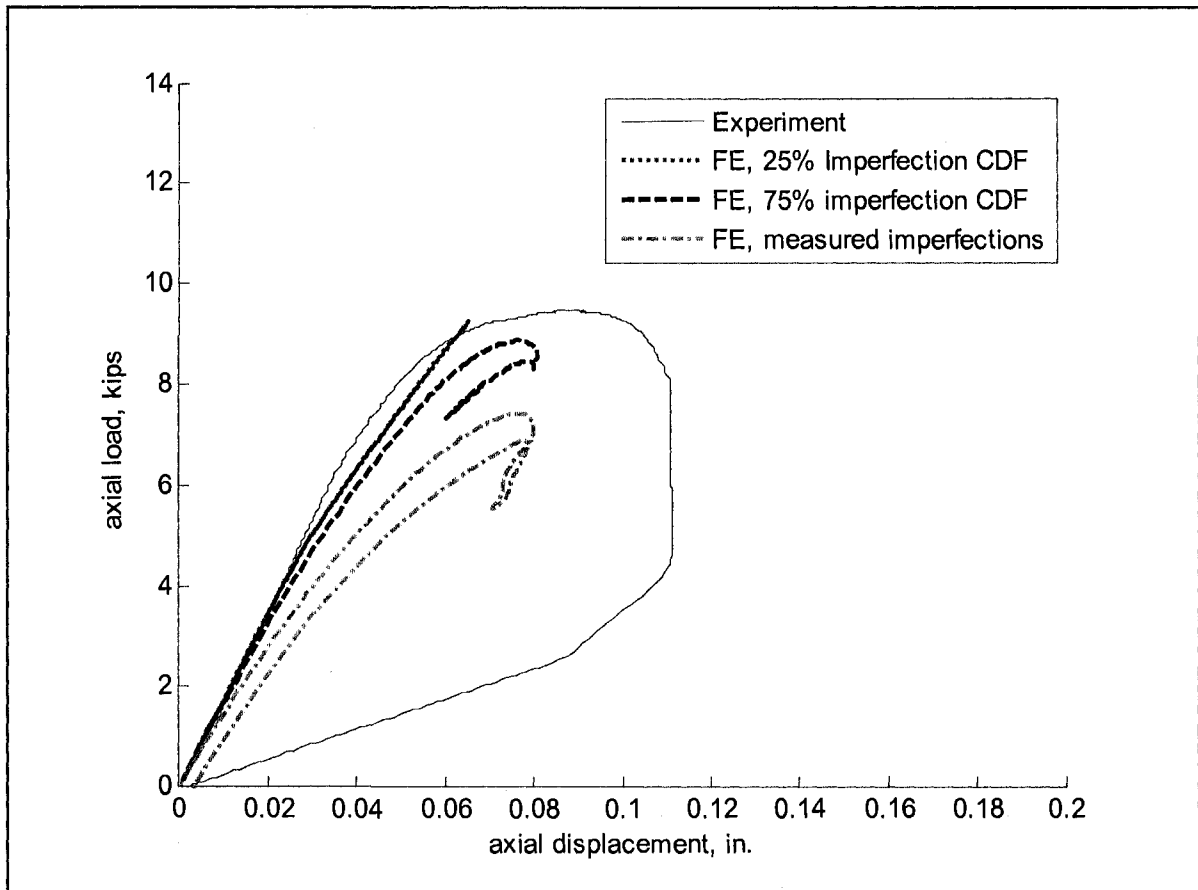
Specimen 362-1-48-NH



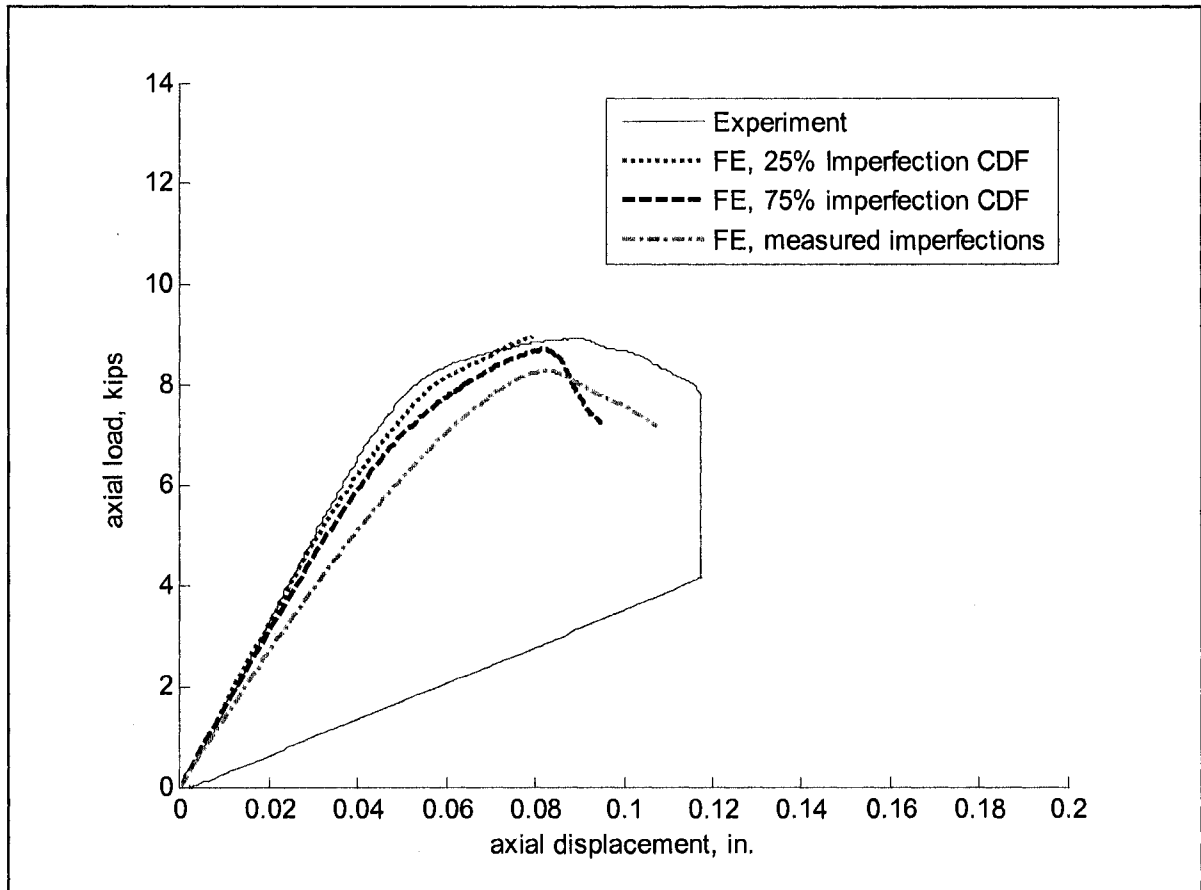
Specimen 362-2-48-NH



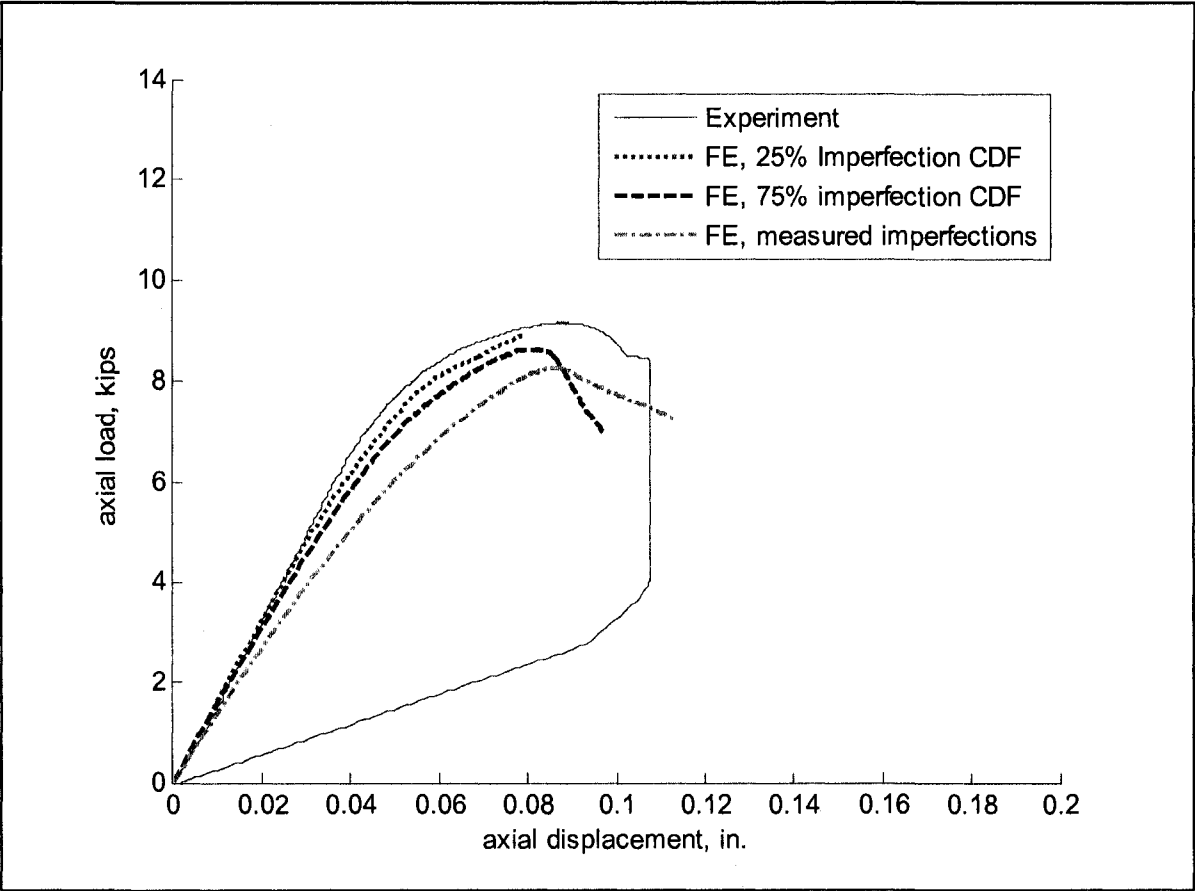
Specimen 362-3-48-NH



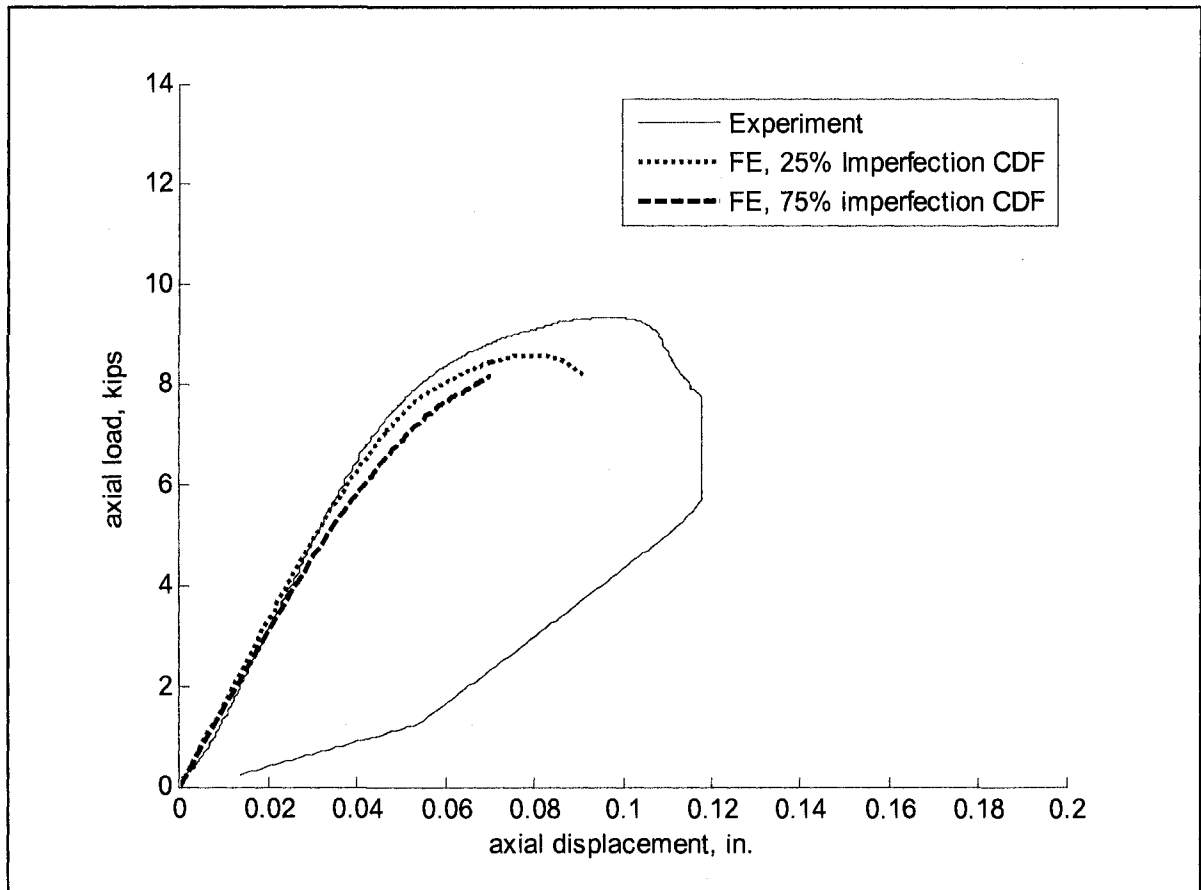
Specimen 362-1-48-H



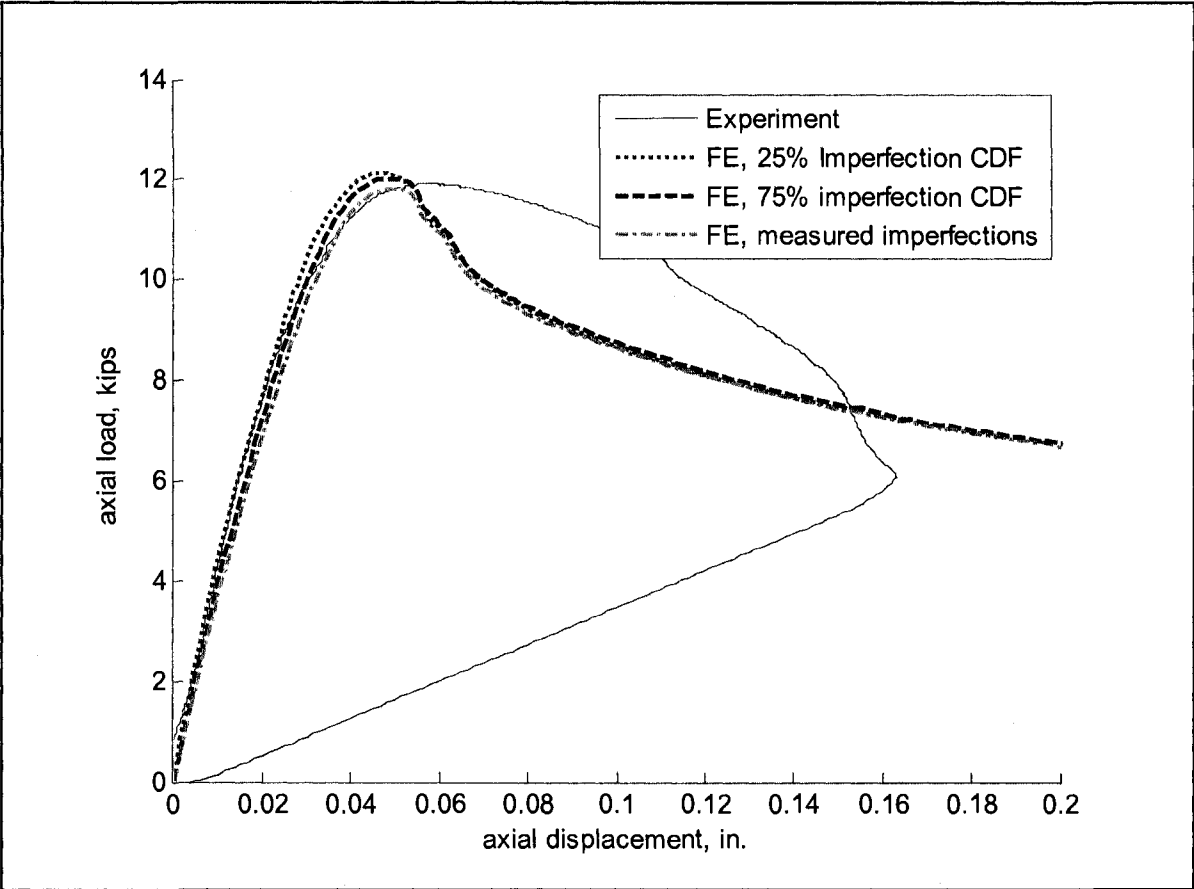
Specimen 362-2-48-H



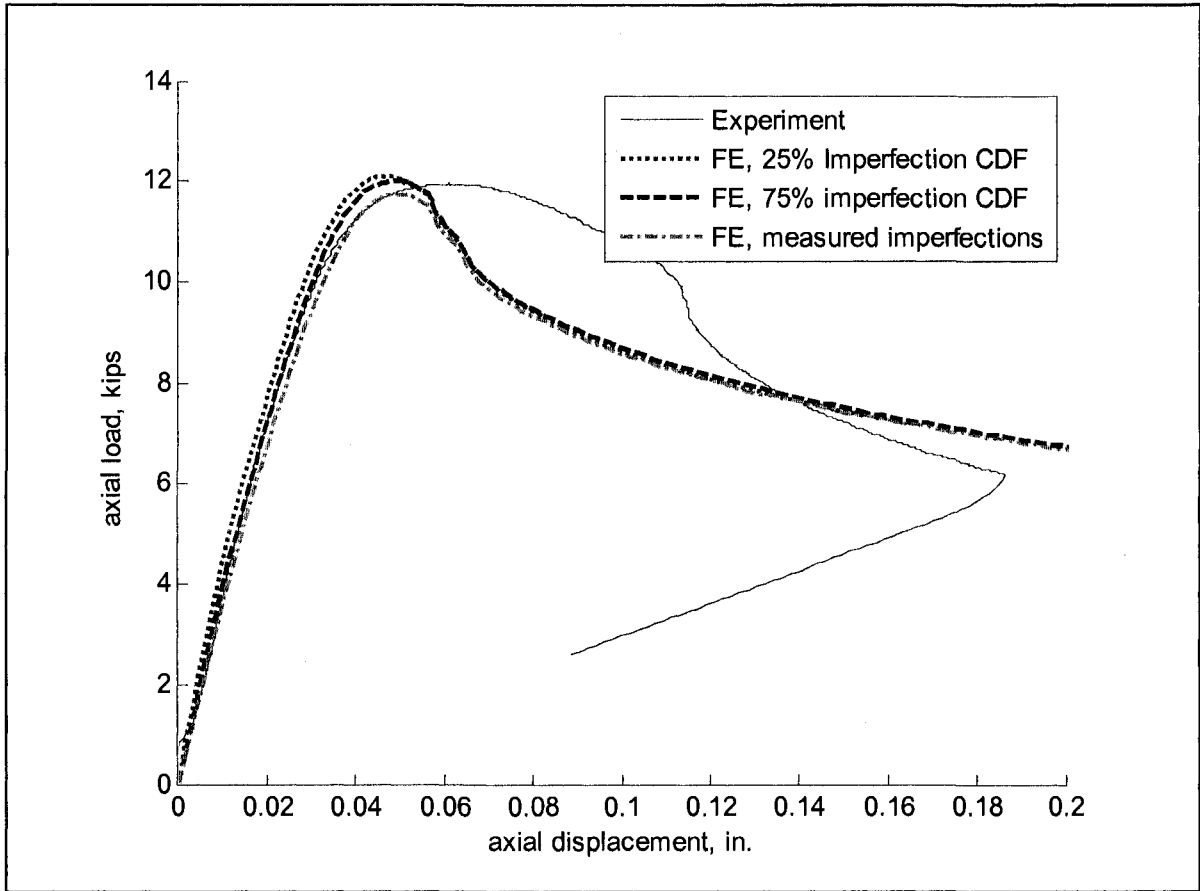
Specimen 362-3-48-H



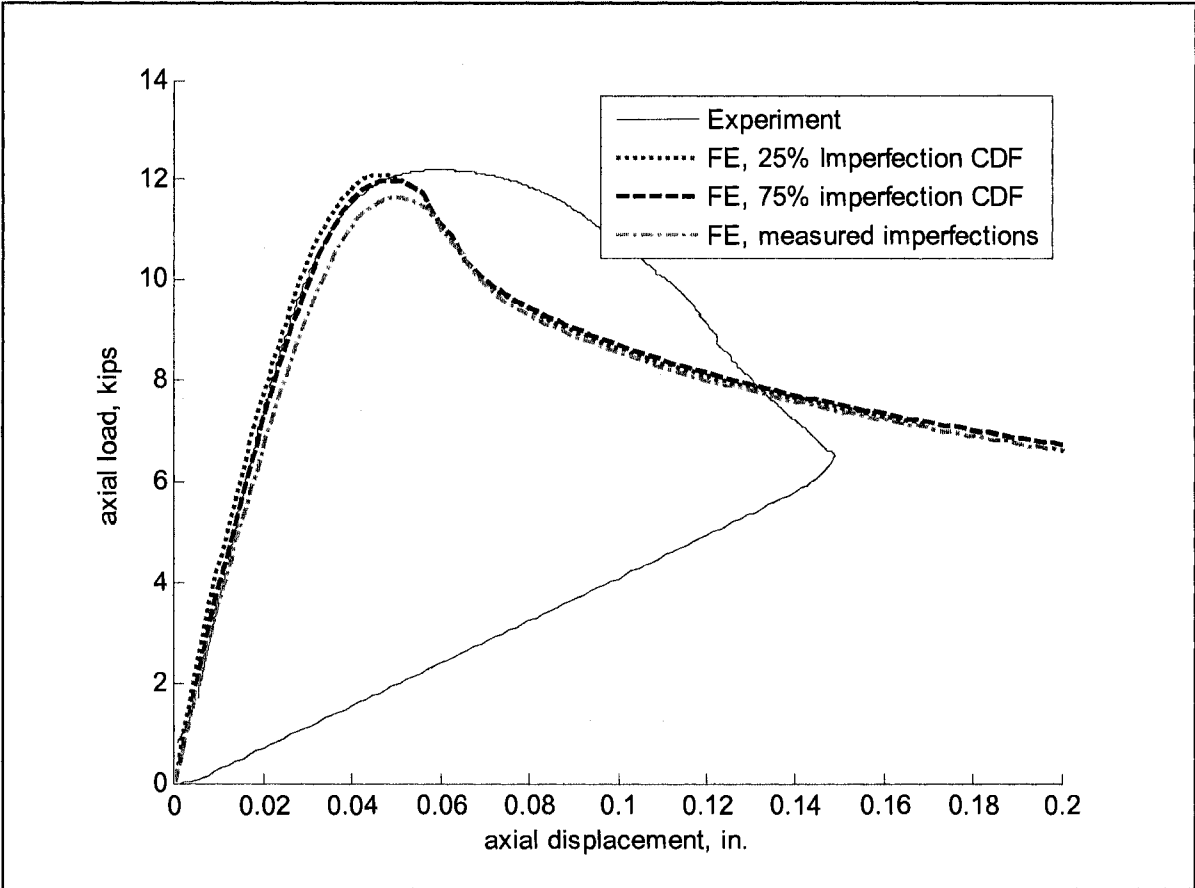
Specimen 600-1-24-NH



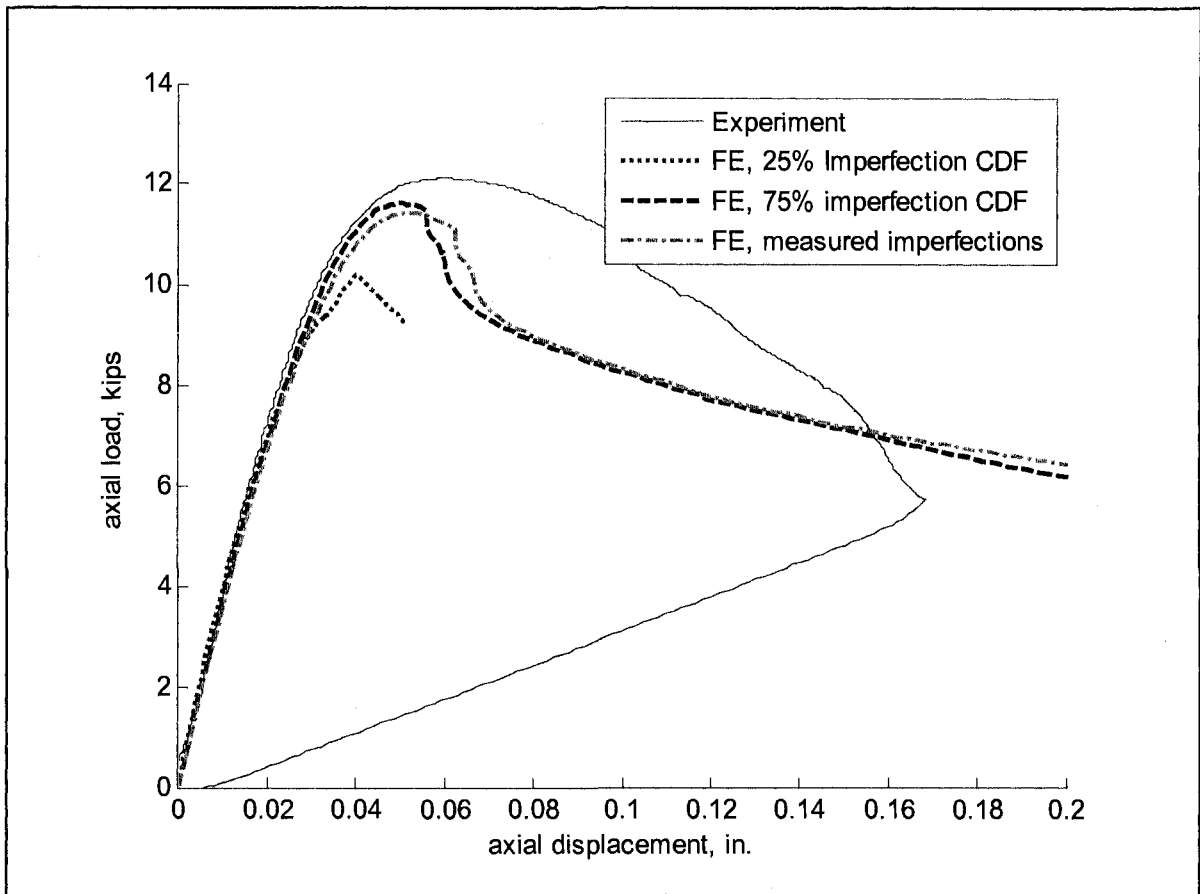
Specimen 600-2-24-NH



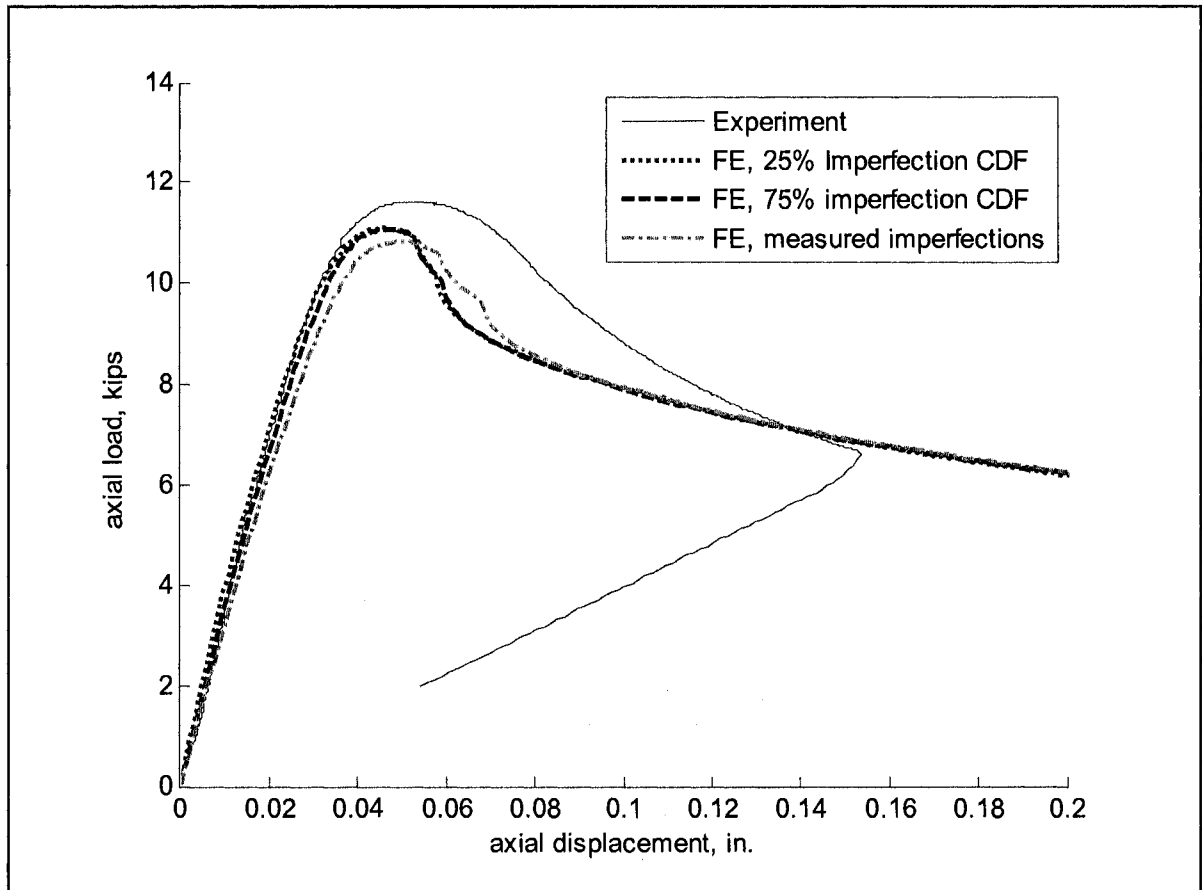
Specimen 600-3-24-NH



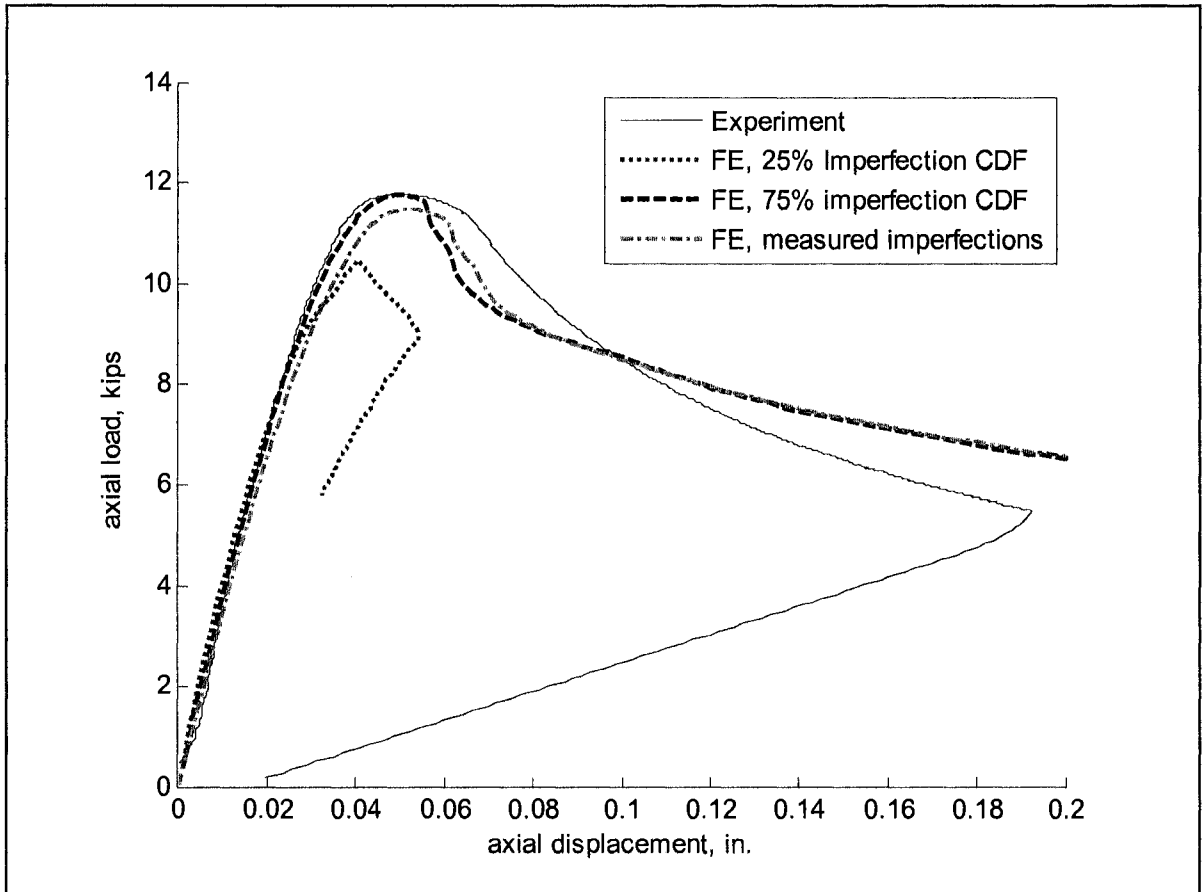
Specimen 600-1-24-H



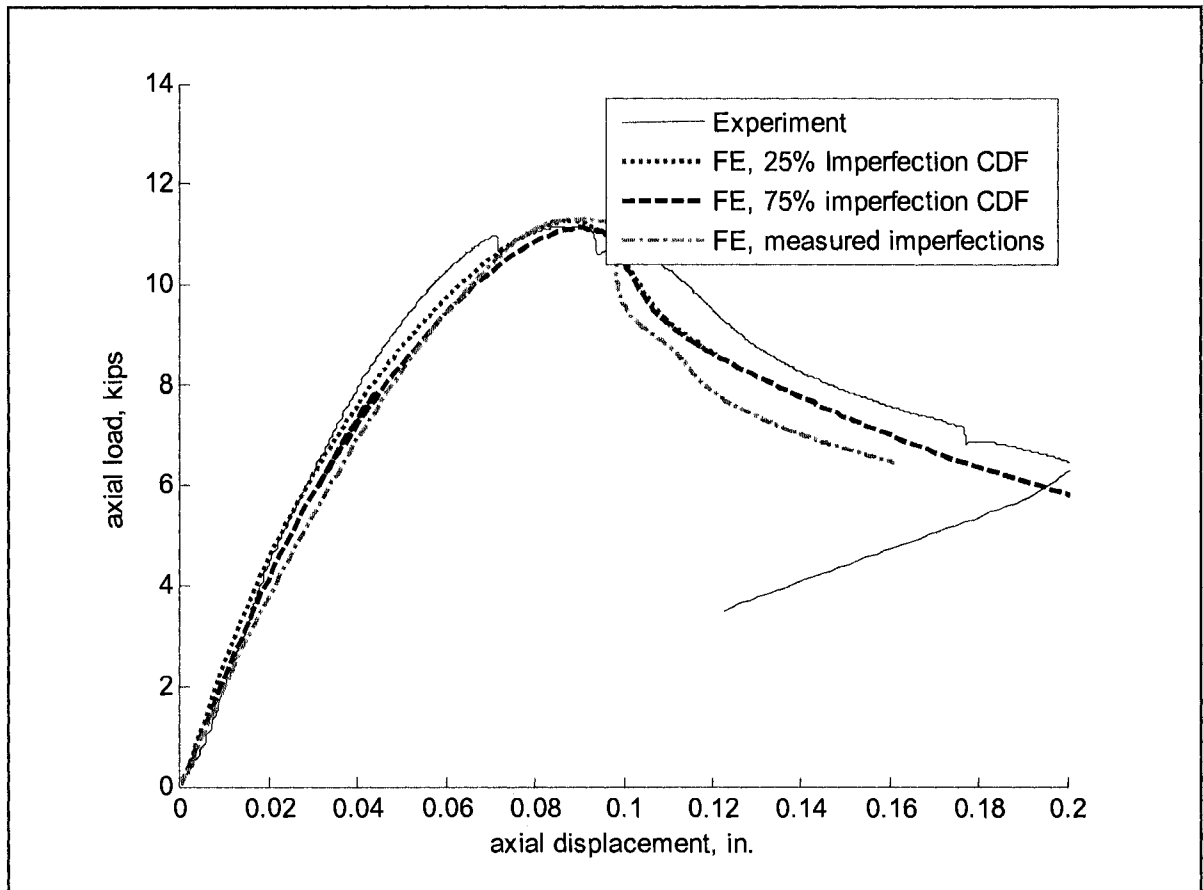
Specimen 600-2-24-H



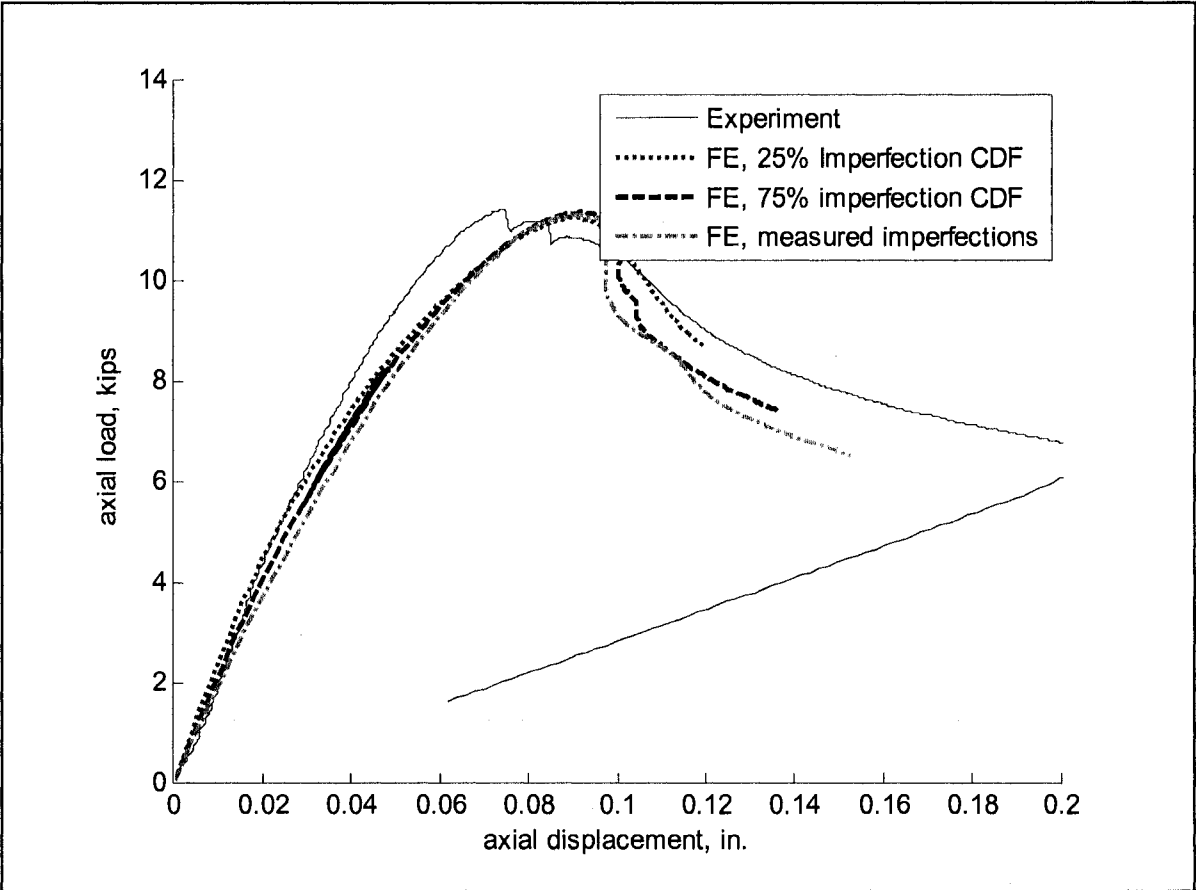
Specimen 600-3-24-H



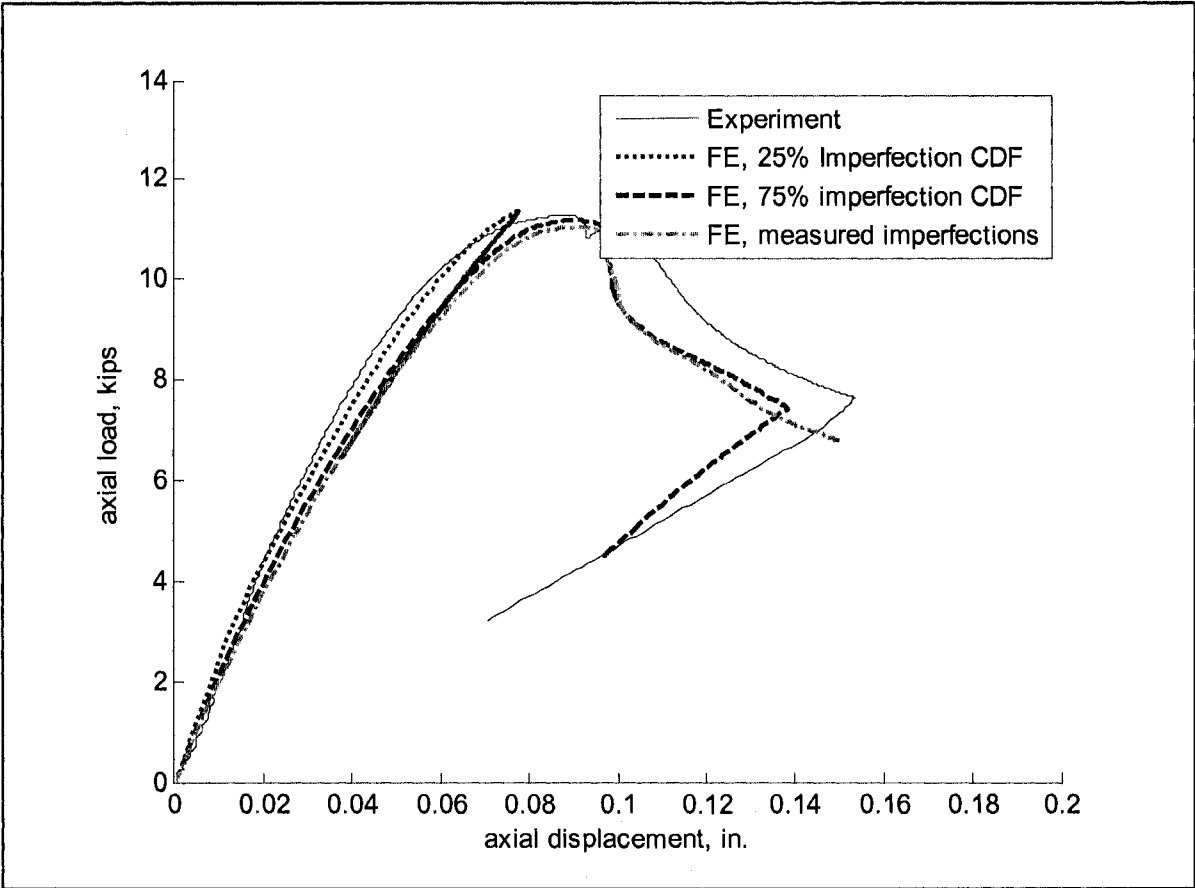
Specimen 600-1-48-NH



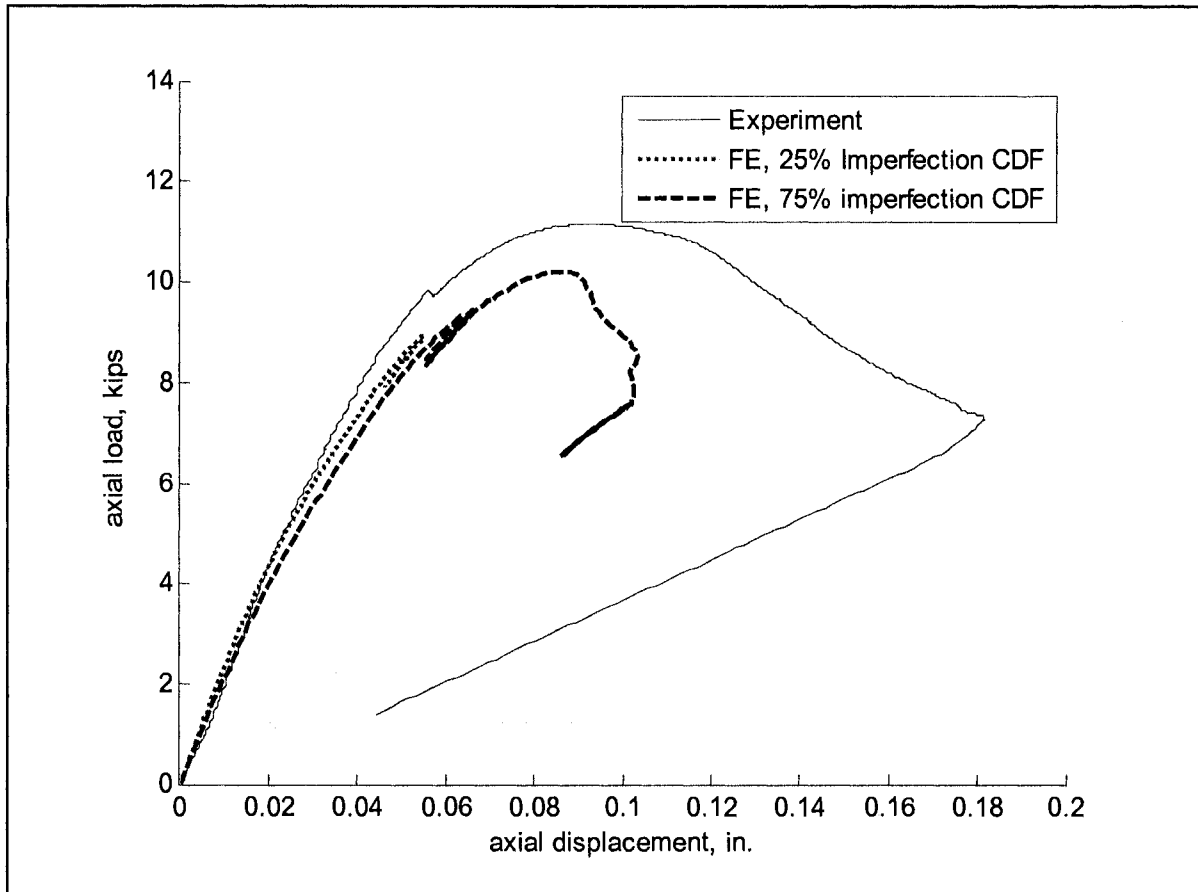
Specimen 600-2-48-NH



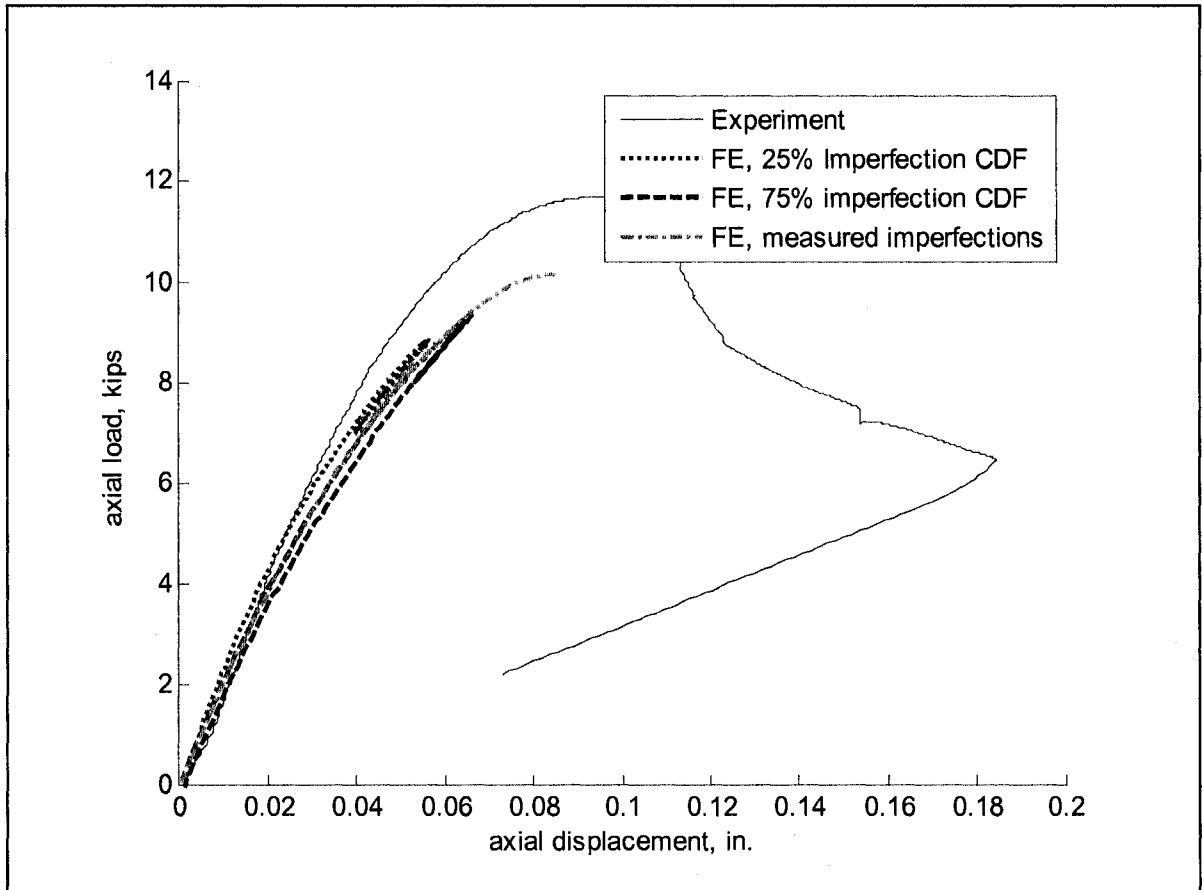
Specimen 600-3-48-NH



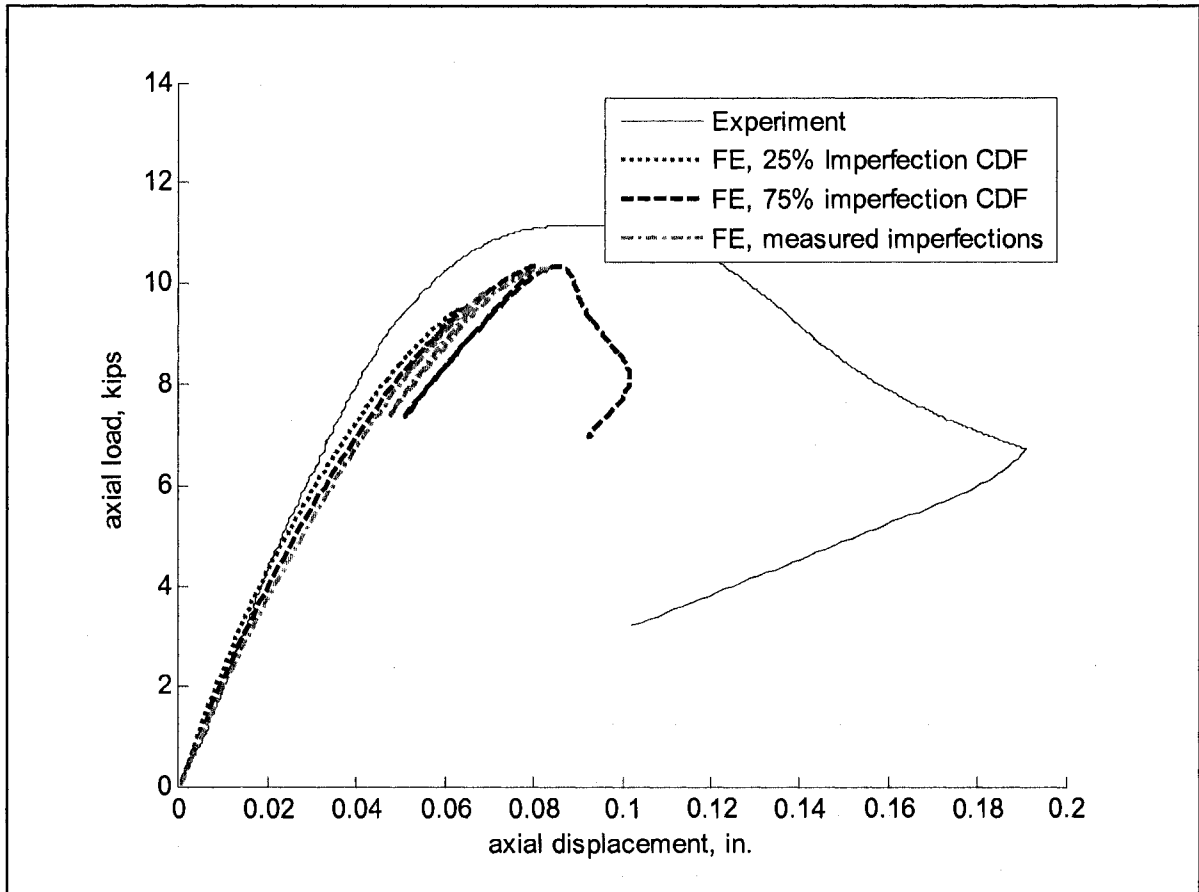
Specimen 600-1-48-H



Specimen 600-2-48-H



Specimen 600-3-48-H



Appendix J Contact simulation in ABAQUS

The friction-bearing end conditions were chosen for the experimental program described in Chapter 5 because they allowed for convenient alignment and testing of the column specimens. These boundary conditions were expected to behave as fixed-fixed, although during the test slipping of the cross-section and lifting off of the specimens were observed for some specimens in the post-peak region of the load-displacement curve. A nonlinear FE study was performed in ABAQUS where the experiment friction-bearing boundary conditions were replicated using contact modeling (Moen and Schafer 2007a). These end conditions allowed deformation of the cross-section at the bearing ends under load (slipping) and lift off of the bearing ends. A master analytical rigid surface was defined to represent the top and bottom platen as shown in Figure J.1 and each surface was assigned a reference node. The rigid surfaces simulate fixed-fixed conditions by restraining the reference node degrees of freedom, and the specimen was loaded by applying an imposed displacement to the bottom surface reference node. Top and bottom node-based slave surfaces were defined to simulate the bearing end of each specimen. The tributary bearing area was defined at each node in the slave surface to ensure that contact stresses were simulated accurately in ABAQUS.

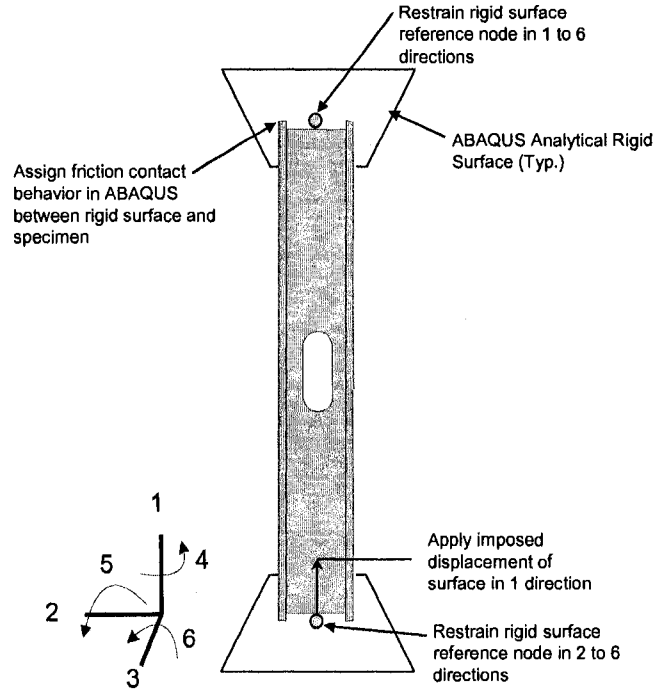


Figure J.1 Contact boundary condition as implemented in ABAQUS

A Coulomb friction model was enforced in ABAQUS between the master and slave surfaces by defining a static and kinetic coefficient of friction, μ_s and μ_k , for steel-on-steel contact. The assumed values for μ_s and μ_k were 0.7 and 0.6 in this study (Oden and Martins 1985). Slip occurs in the model once the shear stress at the contact interface exceeds $\mu_s f_n$, where f_n is the normal contact stress at the bearing surface.

The locations of the rigid surfaces were defined to be in contact with the specimen ends when the first step of the analysis began. This does not guarantee perfect contact in a computational sense, and so the ABAQUS command ADJUST was used to zero the contact surface and avoid numerical instabilities during the first analysis step. The ADJUST command modifies the geometry of the specimen to close infinitesimal gaps, but does not result in internal forces or moments in the specimen.

To evaluate the influence of the contact boundary conditions, the load-displacement response of specimen 600-2-24-NH assuming contact boundary conditions was evaluated against an FE simulation employing the fixed-fixed boundary conditions described in Figure 7.27. The results of the two simulations are almost identical until well into the post-peak range as shown in Figure J.2, demonstrating that the fixed-fixed boundary conditions are a viable approximation to the actual boundary conditions in an FE simulation.

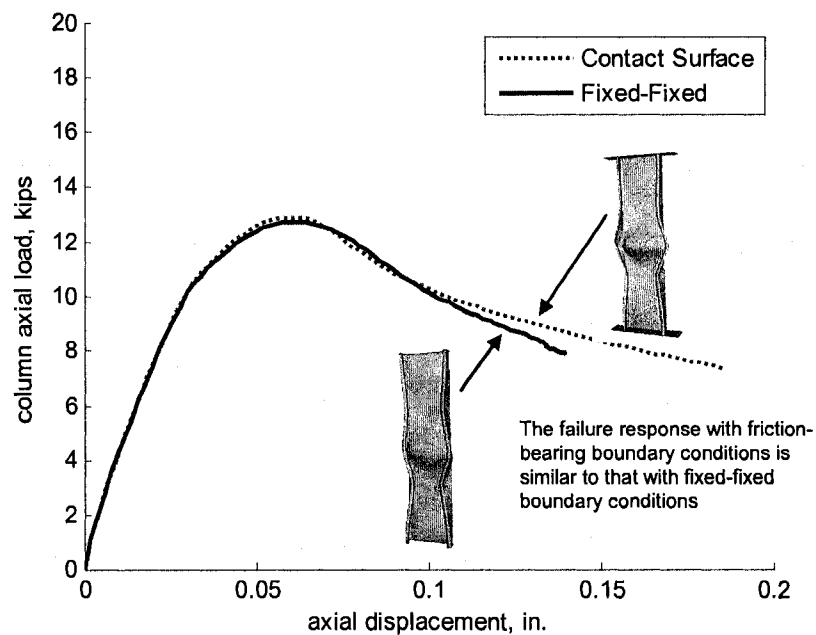


Figure J.2. A comparison of ABAQUS nonlinear solutions considering fixed-fixed and contact boundary conditions for specimen 600-2-24-NH

Appendix K

Simulated column experiments database

The table provided in this appendix summarizes the dimensions, elastic buckling loads, and tested strengths of simulated column experiments described in Section 8.1.10. The letters in the “Study type” column denote simulations considered in the DSM failure mode studies: “D” for the distortional buckling failure study in Section 8.1.2, “G” for the global buckling failure study in Section 8.1.3, and “L” for the local buckling failure study in Section 8.1.4.

The database contains columns with slotted holes or circular holes. To identify the hole type in a specific column, use the following rule: columns with slotted holes always have $L_{hole}=4$ in, and $L_{hole} = h_{hole}$ for columns with circular holes.

The following notation is employed to denote simulated strengths:

P_{test25}	25% CDF local and distortional buckling, no global imperfections
P_{test75}	75% CDF local and distortional buckling, no global imperfections
$P_{test25+}$	25% CDF local and distortional buckling, +L/2000 global imperfection
$P_{test75+}$	75% CDF local and distortional buckling, +L/1000 global imperfection
$P_{test25-}$	25% CDF local and distortional buckling, -L/2000 global imperfection
$P_{test75-}$	75% CDF local and distortional buckling, -L/1000 global imperfection

ID #	SSMA section	L in.	L _{hole} in.	h _{hole} in.	S in.	# of holes	P _{1g} k/ps	P _{ynet} k/ps	P _{1gnet} /P _{1g}	P _{act} k/ps	P _{red} k/ps	P _{em} k/ps	P _{act2} k/ps	P _{act3} k/ps	P _{act4} k/ps	P _{act5} k/ps	P _{act6} k/ps	P _{act7} k/ps	P _{act8} k/ps	Study Type
200	302S137-08	40	4.00	1.32	15	3	27.5	22.0	0.80	28.8	24.0	9.9	11.9	10.8	NaN	NaN	NaN	NaN	NaN	
201	250S182-43	42	4.00	1.28	14	3	16.9	13.5	0.80	13.9	14.9	5.3	7.2	6.67	NaN	NaN	NaN	NaN	NaN	
202	350S182-68	34	4.00	0.00	17	2	30.1	30.1	1.00	33.5	39.4	31.5	22.6	19.4	22.3	18.7	18.3	18.7	18.7	L
203	1000S200-97	88	4.00	0.00	12	7	86.3	86.3	1.00	23.5	25.6	22.9	17.8	16.5	19.4	18	17	15.5	15.5	L
204	350S182-54	24	4.00	0.00	12	2	24.3	24.3	1.00	16.7	24.0	49.4	16.9	15	16.9	15	16.9	15	16.9	L
205	800S200-88	74	4.00	0.00	12	6	53.1	53.1	1.00	11.4	17.4	23.1	14.1	13.9	14	13.2	14.7	14.5	14.5	L
206	550S182-54	42	4.00	0.00	14	3	30.9	30.9	1.00	8.8	14.6	26.0	13.0	12	13.2	12.5	12.7	11.6	11.6	L
208	800S200-54	68	4.00	0.00	13	5	42.5	42.5	1.00	5.8	10.8	23.8	11.6	11.4	11.3	11	11.8	11.9	11.9	L
209	800S250-43	58	4.00	0.00	14	4	31.5	31.5	1.00	4.8	11.1	29.6	12.2	12	12	11.8	12.3	12.2	12.2	L
210	800S182-43	32	4.00	0.00	18	2	26.2	26.2	1.00	4.0	7.8	42.1	10.1	10.1	10.2	10.3	10	9.97	9.97	L
211	800S250-43	74	4.00	0.00	12	6	36.7	36.7	1.00	3.1	7.7	24.9	9.7	9.64	9.64	9.9	9.62	9.4	9.4	L
212	800S182-43	40	4.00	0.00	13	3	31.5	31.5	1.00	2.7	4.4	29.1	8.7	8.94	NaN	8.74	9.32	9.42	9.42	L
213	1000S250-43	80	4.00	0.00	13	6	42.0	42.0	1.00	2.3	5.1	24.2	8.9	8.69	8.62	9.84	8.78	8.72	8.72	L

Appendix L

Simulated beam experiment database

The table provided in this appendix summarizes the dimensions, elastic buckling moments, and tested strengths of simulated beam experiments described in Section 8.2.1. The letters in the “Study type” column denote simulations considered in the DSM failure mode studies: “D” for the distortional buckling failure study in Section 8.2.3 and “L” for the local buckling failure study in Section 8.2.2.

Curriculum Vitae

Cristopher Dennis Moen was born in Tucson, Arizona on October 7, 1973, the son of Dennis and Nancy Moen. After completing his high school degree at Lake Braddock Secondary School, Burke, Virginia, in 1991, he attended the University of Virginia in Charlottesville, Virginia where he received the degree of Bachelor of Science in Civil Engineering in 1995. He continued on at U.Va. and received a Masters of Science degree in Civil Engineering in 1997, during which he conducted high-performance concrete research at the Virginia Transportation Research Council. From 1997 to 2002 he was employed as a bridge engineer for J. Muller International in New York, New York and was involved in the design and construction of the first precast segmental concrete highway bridge constructed in New York City, connecting the Brooklyn-Queens Expressway over Marcy Avenue to the Williamsburg Bridge. He married Estela June Patron on August 10, 2002 in Richmond, Virginia and moved to Baltimore, Maryland shortly thereafter. He continued as a bridge engineer at Parsons Corporation from 2002 to 2004, where he served on the design and construction engineering team for the main spans of the Woodrow Wilson Bridge crossing the Potomac River. He enrolled at Johns Hopkins University in 2004, and received the degree of Doctor of Philosophy in Civil Engineering in 2008, where he studied the stability of thin-walled structures, and specifically the behavior of cold-formed steel structural members. He was hired as an assistant professor in the Via Department of Civil and Environmental Engineering at Virginia Tech in August 2008.